Oscillating Hydrofoil Propulsion for Human-Powered Watercraft Applications

---

A thesis submitted in partial fulfilment

of the requirements for the Degree of

Doctor of Philosophy in Engineering

by Rajan Fernandez

University of Canterbury

2013

Oscillating Hydrofoil Propulsion for Human-Powered Watercraft Applications

by Rajan Fernandez

A thesis submitted in partial fulfilment of the requirements for the Degree of Doctor of Philosophy in Engineering

University of Canterbury, 2013

Unlike conventional propellers, flapping wings may generate large amplitude oscillating forces, which can make them difficult to incorporate into a craft design. This is particularly true for a single, vertically oscillating hydrofoil, as part of a surface water craft where the cyclic lift of the hydrofoil disrupts the craft stability. This thesis begins by reviewing the history of human-powered watercraft with a focus on those having flapping foil propellers. This review combined with a review of the literature provides a balanced overview on how flapping wing propellers are currently designed. Current literature shows that although the mean performance of an oscillating foil has been determined in terms of the Strouhal number and the angle of attack, relatively little describes performance directly in terms of the foil motion. Hence, predicting temporal hydrodynamic forces acting on an oscillating foil is difficult. This provides motivation for research investigating the temporal performance of an oscillating foil directly in terms of its motion.

In this thesis, experimental equipment designed to measure the hydrodynamic forces on a heaving object is presented. Key features of the equipment are analysed to show how measurement accuracy is maintained. Experimental measurements of unsteady hydrodynamic forces acting on a heaving cylinder, flat plate, symmetrical foil, and an asymmetrical foil are analysed with respect to the heaving motion. Firstly, the object motion is limited to one degree of freedom; pure heaving with zero forward velocity, to investigate the start-up conditions of the oscillating hydrofoil propeller. Secondly, these results are expanded on by adding a steady forward velocity component to the object motion to investigate how the hydrodynamic forces on the object are affected by the cross-flow.

Experimental temporal hydrodynamic force measurements presented in this thesis show how the relative composition of hydrodynamic drag and inertia forces change with oscillating frequency, and forward velocity, affecting the phase, magnitude, and profile of the force cycles. This composition is also influenced by the cross-section of the oscillating object and the presence of a free surface. Current marine engineering equations for unsteady hydrodynamic forces on an object in an oscillating flow are validated for a cylinder. However, they are found to contain significant error when predicting the unsteady hydrodynamic forces on an oscillating hydrofoil. Contributions of this thesis link oscillating foil propulsion research to common marine engineering equations with the intent of making flapping wing propeller design more accessible to the general engineering community.

Deputy Vice-Chancellor's Office
Postgraduate Office

UNIVERSITY OF CANTERBURY
Te Whare Wānanga o Waitaha
CHRISTCHURCH NEW ZEALAND

Co-Authorship Form

This form is to accompany the submission of any thesis that contains research reported in co-authored work that has been published, accepted for publication, or submitted for publication. A copy of this form should be included for each co-authored work that is included in the thesis. Completed forms should be included at the front (after the thesis abstract) of each copy of the thesis submitted for examination and library deposit.

Please indicate the chapter/section/pages of this thesis that are extracted from co-authored work and provide details of the publication or submission from the extract comes:
No sections. This work contributed to the motivation of the thesis.

Please detail the nature and extent (%) of contribution by the candidate:
The candidate undertook the research and measurements, and wrote the draft.

The co-author was the supervisor who discussed and reviewed the paper before submission

Certification by Co-authors:
If there is more than one co-author then a single co-author can sign on behalf of all
The undersigned certifys that:

- The above statement correctly reflects the nature and extent of the PhD candidate's contribution to this co-authored work
- In cases where the candidate was the lead author of the co-authored work he or she wrote the text

Name: *Keith Alexander* Signature: Date: *27 March 2013*

Deputy Vice-Chancellor's Office
Postgraduate Office

UNIVERSITY OF CANTERBURY
Te Whare Wānanga o Waitaha
CHRISTCHURCH NEW ZEALAND

Co-Authorship Form

This form is to accompany the submission of any thesis that contains research reported in co-authored work that has been published, accepted for publication, or submitted for publication. A copy of this form should be included for each co-authored work that is included in the thesis. Completed forms should be included at the front (after the thesis abstract) of each copy of the thesis submitted for examination and library deposit.

Please indicate the chapter/section/pages of this thesis that are extracted from co-authored work and provide details of the publication or submission from the extract comes:
Sections 5.2 and 5.3

Please detail the nature and extent (%) of contribution by the candidate:
The candidate undertook the research and measurements, and wrote the draft.

The co-author was the supervisor who discussed and reviewed the paper before submission

Certification by Co-authors:
If there is more than one co-author then a single co-author can sign on behalf of all
The undersigned certifys that:

- The above statement correctly reflects the nature and extent of the PhD candidate's contribution to this co-authored work
- In cases where the candidate was the lead author of the co-authored work he or she wrote the text

Name: *Keith Alexander* Signature: Date: *27 March 2013*

ACKNOWLEDGMENTS

The research presented in this thesis was possible thanks to many people. Here I would like to thank everyone that has contributed to the work presented in this thesis, and to my education at the University of Canterbury.

I would like to thank Associate Professor Dr. Keith Alexander for initiating this project, and for supervising my work.

I would also like to thank Scott Amies, Dave Read, Ken Brown, Jim McClean and Gary Cotton for their efforts building the experimental equipment used for this research. Thanks to Julian Phillips and Gerry Kirk for their guidance with technical issues regarding electrical engineering and programming. I would also like to thank Eric Cox for his efforts transporting setting up experimental equipment. Thanks to Graeme Harris for his ongoing support and guidance with all technical tasks I have thrown at him. Most importantly I would like to thank all of these people for their time, patience and instruction on all the technical engineering tasks involved with this thesis. I firmly believe that the most beneficial skills I have picked up during my post-graduate studies were taught to me by these people in the mechanical engineering laboratory wing.

Thanks to my office mates; Will Bowen, Adam Fuller, Ben Redwood, Alex O'Keefe, Tim Roosen, Rory Horne, Tim Spencer for all good office yarns and guidance with design tasks. These people and their passion for mechanical engineering made my post-graduate studies most enjoyable.

Last but not least I would like to thanks my parents, Linda and Joseph Fernandez, for their ongoing support of my studies.

PUBLICATIONS

R.E. Fernandez and K.V. Alexander: *An experimental investigation assessing the validity of quasi-steady calculations for an oscillating hydrofoil*, OMAE2011 ASME Conference Proceedings (2011), pp. 331-340

R.E. Fernandez and K.V. Alexander: *An experimental study on the effect of submergence on a vertically oscillating hydrofoil at zero translational velocity*. In *Vibration, Structural Engineering and Measurement II*, pp. 459-465, in the Periodical of Applied Mechanics and Materials, Vols. 226-228 (2012)

R.E. Fernandez: *Multi-axis load cell designs employing multiple shear beams*. In *Vibration, Structural Engineering and Measurement II*, pp. 1981-1986, in the Periodical of Applied Mechanics and Materials, Vols. 226-228 (2012)

TO THE READER

This thesis is intended to be read as a digital document (pdf format) as it contains interactive embedded media. Some embedded media is included in Universal 3D (U3D) format. For information on this format please refer to ECMA International Standard ECMA-363.

Not all pdf readers support U3D. Please check that your pdf reader does support U3D to ensure media content will functional properly.

Contents

List of Figures

List of Tables

Nomenclature

α	Angle of attack
α_h	Heave-induced angle of attack
α_{osc}	Ratio of transverse to forward velocity
β	Viscous frequency parameter
$\ddot{\theta}$	Pitch acceleration
$\ddot{h}$	Heave acceleration
$\ddot{s}$	Surge acceleration
$\dot{\alpha_h}$	Rate of heave-induced angle of attack
$\dot{\alpha}$	Rate of angle of attack
$\dot{\theta}$	Pitch velocity
$\dot{E}$	Metabolic power
$\dot{h}$	Heave velocity
$\dot{s}$	Surge velocity
$\dot{u}$	Mainstream flow acceleration
ϵ_d	Dynamic measurement error
$\eta = \frac{P_{out}}{P_{in}}$	Efficiency
η_d	Drag Efficiency
η_o	Overall efficiency
η_p	Propulsive efficiency
λ	Wavelength
ν	Kinematic viscosity of water
ω	Angular frequency
ω_n	Natural frequency
ϕ_h	Estimated heave force phase lag behind heave acceleration
ϕ_s	Estimated surge force phase lag behind heave acceleration
ϕ_{KC}	Keulegan and Carpenter's phase estimate
ρ	Fluid density
θ	Pitch position
θ_c	Crank angular position
A	Platform area ($A = cL$)
A_t	Trailing edge excursion
$a_{\ddot{h}}$	Force sensitivity to heave acceleration
$a_{\dot{h}}$	Force sensitivity to heave velocity
A_{F_h}	Heave force range
A_{F_s}	Surge force range

c	Chord length
$C = \frac{\dot{E}}{v}$	Cost of locomotion
c_a	Added mass coefficient
c_D	Damping coefficient
c_d	Drag coefficient
c_l	Lift coefficient
c_m	Mass coefficient
c_t	Thrust coefficient
$c_{A_{F_h}}$	Heave force range coefficient
$c_{A_{F_s}}$	Surge force range coefficient
d	Submergence depth
E	Young's modulus
f	Oscillation frequency
f_c	Critical oscillation frequency
F_d	Drag force
F_l	Lift force
F_h	Heave force
f_{ns}	Natural vortex shedding frequency
F_s	Surge force
g	Acceleration due to gravity
h	Heave position
h^*	Heave-to-chord ratio
h_0	Heaving amplitude
I	Second moment of area
I_v	Iversen Modulus
J	Foil advance coefficient
k	Gravity-capillary wave number
k_c	Capillary wave number
$K_C = \frac{2\pi h_0}{c}$	Keulegan-Carpenter number
k_g	Gravity wave number
$k_G = \frac{\pi f c}{U}$	Garrick reduced frequency
L	Object/Hydrofoil span
L_c	Connecting rod to crank length ratio
l_c	Crank length
l_r	Connecting rod length
Li	Lighthill number
M	Pitching Moment
m	Mass
m_a	Added mass
m_v	Virtual mass
m_{a_L}	Added mass per unit length
P_{in}	Input power
P_{out}	Output power
$Re_{\dot{h}} = \frac{\dot{h}c}{\nu}$	Reynolds Number based on $\dot{h}$
$Re_{u_e} = \frac{u_e c}{\nu}$	Reynolds Number based on u_e

$Re_u = \frac{uc}{\nu}$	Reynolds number based on u
s	Surge position
S_w	Wetted surface area
$S_{\dot{h}}$	Koochesfahani's (heave velocity based) symmetry parameter
S_h	Heave position based symmetry parameter
SD	Standard deviation
$St = \frac{fA_t}{u}$	Strouhal number
$St_c = \frac{fc}{u}$	Strouhal number based on chord length
St_{ns}	Strouhal number for natural vortex shedding
T	Oscillation Period
t	Time
T_w	Water temperature
u	Mainstream flow velocity
u_d	Dynamic measurement uncertainty
u_h	Heave position uncertainty
u_e	Effective fluid velocity
v	Velocity
V_m	Volume of fluid displaced by an object
V_r	Reduced velocity
W_d	Work done per unit distance to overcome hydrodynamic drag
W_{tot}	Mechanical work done per unit distance of locomotion

Chapter 1

Introduction

The original idea behind this work, to design a human-powered hydrofoil incorporating an oscillating foil propeller, was the concept of Dr. Keith Alexander of the University of Canterbury, Christchurch, New Zealand. This project began in 2008 with several attempts to build a working model-scale watercraft with oscillating hydrofoil propulsion based on quasi-steady calculations (see Section 3.6.1). The failure of these models motivated research in methods for calculating the hydrodynamic forces on an oscillating hydrofoil.

In this chapter, interest in human-powered vehicles is justified and the appeal of flapping wing propellers is explained. The difficulty in designing a oscillating foil propeller for a human-powered hydrofoil with reference to existing knowledge is mentioned before the goals of current research are defined. Finally, an overview of each chapter in this thesis is provided.

1.1 Motivation

1.1.1 Human-powered transport

With rising costs of fossil fuels and growing awareness in the environmental costs of transport interest in 'green' vehicles is high. Strategies to reduce oil consumption and the release of CO_2 include designing more efficient vehicles and adopting other fuel sources (Fulton, 2004). Environmental impacts aside, high-energy transport has been linked to other concerns in social trends including physical inactivity encouraging health problems,

and injuries or deaths resulting from high speed transport (Lobstein, Baur, & Uauy, 2004; Woodcock, Banister, Edwards, Prentice, & Roberts, 2007). Increasing the popularity of human-power transport may address both of these issues by reducing energy costs of transportation while engaging people in physical exercise (Ulrich, 2006).

1.1.2 Flapping Wing Propulsion

Flapping wing propellers have rivalled conventional propellers with their high propulsion efficiency combined with their ability to provide high manoeuvring forces (Read, Hover, & Triantafyllou, 2003). Although modern conventional propellers have reached high efficiencies, with respect to their theoretical maximum, flapping wing propellers have achieved even higher efficiencies by using input mechanical power while also extracting power from the surrounding flow (Beal, Hover, Triantafyllou, Liao, & Lauder, 2006). In the extreme case, passive flapping wing propellers have been designed that are driven entirely by wave power (Daniel, Manley, & Trenaman, 2011; Manley & Willcox, 2010; Terao, 2009).

Conventional hydrofoil watercraft have separate propulsive and lifting devices. These are commonly in the form of a conventional propeller and a fixed wing below the hull. Another advantage of flapping wing propulsion is that it offers the opportunity to consolidate these devices since a single wing can provide both thrust and lift forces. Obviously this requires the wing to be orientated with its span horizontal and to oscillate in the vertical direction.

1.1.3 Flapping Wing Propulsion and Human-Powered Vehicles

The potential for high propulsive efficiency in particular makes flapping wings a notable candidate for application on small low-powered vehicles, such as human-powered vehicles. In fact, flapping hydrofoil propellers have already been employed for this task on vehicles such as the Trampofoil (*Trampofoil*, Accessed 2009). A Trampofoil is an existing, commercially available, human-powered hydrofoil (see Section 2.2.4) that can achieve speeds of up to $27\,\mathrm{km\,h^{-1}}$ ($7.5\,\mathrm{m\,s^{-1}}$) with power provided by a jumping person.

Although a very innovative design, the Trampofoil has several practical limitations.

Firstly, these craft require a moving start at a speed adequate for the main wing to produce enough lift to support the user. This is often done by pushing off a solid structure near the water's edge. Secondly, when a Trampofoil falls below a critical speed, the main wing stalls and the Trampofoil sinks with the rider. Finally, significant user skill is required to use these vehicles which are not like any other. These limitations of the Trampofoil design have motivated the development of a human-powered vehicle which addresses the above issues.

1.1.4 Designing Thrust and Lift Producing Oscillating Hydrofoil Propeller

Due to the oscillatory nature of flapping wing propulsion, high forces in-line with the oscillation direction of the hydrofoil are expected. History shows that the large amplitude oscillatory loading on a vehicle has made designing a balanced surface watercraft difficult (see Chapter 2). This is particularly true for vehicles starting from rest and travelling at slow forward velocities (i.e. high Strouhal number operation). Further review of history and the current literature provides little evidence that engineers have a process for calculating time-dependent hydrodynamic forces acting on an oscillating hydrofoil to simulate vehicle dynamics. This is most likely the reason why a well balanced watercraft, with a seated rider, employing a vertically oscillating thrusting and lifting hydrofoil does not exist to the author's knowledge.

There is a body of research on factors affecting the propulsive performance of an oscillating foil where researchers have presented the time-averaged thrust and lift coefficients for an oscillating foil. Furthermore, a number of studies have focused on correlating propulsive efficiency and mean thrust coefficients with scaling parameters, such as the Strouhal number and angle of attack, rather than the motion of the foil (Figure 1.1). So, although the mean efficiency and mean thrust produced by an oscillating hydrofoil have been well studied, relatively little is known about the nature of the cyclic hydrodynamic forces on an oscillating hydrofoil in terms of the hydrofoil motion. Moreover, since most researchers have studied oscillating hydrofoils operating around their peak efficiency (typically $St \approx 0.3$) little is known about the forces on an oscillating hydrofoil under start-up

conditions, i.e. $u = 0$, $St = \infty$.

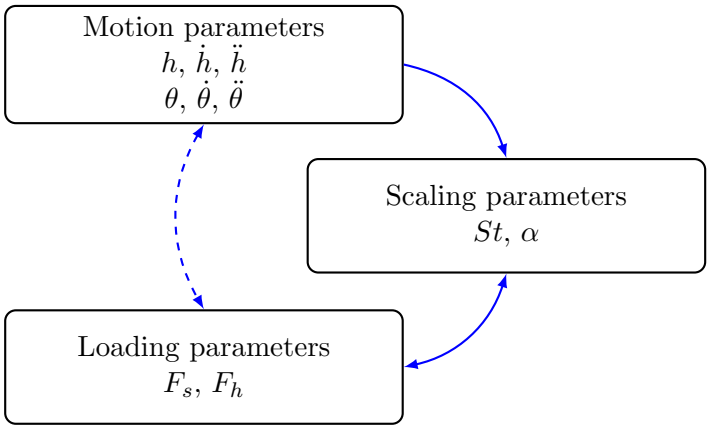

Figure 1.1. Summary of parameter relationships. The mean thrust and efficiency of an oscillating foil has been well researched with respect to scaling parameters. However, the connection between hydrofoil motion and temporal thrust and lift forces (dashed arrow) is not well known.

A method for predicting the time-dependent hydrodynamic forces on an oscillating foil from the foil motion would be useful for successfully simulating the vehicle dynamics. Although several methods exist for modelling the forces on an oscillating foil (e.g. quasi-steady calculations, dynamic calculations, numerical simulations, and prototyping), each has several disadvantages (see Section 3.6). There exist formulas in the field of structural marine engineering for calculating time-dependent hydrodynamic forces on objects in an oscillating flow based on the flow velocity and acceleration (see Section 3.3). However, these formulas rely on empirical coefficients and focus on hydrodynamic forces applied to cylinders. Theoretical model coefficients for other objects can be found in the literature. However, the validity of these coefficients is not well known. This uncertainty in the appropriateness of existing models for calculating the time-dependent hydrodynamic forces on oscillating objects has motivated the current experimental study.

1.2 Research Goals

- The primary aim of this program was to measure the time-dependent hydrodynamic forces on an oscillating hydrofoil to provide an overview of the magnitude and phase of these forces. This data may assist future engineers in designing a human-powered

surface water craft.

- The second goal was to evaluate the validity of existing marine engineering equations for non-cylindrical objects oscillating in initially stagnant water.
- The third goal was to investigate how end effects and the presence of a free surface affect the hydrodynamic forces on vertically oscillating objects with no forward velocity.
- The fourth and final goal was to investigate how forward velocity affects the hydrodynamic forces on vertically oscillating objects.

To achieve these goals, the first task was to design cost-effective experimental equipment to acquire these force measurements accurately with a precision suitable for engineering design. Once this equipment was build and calibrated, the unsteady hydrodynamic forces on several objects were measured under several operating conditions. The variables in the current experiments were, mean submersion depth, end plate diameter, oscillating frequency, fixed pitch angle and forward velocity. Finally the acquired data was analysed with a focus on how these variables affect the amplitude and phase of the hydrodynamic forces.

1.3 Thesis Contributions

This thesis includes several novel contributions to the fields of flapping wing propulsion and marine engineering. To begin, this thesis contains a comprehensive review of existing human-powered hydrofoils, with a focus on those employing flapping wing propulsion. A review of the current literature also provides the reader with some background on flapping wing propulsion technology. The novel design of experimental equipment for measuring the hydrodynamic forces on an oscillating object is presented and its suitability for the current experiments discussed.

Experimental measurements of time-dependent unsteady hydrodynamic forces on several oscillating objects are contributed. This data was captured with test objects undergoing periodic non-sinusoidal heaving under open loop control which is a case not well

covered by the current literature. Although the heaving motion used was near-sinusoidal, it was sufficiently different from pure sinusoidal motion that the heaving acceleration profile was significantly distorted. Measured hydrodynamic forces on a heaving asymmetric hydrofoil, and hydrofoils heaving near a free surface are contributed.

A comparison between experimental data and predictions of common marine engineering equations provides an assessment of the validity of these equations for use with oscillating foils. Further analysis of experimental data investigates the relationship between heaving velocity and acceleration and the measured hydrodynamic forces.

1.4 Chapter Preview

The following content of this thesis begins with a review of the history of human-powered water craft in Chapter 2. Human-powered water craft employing flapping wing propulsion are discussed in detail and compared against one another to distinguish benefits of particular design features.

Chapter 3 is a review of the literature in several relevant fields. Sport science research contributes the expected torque and power output of a person with notes on endurance. Biology publications classifying the locomotion style of winged animals are reviewed since nature was the original inspiration for flapping wing propulsion. Equations used in marine engineering for predicting hydrodynamic forces on structures in unsteady flow are provided. Common state parameters of a flapping wing are defined before the known performance of flapping wing propellers is summarised. Methods currently used to predict the forces on an unsteady foil are explained with mention of their limitations. A brief summary of existing patented craft designs and propulsion mechanisms is provided before this chapter concludes.

In Chapter 4 the design of the experimental equipment is presented, and the experimental procedure used to acquire measurements of the hydrodynamic forces on oscillating test objects is explained. Measurement uncertainties and shortcomings of the experimental method are also discussed in this chapter with supporting material provided in Appendices A to C.

Chapter 5 presents experimental data for the hydrodynamic forces on four test objects undergoing pure heaving motion with no horizontal translational velocity. The results in this chapter provide insight into forces on an oscillating hydrofoil propeller during start-up: a troublesome operating phase avoided by the Trampofoil which requires a gliding start (see Section 2.2.4). This operating state ($u = 0$) for oscillating hydrofoils has been widely neglected until now, with the exception of Lai and Platzer (2000), Alben and Shelley (2005), and Vandenberghe, Childress, and Zhang (2006). The effect of the free surface, heaving amplitude, end plates and object shape are investigated.

In Chapter 6, the test objects still undergo pure heaving motions but an extra degree of freedom is allowed: a non-zero translational velocity in the surge direction ($u \neq 0$). Results show the sensitivity of the hydrodynamic forces on the hydrofoil to forward velocity u and oscillating frequency f for a fixed oscillating amplitude. This study investigates the influence of these two variables on the amplitude and phase of the hydrodynamic forces, even when the Strouhal number (see Section 3.4.1) is held constant.

Finally, in Chapter 7, conclusions and contributions of this thesis are summarised before recommendations for future research are made.

Chapter 2

History of Human Powered Hydrofoils and Oscillating Hydrofoil Propulsion

2.1 Human Powered Hydrofoils History

The history of human powered hydrofoils dates back to the early 1900s. By 1938 Arthur Hill Jr., a commercial fisherman, had a patent on a device which used bird and fish like movements for propulsion (Hill, 1938). Hill applied his 'fishtail drive' to propel vehicles ranging from small model planes up to thirty-five foot boats ("Fishtail drive propels boats and model planes", 1939). When used for boat propulsion, the fishtail drive consisted of a linkage system, driven by human power, which oscillating a pair of fins horizontally.

Bavarian engineer Julius Schuck invented the Wasserläufer and rode it in the river Isar in Munich for Tagesschau, German television news in 1953 (Ehm, 2005). The Wasserläufer has two frames on which the rider stands. Each frame has a hydrofoil as the lowest horizontal member in the frame, and a handle for the rider to control the hydrofoil's angle of attack as shown in Figure 2.1.

In 1965 another German engineer, Wilhelm Schmidt, realised the Knoller-Betz or Katzmayr effect could be exploited in marine propulsion design. This led to the invention of

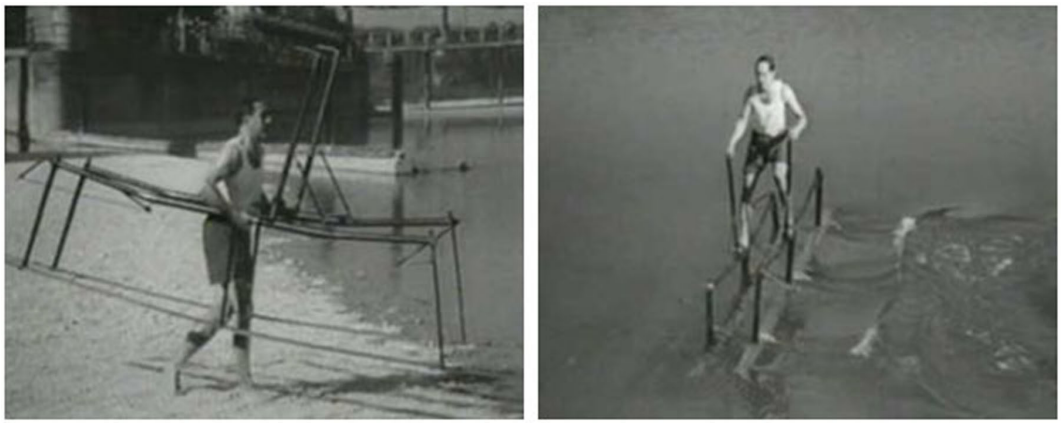

Figure 2.1. The Wasserläufer frames being carried into the water (left) and the Wasserläufer in operation (right) (Tagesschau, 1953)

the wave propeller (Schmidt, 1965a, 1965b). The wave propeller used tandem foils with only the leading foil oscillating. The rear foil was positioned in the oscillating wake of the forward foil to create extra thrust using the Katzmayr effect. In the sixties the U.S. army investigated large amplitude oscillating foil propulsion as an alternative to propellers or jet units in shallow weedy waters (Scherer, 1968).

The Aqueon is a flapping wing propulsion device for divers that was invented by Calvin Gongwer in the 1970's (Gongwer, 1974). Gongwer is the founder and president of the company Innerspace Corporation which manufacture a number of propulsion systems. Since the invention and commercialisation of the Aqueon other companies have developed very similar devices. An example is the PowerSwim that was developed by DARPA (Defence Advanced Research Projects Agency) for use by navy divers (Sofge, 2009). The Aqueon has a front foil that is split in two pieces about the mid-span and share a common pivot axis, and one rear foil. The front foil is forced up and down as the diver's legs bend and straighten. Simultaneously a spring controls the angle of attack of the front foil. Photos of the Aqueon are shown in Figure 2.2. In a letter to Human Power Technical Journal, Gongwer claims that a diver using an Aqueon consumes oxygen at a rate 5 times less than a diver using modern fins swimming at the same speed (Gongwer, 1986-1987). He provides a graph of swimming speed versus air consumption of a diver to illustrate the relative efficiency of the Aqueon to modern fins. He also claims that he has "made various paddle boats and other craft propelled by oscillating foils over the years" (Gongwer, 1986-

1987) and shows a photo of a human powered kayak with two counter-oscillating vertically orientated hydrofoils. This kayak was displayed but not raced at the International Human Power Vehicle Association EXPO-86. A photo of it was published in the following copy of Human Power Technical Journal (Wilson, 1986b).

Oscillating foil propulsion has become popular in the development of diving fins. Traditional diving fins typically have flexible fins and a low aspect ratio where as many fin developments now employ rigid fins with aerodynamic cross-sections. In 1988 Arthur Mosier patented a set of swimming fins that contained a ladder of passively pitching hydrofoils (Mosier, 1988). The DOL-FIN (Smith Aerospace Corp., 2012), developed by Smith aerospace Corporation, is a patented mono-fin that uses a high aspect ratio wing mounted via a flexible element to the diver's boots. Freedom Fins (VortiSeas Innovations LLC, 2012), from VortiSeas Innovations use a low aspect ratio hydrofoil that mounts to the side of a diver's lower leg.

Figure 2.2. A diver using an Aqueon and an Aqueon on the beach. *Photographs courtesy of Rick Iossi* (Iossi, n.d.)

In 1984, aerodynamicists Alan Abott and Alec Brooks designed the Flying Fish in an attempt to break the record race time for human-powered water craft which was currently held by rowing boats (Ehm, 2005). The Flying Fish, shown in Figure 2.3, used catamaran style floats to support the rider before the craft was foil borne. The rider was seated on a regular style bike frame so that they could train on standard bicycles. The Flying Fish also featured a propeller driven by a twisted chain drive to avoid the weight of a gearbox (Art Centre, College of Design, Accessed 2008). Since the Flying Fish was such a successful

design many more similar crafts have been built. The Wet Wing, Flying Magic, Aqua Power and Scafo are some examples. It could be said that the Flying Fish made a new benchmark for human-powered hydrofoil designs.

Figure 2.3. Flying Fish designed by Alan Abott and Alec Brooks. *Photograph courtesy of Steve Finberg* (Finberg, n.d.-b)

The Mutiny on the Boundary Layer (MOBL) was built in 1984 to 1986 by Parker MacCready. It was his first attempt at building a hydrofoil boat with flapping-wing propulsion. Similarly to the Flying Fish, Mutiny on the Boundary Layer used two catamaran style floats for support at low speed and was powered by a rider in the standard cycling position. The boat did achieve flight but required a lot of power from the rider, so flight could only be sustained for approximately 100 seconds (MacCready, 1990a).

In 1986 Einar Jakobsen of Norway wrote an article for Human Power Technical Journal about the working principles of the 'foil propeller'. The article included a photo of him operating his muscle-driven foil-propelled catamaran (Jakobsen, 1986). Since 1978 research had been done in Sweden and Norway on foil propulsion as an alternative to rotatory propellers for higher efficiency. Jakobsen reported that Chalmers University, Gotenburg, Sweden, had been conducting theoretical and practical work and had measured efficiency of up to 75.9 %. The most interesting part about this research on the foil propeller was that it was designed to work as a hybrid marine system which was driven by wave power together with some other power source, most likely an engine. In 1988 a team of stu-

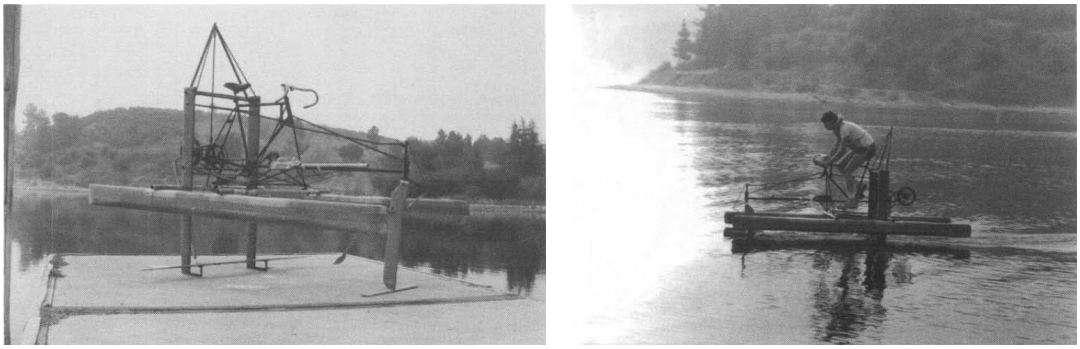

Figure 2.4. Mutiny on the Boundary Layer on a jetty and in operation in the water (Sivertsen, 1990a, 1990b)

dents from Gotenburg entered a boat called the "af Chapman" in the Delft Waterbike Regatta. Previous to the regatta the students had predicted that the af Chapman's foil propeller have an efficiency of 80 %. The af Chapman was described as having a complex transmission with a lot of bearings to transfer power from the feet of the operator into a complex whale-tail like movement. Dave Wilson reported on the regatta in Human Power Technical Journal and stated the "whale-tail concept worked surprisingly well" (Wilson, 1986a). However, in an article (de Man & de Vries, Accessed 2010) on the history of the "af Chapman II", it was stated that its predecessor "was not very successful" and "was propelled by a fish tail propulsion which didn't really work". The af Chapman II was designed to sit two operators back-to-back each with a pedal-power driven crank shaft. The af Chapman II used a rotary propeller rather than a foil propeller and featured ailerons on the main foil to steer and balance the craft.

Parker MacCready's second hydrofoil with flapping-wing propulsion was the Preposterous Pogo Foil which he developed in 1989. This craft also had catamaran style floats but was driven by the rider jumping up and down on a platform while adjusting the hydrofoil's angle of attack via hand controls. The Pogo Foil was a lot simpler and more successful than the Mutiny on the Boundary Layer. A photo of the Pogo Foil is shown in Figure 2.5.

The Decavitator is another famous human-powered hydrofoil which currently holds the world record for the 100 m with a flying start under the International Human Power Vehicle Association (IHPVA) rules. It was designed at MIT by Marc Schafer, Bryon

Figure 2.5. Parker McCready's Pogo Foil. *Photograph courtesy of Parker MacCready* (MacCready, n.d.)

Sullivan, Professor David Gordon Wilson and Professor Mark Drela in 1988 and rebuilt by a team of undergraduate students in 1989 (MIT, Accessed 2009). The Decavitator team was awarded the DuPont prize in 1993. The Decavitator uses catamaran type floats to support the craft before it is foil borne and is propelled by a large air propeller behind the rider. The rider is seated in the recumbent position with a fairing around them to reduce the air drag. Figure 2.6 shows the Decavitator in action.

Figure 2.6. The Decavitator features catamaran style floats and an air propeller. *Photograph courtesy of Steve Finberg* (Finberg, n.d.-a)

Trond Oritsland submitted a brochure for the Ergofoil, which was displayed at a boat show in Oslo, to Human Power Technical Journal in 1991 (Oritsland, 1991). The printed brochure illustration shows a boat with a foil propulsion system similar to that of the Aqueon except driven by the operator's arms via a lever rather than the operator's legs. The Ergofoil employed a hydrofoil with an approximate span and chord length of 1.2 m and 200 mm respectively. This boat could achieve a speed of about $2.5\,\mathrm{m\,s^{-1}}$ with two people rowing. In a 1994 issue of Human Power Technical Journal, Harry Bryan published an article on his pedal-powered fin propelled kayak 'Thistle' (Byran, 1993-1994). This kayak had a single oscillating vertical fin at the rear of the boat in a similar layout to Calvin Gongwer's Kayak. The fin propulsion system used a sprung foil in a very similar way to the Aqueon. The fin was a thin flat flexible piece of polycarbonate plastic. Bryan designed his kayak with the intention of creating a reliable, efficient and relaxing water craft with cruising speed of a lesser priority. The cruising speed of Bryan's Kayak was 7.9 km h.

Greg Ketterman designed the Hobie Cat Mirage kayaks which employ the innovative Hobie 'Mirage Drive' (Industrial Designers Society of America, 2001). Mirage Drive is a pedal powered pair of root flapping fins that are located underneath the kayak. Mirage drive is claimed to be more efficient and quieter than paddling (Company, 2011). The Mirage Drive uses large fins moving slowly, relative to a propeller, to reduce the amount of turbulence produced to create efficient thrust. Mirage Drive fins are flexible and have a stroke that is controlled by the user.

Swedish engineer Alexander Sahlin designed the Trampofoil which was released in 1998 (Ehm, 2005). The Trampofoil, shown in 2.7a, is very similar to the Pogo Foil but does not have any floats. This means that it will sink at low speeds. To launch the Trampofoil the rider is required to push off a jetty and then jump up and down on the platforms to accelerate the craft. The Trampofoil was only made commercially available for a short period of time before production stopped. However, the makers express interest in ideas and proposals to start production again on their website (*Trampofoil*, Accessed 2009).

More recently other devices similar to the Trampofoil have been invented and made commercially available at much lower costs. Such craft include the Pumpabike, Aquaskip-

per and Waterbird. The Pumpabike, designed by South African designer Michael Puzey, features a spring system under the rider's platform that controls the hydrofoil's angle of attack. It is an aesthetically pleasing design with lots of moulded plastic parts. The Pumpabike has also been well marketed and has a starting platform accessory available for purchase (Pumpabike, Accessed 2008). The Aquaskipper is a much simpler design that uses a fibreglass spring link to control the angle of the hydrofoil as the rider jumps up and down. The Aquaskipper was design by Shane Chen for Inventist Inc. in 2003-2004 (Inventist Inc., 2006).

(a) A Trampofoil **(b)** A Pumpabike **(c)** A Aquaskipper

Figure 2.7. The trampofoil and some similar products (Inventist Inc., Accessed 2012; Pacific Blue, Accessed 2012; *[Trampofoil photo]*, Accessed 2012)

Lekhtman patented the Sea Jogger in 2003 (Hanlon, 2005; Lekhtman, 2003). The Sea Jogger is a device which can be dismantled and packed into a carry bag like the Aquaskipper. It has a rigid aluminium frame that is supported by two inflatable pontoons. There are two areas within the frame where the rider can transfer their weight from one side to the other. This motion is transmitted to a pair of flexible oscillating fins at the back of the vehicle which propel the boat forward. Steering is provided with a rudder connected to the handlebars at the front of the boat. Additionally the rider can oscillate the handle bars to propel the boat backwards.

A very recent human-powered hydrofoil is the Flyak, a slim racing style kayak with two hydrofoils mounted to the hull invented by engineers Einar Rasmussen and Peter Ribe in Norway. Each hydrofoil is supported by a single strut in the centreline of the craft. It is driven by a paddle like a normal kayak and once the operator gets the Flyak up to a speed of about $10\,\mathrm{km\,h^{-1}}$ the Flyak lifts onto its foils and its speed dramatically increases.

A single person Flyak has been proven to achieve higher speeds that a regular four man racing kayak. Similar to a Flyak is John Morrell and Kyle Washabaugh's hydrofoil rowing boat called Slip Velocity (Morrell, Accessed 2010). John believes this is the first hydrofoil row boat to have been successfully built and flown. Hydrofoils are still banned in the sport of rowing, so slip velocity cannot be raced in competitions. Slip Velocity used two fixed foils and is described to be remarkably stable while foil borne. The depth of the foils is currently controlled by a skilled rower with the oars, however the periodic nature of the propulsion and varying boat speeds can make this task difficult. It is desired that the boat be able to cruise at a range of speeds so active depth control will be added to the prototype.

2.2 Existing Human-powered Flapping Wing Vehicle Designs in Detail

2.2.1 The Wasserläufer

The Wasserläufer (German for 'water strider', referring to Gerridae) can be described as a pair of hydrofoil stilts. The rider pushes each leg down alternatively while moving the hand controls to control the angle of attack of the hydrofoils. Figure 2.1 shows the Wasserläufer in and out of the water. Figure 2.8 is a series of pictures that shows how the rider is required to move to operate the Wasserläufer. Figure 2.8a shows the start of a cycle with the rider pushing his trailing foot down with the rear handle vertically over the foil. At the same time he is lifting his leading foot up with the front handle slightly behind the front foil to increase its angle of attack. When his trailing foot reaches the bottom of the stroke he moves the rear foil's hand control backwards to increase the rear foil's angle of attack (Figure 2.8b) and moves the front foil's handle vertically over the front foil. The second half of the cycle is symmetrical to the first half with the front foil being pushed down and the rear foot being pulled up until the rider is back in the original position (Figure 2.8c and Figure 2.8d). It is obvious that it would take a lot of coordination and practice to master riding the Wasserläufer, especially since the riders left and right limbs are doing different movements simultaneously. However, when ridden

correctly the Wasserläufer provides a very smooth ride and is able to support the weight of the rider throughout the entire cycle period.

(a) **(b)** **(c)** **(d)**

Figure 2.8. Motion of the Wasserläufer. The Wasserläufer travels to the right of the rider, so is moving left in these photos since the rider is facing out of the page (Tagesschau, 1953)

2.2.2 Mutiny on the Boundary

Mutiny on the Boundary Layer (MOBL) was designed and built by Parker MacCready from 1984. It was the first human-powered flapping-wing propulsion hydrofoil where the foil's motion is controlled by a mechanical link. This made the path of the hydrofoil relative to the rest of the craft very precise. The main features of the MOBL's drive mechanism were the step up gearing, the flywheel, the main oscillating frame and the angle control lever. Firstly, there was a gear ratio of 2:1 between the pedal cranks and the crank that drives the oscillations. In normal operating conditions the rider would be pedalling at 100 rpm to move the crank driving the main oscillating frame at 200 rpm. There was also another step up in the gearing between the crank driving the main oscillating frame and the flywheel so that the flywheel was driven at 1000 rpm. The flywheel was added to the system to help the rider maintain a constant pedalling speed since the mechanism would oppose the rider on its downstroke and then try to speed up the rider's pedalling on its upstroke. The main oscillating frame used a parallel linkage to guide the foil up and down vertically in the water. The main oscillating frame was driven by the crank shaft via a

connecting rod. Finally, the angle control arm, which was also driven by the crankshaft, attached to the rear of the foil. Its phase and attachment radius (which tranlates to pitch angle magnitude) can be adjusted on the driving crank. Its purpose is to control the angle of attack of the foil throughout each cycle. Figure 2.9 is a sketch from Human Power Journal that shows how the Mutiny on the Boundary Layer works.

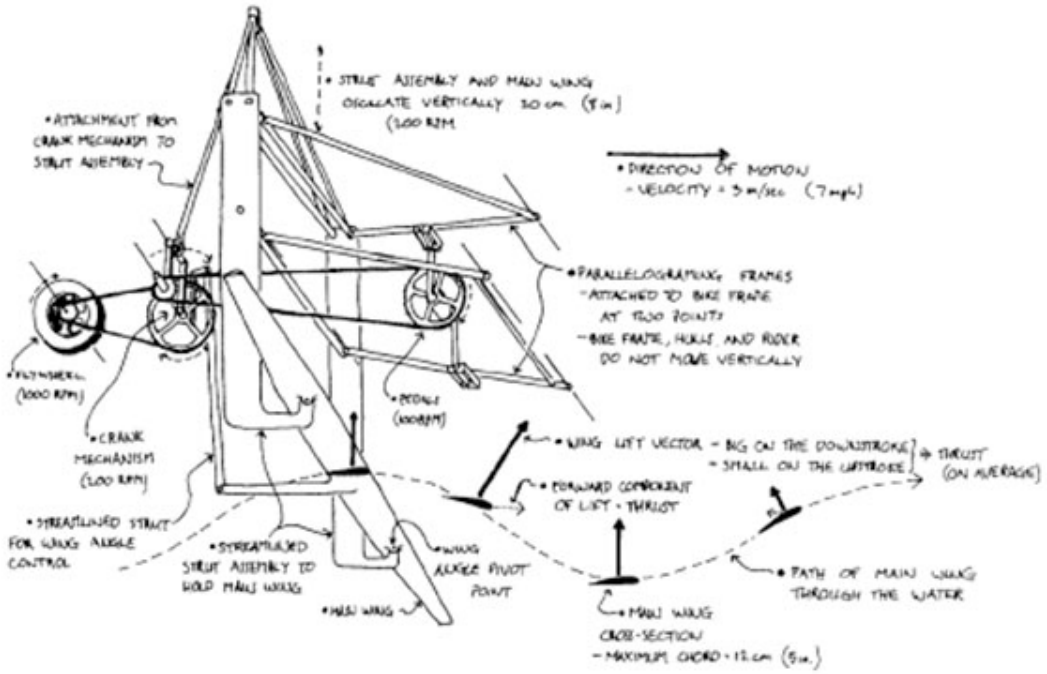

Figure 2.9. A sketch of the Mutiny on the Boundary layer drive mechanism published in Human Power Technical Journal. *Image courtesy of Parker MacCready (MacCready, 1990b)*

2.2.3 The Preposterous Pogo Foil

After building the Mutiny on the Boundary Layer, Parker MacCready went on to develop the Preposterous Pogo Foil. It is a much simpler device than the MOBL and uses the downwards force from the rider jumping on a platform, rather than pedal power, to drive the main foil. Initially the Pogo Foil is supported by its floats on the water before the rider begins jumping. When the rider jumps the Pogo Foil is subject to a force from the rider's feet which makes it moves downwards in the water. As the rider's weight

comes off the platform the floats buoyancy moves the Pogo Foil up and the cycles starts again. The foil is allowed to pivot around its quarter chord and its angle is controlled by a non-linear spring above via a mechanical link. This link is shown in Figure 2.10 which is a sketch of the Pogo Foils design from Human Power Technical Journal. The Pogo Foil accelerates forward using the thrust generated by the foil moving up and down. At some point the front foil will rise up lifting the front of the Pogo Foil out of the water. This will increase the angle of attack of the main foil which will give it more lift so the rear of the boat to become foil borne also. Once foil borne, the downwards force from the rider jumping upwards, forces the main foil downwards generating thrust and increasing its angle of attack. As some of the rider's weight is relieved from the platform the main foil's increased angle of attack enables the main foil to accelerate up quickly to the start position of the cycle.

2.2.4 The Trampofoil

The Trampofoil is effectively just a simplification of the Pogo Foil. It works on the very same principles, but because the Trampofoil does not have any floats it must be launched from a platform. The rider must push off the platform with enough speed so that the Trampofoil can support the rider. If the Trampofoil is travelling at less than approximately $8\,\mathrm{km\,h^{-1}}$ (*Trampofoil Info*, Accessed 2009), it will not be able to support the rider's weight and it will sink. The design is clever in a way since it just ignores the start up problems of flapping-wing propulsion hydrofoils and requires the craft to be launched straight into moving operation. However, it also has the major drawback that if the rider ceases to jump, the device will sink along with the rider. Figure 2.11 is a series of photos showing how an Aquaskipper (or Trampofoil/Pumpabike/Waterbird/etc.) is ridden.

To launch a Trampofoil the rider must hold the main foil about 10 cm below the water surface and push off the jetty while stepping onto the Trampofoil. The Trampofoil will initially glide and support the rider's weight but will slow down and sink if the rider does not start to jump. When the rider jumps on the platform, the force from the rider's feet on the platform and the rider's hands on the handle bars apply a bending moment on the

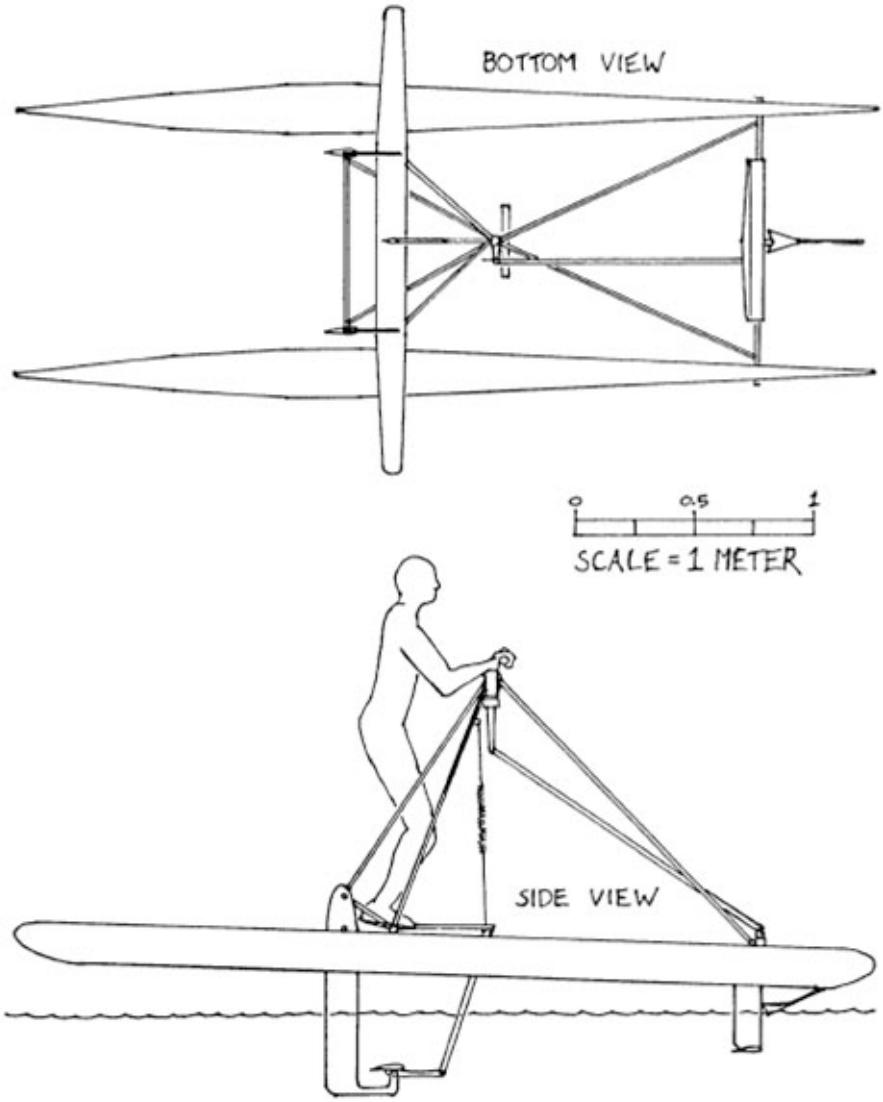

Figure 2.10. Design sketches of the Preposterous Pogo Foil. *Image courtesy of Parker MacCready (MacCready, 1990c)*

Trampofoil frame. This is because the platform and handlebars on the Trampofoil are located between the two foils. It is important that the platform is located in front of the main foil to obtain this moment and for stability. This bending moment causes the front half of the Trampofoil to bend which will pitch the rear half of the Trampofoil downward. The difference between the members of the Trampofoil group of devices is their method for the foils pitch control. The Trampofoil is the simplest device which just uses the flexibility of the main forward pointing composite member of the frame to change the foils pitch.

As the rider pushed down on the platform, the main forward pointing member is subject to a bending moment and deflects so that the rear part of the frame pitches downward relative to its undeflected state. The Aquaskipper and Waterbird use a simple link that includes a fibre glass member as a spring. The fibre glass link is the curved black link that can be seen in the photos in Figure 2.7c. The Pumpabike is slightly more complicated. Pumpabikes make use of a linkage system with a steel spring for the foils pitch control. The link is hidden away under the platform on the Pumpabike.

So the force from the rider jumping is used to pitch the rear of the Trampofoil downward and to push the main foil down through the water. Pushing the foil downward in the water effectively increases the foil's angle of attack and rotates the resultant force vector on the hydrofoil forward. However, by pitching the rear of the craft downward the angle of attack is also decreased. So the overall consequence from jumping on the Trampofoil is temporarily rotating the resultant force vector on the hydrofoil forward. The resultant force vector will then have some forward horizontal component which accelerates the Trampofoil forward. Once the trampofoil is moving forward, the foil's angle of attack cycle will depending on how fast the hydrofoil is pushed down, the moment that rotates the rear of the craft forward and the speed of the Trampofoil. When the rider's feet leave the platform, the Trampofoil has been relieved of the rider's weight and will bend back to its undeformed geometry. This increases the main foil's angle of attack and allows the Trampofoil to quickly gain altitude again. During the hydrofoil's upstroke it may only produce lift and drag since there is no power input. So as the Trampofoil rises it will only decelerate. When the rider lands back on the platform the cycle starts again. There are a lot of clever features in this cycle and the Trampofoil's construction that allowing the Trampofoil to work very well. Some of these features are:

- the simplicity of the Trampofoils construction
- the power source is not attached to the propulsion device
- there is no need for any rotational to linear motion conversions
- the Trampfoil is very light

A very advantageous design feature of the Trampofoil is that the rider, who is the power source and the heaviest component of the system, is not directly attached to the craft. The Trampofoil uses the rider's weight as its source of power throughout the down stroke where the foil is gaining speed. Then as the rider leaves the platform, the craft is relieved of the rider's weight and is allowed to recover height quickly. Therefore the Trampofoil does not have to support the full weight of the rider throughout the entire operating cycle.

The Trampofoil's simple and light construction makes it easy for the user to handle. Hollow members of the frame are filled with closed cell foam so the frame will not sink if left alone in the water. The frame is also capable of providing some support for the rider once the Trampofoil has sunk.

2.2.5 A Comparision of Existing Human-powered Flapping Wing Propulsion Hydrofoils

As discussed in the previous section, the Wasserläufer was the first flapping-wing hydrofoil device that was invented. It was invented in 1953 well before any other device yet was not developed or sold commercially. Soon after Calvin Gongewer tried to market the Aqueon through his company, Innerspace Thrusters Corporation. See Figure 2.12 for the advertisements. The next attempt at a flapping-wing propulsion hydrofoil was Parker MacCready's Mutiny on the Boundary Layer in 1984. This boat was the result of experimental boat building and the application of Wu's Theory (Wu, 1971). After building the MOBL on the Boundary Layer, MacCready continued with his experimental boat building and invented the Preposterous Pogo Foil, which was a much simpler design. MacCready later made a comparison between his two boats saying that the Mutiny on the Boundary Layer was "the overweight over-mechanical, but working, predecessor to the sleeker Pogo Foil" (MacCready, Accessed 2012). In 1998 the original Trampofoil was released for a short period of time before the Trampofoil Company stopped manufacturing them. The Trampofoil is very similar to the Pogo Foil but does not have any flotation devices attached to it. This lack of floatation requires the Trampofoil to be launched from a jetty or other platform just above the water level. It also means that if the rider stops powering

the Trampofoil it will sink. Finally, the most recent flapping-wing propulsion craft are a group of craft that are very similar to the Trampofoil. This group of craft includes models such as the Pumpabike, Aquaskipper and the Waterbird.

From reviewing the successes of the human-powered flapping-wing hydrofoils discussed above, it is clear that the simpler devices have always performed better. However, simpler designs require more human skill and balance to operate than the more complicated designs. The only fully mechanical craft above is the Mutiny on the Boundary Layer which did not perform as well as the simpler craft in the areas of input power requirements and top speeds. The MOBL has been described as an "over-weight and over mechanical device", however it has also been described as quite a reliable craft. The MOBL had a number of features which aimed to make it a more user friendly craft. These features include the catamaran floats for buoyancy and stability at low speeds, and the standard cycling position for the rider.

Nearly all the simpler craft require more skill and experience to operate and do not float by themselves, with the exception of the Pogo Foil. Most of the simpler craft, despite being less user friendly than the MOBL, obtained greater speeds and required less power input so they could be ridden for longer periods of time. Table 2.1 summarises the features of all the human-powered flapping-wing hydrofoils mentioned above and Table 2.2 summarises estimates of their respective operating parameters.

2.3 Other Flapping Wing Propulsion Applications

Flapping wing propulsion technology has been applied in areas other than surface water craft. Some applications include Autonomous Underwater Vehicles (AUVs), Micro Air vehicles (MAVs) and Ornithopers. These types of flapping wing propulsion craft are mentioned briefly below so that the reader may have some appreciation of the broader range of flapping wing propulsion applications.

Flapping wing propulsion is an attractive form of propulsion for Autonomous Underwater Vehicles (AUVs) for a number of reasons. Flapping wing propulsion has been proven to be as efficient as conventional propellers and have the potential to be much more efficient

Table 2.1. Human-powered flapping wing propulsion hydrofoil summary

Boat	Wasserläufer	MOBL	Pogo Foil	Trampofoil	Aquaskipper	Ergofoil
Floats	No	Yes	Yes	No	No	Yes
Stall Speed	-	-	-	$2.5\,\mathrm{m\,s^{-1}}$	$2.2\,\mathrm{m\,s^{-1}}$ (5 mph)	-
Maximum Speed	-	$3.2\,\mathrm{m\,s^{-1}}$ (7 mph)	$5.0\,\mathrm{m\,s^{-1}}$ (11 mph)	$6\,\mathrm{m\,s^{-1}}$	$7.6\,\mathrm{m\,s^{-1}}$ (17 mph)	
Flight Time/Distance	-	$< 100\,\mathrm{s}$	'a few hundred metres'	11.5 km record		*N/A*
	-			30-40 min	-	
Estimated Power	-	400 W (0.5 hp)	-	-	-	-
Take Off Time	$< 1\,\mathrm{s}$	5-10 s	-	*N/A*, must be foil borne		*N/A*
Mass (Weight)	-	110 lb (490 N)	45 lb (200 N)	12 kg (118 N)	25 lb (200 N)	120 kg (1177 N)
Number of driving foils	2	1	1	1	1	1 (second can be mounted)

Data sources: (Inventist Inc., 2006; MacCready, 1990a, Accessed 2012; Oritsland, 1991; Trampofoil, *Accessed 2009)*

Table 2.2. Estimates of the performance parameters for four exsiting flapping wing propulsion hydrofoils at cruising speeds

Boat	Wasserläufer	MOBL	Pogofoil	Trampofoil	Aquaskipper
Cruising Speed ($\mathrm{m\,s^{-1}}$)	2*	3	4.9	4	4
Flapping Amplitude (m)	0.15*	0.1	0.1	0.075*	0.1*
Flapping Frequency (Hz)	1.5*	3.3	2*	2*	2*
Hydrofoil Chord Length (m)	0.2*	0.12	0.12	0.12	0.12
Hydrofoil Span (m)	3*	2	2	2.9	2.13
Heave-to-Chord Ratio	0.75	0.83	0.83	0.63	0.83
Keulegan-Carpenter Number	4.7	5.2	5.2	4.0	5.2
Reynolds Number (based on u) (in water @10°)	306 000	275 000	450 000	367 000	367 000
Reynolds Number (based on $\dot{h}$) (in water @10°)	216 000	190 000	115 000	87 000	115 000
Strouhal Number	0.23	0.22	0.08	0.075	0.1

Data sources: (Inventist Inc., 2006; MacCready, 1990a, Accessed 2012; Trampofoil*, Accessed 2009)*
**Estimates were made via the observation of videos that can be found online at www.youtube.com*

in flows with oncoming vorticity (Anderson, 1996). Efficiency of propulsion is of great importance in AUVs as it governs the overall performance specifications such as physical size, range and payload limits of a AUV. Researchers at Massachusetts Institute of Technology (MIT) concluded that the Tuna had the most desirable shape and movements to base an underwater vehicle platform on (Anderson & Kerrebrock, 2000; Barrett, Grosenbaugh, & Triantafyllou, 1996). MIT developed and tested Robo-Tuna and Robo-Pike, two fish shaped AUVs for the development of high efficiency flapping wing propulsion. These robot designs with actively swimming bodies demonstrated a reduction of the required power at a Reynolds number of 10^6 of greater than 50 % compared with rigid body vehicle configurations.

Underwater animals employing flapping wing propulsion demonstrate agility and manoeuvrability that is currently unmatched by any man made AUV. Work done at MIT with Robo-Tuna concluded that the propulsive efficiency of their current vorticity control (VC) propulsion system provided a similar range and efficiency as conventional propulsion systems. However, the vorticity control propulsion system provided superior vehicle manoeuvrability. MIT then developed a AUV named Finnegan that reassembles a turtle to further investigate the benefits of flapping wing propulsion for the manoeuvrability of AUVs. Finnegan successfully demonstrated superior manoeuvrability over other AUVs such as the REMUS (Stanway, 2008).

There is a lot of interest in Micro Air Vehicles (MAVs) for both civil and military applications. Due to the size of MAVs payloads are very limited and therefore the efficiency of the vehicle is very important. MAVs typically operate at low Reynolds numbers where steady-state aerodynamics are particularly inefficient. Unsteady aerodynamics is seen to be a possible solution to increasing the performance of MAVs (Cleaver, Wang, & Gursul, 2009).

Some of the first motor-powered manned ornithopter flights were achieved by Adalbert Schmid in the 1940s. More recently the human-powered ornithopterindexornithopter, 'Snowbird', was designed and build at the University of Toronto in 2010 (of Toronto Institute for Aerospace Studies, n.d.). Snowbird is claimed to have achieved sustained flight for 19.3 s

2.4 Summary of Existing Designs

So far the only human-powered hydrofoils that have successfully achieved flight with flapping-wing propulsion have required a significant amount of human instinct, skill and balance to operate. No human-powered flapping-wing propulsion hydrofoil craft has been manufactured so that any person, with any skill or experience level, can simply get on and ride. The skill level required for operating such craft could be benchmarked against the skill level required to ride a bicycle.

The only successful designs that have been made commercially available are those that fall into the Trampofoil group of devices. Out of this group, the one that appears to be most successful is the Aquaskipper since they are manufactured relatively cheaply and perform well. Pumpabikes obviously have had a lot of thought put into the aesthetics and associated marketing.

History also shows that the simpler craft, with more rider input into the control of the foils, like the Wasserläufer, Pogo Foil and the Trampofoil type devices have been more successful in the areas of speed and power requirements. A combination of their simplicity and a heavy reliance on human feel and balance as their feedback control, shows that the control of flapping-wing propulsion is quite a difficult thing to master with mechanical devices. Design engineer Parker MacCready stated that "*It remains a strong challenge to the hydrofoil builder to match the simplicity and the cleverness of this early invention (referring to the Wasserläufer)*" (MacCready, 1990a).

(a) lifting in water **(b)** pushing off **(c)** first jump

(d) cruising **(e)** cruising **(f)** swimming back

Figure 2.11. An Aquaskipper being launched from a jetty, cruising and sinking (Grogware, 2007)

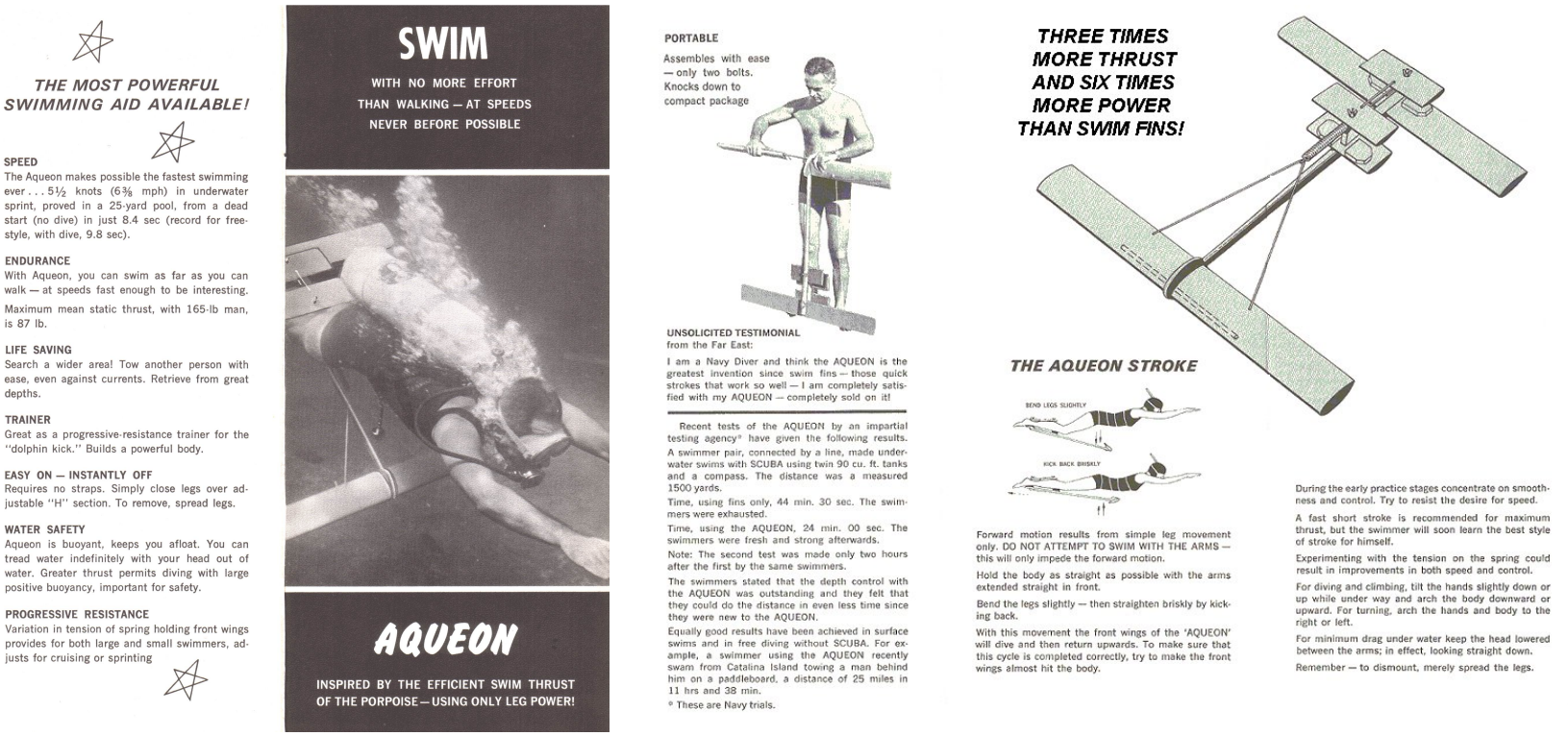

Figure 2.12. Advertisements for the Aqueon. *Photographs courtesy of Innerspace Corporation* (Innerspace Corporation, n.d.)

Chapter 3

Literature and Background Research

This chapter presents a review of the current literature considered relevant to designing a human-powered hydrofoil. Figure 3.1 is an overview of the topics that have been reviewed and the structure of this chapter. Current information useful for designing a human-powered hydrofoil has come from several areas of research including studies of oscillatory and unsteady fluid flows, animal propulsion, vehicle propulsion, aeronautics, ocean structures, energy harvesting, biology, biomimetics, and sport science. The purpose of this review is to summarise published research relevant to designing a human-powered hydrofoil.

This review begins by discussing the capacity of a person to be a power source for a vehicle. Research in this area provides evidence of some key constraints for a human powered vehicle, such as the power that a person can exert for a given duration, which was a short fall of previous designs (see Section 2.2). Since the concept of flapping wing propulsion was inspired by nature, observations of animals that employ flapping wing propulsion are discussed. A review of calculation methods, for hydrodynamic forces acting on an object in unsteady flow, and an object oscillating in steady fluid, are presented. A summary of the parameters used to define the state of flapping foil is followed by a review of the performance of a flapping foil in relation to its state. Finally, this chapter

includes a patent search for existing human-powered water craft that employ flapping wing propulsion.

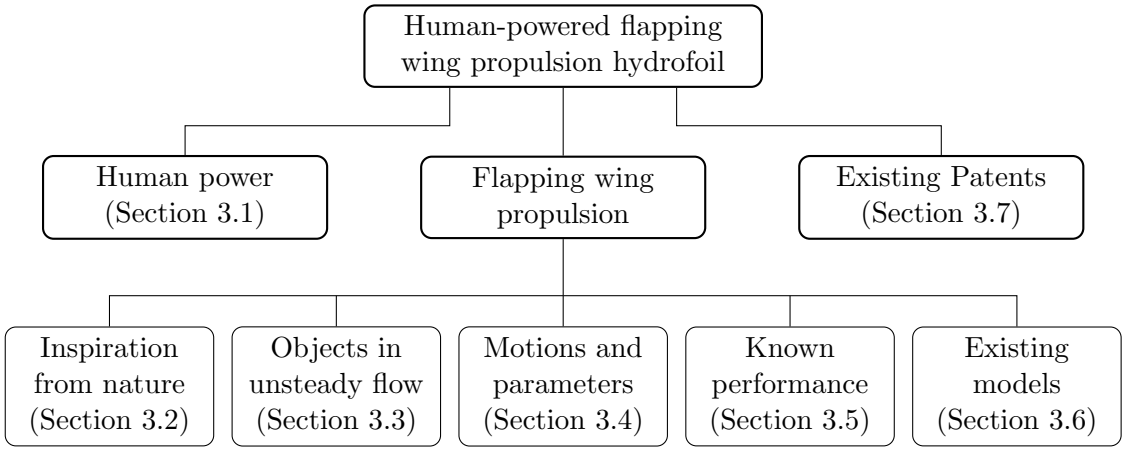

Figure 3.1. Topics of interest for the development of a human-powered flapping wing propulsion watercraft.

3.1 Human Power

According to Schmidt-Nielsen (1972) the 'cost of locomotion' for animals and humans is defined by Equation 3.1. The cost of locomotion quantifies the energy used per unit distance travelled. A high cost of locomotion represents a large amount of energy to move a unit mass per unit distance. This is a useful measure for determining the power required for locomotion of humans and animals and the estimation of their maximum range and travelling speeds. Zamparo et al. (2008) define the cost of locomotion, C, to be the energy cost per unit distance and neglect the weight of the subject (refer to equation 3.2). $\dot{E}$, is the net metabolic power expenditure and v, is the speed of the progression.

$$\text{Energy Cost of Locomotion} = \frac{\text{Metabolic Power}}{\text{Speed}} \tag{3.1}$$

$$C = \frac{\dot{E}}{v} \tag{3.2}$$

The operation of a human-powered watercraft involves a series of energy transfers starting with oxygen entering the operator's respiratory system and ending with the ac-

celeration of water around the water-craft. For each energy transfer there is an associated efficiency. The first transfer involves the operator providing power to drive the vehicle by converting chemical energy in his muscles (food and oxygen) into kinetic energy. In sport science, the net metabolic power a person produces, $\dot{E}$, is proportional to their rate of oxygen consumption, $\dot{V}O_2$. For a pedal-powered vehicle the power produced by the rider may be measured at the crank shaft relatively easily. However, for vehicles with alternative mechanical power transmission devices, determining the power produced from the rider may not be so easy. Dividing the power produced at the crank shaft by the velocity of the vehicle yields the total mechanical work done per unit distance W_{tot}. Zamparo et al. (2008) define the ratio between the total mechanical work per unit distance and the cost of locomotion as in Equation 3.3 to be the overall efficiency η_o. The second transfer is using the energy expenditure of the operator to accelerate water beside the watercraft backwards in order to propel the watercraft forward. This power transfer is commonly done via components of the watercraft such as oars, paddles or hydrofoils. Zamparo et al. (2008) denote the efficiency of this process as the propulsive efficiency, η_p (Equation 3.4) which is the ratio between the work per unit distance to overcome hydrodynamic drag, W_d, and work supplied to the vehicle by the rider per unit distance travelled, W_{tot}. Zamparo et al. (2008) observed that measurements of the overall efficiency did not vary much for vehicles with differing exercise movements such as pedalling, rowing or paddling. Typically η_o is between 0.24 and 0.27. They also observed that measurements taken on land (i.e. on a fixed cycle ergometer) agreed well with the measurements taken on-board a water vehicle (Zamparo et al., 2008). Hence the factors most affecting the cost of locomotion are the propulsive efficiency of the vehicle and external drag on the vehicle. Both these factors can be improved through good vehicle design. Zamparo et al. (2008) also define the efficiency of the entire process as the drag efficiency, η_d, which may be calculated by multiplying the overall efficiency by the propulsive efficiency as in Equation 3.5. Figure 3.2 is an illustration depicting these efficiencies for a human-powered watercraft.

$$\eta_o = \frac{W_{tot}}{C} \tag{3.3}$$

$$\eta_p = \frac{W_d}{W_{tot}} \tag{3.4}$$

$$\eta_d = \eta_o \eta_p \tag{3.5}$$

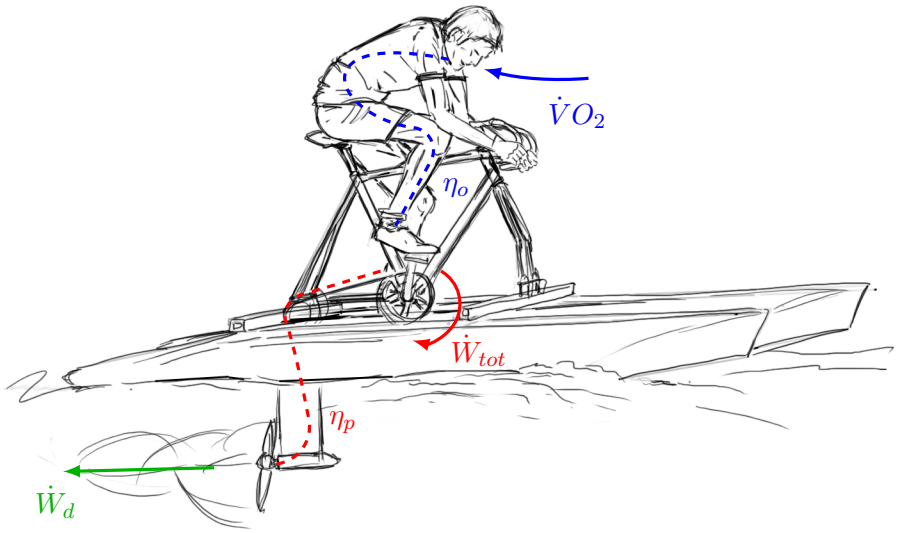

Figure 3.2. Illustration of efficiencies for pedal-driven watercraft (Zamparo et al., 2008).

Designs for human powered craft are constrained by the expected endurance of the rider. It is well known that the power output of a person increases rapidly as exercise duration is decreased (Davies & Rennie, 1968; Morton & Hodgson, 1996) and so the design ride time will dictate the maximum amount of power that can be expected from the rider. The power output of a person is also highly dependent on the type of exercise movement. For example, Davies calculated from force plate measurements that the mean peak power output for jumping was 5.23 hp (3.90 kW) for men and 3.15 hp (2.35 kW) for women and compared these to the mean power output during sustained cycling of 0.33 hp (0.25 kW) for men and 0.25 hp (0.19 kW) for women. Davies (1971) later published that these high power outputs for jumping may be possible due to potential energy stored in the muscle when a person lowered their centre of gravity before accelerating upwards. Harman, Rosenstein, Frykman, Rosenstein, and Kraemer (1988) measured the mean peak power of jumping men consistent with Davies's measurements (3.77 kW) with a jump and

reach test.

Running is another 'weight-bearing exercise' similar to jumping. Weight bearing describes the fact that an athlete's centre of mass does not maintain a constant altitude while running like it would while cycling. The power requirements for running and sprinting have been measured via non-motorised treadmill ergometers (Hawley, 2000). Peak mean power over a stride can exceed 1000 W during acceleration of a sprinter. However, this rapidly declines to about 500 W after the first 30 seconds of sprinting.

A common and practical method of driving a human powered vehicle is with pedal-power since it is a continuous motion that uses some of the larger muscles in the body. Pedal-power is a common method of converting human movements into shaft power to drive human powered vehicles. For an easy to operate human powered watercraft, pedal-power is an obvious choice to consider since most people are able to ride a bicycle without much training. For similar reasons, the majority of experimental data for a person's output power over endurance times have been measured on cycle ergometers (A. V. Abbott & Wilson, 1995; Morton & Hodgson, 1996). This is beneficial for designing a pedal-powered watercraft.

The efficiency of this conversion can be modified simply by changing the ergonomics of the vehicle. It is important that the crank shaft position relative to the rider's seat and the crank length allow for efficient pedalling. In the case of cycling, simply adjusting the seat height to provide the correct spacing between the seat and the pedals is important to ensure good cycling economy (power output to $\dot{V}O_2$ ratio, equivalent to overall efficiency), and to decrease the risk of knee injury (Bini, Hume, & Croft, 2011). Correct gearing between the crankshaft and the propulsive device is essential. Harnish, King, and Swensen (2007) suggest that sufficient gearing options are necessary to allow riders to select their cadence. While pedalling under high load, a low cadence results in the angular velocity of the cranks decreasing faster in the low power phase of pedalling, leading to reduced efficiency. Efficiency will also drop when cadence increases to a higher level, above the cadence ceiling (Harnish et al., 2007). Welbergen and Clijsen (1990) observed little change in a cyclist's power output or oxygen intake for different cycling positions be it sitting or recumbent. Similarly, Ashe et al. (2003) saw no major advantage for untrained cyclists to assume an

aero position, and that changes in cycling posture is mainly beneficial for aerodynamic reasons.

McCartney et al. (1983) measured the peak torque output over a range of crank velocities for males aged 19-23 years participating in a maximal cycling exercise. The torque-velocity relationship for maximal cycling output over a short period of time, 5-30 seconds, was negative and linear much like the torque-velocity relationship of an electric motor (refer to Figure 3.3). Peak mean power was measured to be approximately 1000 W with a crank velocity between 100-140 rpm, which declined linearly to approximately 460 W over the first 30 seconds of maximal effort. McCartney et al. (1983) also found that if the cyclist pedalled with a slower crank velocity (60 rpm) the mean power was lower at the start of a maximal effort test (740 W), but declined at a much slower rate over the duration of the test. Similarly to McCartney et al. (1983), Buśko (2005) also measured that the peak mean power output of untrained but healthy cyclists (with an average age of 21.9 years, height of 182.9 cm and weight of 81.3 kg) was 1000 W at a crank velocity of 120 rpm. Davies and Sandstrom (1989) published similar results for untrained cyclists alongside the mean maximal power of trained sprint cyclists who generated in excess of 1500 W. The maximal power output of both untrained, and trained cyclists, correlated linearly with the mass of the cyclist.

Morton and Hodgson (1996) reviewed the relationship of endurance time and output power for people. These parameters have been modelled with a simple hyperbolic relationship assuming an upper limit for constant power output over long period of exercise known as the 'critical power', and a fixed work capacity for short periods known as the 'anaerobic work capacity'. Morton and Hodgson (1996) extended the hyperbolic model to his own 'three component bioenergetic model', which incorporates these two limits. Figure 3.4 shows the endurance-time curve using Morton's three-component bioenergetic model for a 'typical' fit male subject (Morton, 1990). Note that as the endurance time tends to infinity, the power does not tend to zero, but instead tends to the critical power (208 W). This asymptote represents a maximum sustainable aerobic power output of a person. At the other end of the curve the model appears to have an asymptote at $t = 0$. However, this does not imply that the power output is infinite for infinitesimally short periods. In-

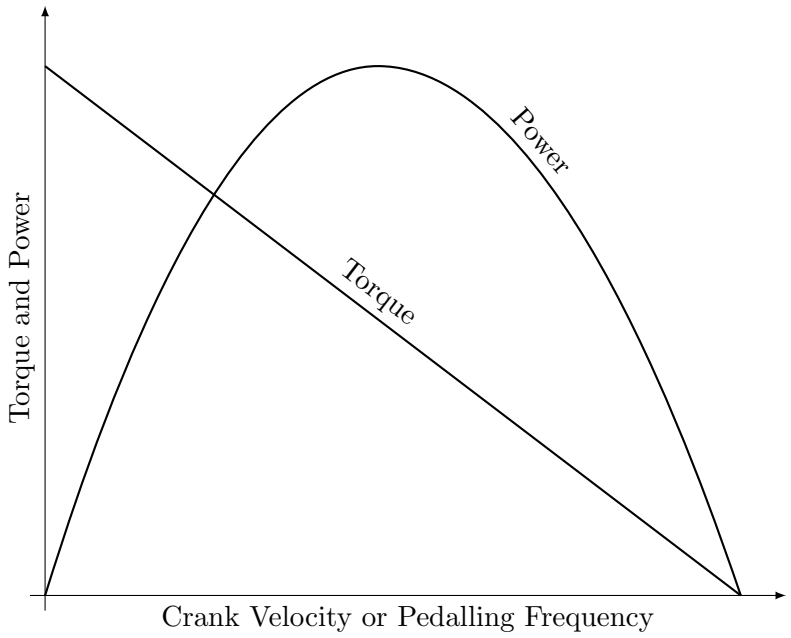

Figure 3.3. Torque-velocity relationship and power curve for maximal cycling. (A. V. Abbott & Wilson, 1995; Buśko, 2005; Hawley, 2000; McCartney et al., 1983)

stead the model suggests that there is an anaerobic time limit for the maximum attainable anaerobic power. For the curve in Figure 3.4, this is 972 W for 6 seconds.

Zamparo et al. (2008) published the drag of two pedal-driven watercraft, a paddle-wheel boat and a water bike, for a range of velocities. The drag curves for these two craft (Figure 3.5) represent the drag of a typically inefficient craft (the paddle-wheel boat), and a more modern, efficient watercraft (the water bike). Drag coefficients deduced from these two drag curves could be used to benchmark drag on a pedal-driven watercraft. Zamparo et al. (2008) evaluated the efficiency of these two pedal-driven watercraft against other non-pedal-driven human-powered watercraft (i.e. a rowing shell and an Olympic kayak). Rowing shells and Olympic kayaks held the highest values for propulsive efficiency and drag efficiency. This could be due to their relatively low cycle frequency and high stride length creating less waste energy in the flow than the relatively high frequency propeller (Pendergast et al., 2003).

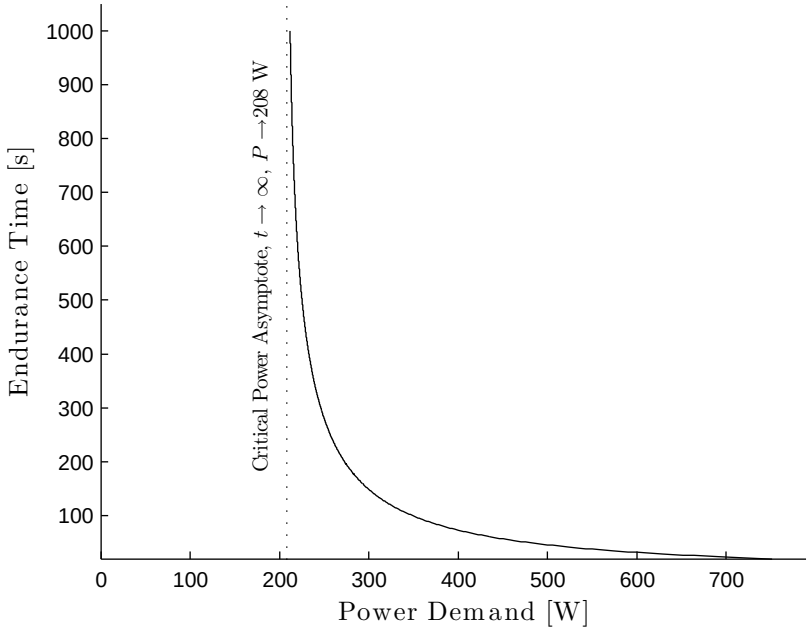

Figure 3.4. Morton's (1990) hyperbolic model for endurance time versus power output for a 'typical' male subject showing critical power

3.2 Inspiration for Flapping Wing Propulsion

There are three types of winged fliers; fixed wing, rotary wing and flapping wing fliers, each with their respective merits and drawbacks. People have observed that nature's choice of these three designs is predominantly the flapping wing variety. It is much less common to find man-made inventions that employ flapping wing propulsion. This is likely due to people having a much better understanding of the other two designs; fixed wing and rotary wing. Water and air are the two most common fluids to find flapping wing fliers in due to their abundance on earth. It is more common to find fliers that operate in a single medium. For example, fliers that are immersed in water (swimmers), such as fishes and submarines, or fliers that are immersed in air, such as birds and insects. However, some fliers operate on the liquid/gas boundary such as hydrofoil boats, hovercraft and some animals. This is a more complex condition to operate in due to the difference in fluid properties, and surface effects.

Airborne flyers, like swimmers, commonly employ flapping wing propulsion in nature.

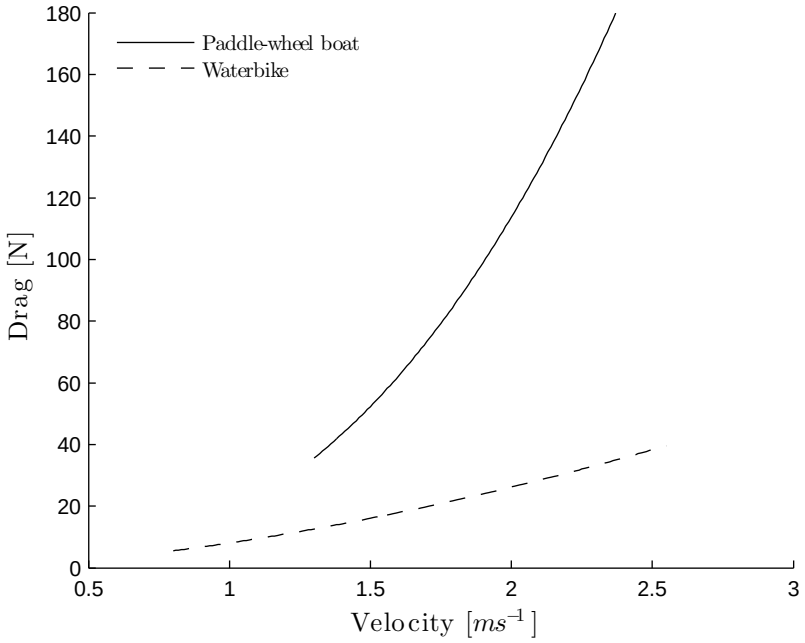

Figure 3.5. Drag of a paddle-wheel boat and a water bike published by Zamparo et al. (2008)

Some parameters are comparable with those of swimmers. However, there are some core differences between flying and swimming. The most notable difference between these two groups is the way they flap their wings. A swimmer's main fin is usually located behind the main body and so must operate in the wake of the main body. In contrast, a flyer's wings are usually located on the side of their body, often extending out some distance avoiding the wake of their body. The different wing locations also affect the type of flapping that is possible. A swimmer moves its tail up and down (or side to side) in a mixture of heaving translation and pitching rotation; a flapping motion (see Section 3.4). However, flyers must rotate their wings along a roll axis while pitching them at the same time. These dorsoventral flapping movements are also referred to as root-flapping motions (*Root-flapping*: see Section 3.4). Even though the movements are different, similar fluid propulsion mechanisms still apply to both forms of flapping wings. Both motions can produce a reverse von Kármán street at certain Strouhal numbers (*Strouhal number*: see Section 3.4.1), and in both forms, peak efficiency is found to fall into the same Strouhal number range (Taylor, Nudds, & Thomas, 2003).

One of the most important differences between the function of a flier and a swimmer, is that a swimmer operates in a medium which has a similar density to that of itself, and so lift forces are not required to maintain its elevation. Breder (1926) states that "...a typical fish might better be likened to a dirigible balloon than to any truly flying animal, which is fundamentally more similar to an aeroplane". For this reason most flapping hydrofoil research has been performed with symmetrical hydrofoils. This would suggest that the literature in the area of aircraft would be more valuable to this project. On the contrary, Gleiss et al. (2011) recorded the movements of four swimming animals and reported that they all had intermittent locomotion styles (i.e. a sequence of alternating flapping and gliding periods) similar to flying animals. Despite the literature's bias to research on symmetrical foils, there are publications on lifting hydrofoils (Lim & Tay, 2010; Tay & Lim, 2009).

The study of fishes has inspired a lot of research in the area of flapping hydrofoil propulsion since they have mastered this type of propulsion through many years of evolution. Researchers have observed different performance measures and given merit to the respective fish. The sailfish is known as the fastest fish in the ocean and has been observed travelling at speeds of up to $110\,\mathrm{km\,h^{-1}}$. The tuna has been noted for its high aspect ratio (hydrofoil like) lunate tail which is relatively small compared with its body (Randall, Conte, & Hoar, 2001). Videler and Kamermans (1985) observed that dolphins travel further (relative to their own body length) per tail-beat than many other species. Other underwater creatures such as octopus and squid propel themselves by creating a jet wake, but they manage to do so without hydrofoil shaped body parts.

Breder (1926) classified fishes into three major categories of swimmers based on how they move their bodies for the purposes of forward locomotion. These categories are named: Anguilliform, Ostraciiform and Carangiform. Anguilliform motion (named after the Anguillidae family of fish) is described to be a serpentine motion like that of a flag waving in the wind. This type of swimmer can be most easily associated with eels. An anguilliform swimmer will move the majority of its body in a wave-type pattern. Ostraciiform motion (named after the Ostraciidae family of fish) is described by Breder (1926) to be a 'wig-wag motion' like a fan. An ostraciiform swimmer looks like it has a hinged

tail that fans rapidly. The body and the tail of the swimmer will hinge back and forth to create thrust, while the hinge point will travel forward in a straight path. Carrangiform motion is displayed by most fish and is the intermediate motion between the two extremes. A carrangiform swimmer changes the direction of their head and then swings their tail around to realign itself. There are more smaller sub-groups within each of the three main classifications of swimming types to further define a swimming style. Thunniform swimming, named after the tuna (Thunnus), is a sub-group of carrangiform swimming that includes swimmers with a relatively stiff body, that only move a small proportion of their body length to oscillate a typically high-aspect ratio lunate tail. Thunniform swimmers are known to travel long distances and be capable of very high speeds.

In 1936 Gray (1936) equated an estimate of a dolphin's muscle power to the drag power on an equivalent rigid body. The conclusion of his analysis was that dolphins should not be able to swim as fast as they do (Gray, 1936). This is known as Gray's Paradox. His hypothesis to explain the paradox was that a dolphin's swimming style maintained laminar flow around its body, and so the drag on its body would be less than his estimate. Explanation of Gray's Paradox eluded scientist for a long time (Fish, 2006) until, recent experiments by Legac, Fish, Williams, and Wei (2007) resolved Gray's Paradox via digital particle image velocimetry (DPIV) flow measurements. They discovered that the propulsive thrust generated by dolphins was in fact approximately 10 times that of Gray's estimate.

Triantafyllou et al. (1993; 1991) compared existing speed, body length and tail-beat frequency data for a range of fish. Their literature review revealed several important correlations between these parameters. For fish with a tail-beat frequency over 5 Hz, a typical cruising tail peak-to-peak amplitude is 20 % of the body length. Tail-beat frequency varies linearly with swimming speed. Finally, most fish cruise within a Strouhal number range of 0.25-0.35. All of these results were observed across a range of Reynolds numbers (10^3-10^6) (*Reynolds number*: see Section 3.4.1).

Not all winged species use their wings for flight. Other phenomena such as Wing-Assisted Incline Running (WAIR) were studied by biologists (Bundle & Dial, 2003; Dial, 2003). The results of these studies include the aerodynamic and inertial propulsion effects

of flapping wings just as publications on flight do and so are indirectly relevant to this thesis. Some of these publications contain theories on the evolution of flight. Understanding the underlying mechanisms for flapping wing propulsion is important in order to understand the evolution of animal propulsion and their high performance wings.

3.3 Force on an Object in an Unsteady Flow

3.3.1 The Morison Equation

The Morison Equation (Equation 3.6), named after J.R. Morison (Morison, Johnson, & O'Brien, 1953), is used to calculate the instantaneous hydrodynamic force acting on an object in an unsteady flow. The Morison equation comprises of an initial term representing the drag forces and a second term representing the inertial forces on the object. The drag term is equivalent to the steady drag on the object and is calculated with the steady drag coefficient c_d (see Equations 3.37).

The inertia term can be decomposed as the sum of the Froude-Krylov force $\rho V_m \dot{u}$ associated with the pressure gradient in an accelerating flow, and a disturbance force $c_a \rho V_m \dot{u}$, where c_a is the added mass coefficient (sometimes referred to as the hydrodynamic mass coefficient) and V_m is the volume of displaced fluid displaced by the object. Combining these two terms leads to the inertia term in the Morison equation (Equation 3.6), where the mass coefficient c_m is equal to $c_a + 1$. In the case of an oscillating object in an otherwise stationary fluid, the Froude-Krylov force is not needed and the inertia term of the Morison equation becomes $c_a \rho V_m \dot{u}$. The theoretical value for c_a is 1. However, experimental results usually show that $c_a < 1$ in practice.

$$F = \frac{1}{2} c_d \rho A u |u| + c_m \rho V_m \dot{u} \tag{3.6}$$

3.3.2 The Relative Motion Morison Equation

The original Morison equation (Equation 3.6) is for oscillating flow over a stationary cylinder. In the case when the cylinder also oscillates, or moves in response to the flow, the relative motion Morison equation applies (Sajonia, 1988). This equation is shown as

Equation 3.7, where x is the time-dependent displacement of the cylinder. Several other extensions of the Morison equation exist, eight of which have been verified by Shafieefar, Massie, and Vugts (1996) who discarded most versions, but not the relative motion Morison equation (Equation 3.6).

$$F = \frac{1}{2} c_d \rho A \left(u + \dot{x}\right) \left|u + \dot{x}\right| + c_a \rho V_m \left(\dot{u} + \ddot{x}\right) + \rho V_m \dot{u} \tag{3.7}$$

3.3.3 The Keulegan-Carpenter Number

When comparing the magnitude of the drag term and the inertia term of the Morison equation, the resulting ratio is proportional to the Keulegan-Carpenter number (Keulegan & Carpenter, 1958). The Keulegan-Carpenter number (sometimes called non-dimensional time (Newman, 1977)) is defined in Equation 3.8 and is used to describe the relative contributions of drag forces and inertia forces of a fluid on an object (Dean & Dalrymple, 1991). V is the amplitude of the fluid oscillation velocity, T is the period of oscillation, and L is some characteristic length of the object. At low Keulegan-Carpenter numbers, the forces on an object will be dominated by inertial effects, and at high Keulegan-Carpenter numbers the forces are predominantly viscous forces.

$$K_C = \frac{VT}{L} = \frac{2\pi h_0}{c} \tag{3.8}$$

For sinusoidal heaving ($V = 2\pi f h_0$), taking the chord length of the foil as the characteristic length, the Keulegan-Carpenter number is proportional to the ratio of heave amplitude to chord length (Equation 3.8). Since the proportional constant in this relationship is 2π the Keulegan-Carpenter could be seen as the angular heave-to-chord ratio. In some fields this ratio of oscillation amplitude to the characteristic length of the object is known as the 'displacement parameter' (Dean & Dalrymple, 1991). However in the field of oscillating foils it is known as the heave-to-chord ratio. The heave-to-chord ratio, h^*, (also known as non-dimensional amplitude of oscillating (Lai & Platzer, 2000), non-dimensional plunge amplitude (Ashraf, Lai, & Young, 2007) or non-dimensional heave amplitude), is

defined by the heaving amplitude divided by the chord length as in Equation 3.9.

$$h^* = \frac{h_0}{c} \tag{3.9}$$

3.3.4 The Iversen Modulus

Before Keulegan and Carpenter (1958) presented the Keulegan-Carpenter number (see Section 3.3.3), Iversen and Balent (1951) presented a similar dimensionless quantity known now as the Iversen Modulus (Journée & Massie, 2001). The Iversen Modulus is the ratio of the product of flow acceleration A and some characteristic length L to the squared flow velocity (Equation 3.10). Since the Iversen Modulus is equivalent to 2π over K_C it was superseded by the preferred Keulegan-Carpenter number.

$$I_v = \frac{AL}{V^2} = \frac{2\pi}{K_C} = \frac{1}{h^*} \tag{3.10}$$

3.3.5 The Viscous Frequency Parameter

For a given oscillating frequency, increasing the Keulegan-Carpenter number inherently increases the maximum oscillating velocity, and therefore the maximum Reynolds number (See Section 3.4.1). Due to this proportionality between these dimensionless parameters, the viscous frequency parameter β (Equation 3.11) (Bearman, Downie, Graham, & Obasaju, 1985; Sarpkaya, 2005), also known as Sarpkaya Beta (Journée & Massie, 2001; Sarpkaya & Isaacson, 1981) or Stokes parameter (Stokes, 1851), is defined as the ratio between the Reynolds number and the Keulegan-Carpenter. The drag and inertia coefficients of an oscillating cylinder are sometimes described in terms of β (Bearman et al., 1985; Sarpkaya, 1986).

$$\beta = \frac{Re}{K_C} \tag{3.11}$$

3.3.6 Mass-Damper Models

Klose (1966) defined the lift coefficient for an oscillating hydrofoil as Equation 3.12, where A is the projected foil area normal to the flow (e.g. $A = cL$ at zero pitch angle),

and α_{osc} is the ratio of transverse oscillating velocity (heaving velocity) $\dot{h}$ to mainstream velocity u. Klose (1966) also defines the lift coefficient to have a component in-phase to the heaving velocity and a 'quadrature' component (assumed to be 90° out of phase with the velocity and hence in-phase with the heave acceleration).

$$c_{Kl} = \frac{2F_l}{\rho u^2 A \alpha_{osc}} \qquad where \qquad \alpha_{osc} = \frac{\dot{h}}{u} \tag{3.12}$$

Similarly to Klose (1966), Newman (1977) and Falnes (2002) also equate the total force on an object in an oscillatory flow to be the sum of a velocity proportional component and an acceleration proportional component as in Equation 3.13. Newman (1977) refers to the coefficients a and b as the apparent damping and apparent mass respectively. Similarly, Falnes (2002) refers to the in-phase and out-of-phase component coefficients as the mechanical impedance Z_m and the radiation impedance Z_r as presented in Equation 3.14. In the case of a submerged oscillating object, the mechanical impedance is represented by mechanical resistance R_m, and the radiation resistance R_r, which represent energy losses in the form of viscous damping and surface wave generation. The radiation impedance is represented by the the mass of the object $i\omega m_m$, and the radiation reactance $X_r = i\omega m_r$, where m_r is the added mass.

$$F = a\dot{u} + bu \tag{3.13}$$

$$\hat{F} = (Z_m + Z_r)\hat{u} = (R_m + R_r + i\omega(m_m + m_r))\hat{u} \tag{3.14}$$

3.3.7 Surface Waves

The dynamics of surface waves generated by a submerged oscillating object may be affected by gravity or surface tension. Waves dominated by the effects of gravity are known as gravity waves, and those dominated by the effects of surface tension are known as capillary waves. Both types of waves have an associated wave number k. They can be found by solving either Equation 3.15 Dean and Dalrymple (1991) or Equation 3.16 respectively. The wave number of a gravity wave depends on the depth of submersion d

and the acceleration due to gravity g, while wave number of a capillary wave depends on the surface tension σ and the density of the heavier and lighter fluids, ρ and ρ' respectively.

$$\omega^2 = gk_g \tanh(k_g d) \tag{3.15}$$

$$\omega^2 = \frac{\sigma}{\rho + \rho'} |k_c|^3 \tag{3.16}$$

The wave length is related to the wave number as per Equation 3.17 (Dean & Dalrymple, 1991). Surface waves with a long wave length are usually dominated by the effects of gravity, while waves with a short wave length are most influence by surface tension. The wavelength dividing these two conditions is known as the critical wavelength λ_c (Equation 3.18), which is about 17 mm for an air-water interface.

$$\lambda = \frac{2\pi}{k} \tag{3.17}$$

$$\lambda_c = 2\pi \sqrt{\frac{\sigma}{(\rho - \rho')g}} \tag{3.18}$$

3.3.8 Drag and Inertia Contributions

The breakdown of the total force on an object in an oscillatory flow in the above models of Klose, Newman and Falnes is different from the Morison Equation (Equation 3.6) because the drag (or damping) term is proportional to velocity rather than velocity squared. Newman (1977) explains that the extremes of the Keulegan-Carpenter number domain, K_C=0 and K_C=∞, can be modelled well with a mass damper model or a steady state drag model respectively. However, when the heave-to-chord ratio is near unity neither model accurately predicts the forces on an oscillating object. For engineering in this range, the Morison equation is usually used as an approximation (Newman, 1977). Table 3.1 shows the modelling suggestions of Journée and Massie (2001) for respective Keulegan-Carpenter number ranges.

Both the steady state model and the mass damper models described previously are for single dimension flows and so may or may not be appropriate for use with oscillating

Table 3.1. Contributions of drag and inertia with model suggestions for Keulegan-Carpenter number ranges (Journée & Massie, 2001).

K_C range	Force contributions	Model Suggestion
$K_C < 3$	Inertia force dominant	Neglect drag and use inertia term from the Morison equation
$3 < K_C < 15$	Inertia forces with linear drag	Mass damper model, i.e. linear drag and inertia
15 $K_C < 45$	Inertia forces with non-linear drag	Morison equation
$K_C > 45$	Drag force dominant	Neglect inertia and use steady state drag equations

foils with some forward velocity (transverse to the oscillation axis). At zero velocity the forces on the foil may be initially approximated with a mass damper model. However, once a jet is established the suitability of this model may change due to the induced flow. Furthermore, the K_C ranges in Table 3.1 are for a cylinder in a sinusoidally oscillating flow and so may now apply to other objects or oscillating flows with higher order harmonics.

3.3.9 The Basset-Boussinesq-Oseen Equation

The Basset-Boussinesq-Oseen (BBO) Equation, named after Alfred Barnard Basset, Joseph Valentin Boussinesq and Carl Wilhelm Oseen, is used to describe the forces on a particle in an unsteady flow at low Reynolds numbers. C. Zhu and Fan (1998) write the BBO Equation for a spherical particle of diameter d_p and density ρ_p moving with velocity U_p in a fluid with a mainstream flow velocity of U_f as Equation 3.19. The equation is in the form of Newton's second law with the left hand side being the mass and acceleration of the particle, and the right hand side being the fluid forces acting on the particle. The terms used to describe the fluid force (from left to right) represent drag, pressure gradients, added mass and the Basset force with the final term representing the sum of other forces on the particle, such as gravity.

$$\frac{\pi}{6}d_p^3\rho_p\frac{\mathrm{d}U_p}{\mathrm{d}t} = 3\pi\mu d_p\left(U-U_p\right) - \frac{\pi}{6}d_p^3\nabla p + \frac{\pi}{12}d_p^3\rho\frac{\mathrm{d}}{\mathrm{d}t}\left(U-U_p\right) + \frac{3}{2}d_p^2\sqrt{\pi\rho\mu}\int_{t_0}^{t}\frac{1}{\sqrt{t-\tau}}\frac{\mathrm{d}}{\mathrm{d}\tau}\left(U-U_p\right)\mathrm{d}\tau + \sum_i F_i \tag{3.19}$$

When the acceleration of an object is sufficiently high, viscous effects cause a temporal delay in the development of the boundary layer. The hydrodynamic force associated with the lagging boundary development is called the Basset force, named after Basset (1888) (also known as the Boussinesq-Basset force or the history term). In unsteady flows, the Basset force contributions significantly towards the precision calculation of hydrodynamic forces (Candelier, Angilella, & Souha, 2004). Although the BBO Equation is commonly applied at low Reynolds numbers ($Re < 1000$), Rostami, Ardeshir, Ahmadi, and Thomas (2006) showed that contributions of the Basset force may still be significant at higher Reynolds numbers. However, the relative contribution of the basset force was shown to decrease as the Reynolds number was increased.

3.4 Flapping Wing Propulsion

In the field of marine engineering the terms surge, sway and heave are used to describe the position of a ship in 3-dimensional space. These three terms refer to a ship's position in the forward-astern, starboard-port and up-down directions respectively. Similarly the orientation of the ship can be described in terms of rotation angles about these three axes (see Figure 3.6). Roll refers to rotation about the surge axis, pitch is rotation about the sway axis and yaw is rotation about the heave axis. In the current literature, these terms are commonly used to describe the motion of a flapping foil.

Terms such as 'flapping' are used loosely throughout the literature to describe the motion of a foil. Figure 3.7 illustrates common modes of 'flapping' motion, and terms used to describe these motions are defined here:

Oscillating: Describes an object going through a periodic motion whether that motion be harmonic, non-harmonic, uni-dimensional, two dimensional or three dimensional.

Can be used when referring to pure heaving, pure pitching or combined pitching and heaving motions.

Pitching: An object undergoing rotational oscillations about an axis located on the object's chord, between $x/c = 0$ and $x/c = 1$, aligned with the object's span. Lai and Platzer (2000) describe a pitching foil to be one that "oscillates about a pivot, resulting in different angles of incidence at difference phases".

Heaving: Describes oscillating linear translation aligned with the heaving axis. Lai and Platzer (2000) also use the term *flapping* to describe this motion. Heaving is also known to as *plunging* in the literature.

Flapping: Combined translational and rotational motion in the heave-surge plane. The translational and rotational motions are usually the same frequency, but often have some phase difference.

Root-flapping: A combination of periodic rotary motion about an axis parallel to the surge axis and rotary motion about the pitching axis.

For the case of a vertically oscillating foil undergoing planar motion (similar to a fish's tail), where the foil's span is always parallel to the sway axis, the foil's position, and orientation, can be fully defined in terms of surge, heave and pitch (see Figure 3.8). In the following experimental work only pure heaving motions are considered to constrain the movement of the foil to a single linear axis. The only axis of rotation considered is pitch.

3.4.1 Unsteady Foil Parameters

Unsteady Angle of Attack

Because of the relative motion between the hydrofoil and the water, there are a number of flow velocities and angles to consider. There are no standard terms or notation for these variables in the current literature. The notation used to express the foil's general motion, and motion relative to the fluid is as follows.

The horizontal velocity of the water relative to the craft, is simply the water velocity u. In the case of a water craft driving through still water this would be the craft speed. The

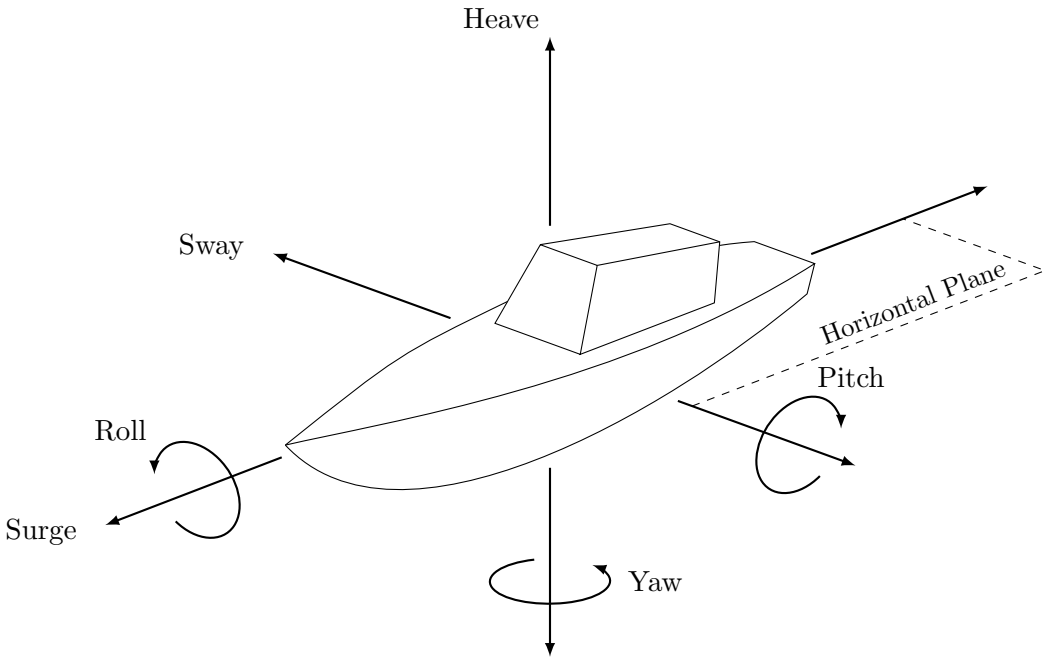

Figure 3.6. Dynamic positioning axes.

heave position, velocity and acceleration (h,$\dot{h}$,$\ddot{h}$) are the foil's vertical position, velocity and acceleration respectively. If the foil has some horizontal component to its oscillating movement, this is the foils' surge position, velocity and acceleration (s,$\dot{s}$,$\ddot{s}$). The pitch angle of the foil with reference to the horizontal is the pitch angle, θ. For harmonic pitching and heaving, the pitch may be out of phase with the heave by phase angle ψ. When pitching leads heaving, ψ is positive.

For a heaving foil, adding the negative heaving velocity vector with the water velocity vector, results in the effective water velocity vector $\hat{u}_e$ (Equation 3.20). As pictured in Figure 3.9, the angle between the effective water velocity and the zero pitch plane is denoted the heave-induced angle of attack, α_h. Heave-induced angle of attack can be calculated with Equation 3.21, assuming the water velocity vector is normal to the heave-sway plane. Knowing the pitch angle, and the heave-induced angle of attack, the instantaneous angle of attack can be found with Equation 3.22. Figure 3.9 shows these

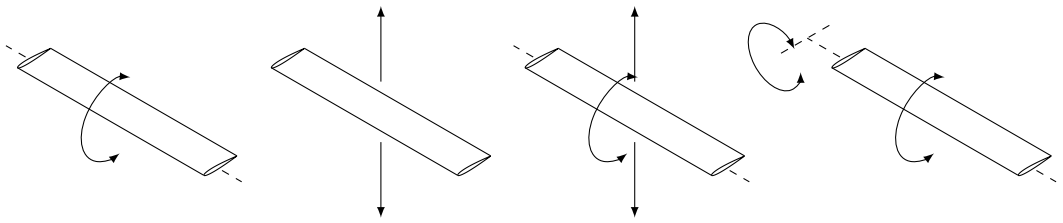

(a) Pitching **(b)** Heaving **(c)** Flapping **(d)** Root flapping

Figure 3.7. Flapping motions.

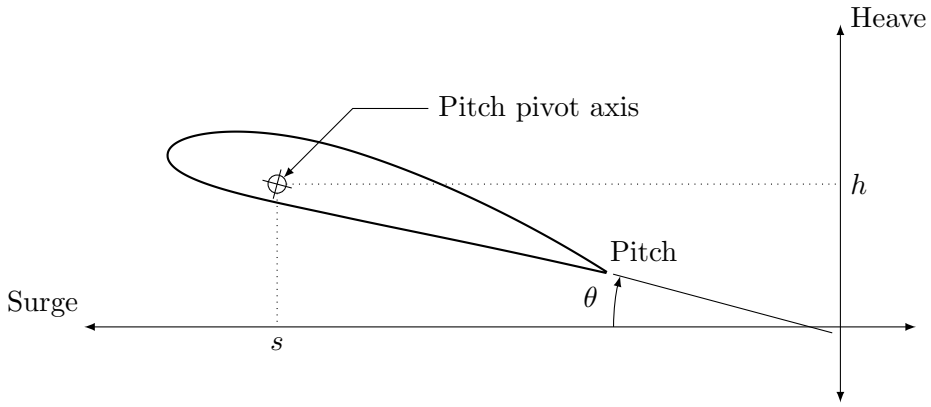

Figure 3.8. Axes defining a vertically oscillating foil's position.

angles and vector velocities.

$$\hat{u}_e = \hat{u} - \hat{\dot{h}} \tag{3.20}$$

$$\alpha_h = tan^{-1}\left(\frac{\dot{h}}{u}\right) \tag{3.21}$$

$$\alpha = \theta - \alpha_h \tag{3.22}$$

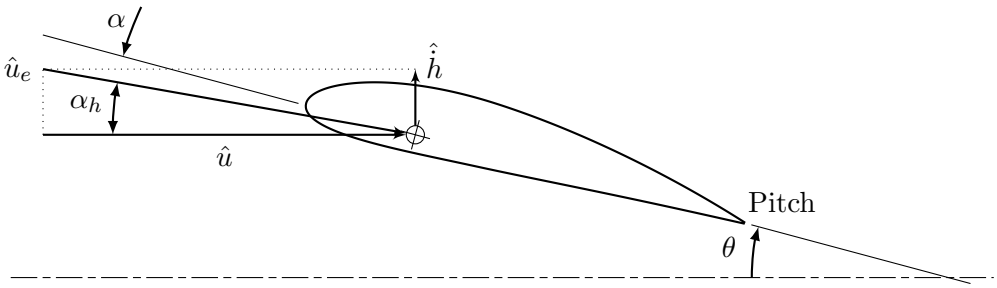

Figure 3.9. Angle of attack of a heaving foil

Strouhal Number

Since G. S. Triantafyllou et al. (1993) revealed that most flapping wing creatures cruise in the Strouhal number range of 0.2-0.4, it is common to find data plotted in the Strouhal number domain. Thrust and lift coefficients as well as efficiencies are usually displayed as a function of the Strouhal number around the area of peak efficiency. Peak efficiency usually occurs around a Strouhal number of 0.3 (G. S. Triantafyllou et al., 1993) so data is usually measured and displayed over the Strouhal range of approximately 0-0.6 (Anderson, Streitlien, Barrett, & Triantafyllou, 1998; Read et al., 2003; G. S. Triantafyllou et al., 1993). Ashraf et al. (2007) used numerical simulations to investigate a much larger range of non-dimensional flapping velocities ($kh = \pi St$) than previously observed in the literature and reported results that agreed with current studies. Furthermore, the Strouhal number is seen as the principal scaling parameter for steadily flapping high aspect ratio foils (M. S. Triantafyllou, Hover, Techet, & Yue, 2005).

The Strouhal number, named after physicist Vincenz Strouhal (1850-1922), is a dimensionless quantity usually associated with oscillating flows. The wake Strouhal number considers the heaving amplitude as well as the flow velocity and frequency of oscillations. The Strouhal number can be calculated with Equation 3.23 where f is the oscillations frequency, V is the flow velocity and D is a characteristic length. Sometimes the flow velocity to oscillating frequency ratio is substituted for the wavelength or stride length λ (Figure 3.10). For an oscillating foil, the flow velocity V is the average mainstream velocity and the characteristic length D is usually taken to be the initial width of the wake. However, since the width of the wake is not known, it is approximated. Other characteristic lengths

used in the literature are the chord length of the foil, and the vertical distance between the leading and trailing edge of a heaving foil (Cleaver et al., 2009). The wake Strouhal number (using the initial wake width as the characteristic length) is the most common dimensionless parameter to display data against. However, some researchers still choose to plot data against the chord based Strouhal number defined in Equation 3.24.

$$St = \frac{fD}{V} = \frac{D}{\lambda} \tag{3.23}$$

$$St_c = \frac{fc}{u} \tag{3.24}$$

For heaving foils, the initial width of the wake is approximated by the trailing edge excursion, A_t (M. S. Triantafyllou et al., 1991), i.e. the heave stroke: $2h_0$ (Equation 3.25). For flapping foils, the trailing edge excursion may not necessarily be equal to the heave stroke. However, it is still usually used as an approximation of the initial wake width. When the heave stroke is used as the characteristic length, and the foil is undergoing simple harmonic motion, the Strouhal number is the ratio between the maximum heaving velocity $2h_0f$ and the mainstream flow velocity u.

$$St = \frac{fA_t}{u} = \frac{2h_0f}{u} \tag{3.25}$$

When oscillations are dominated by rotational motion, i.e. when heaving motions ($2h_0$) contribute little towards the wake width, the Strouhal number may not be considered the governing parameter (G. S. Triantafyllou et al., 1993; M. S. Triantafyllou et al., 1991). In this case the reduced frequency (see Section 3.4.1) multiplied by the pitching amplitude is sometimes used as the primary dimensionless parameter.

In the field of vortex induced vibrations (VIV), the reduced velocity (V_r) is defined as the mean flow velocity V, divided by the response oscillation frequency f_r and a characteristic length of the oscillating section D (usually the diameter of a pipe) (Jaiswal & Vandiver, 2007). This is equivalent to the inverse of the Strouhal number (Equation 3.26), suggesting that flapping wing propulsion and VIV are governed by similar phenomenon

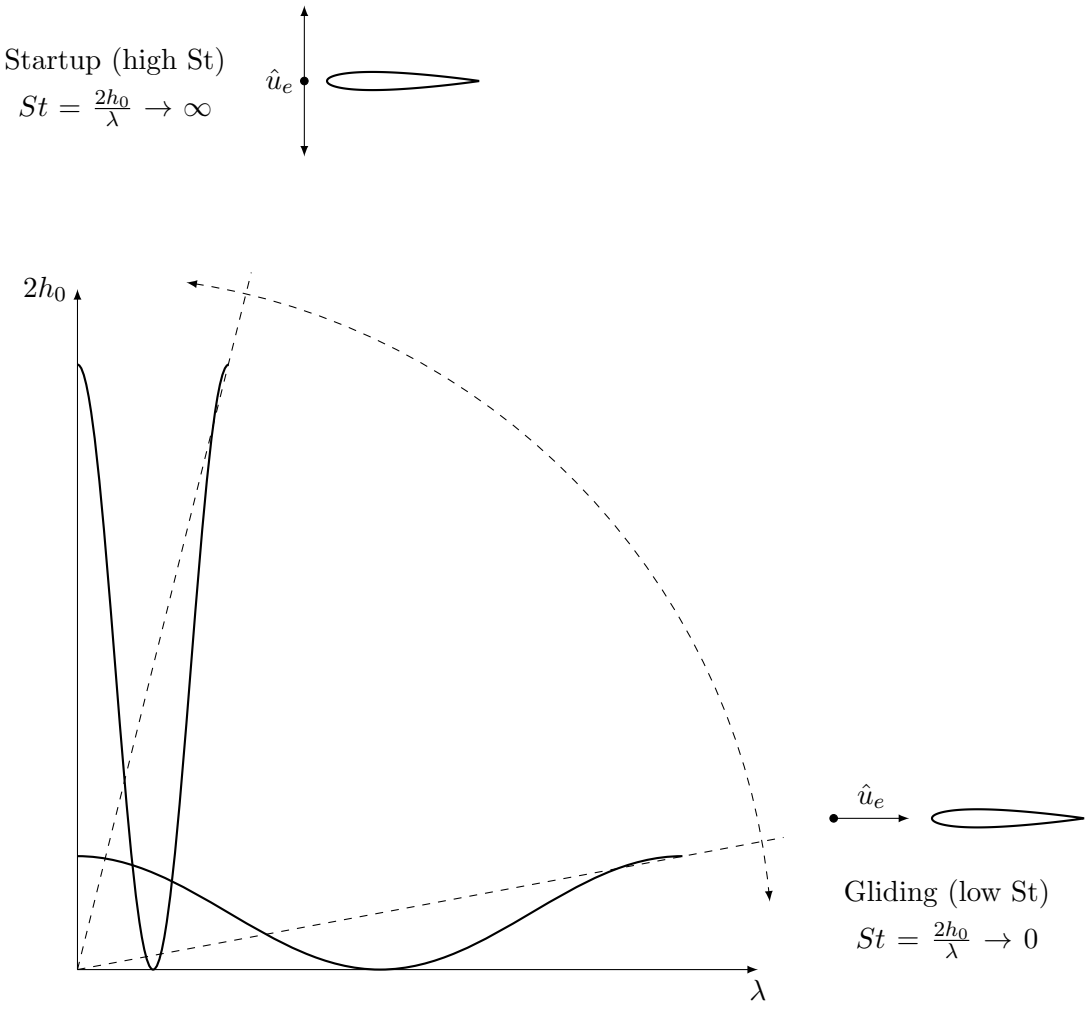

Figure 3.10. Illustrative explanation of the Strouhal number for flapping wing propulsion

(i.e. vortex shedding).

$$V_r = \frac{V}{f_r D} = \frac{1}{St} \tag{3.26}$$

Reynolds Number

As with most fluid flow studies, the Reynolds number is considered as it indicates the flow regime around an object. Equation 3.27 defines the Reynolds number where V is the flow velocity, D is some characteristic length and ν is the kinematic velocity of the fluid. When the Reynolds number is evaluated for steady or unsteady foils, V is the main stream velocity and D is usually the chord length of the foil.

$$Re = \frac{VD}{\nu} = \frac{uc}{\nu} \tag{3.27}$$

The simulations of Visbal (2009) showed that at low Reynolds numbers (3×10^4 - 4×10^4), and Strouhal numbers ($St < 0.12$), the drag on a heaving foil decreased with decreasing Reynolds numbers and Strouhal numbers. Later, simulations of Ashraf, Young, and Lai (2011) showed that at higher Strouhal numbers ($St = 0.32$) the thickness of a symmetrical heaving foil significantly affected its mean thrust and efficiency. Moreover, optimum foil thickness varied over the Reynolds number range of 2×10^2 - 2×10^6. In general, flapping wing propulsion has been proven effective over a wide range of Reynolds numbers (Lighthill, 1970; G. S. Triantafyllou et al., 1993) with thrust and efficiency increasing slightly with increasing Reynolds numbers (M. S. Triantafyllou et al., 2005). Furthermore, G. S. Triantafyllou et al. (1993) observed that animals preferred to cruise around a particular Strouhal number over a large range of Reynolds numbers and concluded that the Strouhal number was the most important parameter for predicting flapping wing performance.

As defined earlier, the effective flow velocity that the foil encounters is the vector sum of the heaving velocity and the mainstream velocity (Equation 3.20). Hence maximum effective flow velocity is a function of heaving velocity, and may be significantly faster than the mainstream flow velocity. If the Reynolds number for an unsteady foil is calculated based on the maximum effective fluid velocity, the Reynolds number may also be signifi-

cantly higher. Equation 3.28 shows the relationship between the steady Reynolds number Re_u, and the unsteady Reynolds number Re_{u_e}. Figure 3.11 is a plot of Re_{u_e} normalised by Re_u as a function of the Strouhal number.

$$Re_{u_e} = \sqrt{1 + (\pi St)^2} Re_s \tag{3.28}$$

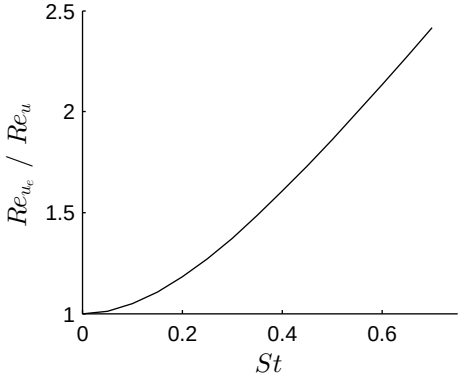

Figure 3.11. Unsteady-to-steady Reynolds number ratio against Strouhal number

Reduced Frequency

Another dimensionless variable used to describe the state of an oscillating foil is the reduced frequency. The reduced frequency is commonly employed as the dimensionless parameter defining the amplitude of a body's pitching oscillations relative to the fluid mainstream velocity in areas such as flutter. Thrust coefficients, lift coefficients, and efficiency were often displayed as a function of reduced frequency. In most recent research, the reduced frequency has largely been superseded by the Strouhal number.

The reduced frequency is defined as the product of a characteristic length and oscillating frequency, divided by the mainstream velocity of the fluid. In more practical terms, MacCready (1986) defines the reduced frequency as "a measure of how many times we flap for each chord length we travel forward". M. S. Triantafyllou, Triantafyllou, and Yue (2000) describes the reduced frequency as "comparing the spatial wavelength of the flow disturbance with the chord length (of the hydrofoil)".

Garrick's (1936) original definition of the reduced frequency, k_G, which most re-

searchers prefer to use is referred to as the 'Garrick reduced frequency' (Harper, Berkemeier, & Grace, 1998; Heathcote, Wang, & Gursul, 2008; Jung & Park, 2005; Klose, 1966; Koochesfahani, 1989; Young & Lai, 2001). The Garrick reduced frequency is defined in Equation 3.29. Other researchers prefer to define the reduced frequency as twice the Garrick reduced frequency, k_{2G} , and use the definition provided in Equation 3.30 (Ashraf et al., 2011; Jones & Platzer, 2001; Lai & Platzer, 2000). In this form, the reduced frequency multiplied by the heave-to-chord ratio ($k_G h^*$) is equivalent to πSt. Ashraf et al. (2011); Jones and Platzer (2001); Lai and Platzer (2000) refer to $k_G h^*$ as the plunge velocity.

Another definition of the reduced frequency is the Garrick reduced frequency over π (Tay & Lim, 2009). This is also referred to as the chord based Strouhal number (Cleaver et al., 2009; Kudela & Kozlowski, 2010; Murray & Howle, 2003) and is defined in Equation 3.24. The inverse of the chord based Strouhal number, Equation 3.31, is known as the foil advance coefficient (Yamaguchi & Bose, 1994).

$$k_G = \frac{\omega c}{2U} = \frac{\pi f c}{U} \tag{3.29}$$

$$k_{2G} = \frac{2\pi f c}{U} \tag{3.30}$$

$$J = \frac{U}{fc} = \frac{1}{St_c} = \frac{\lambda}{c} \tag{3.31}$$

3.5 Flapping Wing Propulsion Performance

Rotary propellers provide a simple, robust, and versatile form of propulsion. They typically only have one time-dependent degree of freedom (the rotational position). The state space of an oscillating foil is comparably large, and so a large amount of research has been done to correlate the performance of an oscillating foil with various parameters. Many of these parameters have been narrowed down to optimum ranges. In this section, a summary of known oscillating foil performance is presented.

3.5.1 Pitching, Plunging, and Angle of Attack

Garrick (1936) analytically predicted that a heaving foil may produce thrust at any oscillating frequency, but a pitching foil may only produce thrust above a critical frequency f_c. Koochesfahani (1989) later showed that the critical frequency was amplitude dependent and that it was higher than Garrick (1936) had predicted. Zhen, Beom-soo, Moo-rong, and Ji-yuan (2008) simulated a hydrofoil undergoing pure pitching about $c/3$ and compared their results with experimental data. Their simulations were validated at low frequencies before the model was used to predict force cycles at higher pitching frequencies ($f > f_c$). They observed the existence of the critical frequency for a pitching foil and frequency proportional phase shift between the angle of attack and force cycle on the foil.

Contrary to Garrick's prediction, it has been shown that heaving foils still create drag at low oscillating frequencies (low St) (Kudela & Kozlowski, 2010; Lai & Platzer, 1999; Yang & Lee, 2006; Young & Lai, 2001). Lai and Platzer (1999) found that a plunging NACA0012 foil begins to make a positive mean thrust for Strouhal numbers over 0.13. Yang and Lee (2006) found that a NACA0010 foil produces thrust from a Strouhal number of 0.08 and mapped its wake structure against reduced frequency and heave-to-chord ratio. Similarly, Kudela and Kozlowski (2010) mapped the wake structure of a heaving foil, with an elliptical cross-section, and found that thrust production was dependent on both Strouhal number and heave-to-chord ratio. Young and Lai (2001) observed significantly different wake structures, for a common reduced frequency (or Strouhal number), by varying the heave amplitude and oscillating frequency of a heaving foil. This would suggest that the hydrodynamic force cycle on the foil, would also vary with independent changes in heave amplitude and frequency.

Lai and Platzer (2000) investigated the velocity field around a heaving NACA0012 foil at zero free-stream velocity, and concluded that the normalised stream-wise wake velocity profile, was independent of oscillating frequency, and may be described by the non-dimensional heave amplitude. Their results showed that the thrust was proportional to the oscillating frequency. Similarly, observation of swimming dolphins has shown linear correlation between tail-beat frequency and velocity. Alben and Shelley (2005) investigated the flow field around an unconstrained heaving ellipse with zero pitch at zero free-stream

velocity and found that interaction between vortices shed on the upstroke and downstroke caused the symmetrical body to accelerate in the surge direction. They also found that the shape of the oscillating ellipse and its density relative to the fluid density affected the stability of the surge velocity. Vandenberghe et al. (2006) showed that this was effect was also applicable to a flat plate with symmetry in the surge and heave planes. They also found that the forward velocity achieve by the oscillating plate was proportional to the peak oscillation velocity.

Combining pitching and heaving motions, expands the state space of an oscillating hydrofoil considerably. The mean thrust and propulsive efficiency of flapping motions are proven capable of exceeding the performance of single degree of freedom motions (Ashraf et al., 2011). The phase difference between pitching and heaving has been shown to play a major role in the efficient generation of thrust. Anderson (1996) suggests that trailing edge vortex shedding is only significant for small oscillation amplitudes ($h^* < 0.5$), while leading edge vortex shedding significantly influences wake structure for large oscillating amplitudes. Furthermore, for efficient thrust generation, a moderately strong vortex should form at the leading edge of the foil, and convect downstream, to combine with the vortex shed at the trailing edge and produce a reverse von Kármán street (see Section 3.5.6) (Anderson, 1996; Guglielmini & Blondeaux, 2004). Hence, the timing between leading and trailing edge vortex shedding is critical, and can be controlled by adjusting the phase between heaving and pitching motions. A phase angle of 90° (pitch leading heave) provides the most robust performance for a flapping foil . However, relatively small gains can be made by varying the phase by ±10° (Read et al., 2003). Read et al. (2003) showed that gains in efficiency were made by using a phase of 80° at low Strouhal numbers. However, the increase in efficiency came with reduction in thrust. Jones and Platzer (2001) and Read et al. (2003) found that efficiency and thrust could be increased by using a phase angle of 100° at high Strouhal numbers. Although phase can modify a flapping foil's performance, Read et al. (2003) conclude that there is no real benefit to phase angles other than 90°.

Hover, Haugsdal, and Triantafyllou (2004) investigated the effect of angle of attack profiles on flapping wing performance. Results yielded that saw-tooth and square wave

angle of attack profiles achieved high thrust and high efficiency respectively, but never both. The cosine wave (half way between a square and saw-tooth wave) achieved reasonably high thrust coefficients as well as high efficiencies. Flow visualisation experiments confirmed that two thrust vortices were shed per cycle with a cosine angle of attack profile, even at high St. They are expected to be shed at points of maximum $\dot{\alpha}$ (Anderson, 1996; Hover et al., 2004). Hover et al. (2004) also observed that for plain heaving motion, two vortices are shed per cycle at low St, but as many as six vortices are shed per cycle at high St. The extra vortices corrupt the thrust wake and reduce thrust and efficiency (see also Section 3.5.6).

Read et al. (2003) showed that small changes in a heaving profile can drastically change the angle of attack profile, due to the $\arctan(x)$ component of the heave-induced angle of attack (see also Appendix D). This can be corrected by modifying either the heaving profile or the pitching profile with higher-order harmonic terms. Read et al. (2003) showed that a corrected heaving profile may vary less than 6 % from a simple harmonic heaving profile. However, small heave corrections have a significant effect on the angle of attack profile. Later Xiao and Liao (2010) investigated how corrected heaving and pitching profiles increased the performance of an oscillating foil and found that modified pitching profiles obtained better thrust and efficiency than modified heaving profiles. In the work of Read et al. (2003) and Xiao and Liao (2010), heaving and pitching motions have pre-prescribed parametric profiles and are forced under closed-loop control or as simulation boundary conditions. The effect of other non-sinusoidal heaving profiles achieved under open-loop control oscillations is not well known. Moreover, this is a case of interest for human-powered oscillating foil propeller design.

Fixed wing stall is due to flow separation and the formation of vortices behind the wing, which disrupts the normal, smooth flow. However, M. S. Triantafyllou and Triantafyllou (1995) highlight that vortex formation behind a flapping wing does not necessarily lead to stall, and in fact may generate thrust. These results demonstrate that the steady stall angle does not apply to unsteady foils. M. S. Triantafyllou and Triantafyllou (1995) found that a flapping foil was most efficient when the maximum angle of attack was between 15° and 25°. Once the angle of attack exceeded 30° significant stall begins to occur. This is

consistent with the maximum angle of attack of a dolphin tail (Fish, 1993).

Even if the upstroke and the downstroke of a foil are symmetrical the load profile on the foil may not be. When plotting force coefficients against angle of attack, it is common to observe a coefficient loop, which is sometimes referred to as a lift, drag or moment hysteresis (Hubel & Tropea, 2009; Hutchison, Brandner, Binns, Henderson, & Walker, 2010; Ko & McCroskey, 1995; Umar, Hamdani, ul Haque, Chaudhry, & Parvez, 2009). Differing upstroke and downstroke force coefficient profiles may be due to an asymmetric foil profile, a non-zero mean angle of attack, wake deflection, or asymmetric velocity, or acceleration profiles. For example, Videler and Kamermans (1985) analysed photo sequences of a swimming dolphin to determine the pitch angle, and 2-D velocity of its tail. Their results showed that the dolphin accelerated on the downstroke and decelerated on the upstroke. Fish (2006) published computer tomography scans showing a dolphin tail cross-section, revealing that the tail has an asymmetrical profile.

3.5.2 Hydrofoil Geometry

Gorelov (2009) investigated the effect of foil thickness on the efficiency of a vertical axis wind turbine, and found that peak efficiency occurred when the thickness was between 18 % to 20 % of the chord length. He noted that this is also the relative thickness of dolphin tails. Mantia and Dabnichki (2011) simulated oscillating symmetrical foils of various thickness, and concluded that thicker sections produced more thrust. This correlation did not explain nature's preference for thin wings. However, when they assumed a constant density for the foils, and compared the thrust per unit mass of foil produced, thin foils were preferred. When mass is a factor, Mantia and Dabnichki (2011) show that it is beneficial to minimise the thickness of an oscillating foil. Mantia and Dabnichki (2011) also simulated the spanwise shape of foils, with constant cross sections, and determined that a small positive (10°) sweep angle, symmetrical about the mid span, gave a slight improvement in the thrust coefficient. Simulations by Ashraf et al. (2011) show that there is some optimal foil thickness, for an oscillating foil, which is dependent on the Reynolds number and the foil's motion profiles.

Ashraf et al. (2011) simulated the influence of camber on thrust produced by a heaving

foil. They concluded that a cambered foil produces the same mean thrust as a symmetrical foil of comparable thickness. However, the thrust profile of an asymmetric foil is asymmetric. Due to interactions with the leading edge vortex, an asymmetric foil will produce more thrust on the downstroke (travelling towards the centre of camber) than on the upstroke.

Ozen and Rockwell (2010) discovered through PIV measurements that leading edge sinusoidal protuberances (as seen on humpback whale flippers) could greatly reduce spanwise flow over a root flapping wing. This may be an alternative solution to end plates, for reducing spanwise flow. Sahin, Sankar, Chandrasekhara, and Tung (2003) investigated the affects of a deformable leading edge on dynamic stall. They found that the leading edge shape effects the stall characteristics of the aerofoil. However, the shape rate of change had little influence.

Some foil profiles are proven to be more suitable for flapping wing propulsion than others. MacCready (Accessed 2012) used a NACA4415 profile for the main wing on his Pogo Foil. The S1020 foil profile was designed by Michael Selig specifically for use in ornithopters (DeLaurier & Harris, 1993). The NACA4415 and the S1020 profiles are very similar. Figure 3.12 shows a comparison of these two profiles. Tay and Lim (2009) considered several asymmetric foil profiles for flapping wing propulsion, and found that the S1020 had the best overall performance of the tested profiles. Surface details aside, Lai and Platzer (2000) suggest that foils with a rounded leading edge, and sharp trailing edge will produce forwards static thrust from zero free stream velocity.

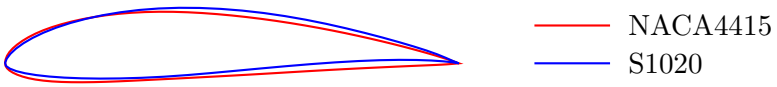

Figure 3.12. A comparison of the NACA4415 and S1020 profiles

3.5.3 Flexible and Sprung Foils

It has been noted that wings of birds and aquatic animals are flexible due to the finite stiffness of bone. Studies have also shown that the chordwise and spanwise flexibility of

an oscillating foil can significantly affect its efficiency. Heathcote et al. (2008) showed that a foil with limited spanwise flexibility can generate greater thrust than a rigid wing. However, a foil with too much spanwise flexibility has a poor thrust coefficient. Heathcote et al. (2008) suggested this was because the wing tips were significantly out of phase with the wing root, which disrupted the reverse von Kármán street. Heathcote et al. (2008) also noted that higher Strouhal numbers demanded stiffer wings to maintain efficiency.

Prempraneerach, Hover, and Triantafyllou (2003) showed that chordwise flexible hydrofoils can be significantly more efficient than rigid hydrofoils, for Strouhal numbers less than 0.45, when the flexibility is properly selected. Prempraneerach et al. (2003) recorded increases in efficiency of up to 36 % relative to a rigid foil. However, the increase in efficiency also came with a small drop in the thrust coefficient. Prempraneerach et al. (2003) concluded that flexible hydrofoils can be very efficient and can be proven to be competitive with rotary propellers. Yamamoto, Terada, Nagamatu, and Imaizumi (1995) also concluded that foils with suitable chordwise flexibility could be used for ship propulsion. Similarly, Chaithanya and Venkatraman's (2008) analysis of a chordwise flexible foil in pure heaving concluded that efficient thrust production was possible with suitable foil flexibility.

Sprung foils have been investigated for possible efficiency gains, and a means of passive controlling pitch. Harper (1997) modelled a sprung foil (see Section 3.6.1) to simulate the stiffness of fish tendons. The model predicted increased efficiency with a suitable spring stiffness. Murray and Howle (2003) explored the use of a spring to reduce a dual actuator (pitching and heaving) propulsion system, to a single actuator system. Murray and Howle (2003) showed that optimal spring stiffness was dependent on oscillating frequency. Furthermore, human-powered hydrofoils such as the Trampofoil, Aquaskipper, Pumpabike, and Aqueon have all successfully employed springs for passive pitch control.

3.5.4 Tandem Hydrofoils

When multiple foils are moving in close proximity, the forces on each foil will differ from forces experienced in the mainstream flow. The interactions between multiple foils have been studied for beneficial effects on their combined performance. When foils are in

pairs, the two common arrangements are biplane arrangement (Figure 3.13a) and, tandem arrangement (Figure 3.13b). The Wasserläufer (see Section 2.2.1), and the Aqueon (see Figures 2.2 and 2.12), are good examples of foils in tandem arrangement oscillating in counter-phase.

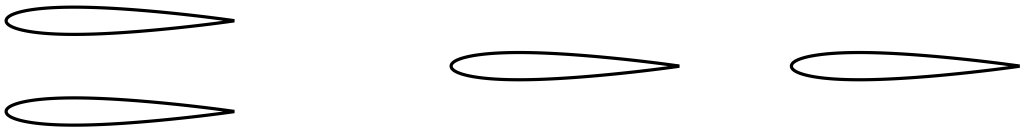

(a) Biplane arrangement. **(b)** Tandem arrangement.

Figure 3.13. Two common arrangements for foil pairs.

Just as an oscillating foil in a steady flow can generate thrust, a steady foil in an oscillating flow can also generate thrust. The later routine is known at the Katzmayr Effect (also known as the Knoller-Betz effect or the Schmidt effect). The observation of flow around fish has made apparent advantages of tandem foils. Akhtar, Mittal, Lauder, and Drucker (2007) observed that a fish will shed a vortex from its head or dorsal fin, then later manipulate the vortex with their tail fin. This vorticity control routine is one reason why fish are suspected to be very efficient swimmers.

Steady or oscillating foils operating sufficiently close to a free surface will generate surface waves. Most conventional hydrofoil boats have a pair of steady foils in tandem configuration. In this layout, the trailing foil travels below the surface waves generated by the leading foil. If the trailing foil is located in the up-wash region of these surface waves (i.e. has an effective flow vector with some positive vertical component), the lift vector inclines forward, reducing drag, and can possibly generate thrust (see Figure 3.15) (Matveev & Duncan, 2005). This effect is also utilised by surfers to propel themselves forward using wave energy. This method of thrust generation could be seen as a steady example of the Katzmayr effect.

Oscillating tandem foils need not be near a free surface to make use of this effect. Instead, the trailing foil may benefit from the wake of the leading foil. Schmidt (1965b) was the first to apply this method of thrust generation when he invented the 'wave propeller'

in 1965. The wave propeller comprised a pair of foils, in tandem arrangement, with only the leading foil oscillating. The idea behind this arrangement was to let the fixed trailing foil exploit the Katzmayr effect, recovering energy from the wake of the leading foil.

Numerical studies by Jones and Platzer (2001) show that the trailing wing in a tandem arrangement should contribute a significant thrust gain (due to the Katzmayr effect). However, Jones and Platzer (2001) were not able to experimentally confirm their predictions and suspected that the viscous drag on the trailing foil may counteract additional thrust production. Tay and Lim (2009) and Lim and Tay (2010) simulated the performance of a single S1020 and tandem S1020 foils. They predicted that varying the streamwise spacing and phase between the leading and trailing foils would considerably vary the thrust, lift and efficiency of the foil pair. They suggest that optimal foil spacing (leading edge to leading edge) is two chords, and that the phase can be varied to maximise either the efficiency, thrust or lift. Akhtar et al. (2007) also found phase to be the key parameter for controlling thrust production. Tay and Lim (2009) and Lim and Tay (2010) predict that tandem foils may have a combined mean thrust coefficient over double that of a single foil.

Jones and Platzer (2001) studied the effects of a solid boundary near an oscillating foil and discovered that thrust increased with decreasing distance from the boundary. At some optimum distance from a wall, the jet velocity (see Figure 3.14c) could be almost doubled compared to free stream equivalents. These affects also apply to foil pairs in a biplane arrangement heaving in counter-phase.

3.5.5 Efficiency of a Flapping Hydrofoil

The efficiency of an oscillating foil is an important measure of its performance. It is also the easiest way to compare the performance of an oscillating foil to the performance of a rotary propeller. The efficiency of an oscillating foil is defined as the ratio of useful propulsive power to the input power (Equation 3.32) (Anderson et al., 1998; Prempraneerach et al., 2003). The input power can be found with Equation 3.34, where F_h and M are the heaving force and pitching moment respectively. The output power can be calculated with Equation 3.33, where F_s is the thrust aligned with the mainstream velocity,

and T is the oscillation period.

$$\eta = \frac{P_{out}}{P_{in}} \tag{3.32}$$

$$P_{out} = \frac{u}{T} \int_0^T F_s(t) dt \tag{3.33}$$

$$P_{in} = \frac{1}{T} \left(\int_0^T F_h \dot{h} dt + \int_0^T M \dot{\theta} dt \right) \tag{3.34}$$

The efficiency of an oscillating foil is dependent on its wake structure. Visualisation and force measurement experiments of Anderson et al. (1998) and Read et al. (2003) confirmed that an oscillating foil is most efficient when one vortex is shed per half cycle at the extremes of the trailing edge excursion ($\dot{\alpha} = 0$), and vortices are arranged in a jet (reverse von Kármán street, see Figure 3.14c). Anderson et al. (1998) concluded that oscillating foils are feasible high efficiency propellers. Later, Hover et al. (2004) showed that the efficiency of oscillating foils were not approaching that of a typical open-ocean propeller. However, Hover et al. (2004) concluded that improvements could be made in the oscillation path, planform design, flap design and flexibility.

Triantafyllou et al. (1993; 1991) has shown by experiment, and through observation of fish, that peak efficiency for a flapping foil occurs in the Strouhal number range of 0.25 to 0.35. M. S. Triantafyllou et al. (2000) suggest that there is an optimum Strouhal number for each motion profile of an oscillating hydrofoil. Later, Anderson et al. (1998) showed that flapping modes of high efficiency typically have two peak efficiencies within the Strouhal number range of 0 to 0.6. The first peak is typically around 0.15, and the second around 0.35. Since the first peak is associated with a low thrust coefficient, the second peak is treated as the true maximum efficiency. Experimental efficiencies exceeding 86 % were achieved during the development of the Robotuna (Anderson et al., 1998; M. S. Triantafyllou & Triantafyllou, 1995).

Jones and Platzer (2001) suggest that large amplitude, low frequency motions should be used to optimize efficiency. Conte, Modarres-Sadeghi, Watts, Hover, and Triantafyllou (2010) investigated the efficiency of fast-starting fish measuring the velocity field around

a model fish undergoing an impulse start driven by a sudden release of stored energy. The high frequency, high acceleration impulse manoeuvre of the model had a hydrodynamic efficiency of only 10 %. Hydrodynamic efficiencies of fast-starting fish were expected to be in the 0.16 to 0.39 range.

Recently, Eloy (2012) has suggested that the optimum Strouhal number for swimming animals is a function of the Lighthill number. The Lighthill number is defined in equation 3.35, where L is the span of the fish tail, u is the swimming velocity, m_{a_L} is the added mass per unit length at the tail tip ($m_{a_L} = \rho\pi L^2$). The drag on the swimmer, F_d is based on S_w, the wetted surface area of the swimmer, and c_d, the drag coefficient ($F_d = c_d \frac{1}{2}\rho u^2 S_w$). Eloy (2012) correlated the Strouhal number with the Lighthill number, from published data, for a range of species, and produced the Strouhal number curve $St \approx 0.75 Li^{\frac{1}{3}}$. (Note: Eloy's equations defining the Lighthill number do not balance. However, his point that the Strouhal number is not the sole parameter specifying efficiency remains).

$$Li = \frac{\pi F_d}{2 m_{a_L} u^2} = \frac{S_w}{L^2} c_d \tag{3.35}$$

3.5.6 Wake Dynamics and Structure

The reaction force, on a body in a flow, is proportional to the flow disturbance it causes. The disturbance is represented by the wake behind the body. Hence, if the wake can be manipulated, the reaction force on the object will also be modified. For this reason, wake structures and dynamics are studied in fields such as flapping wing propulsion, vortex induced vibration (VIV) damping and energy harvesting. For the purposes of biomimetic thrust production, we are most interested in the wake of an unsteady foil. However, applicable research is also done on bodies with simpler geometry, such as circular and semi-circular prisms.

Steady foils with a sharp trailing edge may maintain attached flow at very low Reynolds numbers (see Equation 3.27). As the Reynolds number is increased, an unstable separation region may form around the trailing edge and progress forward. The separation region contains a recirculating flow and is responsible for form drag and stall effects. Once a separation region has formed, the foil is effectively a blunt body and will begin to shed

vortices of alternating signs at frequency f (see Figure 3.14a). This trail of vortices is called a von Kármán vortex street named after fluid dynamicist Theodore von Kármán. An unsteady body ($St \neq 0$), can generate a von Kármán street at lower Reynolds numbers than a steady one. However, Bowlus, Kelly, and Siekmann (1965) observed that by oscillating a hydrofoil, they could significantly reduce flow separation. These results suggest that drag on an oscillating foil can be reduced through either controlling flow separation, or modifying the von Kármán street.

Figure 3.14a shows a typical von Kármán vortex street. Note that the vortices in the top row rotate clockwise and the vortices in the bottom row rotate anti-clockwise. This type of vortex street is associated with drag. Von Kármán and Sears (1938) demonstrated that a flat plate oscillating transverse to a flow could create a reverse von Kármán vortex street (Figure 3.14c). The vortices in the top row rotate anti-clockwise and the vortices in the bottom row rotate clockwise. Reverse von Kármán vortex streets are known to produce thrust and are also referred to as a 'thrust producing wake' or 'jet'. Increasing the oscillating frequency further eventually results in the wake deflecting to one side (Figure 3.14d) (Jones & Platzer, 2001; Kudela & Kozlowski, 2010; Lai & Platzer, 1999).

Since frequency is a continuous variable, there is some frequency at which the wake has no momentum deficit or excess. Koochesfahani (1989) states that this condition occurs when all the alternating vortices are positioned in a straight line (see Figure 3.14b). This vortex street is referred to as a neutral wake. Yang and Lee (2006) define a neutral wake as when the vortex cores lie within ± 0.03 chords of the wake centre line. For a pitching foil this transition occurs when $St \approx 0.18$ (Anderson et al., 1998; Godoy-Diana, Aider, & Wesfreid, 2008; Schnipper, Andersen, & Bohr, 2009).

Figure 3.14 shows wakes where one vortex is shed per half cycle. However, it is possible that more than one vortex is shed during each half cycle. Vortices are either shed one at a time (singles), or in pairs. This leads to a 'S' (single) and 'P' (pair) notation for describing wakes structures. For example, as the oscillating frequency of a heaving foil is increased, Lai and Platzer (1999) and Jones and Platzer (2001) observed the wake transform from a $2S$ drag wake to a $2P$ drag wake, before changing again to a $2S$ thrust wake. Later, Schnipper et al. (2009) presented a model to predict the structure of the wake in terms of

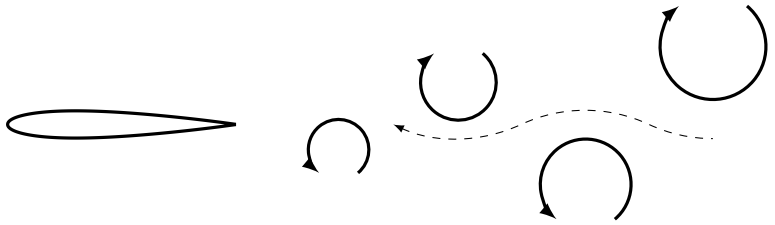

(a) Von Kármán vortex street. Drag producing wake.

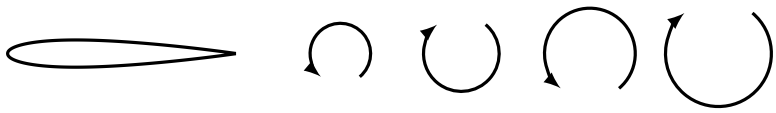

(b) Neutral wake

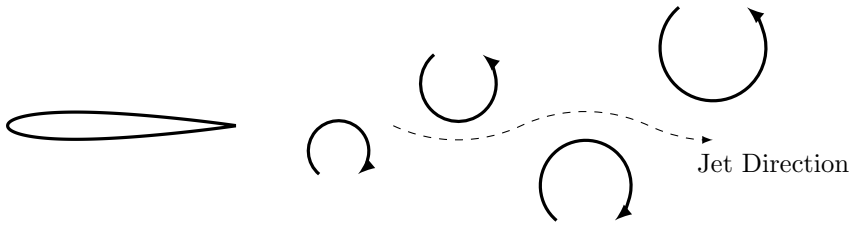

(c) Reverse von Kármán vortex street. Thrust producing wake.

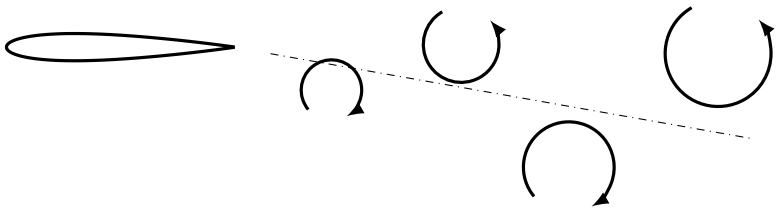

(d) Deflected von Kármán vortex street. Thrust and lift producing wake.

Figure 3.14. The three main types of vortex streets that appear in the wakes of oscillating bodies.

the number of vortices shed per half cycle. Wake structures have been mapped against the Strouhal number and angle of attack (or equivalents) for pitching, heaving and flapping foils (Anderson et al., 1998; Godoy-Diana et al., 2008; Schnipper et al., 2009).

The angle of attack profile has been shown to significantly affect wake structure and thrust production (Anderson, 1996; Godoy-Diana et al., 2008; Hover et al., 2004; Koochesfahani, 1989). Anderson (1996) found that vortex shedding occurs near the point of maximum angle of attack rate. Furthermore, sinusoidal and square wave angle of attack profiles have been shown to provide the 'cleanest' wakes (one strong vortex shed per half cycle) (Anderson, 1996). Koochesfahani (1989) studied the effect of asymmetrical angle of attack cycles on the wake structure. He did this by changing the symmetry parameter, defined by Equation 3.36. Koochesfahani's symmetry parameter describes the relative time of the pitching upstroke to the period of the cycle (Koochesfahani, 1989). He found that asymmetrical pitching cycles (i.e. $S_{\dot{h}} \neq 0.5$), produced multiple small vortices, of the same sign during slow stroke, and a single large vortex on the fast stroke (i.e. a $1S + 1P$ wake). Wakes such as this contain both thrust wake and drag wake structures, which reduces efficiency.

$$S_{\dot{h}} = \frac{T_{\dot{h}>0}}{T} \tag{3.36}$$

For steady foils, the natural vortex shedding frequency f_{ns} (also known as the (also known as the Kármán frequency) varies with the main stream velocity and the angle of attack of the foil (Jung & Park, 2005). For oscillating foils, the vortex shedding frequency is influenced by the oscillating (excitation) frequency f_e as well as the natural shedding frequency f_{ns} of the foil. When the excitation frequency is near the natural shedding frequency, competition between the two frequencies results in 'phase lock-in' (Patnaik, Narayana, & Seetharamu, 1998). For an oscillating cylinder, the boundaries of phase lock-in broaden, on the f_e/f_{ns} domain, as the heave-to-chord ratio increases (Patnaik et al., 1998). During phase lock-in, the lift and drag coefficient cycle amplitudes are amplified. The vortex street is expanded during low frequency lock-in and then compressed during high frequency lock-in.

Although a foil oscillating in planar motion is considered 2-D, the wake that it produces

may have 3-D components. Spanwise flow is not desirable because it represents momentum left in the wake that does not contribute to useful thrust or lift. For steady foils, winglets or end plates are often used to prevent tip vortices and spanwise flow. Koochesfahani (1989) showed that pitching foils produce strong spanwise flow through vortex cores, travelling away from wall boundaries. This may indicate that end plates (essentially wall boundaries) may not be useful for oscillating foils. M. S. Triantafyllou et al. (2000) suggest that 3-D flow will affect oscillating foils less at high frequencies due to the alternating sign of the tip vortices.

3.5.7 Vorticity Control

Fish, such as trout, swim behind obstructions in the flow (such as rocks) to feed, and to reduce their energy expenditure by manipulating the oncoming high energy flow. Beal et al. (2006) showed that even a dead trout (before rigor mortis) can sustain a position behind a semi-circular cylinder in a flow, by extracting energy from the cylinder's wake. A live trout demonstrated this energy extraction process with more precise control (Beal et al., 2006). Similarly Beal et al. (2006) showed that the passive response, of a rigid foil oscillating in the wake of a semi-circular cylinder, was consistent with the motion profile of an efficient, driven, oscillating foil propeller. Liao, Beal, Lauder, and Triantafyllou (2003) also observed that live fish can benefit from swimming in the wake of an upstream object. Fish can obtain optimum thrust by slaloming through oncoming vortices, or minimise their energy expenditure by slaloming between oncoming vortices (Anderson, 1996; Beal et al., 2006). The Kármán Gait is defined as swimming approximately one to two body lengths downstream of a vortex source (to avoid the suction region) while matching their tail-beat frequency to the source with large amplitude lateral body movements.

Gopalkrishnan, Triantafyllou, Triantafyllou, and Barrett (1994) conducted flow visualisation experiments, in which an oscillating foil followed an oscillating cylinder. The separation distance and phase strongly influenced the type of vortex interaction. Three interference modes were defined as: 1) destructive interference (intercepting mode), 2) constructive interference (slalom mode), and 3) intermediate interference (Gopalkrishnan et al., 1994; M. S. Triantafyllou et al., 2002, 2000). Maximum thrust is achieved through

the destructive interference of oncoming vortices, and maximum efficiency was achieved with intermediate interference, that broadened the wake width. M. S. Triantafyllou et al. (2000) found that for good interference, the foil should have a chord length comparable to the oncoming vortex core size. X. Zhang, min Su, Yang, and li Wang (2010) simulated a rigid foil undergoing 2-D heaving and pitching in the wake of a D-cylinder. They discovered the same three modes of vortex interaction as Gopalkrishnan et al. (1994) and Triantafyllou et al. (2002; 2000). X. Zhang et al. (2010) also claimed a fourth, rare interaction mode, where vortices shed from the D-cylinder would not interact with vortices shed by the foil.

3.6 Modelling Flapping Wing Propulsion

This section provides an overview of the current calculation methods, and recent prototype flapping wing propulsion vehicles. Predicting the thrust, lift and flow regime over an oscillating foil still proves to be a difficult task. However, a robust method for calculating the performance of an oscillating foil would be desirable for applying flapping wing propulsion in various applications. There are a number of different methods for predicting the performance of an oscillating foil. The main methods are:

- Quasi-steady calculations
- Calculations using unsteady flow theory
- Computational fluid dynamics (CFD) simulations
- Flow visualisation and measurement experiments

In the following sub-sections, research done using each of these methods is reviewed.

3.6.1 Quasi-steady Calculations

Designers and scientist have persisted used quasi-steady calculations to estimate the forces on oscillating foils (Konstantinov & Yakimov, 1995; MacCready, 1986, 1990a). This method uses the drag and lift equations for a steady foil (Equations 3.37 and 3.38

respectively), with steady drag and lift coefficients c_d and c_l, to estimate the instantaneous hydrodynamic forces on an oscillating foil. However, the appropriateness of this calculation method has not yet been thoroughly investigated. This section summarises how quasi-steady calculations have been employed and developed for predicting the performance of an oscillating foil.

MacCready (1986, 1990a) designed Mutiny on the Boundary Layer by approximating the forces on the hydrofoil with quasi-steady calculations, and considering the unsteady theory contributions of von Kármán and Sears (1938), Garrick (1936), and Wu (1971). MacCready (1990a) suggests that if an oscillating wing "...travels less than about 30 chord lengths forward during a flapping cycle, the quasi-steady analysis begins to have significant (say 10 %) errors.". He then states that if a wing travels less than 30 chord lengths per cycle "...the variability on the wing's wake modifies the flow that the wing encounters, and the analysis is called 'unsteady'.". This limitation does not consider the amplitude of the flapping motion. So, it fails to specify a valid trailing edge excursion Strouhal number range for quasi-steady calculations. However, it does specify that $St_c < 1/30$.

MacCready (1990a) calculated the drag and lift forces on his foil using the foil's steady drag and lift coefficients and Equations 3.37 and 3.38 respectively. In his calculations, he assumes that the thrust is provided by the horizontal component of the inclined lift force vector $\hat{F}_l$, during the downstroke (see Figure 3.15). He also begins the calculations by omitting the drag force on the hydrofoil. He later recognises the drag force as a parasitic term that can only reduce the thrust and efficiency of the hydrofoil. He also states that "one should be careful... that the maximum c_l of the airfoil is not exceeded in the course of flapping". His sample calculations are presented with reference to the reduced frequency but cover the Strouhal number range of 0.06 to 0.25. His calculations present a peak efficiency at St=0.125 with a steep drop off when the Strouhal number is increased to 0.25.

$$c_d = \frac{2F_d}{\rho u^2 cL} \tag{3.37}$$

$$c_l = \frac{2F_l}{\rho u^2 cL} \tag{3.38}$$

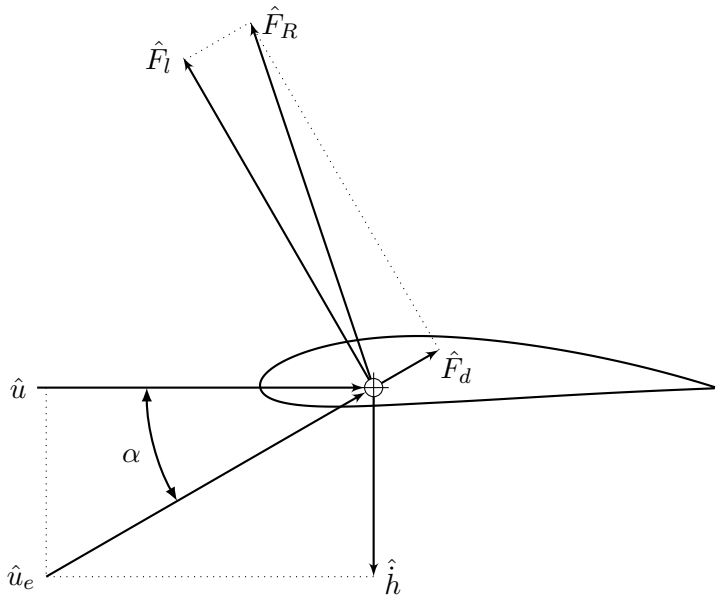

Figure 3.15. Vector diagram of the forces on an unsteady foil used in quasi-steady calculations

To sum up, MacCready's (1990a) quasi-steady calculations were sufficient in getting the Mutiny on the Boundary Layer to fly, but predicted the placement of peak efficiency contrary to more recent research (peak St=0.2-0.4, see Section 3.4.1) (G. S. Triantafyllou et al., 1993). MacCready (1990a) recognised that quasi-steady calculations would be less accurate for small stride lengths, but does not relate this limitation to the Strouhal number. MacCready's (1990a) 30 chord rule can be translated to the condition presented in Equation 3.39. While calculating the thrust force on the hydrofoil, MacCready (1990a) neglected the hydrofoil's drag which may have affected the accuracy of his calculations.

$$15St < h^* \tag{3.39}$$

Harper (1997) expanded on Lighthill's (1970) work by presenting analytical expressions for the dynamic lift, drag, and moment coefficients in terms of the foil's motion parameters. The final expressions can be broken down into three terms that contribute towards the

lift, drag, and pitching moment acting on the foil. The unsteady solution is made up of three components:

1. The quasi-steady solution
2. Mass contributions
3. Wake contributions

The quasi-steady solution describes the hydrofoil's reaction to actuator forces, spring forces, inertia forces, and the quasi-steady lift and drag forces. The hydrofoil is assumed to be similar to a flat plate so weight and buoyancy seem to be neglected. Unlike Equation 3.22, Harper's (1997) angle of attack contains three components: 1) The 'constant' pitch angle, 2) the heave-induced angle of attack, and 3) the pitch-induced angle of attack. The pitch-induced angle of attack is proportional to pitching velocity and is included because, points on the foil further from the pitching axis will experience different heaving rates (and hence heave-induced angles of attack) than points on the foil near the pitching axis.

Harper et al. (1998) modelled a spring driven oscillating foil for potential energy savings. In this model, a linear spring is placed between the actuator and the hydrofoil, to model the elasticity of fish tendons. The spring had one linear and one angular degree of freedom. This model was used to predict the foil's response to a known actuation. It was predicted that the use of springs for energy storage would increase the mechanical efficiency of the oscillating foil, provided a suitable spring stiffness.

Piziali (1994) published a large amount of experimental data for a pitching, symmetrical foil (NACA0015). It is common to find analyses of pitching foils validated against Piziali's (1994) experimental data (Hutchison et al., 2010; Ko & McCroskey, 1995; Umar et al., 2009). His data includes steady measurements, quasi-steady measurements (at a frequency of one cycle per minute), and unsteady measurements for a range of mean angles of attacks, oscillation amplitudes, and frequencies.

3.6.2 Dynamic Calculations

In contrast to Section 3.6.1, the unsteady hydrodynamic forces on a foil have also been calculated with analytically. Some of the earliest research on flapping foils stemmed from

research done on wing flutter, such as the work done by Theodorsen (1935). In the mid 1930s, Garrick (1936) considered a 2-D aerofoil oscillating with three degrees of freedom; vertical motion, pitching motion, and angular oscillations of an aileron. The solution to this problem included Bessel functions of the first and second kind, of argument k, the reduced frequency (see Section 3.4.1). A common criticism of Theodorsen's (1935) work was that the equations were complex, and that it was hard to make physical sense of his research. For this reason it could not be properly applied. Von Kármán and Sears (1938) tried to make this work more accessible to engineers and created their 'unified theory' of unsteady aerodynamics. Designers have used Garrick's (1936) model to predict the forces on a flapping wing, however, one major limitation is that the model assumes a small oscillation amplitude. For this reason Garrick's theory is limited to very low Strouhal numbers. This has been confirmed with experimental data (Lai & Platzer, 1999).

The Wu-Siekmann theory of swimming hydrofoils is an analytical model to predict the performance of a flexible foil (Siekmann, 1962, 1963; Wu, 1961). Their approach was to model a rigid foil with a finite number of hinges. In this model, the foil is assumed to be thin and is modelled as a flat plate. Bowlus et al. (1965) experimentally validated this theory and concluded that it can successfully predict the thrust of an oscillating foil whether rigid or hinged. Bowlus et al. (1965) did not draw any conclusion on the validity of the lift and moment predictions since their lift and moment data was too scattered to analyse. Their experiments were conducted in the Strouhal number range of 0 to 0.05, which is far from the placement of peak efficiency ($St \approx 0.3$) (G. S. Triantafyllou et al., 1993).

Lighthill (1970) first used oscillating foil theory to model different types of fish propulsion in 1970. He recognised that quasi-steady calculations for flapping wing propulsion would only be good when inertial forces were low, and viscous forces dominate (i.e. high K_C) without providing a quantitative boundary between the two cases. Furthermore, he notes that an additional force in unsteady motion is required to accelerate a mass of water around a swimming body. This mass of water is called 'virtual mass' (see Section 3.3). Swimming techniques with high efficiency are thought to be those that utilize virtual mass effects. Lighthill's (1970) linear theory was compared against the experimental results of

Anderson et al. (1998) over the Strouhal number range of 0 to 0.6 for low angles of attack. Linear and non-linear theory disagreed with experimental results for thrust and power coefficients for certain Strouhal number and angle of attack combinations. Efficiency predictions disagreed with linear theory, for all Strouhal numbers, and a number of flapping profiles.

Discrete vortex models have also been used to predict the flow field around an oscillating foil. Kelly, Mason, Anhalt, Murray, and Burdick (1998) used the substitution vortex model to predict the placement and strength of vortices shed from a thin oscillating aerofoil to investigate carangiform locomotion control.

3.6.3 Numerical Simulations

Computational fluid dynamics (CFD) has become a popular method for modelling fluid flow. With recent progress in numerical models, some oscillating foil simulations have agreed well with experimental data (Platzer & Jones, 2000; Umar et al., 2009). Large amounts of work have been done on validating and improving numerical methods for simulating the flow over an oscillating foil. Studies have shown that attached flows can be modelled very well. However, simulating dynamic stall and leading edge vortices is difficult (Jones & Platzer, 2001; Ko & McCroskey, 1995).

Umar et al. (2009) modelled a pitching symmetrical foil for reduced frequencies between 0.1 and 0.3. Their results agreed reasonably well against Piziali's (1994) data. Münch et al. (2007) validated numerical simulations with water tunnel tests for a pitching foil. The result of this study was the transfer function between a pitching foil's angular displacement and pitching torque. Other recent work includes, CFD simulations of the reverse von Kármán street shed by an oscillating foil, and the relationship between the wake structure and the thrust produced by an oscillating foil. Most simulations use a symmetrical foil, however, recently Tay and Lim (2009) studied the effect of non-symmetrical foil shapes on the lift, drag, and efficiency of a flapping foil.

3.6.4 Prototyping

The most successful program for designing a human-powered flapping wing craft was Parker MacCready's development of the Pogo Foil. MacCready developed the Pogo Foil through several years of experimental boat building (MacCready, Accessed 2012), which shows that at this time there was not sufficient design data, or existing design process, prescribing the details of flapping wing propulsion. Although plenty of research has been done in the field of flapping wing propulsion over recent decades, still no design process exists for engineers to design water craft utilising this technology. MacCready (1990a) discusses the development of the 'Mutiny on the Boundary Layer' and the 'Preposterous Pogo Foil' in Human Power, the technical journal of the IHPVA. Two clear conclusions from this development program, and reasons why the Pogo Foil was more successful than the MOBL were: 1) the Pogo Foil was a much simpler device and 2) the Pogo Foil gave the pilot more feedback on the forces applied to the main wing and more control over the wing's motion.

Recently undulating fins have been developed for wave power propulsion. Y. Zhang, Song, Yang, and Low (2008) developed an oscillating fin capable of undulating and root flapping motions. Delta Prototypes in Poland developed the Kalmar prototype, which employs a 'hydro wing' propeller (Gordon, 2010; Samek & Latacz, 2007). The hydro-wing consists of a series of horizontal rods, transverse to the boat, which oscillate out of phase in vertical root-flapping motion. There are two series of rods, one on each side of the keel. Each set is connected with a latex film, which undergoes an undulating motion. This model would be a good example of rajiform swimming as demonstrated by most stingrays (Breder, 1926).

Yutaka Terao invented the Suntory Mermaid II ship, which employs a Wave Devouring Propulsion System (WDPS). WDPS uses ocean waves to passively control the pitching motion of a hydrofoil. Enough thrust is generated to enable the ship to drift against waves. The Suntory Mermaid II took 110 days to travel 7800 km from Hawaii to Japan in 2008 (Terao, 2009). The 'Wave Glider', developed by Liquid Robotics, also employs a system similar to the WDPS to generate thrust from wave energy allowing it to drift around the ocean (Daniel et al., 2011; Manley & Willcox, 2010). Unlike the Suntory Mermaid

II, the wave glider has an array of hydrofoils to create thrust and consists of two main assemblies; a buoyant board, which floats at the surface, and the hydrofoil array, which is submersed below. The Wave Glider is used as an autonomous ocean instrumentation platform powered by wave energy and solar power.

3.7 Patent Search

A range of propulsion units and entire vehicles, which employ oscillating hydrofoil propulsion have been patented within the last century. Gongwer (1974) patented the Aqueon and an oscillating hydrofoil propulsion boat (Gongwer, 1987). Michael Puzey may have been the first person to submit a patent application for a Trampofoil type vehicle when he applied to patent the Pumpabike design in 1997 (Puzey, 1997). Puzey recieved the patent in August 2000 (Puzey, 2000). At almost the same time as Puzey's submission, Sahlin (1998) submitted an application to register the Trampofoil design in Sweden. Lekhtman (2003) has patented the SeaJogger, Chen (2006; 2008; 2010a; 2010b) holds multiple patents on the Aquaskipper and another for a device, which seems to operate in a similar way to the Wasserläufer (Chen, 2002). Schmidt (1965b) patented the wave propeller. Latacz has applied to patent the Kalmar's 'hydro wing' propeller (Samek & Latacz, 2007). The Massachusetts Institute of Technology (MIT) holds a patent on propulsion systems employing flapping foils as a result of Triantafyllou's work (M. S. Triantafyllou, 1995, 1998). MIT also holds a patent for a human powered marine vehicle that has a rigid front section and a flexible rear section, which moves in a fish-like motion (M. S. Triantafyllou, 1999). Recently Grande (2011) has applied to patent a propulsion device for driving vehicles. The device features eccentric components to convert a rotational motion into an oscillating motion to drive a flapping foil.

3.8 Literature Summary

The literature presented in this chapter supports the need for further investigation of flapping wing propulsion for human-powered hydrofoils. Flapping foils were shown to be as efficient as rotary propellers and have significant advantages for manoeuvrability. The

characteristics of the two types of propeller are very different. Flapping wings produce pulsing, high force, low frequency thrust (MacCready, 1986; Platzer & Jones, 2000) while rotary propellers utilise continuous motion to provide relatively steady thrust. These characteristics have enabled rotary propellers to be more easily incorporated into watercraft. Nevertheless, flapping wing propulsion was evaluated as a viable form of marine propulsion if implemented properly.

The implementation of flapping wing propulsion on Parker MacCready's Mutiny on the Boundary Layer (see Section 2.2.2) resulted in several important observations. Two of these observations were that 1) the craft reacted strongly to the hydrodynamic forces acting on the hydrofoil during start-up, and 2) the hydrodynamic forces on the hydrofoil back-driving the craft drivetrain made pedalling at a near constant velocity difficult and warranted a flywheel to smoothly operate the craft. To improve MacCready's design or to design a new pedal powered vehicle with flapping wing propulsion, it would be useful to simulate vehicle dynamics before constructing the craft. However, the one unknown force on the vehicle that may not be assumed steady is the hydrodynamic force on the hydrofoil as it is driven through the water. Hence, the application of flapping wing propulsion is currently pending on a robust method for predicting the hydrodynamic forces on an oscillating hydrofoil.

Performance characteristics of an oscillating foil are usually expressed in terms of the Strouhal number, and are rarely related directly to the motion of the foil. Furthermore, most performance studies focus on the mean hydrodynamic loads exerted on the foil, rather than time-dependent load cycles. This is fine for foils undergoing predefined parametric motion profiles such as a sinusoidal motion. However, the Strouhal number alone is not sufficient for characterising non-parametric motions.

Analytical calculations of loads and flow fields are proven to be reliable at very low Strouhal numbers where the assumption of small oscillating amplitudes holds. Quasi-steady calculations, based on steady lift and drag coefficients, have been used to estimate the time-dependent hydrodynamic loads on oscillating foils. However, the limits of quasi-steady calculation on the Strouhal number domain have not clearly been established. Most recently, numerical models have been developed to predict the flow around an oscillating

foil. Simulations at low Strouhal numbers with attached flow or trailing edge vortex shedding have been most successful. Leading edge vortex shedding has been more difficult to model.

Since most watercraft are required to start from rest, calculating the hydrodynamic forces acting on a oscillating hydrofoil undergoing high Strouhal number operation, also referred to as 'piston mode' operation (Anderson et al., 1998), is very important. However, methods for calculating the hydrodynamic forces on an object undergoing high Strouhal number oscillations, without using numerical models (CFD), are limited to the marine engineering equations mentioned in Section 3.3. These equations are typically used for calculating the hydrodynamic forces on a cylinder in a oscillating flow, such as a pile in the ocean, and are not well validated for object of other geometry. Moreover, since oscillating hydrofoils undergoing high Strouhal number operation are known to have poor propulsive efficiency, little work has focused on thrust coefficients for this case.

In this thesis, experimental work focusing on the direct relationship between the motion of an oscillating object and the hydrodynamic forces on that object is presented. More specifically, the validity of the aforementioned marine engineering equations for calculating time-dependent hydrodynamic forces on an oscillating cylinder is established before their application to other object geometries, such as flat plates hydrofoils, is investigated. The focus of this work was not to optimise the motion of an oscillating foil for human powered foil applications, but to validate if these marine engineering equations may aid this process. Hence, in order to simplify the validation procedure, i.e. the requirements for the experimental equipment and data analysis methods, the current work only focuses on single degree of freedom oscillations: pure heaving motion. The aim of this contribution was to make oscillating foil propellers more accessible to engineers for application in vehicle design.

Chapter 4

Experimental Equipment and Procedure

4.1 Experiment Objectives

To assist in the design of a flapping wing propulsion surface watercraft, quantitative measurements of thrust, and lift force cycles on an oscillating hydrofoil were collected and analysed. The aim was to record experimental data that could relate the motion of an oscillating hydrofoil to the propulsive force it was generating. To have a fully defined set of experimental data the variables that need to be recorded are the water velocity, the position and pitch of the hydrofoil, the vertical lift force and the horizontal drag forces acting on the hydrofoil. While all of these variables may be time dependent, some can be fixed to a constant value. In the experiments discussed in this thesis, the hydrofoil pitch is held constant with time to limit degrees of freedom. Hydrodynamic forces on a symmetrical and asymmetrical heaving hydrofoils were measured. Hydrodynamic forces on bodies with simple geometry, like a circular cylinder and a flat plate of finite thickness were studied to assist in understanding, and modelling of, the forces on the oscillating hydrofoils.

4.2 Mechanical Design

Initial test equipment designs proved to be troublesome with poor performance resulting in data that was not suitable for drawing any quantitative conclusions. Reports in the literature revealed that other researchers also had to carefully design their experimental equipment to avoid structural resonance (Flores, 2003; G. S. Triantafyllou et al., 1993).

Figure 4.1 is an image of the final test rig design and Figure 4.2 is a schematic of its working elements. A pair of Watt's linkages were chosen to guide the linear heaving motion, since the bearings required for the linkage were more cost effective than those required for a linear slide system. A Watt's linkage has a range of movement where the centre point of the middle link is approximately linear. However, the linearity of the path deteriorates in the extremities of the motion range. Figure 4.3 shows the linkage's deviation from a linear path. Short linkage lengths provide a very stiff linkage and have a high natural resonant frequency but longer links minimise the non-linearity in the stroke path. The length of the links was chosen to be the minimum length that would provide less than 0.5 % horizontal deviation from the vertical linear path at the maximum design stroke.

The oscillating assembly held by the Watt's linkages holds the load cell assembly in series with the struts and the test object. The mass and stiffness of all the oscillating components are critical in defining the structure's natural frequency (See section 4.6). The mass of the oscillating components was minimised to decrease stress on the drive train and increase the structure's resonant frequencies.

The key parameters affecting the resonant frequencies of the struts and the test object are the length of the struts and the mass of the test object. Each strut can be considered a cantilever beam with a concentrated mass (the test object) on the end. Equation 4.1 is the governing equation of the natural frequency ω_n for a beam of this type. The mass of the beam and the concentrated mass are denoted by m_b and m respectively. The length, elastic modulus and the moment of inertia of the beam's section are denoted by l, E and I respectively. It is clear that the length of the beam is the most influential parameter and should be minimised to maximise the natural frequency. The mass and the length of the beam were minimised along with the mass of the test object, while I was increased

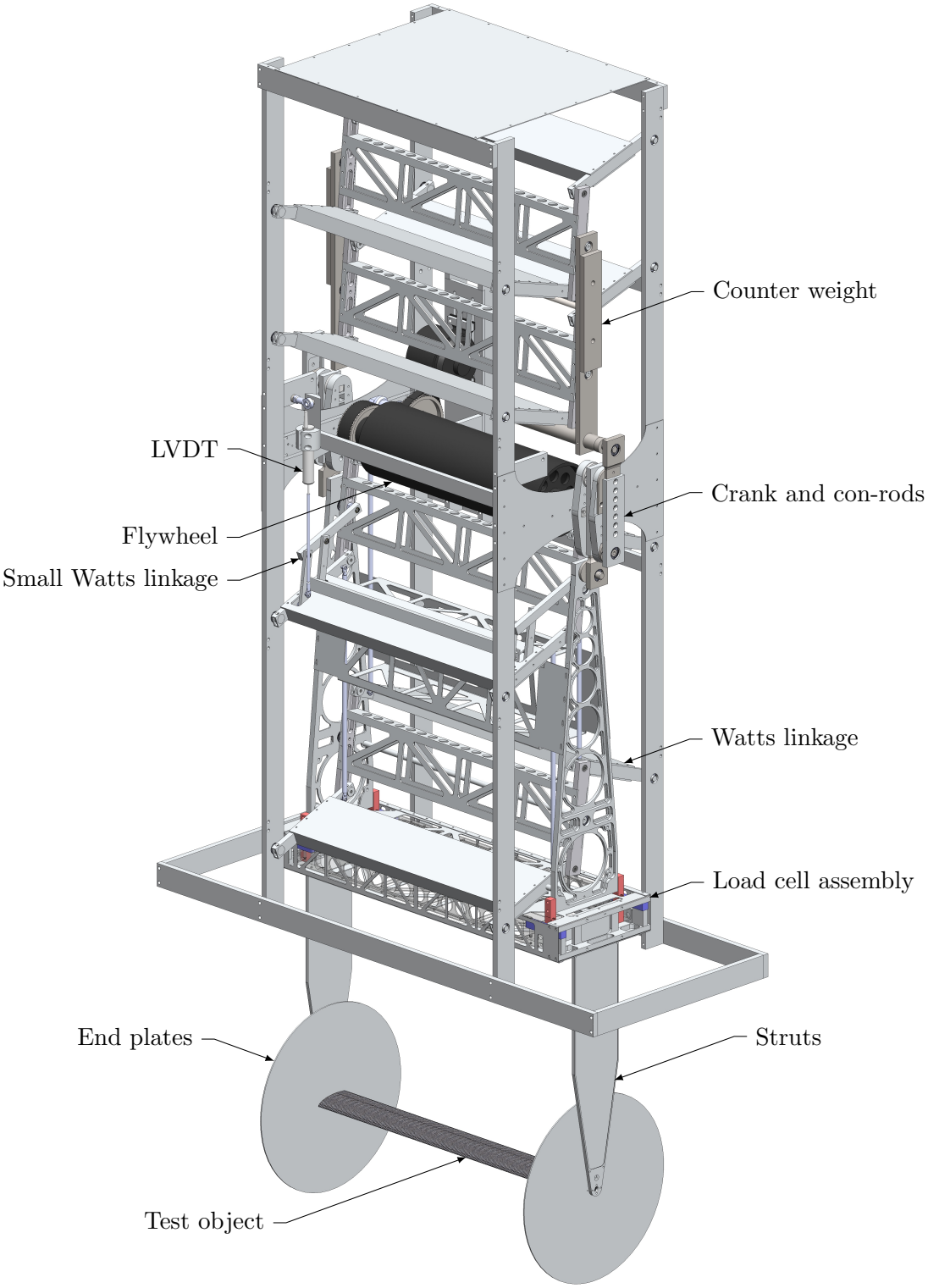

Figure 4.1. Image of the testing equipment design

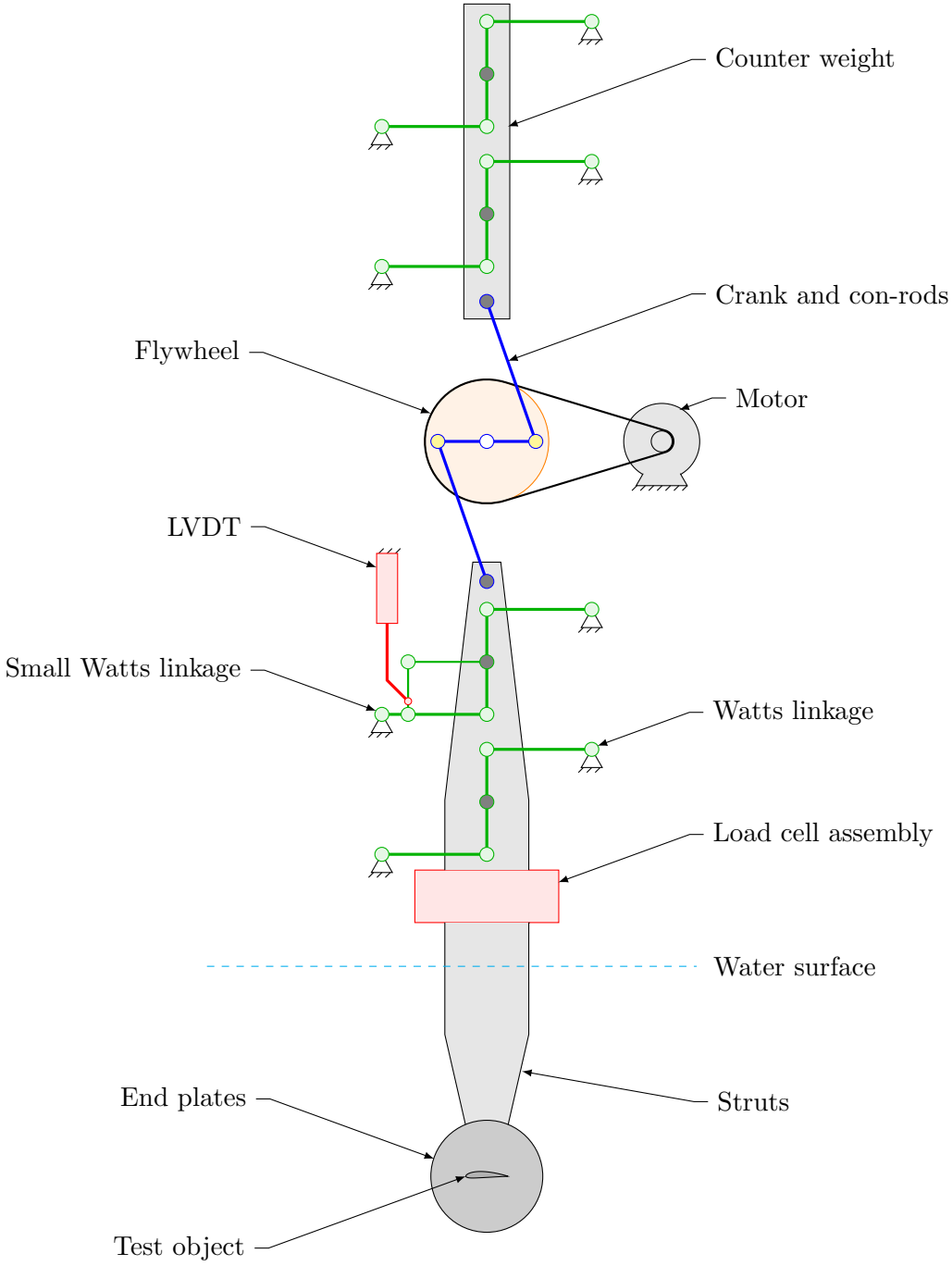

Figure 4.2. Schematic of the testing equipment design

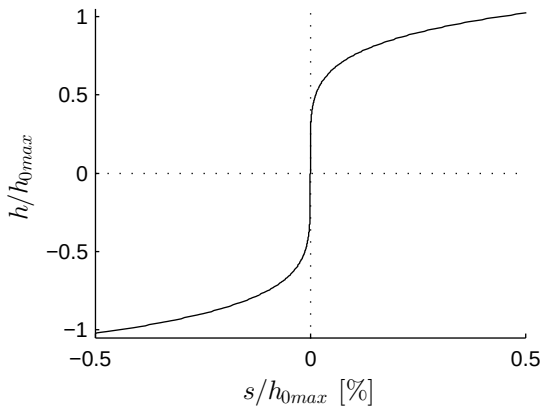

Figure 4.3. Horizontal deviation in the Watt's linkage path

to maximise the natural frequency of the lower oscillating assembly in the stream wise direction. The struts were kept slender to minimise their drag. This meant compromising their moment of inertia about a streamwise axis. Tension wires were added to the struts, in order to prevent oscillations in bending transverse to the mainstream flow.

$$\omega_n = \sqrt{\frac{3EI}{l^3\left(m + 0.23m_b\right)}} \tag{4.1}$$

A counter-balance weight of equal mass to the lower oscillating assembly is driven by the crank shaft 180 degrees out of phase with the lower oscillating assembly. This provides a facility for storing the gravitational potential energy of the lower oscillating assembly as it plunges downwards, which is later returned on the upstroke. A flywheel was used to increase the rotational inertia of the crank shaft. This allowed the test rig to operate more smoothly, especially at low oscillating frequencies. The counter balance and the flywheel both smooth the power requirements from the motor and relieve oscillating loads on the drive train. The oscillations were driven by a DC motor with open loop control. Open loop control was chosen because it represents more accurately pedal power drive characteristics than closed loop control. Power was transmitted to the lower oscillating assembly and the counter-balance via synchronous belts and a crank and connecting rod arrangement. The length of the cranks was made adjustable so that the heaving amplitude could be changed.

4.3 Test Objects

Four test objects were used in the current experiments (see Figure 4.4). Their properties are listed in Table 4.1. The first object, in order of increasing complexity, was a cylinder with a diameter of 60.4 mm. Second was a flat plate with a chord length of 51 mm and thickness of 6 mm. The last two objects were, a NACA0012 symmetrical hydrofoil, and a NACA4415 asymmetrical hydrofoil. Each hydrofoil had a chord length of 60 mm. The NACA0012 was chosen for testing because it is the most common foil profile used in the relevant literature, and hence is a good control profile. The NACA4415 section was chosen since MacCready (1990a; Accessed 2012) proved it to be a suitable foil profile for flapping hydrofoil propulsion. Tay and Lim (2009) also found a S1020 profile, which is very similar to the NACA4415 profile (see Figure 3.12), to be the best overall foil for high thrust and lift production with good efficiency when compared to other sections. All objects had a span of 600 mm.

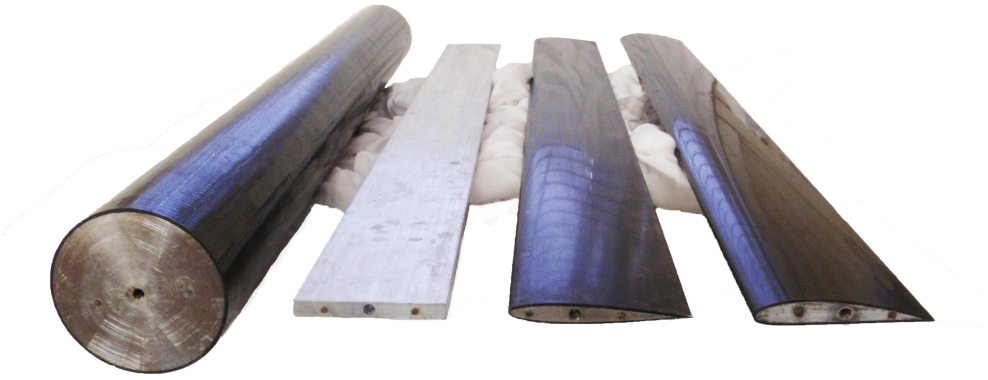

Figure 4.4. Test objects used the experiments.

4.4 NIWA's Towing Tank

Experiments were conducted at the National Institute of Water and Atmospheric Research (NIWA) towing tank located in Kainga, Christchurch. The towing tank is 50 m long, 1.8 m wide and 1.75 m deep. Figure 4.5 is a view looking down the towing tank.

Table 4.1. Properties of the test objects.

	Cylinder	Flat Plate	NACA0012	NACA4415
Profile (Scale 1:2)	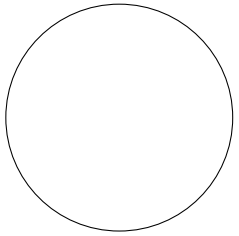	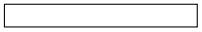		
Chord length/ diameter (mm)	60.4	51.0	60	60
Span (mm)	600	600	600	600
Thickness (mm)	60	6	7.2	9.3
Material	Carbon fibre, foam and Aluminium	Aluminium	Carbon fibre, foam and Aluminium	Carbon fibre, foam and Aluminium
Weight (g)	315	492	205	195

The towing car has a maximum towing speed of $3\,\mathrm{m\,s^{-1}}$. Figure 4.6 shows the oscillator mounted to the front of the towing car.

Figure 4.5. A view of the tow tank in the direction that the experiments were done.

The testing equipment was mounted to the front section of the towing car's chassis and was adjusted to be aligned with the towing car's direction of travel. The vertical alignment of the test rig's pitch angle was the most important. The load cell vertical measurement axis was aligned with the true vertical by placing a weight on the load cell and adjusting the pitch of the test rig until no horizontal load was measured. The test rig's yaw was set by placing a string in tension across the width of the tow tank, square to the towing car's rails, and adjusting both struts to have an equal clearance to the string. The roll angle of the test rig is least critical to the measurements and was checked with a spirit level. The mean heave position of the test object was $295\pm5\,\mathrm{mm}$ below the water surface for all experiments, except those investigating submergence depth.

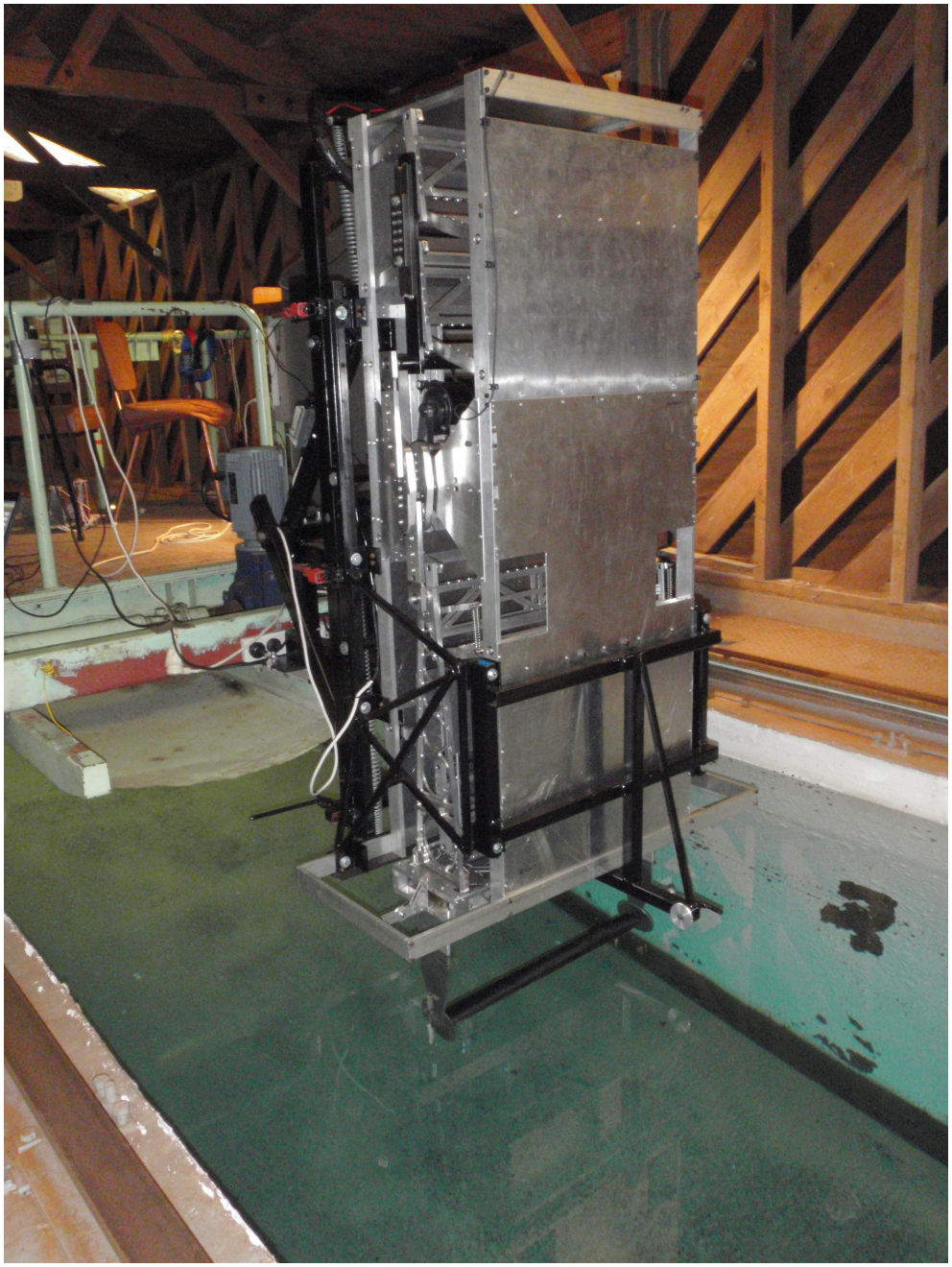

Figure 4.6. Experimental equipment on the towing car at NIWAs towing tank.

4.5 Instrumentation and Data Acquisition

The oscillator was fitted with instrumentation to record and display the vertical position, velocity and acceleration of the test object as well as the streamwise and vertical forces on the test object. The vertical position was measured at the Watt's linkage with a Linear Variable Differential Transformer (LVDT). Since a LVDT with a 40 mm range was available the LVDT was attached to the main Watt's linkage via a small Watt's linkage to scale down the vertical movement of the strut carriage.

Initially a Trans-tek Linear Velocity Transducer (LVT) and an accelerometer were used to measure the velocity and the acceleration of the oscillations respectively. When the LVT and accelerometer were first installed, sample data was recorded to compare the differentiated position signal to the direct measurements of heave velocity and acceleration. The study revealed that both direct and indirect methods yield the same result. The LVT was supplied with its calibration constants from Trans-tek. However, there are many ways that the LVT calibration may change. There was no known practical method for calibrating the LVT once it was installed, and so the LVT was not an attractive sensor to use. The LVDT however can be calibrated quickly before every run (see Section 4.8.1). The level of noise in the accelerometer signal was much larger than the noise level in the LVDT signal, which reduced the appeal of the accelerometer. For these reasons the heave velocity and acceleration were measured indirectly via differentiating the heave position signal.

The horizontal and vertical forces on the test object were measured via an assembly of binocular shear beam load cells. Four load cells of 5 kg capacity each supported the load on the test object in either the horizontal or vertical direction. Figure 4.7 highlights the position and orientation of the load cells in the load cell assembly. The design is essentially the same as Heglund's (1981) force plate, but constructed from commercially available load cells rather than specific transducer elements. Even though ideally, the force measurement sensor would be directly connected to the test object at the end of the struts, the load cells were chosen to be located above the waterline so that waterproofing would not be required. This means however that the hydrodynamic forces on the struts were measured as well as on the test object. The strut forces were measured separately and

subtracted from the data. An advantage of putting the load cell assembly above the water line is that it locates the weight of the load cell assembly closer to the supporting frame work of the test rig, which increases the natural frequency of the test equipment. The load cell assembly must have a high bending stiffness to increase the natural frequency of the struts. However, the shearing stiffness across each load cell must not be so high as to reduce the sensitivity of each load cell. To fulfil both of these requirements, the load cell spacing in the streamwise direction was made large to maximise their combined second moment of area. Refer to sections 4.2 and 4.6 for more details of resonance design. This load cell assembly design has a very low amount of dependence between the two axes of measurement. See Appendix A for details on its calibration.

The position of the towing car was measured with an Omron E6C2-CWZIX 1000 P/R incremental encoder driven by the left rear wheel of the car. Using quadrature encoding, a resolution of 0.35 mm was possible. Car velocity samples were calculated by dividing the distance travelled by the car over every ten increments of the encoder (3.5 mm) and dividing by the respective elapsed time. The mean velocity of the car and the steadiness (velocity distribution) of the car could then be evaluated.

Due to the large thermal mass of the tank water, the variation in water temperature was minimal over the duration of an experiment. The water temperature was checked approximately hourly with two digital thermometers, at different depths from the water surface, near the centre of the tank's length. The recorded water temperature was the mean of these two water temperature measurements.

Instrument voltages were measured with a National Instruments CompactDAQ chassis. A National Instruments NI9237 24-bit analogue input module was used to power the strain gauges and sample the load cell's output. A NI9239 24-bit analogue input module was used to sample the LVDT's output voltage. A NI9263 16-bit analogue output module was used to generate a voltage to apply to the motor speed controller's input. An internal counter in the CompactDAQ was used to keep trace of the rotary encoder's position. A NI9401 digital I/O module was used to generate a trigger signal, for sampling the encoder's position, at the same rate as the load cell and LVDT channels. Data acquisition was achieved with National Instruments LabView software.

Figure 4.7. Load cell assembly design. Red load cells measure drag/thrust (surge forces) and blue load cells measure lift/downforce (heave forces).

4.6 Structural Spectrum Analysis

As with any oscillating system, structural resonance is an important phenomenon. The impact response of the structure was evaluated for loads in the heave, surge and sway axis. Figure 4.8 is an example of the the power density spectrum of the experimental equipment's response to impact loads in each of these axes, with the NACA4415 foil and two chord length diameter aluminium end plates (290 g total mass) mounted, with a 0° pitch angle. Table 4.2 summarises the primary and secondary impact response frequencies of the experimental equipment in this configuration.

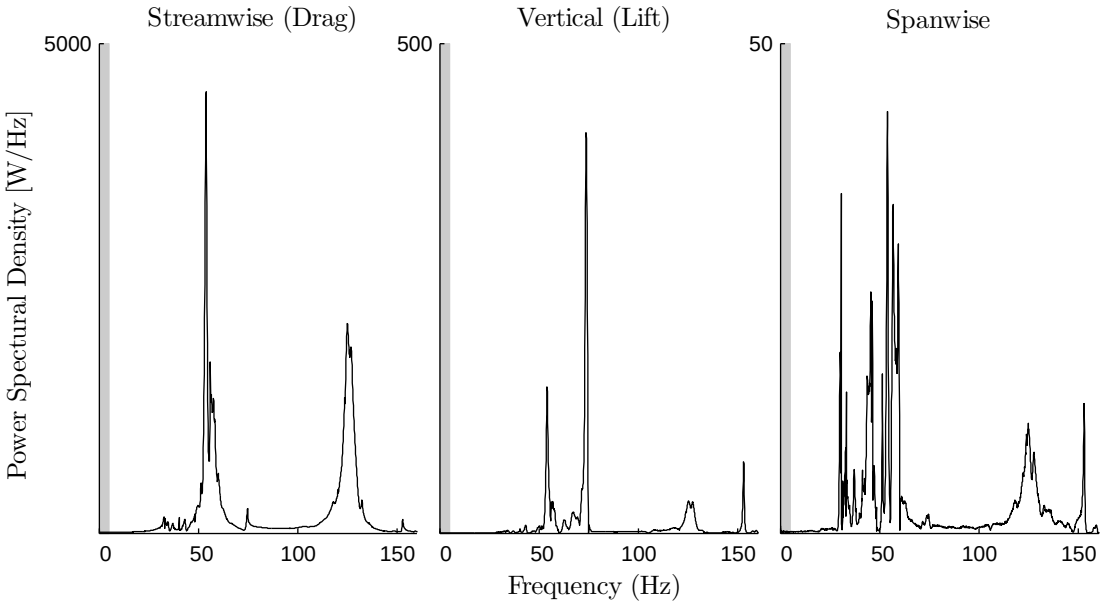

Figure 4.8. Power density spectrum for impact loading of the experimental equipment

Table 4.2. Primary and secondary fundamental natural frequencies of the experimental equipment with the NACA4415 with $2c$ diameter end plates mounted

Forcing direction	Primary [Hz]	Secondary [Hz]
Streamwise (Surge)	54	125
Vertical (Heave)	74	153
Spanwise (Sway)	31	33

The lowest frequency response of the equipment was in the spanwise direction due to

the strut's lack of stiffness in this axis. The struts were designed to be slender to minimise their drag area. However, this leads to minimised stiffness in the spanwise direction, and hence a low natural frequency. Initially, the frequency response of the strut to impact loading in the sideways direction was 25 Hz. This was increased to over 30 Hz with the addition of guy wires which support the struts from deflecting in the spanwise direction. Given that the operating frequency of the equipment was less than 5 Hz, the natural frequencies of the structure were acceptable and were attenuated with a low pass filter.

Changing objects attached to the struts in the experimental equipment, or adjusting an object's pitch angle, changes the equipment's natural frequency. When the mass at the end of the struts is increased the resonant frequencies should decrease according to Equation 4.1. The inertia of several masses mounted to the struts was measured to quantify the accuracy of dynamic force measurements acquired with the experimental equipment (see Appendix B). The results of these tests also provided insight to the frequency response of the equipment under various oscillating inertia loads. Figure 4.9 shows the point-wise dynamic measurement error (Equation B.2: $\epsilon_d = F_h - m\ddot{h}$) over the working oscillation frequency range for various masses mounted to the struts. The maximum dynamic error increases linearly with the oscillating frequency. However, the error has a peak towards the end of the working frequency range for the heavier two masses. This shows that the experimental equipment has some structural resonant frequency which enters the working frequency range once enough mass is mounted to the struts. The effect of this resonance is a distortion in the force cycle profile. Figure 4.10 shows the measured inertia cycle with the expected inertia cycle ($m\ddot{h}$) of a 3.208 kg mass oscillating at 3.8 Hz. The point-wise dynamic error is most prominent near the heaving force peaks, where heaving acceleration and inertia forces are at a maximum. Refer to Appendix B for more detail on the effects of the heave axis compliance.

Dynamic error relative to the cycle amplitude decreases with frequency. However, the resonant effect shown in Figure 4.9 begins to magnify dynamic errors when the equipment is under high in-phase load. Hence, there is a relative dynamic error minimum around 2.8 Hz (see Figure B.5) just before resonant effects begin. Furthermore, the best operating frequency range, with minimal resonant effects when the equipment is under high in-

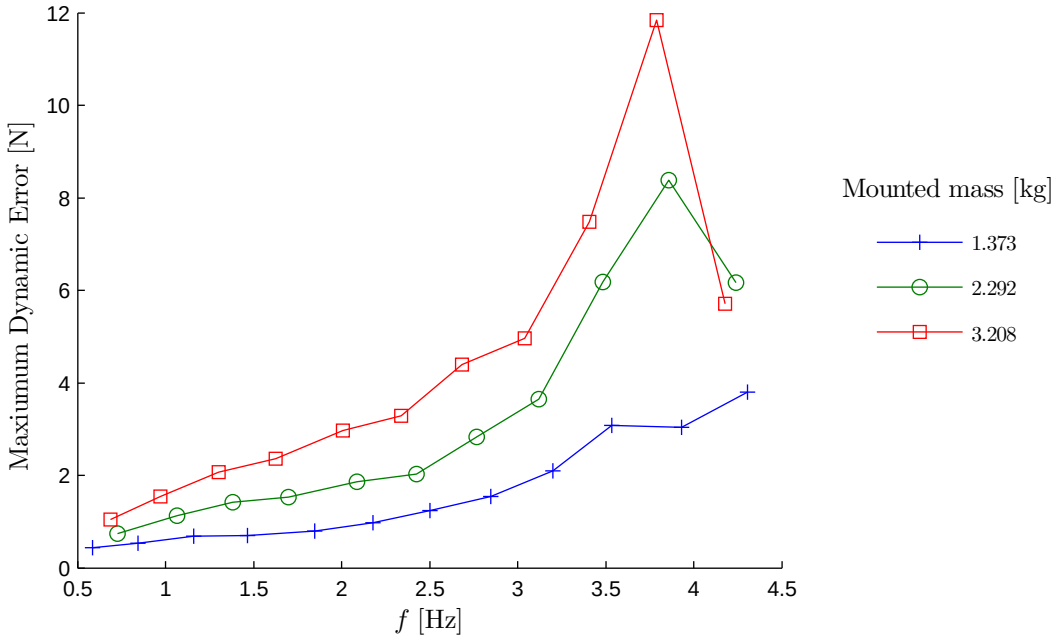

Figure 4.9. Maximum point-wise dynamic error as a function of oscillating frequency.

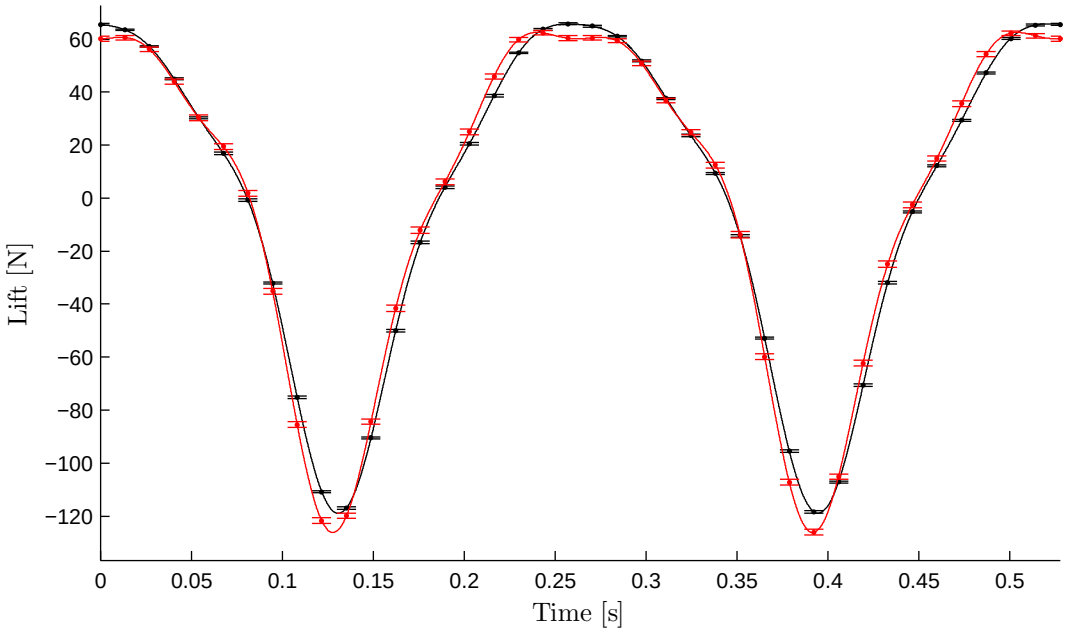

Figure 4.10. Measured (red) and expected ($m\ddot{h}$, black) inertia of 3.208 kg mass oscillating at 3.8 Hz.

phase load, is when the oscillating frequency is less than 3.5 Hz. Keeping in mind that the results discussed in this section and in Appendix B used the maximum expected inertia forces, this resonant effect is not expected to significantly degrade the majority of force measurements presented in later chapters. Furthermore, later results are presented with dynamic uncertainty bounds (defined in Appendix B) which indicates a region where the true, undistorted force cycle is expected to lie with 95 % confidence.

4.7 Data Filtering

Since frequencies above three times the driving frequency (0.5 Hz to 5.0 Hz) were considered as artefacts from structural vibration, a low-pass filter with a 15 Hz pass band edge was chosen. Flores (2003) also chose to attenuate frequencies above three times the driving frequency while measuring forces on a foil during an impulsive start. All data channels were filtered with a digital least squares finite impulse response (FIR) filter. The magnitude and phase response for this filter is shown in Figure 4.11. This design has a short transition band and a linear phase response. The linear phase response is particularly desirable since it provides a constant group delay and phase delay. The group and phase delay for this filter are 2.5×10^4 samples and 15.71 rad Hz^{-1} respectively. Passband ripple gain was less than 3.2×10^{-3} dB and the stop band attenuation was 71 dB.

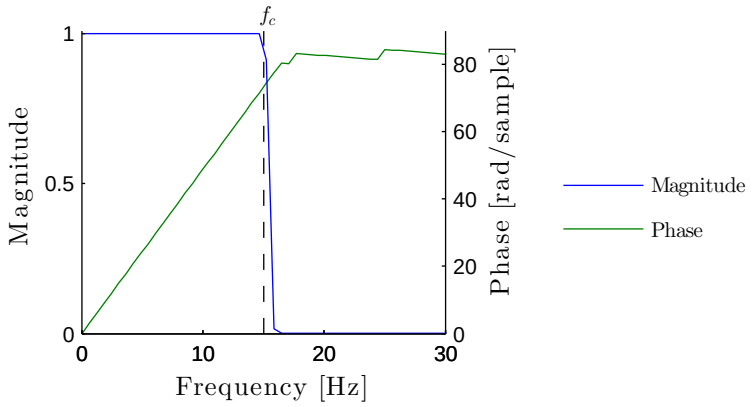

Figure 4.11. The transfer function of the digital low pass filter used to filter the experimental data.

4.8 Procedure

4.8.1 Calibration of Instruments

The towing car wheels are machined steel and have a diameter of 450 mm. To monitor the wheel circumference over time, the towing car rails have an original distance of 18 wheel revolutions precisely marked on the side. To check the wheel circumference, the car is positioned with the marking on the wheel adjacent to the first rail marking and rolled forward until the mark is over the second rail marking. Since the encoder has 1000 pulses per revolution it has a quadrature resolution of 0.35 mm. This resolution is large enough to see with the naked eye and so the number of encoder pulses between the two rail markings is also monitored. Furthermore, the distance between the two rail markings is known and so the distance travelled per increment of the the encoder can be calculated precisely.

Before each run the LVDT was calibrated by oscillating the equipment at approximately 0.8 Hz and measuring the minimum and maximum output voltages. Knowing the physical oscillation amplitude, h_0, the gain and offset of the LVDT signal were calculated to properly scale the LVDT signal.

Calibration of the load cell assembly involved the measurement of several gain factors. The gain of each individual load cell was measured in both its positive and negative load directions since each load cell was used for measuring an oscillating load. The load cell gain for measuring a positive load may be slightly different for that of a negative load due to minor asymmetry of the load cell physical geometry (Figure 4.12). To illustrate this, example strains (obtained via finite element analysis) for positive and negative loads applied to the load cell pictured in Figure 4.12 are listed in Table 4.3, along with the sensitivity of the load cell in each direction (Equation 4.2). The gain for each load cell was taken as the average of its positive and negative load gains.

$$S = \frac{V_S}{V_{Ex}} = \frac{1 + GF\epsilon_2}{2 + GF\epsilon_1 + GF\epsilon_2} - \frac{(1 + GF\epsilon_4)}{2 + GF\epsilon_3 + GF\epsilon_4} \tag{4.2}$$

Having assigned a gain factor to each load cell, their signals could be combined in the correct proportions to one another. After the individual signals were added together, a

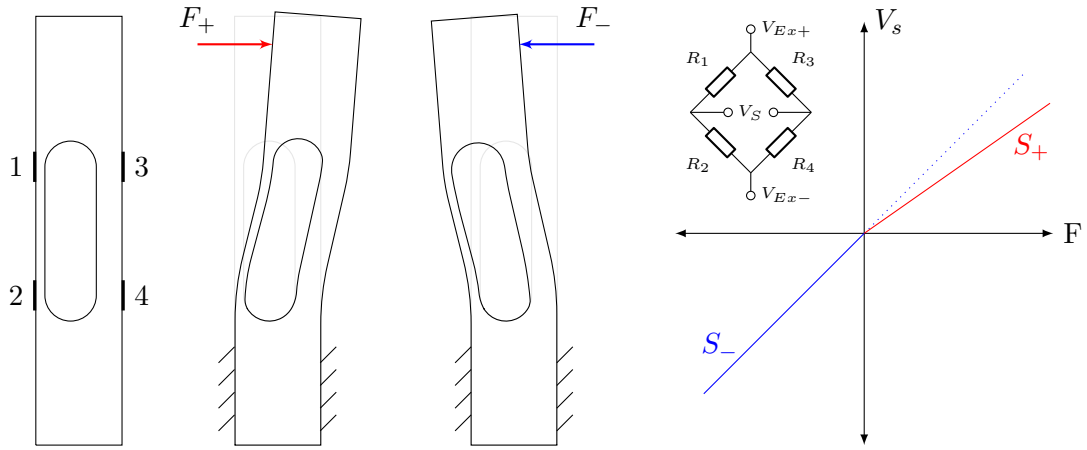

Figure 4.12. Asymmetrical deflection of shear beam load cells.

Table 4.3. Example strain and sensitivity for bidirectional loading of the load cells pictured in Figure 4.12

Force direction	F_+	F_-
ϵ_1	-2.09×10^{-4}	7.01×10^{-5}
ϵ_2	4.93×10^{-5}	-2.03×10^{-4}
ϵ_3	2.05×10^{-4}	-1.17×10^{-4}
ϵ_4	-1.21×10^{-4}	2.67×10^{-4}
Gain factor	2	2
Sensitivity	3.37×10^{-5}	5.57×10^{-5}

final gain G_f was applied to the sum to scale the final output signal. This final gain is particularly important for remote loads applied to the load cell assembly that do not act through the load cell gauging centre, such as in the surge force measurement axis. Finally, to compensate for asymmetry of the individual load cells, and the load cell assembly itself, an asymmetrical gain factor G_a was applied to the positive heave force and surge force measurements only. Figure 4.13 illustrates the order that gains are applied to the load cell signals.

At the start of a days testing, the air temperature at the towing tank was typically below 10 °C. These low temperatures meant that the load cells required longer warm-up periods than if they were started at room temperature. The load cell signals would cease drifting typically 15 to 20 minutes after the excitation voltage was applied. Before each experiment, a known calibration weight was applied separately to the surge force axis

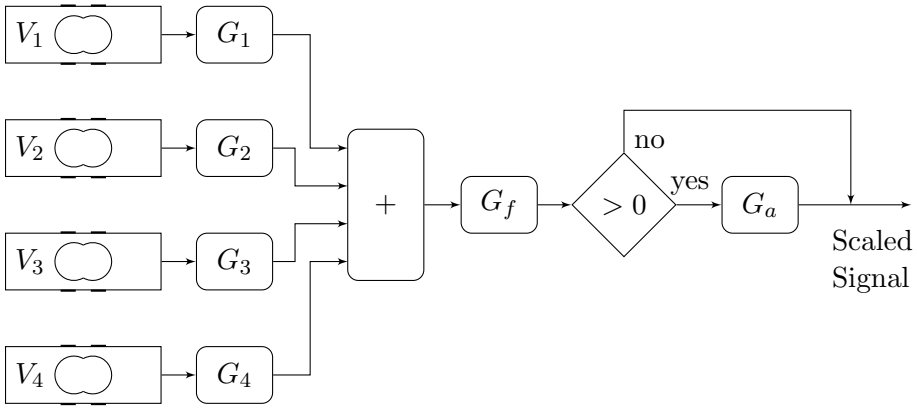

Figure 4.13. Gains applied to the load cell signals.

and the heave force axis to set the final gain of each axis. Horizontal drag (surge) and vertical lift (heave) force measurements were calibrated and recorded in units of kilograms-force to be compatible with the static calibration method of hanging weights. Force measurements were converted to units of newton during post-processing by multiplying them with the gravitational acceleration constant of $9.81\,\mathrm{m\,s^{-2}}$. Once the gains were set, the test equipment was lowered so that the test object was at the required submersion. At this point, the crankshaft was positioned at top dead centre and the load cell offsets were set so that the output forces would read zero. Since the test object would stay fully submerged while oscillating, changes in buoyancy were due to the varying submergence of the struts. Forces on the struts were measured separately and subtracted from the final results (see Section 4.9).

4.8.2 Acquiring data

Before any type of measurement the data signal gains were set as described in Section 4.8.1. Next, the appropriate test object was mounted to the struts at the required pitch angle. Each test object had two 2 mm locating pins at each end, which aligned it to each end plate in a fixed orientation. The pitch angle of the end plates was set by aligning the appropriate degree mark etched into the end plate with the vertical line scribed into the strut above the mounting bolt centre (see Figure 4.14).

To record data at zero translational velocity, the towing car was positioned near but

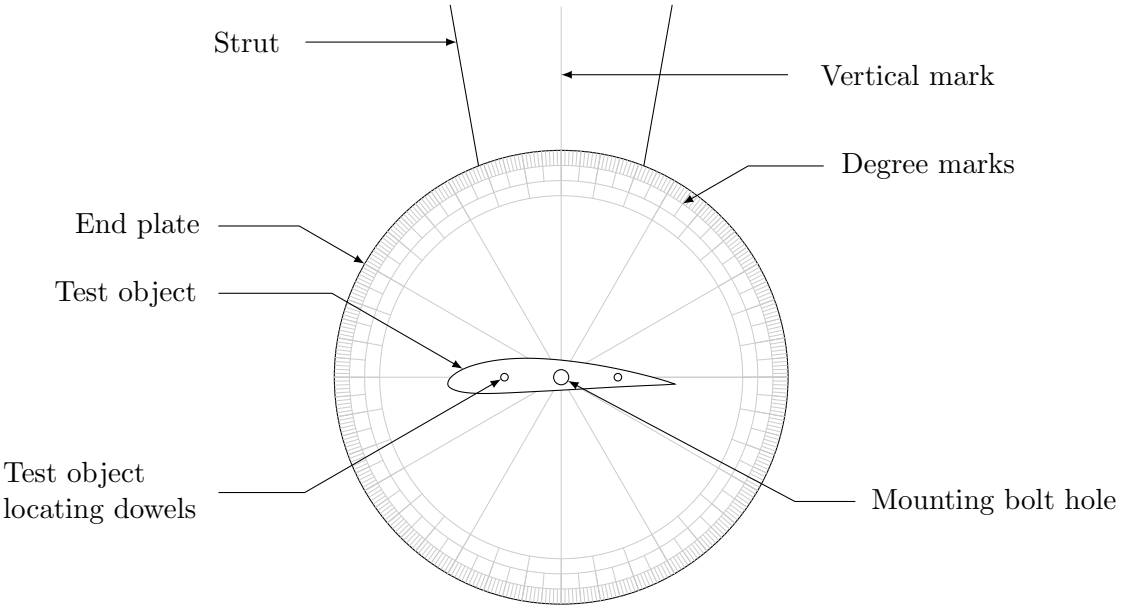

Figure 4.14. Marks on the end plates and struts used to set the pitch angle of the test object (⌀120 mm end plate with 60 mm chord foil shown at half scale).

not at the centre of the tank to avoid symmetrical wave generation. Initially the water was still when the equipment was made to start oscillating at a low frequency. The equipment would be allowed to run at steady state for about 10 seconds to avoid measuring effects of an accelerating oscillating frequency. Data was then recorded for approximately 50 cycles. An additional 3 seconds was added to the data logging time to allow for the group delay of the low-pass filter. Once the measurement was complete, the oscillating frequency was increased, the system would wait 10 seconds for the hydrodynamic forces to establish a new routine, and data was recorded as with the first measurement. This sequence was repeated until data was acquired for all the oscillating frequencies of interest.

To record data at non-zero translational velocities, the towing car was initially positioned at the start of the tank and the test equipment was made to oscillate at a prescribed rate before the car was accelerated to the appropriate speed. Once the car speed was steady, data was recorded until the end of the tank or 50 cycles had been recorded. The car was then returned to the beginning of the tank at low speed to not excite the

water in the tank to much. After runs at high translational velocities or high oscillating frequencies, the water was allowed approximately one minute to settle before the next run commenced.

For each different test object and end plate configuration, the test equipment was oscillated in air over a range of oscillating frequencies to measure the inertia of the equipment bearing on the load cells. Assuming that the aerodynamic forces in air are negligible, these measurements provided us with the inertia of the oscillating equipment. Similar techniques has also been used by Beal et al. (2006), Yu (1945), Anderson et al. (1998), Klose (1966) and Bishop and Hassan (1964) to find the inertia of experimental equipment. Similarly, the hydrodynamic forces and inertia of the struts alone were measured so that they could be subtracted later from the measurements with the test object mounted.

4.9 Data Analysis

As mentioned in Section 4.5, measurements consisted of contributions from the hydrodynamic forces on the struts (including changes in buoyancy), the inertia of the struts, the inertia of the mounted object and the hydrodynamic forces on the object. The only force that is of interest is the hydrodynamic forces on the object and so the rest must be subtracted from the measurements. Each final data set, adjusted for inertia and strut forces, is the result of four separate force cycle measurements: 1) strut and end plate inertia recorded in air, 2) strut, end plate and object inertia forces recorded in air, 3) hydrodynamic forces on the struts and end plates, and 4) the hydrodynamic forces on the struts, end plates, and the mounted object. Figure 4.15 shows how these measurements are combined to yield the hydrodynamic forces on the test object.

4.9.1 Calculating Data Spread

An overview of the process used to find the average cycle in a continuous measurement of a repeating cycle is illustrated in Figure 4.17. First, the continuous signal was separated into individual sample cycles. To do this, the maximum positive heave displacement point was used to index the start and finishing points of cycles in other signals as illustrated in

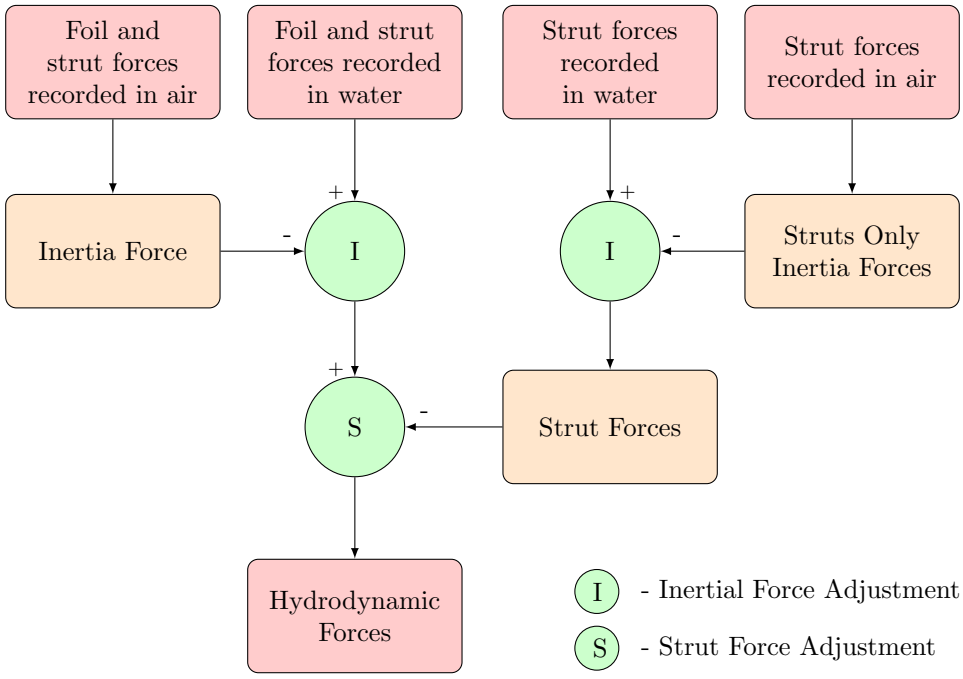

Figure 4.15. The process for removing inertial forces and strut forces from the experimental data.

Figure 4.16. Hence force cycle results presented in later chapters all represent the force cycle on the relevant object on the downstroke followed by that of the upstroke.

Due to variation in cycle period, each cycle sample may contain a different number of data points and so each cycle sample must be interpolated to a common number of data points in length before point-wise averaging can be performed. Point-wise averaging involves averaging samples that all represent the cycles magnitude at a certain position in the cycles period. Given that each of n vector cycle samples are m data points in length, they can be consolidated into a $m \times n$ array (as drawn in Figure 4.17) and the point-wise mean cycle can be found by taking the mean of each column. One limitation of this method is that it does not evaluate temporal variations in the data well.

The sample standard deviation s is known to consistently underestimate the population standard deviation σ for small sample sizes, n (Gurland & Tripathi, 1971). Due to the limited tank length, limited oscillation cycles could be recorded continuously at high

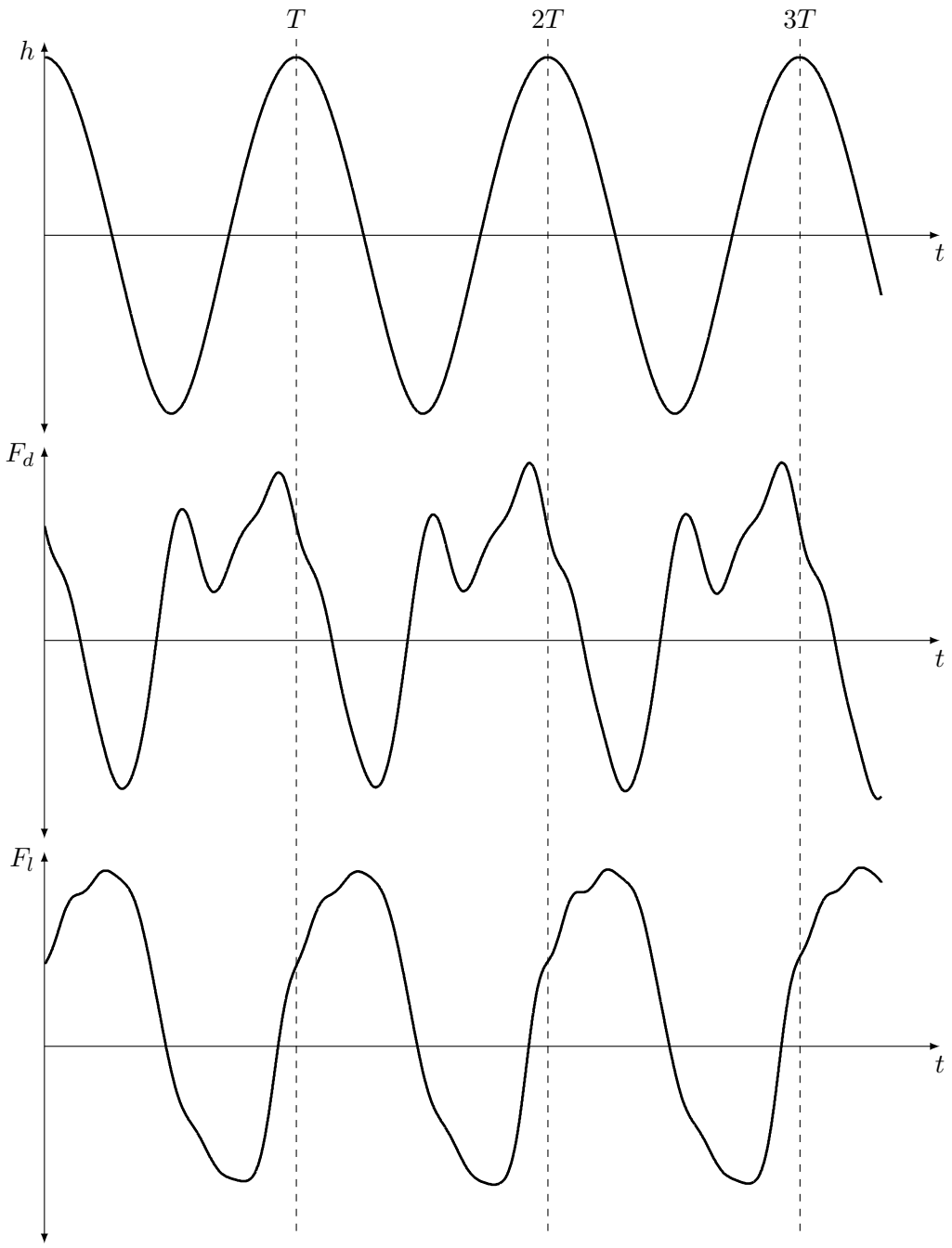

Figure 4.16. Schematic of the heave position signal h being used to index and separate the surge and heave force cycles

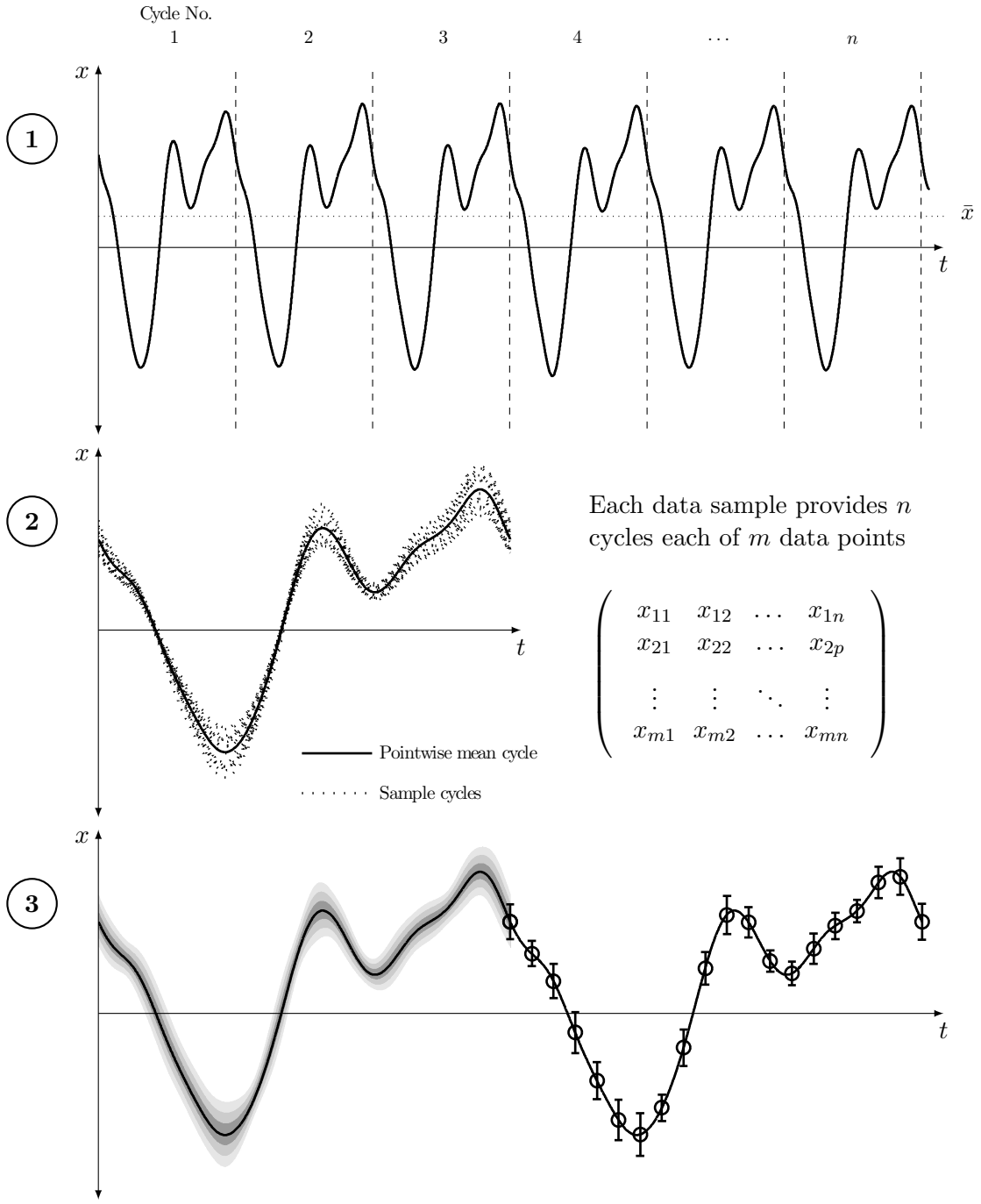

Figure 4.17. A schematic of the point-wise cycle averaging process. 1 - separating the sample into individual cycle samples. 2 - interpolating each sample cycle to a common length of data points. 3 - point-wise averaging and variation statistics; shaded standard deviations and $\pm 2\,\mathrm{SD}$ error bars.

car velocities. To prevent the standard deviation from being underestimated, standard deviations were multiplied by the correction factor c_n, defined in Equation 4.3, where Γ is the gamma function. For sample sizes greater than 26 samples, the correction is less than 1 %. Cycle means were added together on a point-wise basis. Cycle uncertainties were also added point-wise using Equation 4.4 (Castrup & Castrup, 2010).

$$c_n = \sqrt{\frac{n-1}{2}} \frac{\Gamma\left(\frac{n-1}{2}\right)}{\left(\frac{n}{2}\right)} \tag{4.3}$$

The velocity of the towing car was derived from position measurements obtained via an incremental encoder (see Section 4.5). The position of the car was sampled at the same rate as the force and heave position measurements, which resulted in over-sampling. The velocity of the tow towing car was calculated every hundred increments of the encoder to ensure small calculation errors while maintaining a good velocity sampling frequency.

4.9.2 Hydrodynamic Force Phase Estimation

For engineering applications, the main characteristic of interest in the heave force profile is its magnitude. At a minimum of detail for design purposes the magnitude and phase of the cycle maximum and minimum should be known. As mentioned in Section 3.3.7, the heave motion in the current experiments is not purely sinusoidal, but is the composition of several harmonics. This makes defining the phase of the heave motion cycles and force cycles difficult. Keulegan and Carpenter (1958) also recognised these two points and defined the phase of their measured force cycles as $\phi_{KC} = \pi - \theta_m$ where θ_m is the phase at which the maximum hydrodynamic force occurs. They also define their fluid velocity with the function $u = u_0 \cos(\omega t)$ where u_0 is the half-amplitude of the fluid velocity. These definitions essentially describe the force cycle phase as the phase by which the maximum hydrodynamic force leads the maximum fluid velocity (Figure 4.18). Since Keulegan and Carpenter (1958) used a sinusoidally oscillating flow in their experiments, by symmetry this phase also describes how much the minimum hydrodynamic force leads the minimum fluid velocity.

In the current study, with hydrodynamic forces expected to be dominated by inertial effects, it was considered more appropriate to define the phase of the heave forces relative

to the phase of the heave acceleration signal. Hence, the phase of a force cycle ϕ was defined as the lag between the heave acceleration and the hydrodynamic force. Since the heaving motion and resultant hydrodynamic forces are not sinusoidal, but are composed of several harmonics (see Section D.2), the phase of a force cycle was estimated by the phase difference between a characteristic point in the force cycle and the corresponding characteristic point in the heave acceleration cycle. For example, the heave force phase at maximum heave position $\phi^{\wedge}_{h\downarrow}$ was defined as the phase lag between the peak acceleration at top dead centre, and the following peak heave force. Force cycle phase was estimated at four points $\phi^{\wedge}_{\downarrow}$, $\phi^{0}_{\downarrow}$, $\phi^{\wedge}_{\uparrow}$ and $\phi^{0}_{\uparrow}$ as shown in Figure 4.19. To estimate the average phase of a force cycle $\bar{\phi}$, the mean of these four estimates was used. Subscripts s and h signify surge and heave force cycle phase estimate respectively.

4.10 Error Identification

Data was acquired from the National Instruments CompactDAQ in LabView's waveform data type at a sample rate of 10 kHz. The specified internal timing accuracy of the CompactDAQ is 50 ppm (0.005 %). The magnitude of this accuracy is negligible and so the uncertainty in sample timing was neglected in data and error analyses.

Since the LVDT was the source of not only heave position measurements, but heave velocity and acceleration measurements, it was calibrated regularly (as described in Section 4.8.1) to ensure that these measurements were precise. Sources of uncertainty in the heave position measurements include play in the Watt's linkage that the LVDT was mounted to, and temperature changes. Although no systematic process was used to evaluate the repeatability of the heave position measurements, the measured position of the oscillating assembly was checked to be correct at top dead centre and bottom dead centre regularly. The error of the position measurement at these two locations was always less than 0.1 mm. With this observation, and making the assumption that the heave position measurement errors are normally distributed, and the 95 % confidence interval for the heave position measurements is ± 0.1 mm, the standard deviation, or uncertainty (Castrup & Castrup, 2010), of the heave position measurements is 0.051 mm.

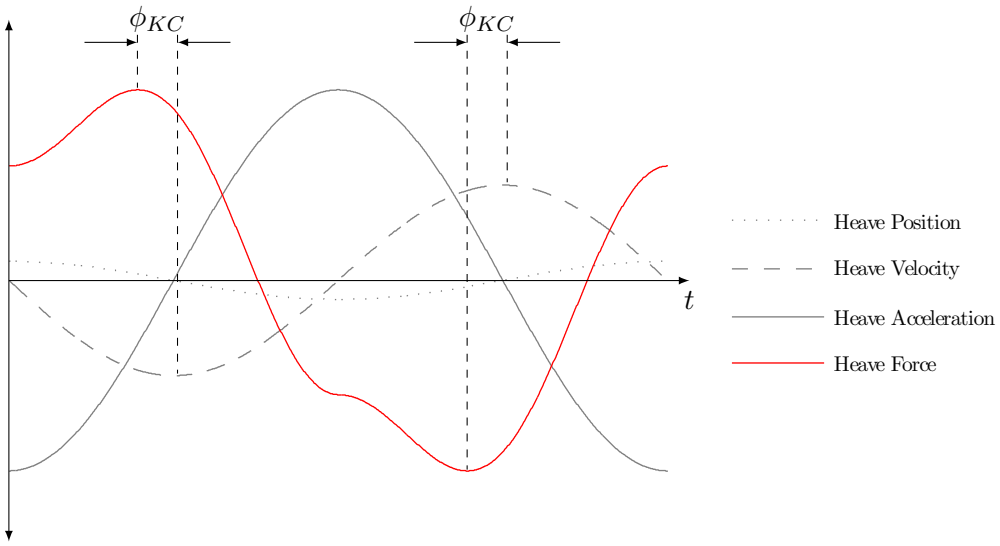

Figure 4.18. Keulegan and Carpenter's (1958) definition of hydrodynamic force phase.

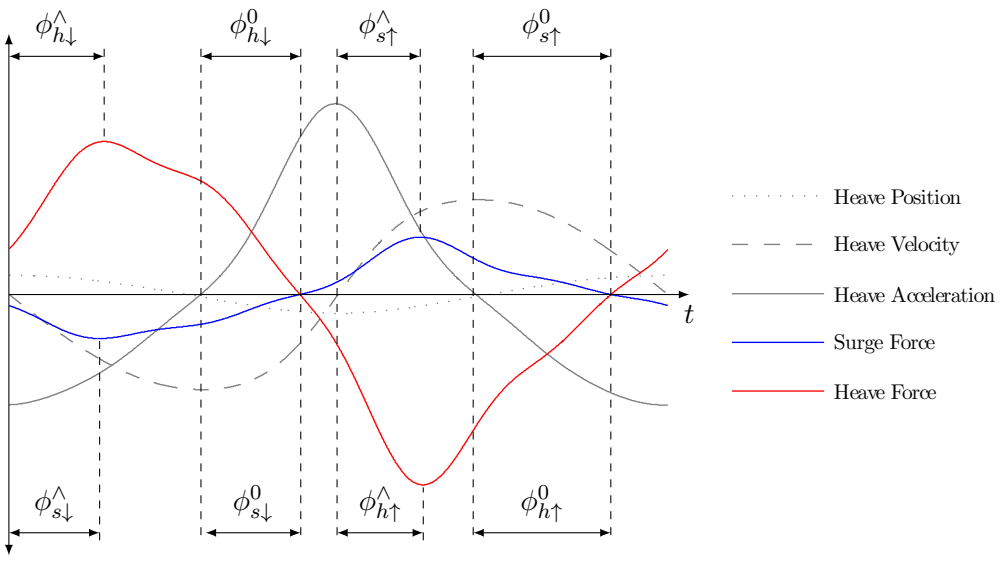

Figure 4.19. Notation used for describing how hydrodynamic forces lag the heaving acceleration.

Heave velocity was derived from the heave position measurement by taking the difference between two successive position measurements and multiplying by the sampling frequency. The heave acceleration was calculated from the heave velocity using the same process. As mentioned above, the sample measurement timing uncertainty was negligible and so the uncertainty of the heave velocity was equal to the sum of the two position measurement uncertainties. Equation 4.4 (Castrup & Castrup, 2010) is the general formula used for the addition of uncertainties. Apply Equation 4.4 to the addition of two position measurements, each with uncertainty u_h, Equations 4.5 and 4.6 present expressions for the uncertainty of the calculated heave velocity and acceleration respectively.

$$u_{\dot{h}} = \sqrt{u_1^2 + u_2^2 + 2\rho_{1,2}u_1u_2} \tag{4.4}$$

$$u_{\dot{h}} = \sqrt{{u_h}^2 + {u_h}^2 + 2u_h^4} = \sqrt{2{u_h}^2 + 2u_h^4} \tag{4.5}$$

$$u_{\ddot{h}} = \sqrt{{u_h}^2 + 2^2{u_h}^2 + {u_h}^2 + 2(2)u_h^4 + 2(2)u_h^4 + 2u_h^4} = \sqrt{6{u_h}^2 + 10u_h^4} \tag{4.6}$$

The uncertainty of measurements made with the load cell assembly was evaluated by repeated static and dynamic measurements of known loads. Appendix A contains a statistical analysis of repeated measurements taken with the load cell assembly. These sample measurements resulted in successive measurements taken with the load cell assembly having a symmetrical uncertainty of 0.12 N associated with them. The load cell assembly displayed very good linearity in both the heave and surge axis (Figures A.2 and A.3). To check that the output of the load cell assembly was independent of where the load was applied along the test object span, measurements were taken with weights applied to the centre of the object, next to the left strut and the right strut. Measurements applied at the length of the object span deviated less than 0.2 % from the applied load. The hydrodynamic load on the object was assumed to be reasonably evenly distributed across the object span and so this bias was neglected. The independence of the two force measurement axes were checked by applying a load purely along an axis and recording the load measurement in the orthogonal axis (Section A.1). The cross-talk between the two

channels was less than 0.2 % (see Figures A.6 and A.7). The independence of the two load axes was also checked by applying a two-component load in each axis (Section A.2).

Due to the limited stiffness of the experimental equipment, the response of the struts and test object is not in-phase with the excitation oscillation. Hence, the force measurements differ from those that would be acquired with rigid equipment. The effect of this error is discussed in detail in Appendix B. Heave forces presented as a function of time in subsequent chapters are shown with their $\pm 2\,\mathrm{SD}$ uncertainty bounds and dynamic confidence bounds. The dynamic confidence bounds indicate the point-wise interval, in which the true force cycle (free from dynamic error) is expected to lie with 95 % confidence.

Before and after each experiment, the load cell assembly gains were checked. No significant load cell drift was ever encountered during the course of a day's testing. The offset of the load cell's signal was checked before and after every 2 to 3 low speed runs ($u \leq 2.5\,\mathrm{m\,s^{-1}}$). At higher speeds the offset was checked before and after every run since water would sometimes splash up onto the load cell assembly and add extra downforce to the measurements. As part of the load cell assembly was above the water surface, some load due to aerodynamic drag would be measured. Due to the density of water being approximately a thousand times that of air, any aerodynamic loads were considered of negligible magnitude relative to the measured hydrodynamic loads and were ignored. The experimental equipment was rigidly attached to the towing car chassis using bolts for good alignment with the water channel (see Section 4.4). The rigid mounting of the test equipment also allowed for vibration from the car to be transmitted to the test equipment and be felt by the load cell assembly. Constant vibration sources included the car's electric drive motor and mechanical transmission. Irregular vibration sources included small debris on the rails, or movement of the driver. To minimise artefacts due to irregular vibrations, the rail tracks were kept very clean and people on the car during data acquisition were required to be seated and still. Averaging several hydrodynamic force cycles reduced the effect of any remaining artefacts due to unavoidable irregular vibration sources.

As mentioned in Section 4.9 the velocity of the towing car was calculated every hundred increments of the rotary encoder to maintain a reasonable velocity sample frequency and hence capture velocity fluctuations of the towing car. Again assuming the sample timing

uncertainty to be negligible, the uncertainty of each velocity calculation is equal to the position resolution relative to the measured displacement (1 %). Although this seems coarse, the uncertainty of the velocity sample's mean is reduced to the position resolution relative to the total displacement of the towing car (during one data log). Hence, the longer data was recorded for, the lower the uncertainty of the mean velocity. Since up to 50 cycles would be recorded per run, the shortest towing car total displacement occurred when the car velocity was low and the oscillating frequency was high (i.e. high Strouhal number measurements). During these runs the total car displacement was typically 7 m to 8 m. Over these displacements the resolution of the encoder is negligible ($< 5 \times 10^{-3}$ %).

It was important that measurements recorded at non-zero velocity were acquired when the towing car velocity was constant to avoid inertial forces contributing to the surge force measurements. For all oscillating frequencies and translational velocities, 95 % of velocity samples lay within ± 0.7 % of the mean velocity. This variation is considered to have negligible effect on the results.

4.11 Presentation of Data

As mentioned in the previous section, heave force cycles presented in later chapters, plotted against time, are shown with their ± 2 SD uncertainty bounds (inner error bars) and dynamic confidence bounds (see Appendix B). Surge force cycles are not expected to contain the same dynamic uncertainty as the heave force cycles (due to smaller cycle amplitudes) and so surge force cycles are presented with error bars representing ± 2 SD bounds of the sample. Error bars have been omitted for clarity in some plots showing multiple heave force cycles or surge force cycles as a function of time. In these cases errors are usually small. However, typical errors may be found in Appendices E to H.

In later chapters, cyclic hydrodynamic forces are presented as a function of time similar to those shown in Figure 4.17. As mentioned in Section 4.9, points of maximum heave position were used to index the beginning and end of individual force cycles so that individual cycle samples may be compared. For this reason cyclic data presented as a function of time (or normalised time) will begin at the top of the heave downstroke, i.e. at

$t = 0$, $h(t) = h_0$. Furthermore, approximately the first half of a cycle period ($0 < {}^{t}/_{T} < 0.5$) represents the data during the downstroke motion while the second half of the cycle period ($0.5 < {}^{t}/_{T} < 1$) represents data during the upstroke motion.

Hydrodynamic forces were analysed with respect to the unsteady motion of the foil, i.e. the heaving velocity and acceleration. Hence, with two degrees of freedom, some data was best displayed as a surface plot to visualise dependencies between variables. It can be difficult to visually evaluate a functional fit to measured data from a single viewing angle, and so some surface plots included in the results are done so in U3D format. These plots can be activated and deactivated by clicking on the figure.

The conventions declared in this section for the presentation of results will be upheld throughout the results chapters unless otherwise stated.

4.12 Verification of the Experimental Method

4.12.1 Heaving consistency

As discussed in Section 4.8.2, the mode of measuring the forces on the test object was not by direct measurement. Measured force signals initially contain components of unwanted quantities, i.e. the object and strut inertia, as well as hydrodynamic forces on the struts, which must all be subtracted from the data. This section discusses the checks performed to verify this method.

The consistency of the input power from open loop control makes it easier for the oscillating loads on the test object to back-drive the transmission and hence vary the heaving profile. MacCready (1990a) overcame this issue on the Mutiny on the Boundary layer by adding a flywheel to the drive-train. A flywheel was added to the crankshaft of the experimental equipment for the same reason: to avoid the distortion of the heaving profile when the test object was subject to hydrodynamic cyclic forces. In the process of subtracting the measured hydrodynamic forces on the struts and the inertia of the equipment, it was assumed that the forces on the test object whilst oscillating in water do not distort the heaving position, velocity and acceleration profiles from those in air. Even with the presence of the flywheel, this assumption required validation.

The flat plate was chosen as the test object for this study because it was expected to be subject to high hydrodynamic reaction forces (added mass and drag) due to its flat geometry. The flat plate was mounted to the test rig and oscillated in air and water to compare changes in the heaving profile. This test was also performed with only the ⌀320 mm end plates mounted to the struts for comparison. Figures 4.20 and 4.21 show the effect of hydrodynamic forces on the heaving velocity and acceleration profiles respectively. Figure 4.22 summarises the effect of hydrodynamic reaction forces on the heaving profile of the flat plate. It also shows how the hydrodynamic reaction forces alter the heaving profile of the struts with the ⌀320 mm end plates mounted.

Referring to Figure 4.20, the wet and dry heaving velocity profile of the flat plate varies less than ±2.3 % provided the oscillating frequency is greater than 2 Hz. Similarly, once the oscillating frequency exceeds 2 Hz the wet and dry heaving acceleration profiles vary less than ±3.5 %. This settling of the heaving velocity and acceleration profiles, at oscillation frequencies above 2 Hz, is also evident in Figure 4.22 where the plot becomes almost horizontal. When no test object is mounted, the difference between the wet and dry heaving profiles tends to zero as oscillating frequency is increased (see Figure 4.22). The struts, with end plates mounted, have only a small cross-sectional area normal to the heaving axis, and so do not displace a large amount of water. Hence, the hydrodynamic force on the struts is relatively small. As the oscillating frequency increases, the flywheel gains momentum and the hydrodynamic forces on the struts become less significant. In this case the flywheel is large enough to smooth changes in torque on the drive-train due to the hydrodynamic forces. When the flat plate is mounted to the struts (at θ=0), the cross-sectional area normal to the heave axis is significantly larger, and so are the hydrodynamic forces. Furthermore, the torque cycle on the drive-train due to hydrodynamic forces has a larger amplitude. In this case, although the flywheel provides significant energy storage to smooth the velocity of the crank shaft, at frequencies above 2 Hz the flywheel smoothing effect is limited.

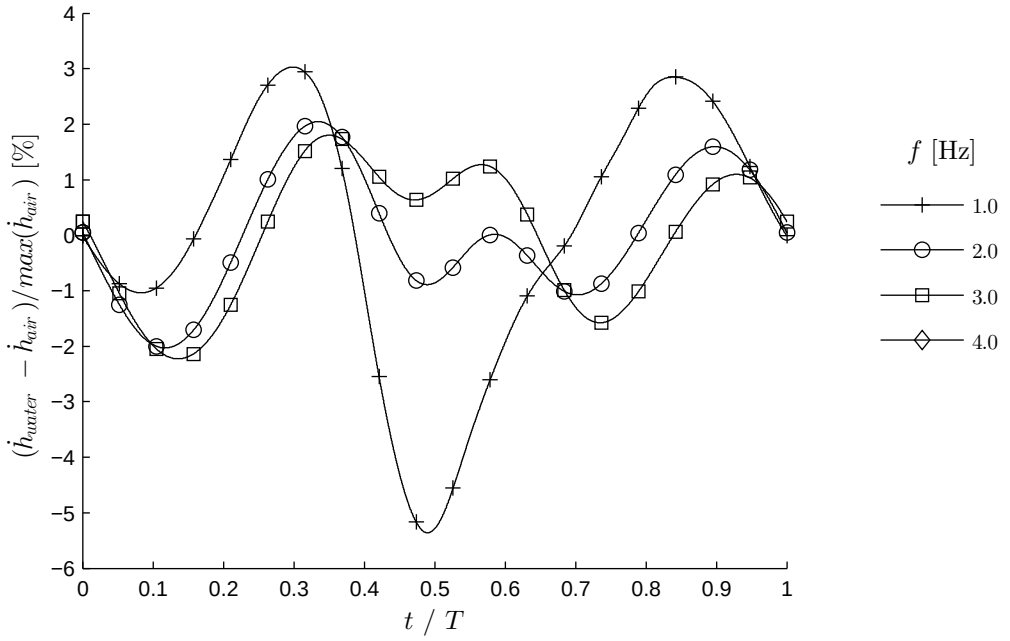

Figure 4.20. Comparing the heave velocity profile for the flat plate oscillating in water to the foil oscillating in air. h_0/c=0.75

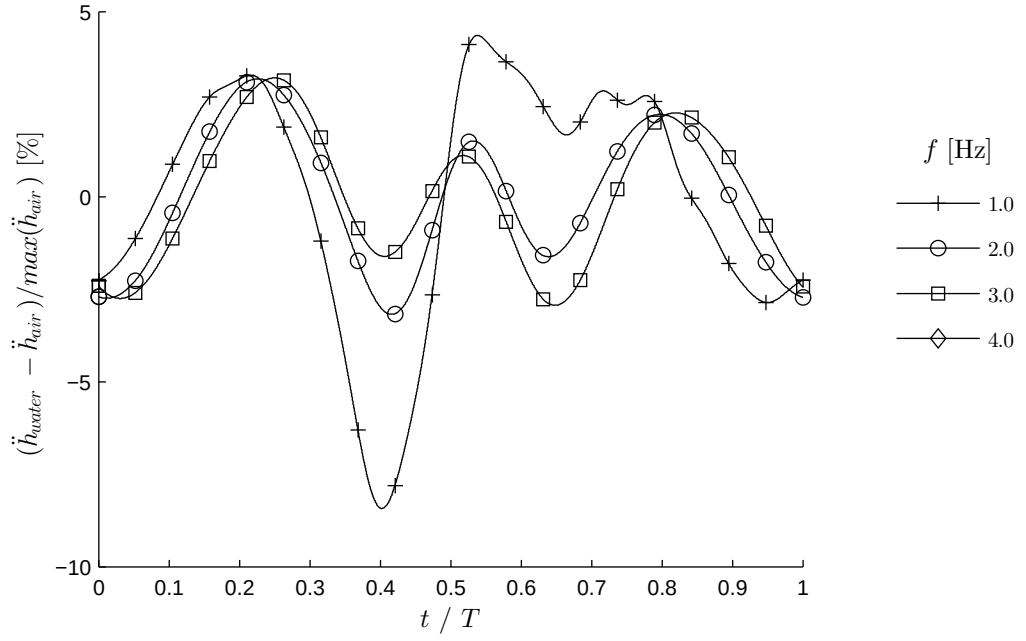

Figure 4.21. Comparing the heave acceleration profile for the flat plate oscillating in air to the foil oscillating in water. h_0/c=0.75

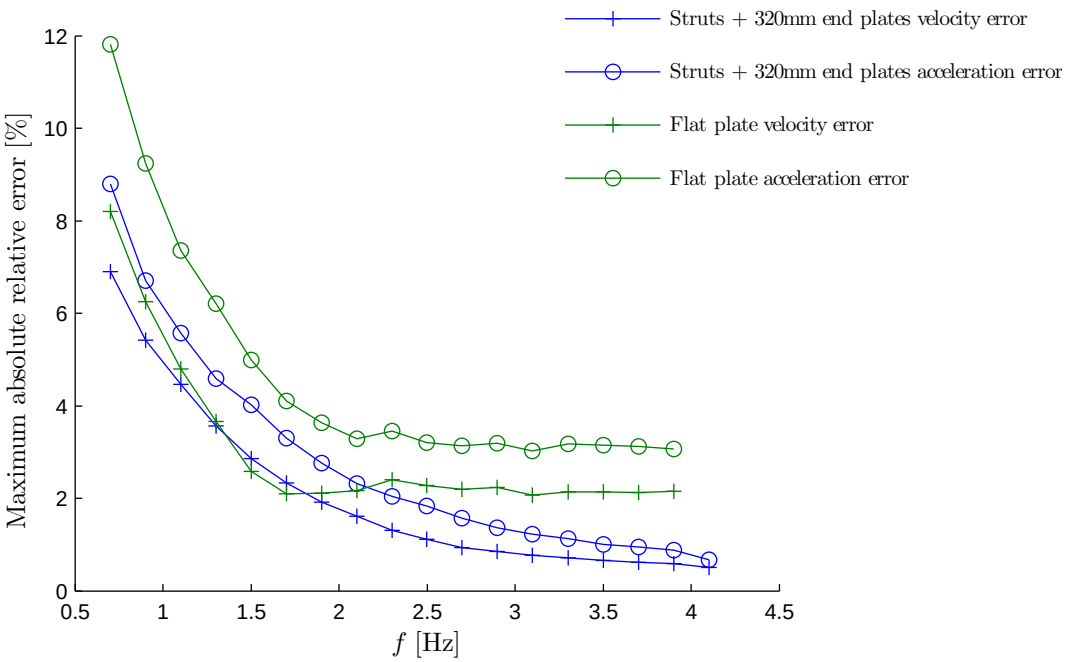

Figure 4.22. Maximum relative point-wise error between heaving velocity and acceleration in air and water versus oscillating frequency. h_0/c=0.75

4.12.2 Repeatability of Measurement

As mentioned in Section 4.9, the length of the towing tank limited the number of cycles that could be recorded in a single run. Since both the towing car and the experimental equipment motors were under open loop control, it was considered fair that only force cycles recorded in a continuous run were compared against one another. If force measurements exhibit inadequate consistency, the combined measurement uncertainties after the cycle subtraction process (Section 4.9) would expand data uncertainties rapidly. Referring to Figure B.6 in Appendix B, the spread of force data about the point-wise cycle mean was relatively insensitive to the heave force cycle range for continuous force measurements. However, this does not show that the same force cycle could be captured again in an independent run.

To check that force measurements where repeatable, repeated measurements were taken at three different states (see Table C.1). The difference between three independent runs at the same state was small. Example plots of the repeated measurements are

shown in Appendix C. When the cycle periods were normalised to remove small temporal biases, the maximum point-wise bias between the repeated force measurements shown in Figures C.1 to C.3 was 1.2 % and 0.9 % of the cycle range for surge and heave force measurements respectively. Furthermore, the maximum mean biases were smaller than the 95 % confidence intervals for the mean assuming a student's t-distribution (±1.3 % and ±1.4 % for the mean surge and heave cycles respectively). Even though the measurements were highly repeatable, especially at high oscillating frequencies, they contained systematic error due to the finite stiffness of the load cell assembly. This error is discussed in Appendix B.

4.12.3 Contributions of Inertia and Hydrodynamic Forces on the Struts

As mentioned in Section 4.5, measurements of the hydrodynamic forces on the test object were made indirectly. Raw force measurements contained contributions from hydrodynamic forces on the struts, and the inertia of components bearing on the load cell assembly. The final surge and heave force data (on the test object alone) relies on the removal of these force components from the raw data as described in Section 4.9. Figure 4.23 and Figure 4.24 illustrate the contributions of hydrodynamic forces on the struts, and inertial forces to the raw measured surge and heave forces on an oscillating NACA4415 hydrofoil (θ=0) at low and high Strouhal numbers (low St: f=1.8, u=2.0, high St: f=3.6, u=0.5).

Figure 4.23 shows that inertial forces in the surge direction, which could have arisen from the Watt's link surge error (see Section 4.2), or unsteady translational velocities (see Section 4.10) are of negligible magnitude relative to hydrodynamic surge forces. Figure 4.23a shows that the strut drag force offsets the surge force cycle but has little contribution to the surge force profile. Hence, the amplitude of the strut drag cycle is small compared to the range of the surge force cycle. This strut drag offset becomes smaller as the Strouhal number is increased.

Both Figure 4.24a and Figure 4.24b show that hydrodynamic heave force on the struts is minor compared to that on the foil. This is due to their small cross-sectional area in the horizontal plane. Inertia is the dominant unwanted force component in the heave axis.

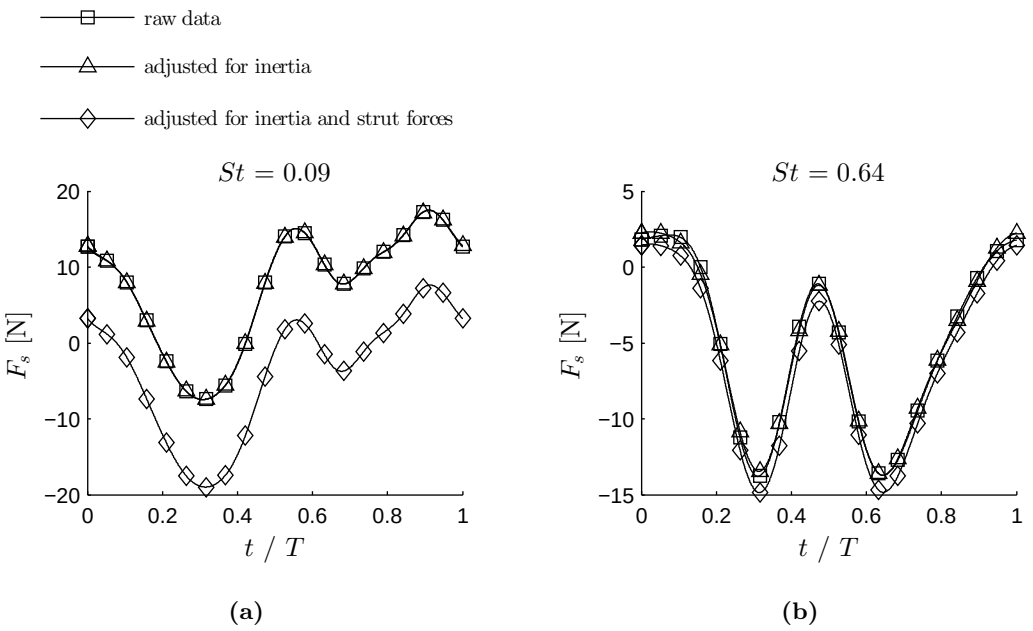

Figure 4.23. Contributions of inertia and hydrodynamic forces on the struts to the total measured surge forces.

Figure 4.24b shows that inertia of the measurement equipment has a larger contribution to the measured lift at higher Strouhal numbers where the oscillation frequency is high. Also note at high Strouhal numbers the difference between the unadjusted and adjusted force cycle profiles and phase. At high St, the contributions of in-phase and out-of-phase forces on the test object in the heave axis are comparable. Once the object inertia force is removed from the measurements, the balance between the in-phase and out-of-phase forces changes resulting in a change in phase and profile.

To sum up, the hydrodynamic forces on the struts, and the inertia of components bearing on the load cell assembly contribute the least to the surge force measurements at high Strouhal numbers, and least to heave force measurements at low Strouhal numbers. At low Strouhal numbers the hydrodynamic forces on the strut contribute a near constant surge offset relative to the surge force cycle range. At high Strouhal numbers, the removal of the dry inertia force aligned with the heave axis significantly changes the balance between in-phase and out-of-phase forces on the load cell assembly. In this case the removal

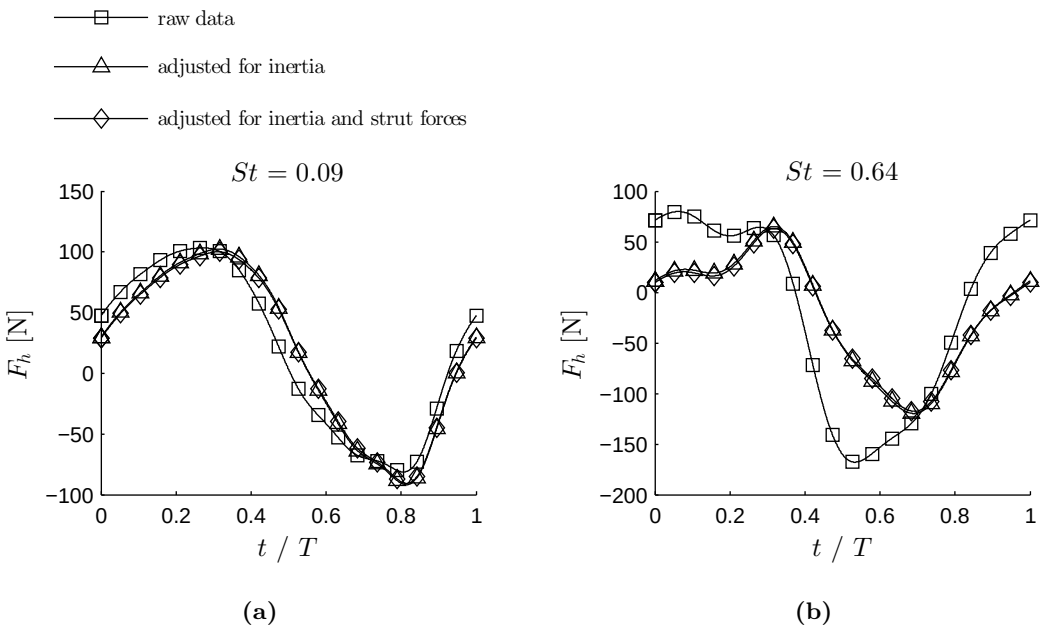

Figure 4.24. Contributions of inertia and hydrodynamic forces on the struts to the total measured heave forces.

of the unwanted inertia forces causes the most drastic modification to the raw measured heave force cycle.

Chapter 5

Hydrodynamic Forces on a Heaving Object with Zero Forward Velocity

5.1 Introduction

The hydrodynamics of oscillating foils has been extensively studied over the finite Strouhal number range. However, little attention has been given to objects oscillating at zero free-stream velocity ($St{=}\infty$). Lai and Platzer (2000) showed that thrust produced by a heaving NACA0012 foil at zero free-stream velocity was proportional to the oscillating frequency. Similarly, Vandenberghe et al. (2006) showed that the surge velocity achieved by a heaving flat plat starting from rest was proportional to the heaving velocity. However, the influence of other variables such as the heave amplitude, submersion depth, end effects, and object orientation are not well known.

Up until now, vehicles such as the Trampofoil have avoided operating under this condition by launching with a 'rolling start' (see Section 2.2.4). Like the Trampofoil the Wasserläufer lacks sufficient buoyancy to support the rider at rest. However, the Wasserläufer can start from rest using an impulse start, exploiting the added mass of its hydrofoils. The added mass of a cylinder has been studied extensively. However, the

theoretical added mass associated with other objects has not been well validated.

5.1.1 Objectives

In Section 3.3 two existing models for calculating the hydrodynamic forces on an object in a 1D oscillatory flow were reviewed. Both models equate the in-phase (inertial) hydrodynamic forces to the product of the heave acceleration and the virtual mass of the object. However, drag forces were modelled differently. The suitability of each model is subject to the relative contributions of the in-phase and out of phase hydrodynamic forces, which can be evaluated with the heave-to-chord ratio or the Keulegan-Carpenter number. Low values of K_C ($K_C < 3$ (Journée & Massie, 2001)) suggest that inertial forces dominate and a mass damper model should be used. Alternatively high values of K_C indicate drag dominated hydrodynamic forces which will be best modelled by the Morison Equation. However, this guideline to model selection assumes drag is proportional to the heaving velocity squared as in the Morison equation (Equation 3.6), causing a bias outcome. Furthermore, other factors such as object geometry and the frequency of the oscillating flow do not contribute to this decision. An objective of the following experiments was to determine the suitability of the Morison equation and the mass damper model for modelling the hydrodynamic forces on the four test objects in the K_C range of interest.

5.1.2 Overview of Tests

In this chapter, measurements of hydrodynamic forces on oscillating objects in initially stagnant water are presented. Firstly the effects of the free surface and span-wise flow are considered in Section 5.2 to specify adequate submersion and end plate size for the subsequent experiments. Secondly, measured hydrodynamic forces on a cylinder are presented in Section 5.4 and compared with other published results. The cylinder heave amplitude is varied to observe the influence of the heave-to-chord ratio on the hydrodynamics forces. Thirdly, the hydrodynamic forces on the flat plate are presented in Section 5.5 and are compared with the hydrodynamic forces on the cylinder. The effect of non-zero pitch angles on the hydrodynamic forces is shown in this section. These results demonstrate

the effect of object geometry on its added mass. Finally, the hydrodynamic forces on the NACA0012 and the NACA4415 oscillating at zero translational velocity are presented in Section 5.6 and compared to the results of the previous two test objects.

To maintain similarity with full scale human-powered flapping wing propellers (see Table 2.2) the heave-to-chord ratio in the following experiments was h_0/c=0.88 for the flat plate and h_0/c=0.75 for all other test objects. The Reynolds number based on maximum heaving velocity was limited by the capacity of the load cell assembly and the power of the motor driving the oscillations. However, it ranged up to about 58 000 which was considered close enough to that of the Trampofoil (Re_h ≈87 000). The covered Reynolds number ranges for each heave-to-chord ratio investigated are shown in Table 5.1.

5.2 Free Surface Effects

The presence of a free surface or wall affects the hydrodynamic forces on a steady or unsteady object in a flow. Existing human-powered flapping wing hydrofoils (such as the vehicles discussed in Section 2.2) operate at a submergence shallow enough that the free surface interacts with the foil. This is evident in the surface waves generated behind one of these vehicles. Hence, to design a new vehicle the effect of the free surface on propulsion should be considered. Knowing the effect of a free surface on an oscillating foil is not only useful for design, but also in the laboratory, and for experiment error analysis. Currently experimental studies have justified the working depth of an oscillating foil for thrust measurements to be independent of the free surface (Hover et al., 2004). However the effect of the free surface on thrust production has not yet been well described.

5.2.1 Background

The lift and drag coefficients of a steady foil at non-zero forward velocities and low submersion depths are known to vary significantly from those at higher submergence (Matveev & Duncan, 2005; Xie & Vassalos, 2007; Yasko, 1988). Daskovsky (2000) and Wadlin, Shuford, and McGehee (1955) both modelled the lift reduction of a steady foil in the proximity of the free surface with potential flow theory. The lift reduction is sensitive to the

submersion depth, chord length and the span of the foil. Q. Zhu, Liu, and Yue (2006) modelled a foil heaving near a free surface and concluded that the thrust coefficient is also sensitive to the submersion depth, chord length and the span of the foil.

As well and the mean lift, the free surface may also effect the phase and magnitude of the hydrodynamic forces though altering added mass contributions. The added mass of an object is often found by comparing its natural frequency in multiple mediums (Chen, Wambsganss, & Jendrzejczyk, 1976; Pabst, 1930; Yu, 1945). Amabili (1996) suggests that the natural frequency, and hence the added mass of a vibrating plate change with distance from fluid boundaries. Furthermore, theory predicts that the natural frequency of the object will decrease with depth from a free surface and increase with distance from a wall. If this is true, added mass contributions would be expected to increase with submergence depth, decreasing the lag between heave acceleration and heave force.

When using an oscillating foil for propulsion the aim is to transfer kinetic energy from the foil to the fluid. Like most processes this transaction has an associated efficiency. In the case of an ideal propeller, all the wake momentum would be aligned with the main stream flow direction. In reality, wake momentum in the main stream direction equates to useful thrust while the remaining components of momentum are wasted energy. For a submerged foil oscillating near a free surface, energy is lost in the wake and through generating surface waves. Grue, rn, and Plam (1988) states that the generation of surface waves is associated with a considerable amount of wasted energy.

5.2.2 Procedure

The effect of a free surface on a submerged oscillating object may depend on the amplitude of the oscillations, the mean submergence, the frequency of the oscillations and the size and shape of the object. In this investigation we hold the amplitude of the oscillations constant while varying the oscillation frequency and submergence of the test objects described in Section 4.3. Grue et al. (1988) states that free surface effects are most prominent when $^{Uf}/_{g} < {}^{1}/_{4}$, i.e. when either the forward velocity or oscillating frequency of the foil is small. So the current experiments were performed with a zero main stream velocity which was assumed to be the case where surface effects will be most prominent.

Figure 5.1 is a diagram of the oscillation variables. In the following experiments the heave amplitude h_0 was 45 mm ($h^* = 0.88$ for the flat plate and $h^* = 0.75$ for all other objects). Measurements were recorded at five different submersion depths. For all tests, except those investigating end effects, test bodies were fitted with ⌀320 mm (5.3 chord lengths) end plates to avoid significant span-wise flow. Experiments were repeated for the NACA4415 foil with ⌀120 mm (2 chord lengths) end plates and no end plates to determine if span-wise flow significantly affects the hydrodynamic loads on the foil.

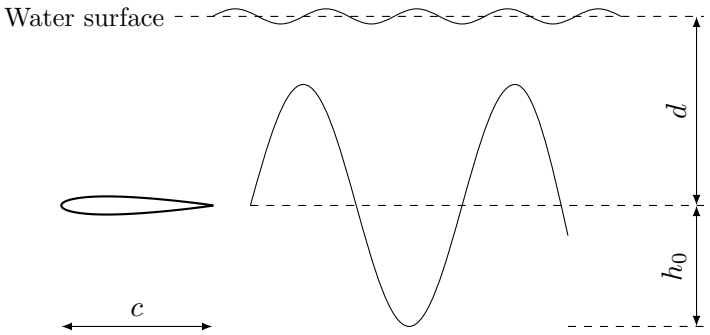

Figure 5.1. Submergence study parameters

In the following experiments, the capillary wave number goes beyond 220 m^{-1} resulting in corresponding wave lengths approaching the critical wave length. In this case we can expect surface waves to be effected by both gravity and surface tension (see Section 3.3.7), in which case the gravity-capillary wave number can be found with Equation 5.1. Furthermore, since the tank depth (see Section 4.4) is greater than half of the longest expected wave length ($\approx$ 125 mm) the tank can be considered as deep water.

$$\omega^2 = \left(gk + \frac{\sigma}{\rho}k^3\right)\tanh\left(kd\right) \tag{5.1}$$

To compare the two independent variables, oscillating frequency and submersion depth, the oscillating frequency was converted to the wave number k by solving Equation 5.1, and then non-dimensionalised with the object chord length similarly to the submersion depth. A water surface tension of $\sigma = 0.0742\,\mathrm{N\,m}^{-1}$ and density of $\rho = 1000\,\mathrm{kg\,m}^{-3}$ were used. To estimate the power required to oscillate a test object, Equation 3.34 can be simplified

to Equation 5.2 because the object does not change pitch with time.

$$\bar{P}_{in} = \frac{1}{T}\int_0^T F_h \dot{h} dt \tag{5.2}$$

5.2.3 Non-thrusting objects

A Cylinder Heaving Beneath a Free Surface

Mean surge force on the cylinder remained relatively constant and near zero over the test kc domain when the cylinder remained entirely submerged throughout a heaving cycle (Figure 5.2a). The mean heave force on the oscillating cylinder also remained near zero when the cylinder remained entirely submerged. As the cylinder approached the free surface the mean heave force became more positive as there became less water resisting motion on the upstroke. Figure 5.2b shows that the mean heave force on the cylinder is independent of the free surface over the tested range of kc for depths greater than $3.3c$. At the submersion depth of $3.3c$ the mean heave force has a sharp local minimum at approximately $kc = 3.9$. This represents the start of ventilation. At submergences deeper than this ventilation did not occur.

At shallow submergence there are large spikes in the heave force phase, particularly at high oscillating frequencies (Figure 5.2c). These phase shifts are suspected to be related to observed strong spanwise oscillations of fluid at the surface between the struts (see Figure 5.3), which could be driven by a three-dimensional instability in the induced flow around the cylinder known as the Honji instability (Honji, 1981; Tatsuno & Bearman, 1990). This is likely since the Keulegan-Carpenter number of this experiment was beyond that required for stability ($K_C < 0.3$) over the studied viscous-frequency parameter range ($1\ 950 < \beta < 12\ 410$) (Suthon & Dalton, 2012). Furthermore, the observed spanwise sloshing is suspected to be a result of the water resonating between the struts in the spanwise direction when the wavelength of the Honji instability became tuned to the cylinder span. Note that each set of peaks in Figure 5.2c occur in order of submergence from shallowest to deepest indicating that the submersion depth may influence wave making due to spanwise flow. Although Honji (1981) found that end plates had little affect on the three-dimensional stability of the flow, here end plate size may play a role in the entrapment of

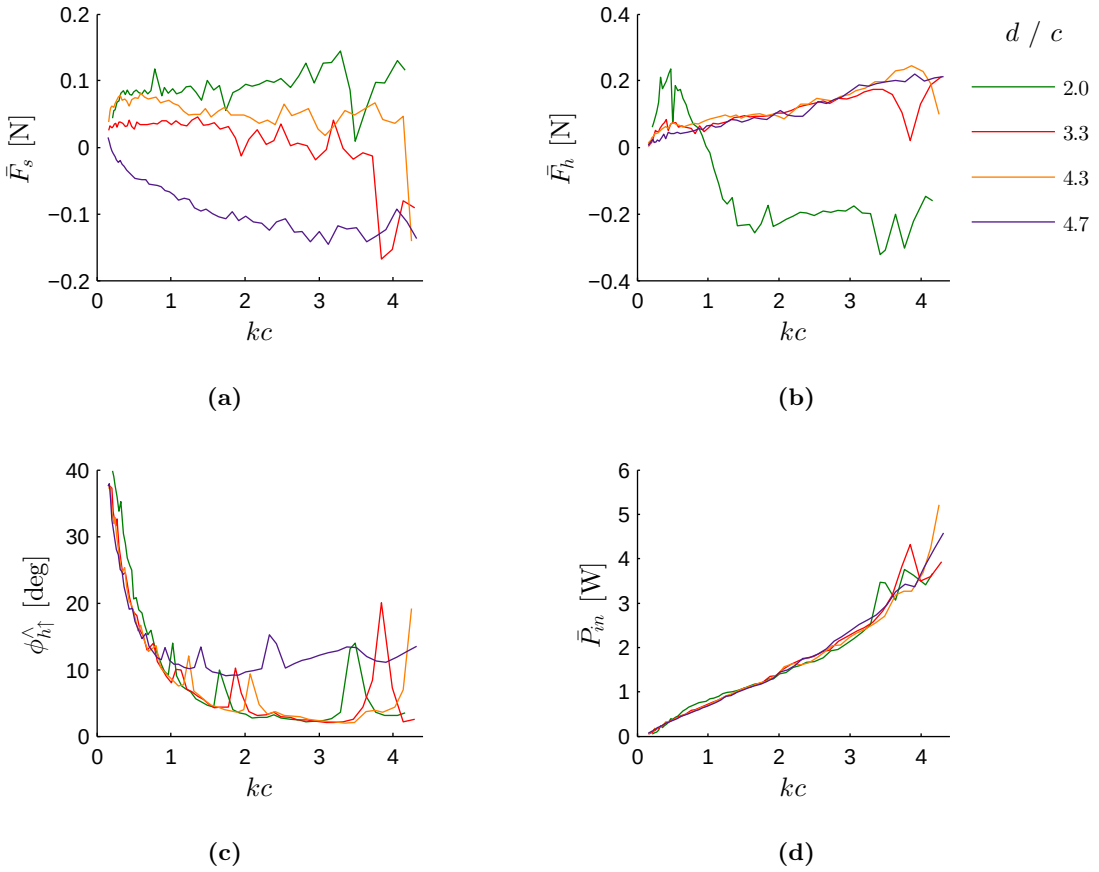

Figure 5.2. The effect of the free surface on the hydrodynamic forces on a heaving cylinder. $u = 0$, $h^* = 0.75$

standing surface waves created by the spanwise flow.

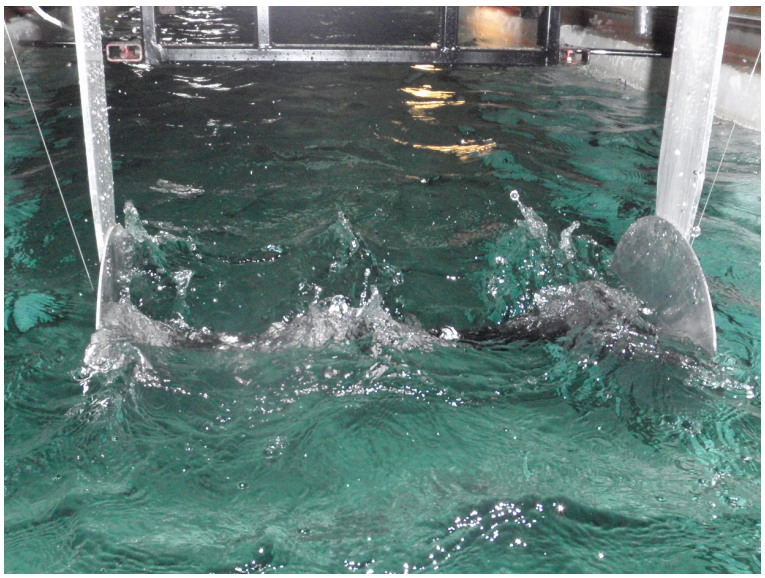

Figure 5.3. The oscillating cylinder created standing surface waves along its length for some oscillating frequencies an submergence depths.

Figure 5.4 shows sample heave force cycles on the cylinder for three submergences. The heave profile for these results is near cosine, i.e. maximum heave occures at $t/T = 0$ and minimum heave at $t/T \approx 0.5$. At a submergence of $d = 0.9c$, the cylinder comes in contact with the free surface at maximum heave position, which clearly affects the heave force cycles, particularly at lower oscillating frequencies. As the oscillating frequency is increased the difference in the heave force cycles for $d = 2.0c$ and $d = 3.3c$ becomes less with the exception of $kc = 3.5$ (Figure 5.4d). Here the change in the heave force profile corresponds to the phase shift peak seen in Figure 5.2c. At this combination of oscillating frequency and submergence the cylinder appears to be in a state tuned to forcing the free surface resulting in a significantly different heave force profile from other oscillating frequencies. Normally the cylinder heave force profile is dominated by inertial (in-phase) forces (see Section 5.4). However, under this tuned state, the heave force profile has a larger out-of-phase component resulting in a heave force cycle more similar to those generated by the flat plate (e.g. Figure 5.9).

Figure 5.2c shows that the cylinder heave force phase decreases as the oscillating frequency and kc are increased. The small phase lag of the cylinder heave force suggests

that heave force is dominated by inertial force contributions. This has a drastic effect on input power required to oscillate the cylinder calculated with Equation 5.2. Notice how the power to oscillating the cylinder (Figure 5.2d) is much lower than what the flat plate requires for the same kc (Figure 5.5d). The input power to oscillate these two objects is also compared in Figure 5.18.

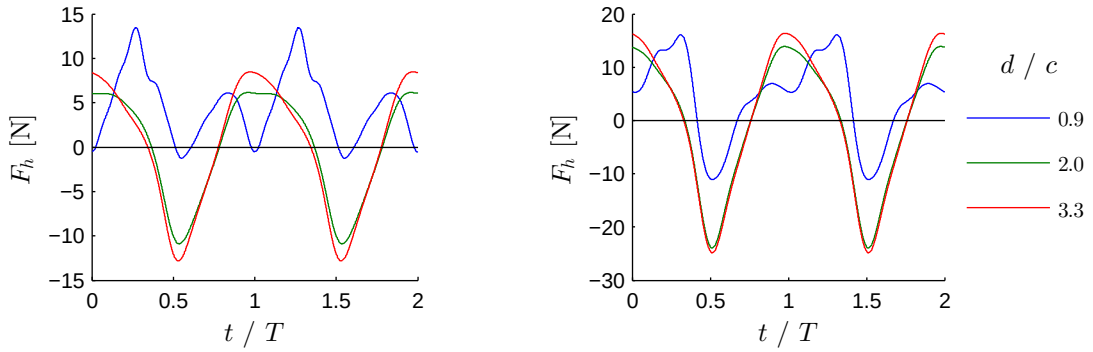

(a) $kc = 0.8$ **(b)** $kc = 1.5$

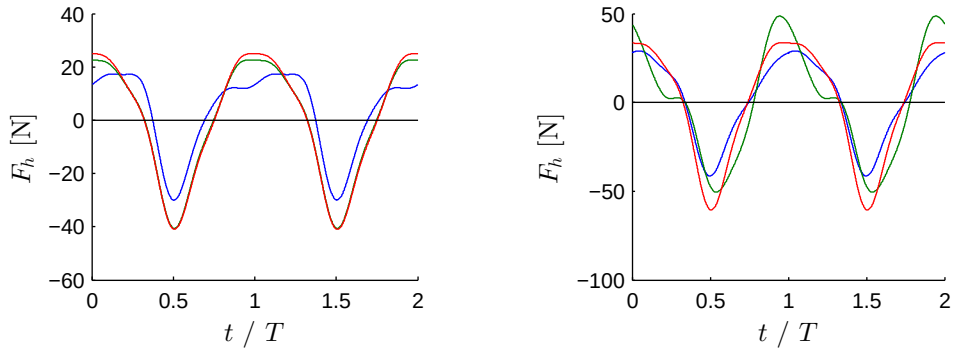

(c) $kc = 2.5$ **(d)** $kc = 3.5$

Figure 5.4. Heave force cycles at varying submergence for a cylinder against non-dimensionalised time. $u = 0$, $h^* = 0.75$

A Flat Plate Heaving Beneath a Free Surface

Since the cylinder is symmetrical in the plane normal to the surge axis, the near zero surge forces shown in Figure 5.2a were expected. Since the flat plate orientated at $\theta = 0$ is also symmetrical in the plane normal to the surge axis, the mean surge forces were

also expected to be zero. However, Figure 5.5a shows that the mean surge force has a small linear dependence on oscillating frequency. However, since the bias direction is not consistent between runs these small bias are considered to be random and insignificant. These small bias in surge force may be due to a small initial flow in the tank or the precision that the plate pitch could be set. Figure 5.5b shows the effect of the free surface on the mean heave force of a oscillating flat plate. Similar to the cylinder, heave forces on the flat plate with a submergence of $d \geq 3.9c$ appear to be consistent, suggesting that these depths are sufficient for minimising free surface effects.

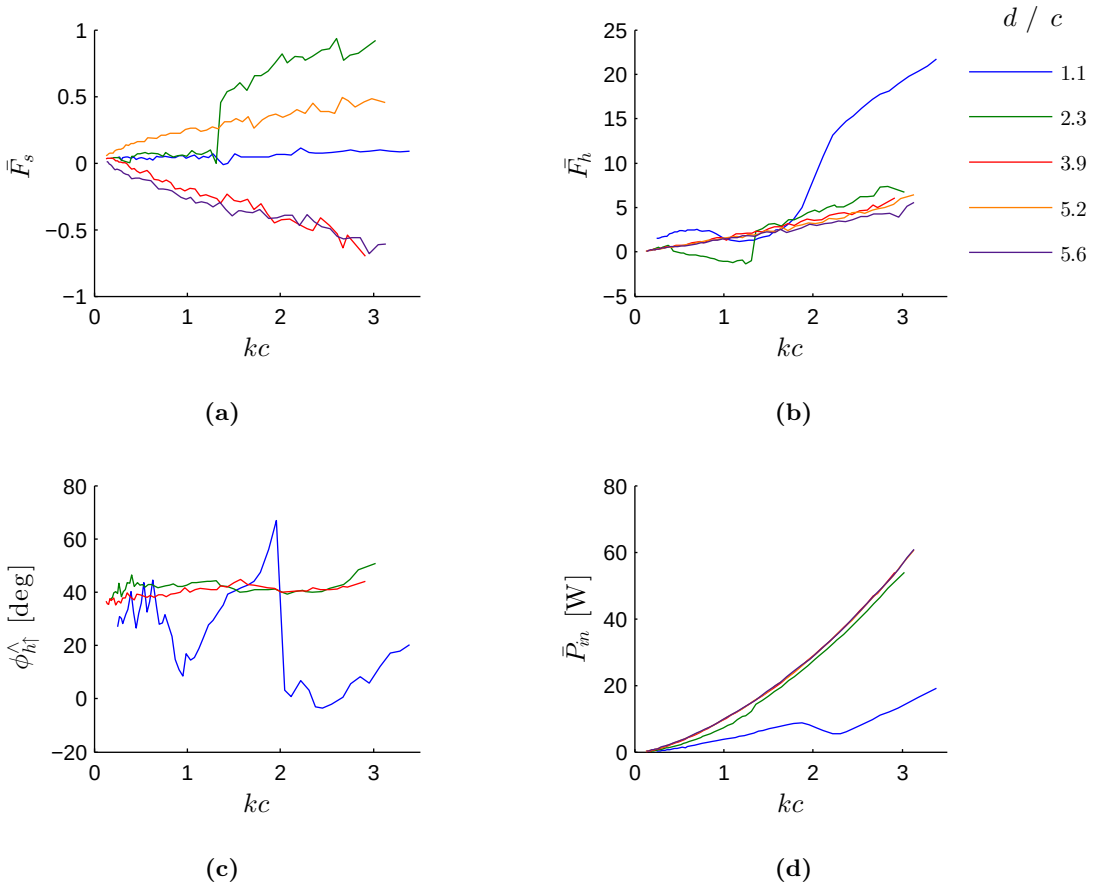

Figure 5.5. The effect of the free surface on the hydrodynamic forces on a heaving flat plate. $u = 0$, $h^* = 0.88$

At shallow submergence ($d = 1.1c$) the flat plate was observed going through three regimes of interaction with the free surface (Figure 5.6). The heave force phase (Figure 5.5c) shows two distinct discontinuities at $kc = 1$ and $kc = 2$ where the type of interaction

mode changed. At low oscillating frequencies ($kc < 1$), the plate generated surface waves that increased in amplitude as the oscillating frequency was increased. For the mid range of oscillating frequencies ($1 < kc < 2$) the plate would disperse water on its downstroke which would collapse on the plates top surface during its upstroke. The collision between the falling water wave and the plate accelerating upwards would results in water being thrown into the air as shown in Figure 5.7. The falling water impacting the top surface on the plate is a likely cause for the decreased mean heave force between $kc = 1$ and $kc = 2$ in Figure 5.5b. The surface waves generated during this regime where of much smaller amplitude than the previous regimes. Finally, at high oscillating frequencies ($kc > 2$) the plate would continue to displace water on its downstroke. However, the water did not have time to collapse on top of the plate after being displaced, leaving the top surface of the plate constantly exposed to air (Figure 5.8). Figure 5.9 shows how this affect caused a significant bias and a reduction in amplitude in the plate heave force cycle when $d = 1.1c$. Furthermore, Figure 5.5d shows how the reduction in heave force amplitude significantly reduces the input power required to oscillate the flat plate under this condition.

Figure 5.5c shows that the flat plate heave force phase was much more consistent that the heave force phase of the cylinder for submersion depths greater than $1.1c$ (Figure 5.2c). The observed surface patterns over the flat plate were consistently chordwise for all oscillating frequencies, with little spanwise wave generation as observed over the cylinder. Figures 5.7 and 5.8 show water being displaced by the flat plate evenly across its span.

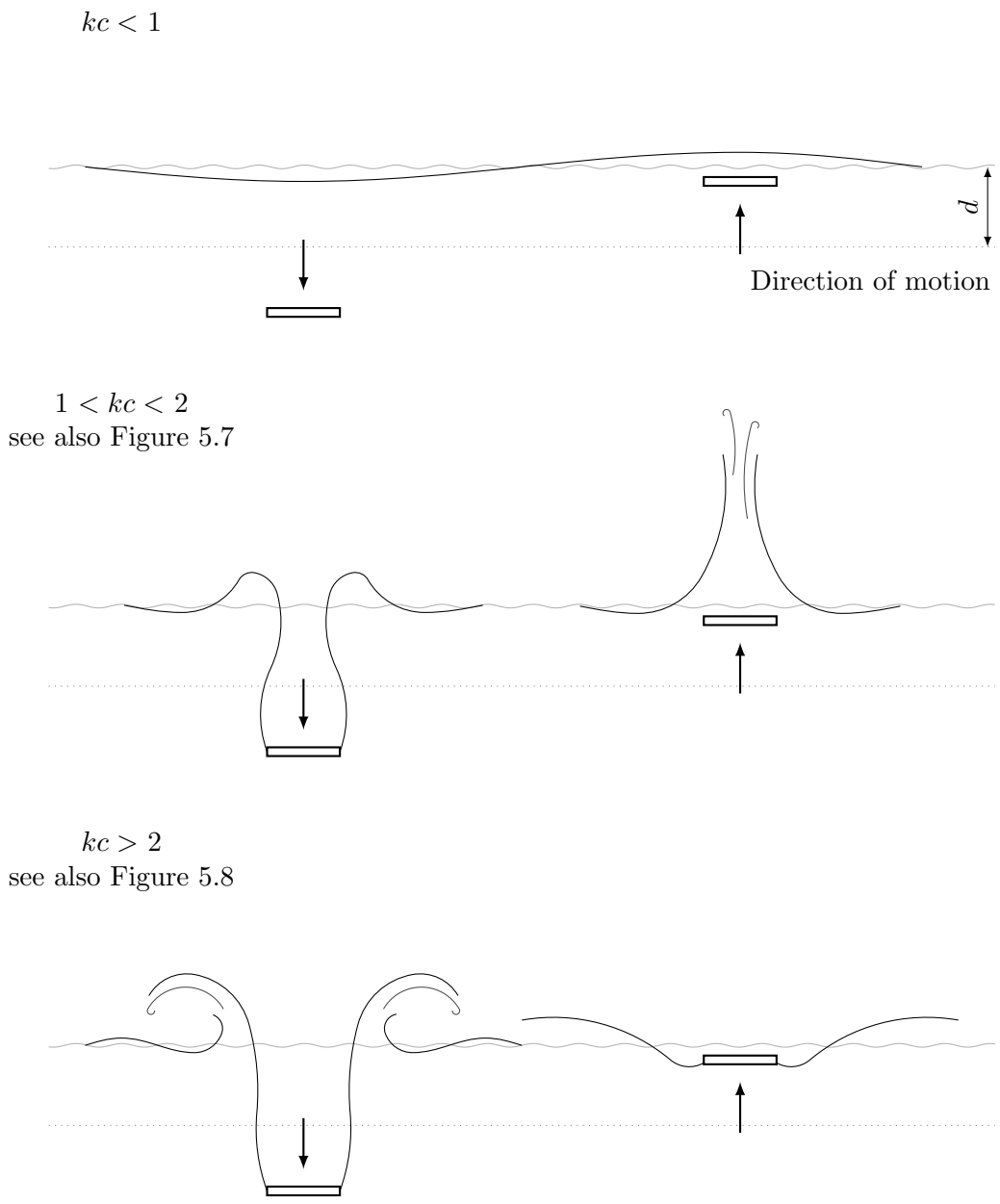

Figure 5.6. Three observed interactions between a heaving flat plate and the free surface. $u = 0$, $h^* = 0.88$, $d = 1.1c$

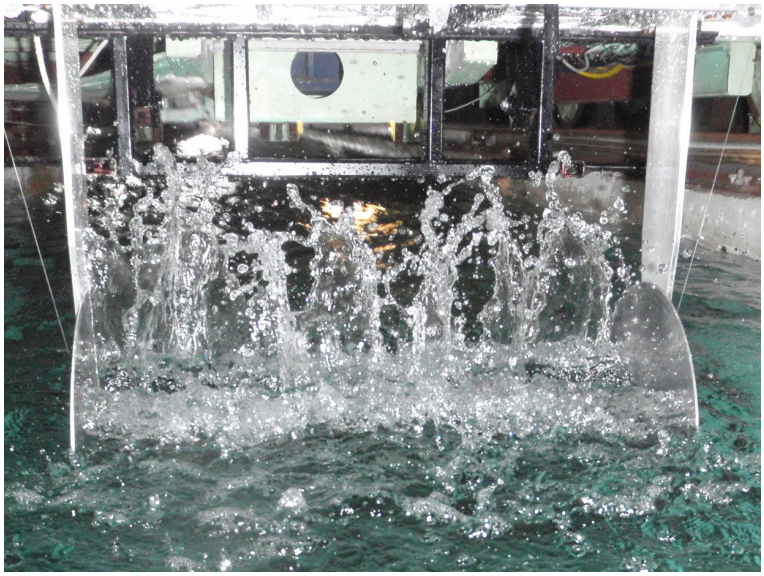

Figure 5.7. The flat plate heaving at low submersion depth, $d = 1.1c$, with a medium oscillating frequency ($1 < kc < 2$). $u = 0$, $h^* = 0.88$

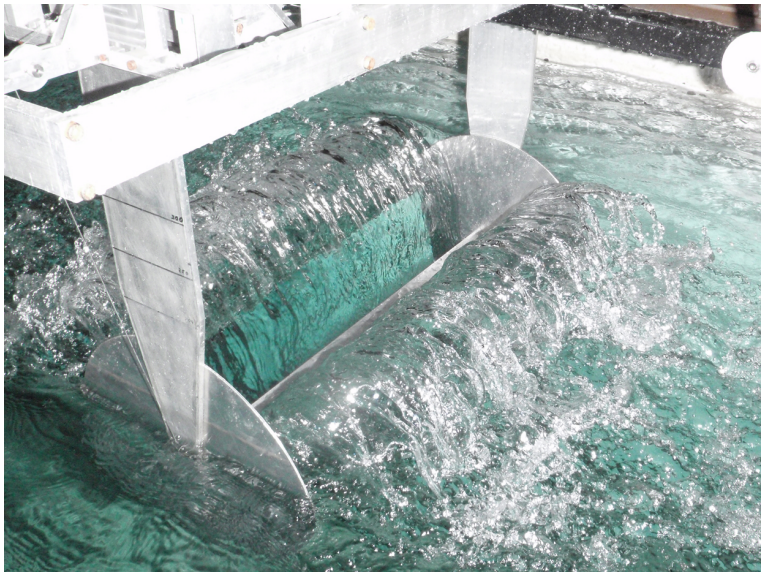

Figure 5.8. The flat plate heaving at low submersion depth, $d = 1.1c$, with a high oscillating frequency ($kc > 2$). $u = 0$, $h^* = 0.88$

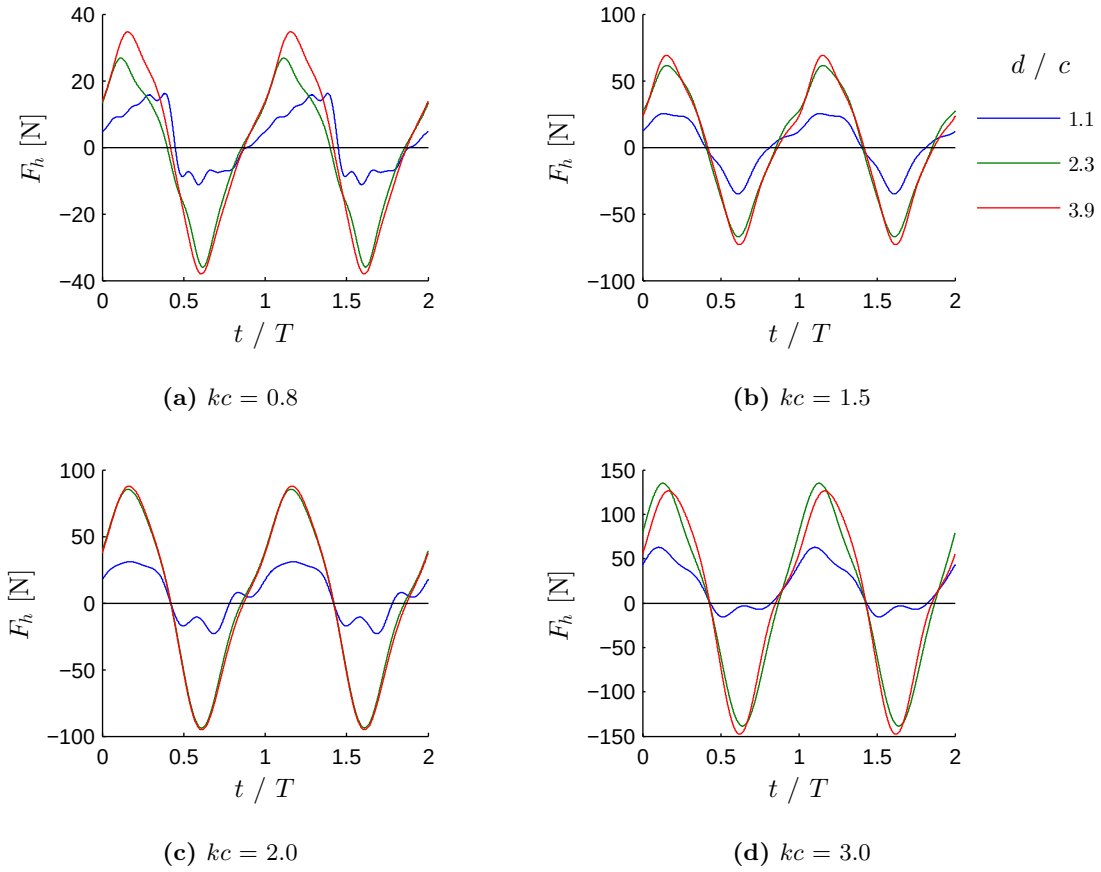

(a) $kc = 0.8$ **(b)** $kc = 1.5$

(c) $kc = 2.0$ **(d)** $kc = 3.0$

Figure 5.9. Heave force cycle at varying submergence for a flat plate against non-dimensionalised time. $u = 0$, $h^* = 0.88$

5.2.4 Thrust Producing Objects

A NACA0012 Heaving Beneath a Free Surface

Figure 5.10a shows the mean thrust produced by the NACA0012. The mean thrust produced was relatively unaffected by the changes in submersion, even with as little depth as 2.1 chord lengths. Unlike the other test objects, the NACA0012 produced a small negative mean heave force. However, the mean heave force data contains a lot of variation beyond $kc = 1.8$ (Figure 5.10b). Similar to the other test objects the mean heave force on the NACA0012 was affected by the free surface once the submersion was decreased to $d = 2.1c$. Also similar to the flat plate and the NACA4415, the NACA0012 began to ventilate (Figure 5.11) at a submergence of $d = 2.1c$ when kc exceeded about 3.

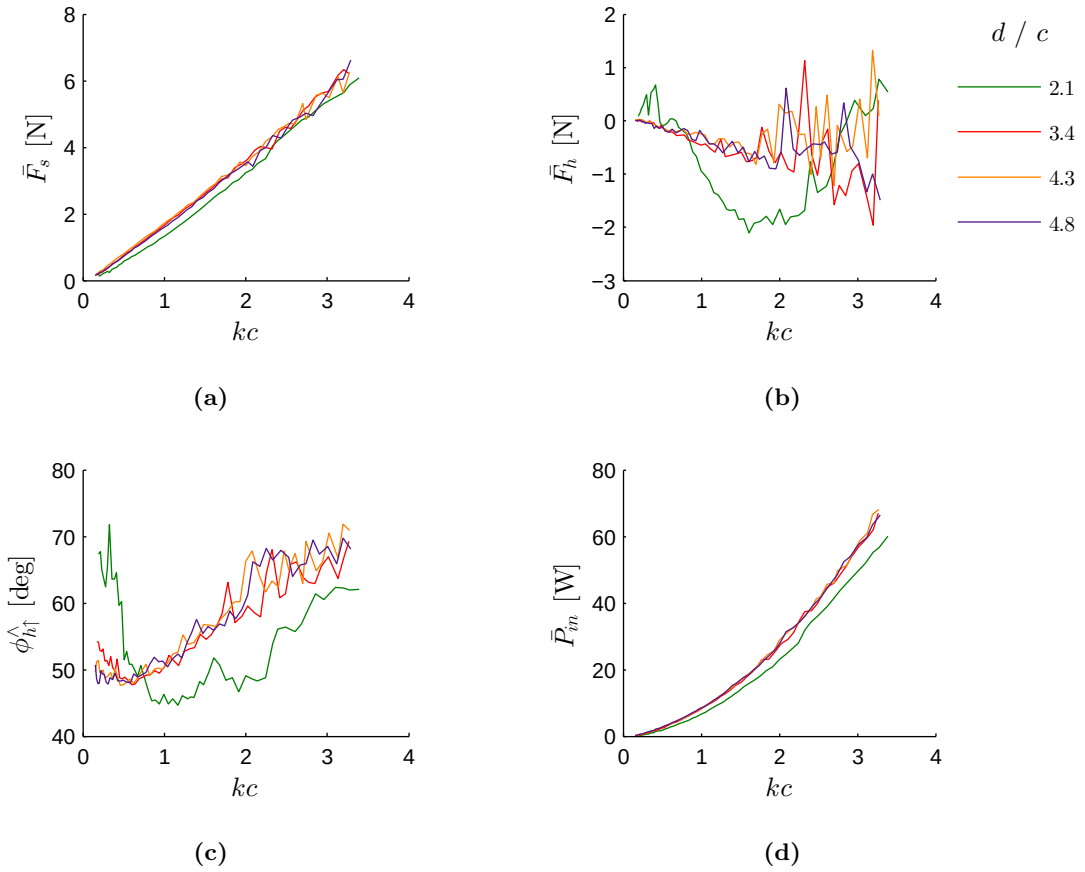

Figure 5.10. The effect of the free surface on the hydrodynamic forces on a heaving NACA0012. $u = 0$, $h^* = 0.75$

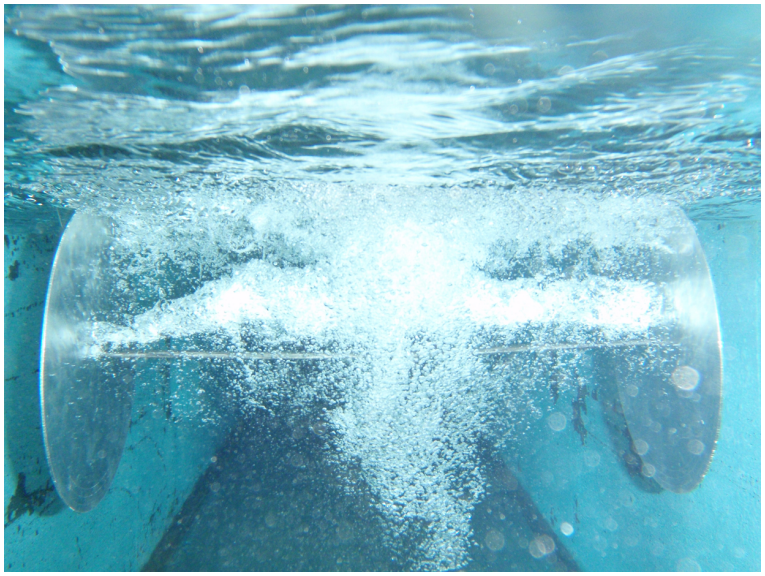

Figure 5.11. Air being drawn below the water surface by the NACA0012 at a submersion depth of $d = 2.1c$. $u = 0$, $h^* = 0.75$

A NACA4415 Heaving Beneath a Free Surface

Figure 5.12a shows the mean thrust produced by the NACA4415 over the tested kc domain. Notice that for a submersion depth of $d = 2.1c$, the mean thrust produced by the foil for $kc < 1$ is low relative to that produced at deeper submersion. However, once $kc > 1$, the oscillating foil becomes tuned to the free surface and the amount of thrust produced exceeds that at deeper submersion. The foil continues to produce thrust in excess of that at deeper submersion depths until $kc = 3.1$ where the foil began to ventilate, similar to the NACA0012 and the flat plate.

These two discontinuities in the thrust produce by the foil, at $kc \approx 1$ and $kc \approx 3$, also appear to affect the mean heave force, heave force phase and mean input power shown in Figures 5.12b to 5.12d. Notice that coincident to the increase in thrust production, the mean heave force also increases to beyond that experienced at deeper submersion depths. However, the range of the heave cycle is unaffected (Figure 5.14). Both these performance properties of the NACA4415 would be advantageous for a water craft starting from rest.

Figure 5.13 shows an example of the thrust cycle produced by the NACA4415 at two different oscillating frequencies. At low frequency (Figure 5.13a) the foil produces thrust

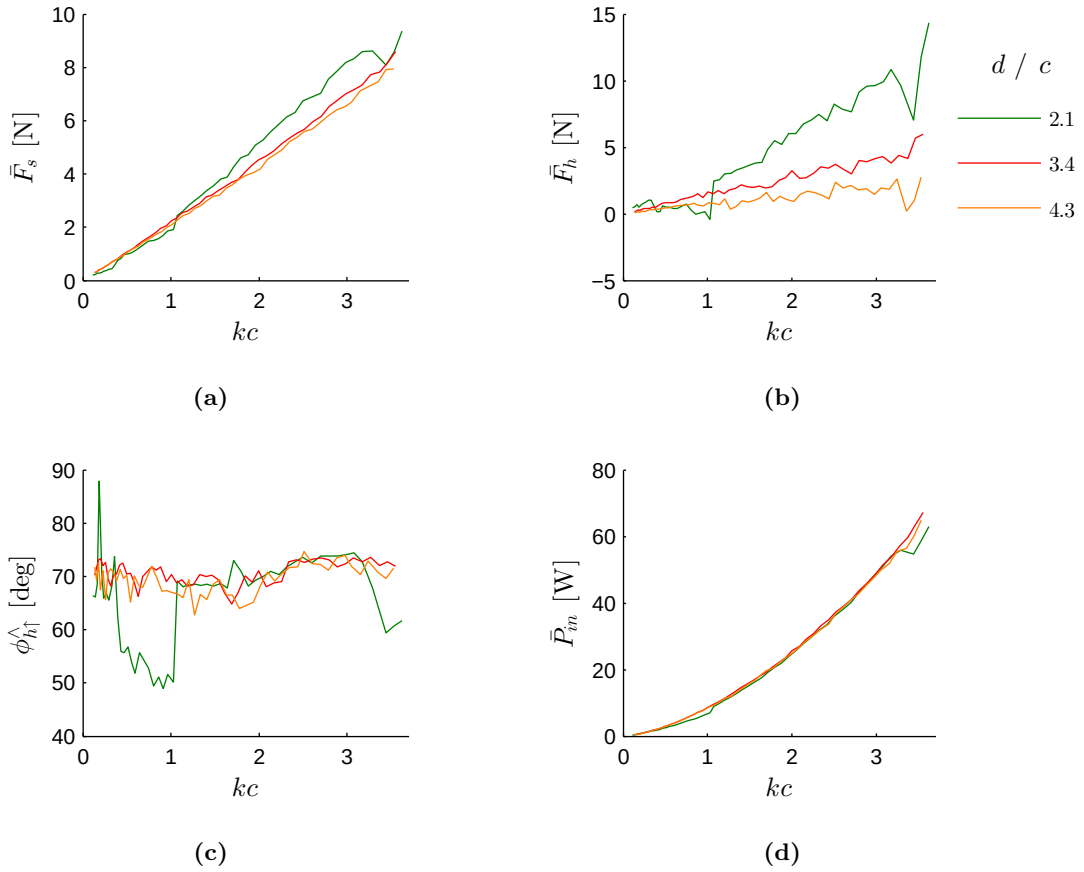

Figure 5.12. The effect of the free surface on the hydrodynamic forces on a heaving NACA4415. $u = 0$, $h^* = 0.75$

throughout the entire heaving cycle with more thrust being produced on the upstroke ($0.5 < t/T < 1$) than the downstroke ($0 < t/T < 0.5$). Furthermore, the downstroke thrust is relatively small compared with the thrust produced with deeper submersion. When the oscillating frequency is higher (Figure 5.13b), downstroke peak thrust increased to exceed the thrust produced with deeper submersion while the upstroke thrust remains the same.

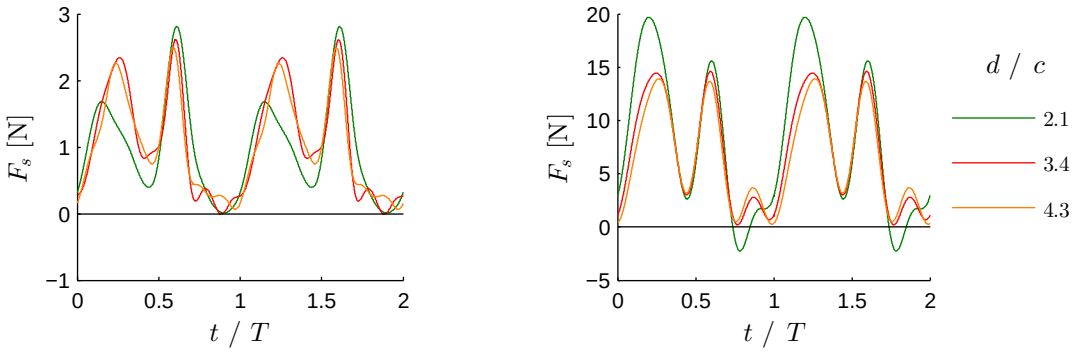

(a) $kc = 0.5$ **(b)** $kc = 3.0$

Figure 5.13. The effect of the free surface on the thrust produced by a NACA4415. $u = 0$, $h^* = 0.75$

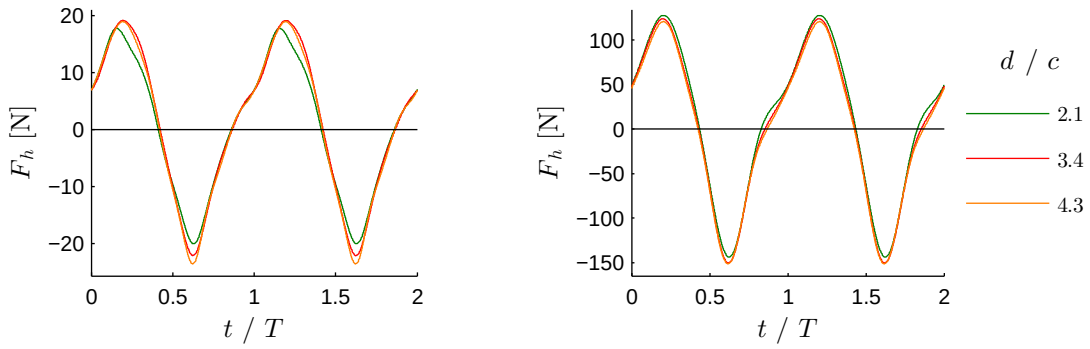

(a) $kc = 0.5$ **(b)** $kc = 3.0$

Figure 5.14. The effect of the free surface on the heave cycle of the NACA4415. $u = 0$, $h^* = 0.75$

5.3 End Effects

To investigate the effect of different end conditions on a test object heaving with no forward translational velocity, the forces on the NACA4415 were measured at different submersion depths with three different end conditions: no end plates, $\varnothing 2c$ end plates and $\varnothing 5.3c$ end plates (Figure 5.15). Figures 5.16 and 5.17 show the heave force cycles on the NACA4415 for a submergence of $d = 4.3c$, where free surface effects are considered minimal, and a submergence of $d = 2.1c$, where the free surface was shown to influence the thrust produced by the NACA4415 in the previous section.

When operating at depth, i.e. $d > 3.5c$, Figures 5.16a and 5.16b show that the amplitude of the heave force cycle increases slightly with increasing end plate size. The affect of the end plates is more noticeable in the surge force results. Figure 5.16c shows that at low oscillating frequencies, when the $2.0c$ end plates were mounted, the surge cycle amplitude increased causing an increase in the mean thrust developed by the foil. Increasing the end plate size to $5.3c$ also increases the mean thrust. However, with the $5.3c$ end plates the thrust profile peaks become more similar in magnitude and more like the typical thrust pattern of a symmetrical foil undergoing sinusoidal heaving (Ashraf et al., 2011). Similarly, at a higher oscillating frequency (Figure 5.16d), mean and peak thrust increased with end plate size. Here it is more apparent that the gains in mean thrust originate from increased peak thrust on the foil downstroke. The peak thrust on the foil upstroke appears to be less sensitive to end plate diameter at higher oscillating frequencies.

Figure 5.17c shows that with the free surface nearer to the foil mean heave position the mean thrust produced by the foil at low oscillating frequencies ($kc < 1$) is low due to reduced peak thrust values, particularly on the downstroke. At higher oscillating frequencies (Figure 5.17d) the foil thrust is less affected by the shallow submersion depth. Mean thrust decreases slightly with no end plates. However, the $2.0c$ end plates help to maintain good mean thrust. Figure 5.17d shows that the thrust gains at shallow submergence with the NACA4415 could only be achieved with the large $5.3c$ end plates fitted. In this case the downstroke thrust peaks at almost three times that achieved with no end plates. This increase in downstroke peak thrust also substantially raises the cycle mean thrust to 66 % more that than with no end plates.

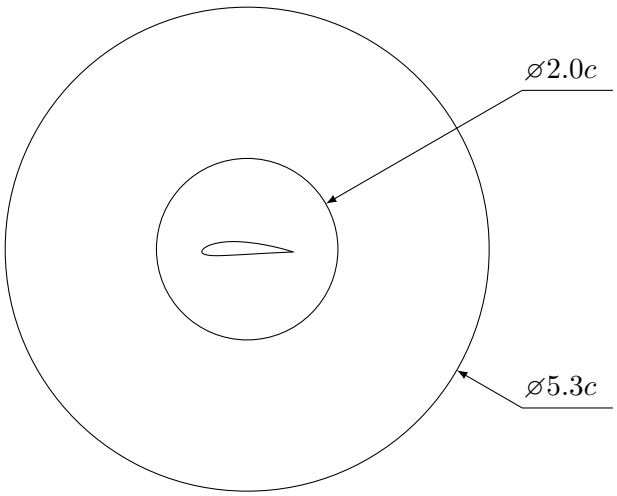

Figure 5.15. The two end plate sizes used for the end effects study. Scale = 1:5).

The mean input power required to oscillate the NACA4415 foil (calculated with Equation 5.2) with different end plates is shown in Figure 5.18. The input power required to oscillate the cylinder, flat plate and the NACA0012 is also shown for comparison. The use of end plates with the NACA4415 requires a higher mean input power than without the end plates. This is due to the increased amplitude of the heave force cycle when end plates are fitted, as shown in Figures 5.16 and 5.17.

Figure 5.19 shows that for a submersion depth deep enough that the foil is not influenced by the free surface ($d = 4.3c$ in this case), the extra input power required with end plates fitted is roughly proportional to the extra mean thrust developed. Hence the power per unit thrust is not effected. However, over the range $1 < kc < 3$ the heaving NACA4415 becomes tuned to the free surface resulting in increased thrust production (see Section 5.2.4). Figure 5.19 shows that during this regime the power per unit thrust is reduced by approximately 14 % when the $5.3c$ end plates were fitted. Furthermore, Figure 5.19 shows that power savings actually began from approximately $kc = 0.3$, where there was a sudden reduction the heave force phase lag (Figure 5.10c).

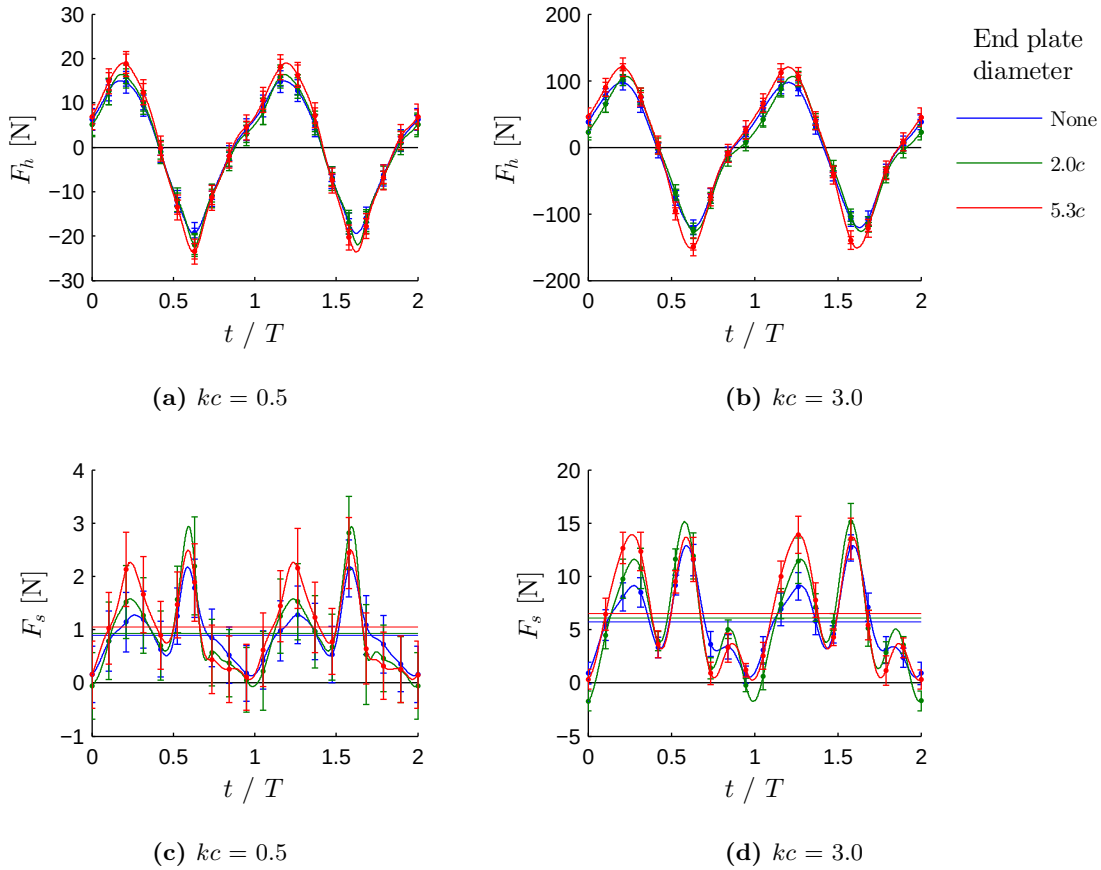

(a) $kc = 0.5$ **(b)** $kc = 3.0$

(c) $kc = 0.5$ **(d)** $kc = 3.0$

Figure 5.16. The effect of end plate size on the heaving and surging forces produced by a heaving NACA4415 at a submersion depth of $d = 4.3c$. Coloured horizontal lines mark the mean force.

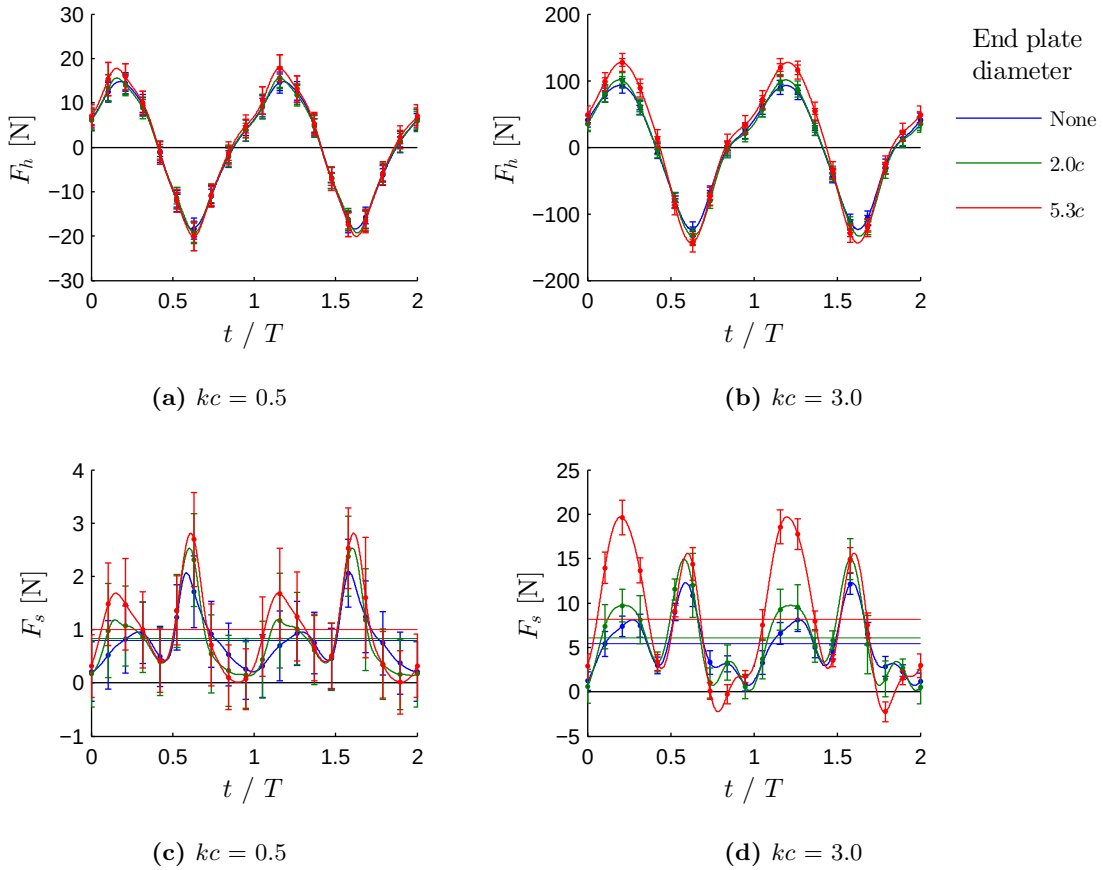

(a) $kc = 0.5$ **(b)** $kc = 3.0$

(c) $kc = 0.5$ **(d)** $kc = 3.0$

Figure 5.17. The effect of end plate size on the heaving and surging forces produced by a heaving NACA4415 at a submersion depth of $d = 2.1c$. Coloured horizontal lines mark the mean force.

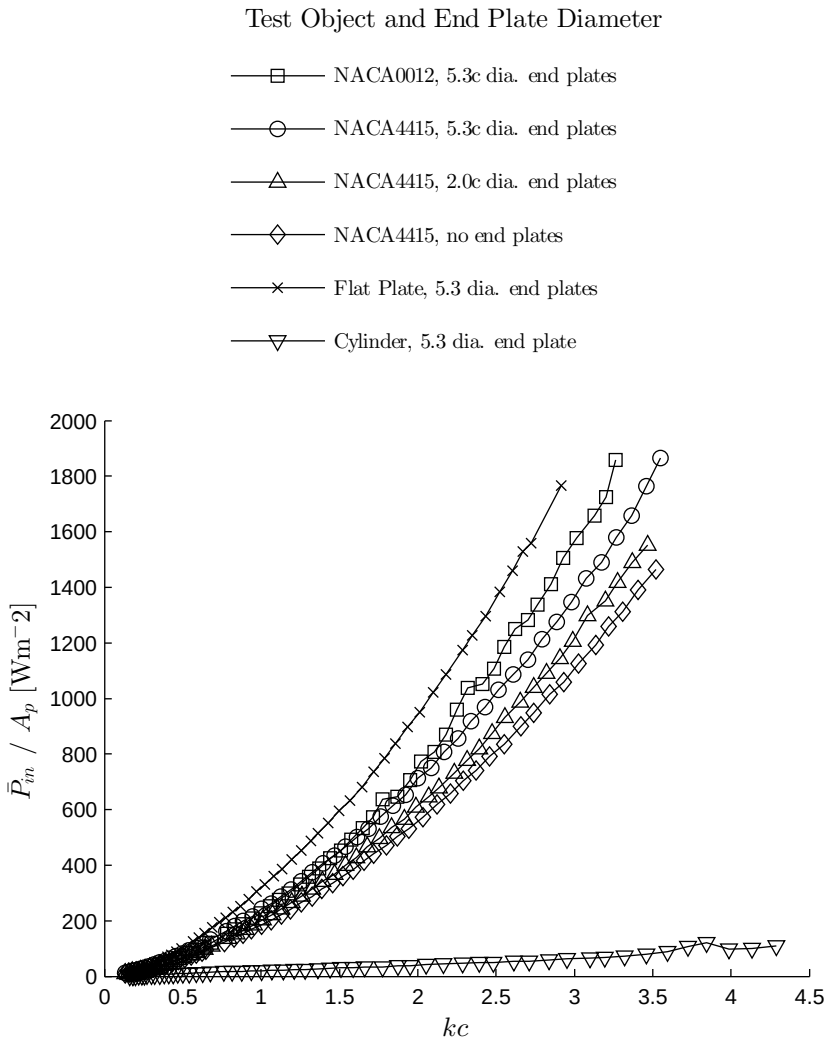

Figure 5.18. Input power to oscillate test objects in water. Flat plate; $h^* = 0.88$, $d = 3.9c$, All other objects $h^* = 0.75$, $d = 3.3c$

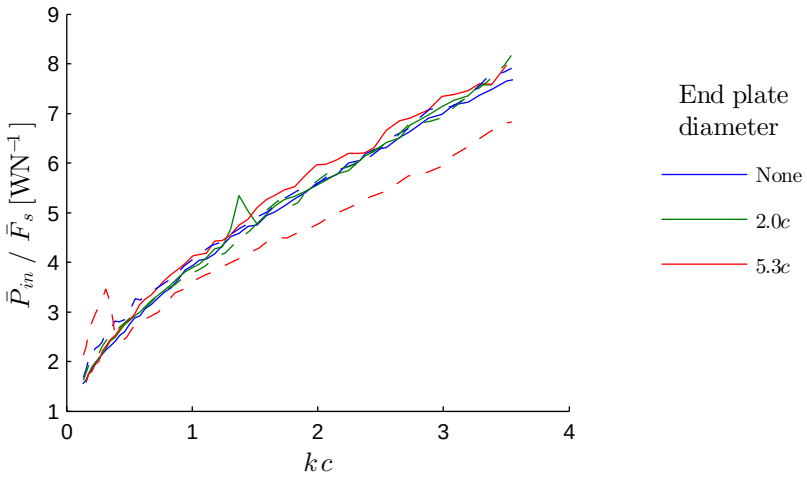

Figure 5.19. The effect of end plates on input power and mean thrust of a NACA4415. Dashed lines represent shallow submersion, $d = 2.1c$, and solid line represent deep submersion, $d = 4.3c$. $u = 0$

5.4 A Heaving Cylinder with Zero Forward Velocity

In this section, the hydrodynamic forces on an oscillating cylinder with no translational velocity are presented. The effect of heave amplitude and heave profile on the hydrodynamic forces are discussed. This study was conducted for two reasons. Firstly, the simplistic geometry of a cylinder makes it the ideal object to begin a study. Due to its rotational symmetry, pitch angle may be discarded as a variable to simplifying data collection and analysis. Secondly, there exist far more literature for the hydrodynamic forces on a cylinder than any other shape. This enables the current findings to be easily compared to the literature, for the purposes of validating the experimental equipment design presented in Chapter 4.

Unsteady hydrodynamic forces on the cylinder where recorded, as described in Section 4.8.2, for various heave amplitudes and oscillating frequencies. The heave amplitude was changed by changing the crank length. The cylinder was mounted with the ⌀320 mm (⌀5.3c) end plates. Table 5.1 lists the four heave-to-chord ratios studied in this experiment with the corresponding oscillating frequency range and other dimensionless quantities.

Table 5.1. Parameter space for the study of heave amplitude on a cylinder. Cylinder diameter 0.06 m.

h^*	K_C	f [Hz]	$\dot{h}_{max}$ [m s^{-1}]	Re_h	β
0.25	1.57	0.73 - 5.20	0.07 - 0.50	3 250 - 23 020	2 070 - 14 660
0.50	3.14	0.83 - 5.13	0.16 - 0.97	7 440 - 44 720	2 370 - 14 240
0.75	4.71	0.63 - 4.29	0.19 - 1.22	9 200 - 58 520	1 950 - 12 410
1.00	6.28	0.46 - 3.81	0.21 - 1.38	9 580 - 64 230	1 530 - 10 220

5.4.1 Mass and Damping Coefficients

Figure 5.20 shows surface plots of the heaving force as a function of heaving velocity and acceleration for each heave-to-chord ratio. A flat plane, with the general form of Equation 5.3, was fitted to each set of data with a high goodness of fit. The coefficients, with their respective confidence intervals are shown in Table 5.2.

$$F_h(\dot{h}, \ddot{h}) = a_0 + a_{\dot{h}}\dot{h} + a_{\ddot{h}}\ddot{h} \tag{5.3}$$

Table 5.2. Flat plane fit coefficients and coefficients of determination for the oscillating cylinder heave force data for various heave-to-chord ratios. Data plots are shown in Figure 5.20.
Coefficient 95 % confidence interval are show in brackets.

h^*	K_C	a_0	$a_{\dot{h}}$	$a_{\ddot{h}}$	R^2	$RMSE$
0.25	1.57	0.0323	1.2668	1.7625	0.9995	0.153
		(±0.0008)	(±0.0048)	(±0.0002)		
0.50	3.14	0.0363	2.9368	1.6898	0.9979	0.597
		(±0.0032)	(±0.0095)	(±0.0004)		
0.75	4.71	0.0567	5.0114	1.6522	0.9881	1.472
		(±0.0052)	(±0.0127)	(±0.0006)		
1.00	6.28	0.0321	7.4293	1.5209	0.9825	1.764
		(±0.0083)	(±0.0176)	(±0.0010)		

It is known that when $K_C < 3$, i.e. for $h^* = 0.25$, the hydrodynamic forces on a cylinder should be inertia dominant and may be modelled by a linear fit in $\ddot{h}$ neglecting drag (see Section 3.3.8). This fit is equivalent to Equation 5.3 with $a_{\dot{h}} = 0$. Table 5.3 contains the coefficients for this type of fit with corresponding goodness of fit indicators.

Figure 5.21 shows how the coefficient of determination of a linear mass-damper model

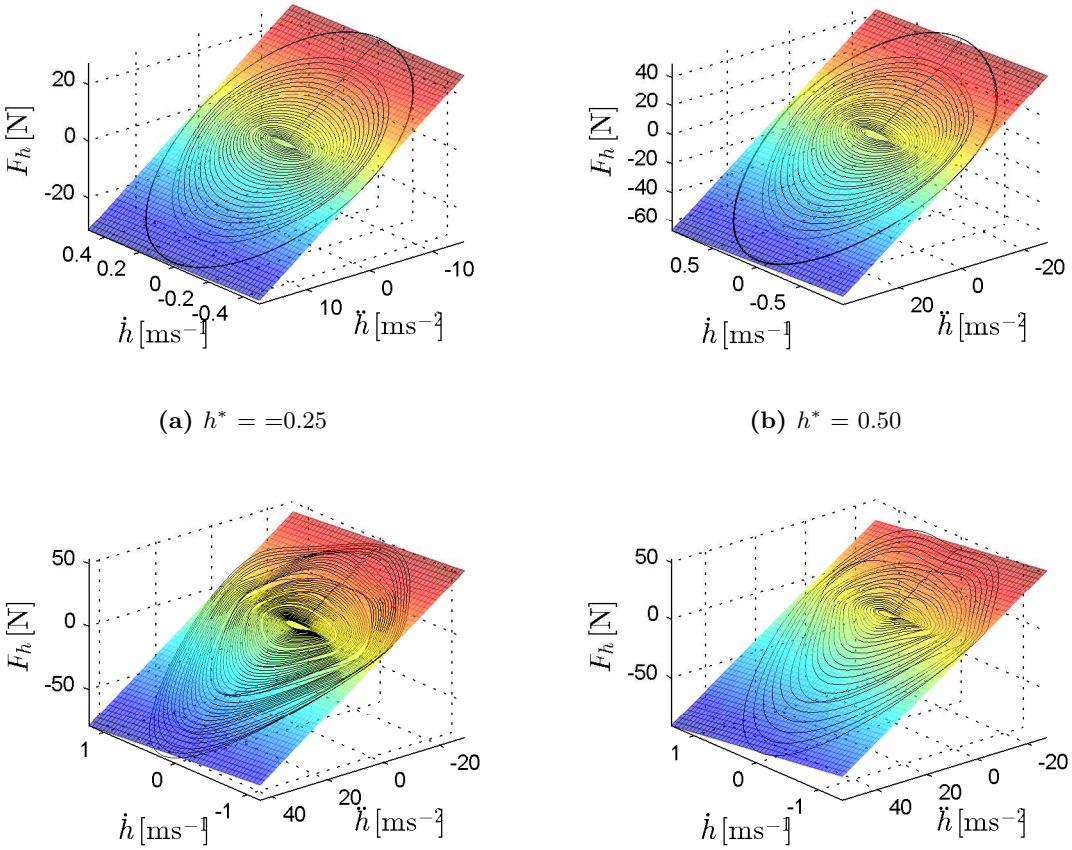

(a) $h^* = =0.25$ **(b)** $h^* = 0.50$

(c) $h^* = 0.75$ **(d)** $h^* = 1.00$

Figure 5.20. Heave force on a cylinder undergoing pure heaving at zero translational velocity plotted against heaving velocity and acceleration.

fit and a linear mass model fit decay with K_C. Clearly when drag is neglected ($a_{\dot{h}} = 0$) R^2 decays much more rapidly with increasing K_C. Once h^* exceeds 0.5 ($K_C > 3.1$), R^2 begins to rapidly decrease and the root mean square error (RMSE) of the linear mass model begins to exceed 200 % that of the mass-damper model. Hence a linear mass model should only be used for small heave amplitudes, i.e. $K_C < 3$. Assuming a threshold of $R^2 = 0.9$ for a good fit, extrapolating the current results shows the linear mass-damper model fits the data well for $K_C < 14$. This is in good agreement with Journée and Massie (2001) who suggests that a linear mass-damper model is valid for $K_C < 15$ (see Table 3.1).

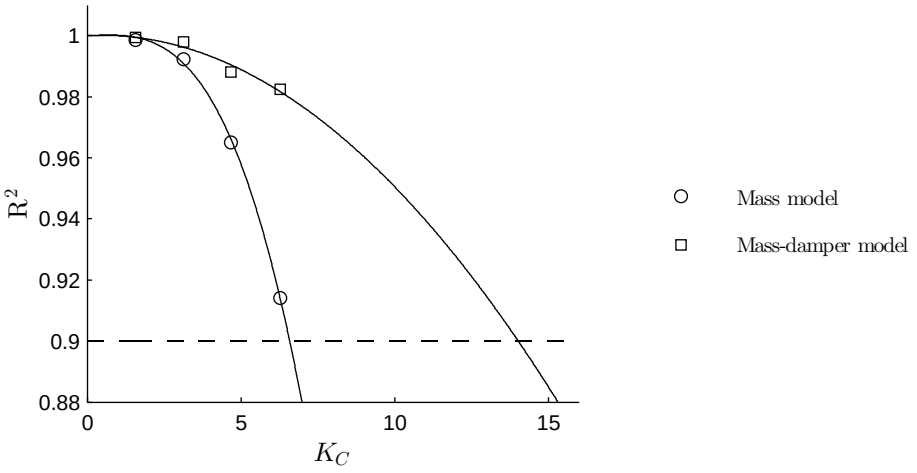

Figure 5.21. RMSE of a linear mass model fit and a linear mass-damper model fit for a heaving cylinder over a range of K_C.

5.4.2 Heaving Profile

Notice that when heave velocity and acceleration are plotted on orthogonal axis, as in Figure 5.20, the plot is a smooth oval shape at low heave-to-chord ratios but distorts as the heave-to-chord ratio is increased. This is due to changes in the connecting rod to crank length ratio. When the crank lengths were changed between runs, the connecting rod lengths where also changed to ensure the zero heave position was at the centre of the Watts linkage stroke, and hence minimise surging error (see Section 4.2). However, the change in connecting rod length was small relative to the change in crank length causing the con-rod to crank length ratio to decrease as the heave amplitude was increased. Figure 5.22 shows how the fixed offset between the crank axis and the zero heave position causes the con-rod to crank length ratio to change with changes in the crank length (or heaving amplitude). Furthermore, Equation 5.4 is the relationship between the con-rod to crank length ratio L_c and the crank length l_c (equivalent to heave amplitude) for some fixed zero heave offset, y_{h_0}. Table 5.4 contains the connecting rod to crank length ratios for each heaving amplitude used in the experiments.

$$L_c = \sqrt{\frac{y_{h_0}^2}{l_c^2} + 1} \tag{5.4}$$

Crank and connecting rod linkages are robust means of converting rotary motion to oscillating linear motion. When a large con-rod to crank length ratio is used, the output linear motion is very near sinusoidal. However, small con-rod to crank length ratios distort the sinusoidal output with frequencies higher than the crank frequency. Appendix D discusses the extent of this effect in more detail.

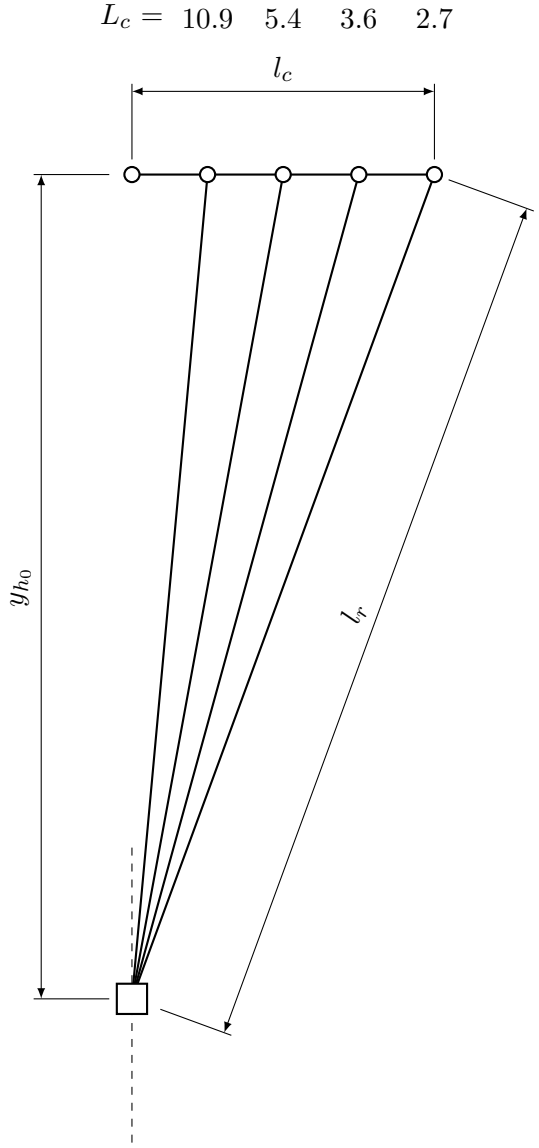

Figure 5.22. Variation of the con-rod to crank length ratio for changes in crank length with a fixed zero heave position.

5.4.3 The Appropriateness of the Morison Equation

Fitting the data with the Morison equation (Equation 3.6), i.e using quadratic drag, provides a better fit than when drag was neglected, but not as good as using a linear drag model. The coefficients for a Morison fit are shown in Table 5.5. The RMSE of the Morison equation fit increased with increasing heave-to-chord ratio faster than the RMSE of the mass-damper model fit. The RMSE of the Morison equation fit exceeded that of the mass-damper model fit by 24 % when $h^* = 1$. This result again supports K_C bounds for the unsteady hydrodynamic force models set out by Journée and Massie (2001) who suggests that the full Morison equation should not apply until $K_C > 15$.

Although the data presented here supports a mass-damper model for calculating the temporal hydrodynamic forces on an oscillating cylinder, a substantial amount of research has been done finding drag and inertia coefficients assuming the Morison equation. Since many applications using the Morison equation are at high Reynolds numbers and viscous frequency parameter, e.g. full scale structure in the offshore industry, it is important to have experimental data for these cases. Sarpkaya (1976) realised that there was a lack of experimental data at high Reynolds numbers and made significant experimental contributions. Later Sarpkaya (1986) compared experimental results to theory finding that drag and inertia agreed with theory for small Keulegan-Carpenter numbers ($K_C < 0.8$) when β was small ($\beta < 1380$). However, coefficients differed substantially from theory with $\beta = 11\ 240$ and when the surface roughness of the cylinder increased. This showed the importance of having access to reliable drag and inertia coefficients when applying the Morison equation. Fortunately more recent experiments and simulations have been done at higher values for Re and β. Table 5.6 is included to compare the current results for Morison equation drag and inertia coefficients to those found in the literature.

Beyond variation in experiment design or simulation conditions, there are also several methods for calculating Morison equation coefficients which leads to added variation in the results (Journée & Massie, 2001). Shafiee-far et al. (1996) found that Fourier analysis and less square fitting techniques yield nearly the same coefficients when validating the Morison equation. Other simpler methods, such as Morison's original method are considered to lack accuracy (Journée & Massie, 2001).

Two methods were used to calculate the added mass and drag coefficients for the current data. Firstly Morison's method, were the added mass coefficient is calculated at points of zero heave velocity and the drag coefficient is calculated at points of zero acceleration. Secondly, these coefficient were calculated via a least squares fit of the heave force surfaces shown in Figure 5.20. Figure 5.23 shows these coefficients plotted with those found in the literature (Table 5.6). Note that the added mass coefficients derived via either calculation method are near equivalent. However the drag coefficients calculated via surface fitting tend to be less than those calculated using Morison's method.

In the results of Sarpkaya (1976) ($2.5 < K_C < 6.5$, $1107 < \beta < 8370$), the inertia coefficient of a cylinder in an oscillating flow takes a value just above 2 at low K_C and slowly decreases with K_C and is relatively insensitive to β. The current results agree with this trend and take similar values to many other results from the literature (Table 5.6 and Figure 5.23b).

Results of Sarpkaya (1976) showed that the drag coefficient varies considerably with β, approximately halving in magnitude when β is increased from 784 to 5260. In addition, as β increases, the sensitivity of the drag coefficient to K_C decreases. Although the results of Sarpkaya (1976) do not explore values of β quite as high as the current study, results of Sarpkaya (1986) and simulations of Rashid et al. (2011) show that the drag coefficient declines as β is increased further up to values as high as 11 240. The current results, with β as high as 14 660 suggest that the drag coefficient continues to decline as β increases. Note the variation in coefficient values presented in Figure 5.23a shows how sensitive the drag coefficient is to β and further supports the conclusion that the Morison equation is not a suitable model for the hydrodynamic forces on a cylinder over this Keulegan-Carpenter number range.

5.4.4 Cross-flow Forces

As the heave amplitude was increased, surge position amplitude due to the Watt's linkage error (see Section 4.2) was also increased. Consequently the surge force amplitude due to inertia forces also increased. However, Figure 5.24 shows that when $K_C = 4.7$ and $K_C = 6.3$, the surge force range increases relative to the measured inertia force range

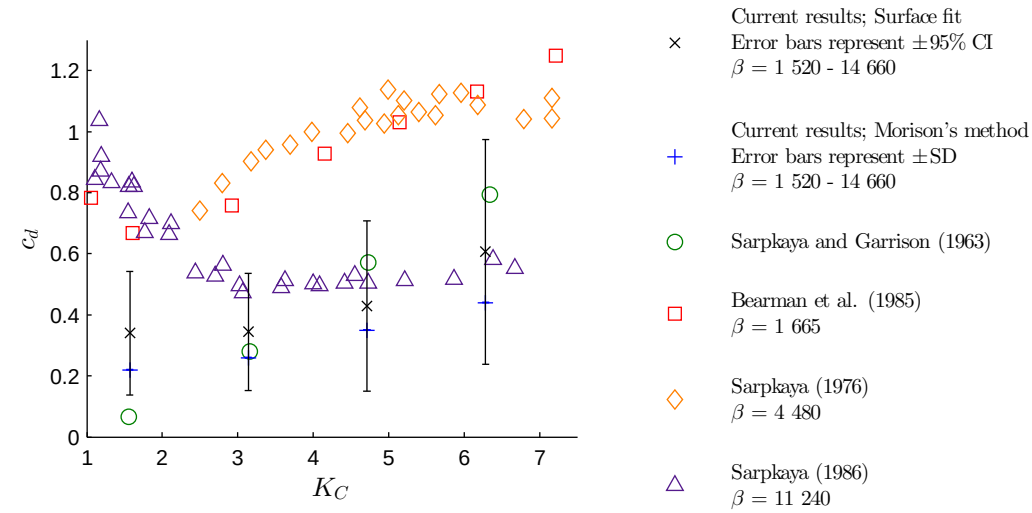

(a)

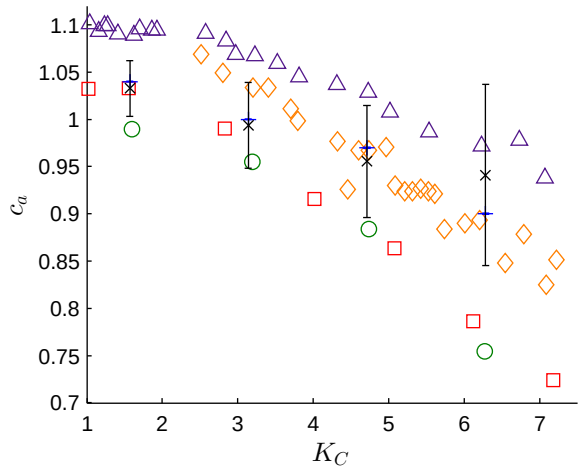

(b)

Figure 5.23. A comparison of current experimental Morison equation coefficients with values from the literature.

(ignoring resonant peaks). This indicates that surge forces due to the induced flow increase in amplitude as K_C increases. Figure 5.24d shows that when $K_C = 6.3$ ($h^* = 1.00$) the hydrodynamic surge forces are clearly larger than the inertia forces and begin to take a negative bias due to asymmetry in the surge for cycle.

Tatsuno and Bearman (1990) found that in the high β, low K_C number range of the current experiments, we can expect three-dimensional instability in the induced flow, with longitudinal vortices being shed and possibly irregular switching of flow convection direction. Furthermore, simulations of Iliadis and Anagnostopoulos (1998) predict that asymmetrical vortex shedding should occur under the current experimental conditions when $K_C > 3.5$. Experimental findings of Bearman et al. (1985) are also in agreement. This asymmetrical vortex shedding is likely to be the cause of the higher surge force amplitudes shown in Figures 5.24c and 5.24d when $K_C > 3.5$.

5.4.5 Heave Force Phase

Keulegan and Carpenter (1958) found that the in-line hydrodynamic forces on a cylinder in an oscillating flow lead the heaving velocity and was dependent K_C. Later, Bishop and Hassan (1964) showed that the phase of the hydrodynamic forces of a cylinder oscillating in water were also dependent on the oscillating frequency. Both of these studies involved sinusoidal oscillations. Figure 5.25 shows that with the current non-sinusoidal heaving (see Section 5.4.2) the timing of peak and zero heave force relative to the heave acceleration also depends on the heaving profile (see Section 4.9.2 for notation). For instance, Figure 5.25a shows that with the current heaving motion, the lag of peak heave force following peak heave acceleration near TDC is less sensitive to oscillating frequency than other points in the cycle. Heaving motion aside, the results show that over the current K_C range, higher K_C generally leads to lower lag between heave acceleration and the heave force. This is due to the heave force having an increasing sensitivity to heave velocity with increasing K_C as shown in Figure 5.20.

Figure 5.26 compares the mean phase lag (neglecting variation due to oscillating frequency and heave motion profile) for a given Keulegan-Carpenter number with the results of Keulegan and Carpenter (1958) and Bishop and Hassan (1964). The current results

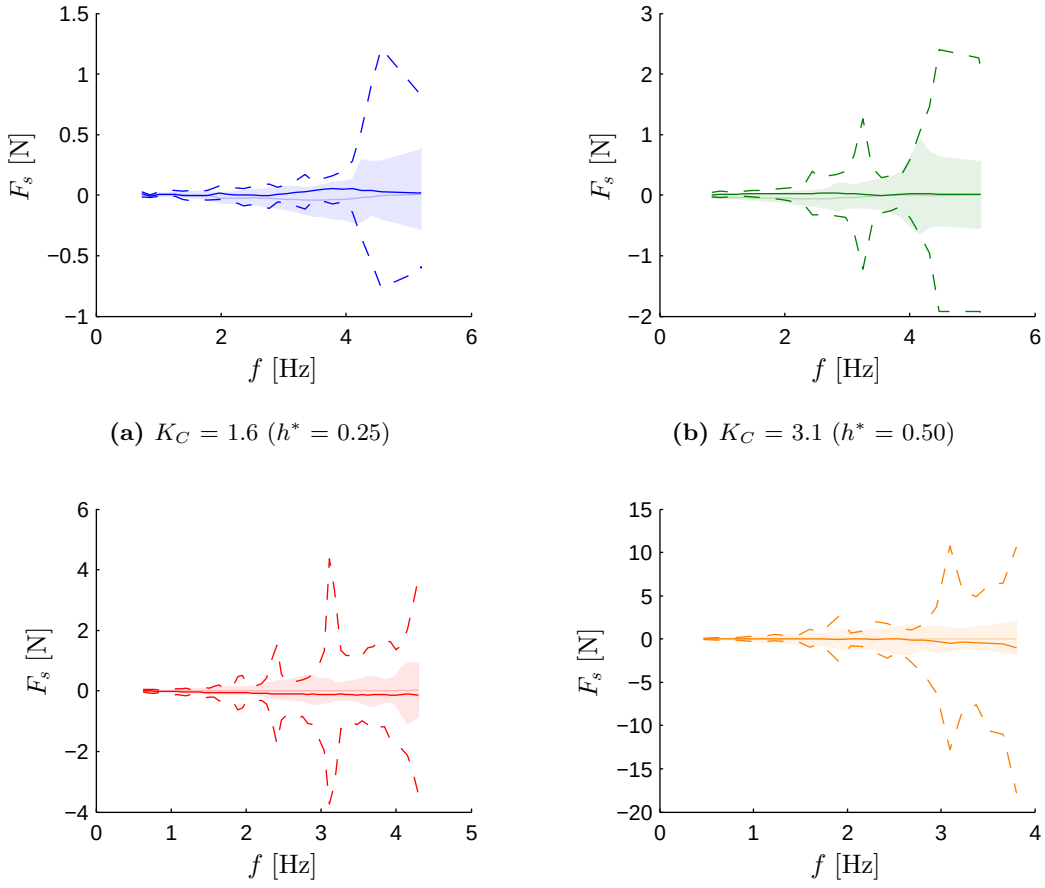

(a) $K_C = 1.6$ ($h^* = 0.25$)

(b) $K_C = 3.1$ ($h^* = 0.50$)

(c) $K_C = 4.7$ ($h^* = 0.75$)

(d) $K_C = 6.3$ ($h^* = 1.00$)

Figure 5.24. Surge force cycle maximum (upper dashed line), minimum (lower dashed line) and mean (centre solid line) for a cylinder oscillating in water, $u = 0$. Surge force range for oscillations in air, i.e. typical inertia measurement due to equipment imbalance and vibration is shown for reference (shaded area with mean shown as light coloured solid line).

Table 5.3. Flat plane fit coefficients with no drag sensitivity and coefficients of determination for the oscillating cylinder heave force data for various heave-to-chord ratios. Data plots are shown in Figure 5.20.
Coefficient 95 % confidence interval are show in brackets.

h^*	K_C	a_0	$a_{\ddot{h}}$	R^2	$RMSE$
0.25	1.57	0.0323	1.7627	0.9985	0.2584
		(±0.0013)	(±0.0003)		
0.50	3.14	0.0363	1.6895	0.9923	1.1518
		(±0.0061)	(±0.0008)		
0.75	4.71	0.0567	1.6495	0.9650	2.5263
		(±0.0089)	(±0.0011)		
1.00	6.28	0.0321	1.5064	0.9140	3.9114
		(±0.0184)	(±0.0022)		

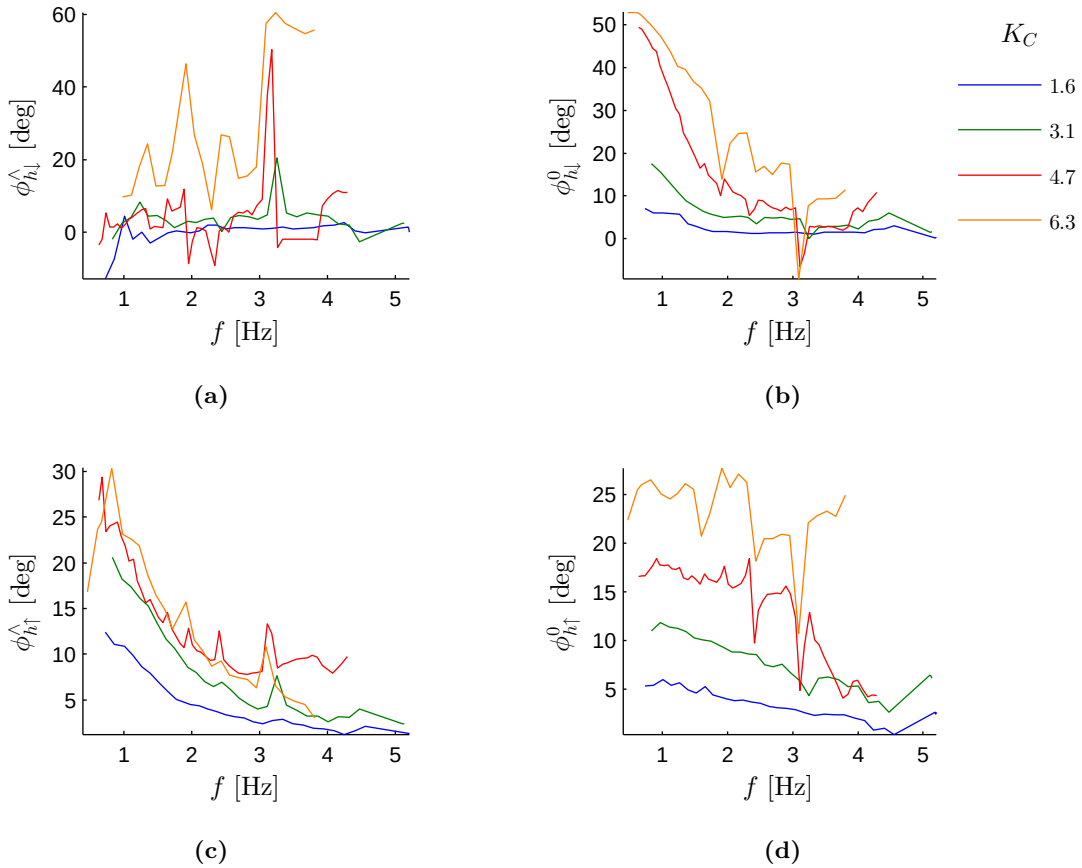

Figure 5.25. Timing of peak and zero heave force on the cylinder. $u = 0$

Table 5.4. Connecting rod to crank length ratios for each heaving amplitude used in this study.

h_0 [mm]	L_c
15	10.9
30	5.4
45	3.7
60	2.9

Table 5.5. Morison equation drag and added mass coefficients with coefficients of determination for the oscillating cylinder heave force data for various heave-to-chord ratios. Data plots are shown in Figure 5.20.
Coefficient 95 % *confidence interval are show in brackets.*

h^*	K_C	c_d	c_a	R^2	$RMSE$
0.25	1.57	0.2208	1.0393	0.9994	0.166
		(±0.0010)	(±0.0010)		
0.50	3.14	0.2602	0.9964	0.9973	0.678
		(±0.0010)	(±0.0010)		
0.75	4.71	0.3475	0.9741	0.9843	1.695
		(±0.0011)	(±0.0011)		
1.00	6.28	0.4413	0.8967	0.9731	2.186
		(±0.0014)	(±0.0014)		

and those of Bishop and Hassan (1964) appear to vary linearly with K_C. However, the results of Keulegan and Carpenter (1958) show a non-linear relationship with K_C, which if extrapolated would have a mean phase of approximately 7° when $K_C = 0$. This may be because Keulegan and Carpenter's experiments were conducted with a stationary cylinder in an oscillating flow, while the current experiments and those of Bishop and Hassan (1964) were conducted with an oscillating cylinder in an initially stationary fluid.

5.4.6 Suitability of the Experimental Equipment Design

In Section 5.4.1, a linear mass-damper model was shown to provide the best fit to the measured hydrodynamic forces on the heaving cylinder ($u = 0$, $1.6 < K_C < 6.3$). It was also concluded that the drag term in this model could be neglected at low Keulegan-Carpenter numbers ($K_C < 3$). These result are in good agreement with the model validity recommendations of Journée and Massie (2001) (see Section 3.3.8). In Section 5.4.3 added

Table 5.6. A comparison of current experimental Morison equation coefficients with values from the literature.

Source	h^*	K_C	c_d	c_m	c_a	Conditions
Current Results	0.25	1.57	0.34	-	1.03	β = 2 070 - 14 660
Morison's method	0.50	3.14	0.34	-	0.99	β = 2 370 - 14 240
	0.75	4.71	0.43	-	0.96	β = 1 950 - 12 410
	1.00	6.28	0.61	-	0.94	β = 1 530 - 10 220
Current Results	0.25	1.57	0.22	-	1.04	β = 2 070 - 14 660
Surface fit	0.50	3.14	0.26	-	1.00	β = 2 370 - 14 240
	0.75	4.71	0.35	-	0.97	β = 1 950 - 12 410
	1.00	6.28	0.44	-	0.90	β = 1 530 - 10 220
Sarpkaya and Garrison	0.25	1.57	0.07	1.99	0.99	
(1963)	0.50	3.14	0.28	1.95	0.95	
	0.75	4.71	0.57	1.86	0.86	
	1.00	6.28	0.79	1.75	0.75	
Bearman et al. (1985)	0.16	1.00	0.83	2.01	1.01	β = 1 665
	0.32	2.00	0.63	2.01	1.01	β = 1 665
	0.64	4.00	0.88	1.90	0.90	β = 1 665
	0.95	6.00	1.10	1.74	0.74	β = 1 665
Sarpkaya (1976)	0.50	3.10	0.89	2.05	1.05	β = 4 480
	0.75	4.70	1.05	1.95	0.95	β = 4 480
	1.00	6.30	1.12	1.87	0.87	β = 4 480
Sarpkaya (1986)	0.25	1.57	0.72	2.10	1.10	β = 11 240
	0.50	3.14	0.50	2.03	1.03	β = 11 240
	0.75	4.71	0.50	1.95	0.95	β = 11 240
	1.00	6.28	0.54	1.90	0.90	β = 11 240
Rashid, Vartdal, and Grue (2011)	0.16	1.00	0.23		1.03	β = 11 240
(simulation)	0.32	2.00	0.18		1.01	β = 11 240
	0.64	4.00	0.36		0.95	β = 11 240
Sajonia (1988)	N/A		0.93	1.73	0.73	free-to-surge
Troesch and Kim (1991)	0.08	0.50	0.85	2.00	1.00	β = 48 600
Otter (1990)	< 0.15	< 0.94			1.09	
Clauss, Lehmann, and Ostergaard (1992)	< 1.6	< 10	0.60	2.00	1.00	$Re > 10^5$

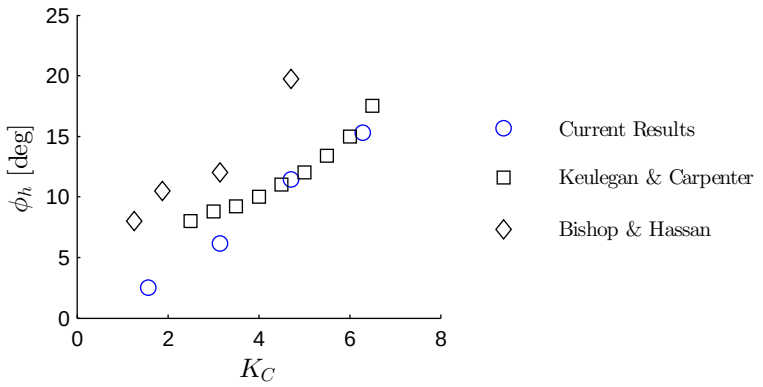

Figure 5.26. Mean heave force lag versus K_C for a cylinder. (Bishop & Hassan, 1964; Keulegan & Carpenter, 1958)

mass and drag coefficients calculated from the current experimental measurements were compared to values found in the literature.

The current calculated drag coefficients fell below values found in the literature (Figure 5.23a). However, this was justified because of the higher value of β in the current experiments. The drag coefficient for $K_C = 4.7$ agreed well with the results of Sarpkaya and Garrison (1963) and Sarpkaya (1986), which was good since subsequent testing would be performed at this Keulegan-Carpenter number. Furthermore, the current calculated added mass coefficient was well centred amongst the results of Bearman et al. (1985), Sarpkaya and Garrison (1963) and Sarpkaya (1976, 1986) under this condition of $K_C = 4.7$. (Figure 5.23b).

These points of agreement between the current results and the literature instilled confidence that the current experimental equipment design (see Section 4.2) was adequate for measuring hydrodynamic forces on the cylinder. Furthermore, with these results, it was deemed adequate for continuing the current programme to provide force data on the other test objects (see Section 4.3). Data that is presented and discussed in the proceeding chapters.

5.5 A Heaving Flat Plate with Zero Forward Velocity

In this section the forces on an oscillating flat plate of finite thickness are presented. Similarly to the study on the cylinder, this section is included to show the time-dependent hydrodynamic forces on an object with simple geometry. However, the flat plate is more similar to a foil than a cylinder is (see Section 4.3). The flat plate was chosen with similar thickness, relative to its chord length, as the foils had. However, with its flat faces, and identical leading and trailing edge geometry, the flat plate was not expected to create thrust at zero pitch angle like the foils were.

The following data was collected with a heave-to-chord ratio of 0.88 ($h_0 = 45\,\text{mm}$, $c = 51\,\text{mm}$) and zero forward velocity. The oscillating frequency was varied between approximately 0.6 Hz and 3.9 Hz while pitch angle was varied from 0° to 90° in increments of 10°.

5.5.1 Object Shape

Before the hydrodynamic forces on the flat plate and the foils are examined in the following sections, a brief overview on how the object shape influences the heave force profiles is provided here. Figure 5.27 shows the typical heave force cycle of each test object oscillating in initially stagnant water with zero pitch. These heave force cycles have been normalised by their maximum absolute value so that their profiles can be compared. Notice that the phase and profile of the flat plate heave force cycle is significantly different from that of the cylinder. Furthermore, the two foils have a very similar heave force profile and phase to the flat plate. Later this is shown to also be true for some larger pitch angles in Section 5.6.2.

As found in Section 5.4, the heave force acting on the cylinder is near in-phase with the heaving motion. Here the heave force on the flat plate and the foils lags the heaving motion by almost one quarter of the period. This lag for each of these signals appears to be very consistent if the points of zero heave are taken as a reference. However, the points of peak heave vary with object shape.

Also note that the heave force profiles are not symmetrical about zero heave, nor

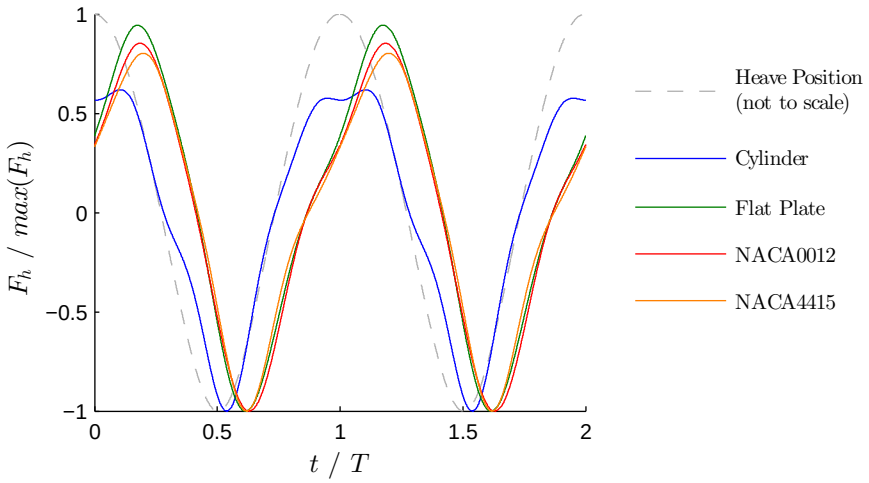

Figure 5.27. Normalised heave force profiles for different shape test objects. $u = 0$, $h^* = 0.88$, $\theta = 0°$

similar for the upstroke and downstroke portions of the heaving motion. This is due to the heaving acceleration profile being asymmetrical about zero heave acceleration and the phase of peak heave force being dependent on the magnitude of the preceding peak in heave acceleration. This observation is presented in more detail in Section 5.6.1.

The magnitude of the heave forces generated by the flat plate were compatible to those generated by the foils. However, both the flat plate and the foils generated much larger heave forces than the cylinder did. Figure 5.28 compares the maximum and minimum heave forces generated by each test object over the tested oscillating frequency range. Peak heave force on the flat plate or the foils was 2.5 - 4.5 times higher than the peak heave force on the cylinder (Table 5.7). This indicates that flatter objects either have a higher virtual mass or create more drag.

Table 5.7. Peak heave force values normalised by the cylinder peak heave force values. Mean values are shown with 2 SD uncertainty. $(0.8 < f < 3.7)$

Test Object	Flat Plate	NACA0012	NACA4415
Min. heave force	2.76 ±0.28	2.96 ±0.42	2.79 ±0.26
Max. heave force	3.90 ±0.30	4.20 ±0.30	3.55 ±0.26

The power required to oscillate the flat plate or a hydrofoil foil ($\theta = 0$) at a given frequency was approximately ten times more than for the cylinder (Figure 5.18). As

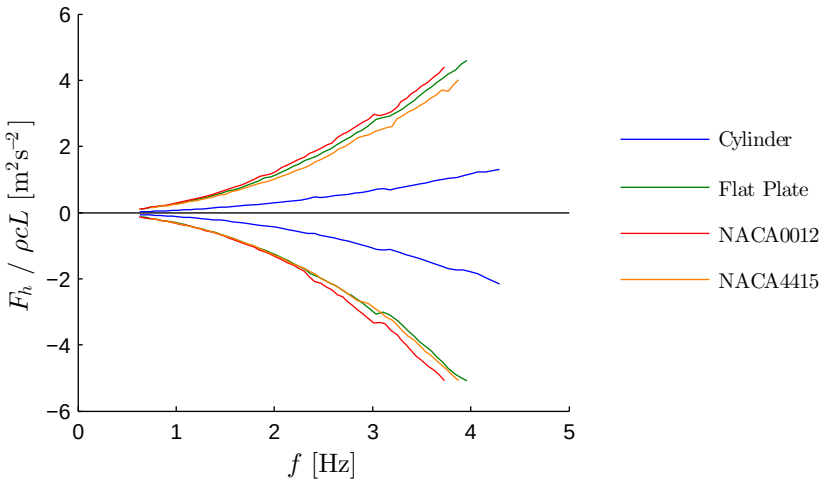

Figure 5.28. Heave force range normalised by plan form area for different shape test objects. $u = 0$, $h^* = 0.88$, $\theta = 0°$

a flat plate normal to a flow generates more drag than a cylinder under steady state conditions, it is not surprising that the flat plate also requires a more input power under unsteady conditions. As presented in Section 5.2.3, the calculated mean input power for the cylinder is relatively small due to the heave force cycle having a relatively high out-of-phase component. Similarly, because the flat plate and the foils have a much higher in-phase component to their heave cycles, the mean input power required is much higher.

5.5.2 Hydrodynamic Forces at Zero Pitch

In the case of the flat plate heaving with zero pitch and no forward velocity ($\theta = u = 0$), heave forces are large and surge forces are relatively small due to the projected area of the plate normal to these directions. Figure 5.29 shows the heaving velocity and acceleration profiles with the typical resultant heave and surge force profiles under these conditions.

5.5.3 Evaluating Existing Models

A Visual Comparison of Model Fits

Figure 5.30 shows the measured surge and heave forces plotted against heaving velocity and acceleration. Unlike the results of the cylinder, the heave forces do not fall into a plane

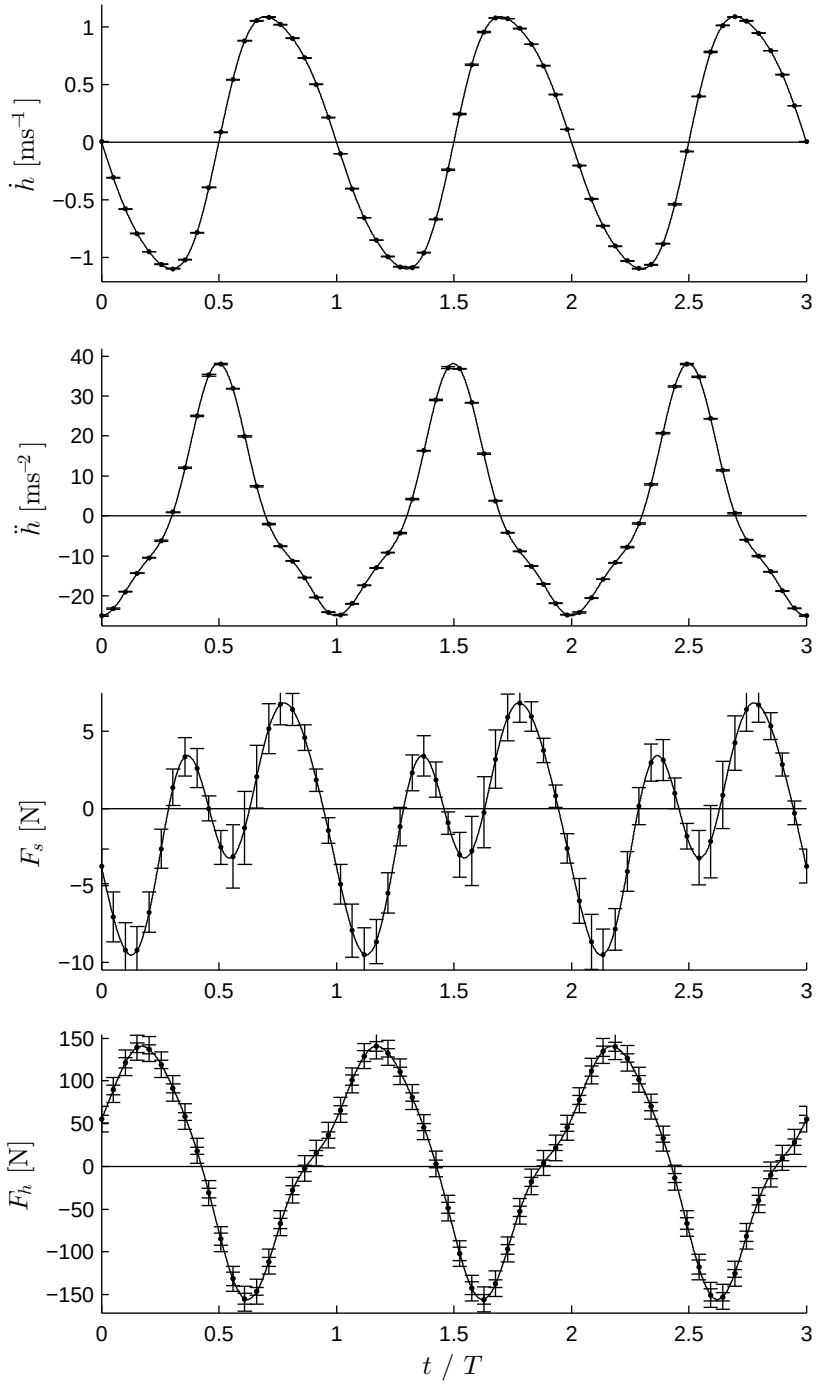

Figure 5.29. Typical profiles of surge and heave forces on a flat plate as a function of normalised time. $u = 0$, $h^* = 0.88$, $\theta = 0°$

over this domain and so may not be modelled with linear added mass and damping. Upon further inspection of this surface it is also clear that the data may not be fitted well with a function in the form of the Morison equation (Equation 3.6).

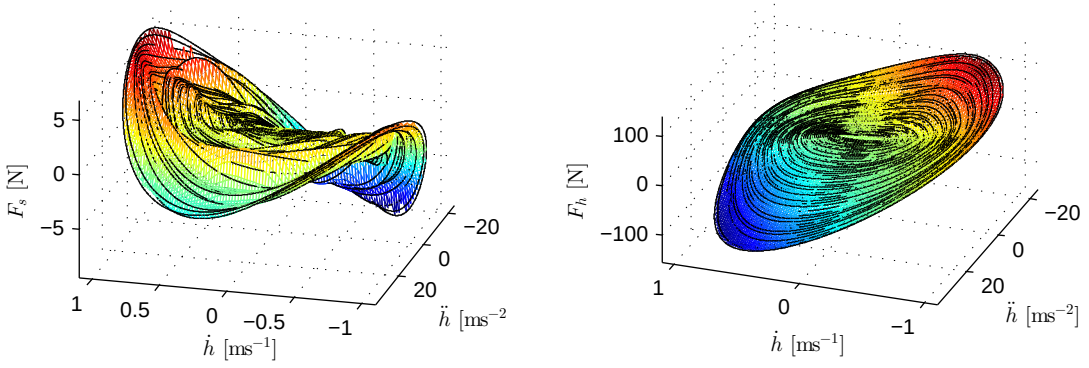

(a) **(b)**

Figure 5.30. Surge and heave forces on a flat plate as a function of heave velocity and heave acceleration. $u = 0$, $h^* = 0.88$, $\theta = 0°$

Figure 5.32 shows a measured heave force cycle alongside a linear mass-damper model, a fit using the Morison equation, and a quasi-steady estimate of the heave forces. The mass and damping (or drag) coefficients for the fits (Table 5.8 and Table 5.9) were found by fitting the surface shown in Figure 5.30b. Figure 5.31 shows the surface fits with the experimental data. The drag coefficient used for the quasi-steady estimate was $c_d = 1.9$.

A Comparison of the Current Model Coefficients with the Literature

Potential flow theory predicts that the added mass of a thin flat plate is equivalent to that cylinder with a diameter equal to the plate chord length, i.e. $m_a = \pi/4\rho c^2 L$ (Newman, 1977; Payne, 1981). However, the virtual mass of a real flat plate is dependent on its aspect ratio, thickness, and structural vibration modes Payne (1981); Yadykin, Tenetov, and Levin (2003); Yu (1945). Table 5.9 compares the current Morison equation fit coefficients with other values found in the literature. The experiments of Keulegan and Carpenter (1958) were performed with under similar conditions. However, in their experiments the plate was fixed and the flow oscillated. As mentioned in Section 3.3.1,

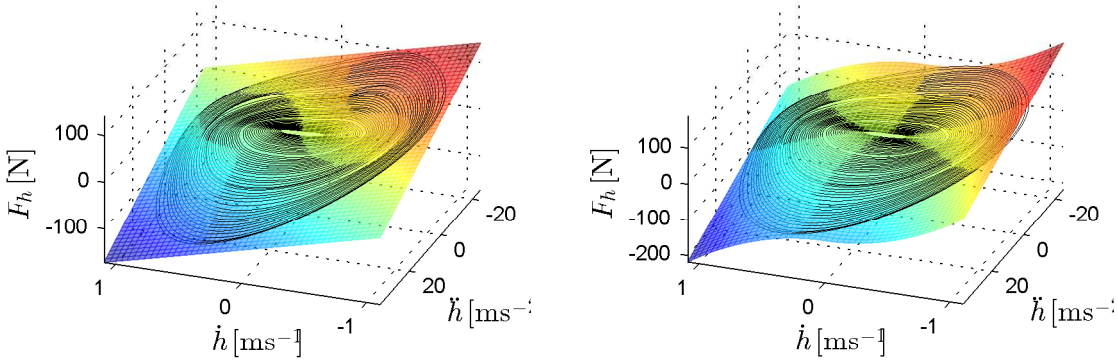

(a) **(b)**

Figure 5.31. Heave forces on the flat plate fitted with (a) a linear mass-damper model ($R^2 = 0.90$) and (b) the Morison equation ($R^2 = 0.94$). $u = 0$, $h^* = 0.88$, $\theta = 0°$

the difference between the hydrodynamic forces for these cases is the Froude-Krylov force which increases the added mass coefficient by one. As seen in Table 5.9, the added mass coefficient c_a for the current experiment is in good agreement with the inertia coefficient c_m of Keulegan and Carpenter (1958). Furthermore, the current added mass m_a agrees with theory for the virtual mass m_v of a plate of finite thickness. These similarities may suggest that a Froude-Krylov force does act on a flat plate under going vertical oscillations in an otherwise still fluid. This effect could be due oscillatory local flow induced by the heaving plate.

The current drag coefficient c_d is very high when compared to that of a steady plate, or the results of Morison et al. (1953). However, the current drag coefficient fits well between the results of Keulegan and Carpenter (1958) from experiments at slightly higher and lower K_C. Again, this is because the experiments of Keulegan and Carpenter (1958) were performed very similar conditions to the current experiments.

Selection of the Best Model

As expected a quasi-steady fit (see Figure 5.32) is highly inappropriate at high Strouhal numbers with a mean RMSE over the covered frequency range of 26 % of the heave force

Table 5.8. Coefficients for flat plate heave force fits. $u = 0$, $\theta = 0°$

Mass-Damper Model	$a_{\dot{h}}$ $[\mathrm{kg\,s^{-1}}]$	$a_{\ddot{h}}$ [kg]	$Re_{\dot{h}}$	K_C
Current Results	65.29	2.70	6.3×10^3 - 41.3×10^3	5.5

Table 5.9. Coefficients for flat plate heave force fits. $u = 0$, $\theta = 0°$

Morison equation	c_d	m_v [kg]	m_a [kg]	c_m	c_a	$Re_{\dot{h}}$	K_C
Current Results	6.45		2.70			6.3×10^3 - 41.3×10^3	5.5
V_m the volume of the flat plate					14.71		
V_m the volume of an equivalent cylinder					2.20		
Steady drag coefficient (Det Norske Vertias, 2011)	1.90					$> 10 \times 10^3$	
Potential flow theory value (Newman, 1977)		2.45	1.23	2.00	1.00		
For a plate with to chord/thickness = 8.5 (Det Norske Vertias, 2011)		2.65	1.43	2.16	1.16		
Keulegan and Carpenter (1958)	5.21			2.22		12.8×10^3	8.8
(Plate; $c = 50.8\,\mathrm{mm}$, $L = 520\,\mathrm{mm}$)	8.04			2.16		5.9×10^3	4.1
Morison et al. (1953) (Plate; $c = 25.4\,\mathrm{mm}$, chord/thickness = 8)	1.20			0.42		15.0×10^3	

range. The quasi-steady estimate significantly lags the measured heave force cycle and underestimates its magnitude by approximately 84 %. The linear mass-damper model and Morison equation fits are both in phase with the measured heave force cycle. Although both fits predict the point of zero heave force on the upstroke precisely, the timing of the predicted zero heave force leads the measured heave force slightly on the downstroke. This affects the position based symmetry parameter which may contribute to the mean heave force being underestimated as shown in Table 5.10.

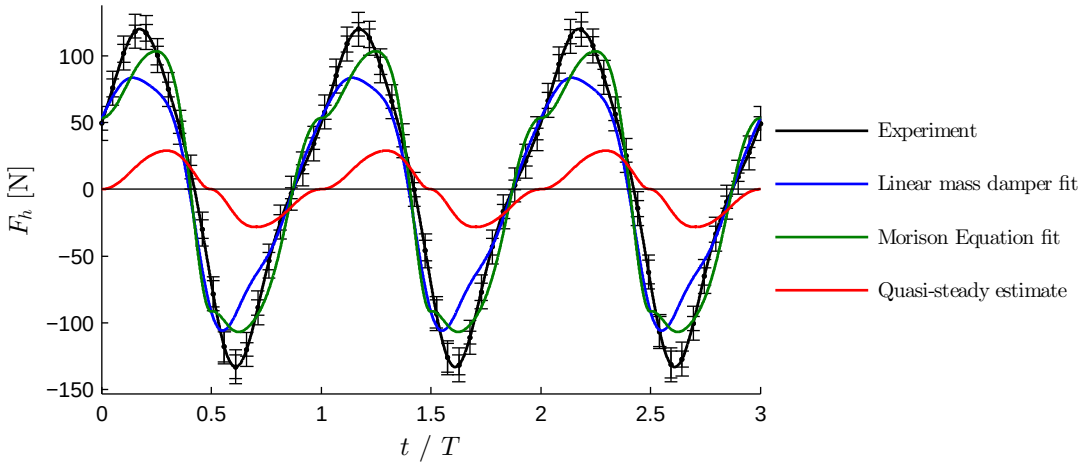

Figure 5.32. Measured heave forces on the flat plate compared to a linear mass-damper model fit, a Morison equation fit, and a quasi-steady estimate. $f = 3.7\,\text{Hz}$, $u = 0$, $h^* = 0.88$, $\theta = 0°$

Table 5.10. Mean heave forces for the cycles shown in Figure 5.32.

	Experiment	Mass-damper fit	Morison fit	Quasi-steady
Mean heave force [N]	4.25	0.02	0.19	0.05

Figure 5.33 shows the RMSE of the two data fits and the quasi-steady estimate relative to the measured heave force range. Both the Morison equation fit and the quasi-steady estimate maintain as consistent relative RMSE over the investigate frequency range. However, the linear mass-damper model fit does not scale with frequency well.

Although the Morison equation fit maintains a low relative RMSE around 8 %, minimum heave is consistently underestimated by approximately 18 % and maximum heave

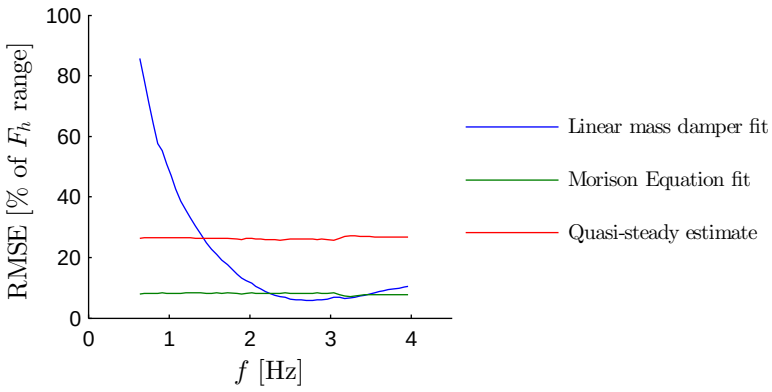

Figure 5.33. RMSE a linear mass-damper model fit, a Morison equation fit, and a quasi-steady estimate for the heave forces on the flat plate plotted against oscillating frequency. $u = 0$, $h^* = 0.88$, $\theta = 0°$

by up to 15 %. Figure 5.34 shows the ratio of minimum-to-maximum heave for the measured heave forces with that for the linear mass-damper fit, Morison equation fit, and the quasi-steady estimate over the investigated oscillating frequency range. Since the minimum-to-maximum ratio of the heave velocity profile is approximately 1, but that of the heave acceleration profile is approximately 1.75, it may be used to estimate which profile has more influence on the heave force cycle. The measured heave forces exhibit a relatively consistent minimum-to-maximum heave ratio over the oscillating frequency range that suggests that its profile scales well with oscillating frequency.

The minimum-to-maximum heave force ratio of the linear mass-damping model linearly increases as the oscillating frequency increases. This is expected since the contribution of the heave acceleration dependent forces ($a_{\ddot{h}}\ddot{h}$) relative to heave velocity dependent forces ($a_{\dot{h}}\dot{h}$) increase linearly with oscillating frequency (Equation 5.5), and the magnitude of the heave acceleration maximum and minimum are not equal (see Appendix Section D.2). Similarly, the minimum-to-maximum heave force ratio of the Morison fit tends to that of the quasi-steady estimate at low frequencies ($f < 1.5$ Hz) as the inertia term becomes small compared to the drag term.

$$\frac{|\ddot{h}|}{|\dot{h}|} \propto \frac{\omega^2 h_0}{\omega h_0} = \omega \tag{5.5}$$

The above results show that the heave forces on the flat plate differed substantially

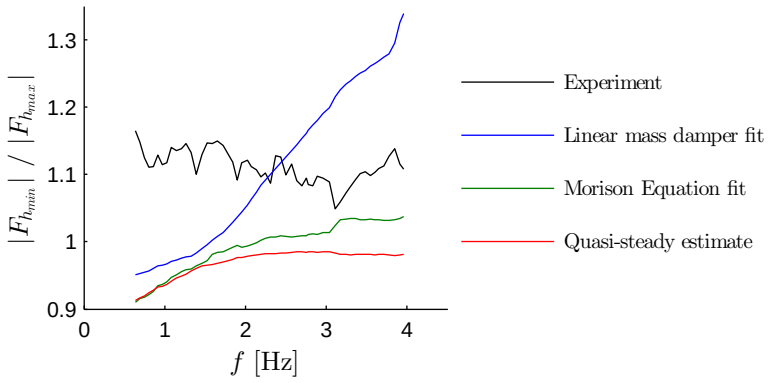

Figure 5.34. Ratio of minimum-to-maximum heave force for the measured data, the linear mass-damper model fit, the Morison equation fit, and the quasi-steady estimate.

from those on the cylinder, and confirmed that quasi-steady calculations of heave forces at high St contain very large errors. The heave forces on the flat plate could not be modelled well with a linear mass-damper model, and so the Keulegan-Carpenter number ranges that define model applicability for a cylinder (see Section 3.3.8) are unlikely to apply for flat plates or other flat shape objects such as hydrofoils. Although the Morison equation may provide a reasonable estimate for the heave force cycle on a flat plate, the profile and magnitude of the heave force cycle it predicts are less than ideal. As seen in Figure 5.32, significant errors in the Morison equation fit occur around the points of maximum and minimum heave force which are underestimated. The shape of the calculated force cycle in these areas is also not like that of the measured heave force cycle.

5.5.4 Change in Hydrodynamic Forces with Pitch

Figure 5.35 shows that the heave force range is greatest when the plate is orientated normal to the heave direction ($theta = 0°$). As the plate pitch of the increases, the heave force range steadily decreases to near zero when the pitch reaches 90°. The surge forces on the plate increase as the pitch increases to around 45° and then decrease as the pitch is increased to 90°. In the following subsections the magnitude, phase and profile of the heave and surge forces are investigated with respect to the pitch angle.

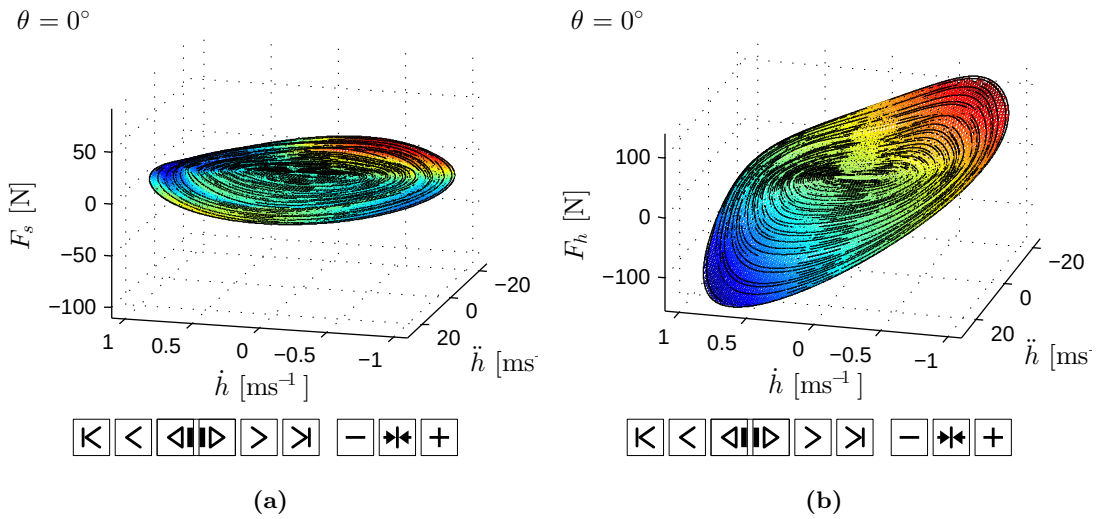

(a) **(b)**

Figure 5.35. Surge and heave forces and on the flat plate as a function of heaving velocity and acceleration for pitch angles θ=0° to θ=90° in 10° increments. $u = 0$, $h^* = 0.88$

Heave Force Range

Although the mean heave force on the flat plate increases linearly with oscillating frequency (Figure 5.5b), the range of the cycle increases quadratically. This suggests that the heave force on the flat plate is predominantly due to inertial effects ($\propto \ddot{h}$) or quadratic drag ($\propto \dot{h}^2$). Assuming that the heave forces are inertia dominant, the heave force range A_{F_h} was correlated against the heave acceleration range $A_{\ddot{h}}$ in this section. Figure 5.36a shows that the relationship between these two quantities is linear, and so a proportionality constant $c_{A_{F_h}}$ may be calculated for each pitch angle with Equation 5.6. The heave force range coefficient $c_{A_{F_h}}$ describes how quickly the heave force cycle range increases with the heaving acceleration range, which are proportional to the oscillating frequency squared. If heave forces are purely in-phase with the heave acceleration, then $c_{A_{F_h}}$ represents the virtual mass of the plate. Figure 5.36b shows how $c_{A_{F_h}}$ varies with the pitch of the flat plate.

Yu (1945) considered that the theoretical added mass of a thin flat plate should be proportional to $M_0 cos^2(\theta)$ where M_0 was the added mass of the plate oscillating in the direction of its normal, i.e. $\theta = 0°$. This relationship agreed with his experimental results

except for when the pitch was near 90° due to the real plate having a finite thickness.

Assuming that the change in heave force amplitude with pitch is predominantly due to a change in added mass, then $c_{A_{F_h}}$ should also be proportional to $cos^2(\theta)$ (or equivalently $cos(2\theta)$). However, Figure 5.36b shows that a function of this form does not fit the current results well. However, if the thickness of the plate is considered (Figure 5.37) the heave force range coefficient should be proportional to the pitch as in Equation 5.7, where t_p is the plate thickness. Figure 5.36b shows that this function provides a better fit to the experimental results suggesting that the thickness of the plate significantly affects its added mass. In this case, particularly for pitch angles between 10° and 60°.

$$c_{A_{F_h}} = \frac{A_{F_h}}{A_{\ddot{h}} \rho c L} \tag{5.6}$$

$$c_{A_{F_h}}(\theta) = \left(\frac{c_0 - c_{90}}{2}\right)\left(cos(2\theta) + \frac{t_p sin(2\theta)}{c}\right) + \left(\frac{c_0 + c_{90}}{2}\right) \tag{5.7}$$

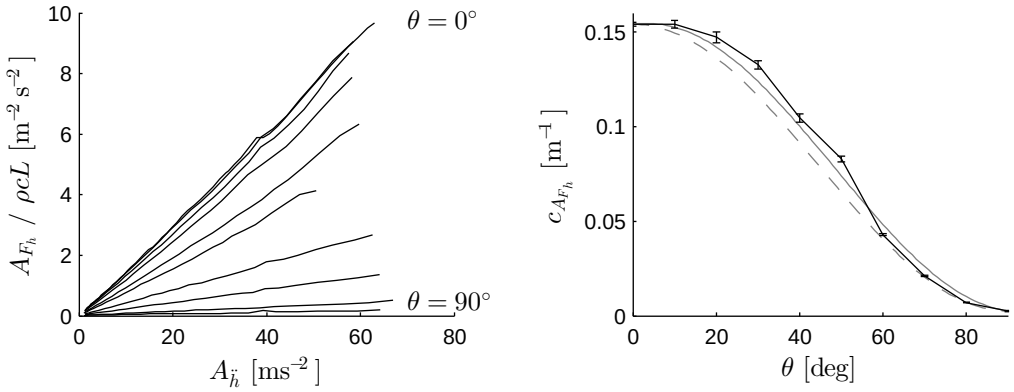

Figure 5.36. (a) Heave force range is proportional to the heave acceleration range and (b) the proportionality constant $c_{A_{F_h}}$ as a function of pitch angle θ. A function proportional to $cos(2\theta)$ is shown as a grey dashed line, and a function of the form Equation 5.7 is shown as a solid grey line for reference. $u = 0$, $h^* = 0.88$

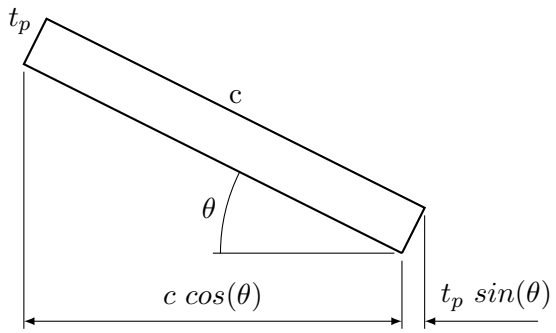

Figure 5.37. The projected chord length of flat plate with finite thickness.

Surge Force Range

Figure 5.38 shows how the surge force range coefficient changes with the pitch angle of the plate. Since the $c_{A_{F_h}}$ was approximately proportional to $cos(2\theta)$, it was reasonable to expect $c_{A_{F_s}}$ to be proportional $sin(2\theta)$. As shown in Figure 5.38 this was not the case and $c_{A_{F_s}}$ varies almost linearly with pitch.

Notice in Figure 5.38b that the surge force range coefficient $c_{A_{F_s}}$ is larger at $\theta = 0°$ than at $\theta = 90°$. This is because at $\theta = 0°$ the flat plate has a much larger projected area in the heave direction leading to higher Reynolds numbers and flow separation. For a cylinder, asymmetrical vortex shedding begins to occur at high Reynolds number (see Section 5.4.4) leading to oscillating surge forces. These results agree with the simulations of Alben and Shelley (2005) which show that surge forces on ellipses with higher aspect ratios (i.e. with geometry similar to that of the flat plate) begin to grow at lower heave velocity based Reynolds numbers than they do for ellipses with lower aspect ratios (i.e. with geometry similar to a cylinder).

Although the current results agree with Alben and Shelley (2005) and Vandenberghe et al. (2006) that surge forces may be generated at zero free-stream velocity by heaving objects with symmetry in the surge plane, Figure 5.38b shows that surge forces generated in this way are relatively small compared to surge forces generated from flow deflection when the plate plane is neither parallel or perpendicular to the heave axis. Interpolating the data reveal that peak $c_{A_{F_s}}$ does not occur at $\theta = 45°$, but at $\theta = 50°$. This bias may also be due to the difference between $c_{A_{F_s}}(0)$ and $c_{A_{F_s}}(90)$.

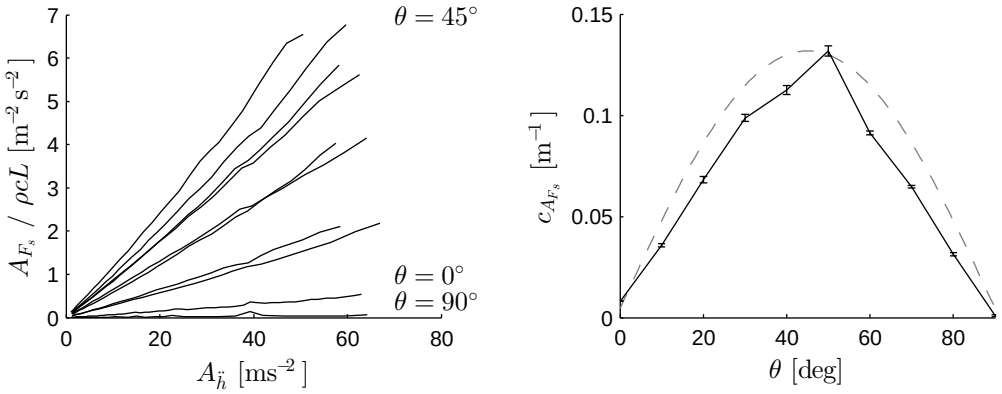

(a) **(b)**

Figure 5.38. (a) Surge force range is proportional to the surge acceleration range and (b) the proportionality constant $c_{A_{F_s}}$ as a function of pitch angle θ. A function proportional to $sin(2\theta)$ is shown as a grey dashed line for reference. $u = 0$, $h^* = 0.88$

Heave and Surge Force Phase

Keulegan and Carpenter (1958) found the the forces on a flat plate in an oscillating flow lead the flow velocity by 33° when $K_C = 5.5$. Assuming a sinusoidal flow velocity, this is equivalent to a phase lag behind the flow acceleration (ϕ_h) of 57°. Similarly, the mean heave force lag (see Section 4.9.2) for the current results with $\theta = 0$ was $\bar{\phi_h} = 52.4°$ over the tested oscillating frequency range. This result is slightly lower than that of Keulegan and Carpenter (1958), which is likely to be because of the non-sinusoidal heaving motion in the current experiments.

Figure 5.39 shows how much the heave force lags behind points of peak or zero heave acceleration. The phase of peak heave force on the downstroke shows a strong dependency on oscillating frequency (Figure 5.39a). Note that at low oscillating frequencies, the downstroke heave forces becomes in-phase with heave velocity indicating a strong contribution of drag forces supporting Equation 5.5. In contrast, peak heave force on the upstroke is relatively insensitive to oscillating frequency (Figure 5.39c). This is likely due to the peak heave acceleration initiating the downstroke being approximately half the magnitude of the peak heave acceleration initiating the upstroke (because of the crank and con-rod mechanism, see Appendix D), leading to a lower relative contribution of in-phase hydrodynamic

force.

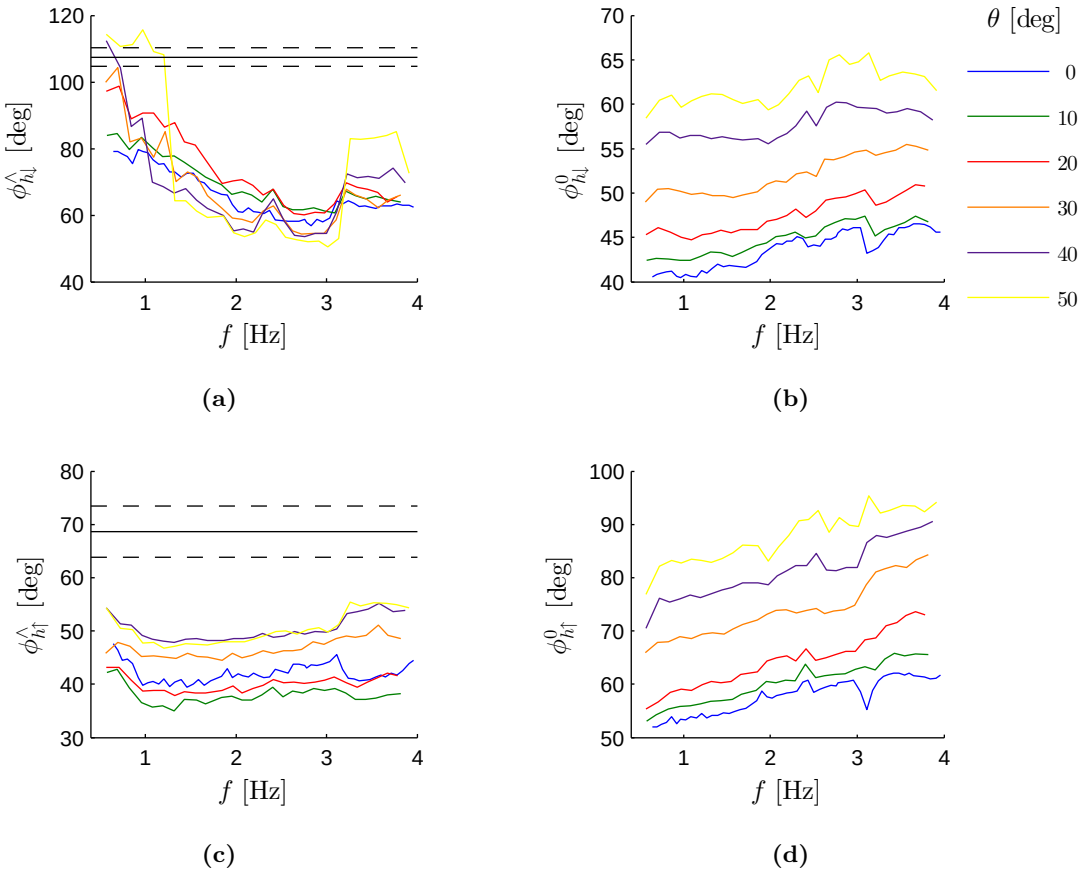

Figure 5.39. Timing of peak and zero heave force on the flat plate at various pitch angles. The mean timing of peak heave velocity following peak heave acceleration is shown with a solid black line with ±2 SD bounds of this value shown as dashed black lines. $u = 0$, $h^* = 0.88$

Figure 5.40 shows the heaving velocity and acceleration profiles with the typical resultant heave and surge force profiles for the heaving plate with a pitch angle of 40°. Note that with a non-zero pitch angle, surge forces may take a similar profile to the heave forces. Furthermore, these large surge forces slightly lag the heave acceleration and are in-phase with the heave force cycle.

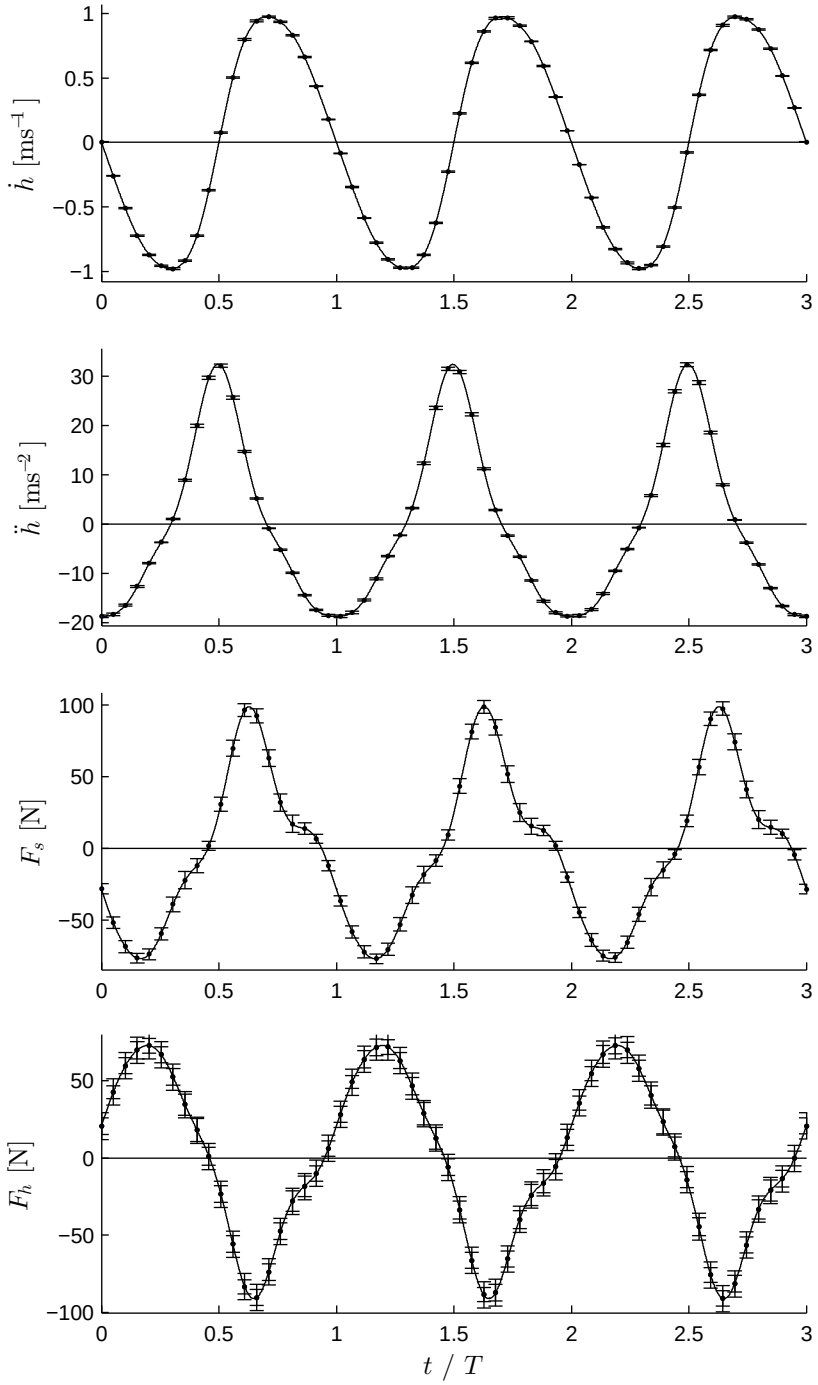

Figure 5.40. Typical profiles of surge and heave forces on a flat plate as a function of normalised time. $u = 0$, $h^* = 0.88$, $\theta = 40°$

5.6 Heaving Hydrofoils with Zero Forward Velocity

In this section, the forces on two different hydrofoils heaving with no forward velocity are presented. The flow regime around hydrofoils undergoing high Strouhal number oscillations is referred to 'piston mode' and is characterised by strong simultaneous vortex shedding from the leading and trailing edges of the hydrofoil (Anderson et al., 1998). This mode of operation is known to have poor propulsive efficiency and so little work has focused on thrust coefficients for this case. However, since most watercraft are required to start from rest, characteristics of the hydrodynamic forces acting on a oscillating hydrofoil propeller operating in piston mode would be useful for design. The goal of this section is to contribute experimental data in this area, and to relate this data to existing hydrodynamic force models for cylinders.

Forces on each heaving hydrofoil were measured using the same procedure that was used for the cylinder and the flat plate. The pitch angle of the NACA4415 was varied from $-90°$ to $90°$. However, since the NACA0012 is a symmetrical foil, only pitch angles from $0°$ to $90°$ were studied.

5.6.1 Hydrodynamic Forces at Zero Pitch

Figure 5.41 shows the surge and heave forces on the heaving NACA0012 with zero pitch and zero forward velocity. As shown in Section 5.5.1, the heave forces are very similar to those on the flat plate. However, the surge force range is larger and has a definite positive bias. This result agrees with Lai and Platzer (2000) who found that shapes with a rounded leading edge and sharp trailing edge will produce a net forward thrust even when $u = 0$.

Figure 5.42 shows the typical heave velocity and acceleration profiles with the surge and heave force profiles for the NACA0012 under these conditions. The surge force profile clearly shows that net thrust is being produced as the surge force rarely falls below zero. As the NACA0012 is a symmetrical foil, the surge force profile would have been symmetric under sinusoidal heaving conditions (Ashraf et al., 2007). However, since the heaving position profile of the current experiments is not sinusoidal, higher order harmonics in the heave position (see Section 5.4.2) distort the heave velocity and acceleration profiles

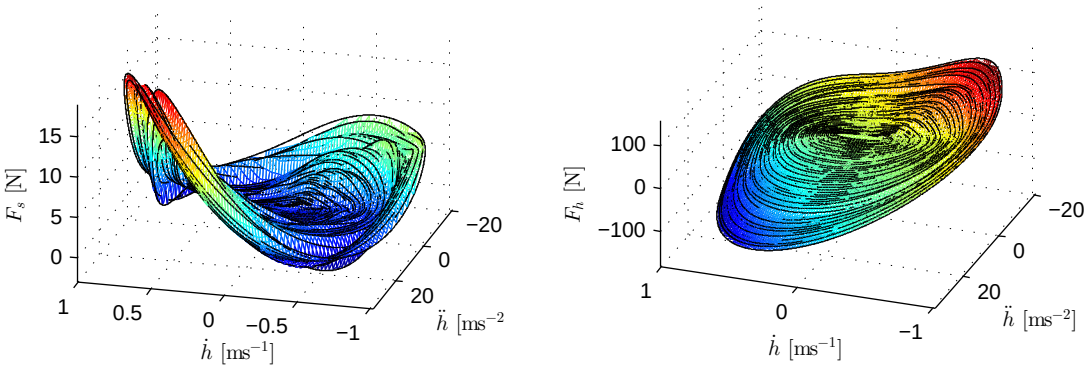

(a) **(b)**

Figure 5.41. Surge and heave forces on a NACA0012 as a function of heave velocity and heave acceleration. $u = 0$, $h^* = 0.75$, $\theta = 0°$

significantly and cause the surge profile to become asymmetric.

As shown in Figure 5.42, points of maximum and minimum heave velocity are equal in magnitude. However, points of maximum and minimum heave acceleration differ in magnitude due to the crank and con-rod mechanism used to drive the heaving motion (see Appendix D). Notice in Figure 5.42 that the magnitude of each surge force peak is roughly proportional to the magnitude of the preceding heave acceleration peak. This suggests that surge forces are most sensitive to heave acceleration when $u = 0$ and $\theta = 0$. Figure 5.43 supports this observation, showing the correlation between peak heave acceleration and the magnitude of the proceeding surge force peak ($R^2 = 0.9759$).

Figure 5.44 shows the surge and heave forces on the NACA4415 as a function of heaving velocity and acceleration. Again, the heave forces on the NACA4415 with zero pitch and zero forward velocity are very similar to the flat plate and the NACA0012 (see Section 5.5.1). However, the surge forces are very different. This leads to the conclusion that surge forces (when $u = 0$) are more sensitive to object geometry than heave forces are.

Figure 5.45 further illustrates how the surge force profile of the NACA4415 is quite different from that of the NACA0012. The NACA4415 produces three thrust pulses per cycle rather than two. This suggest that the NACA4415 produces a 1S + 1P wake rather than a 2S wake like the NACA0012 (when $u = 0$, $\theta = 0$). Since a 1S + 1P wake does not

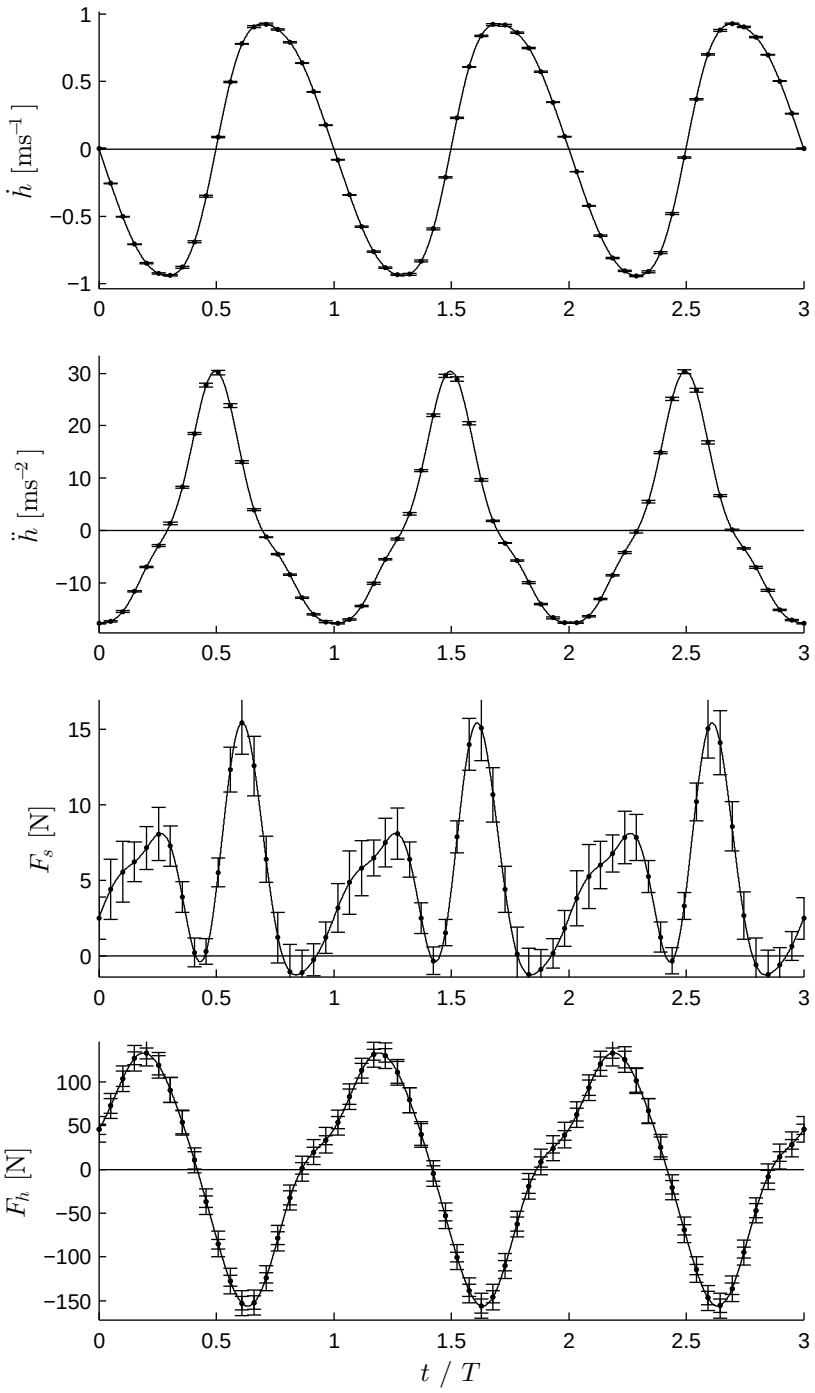

Figure 5.42. Typical profiles of surge and heave forces on a NACA0012 as a function of normalised time. $u = 0$, $h^* = 0.75$, $\theta = 0°$

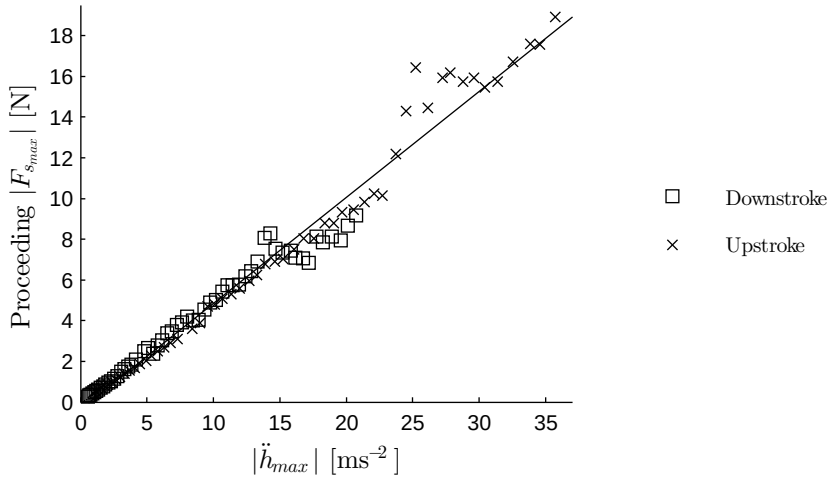

Figure 5.43. Peak heave acceleration versus the magnitude of the proceeding thrust peak for heaving NACA0012. $u = 0$, $h^* = 0.75$, $\theta = 0°$

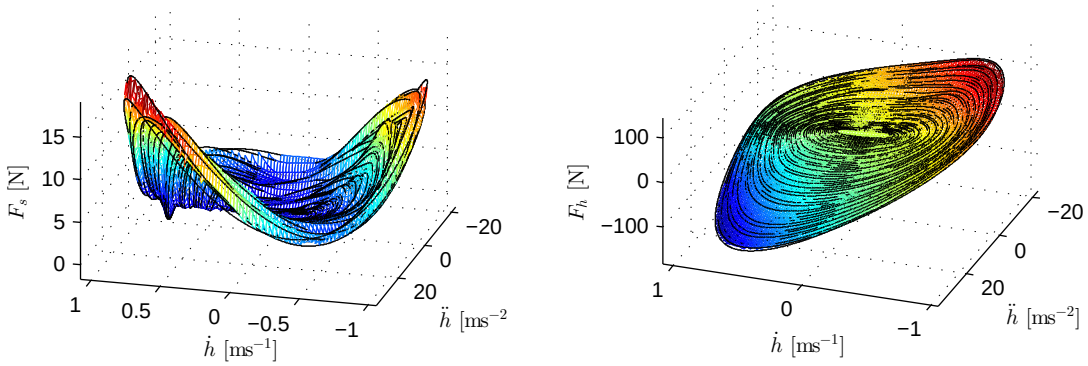

(a) **(b)**

Figure 5.44. Surge and heave forces on a NACA4415 as a function of heave velocity and heave acceleration. $u = 0$, $h^* = 0.75$, $\theta = 0°$

facilitate an efficient jet (see Section 3.5.6) this would in turn suggest that the heaving motion produced by the crank and conrod arrangement is not well suited to the NACA4415 when $u = 0$.

The main thrust pulse produced by the NACA4415 on the upstroke and the downstroke are of similar magnitude, unlike the two main thrust pulses produced by the NACA0012. However, this may change with end plate size as shown in in Section 5.3. Figure 5.46

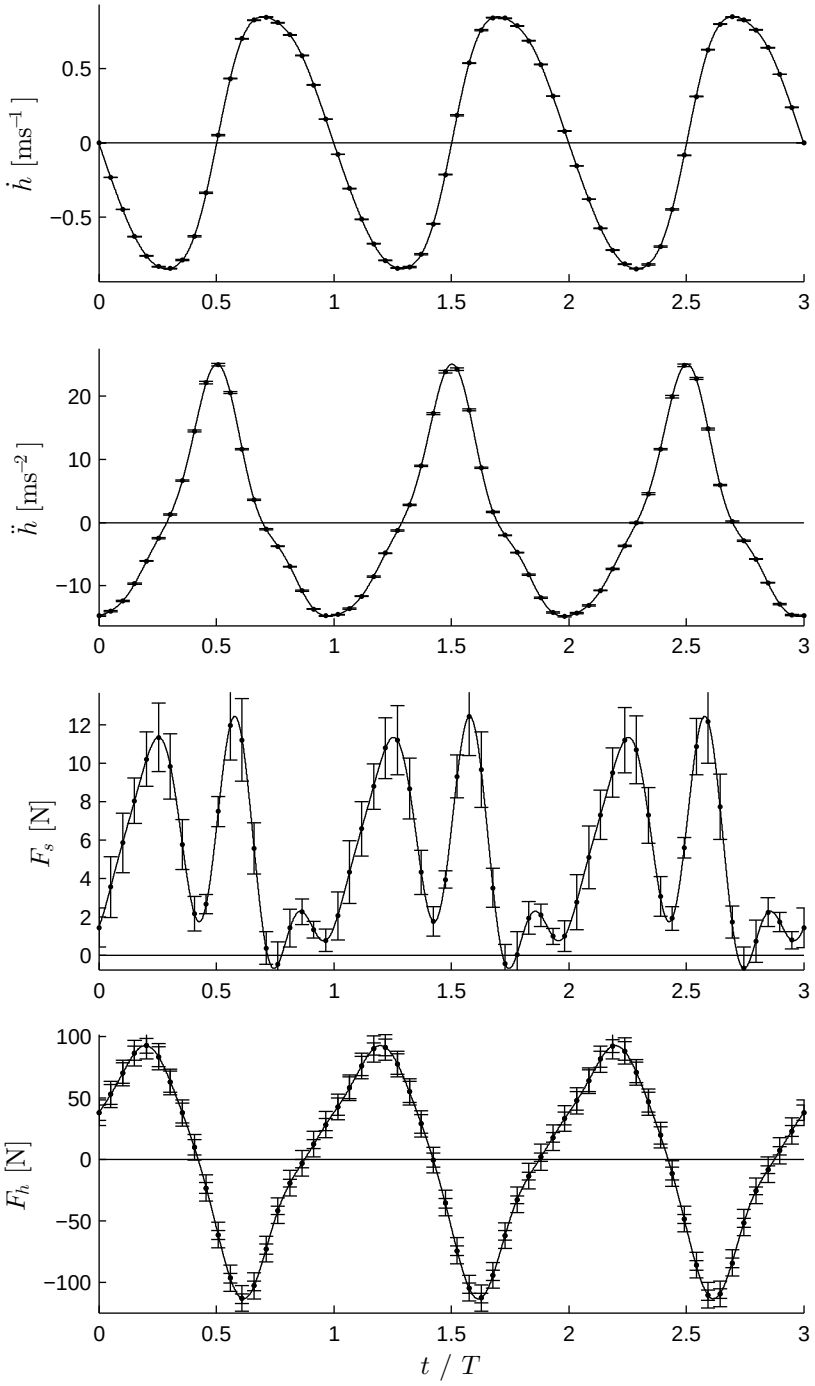

Figure 5.45. Typical profiles of surge and heave forces on a NACA4415 as a function of normalised time. $u = 0$, $h^* = 0.75$, $\theta = 0°$

shows each thrust pulse produced by the NACA4415 is proportional to the magnitude of the proceeding heave acceleration peak. In contrast to Figure 5.43, the constant of proportionality for this relationship is different for the upstroke and the downstroke due to the NACA4415 asymmetry.

On the downstroke, the relative flow impinges on the bottom surface of the NACA4415 which is just slightly flatter than that of the NACA0012 (Figure 5.47). On the upstroke top surface of the NACA4415 faces the relative flow which is more rounded than that of the NACA0012. Figure 5.47 shows that the difference between the top surface of the NACA0012 and that of the NACA4415 is more than the difference between the lower surfaces. However, surprisingly the slight flattening of the lower surface has a larger effect on thrust generation than bulging of the top surface (Figure 5.46).

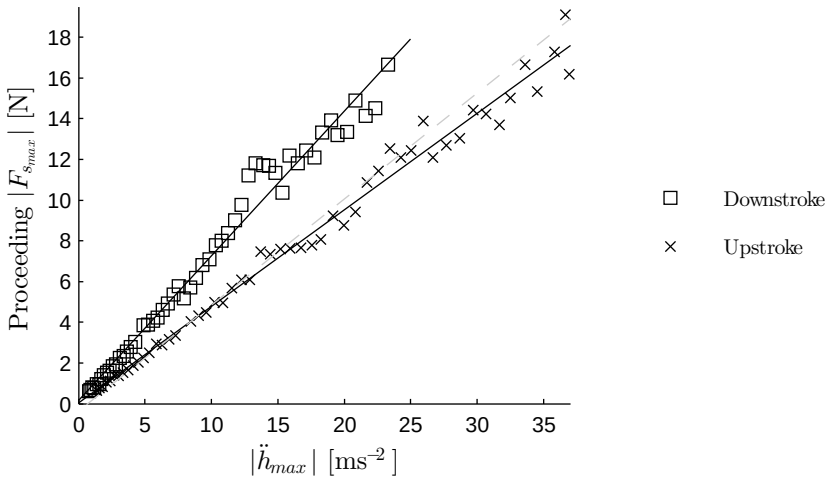

Figure 5.46. Peak heave acceleration versus the magnitude of the proceeding thrust peak for heaving NACA4415. The line of best fit for the NACA0012 (Figure 5.43) is shown for comparison. $u = 0$, $h^* = 0.75$, $\theta = 0°$

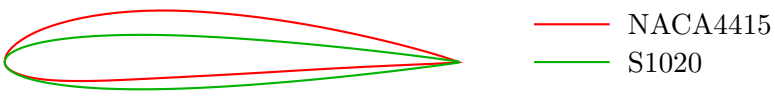

Figure 5.47. A comparison of the NACA415 and S1020 profiles

Heave Force Fit

In Section 5.5.3 the heave forces on the flat plate were fitted with the Morison equation and a linear mass-damper model. Neither of these models were capable of providing a good fit to the measured heave force profiles. Similarly to Figure 5.31, Figures 5.48 and 5.49 show how these models fit the measured heave forces on a NACA0012 and NACA4415 respectively. Tables 5.11 and 5.12 list the coefficients of these fits and compare them to those for the flat plate and the cylinder. The flat plate and hydrofoils have similar fit coefficients due to them having similar heave force profiles (see Figure 5.27). However, the cylinder has significantly smaller drag and added mass coefficients.

Table 5.11. Mass-damper model coefficients for different objects. $u = 0$, $\theta = 0°$

	$a_{\dot{h}}$ [kg s^{-1}]	$a_{\ddot{h}}$ [kg]	$Re_{\dot{h}}$	K_C
Cylinder	5.01	1.65	9.2×10^3 - 58.9×10^3	4.7
Flat Plate	65.29	2.70	6.3×10^3 - 41.3×10^3	5.5
NACA0012	76.52	3.36	8.6×10^3 - 49.4×10^3	4.7
NACA4415	72.76	2.91	10.7×10^3 - 54.8×10^3	4.7

Table 5.12. Morison equation coefficients for different objects. $u = 0$, $\theta = 0°$ (c_a *calculated with* V_m *the volume of an equivalent cylinder*)

	c_d	c_a	$Re_{\dot{h}}$	K_C
Cylinder	0.35	0.97	9.2×10^3 - 58.9×10^3	4.7
Flat Plate	6.45	2.20	6.3×10^3 - 41.3×10^3	5.5
NACA0012	6.97	1.98	8.6×10^3 - 49.4×10^3	4.7
NACA4415	6.24	1.72	10.7×10^3 - 54.8×10^3	4.7

Surge Force Fit

The surge forces produced by the NACA0012 fall into a saddle shape surface when plotted against heave velocity and acceleration. Furthermore the curve of the saddle seems parabolic. Figure 5.50 shows this surface fitted with a 2-dimensional second order polynomial in the form of Equation 5.8. The coefficients of the fit are shown in Table 5.13.

The RMSE of this fit is plotted against oscillating frequency in Figure 5.50b. The fit

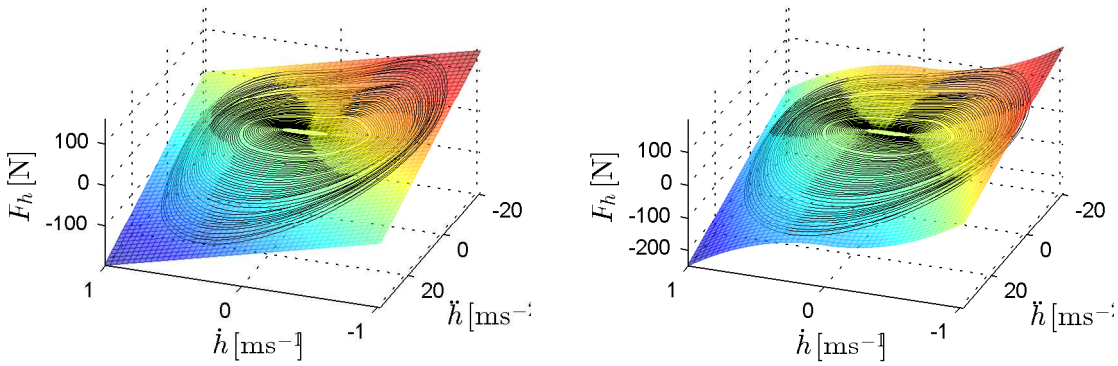

(a) **(b)**

Figure 5.48. Heave forces on the NACA0012 fitted with (a) a linear mass-damper model ($R^2 = 0.86$) and (b) the Morison equation ($R^2 = 0.93$). $u = 0$, $h^* = 0.75$, $\theta = 0°$

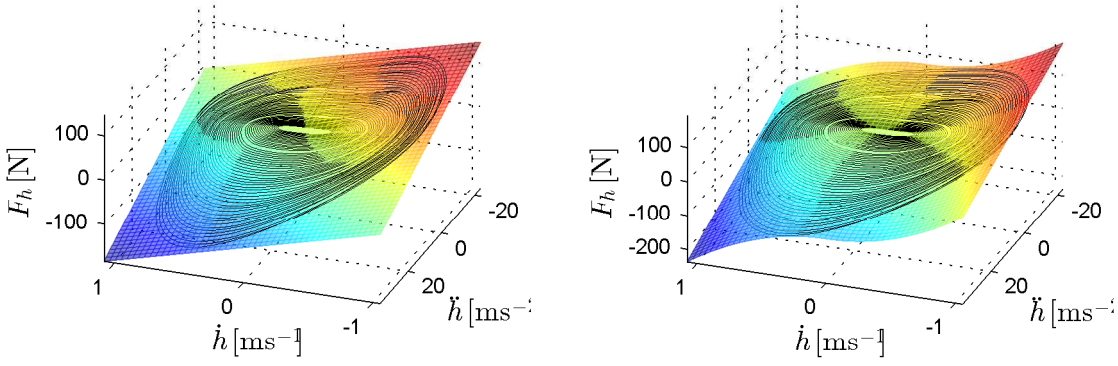

(a) **(b)**

Figure 5.49. Heave forces on the NACA4415 fitted with (a) a linear mass-damper model ($R^2 = 0.89$) and (b) the Morison equation ($R^2 = 0.95$). $u = 0$, $h^* = 0.75$, $\theta = 0°$

RMSE relative to the cycle range becomes smaller as the oscillating frequency increases. However, even at high oscillating frequencies the fit still contains significant error ($> 10\,\%$ of the cycle range). Even when the oscillating frequency is high and the RMSE is reasonable, the fit provides a poor estimate of the cycle profile (Figure 5.51). This means that the fit provides a poor estimate of the timing and magnitude of the peak surge forces, which are most useful to know for design. As shown in Figure 5.51, the timing of the first surge pulse and the timing between each surge pulse are not accurately described by the data fit. Hence, it is clear that a parabolic model in the form of Equation 5.8 is inadequate for predicting these surge forces. Also refer to Section 5.6.2 for further comments on the surge force lag for the NACA0012.

$$F_s = a_{00} + a_{10}\dot{h} + a_{01}\ddot{h} + a_{20}\dot{h}^2 + a_{11}\dot{h}\ddot{h} + a_{02}\ddot{h}^2 \tag{5.8}$$

Table 5.13. Two-dimensional second order polynomial fit coefficients (Equation 5.8) for surge forces on a NACA0012. $u = 0$

	a_{00}	a_{10}	a_{01}	a_{20}	a_{11}	a_{02}
Mean	0.196	0.872	0.031	6.933	0.631	0.007
95 % CI	±0.005	±0.009	±0.001	±0.017	±0.001	±0.000

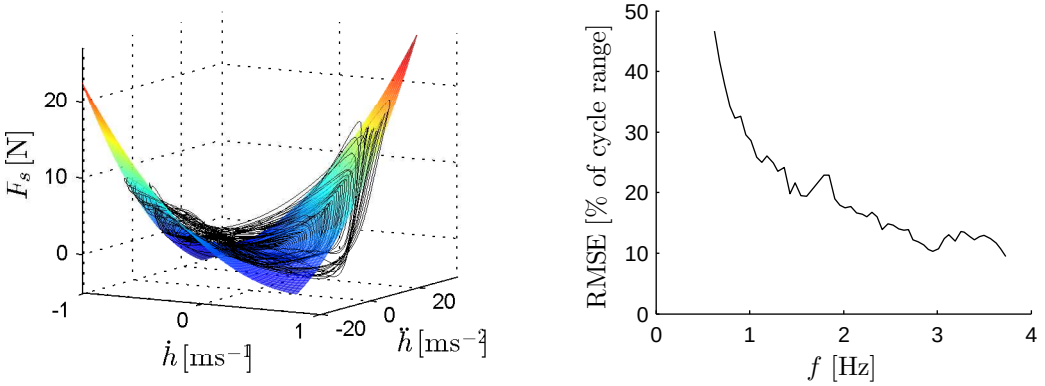

(a) **(b)**

Figure 5.50. (a) NACA0012 surge data fitted with a 2-dimensional second order polynomial with (b) the RMSE of this fit for each oscillating frequency.

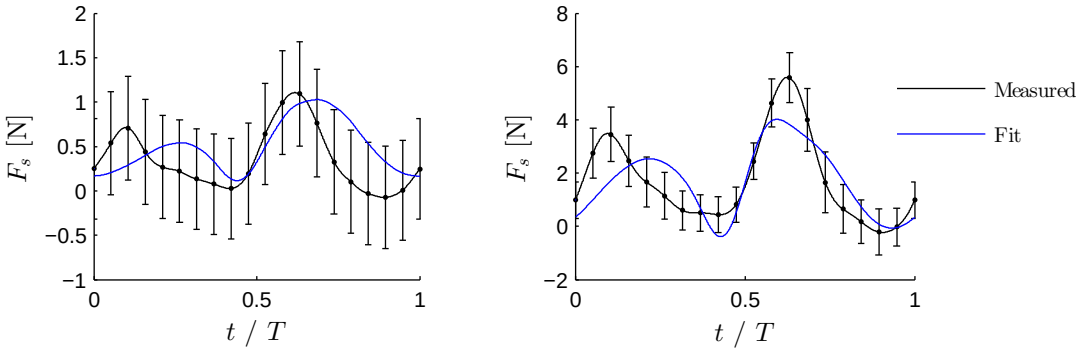

(a) $f = 1.0\,\text{Hz}$ **(b)** $[f = 2.1\,\text{Hz}$

Figure 5.51. Measured surge force cycles on NACA0012 with a 2-dimensional second order fit (Equation 5.8) shown.

5.6.2 Change in Hydrodynamic Forces with Pitch

Figure 5.52 and Figure 5.53 shows how the heave and surge forces on the NACA0012 and the NACA4415 change with pitch respectively. Similar to the flat plate (Figures 5.35), as the hydrofoil pitch is increased the surge force profile becomes similar to the heave force profile. This suggests that the hydrodynamic forces on a 'flat' object, such as a thin hydrofoil, may simply be approximated by the force on a flat plate once hydrodynamic forces are dominated by flow deflection forces (see Section 5.5.4). To confirm this, Figure 5.54 shows the heave and surge force cycles on the flat plate, the NACA0012 and the NACA4415 heaving with a pitch angle of 40°. Here, the small differences in object geometry do not significantly influence the resultant hydrodynamic forces.

Heave and Surge Force Phase

Figure 5.55 shows the heave force lag behind points of peak and zero heave acceleration for the NACA0012 on the downstroke. Again, the results show that the heave forces on the NACA0012 are very similar to those on the flat plate (Figure 5.39). However, note that when the pitch angle is zero, the heave force lag at low frequency is much less than when the pitch is increased. This is surprising since at low oscillating frequencies, heave force lag usually increases due to higher relative contributions of drag forces, such as in Figure 5.55a when $\theta \geq 10°$.

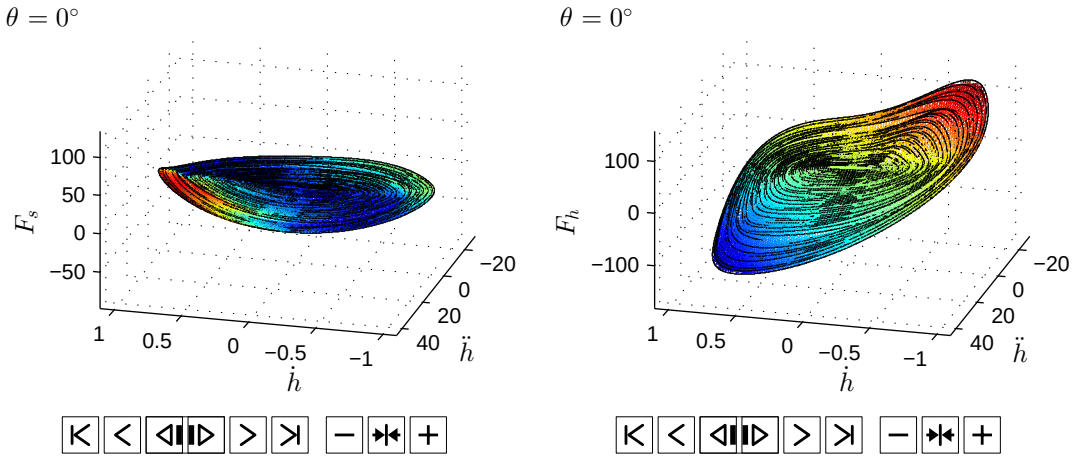

(a) **(b)**

Figure 5.52. Surge and heave forces and on the NACA0012 as a function of heaving velocity and acceleration for pitch angles θ=0° to θ=90° in 10° increments. $u = 0$, $h^* = 0.75$

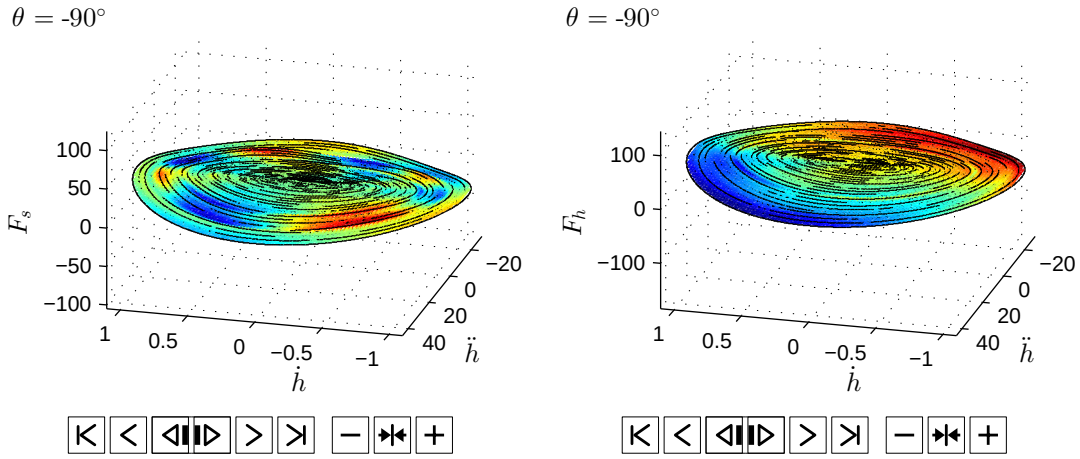

(a) **(b)**

Figure 5.53. Surge and heave forces and on the NACA4415 as a function of heaving velocity and acceleration for pitch angles θ=−90° to θ=90° in 10° increments. $u = 0$, $h^* = 0.75$

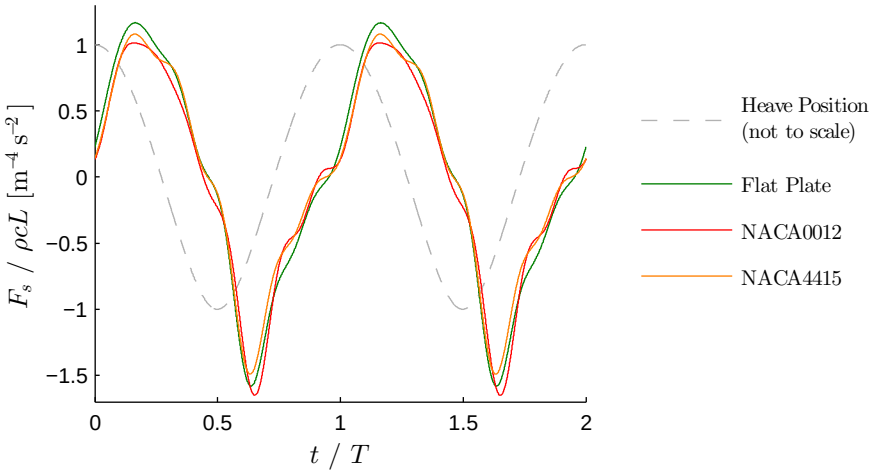

(a)

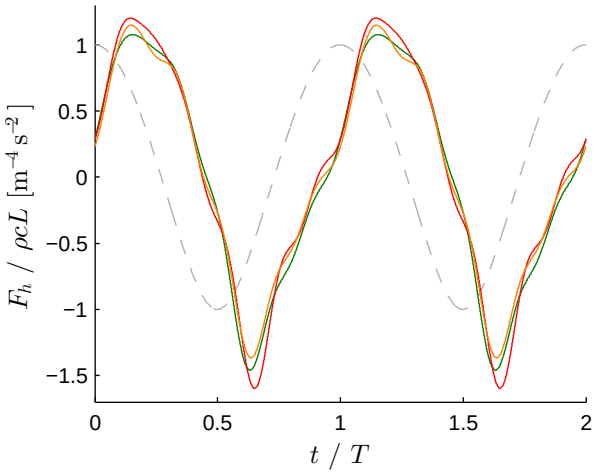

(b)

Figure 5.54. Comparison of the heave and surge forces on the flat plate, NACA0012 and NACA4415. $f \approx 2.5\,\text{Hz}$, $u = 0$, $h^* = 0.75$, $\theta = 40°$

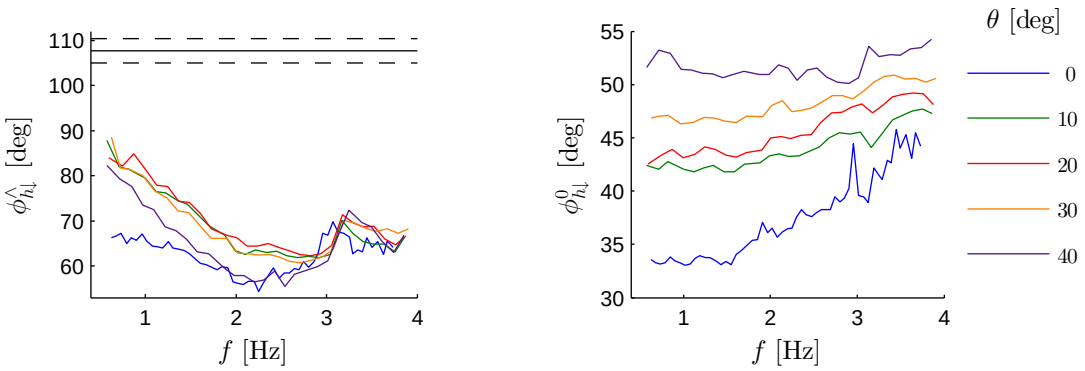

(a) **(b)**

Figure 5.55. Timing of peak and zero heave force on the NACA0012 at various pitch angles. The mean timing of peak heave velocity following peak heave acceleration is shown with a solid black line with ±2 SD bounds of this value shown as dashed black lines. $u = 0$, $h^* = 0.75$

As with the heave force phase, the surge force phase is quite consistent when $\theta \geq 10°$ (Figure 5.56). However, when the $\theta = 0°$ the timing of peak surge forces are very different. Furthermore, the surge force profile is also very different as it contains two thrust peaks rather than one thrust peak and one drag peak (Figure 5.57). This implies that the flow regime at zero pitch is substantially different from with a non-zero pitch. As suggested in Section 5.5.4, the surge forces when $\theta = 0°$ are thought to be predominantly due to asymmetrical vortex shedding, while the surge forces when $\theta \geq 10°$ are thought to be due to flow deflection (Figure 5.58).

The difference in heave and surge force phase lag between when $\theta = 0°$ and when $\theta \geq 10°$ is larger for the NACA0012 than the flat plate. This is suggested to be due to the blunt leading edge and sharp trailing edge of the foil promoting stronger asymmetry in vortex shedding. This strong asymmetric vortex shedding is known to result in the formation of a jet behind the trailing edge (Lai & Platzer, 2000) (Figures 5.58a and Figure 5.58b). Furthermore, this jet will always flow in the same direction: towards the trailing edge (Figure 5.58b). This is not guaranteed to happen for objects with symmetry in the surge plane such as the flat plate in Section 5.5 and Figure 5.58a.

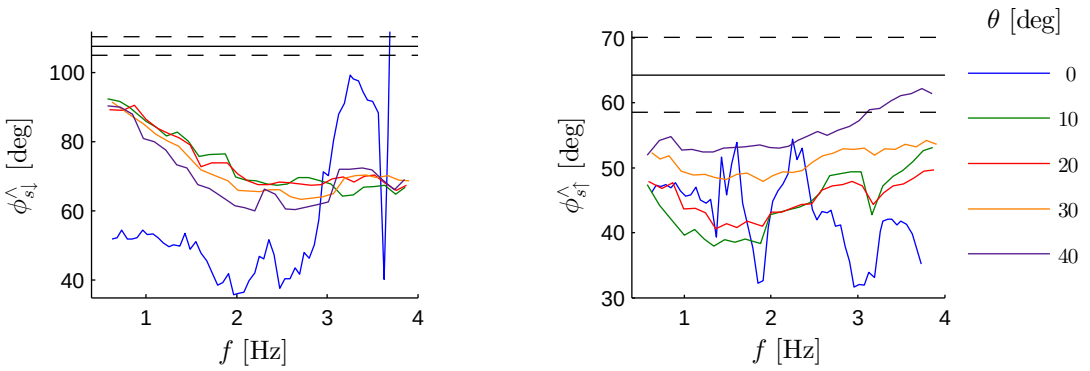

(a) **(b)**

Figure 5.56. Timing of peak surge force on the NACA0012 at various pitch angles. The mean timing of peak heave velocity following peak heave acceleration is shown with a solid black line with ±2 SD bounds of this value shown as dashed black lines. $u = 0$, $h^* = 0.75$

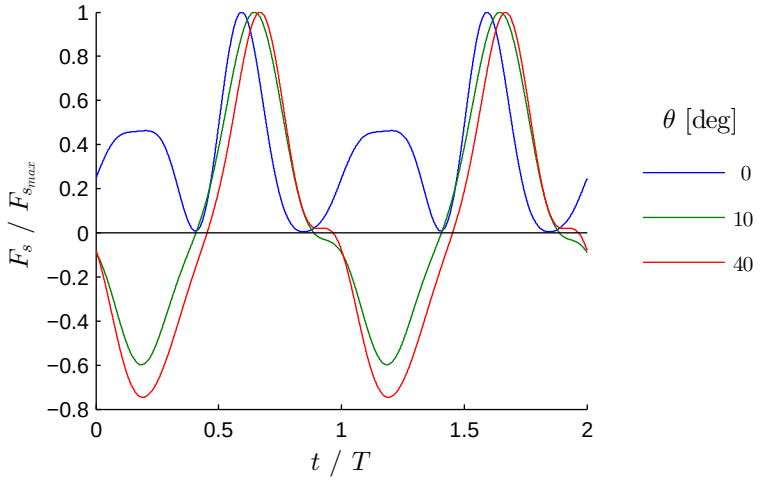

Figure 5.57. Normalised surge force cycles on the NACA0012 at various pitch angles. $u = 0$, $h^* = 0.75$

Force Cycle Range

Figure 5.59a and Figure 5.60a show how the surge force range coefficients change with pitch for the NACA0012 and the NACA4415 respectively. Similar to the flat plate, $c_{A_{F_s}}$ and $c_{A_{F_h}}$ are greater with a pitch angle of 0° than with a pitch angle of 90°. This could be expected for $c_{A_{F_h}}$ since both the hydrofoils and the flat plate are less streamlined

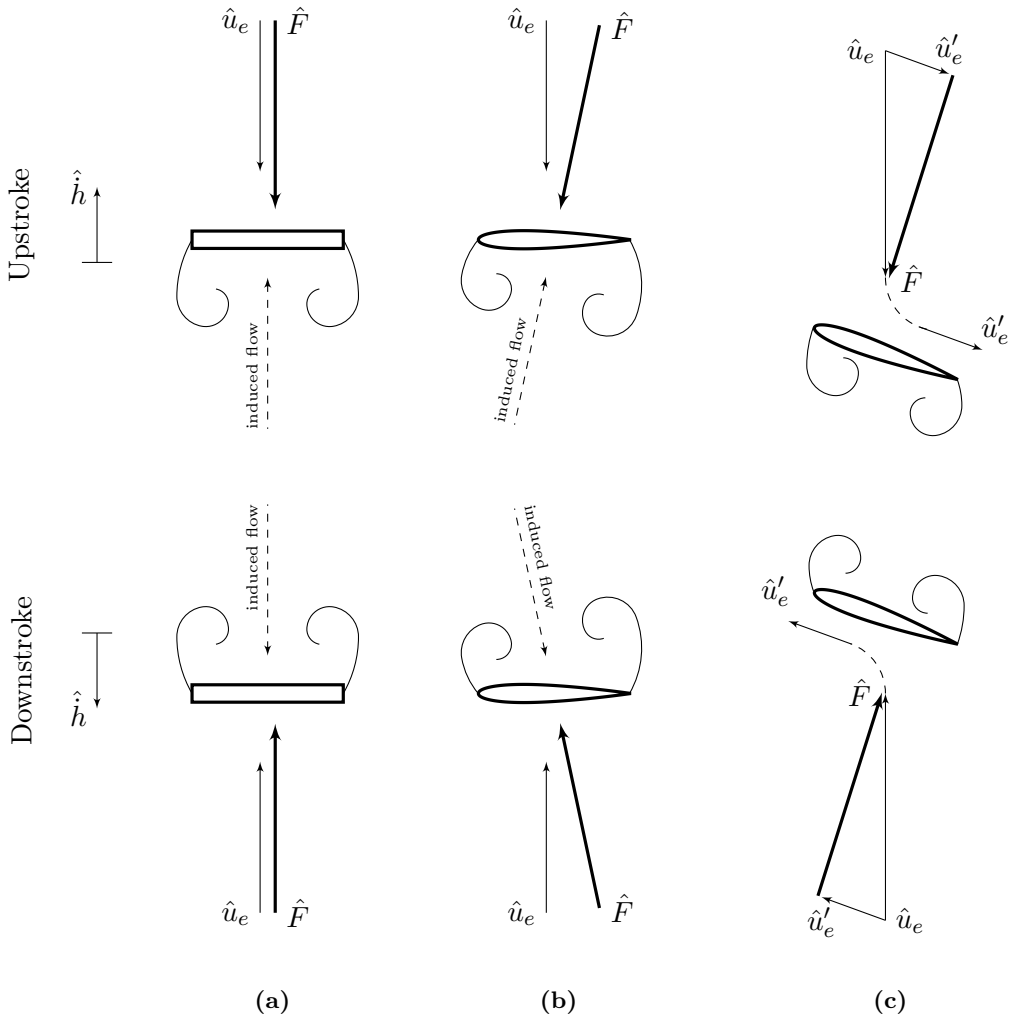

Figure 5.58. (a) & (b) Leading and trailing edge geometry influences the symmetry of vortex shedding and surge force direction on a heaving flat object ($u = 0$, $\theta = 0°$). (c) Surge forces generated from flow deflected by a heaving flat object($u = 0$, $\theta \neq 0°$).

with regards to the effective flow when $\theta = 0°$. Hence the drag coefficient increases with decreasing pitch. The higher surge force range coefficient at $\theta = 0°$ than $\theta = 90°$ can be explained by a higher Reynolds number promoting stronger asymmetrical vortex shedding as mentioned in Section 5.5.4. However, $c_{A_{Fs}}$ for the foils at $\theta = 0°$ (Figure 5.59a and 5.60a)) are approximately twice that for the flat plate at $\theta = 0°$ (Figure 5.38b). This is believed to be due to the foils having a geometrical difference between their leading edge

and trailing edge which further promotes strong asymmetrical vortex shedding (Figure 5.58b). For both foils, the maximum surge force range coefficient occurs at $\theta = 40°$ when pitch is positive, unlike the response of the flat plate where the maximum $c_{A_{F_s}}$ was at $\theta = 50°$. This is most likely due to asymmetrical vortex shedding increasing $c_{A_{F_s}}$ over the pitch range $0° < |\theta| < 40°$.

In Section 5.5.4, a function proportional to $cos(2\theta)$ (plus a correction for the plate thickness, Equation 5.7) provided a good fit for $c_{A_{F_h}}$ of the flat plate. When $|\theta| > 40°$, a function of this form also provides a good fit for $c_{A_{F_h}}$ of the hydrofoils. However, when $|\theta| < 40°$, $c_{A_{F_h}}$ deviates from this fit significantly. The exception to this observation is when the NACA4415 has a negative pitch angle. In this scenario, the $c_{A_{F_h}}$ for the NACA4415 is similar to that of the flat plate and may be fit well with a function proportional to $cos(2\theta)$ (Figure 5.60b). The poor agreement with the fit for $c_{A_{F_h}}$ at low pitch angles suggests again that asymmetrical vortex shedding from the foil leading and trailing edges has a significant effect on the heave forces when the pitch angle is small, i.e. $\theta < 40°$. When $\theta > 40°$, the flow around the foils is expected to be similar to the flow around the flat plate since the magnitude of the heave forces are so similar.

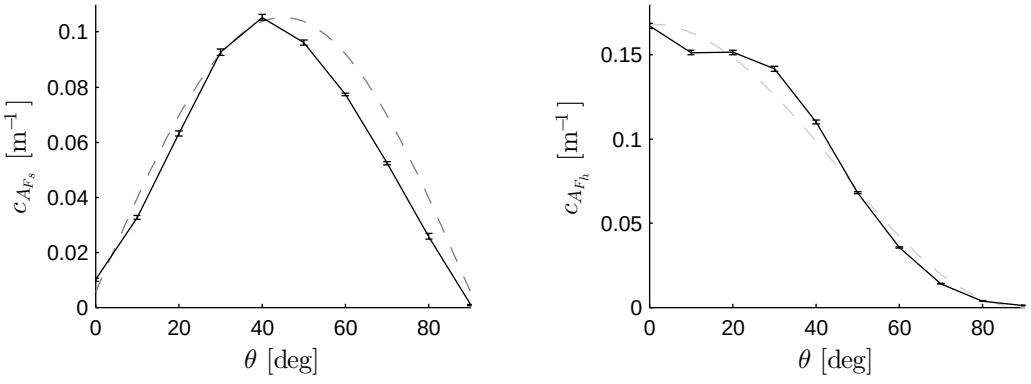

(a) **(b)**

Figure 5.59. (a) Surge and (b) heave force range coefficients for the NACA0012 as a function of pitch angle θ. A function proportional to $sin(2\theta)$ or $cos(2\theta)$ are shown in each figure as a grey dashed line for reference.

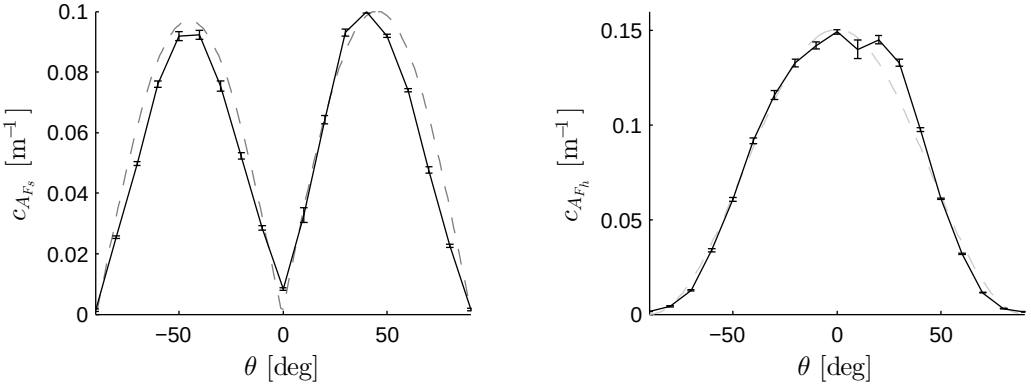

(a) **(b)**

Figure 5.60. (a) Surge and (b) heave force range coefficients for the NACA4415 as a function of pitch angle θ. A function proportional to $|sin(2\theta)|$ or $cos(2\theta)$ are shown in each figure as a grey dashed line for reference. $u = 0$, $h^* = 0.75$

5.7 Summary

In this chapter, experimental measurements of the hydrodynamic forces on heaving objects with no forward velocity were presented. These time-dependent hydrodynamic force measurements were compared with force predictions of existing ocean engineering models, showing that these models have limited applicability under these conditions. The influence of submergence, end plates, object shape, pitch angle and oscillating frequency was investigated to provide an overview of the hydrodynamic force sensitivity to these parameters. In particular, the affect of these variables on the phase, magnitude and profile of the force cycles was outlined. These experiments yielded the following outcomes:

Submergence

- A submergence of 3 chord lengths was sufficient to avoid the free surface significantly affecting the hydrodynamic forces on a heaving object.
- A shallow submersion depth ($d \approx 2c$) provided a significant increase in the thrust production of a NACA4415, particularly when large end plates ($\varnothing$ 5.3c) were fitted. Simultaneous to the increase in mean thrust came an increase in mean lift. Both of these results would be beneficial for a hydrofoil during start-up.

3D Flow Effects

- Spanwise flow generation is stronger with a cylinder than a flatter object. This effect is thought to be due to the Honji instability.
- The use of end plates on a heaving NACA4415 increased downstroke thrust at all submersion depths. They also enabled positive interaction with the free surface which amplified thrust generation as described in the prior submergence summary.

Object Shape and Orientation

- The shape of heaving two-dimensional objects was shown to significantly affect the resulting heave forces. Heave forces on flatter objects (i.e. flat plates or hydrofoils) contained both in-phase and out-of-phase force contributions leading to a resultant force cycle that lags flow acceleration but leads flow velocity.

- At zero pitch and zero forward velocity, the surge force profile was very sensitive to object shape. Hence under this condition, the thrust produced by each shape was very distinct. Furthermore, objects with the right shape heaving with zero pitch can provide thrust during a stationary start.

- At non-zero pitch (especially when $|\theta| > 40°$) and zero forward velocity, the heave and surge forces on 'flat' objects like flat plates or hydrofoils were relatively insensitive to detail of object shape, i.e. the sharpness of the leading and trailing edges, or the curvature of the upper and lower surfaces.

- At zero pitch, surge forces are suggested to be due to asymmetric vortex shedding, and at non-zero pitch angles surge forces are suggested to be dominated by flow deflection. The phase lag of both surge and heave forces is lower when asymmetric vortex shedding is dominant.

Heaving Motion

- Most previous studies use a sinusoidal oscillating profile. However, in the current study the heave motion was just near sinusoidal and under open-loop control. Results showed that very small changes in the heave position profile cause larger changes in the heave velocity and acceleration profiles, which in turn has a significant influence on the surge force profile. In the current results, the magnitude of peak acceleration was found to influence the magnitude of peak surge force on a heaving hydrofoil with zero pitch.

Model Validity

- Morison equation added mass and drag coefficients for a cylinder were calculated from experimental force measurements that agreed with other values found in the literature. The current experimental results for the hydrodynamic forces on the cylinder also supported the Keulegan-Carpenter ranges for model selection set out by Journée and Massie (2001) (see Section 3.3.8). These results provided confidence that the experimental equipment was fit for gathering credible data.

- Although a linear mass-damper model provided a good fit to the measured heave forces on the cylinder over the given Keulegan-Carpenter number range, it provided a poor fit to the measured heave forces on the flat plate and the foils. The Morison Equation provided a better fit than the linear mass-damper model for these objects. However, it failed to properly describe the forces around the areas of maximum and minimum heave force.

The results presented in this chapter provide designers with insight into the characteristics of hydrodynamic forces on a heaving cylinder, flat plat, or hydrofoil with a fixed pitch angle. The drag and added mass coefficients fitted to the current experimental data may be used to estimate the magnitude of hydrodynamic forces on a heaving foil. However, this is not recommended since small changes in the heaving motion profile have a significant affect on the hydrodynamic forces of the hydrofoil. Particularly the magnitude and phase of peak surge forces.

Designers should consider a shallow mean submergence depth for an oscillating foil propeller during start-up to exploit thrust gains from free surface effects. Furthermore, to maximise these effects end plates should by used. Although net positive thrust can be achieved with a fixed pitch heaving hydrofoil (even with $\theta = 0°$) due to asymmetrical vortex shedding from the leading and trailing edges, much larger thrust forces can be achieved by deflecting flow with a non-zero pitch angles. Hence, pure heaving motions are not ideal for start-up operation.

Chapter 6

Hydrodynamic Forces on a Heaving Object for Finite Strouhal Numbers

6.1 Introduction

The hydrodynamic forces on an oscillating cylinder in a flow have been extensively studied in the fields of vortex-induced vibrations (VIV) and ocean engineering. Several different flow regimes have been observed that can be associated with different oscillation states. Moreover, each state can be associated with a certain hydrodynamic force response. Although the mean hydrodynamic forces on an oscillating foil have been well studied (see Section 3.5), relatively little work has focused on the time-dependent attributes of these forces. Furthermore, little work has focused on the time-dependency of the hydrodynamic forces on an oscillating 'flat' object in a flow, such as a flat plate or a hydrofoil.

A historical review of vehicle design (Chapter 2) has shown that the transition from high Strouhal number operation during start-up to cruising speed operation is difficult. As mentioned in Section 2.2.4, vehicles such as the Trampofoil have avoided this transition entirely by demanding a 'rolling start'. Vehicles such as the Mutiny on the Boundary Layer, the Wasserläufer and the Pogo Foil have successfully dealt with this phase. However,

MacCready (Accessed 2012) described the launch procedure of the Pogo Foil as "*a magical and difficult-to-master moment.*". With more knowledge of how the time-dependent hydrodynamic forces on an oscillating foil propeller change with forward speed, designing and simulating a more user-friendly vehicle may be possible.

6.1.1 Objectives

In Chapter 5, the hydrodynamic forces on a oscillating cylinder ($u = 0$, $0.25 < h^* < 1$) could be modelled well with a linear mass-damper model (see Section 3.3.6). However, neither the mass-damper model nor the Morison equation could satisfactorily fit the measured forces on a flat plate or a hydrofoil ($u = 0$, $h^* = 0.75$). The goal of the following experiments was to measure the hydrodynamic forces acting on oscillating test objects travelling with some steady forward velocity in the surge direction ($u \neq 0$, $h^* = 0.75$), to investigate how this forward velocity affects the phase and magnitude of the forces.

6.1.2 Overview of Tests

In this chapter, measurements of hydrodynamic forces on oscillating objects travelling forward through water at constant velocity are presented. Firstly, the the significance of 3-dimensional flow on the hydrodynamic forces is investigated in Section 6.2 by varying the diameter of circular end plates. Secondly, the unsteady hydrodynamic forces on a pair of vertical surface piercing plates are presented in Section 6.3 to illustrate the appropriateness of quasi-static calculations for predicting drag forces on a pair of heaving struts. Next the hydrodynamic forces on a heaving cylinder are shown in Section 6.4 and compared to other published results found in the literature. Finally, the hydrodynamic forces on the flat plate and the two hydrofoils (see Section 4.3) are presented in Section 6.5 and Section 6.6 respectively and compared to those on the cylinder.

The experiments in this chapter were conducted at the 4 forward velocities and 5 oscillating frequencies shown in Table 6.1 to cover the Strouhal number range of 0.07 to 0.72. This matrix of Strouhal numbers is centred about the peak efficiency of an oscillating foil (see Section 3.4.1). However, it contains different velocity/frequency pairs that have the same Strouhal number. This is important since parameter pairs such as

these may provide the same mean thrust and lift coefficients but have very different thrust and lift force profiles. The Reynolds number based on forward velocity u was limited by the speed of the towing car and the length of the towing tank to about 93 000. This is about four times less than the estimated Re_u for the Trampofoil (see Table 2.2) but was considered acceptable since oscillating wings have been shown to be relatively insensitive to Re_u compared to St (G. S. Triantafyllou et al., 1993). The Reynolds number for each forward velocity and test object is listed in Table 6.2. Test objects were always fitted with ⌀320 mm end plates (except for in the end plate diameter study). All tests were done at a submersion depth of approximately 300 mm and had a heave amplitude of 45 mm.

Table 6.1. Approximate Strouhal numbers for runs with some forward velocity.

		u [m s^{-1}]			
		0.5	1.0	1.5	2.0
f [Hz]	1.6	0.29	0.14	0.10	0.07
	2.2	0.40	0.20	0.13	0.10
	2.8	0.50	0.25	0.17	0.13
	3.4	0.61	0.31	0.20	0.15
	4.0	0.72	0.36	0.24	0.18

Table 6.2. Approximate chord based Reynold numbers for runs with some forward velocity.

	u [m s^{-1}]			
	0.5	1.0	1.5	2.0
Cylinder and hydrofoils	23 440	46 890	70 330	93 770
Flat plate	19 930	39 850	59 780	79 700

6.2 End Effects

The lift force on a steady foil with a finite span is lower than one of an infinite span. The reduction in lift is due to 3-dimensional flow at the end of the foil span, induced by the pressure difference between the upper and lower surfaces of the foil. To reduce end effects on a steady foil, it is common to taper the foil towards the end of its span or fit end plates to the foil. An oscillating foil may induce 3-D flow structures in its wake (Hall &

Hall, 1996; Koochesfahani, 1989). However, the significance of end effects as described above is unclear. Furthermore, it is unclear if end plates have a beneficial affect on lift and thrust cycles.

Objects that produce lift are more susceptible to end effects because of the pressure difference they generate across them. Hence, out of the test objects used in the current experiments (see Section 4.3) the NACA4415 would be most likely to suffer from end effects. To estimate the significance of end effects in the experiments to follow, the hydrodynamic forces on the NACA4415 were recorded with different size end plates over a range of Strouhal numbers.

6.2.1 End Effects on a Heaving NACA4415

Section 5.3 showed that end effects may reduce the thrust produced by an oscillating foil with zero forward velocity ($St = \infty$). Figures 6.1 and 6.2 show how end plate size affect the surge and heave force cycles on an oscillating foil with some forward velocity respectively ($St \neq \infty$).

At a low Strouhal number ($St = 0.09$) peak surge force was reduced by approximately 17 % in the absence of end plates (Figure 6.1b). Furthermore, peak surge force was attenuated on both the upstroke and the downstroke with no end plates mounted. Although this reduction in peak surge force is relatively small, it significantly affects the mean surge force. When no end plates were used, the mean surge force was approximately 50 % less that when the end plates were mounted. Figure 6.1a shows that once the Strouhal number was increased to 0.26, peak surge force on the upstroke was not significantly affected by the presence of end plates. However, peak surge force on the downstroke remained significantly higher when the end plates were present.

Figure 6.2 shows that end plate size has no significant effect on the heave force cycle when the oscillating NACA4415 was travelling forward. Comparing the heave force cycles shown in Figure 6.2 ($u \neq 0$) to those in Figures 5.16 and 5.16 ($u = 0$), suggests that end plates influence the heave force cycle most when u is zero ($St = \infty$) and the end plate diameter is sufficiently large ($>5c$).

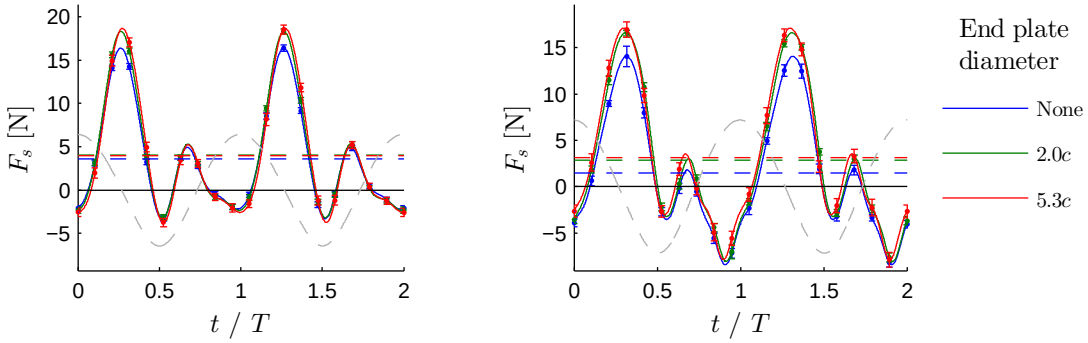

(a) f=2.8, u=1.0, St=0.26 **(b)** f=1.8, u=2.0, St=0.09

Figure 6.1. The effect of end plate diameter on surge force cycles for finite Strouhal numbers. Coloured dashed lines indicate mean surge force. Grey dashed line indicates heave position (not to scale). $\theta = 0°$, $h^* = 0.75$

6.3 Strut forces

As mentioned in Section 4.12.3, the heave forces on the struts were considered insignificant relative to the heave forces on a test object during the current experiments. Furthermore, the amplitude of surge forces on the struts was insignificant relative to the amplitude of the surge forces on the test object and so could be considered as a near constant drag force. Figure 6.3 shows that the mean unsteady strut drag was equivalent to the measured steady strut drag ($h = 0$) over the range of forward velocities u covered in the current experiments.

Although the surge force cycle on the struts did not significantly affect the primary results of the current experiments, they are reviewed in this section to show that quasi-steady calculations are limited in application here as they are for the test objects. Calculating the drag on unsteady struts will be important when strut drag is comparable to thrust produced by the foil. The following force measurements where made with only the struts mounted to the load cell assembly. Similarly to the experiments with test objects mounted, inertial forces were subtracted from the force measurements as described in Section 4.9.

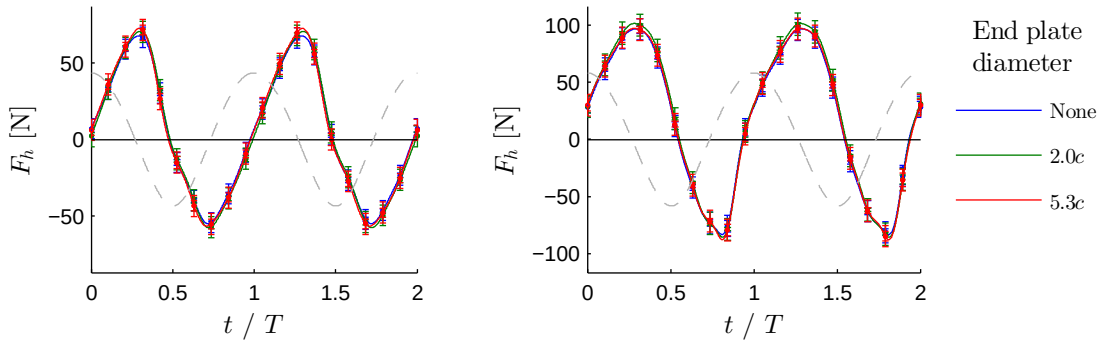

(a) f=2.8, u=1.0, St=0.26 **(b)** f=1.8, u=2.0, St=0.09

Figure 6.2. The effect of end plate diameter on heave force cycles for finite Strouhal numbers. Grey dashed line indicates heave position (not to scale). $\theta = 0°$, $h^* = 0.75$

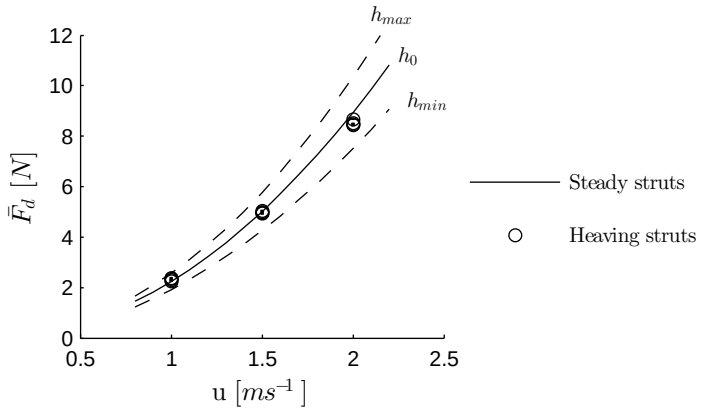

Figure 6.3. Comparison of steady and unsteady mean drag on the struts. Steady mean drag is shown for the maximum, minimum and mean heave positions.

6.3.1 Unsteady Hydrodynamic Forces on Surface-Piercing Heaving Plates

Figure 6.4 shows the measured unsteady drag on the struts with the drag predicted with quasi-steady calculations. Quasi-steady drag was calculated by interpolating between the steady drag curves of the struts positioned at the maximum heave position and minimum heave positions (see Figure 6.3). Although the uncertainties are large, these results still provide an idea of when quasi-steady calculations are most valid and where the largest errors will occur.

It is not surprising that quasi-steady calculations appear to be adequate when the

oscillating frequency and the forward velocity are both low (Figure 6.4a). When the forward velocity is increased the phase and amplitude of the measured forces agree with the quasi-steady estimate (Figure 6.4b). However, the measured forces are slightly smaller than predicted.

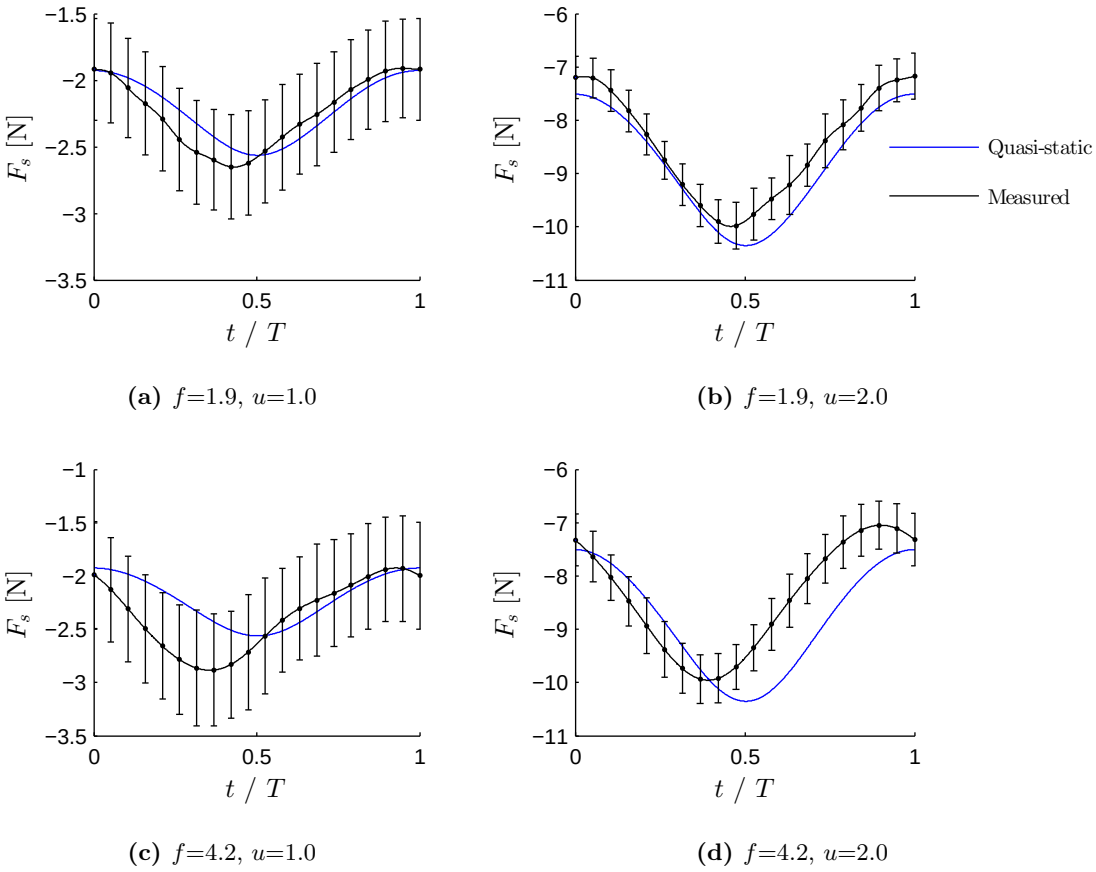

(a) f=1.9, u=1.0

(b) f=1.9, u=2.0

(c) f=4.2, u=1.0

(d) f=4.2, u=2.0

Figure 6.4. Strut drag cycles for different oscillating frequencies and translational velocities.

6.4 A Heaving Cylinder with Non-Zero Forward Velocity

Similar to Chapter 5, the results presented in this chapter begin with the forces on the cylinder since it has the simplest geometry, no pitch angle, and is the most commonly studied object in the literature. In this section we present measured forces on a heaving cylinder at different forward velocities and compare the results to those for a cylinder

with no forward velocity presented previously in Section 5.4. The current results are also compared to the results found in the literature to verify that the experimental equipment was capable of providing credible measurements. The following force measurements were acquired at the approximate oscillating frequencies and forward velocities shown in Table 6.1, while the heave-to-chord ratio remained fixed at $h^* = 0.75$.

The natural vortex shedding frequency f_{ns} of a smooth cylinder in a flow with velocity u can be calculated with the Equation 6.1 (Prud'homme, 2010), where D is the diameter of the cylinder. The natural vortex shedding frequency of the cylinder is plotted against Re_u in Figure 6.5 with the test oscillating frequencies and Reynolds numbers marked. Note that there are two runs where the forced oscillation frequency is near the natural vortex shedding frequency. Competition between the two frequencies may have an influence on the force measurements (see Section 3.5.6). However, since the heaving motion is not purely sinusoidal, the extent of this effect is unknown.

$$St_{ns} = \frac{f_{ns}D}{u} = 0.198\left(1 - \frac{19.7}{Re_u}\right), \qquad 2 \times 10^2 < Re_u < 2 \times 10^5 \tag{6.1}$$

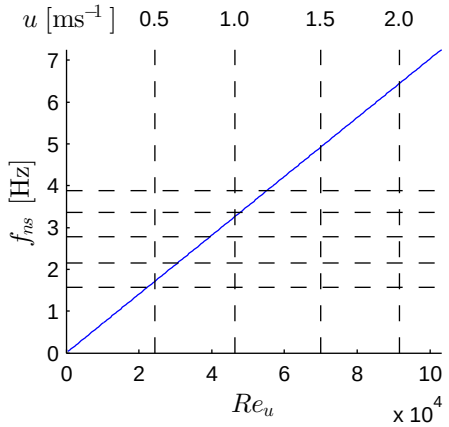

Figure 6.5. The natural vortex shedding frequency of the cylinder (Equation 6.1) over the tested Reynolds number range. Dashed lines mark the experimental mean oscillating frequencies f and Reynolds numbers based on forward velocity Re_u.

6.4.1 Force Phase and Amplitude

Figure 6.6 shows the heave and surge force cycles on the heaving cylinder as it progresses forward in the surge direction at four different velocities. At speeds of up to approximately 8.3 chords per second (Figure 6.6a) the heave and surge forces are very similar to those with zero forward velocity. However, now the maximum heave force is not linear with heave velocity and acceleration, but instead takes a the relationship shown in Figure 6.7. Here peak heave force exceeds that experienced when $u = 0$ and also lags the peak heave acceleration. Consequently, the coefficients of determination for a linear mass-damper fit decreases from 0.9881 ($u = 0\,\mathrm{m\,s^{-1}}$, see Section 5.4.1) to 0.9609 ($u = 0.5\,\mathrm{m\,s^{-1}}$)).

At speeds faster than 8.3 chords per second (Figures 6.6b to 6.6d), the heave and surge force profiles remain similar to those when $u = 0$ when the oscillating frequency is sufficiently high. However, when the oscillating frequency is reduced both the heave and surge forces undergo a sudden phase shift and reduction in amplitude. This sudden change in the hydrodynamic forces is due to a change in vortex shedding mode as natural vortex shedding induced by the forward velocity competes with vortex shedding caused by the heaving oscillations (Carberry, Sheridan, & Rockwell, 2001). Once the vortex shedding regime has changed, the force measurement standard deviation relative to the mean cycle range increased rapidly. This indicated that the forces on the cylinder were less consistent while vortex shedding modes were competing.

The wake structure map produced by Williamson and Roshko (1988) shows that the wake changes from a 2S structure for short wavelengths to a 2P structure when the wave length is increased (i.e. St is decreased). In this case, for runs of constant u, this means that the cylinder will have a 2S wake at high oscillating frequencies (i.e. high St) and a 2P wake at low oscillating frequencies (i.e. low St). Figure 6.6 shows that as the forward velocity was increased, the oscillating frequency required for the jump between states also increased. Similarly, Bishop and Hassan (1964) found that the jump between states occurred at higher oscillating frequencies for higher forward velocities.

To illustrate this more clearly, Figure 6.8 shows the contributions of frequency components two and three times the oscillating frequency in the heave force response against the

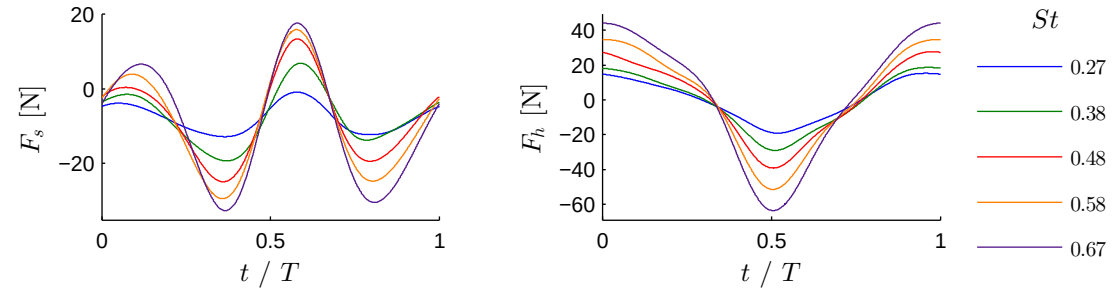

(a) $u = 0.5\,\mathrm{m\,s^{-1}}$

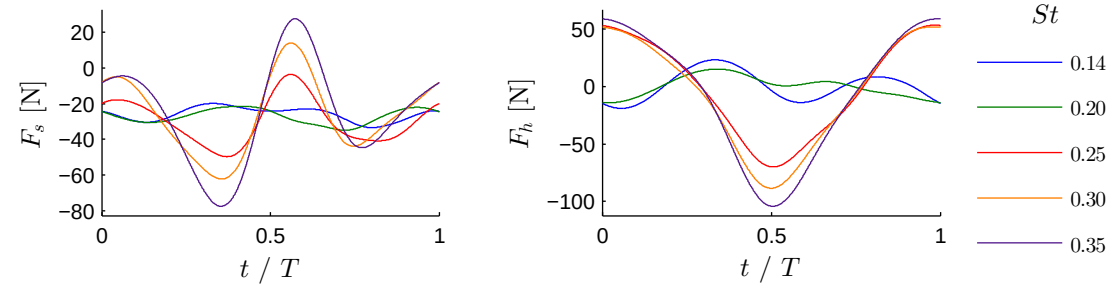

(b) $u = 1.0\,\mathrm{m\,s^{-1}}$

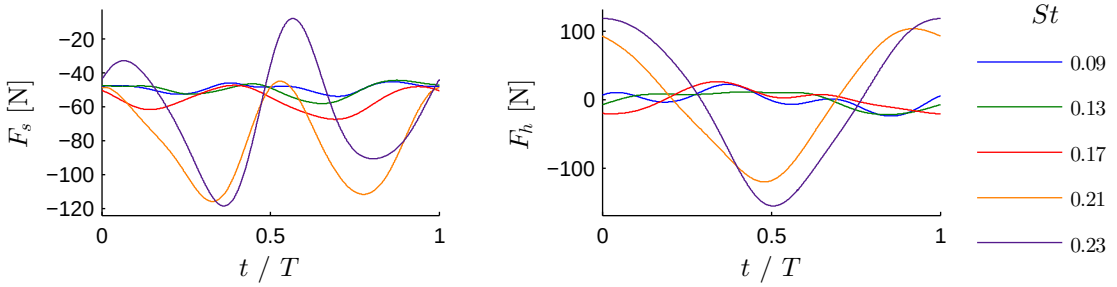

(c) $u = 1.5\,\mathrm{m\,s^{-1}}$

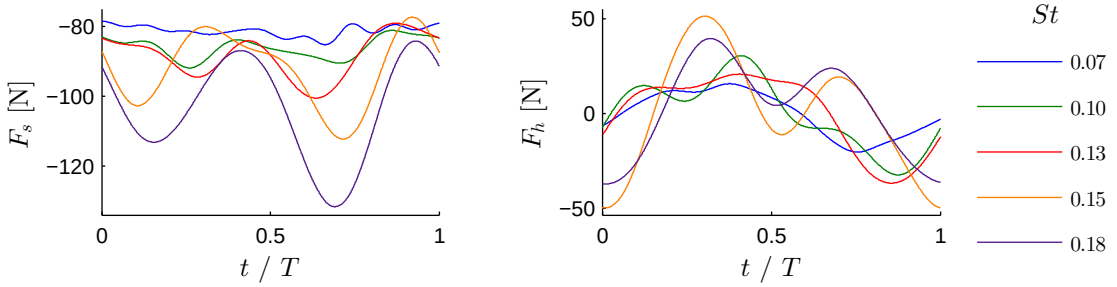

(d) $u = 1.9\,\mathrm{m\,s^{-1}}$

Figure 6.6. The effect of forward velocity on the heave force cycle of a heaving cylinder. $h^* = 0.75$

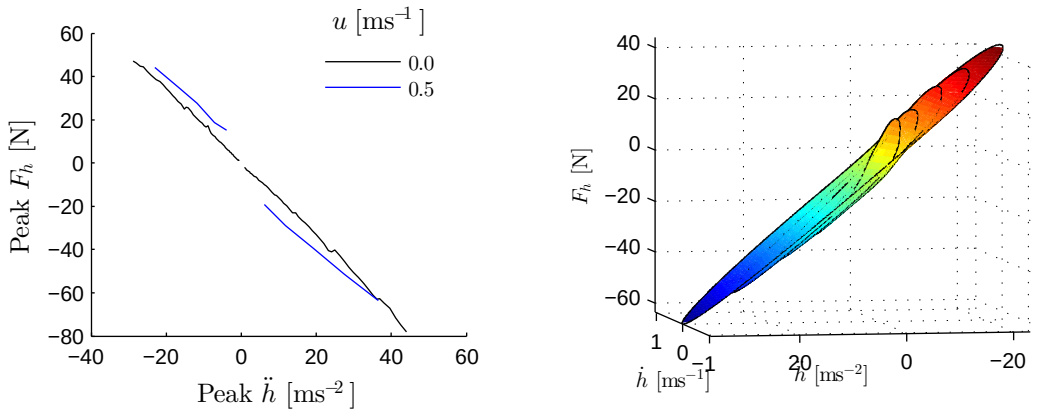

Figure 6.7. Peak acceleration versus peak heave force. $u = 0.5\,\mathrm{m\,s^{-1}}$, $h^* = 0.75$

Strouhal number. Notice that when the Strouhal number was decreased to $St = 0.14$, the heave force cycle was dominated by a component twice the oscillating frequency indicating that a 2P wake had been established. When the Strouhal number was decreased further ($St < 0.13$), the heave force response was dominated by frequency components with one and three times the oscillating frequency. This suggests that at very low Strouhal numbers ($St < 0.13$), the wake becomes more complex with more vortices being shed per cycle. Furthermore, it suggests that the von Kármán street is carried by a wake undulating at the oscillating frequency as found by Koochesfahani (1989).

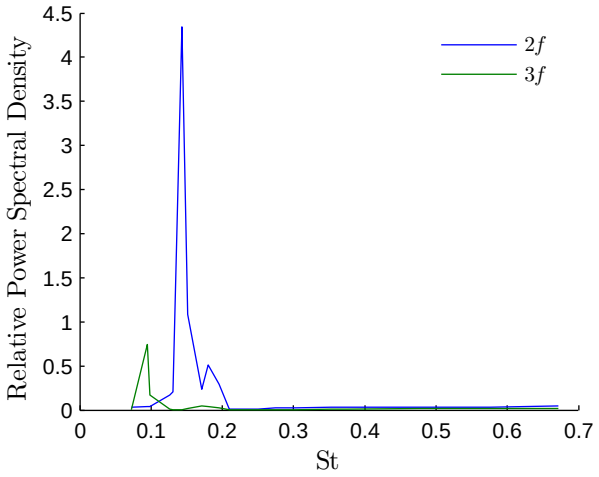

Figure 6.8. The relative contributions of frequencies two and three times the oscillating frequency in the heave force response of an oscillating cylinder with non-zero forward velocity . $h^* = 0.75$

6.4.2 Suitability of the Experimental Equipment Design

Williamson and Roshko (1988) found that the critical point where the wake structure changes from a 2S structure to a 2P structure is when $\lambda \approx 4c$ for $h^* = 0.75$. However, the abrupt change in hydrodynamic forces should not be expected until the $\lambda \approx> 5.1c$ (Williamson and Roshko (1988) Figure 4). Carberry et al. (2001) also studied this discontinuity of hydrodynamic forces and found that the sudden jump occurred when the ratio of forcing oscillating frequency to natural vortex shedding frequency (f/f_{ns}) became greater than 0.81. Similarly, Bishop and Hassan (1964) found that the critical Strouhal number ratio for $h^* = 0.75$ is in the range of $0.92 < St_c/St_{ns} < 0.96$ depending on whether f is increasing or decreasing.

Figure 6.9 shows the boundary where the hydrodynamic forces suddenly change in the current results. Boundary conditions found in the literature are also shown for comparison. The boundary found by Bishop and Hassan (1964) and Williamson and Roshko (1988) occurs at frequency ratio f/f_{ns} closer to unity that the the current results and that of Carberry et al. (2001). The current results suggest that the wake changes structure with a frequency ratio of $f/f_{ns} = 0.78$, which is very similar to the result of Carberry et al. (2001) ($f/f_{ns} = 0.81$).

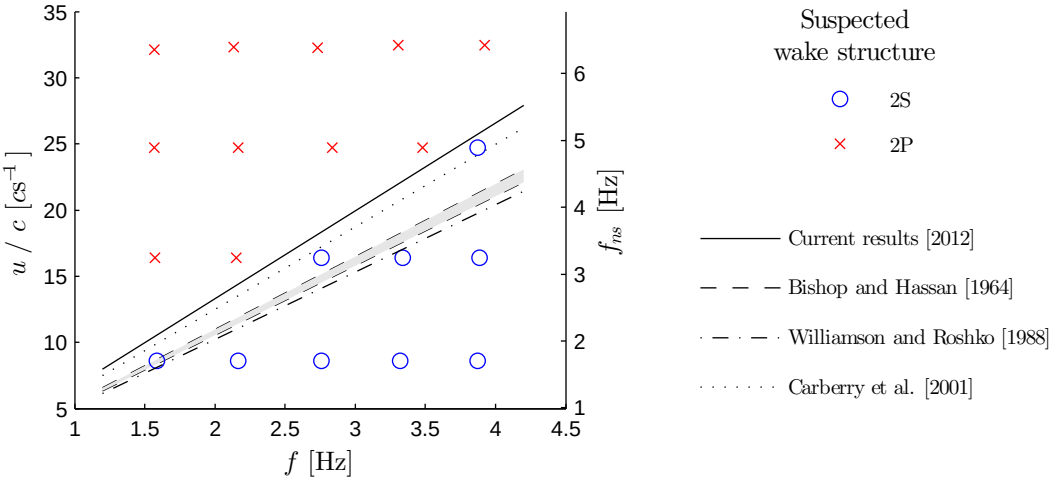

Figure 6.9. Transition point for the sudden change in hydrodynamic force phase and amplitude on the cylinder. $h^* = 0.75$

Possible reasons for the current result having a slightly lower boundary frequency ratio

are, the non-sinusoidal heaving motion, a higher Reynolds number, or error in the predicted natural vortex shedding frequency. The experiments of Bishop and Hassan (1964), Williamson and Roshko (1988), and Carberry et al. (2001) were all done at Reynolds numbers of $Re_u \leq 10^4$. Table 6.2 shows that the current experiments were conducted in the range of $10^4 < Re_u < 10^5$, roughly one to two orders of magnitude higher than the previously mentioned experiments. The natural vortex shedding frequency of the cylinder in the current experiments was calculated with Equation 6.1, which is considered an approximation for St_{ns} over the range of $2 \times 10^2 < Re < 2 \times 10^5$. However, the natural vortex shedding frequency is known to vary with surface roughness. Over prediction of the natural vortex shedding frequency could be a reason for the slightly low boundary frequency ratio.

The current results positioned the change in wake structure boundary in a similar place to those found in the literature, and very close to the recent results of Carberry et al. (2001). Thus, the experimental equipment was deemed adequate for accurately measuring unsteady hydrodynamic forces on the cylinder. Moreover, it was also considered suitable to proceed with acquiring credible measurements of the unsteady hydrodynamic forces on the flat plate and foils that presented in the following sections.

6.5 A Heaving Flat Plate with Non-Zero Forward Velocity

In Chapter 5, the hydrodynamic forces on a 'flat' object, such as a flat plate or a hydrofoil were shown to be very different from those on a cylinder oscillating with no forward velocity. The purpose of this section is to compare the time-dependent hydrodynamic forces on a 'flat' object with those on a cylinder when they are oscillating with some non-zero forward velocity. These experiments were also performed to study the hydrodynamic forces on a 'flat' object with elementary geometry so that they could be compared to the forces on other 'flat' objects with more complex geometry, specifically the hydrofoils studied in Section 6.6. For this reason, the dimensions of the flat plate were chosen to be similar to the hydrofoils (see Section 4.3) used in the following experiments. The following data was collected for several different combinations of forward velocity and oscillating

frequency (see Table 6.1) while the heave-to-chord ratio remained fixed at $h^* = 0.88$.

6.5.1 Hydrodynamic Forces at Zero Pitch

Figure 6.10 shows the measured hydrodynamic force cycles on the flat plate with zero pitch operating under the approximate oscillating frequencies and forward velocities set out in Table 6.1.

Surge Force Profile

At slow forward velocity ($u = 0.5\,\mathrm{m\,s^{-1}}$) and higher St the surge force cycle has a wavy profile that alternates sign about a near zero mean (Figure 6.10a). With this profile, peak positive surge force occurs around the points of maximum heave velocity, and peak negative surge force lags points of peak heave acceleration. When the forward velocity is increased to $u = 1\,\mathrm{m\,s^{-1}}$, the amplitude of these wavy surge force cycles decreases for a given oscillating frequency. Figure 6.11 shows that when operating under these high Strouhal number conditions the mean drag coefficient of the plate is less than when the plate is steady.

When the Strouhal number is sufficiently low (approximately $St < 0.2$), the positive thrust peaks in the the surge force cycle reduce to near zero and the cycle takes a distinctly different profile. During this transition, the points of peak negative surge force, i.e. points of peak drag, advance in phase (Figure 6.10b), similarly to the drag on the struts as shown in Section 6.3. The surge force cycle also has definite negative bias, i.e. there is always a net drag force on the plate, and the mean unsteady drag coefficient is now higher than the steady drag coefficient (Figure 6.11). Figure 6.12 shows that this sudden change in surge force profile at $St = 0.2$ corresponds to points of peak negative surge force changing from lagging peak heave acceleration to leading peak heave acceleration.

Heave Force Range

Figure 6.13 shows that as the plate gains forward velocity (i.e. as the Stouhal number reduces from infinity), the heave force range coefficient reduces from that when there was zero forward velocity. This is good, since these large vertical oscillating forces are not

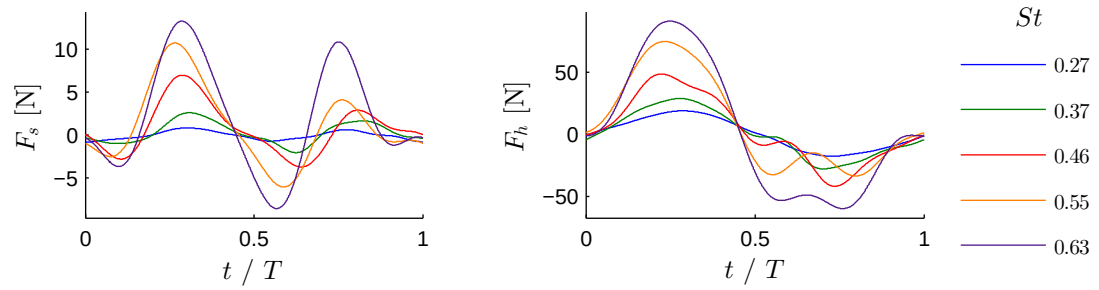

(a) $u = 0.5\,\mathrm{m\,s^{-1}}$

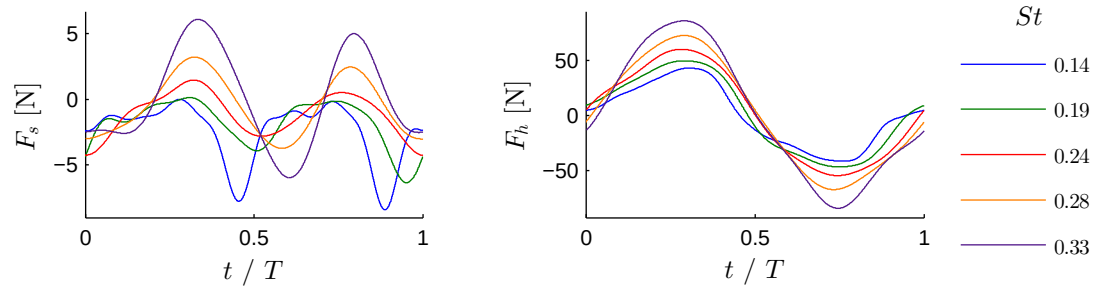

(b) $u = 1.0\,\mathrm{m\,s^{-1}}$

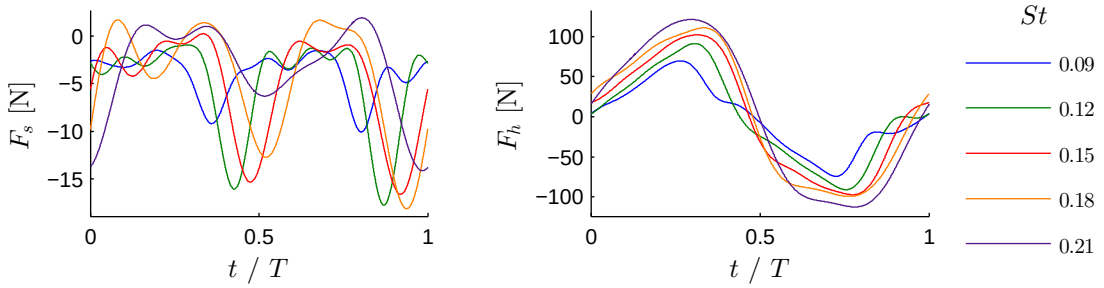

(c) $u = 1.5\,\mathrm{m\,s^{-1}}$

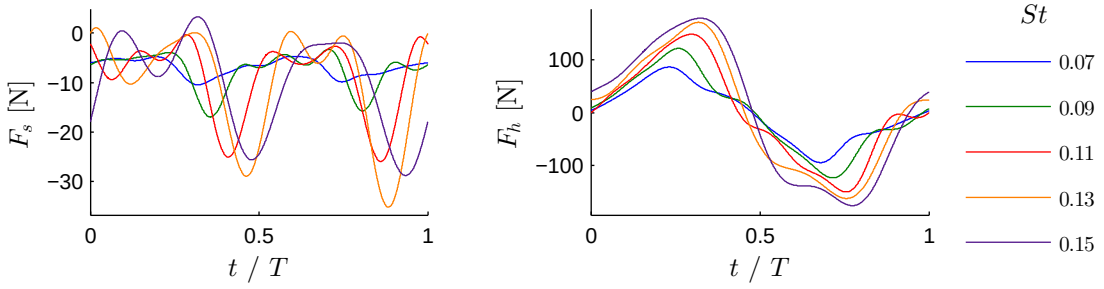

(d) $u = 2.0\,\mathrm{m\,s^{-1}}$

Figure 6.10. The effect of forward velocity on the heave force cycle of a heaving flat plate. $\theta = 0°$, $h^* = 0.88$

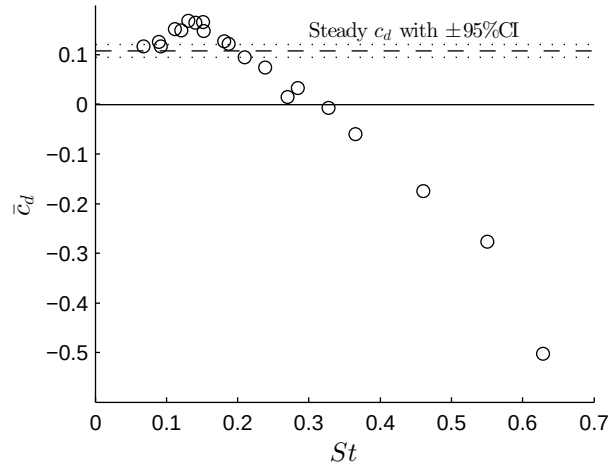

Figure 6.11. Mean drag coefficient against Strouhal number for the heaving flat plate. $\theta = 0°$, $h^* = 0.88$

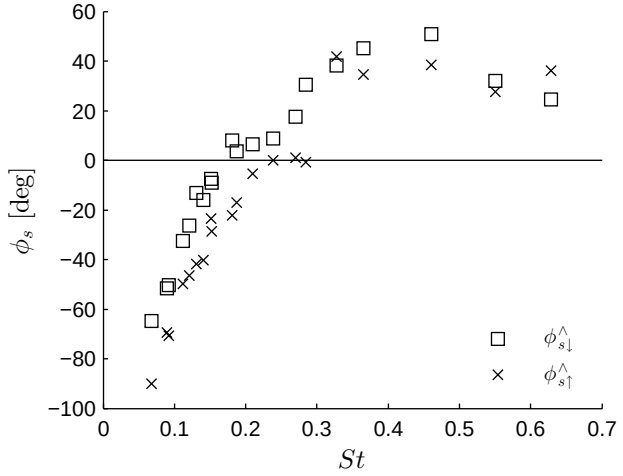

Figure 6.12. Surge force phase against Strouhal number for the heaving flat plate. $\theta = 0°$, $h^* = 0.88$

wanted on a watercraft. However, as the Strouhal number reduces to approach 0.2 the heave force coefficient rises again and returns to its original value when $u = 0$. When $St < 0.2$ the heave force range increases quickly. This is most likely due the increased effective velocity that the plate encounters when heaving at fast forward velocities.

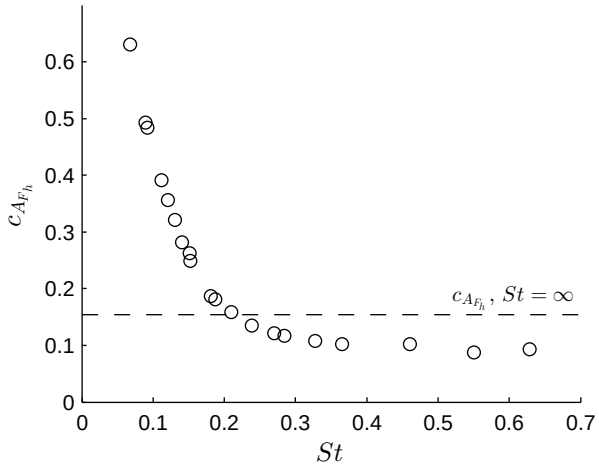

Figure 6.13. Heave force range coefficient against Strouhal number for the heaving flat plate. $\theta = 0°$, $h^* = 0.88$

6.6 Heaving Hydrofoils with Non-Zero Forward Velocity

The results in Chapter 5 showed that although both hydrofoils and flat plates are geometrically similar 'flat' objects, asymmetry of the hydrofoils in the surge plane made them superior propellers when $u = 0$. However, the heave forces on the foils and the flat plate were very similar. In the previous section, the hydrodynamic forces on an oscillating flat plate with some non-zero forward velocity were presented. In this section, the hydrodynamic forces on two different hydrofoils are presented and compared to those on the flat plate. The following force measurements were collected at the approximate forward velocities and oscillating frequencies shown in Table 6.1, while the heave-to-chord ratio remained fixed ($h^* = 0.75$).

6.6.1 Hydrodynamic Forces at Zero Pitch

Figure 6.14 and Figure 6.15 show the hydrodynamic force cycles on the NACA0012 and NACA4415 respectively, both with a pitch angle of 0° oscillating under the conditions set out in Table 6.1. These figures show that the surge force cycle of either foil undergoes the most significant changes in profile while $u = 0.5\,\mathrm{m\,s^{-1}}$. This transition occurs at a higher Strouhal number, than with the flat plate or the cylinder where the most significant

changes in the surge force profile occurred at $u = 1\,\mathrm{m\,s^{-1}}$ ($St \approx 0.2$).

Surge Force Profile

Results in Section 5.6.1 showed that the NACA0012 had an asymmetrical surge force cycle when $u = 0$. Since the NACA0012 is a symmetrical foil, this was attributed to the non-sinusoidal heaving motion. Figure 6.14 shows that as the heaving NACA0012 gains forward velocity, the surge force profile regains symmetry, producing equal size thrust peaks on the upstroke and the downstroke. Similarly, as the NACA4415 gains forward velocity, its surge force profile develops to produce more thrust on the downstroke than the upstroke (Figure 6.15).

Even though the NACA0012 and the NACA4415 thrust profiles are very different when the forward velocity is increased, Figure 6.16 shows that their mean thrust coefficients are similar. This is most likely due to these hydrofoils having a similar thickness (Ashraf et al., 2007). Figure 6.16 also shows that the current results agree well with the results of Ashraf, Young, and Lai (2012). However, the simulations of Tuncer, Walz, and Platzer (1998) predict that the NACA0012 thrust coefficient will decrease with increased at high Reynolds numbers ($Re > 10^6$).

Heave Force Range

Similar to the flat plate, the heave force range coefficient decrease as the hydrofoils gain forward velocity. The heave force coefficient reaches a minimum at approximately St=0.56 and then increases as St decreases (Figure 6.17). The NACA4415 maintains the lowest heave force range coefficient throughout the tested St range, and has a lower heave force range coefficient than when $St = \infty$ until $St < 0.15$.

Hydrofoil Shape

As shown in Section 5.5.1 the heave force profiles of the flat plate, NACA0012 and the NACA4415 were near equal when $u = 0$ ($St = \infty$). Comparing Figure 6.14 with Figure 6.15 shows that the heave force profile of the NACA0012 and the NACA4415 remain similar with forward velocity. However, as the Strouhal number decreases, the NACA4415

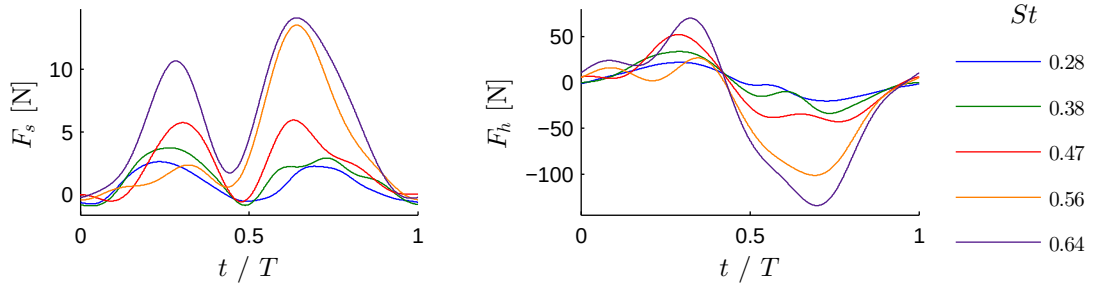

(a) $u = 0.5\,\mathrm{m\,s^{-1}}$

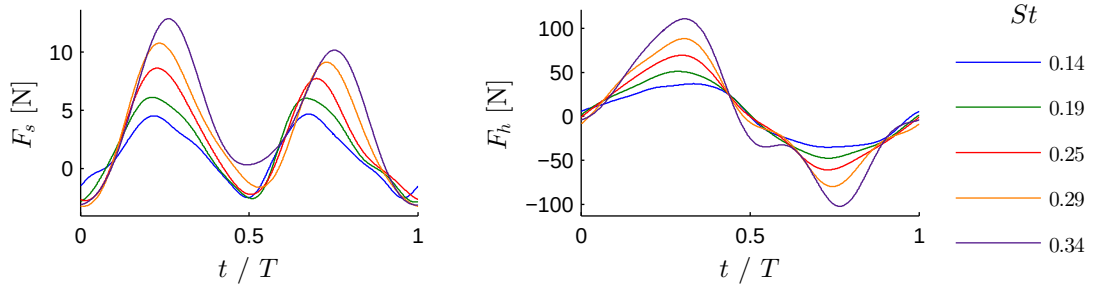

(b) $u = 1.0\,\mathrm{m\,s^{-1}}$

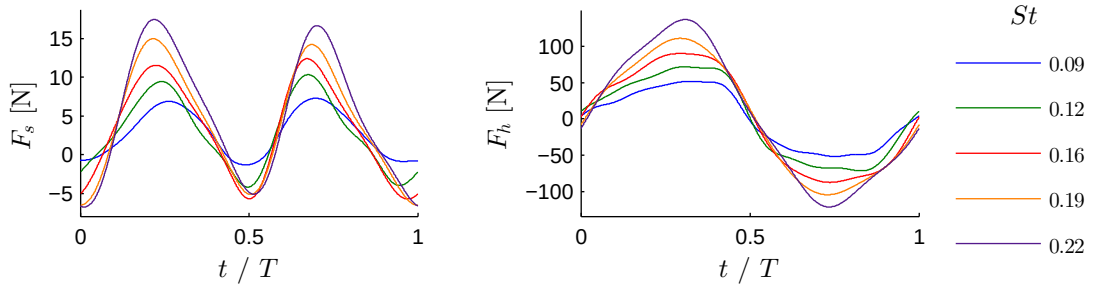

(c) $u = 1.5\,\mathrm{m\,s^{-1}}$

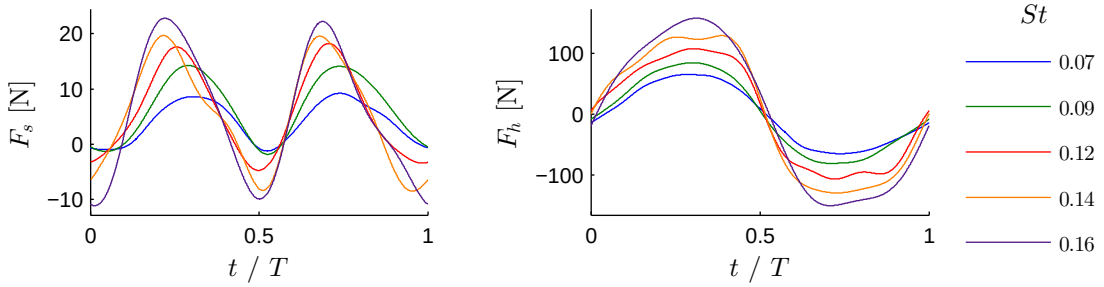

(d) $u = 2.0\,\mathrm{m\,s^{-1}}$

Figure 6.14. The effect of forward velocity on the heave force cycle of a heaving NACA0012. $\theta = 0°$, $h^* = 0.75$

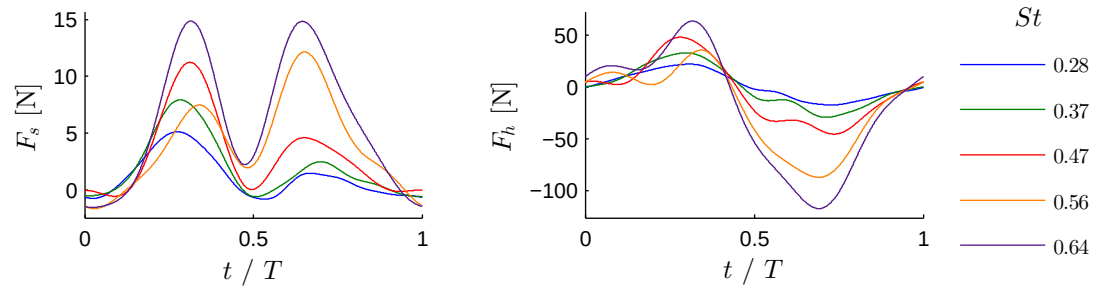

(a) $u = 0.5\,\mathrm{m\,s^{-1}}$

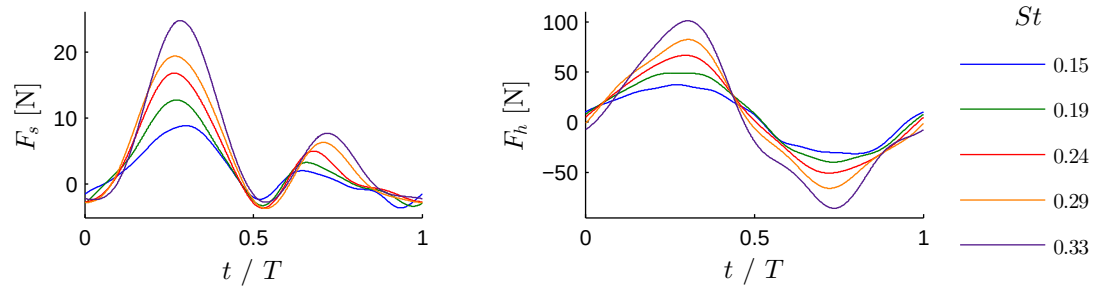

(b) $u = 1.0\,\mathrm{m\,s^{-1}}$

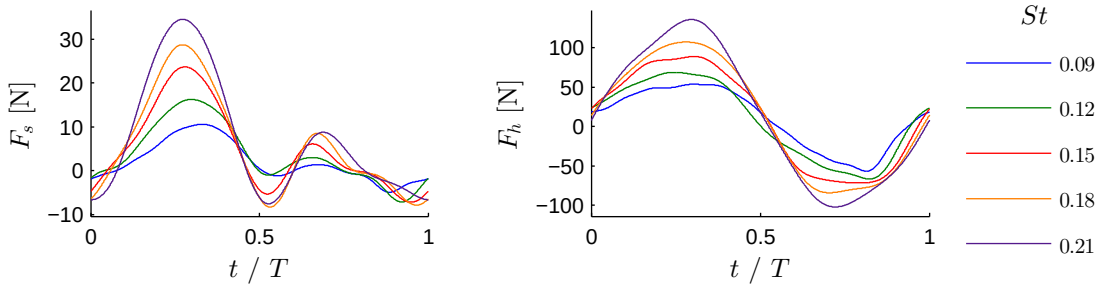

(c) $u = 1.5\,\mathrm{m\,s^{-1}}$

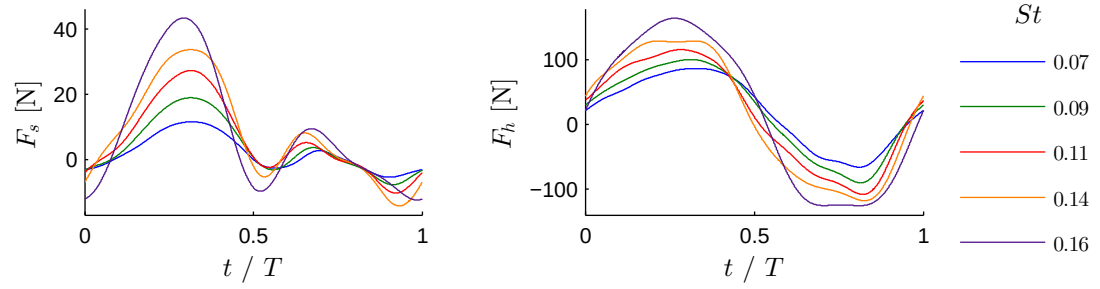

(d) $u = 2.0\,\mathrm{m\,s^{-1}}$

Figure 6.15. The effect of forward velocity on the heave force cycle of a heaving NACA4415. $\theta = 0°$, $h^* = 0.75$

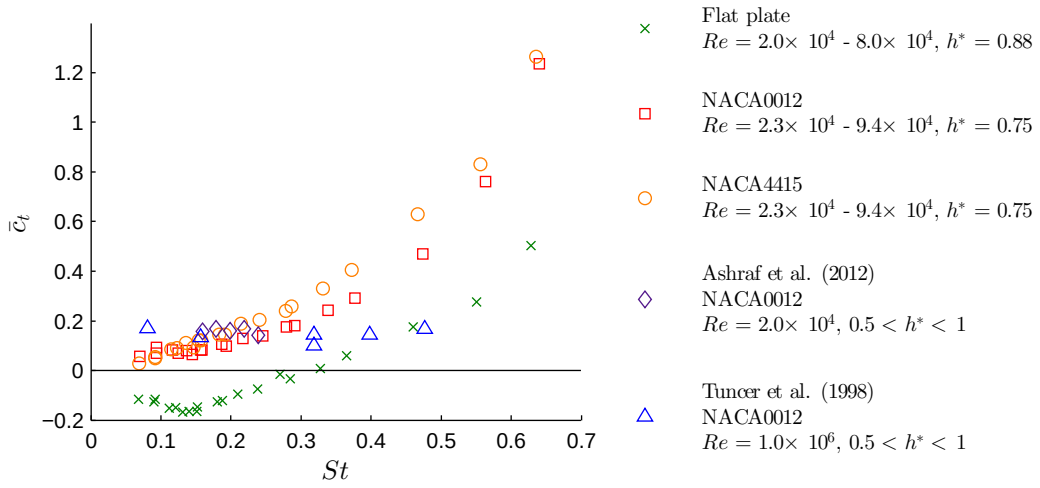

Figure 6.16. Mean thrust coefficient against Strouhal number for a heaving NACA0012 and NACA4415. $\theta = 0°$, $h^* = 0.75$

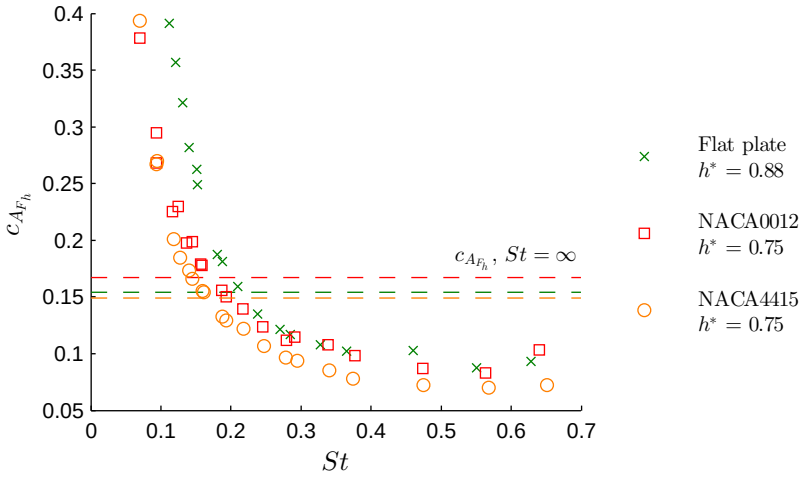

Figure 6.17. Heave force range coefficient against Strouhal number for a heaving NACA0012 and NACA4415. $\theta = 0°$, $h^* = 0.75$

camber begins to affect the heave force cycle bias. Figure 6.18 shows that once $St < 0.28$ the NACA4415 lift coefficient increases, tending towards its steady state lift coefficient at $St = 0$ while the the NACA0012 and flat plate lift coefficients remain near zero. As with lift on steady foils, the increased NACA4415 mean lift coefficient does not come without cost. Figure 6.16 shows that when $St < 0.28$ the mean thrust coefficient decreases relative to that of the NACA0012.

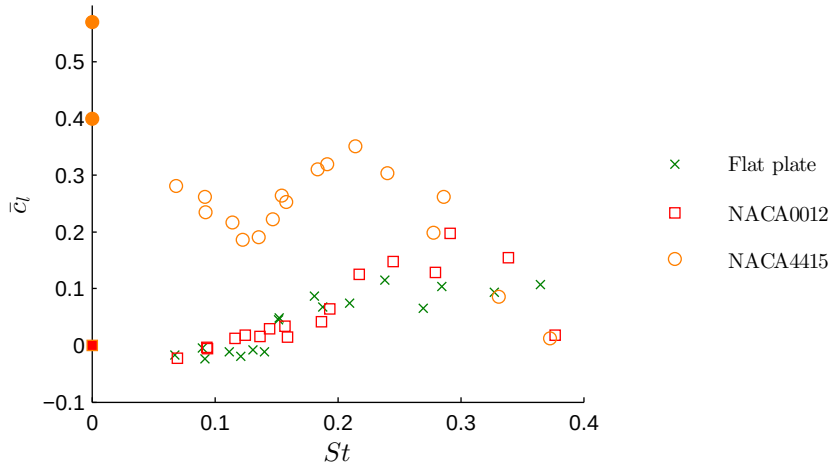

Figure 6.18. Mean lift coefficient against Strouhal number for a heaving flat plate, NACA0012, and NACA4415. $\theta = 0°$, $h^* = 0.75$. Solid markers represent steady lift coefficients: NACA4415; $c_l = 0.4$, $Re = 3 \times 10^6$ (I. H. Abbott et al., 1945), $c_l = 0.57$, $Re = 10^6$ (Reuss et al., 1995)

Figure 6.19 shows the efficiency of each hydrofoil against the Strouhal number. To evaluate the efficiency the input and output power were calculated with Equations 5.2 and 3.33 respectively, so inherently as $St \to \infty$ the efficiency tends to zero. The NACA4415 maintains a higher efficiency than the NACA0012 while $St > 0.1$. This could be attributed to its slightly higher thrust coefficient (Figure 6.16) or its lower heave force cycle range (Figure 6.17) over this domain. However, at approximately $St = 0.1$, the efficiency of the NACA4415 reaches a maximum and then decreases as St decreases. This is because of the NACA4415 mean lift coefficient increasing rapidly simultaneous to a decrease in the mean thrust coefficient.

It is not surprising that the simulations of Lewin and Haj-Hariri (2003) predicted that the propulsive efficiency of an ellipse is low due to its symmetrical geometry in the surge plane. However, the simulations of Ashraf et al. (2012) predicted that the efficiency of a heaving NACA0012 would be similar ($\eta \approx 5\,\%$). The experimental current results show that a heaving NACA0012 can achieve higher efficiencies than predicted in these simulations and confirm that objects with a blunt leading edge and a sharp trailing edge make more efficient propellers.

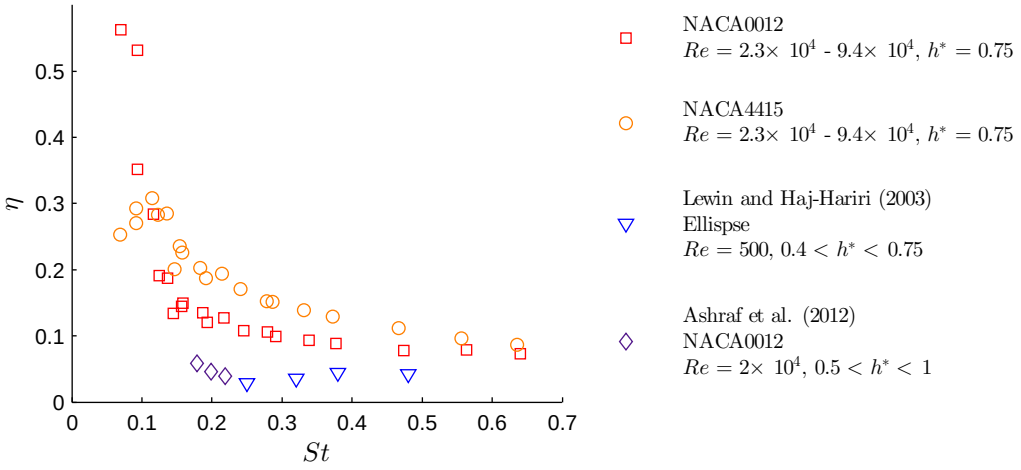

Figure 6.19. Efficiency against Strouhal number for a heaving NACA0012 and NACA4415. $\theta = 0°$, $h^* = 0.75$

6.7 Summary

In this chapter, experimental measurements of the hydrodynamic forces on heaving objects with some forward velocity were presented. The current results confirmed that when the oscillating frequency competes with the natural shedding frequency of a cylinder, hydrodynamic forces on the cylinder will undergo a sudden change. Alignment of these results with existing literature validated that the functionality of the current experimental equipment design was adequate for the current tests. Subsequent experiments investigated if this sudden change in hydrodynamic forces was also applicable to a heaving flat plate or hydrofoil. The outcomes of these experiments are as follows:

End Effects

- Forward velocity causes a small decrease in peak surge force when end plates are not used. However, the change in peak surge force may significantly affect the surge cycle mean.

- End plate diameter does not significantly affect the heave force cycle when forward velocity is increased. The heave force cycle is most influenced by end plate diameter at start-up, i.e. $u = 0$.

Strut Forces

- As with steady surface piercing plates, forward velocity reduces the drag coefficient of struts due to the formation of an air cavity at the surface behind the struts. Increasing the oscillating frequency of surface piercing struts leads to an advance in the drag cycle phase.

Object Shape

- As shown in Section 5.6.1, a heaving symmetrical hydrofoil does not necessarily produce a symmetrical surge force cycle when $u = 0$ and $\theta = 0°$. In this case, the heaving motion significantly affects the symmetry of the hydrodynamic forces. When forward velocity is increased, the heaving motion is less significant and the object shape has a stronger influence on the force cycle symmetry.

- Hydrofoil camber will not significantly affect the heave forces on a heaving hydrofoil ($\theta = 0°$) until the Strouhal number is sufficiently low. In the current experiments, the NACA4415 mean lift coefficient was not higher than that of the symmetrical NACA0012 until $St < 0.28$.

In terms of design for human-powered vehicles, asymmetrical foils will provide net lift while cruising, i.e. at low Strouhal numbers, as well as while gliding. However, as shown in Chapter 5, heaving motion becomes the dominant variable at high Strouhal numbers and heave forces become less sensitive to small differences in object shape. It was already well known that end plates can contribute towards maintaining a high lift-to-drag ratio while gliding. These results suggest that end plates should also be used to maintain peak thrust during high Strouhal number operation. Although the drag on oscillating struts was found to advance in phase with increased oscillating frequency, at low oscillating frequencies the drag on the struts may be adequately predicted with quasi-steady calculations.

Chapter 7

Conclusion

The original motivation behind this thesis was the goal of designing a human-powered hydrofoil incorporating an oscillating foil propeller. A requirement of the design was that the hydrofoils should be able to start from rest without the assistance of any external structure. The review of experimental craft building presented in Chapter 2 revealed that very few designs have achieved this. Two designs that did achieve this goal were Parker MacCready's Mutiny on the Boundary Layer and Pogo Foil. Both of these watercraft required a lot of power from the rider and had poor efficiency. Parker MacCready designed the MOBL and the Pogo foil using quasi-steady calculations and analytical theory. Both of these methods are known to have significant errors at high Strouhal numbers, i.e. during start-up from rest.

A review of the literature revealed that ocean engineering equations exist for calculating the time-dependent hydrodynamic forces on a cylinder under these conditions. These equations could be used to model the hydrodynamic forces on an oscillating hydrofoil during start-up to simulate vehicle dynamics. However, the validity of these equations for predicting hydrodynamic forces on a hydrofoil was not known. Furthermore, added mass and drag coefficients for hydrofoil with large angles of attack could not be found. Hence the primary objective of this thesis became to measure the time-dependent hydrodynamic forces on an oscillating hydrofoil to provide an overview of the magnitude and phase of these forces. This data was then used to evaluate the validity of the ocean engineering equations for predicting hydrodynamic forces on hydrofoils.

To achieve these objectives experimental equipment was designed to measure the hydrodynamic forces on oscillating objects. The measured hydrodynamic forces on a heaving cylinder were compared to results found in the literature to verify that the measurements were credible. The experimental results presented in this thesis have further revealed the complexity of hydrodynamic forces acting on oscillating objects and clarified the validity of the Morison equations and mass-damper model for application in this field. Results have also uncovered several relevant points of interest for designing a vertically oscillating hydrofoil propeller.

7.1 Summary of Results

7.1.1 Hydrodynamic Force Model Validity

For a Heaving Object with Zero Forward Velocity

Measured time-dependent heave forces on a cylinder can be adequately described with a linear mass-damper model at low Keulegan-Carpenter numbers. The current results support the Keulegan-Carpenter number range for mass-damper model set out by Journée and Massie (2001). Hydrodynamic forces on 'flat' objects such as a plate or a hydrofoil were shown to differ significantly in phase and profile from those on a cylinder. The Morison equation provided a better fit than the linear mass-damper model for the forces on these objects. However, neither model was considered a good fit, particularly around the points of maximum and minimum heave force which were typically underestimated. Thus the current study concluded that the mass-damper model and the Morison equation were limited when predicting unsteady hydrodynamics forces on heaving objects with significantly different geometry from a cylinder and a heave-to-chord ratio of 0.75 or 0.88.

7.1.2 Heaving Motion

The current experiments were done with a crank and connecting rod mechanism driving the heaving motion. Due to this mechanism having a low connecting rod to crank length ratio and the drive motor being under open-loop control, the resulting heaving motion was non-sinusoidal. Results show that small changes in the heave position profile cause larger

changes in the heave velocity and acceleration profiles due to higher order harmonics. Consequently, the heave acceleration profile in the current experiments was non-sinusoidal which had a strong influence on the surge force profile of a heaving hydrofoil with zero pitch and no forward velocity. Under these conditions, the magnitude of peak heave acceleration was shown to be proportional to the magnitude of the proceeding peak in the surge force cycle. The constant of proportionality was dictated by the shape of the upper and lower surfaces of the hydrofoil.

7.1.3 Object Shape

The shape of an object was shown to significantly affect the hydrodynamic forces on it whilst heaving. For example, the hydrodynamic forces on a cylinder were distinctly different from those on flatter objects such as a flat plate or a hydrofoil with similar dimensions. These flatter shapes typically generated larger heave forces with peaks lagging peak heave acceleration but leading peak heave velocity. At zero pitch and zero forward velocity the surge forces were very sensitive to object shape. Objects with asymmetry in the surge plane, such as a hydrofoil generated useful thrust under these conditions due to asymmetrical vortex shedding. Moreover, the time-dependent profile of the thrust produced was distinctly characteristic of the object shape. At non-zero pitch and zero forward velocity the heave and surge forces on a 'flat' object were relatively insensitive to the specific object shape, especially when pitch was greater than 40°. Under these conditions the heave and surge forces on the object are thought to be dominated by flow deflection.

At zero pitch and zero forward velocity, the forces on a heaving hydrofoil were strongly influenced by the heaving motion. As the forward velocity was increased, the thrust produced by a hydrofoil quickly developed to reflect the hydrofoil shape. For example, a symmetrical foil will produce equal thrust on the upstroke and the downstroke while a cambered foil will produce more thrust when travelling towards the centre of camber. Similarly, heave forces on a hydrofoil were relatively insensitive to camber until the Strouhal number was sufficiently low. In the case of the tested NACA4415, a heave force bias due to its cambered shape was not prominent until the Strouhal number fell below 0.28.

Furthermore, once the mean lift coefficient began to increase, the mean thrust coefficient decreased faster with a decreasing Strouhal number indicating that lift-induced drag also applies to unsteady hydrofoils.

Many analytical studies of oscillating hydrofoil propulsion assume the hydrofoil to be a thin flat plate. The current experimental study has shown that although the heave forces on a flat plate may be similar to those on a hydrofoil, the thrust generated by a hydrofoil is very different from that of a flat plate. Hence, this assumption will inherently limit the validity of an analysis.

7.1.4 Submergence

Proximity of the free surface can significantly affect the propulsive forces generated by a heaving hydrofoil with a heave-to-chord ratio of 0.75 (Figure 7.1). For obtaining force measurements on a heaving object with zero forward velocity, a submersion depth of 3 chord lengths was found to be sufficient to avoid significant free surface effects. Once the submersion depth was decreased to a approximately one chord length ventilation became a common issue for a heaving flat plate. Moreover, the mode of interaction between the heaving flat plate and the free surface was observed to change at integer values of the product of the gravity-capillary wave number and the plate chord length, kc. A heaving asymmetric NACA4415 hydrofoil operating at a submergence depth of 2.1 chord lengths lead to significant increases in mean thrust and lift when $kc > 1$. The increase in mean thrust was caused by a significant increase in peak thrust on the downstroke. Water craft employing an oscillating foil for lift and thrust would benefit from operating under this condition at start-up as it would decrease the time for the craft to become foil-borne.

7.1.5 End Plates

The use of end plates and end plate size was found to affect heave and surge forces differently under different operating conditions. Figure 7.2 summarises the effect of fitting end plates to a heaving hydrofoil.

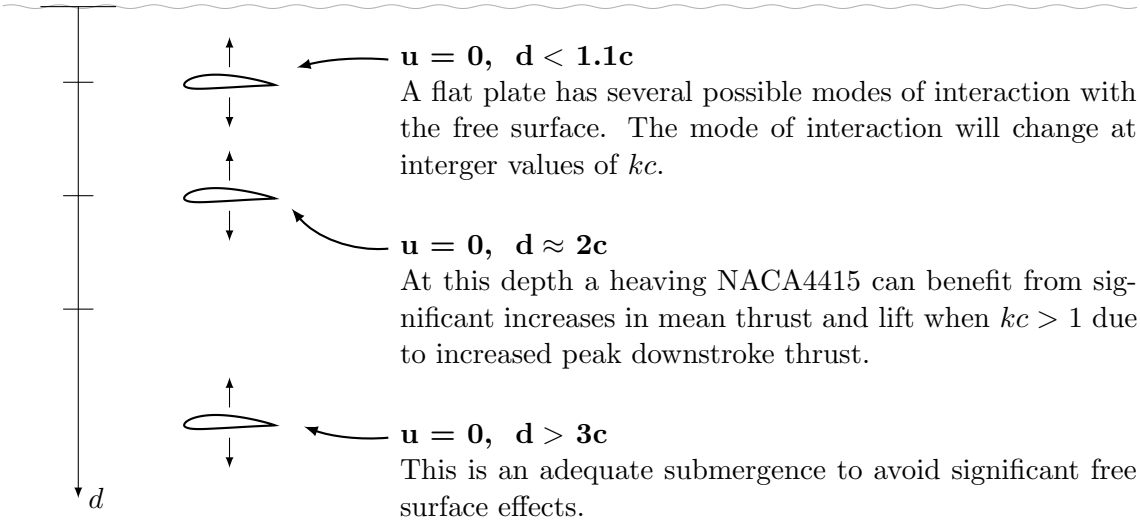

Figure 7.1. The effect of submersion depth on a heaving flat plate ($h^* = 0.88$) or a hydrofoil ($h^* = 0.75$). $\theta = 0°$, $0 < kc < 4.2$

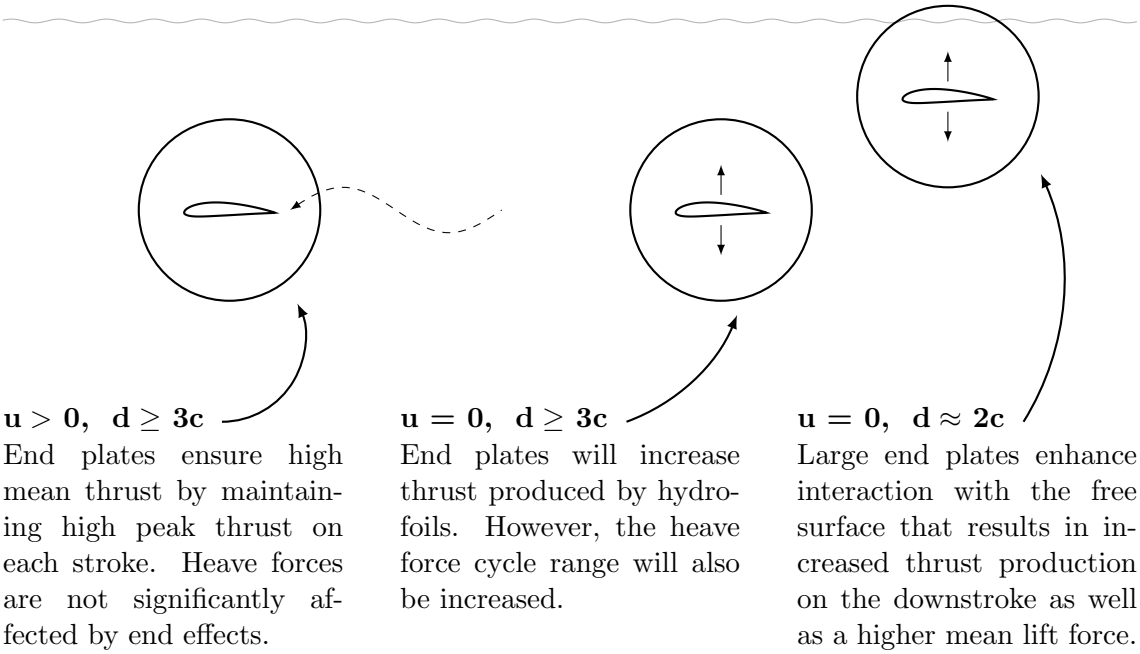

Figure 7.2. The effect of end plates on a heaving hydrofoil. $h^* = 0.75$, $\theta = 0°$

7.2 Implications for Watercraft Design

Neither the mass-damper model nor the Morison equation provided a good fit to measured hydrodynamic forces on a heaving flat plate or hydrofoil. Hence, neither of these models would be appropriate for modelling the vehicle dynamics of a human-powered surface watercraft with flapping wing propulsion. It is recommended that future work be done on creating an alternative model to better fit the experimental data presented in this thesis. In the meantime it is important that flapping wing propeller designers consider that although the mean thrust produced by heaving foil increases linearly with oscillating frequency, the heave force cycle range will increase quadratically, and hence significantly affect vehicle dynamics.

Designers should consider shallow mean submergence depths for oscillating foil propellers during start-up to exploit thrust gains from free surface effects. However, the characteristics of these thrust gains will be dependent on the choice of hydrofoil shape. Asymmetrical foils will provide net lift while cruising, i.e. at low Strouhal numbers, as well as while gliding. However, heaving forces during high Strouhal number operation, i.e. during start-up, are less sensitive to object shape than they are to heaving motion. Hence, vehicle dynamics during start-up will also be more sensitive to hydrofoil motion than hydrofoil shape. Although hydrofoil motions were limited to pure heaving in the current study to simplify data analysis, pure heaving motions are not ideal for start-up operation since they are associated with weak thrust production and low efficiencies. Hence, it is recommended that designers consider mixed heaving and pitching motions for oscillating foil propellers.

7.3 Recommendations for Further Research

The work presented in this thesis focused only on correlating the motion of an oscillating object with the unsteady hydrodynamic forces exerted on it. The measured forces are the result of a complex induced flow in the fluid. The discussion around the results presented in this thesis may only speculate on what flow patterns cause the captured force measurements. Further research could involve flow visualisation work to investigate the

flow dynamics behind the current force measurements.

The degrees of freedom of the foil were limited in the current work. Further work could be done investigating more complex object motion such as movements involving simultaneous surging, heaving or pitching. However, it is recommended that further interpretation and modelling of the current data would be beneficial. In particular, modelling the hydrodynamic forces on the flat plate as it heaves with no forward velocity since this is a fundamental case that is not well understood. Once this case is modelled well, modelling the forces on a foil may follow more easily due to the similar object geometry.

One of the largest issues that needs to be addressed when designing a surface watercraft with an oscillating hydrofoil propeller is the stability of the watercraft as it is subject to large oscillating loads during the start-up phase. Using the data presented in this thesis, the phase and magnitude of these forces may be estimated with reasonable precision allowing scale prototype water craft employing a single, or multiple oscillating hydrofoils for thrust and lift to be designed and simulated.

References

Abbott, A. V., & Wilson, D. G. (Eds.). (1995). *Human-powered vehicles*. Human Kinetics.

Abbott, I. H., Von Doenhoff, A. E., & Stivers, L., Jr. (1945, January). *Summary of airfoil data* (Tech. Rep. No. NACA-TR-824).

Akhtar, I., Mittal, R., Lauder, G. V., & Drucker, E. (2007). Hydrodynamics of a biologically inspired tandem flapping foil configuration. *Theoretical and Computational Fluid Dynamics*, *21*(3), 155-170.

Alben, S., & Shelley, M. (2005). Coherent locomotion as an attracting state for a free flapping body. *Applied Mathematics*, *102*(32), 1116311166.

Amabili, M. (1996). Effect of finite fluid depth on the hydroelastic vibrations of circular and annular plates. *Journal of Sound and Vibration*, *193*(4), 909-925.

Anderson, J. M. (1996). *Vorticity control for efficient propulsion.* Phd thesis, Massachusetts Institute of Technology.

Anderson, J. M., & Kerrebrock, P. A. (2000). The vorticity control unmanned undersea vehicle (VCUUV): An autonomous robot tuna. *The Draper Technology Digest*, 63-70.

Anderson, J. M., Streitlien, K., Barrett, D. S., & Triantafyllou, M. S. (1998). Oscillating foils of high propulsive efficiency. *Journal of Fluid Mechanics*, *360*, 41-72.

Art Centre, College of Design. (Accessed 2008). *Athropropulsion.* `http://www.artcenter.edu/exhibit/anthro/fish.html`.

Ashe, M. C., Scroop, G. C., Frisken, P. I., Amery, C. A., Wilkins, M. A., & Khan, K. M. (2003). Body position affects performance in untrained cyclists. *British Journal of Sports Medicine*, *37*, 441-444.

Ashraf, M. A., Lai, J. C. S., & Young, J. (2007, December). Numerical analysis of flapping wing aerodynamics. In *the proceedings of the* 16^{th} *Australasian Fluid Mechanics Conference* (p. 1283-1290). Crown Plaza, Gold Coast, Australia.

Ashraf, M. A., Young, J., & Lai, J. C. S. (2011). Reynolds number, thickness and camber effects on flapping airfoil propulsion. *Journal of Fluids and Structures*, *27*, 145-160.

Ashraf, M. A., Young, J., & Lai, J. C. S. (2012). Oscillation frequency and amplitude effects on plunging airfoil propulsion and flow periodicity. *AIAA Journal*, *50*(11), 2308-2324.

Barrett, D., Grosenbaugh, M., & Triantafyllou, M. (1996, June). The optimal control of a flexible hull robot vehicle propelled by an oscillating foil. In *the proceedings of the 1996 Symposium on Autonomous Underwater Vehicle Technology* (p. 1-9).

Basset, A. B. (1888). *A treatise on hydrodynamics with numerous examples* (Vol. 2). Cambridge University Press.

Beal, D. N., Hover, F. S., Triantafyllou, M. S., Liao, J. C., & Lauder, G. V. (2006). Passive propulsion in vortex wakes. *Journal of Fluid Mechanics*, *549*, 385-402.

Bearman, P. W., Downie, M. J., Graham, M. R., & Obasaju, E. D. (1985). Forces on cylinders in viscous oscillating flow at low keulegan-carpenter numbers. *Journal of Fluid Mechanics*, *154*, 227-356.

Bini, R., Hume, P. A., & Croft, J. L. (2011). Effects of bicycle saddle height on knee injury risk and cycling performance. *Sports Medicine*, *41*(6), 463-476.

Bishop, R. E. D., & Hassan, A. Y. (1964, January). The lift and drag forces on a circular cylinder oscillating in a flowing fluid. In *Mathematical and Physical Sciences* (Vol. 277, p. 51-75).

Bowlus, G. H., Kelly, H. R., & Siekmann, J. (1965). On the swimming of hinged hydrofoils. *Ingenieur-Archiv*, *34*, 339-352.

Breder, C. M., Jr. (1926, September). Locomotion of fishes. *Zoologica: N.Y. Zoological Society*, *4*(5), 159-297.

Bundle, M. W., & Dial, K. (2003, August). Mechanics of wing-assisted incline running (WAIR). *The Journal of Experimental Biology*, *206*, 4553-4564.

Buśko, K. (2005). Power output and mechanical efficiency of human muscle in maximal cycle ergometer efforts at different pedalling rates. *Biology of Sport*, *22*(1), 35-51.

Byran, H. (1993-1994). Fin power - success comes from copying nature. *Human Power*, *11*(1), 6-9.

Candelier, F., Angilella, J. R., & Souha, M. (2004). On the effect of the boussinesqbasset force on the radial migration of a stokes particle in a vortex. *Physics of Fluids*, *16*(5), 1765-1776.

Carberry, J., Sheridan, J., & Rockwell, D. (2001). Forces and wake modes of an oscillating cylinder. *Journal of Fluids and Structures*, *12*, 523-532.

Castrup, S., & Castrup, H. T. (2010, July). *Measurement uncertainty analysis principles and methods, nasa measurement quality assurance handbook annex 3* (Tech. Rep. No. NASA-HDBK-8739.19-3). National Aeronautics and Space Administration.

Chaithanya, M. R., & Venkatraman, K. (2008, August). Hydrodynamic propulsion of a flexible foil. In *the proceedings of the* 12^{th} *Asian Congress of Fluid Mechanics* (p. 1-5). Daejeon, Korea.

Chen, S. (2002, October). *Personal watercraft.* Patent US 6,468,118.

Chen, S. (2006, April). *Self propelled hydrofoil device.* Patent US 7,021,232 B2.

Chen, S. (2008, October). *Collapsible self propelled hydrofoil device.* Patent US 7,434,530.

Chen, S. (2010a, October). *Self-propelled hydrofoil device with flexible steering assembly.* Patent US 7,819,074.

Chen, S. (2010b, October). *Self propelled hydrofoil device with leverage-based control of drive foil.* Patent US 7,802,534.

Chen, S., Wambsganss, M., & Jendrzejczyk, J. (1976). Added mass and damping of a vibrating rod in confined viscous fluids. *Journal of Applied Mechanics*, *43*(2), 325-329.

Clauss, G., Lehmann, E., & Ostergaard, C. (1992). *Offshore structures: Conceptual design and hydromechanics* (Vol. 1). Springer-Verlag.

Cleaver, D. J., Wang, Z., & Gursul, I. (2009, June). Lift enhancement of oscillating airfoils. In *the proceedings of the* 39^{th} *AIAA Fluid Dynamics Conference.* San Antonio, Texas,

USA.

Company, H. C. (2011). *Hobie kayaking.* `http://www.hobiecat.com/kayaking/`.

Conte, J., Modarres-Sadeghi, Y., Watts, M. N., Hover, F., & Triantafyllou, M. (2010, September). A fast-starting mechanical fish that accelerates at 40 ms^{-2}. *Bioinspiration and Biomimetics*, *5*(3).

Daniel, T., Manley, J., & Trenaman, N. (2011, June). The wave glider - enabling a new approach to persistent ocean observation and research. *Ocean Dynamics*, *61*, 1509-1520.

Daskovsky, M. (2000). The hydrofoil in surface proximity, theory and experiment. *Ocean Engineering*, *27*, 1129-1159.

Davies, C. T. M. (1971). Human power output in exercise of short duration in relation to body size and composition. *Ergonomics*, *14*(2), 245-256.

Davies, C. T. M., & Rennie, R. (1968, February). Human power output. *Nature*, *217*, 770-771.

Davies, C. T. M., & Sandstrom, E. R. (1989). Maximal mechanical power output and capacity of cyclists and young adults. *European Journal of Applied Physiology*, *58*, 838-844.

Dean, R. G., & Dalrymple, R. A. (1991). *Water wave mechanics for engineers and scientists.* World Scientific.

DeLaurier, J. D., & Harris, J. M. (1993, October). A study of mechanical flapping-wing flight. *Aeronautical Journal*, *97*(968), 277-286.

de Man, P., & de Vries, L. (Accessed 2010). *Story of the Af Chapman II.* `http://www.waterbike.eu/Articles/Af_Chapman_2/article_Af_Chapman_2.html`.

Det Norske Vertias. (2011, April). *Recommended practice - modelling and analysis of marine operations* (Tech. Rep. No. DNV-RP-H103). DNV.

Dial, K. (2003, January). Wing-assisted incline running and the evolution of flight. *Science*, *299*, 402-404.

Ehm, M. (2005). *History of human powered hydrofoils - all hydrofoils from 1953 to 2005.* `http://www.human-powered-hydrofoils.com/history.html`.

Eloy, C. (2012). Optimal strouhal number for swimming animals. *Preprint version - currently submitted to JFS*.

Falnes, J. (2002). *Ocean waves and oscillating systems.* Cambridge University Press.

Finberg, S. (n.d.-a). *[Decavitator photo].* Retrieved from `http://lancet.mit.edu/decavitator/StillImages.html`.

Finberg, S. (n.d.-b). *[Flying Fish photo].* Retrieved from `http://lancet.mit.edu/decavitator/StillImages.html`.

Fish, F. E. (1993). Hydrodynamics of swimming dolphins. *Journal of Experimental Biology*, *185*, 179-1993.

Fish, F. E. (2006, June). The myth and reality of gray's paradox: implication of dolphin drag reduction for technology. *Bioinspiration & Biomimetics*, *1*(2), R17-R25.

Fishtail drive propels boats and model planes. (1939, October). In R. J. Brown (Ed.), (Vol. 135, p. 103). Bonnier Corporation.

Flores, M. D. (2003). *Flapping motion of a three-dimensional foil for propulsion and maneuvering of underwater vehicles.* Unpublished master's thesis, Massachusetts Institute of Technology.

Fulton, L. (2004, April). *Reducing oil consumption in transport: Combining three approaches* (Tech. Rep. No. EET/2004/01). International Energy Agency.

Garrick, I. E. (1936). *Propulsion of a flapping and oscillating airfoil* (Tech. Rep. No. NACA-TR-567). National Advisory Committee for Aeronautics.

Gleiss, A. C., Jorgensen, S. J., Liebsch, N., Sala, J. E., Norman, B., Hays, G. C., ... Wilson, R. P. (2011, June). Convergent evolution in locomotory patterns of flying and swimming animals. *Nature Communications*, *2*.

Godoy-Diana, R., Aider, J.-L., & Wesfreid, J. E. (2008, January). Transitions in the wake of a flapping foil. *Physical Review E*, *77*.

Gongwer, C. (1974, April). *Swimmer propulsion device.* Patent US 3,802,008.

Gongwer, C. (1986-1987). Letter/report. *Human Power*, *5*(4), 7.

Gongwer, C. (1987, August). *Watercraft propulsion device.* Patent US 4,688,994.

Gopalkrishnan, R., Triantafyllou, M. S., Triantafyllou, G. S., & Barrett, D. (1994). Active vorticity control in a shear flow using a flapping foil. *The Journal of Fluid Mechanics*, *274*, 1-21.

Gordon, L. (2010, November). This "undulating propeller" drives watercraft using wave motion. *Machine Design*, *82*(20), 51.

Gorelov, D. N. (2009). Analogy between a flapping wing and a wind turbine with a vertical axis. *Journal of Applied Mechanics and Technical Physics*, *50*(2), 297-299.

Grande, B. (2011, June). *Propeller device, vehicle drive unit and energy conversion unit.* Patent Application US 2011/0150650 A1.

Gray, J. (1936, August). The propulsive powers of the dolphin. *The Journal of Experimental Biology*, *13*, 192-199.

Grogware. (2007). *[Aquaskipper photos].* Retrieved from `http://www.grogware.com/aquaskipperphotos.php`.

Grue, J., rn, A., & Plam, E. (1988). Propulsion of a foil moving in water waves. *Journal of Fluid Mechanics*, *186*, 393-417.

Guglielmini, L., & Blondeaux, P. (2004, March-April). Propulsive efficiency of oscillating foils. *European Journal of Mechanics B/Fluids*, *23*(2), 255-278.

Gurland, J., & Tripathi, R. C. (1971, October). A simple approximation for unbiased estimation of the standard deviation. *The American Statistician*, *25*(4), 30-32.

Hall, K. C., & Hall, S. R. (1996, May). Minimum induced power requirements for flapping flight. *The Journal of Fluid Mechanics*, *323*, 285-315.

Hanlon, M. (2005). *SeaJogger allows you to walk on water.* `http://www.gizmag.com/go/4392/`.

Harman, E. A., Rosenstein, M. T., Frykman, P. N., Rosenstein, R. M., & Kraemer, W. J. (1988). *Estimation of human power output from maximal vertical jump and body mass* (Tech. Rep. No. AD-A218 194). Exercise Physiology Division, USARIEM.

Harnish, C., King, D., & Swensen, T. (2007). Effect of cycling position on oxygen uptake and preferred cadence in trained cyclists during hill climbing at various power outputs. *European Journal of Applied Physiology*, *99*, 387-391.

Harper, K. A. (1997). *Modeling the dynamics of carrangiform swimming for application to underwater robot locomotion.* Unpublished master's thesis, Boston University, College of Engineering.

Harper, K. A., Berkemeier, M. D., & Grace, S. (1998, July). Modeling the dynamics

of spring-driven oscillating-foil propulsion. *IEEE Journal of Oceanic Engineering*, *23*(3), 285-296.

Hawley, J. A. (Ed.). (2000). *Running.* Blackwell Science.

Heathcote, S., Wang, Z., & Gursul, I. (2008). Effect of spanwise flexibility on flapping wing propulsion. *Journal of Fluids and Sturctures*, *24*, 183-199.

Heglund, N. C. (1981). A simple design for a force-plate to measure gound reaction forces. *Journal of Experimental Biology*, *93*, 333-338.

Hill, A. D., Jr. (1938, March). *Propelling mechanism.* Patent US 2,173,415.

Honji, H. (1981). Streaked flow around an oscillating circular cylinder. *Journal of Fluid Mechanics*, *107*, 509-520.

Hover, F. S., Haugsdal, O., & Triantafyllou, M. S. (2004). Effect of angle of attack profiles in flapping foil propulsion. *Journal of Fluids and Structures*, *19*, 37-47.

Hubel, T. Y., & Tropea, C. (2009). Experimental investigation of a flapping wing model. *Experimentals in Fluids*, *46*, 945-961.

Hutchison, S. R., Brandner, P. A., Binns, J. R., Henderson, A. D., & Walker, G. J. (2010, December). Development of a CFD model for an oscillating hydrofoil. In *the proceedings of the* 17^{th} *Australasian Fluid Mechanics Conference.* Auckland, New Zealand.

Iliadis, G., & Anagnostopoulos, P. (1998). Viscous oscillatory flow around a circular cylinder at low keulegan-carpenter numbers and frequency parameters. *International Journal for Numercial Methods in Fluids*, *26*, 403-442.

Industrial Designers Society of America. (2001). *Design secrets: 50 real-life projects uncovered. products* (Vol. 1). Rockport Publishers.

Innerspace Corporation. (n.d.). *[Aqueon advertising].* Retrieved from `http://www.innerspacethrusters.com/Aqueon.htm`.

Inventist Inc. (2006). *Human powered hydrofoil history.* `http://www.inventist.com/index.php?option=com_content&task=view&id=25`.

Inventist Inc. (Accessed 2012). *[Aquaskipper image].* Retrieved from `http://www.inventist.com/`.

Iossi, R. (n.d.). *[Diving photos].* Retrieved from `http://fksa.org/showthread.php?t=4372`.

Iversen, H. W., & Balent, R. (1951, May). A correlating modulus for fluid resistance in accelerated motion. *Journal of Applied Physics*, *22*(3), 324-328.

Jaiswal, V., & Vandiver, J. K. (2007, June). VIV response for long risers with variable damping. In *the proceedings of the* 26^{th} *International Conference on Offshore Mechanics and Arctic Engineering.* San Diago, California, USA.

Jakobsen, E. (1986). Foil propulsion at sea. *Human Power - Technical Journal of the IHPVA*, *5*(3), 7-9.

Jones, K. D., & Platzer, M. F. (2001, May). On the use of vortex flows for the propulsion of micro-air and sea vehicles. In *RTO-MP-069(I).* Loen Norway.

Journée, J. M. J., & Massie, W. W. (2001). *Offshore hydrodynamics* (First Edition ed.). Delft University of Technology.

Jung, Y. W., & Park, S. O. (2005). Vortex-shedding characteristics in the wake of an oscillating airfoil at low reynolds number. *Journal of Fluids and Structures*, *20*, 451-464.

Kelly, S. D., Mason, R. J., Anhalt, C. T., Murray, R. M., & Burdick, J. W. (1998, June). Modelling and experimental investigation of carangiform locomotion for control. In *the proceedings of the American Control Conference.* Philadelphia, Pennsylvania, USA.

Keulegan, G. H., & Carpenter, L. H. (1958, May). Forces on cylinders and plates in an oscillating fluid. *Journal of Research of the National Bureau of Standards*, *60*(5), 423-440.

Klose, G. J. (1966). *Unsteady forces on oscillating hydrofoils.* Phd thesis, California Institute of Technology.

Ko, S., & McCroskey, W. J. (1995, January). Computations of unsteady seperating flows over an oscillating airfoil. In *the proceedings of the AIAA* 33^{rd} *Aerospace Sciences Meeting.* Reno, NV.

Konstantinov, G. A., & Yakimov, Y. (1995). Calculation of the thrust of a wave-prowered marine propelling device. *Fluid Dynamics*, *30*(3), 453-456.

Koochesfahani, M. M. (1989, September). Vortical patterns in the wake of an oscillating airfoil. *American Institute of Aeronautics and Astronautics Journal*, *27*(9), 1200-1205.

Kudela, H., & Kozlowski, T. (2010). Hydrodynamic effects produced by plunging foil in a fluid. *Chemical and Process Engineering*, *31*, 579-588.

Lai, J. C. S., & Platzer, M. F. (1999, December). Jet characteristics of a plunging airfoil. *AIAA Journal*, *37*(12), 1529-1537.

Lai, J. C. S., & Platzer, M. F. (2000, November). Characteristics of a plunging airfoil at zero freestream velocity. *AIAA Journal*, *39*(3), 531-534.

Legac, P., Fish, F., Williams, T., & Wei, T. (2007, November). DPIV measurements on dolphins: Examining gray's paradox. In *the proceedings of the* 60^{th} *Annual Meeting of the Divison of Fluid Dynamics* (Vol. 52). Salt Lake City, Utah.

Lekhtman, G. (2003). *Feet-propelled water vehicle.* Patent US 6595813 B1.

Lewin, G. C., & Haj-Hariri, H. (2003). Modelling thrust generation of a two-dimensional heaving airfoil in a viscous flow. *Journal of Fluid Mechanics*, *492*, 339-362.

Liao, J. C., Beal, D. N., Lauder, G. V., & Triantafyllou, M. S. (2003). The karman gait: novel body kinematics of rainbow trout swimming in a vortex street. *The Journal of Experimental Biology*, *206*, 1059-1073.

Lighthill, M. J. (1970). Aquatic animal propulsion of high hydromechanical efficiency. *Journal of Fluid Mechanics*, *44*(2), 265-301.

Lim, K. B., & Tay, W. B. (2010). Numerical analysis of the S1020 airfoils in tandem under different flapping con figurations. *Acta Mechanica Sinica*, *26*(2), 191-207.

Lobstein, T., Baur, L., & Uauy, R. (2004, May). Obesity in children and young people: a crisis in public health. *Obesity Reviews*, *5*, 485.

MacCready, P. (n.d.). *[Pogo Foil photo].* Retrieved from `http://faculty.washington.edu/pmacc/pogo_foil.htm`.

MacCready, P. (1986). Features of flapping wing propulsion. In A. Abbott (Ed.), *the Third International Human Powered Vehicle Scientific Symposium Proceedings* (p. 45-52). Seal Beach, CA, USA.

MacCready, P. (1990a). Hydrofoil boats with flapping-wing propulsion. *Human Power*, *8*(1), 9-16.

MacCready, P. (1990b). *[Sketched schematic of the Mutiny on the Boundary Layer].* Human Power, 8(1): p14.

MacCready, P. (1990c). *[Sketch of the Pogo Foil].* Human Power, 8(1): p15.

MacCready, P. (Accessed 2012). *The pogo foil - a human powered boat with flapping wing propulsion.* `http://faculty.washington.edu/pmacc/Research/pogo_foil.htm`.

Manley, J., & Willcox, S. (2010). The wave glider: A new concept for deploying ocean instrumentation. *IEEE Instrumentation & Measurement Magazine*, *13*(6), 8-13.

Mantia, M. L., & Dabnichki, P. (2011). Effect of the wing shape on the thrust of flapping wing. *Applied Mathematical Modelling*, *35*, 4979-4990.

Matveev, K., & Duncan, R. (2005). Development of the tool for predicting hydrofoil system performance and simulating motion of hydrofoil-assisted boats. In *the proceedings of the High Speed and High Performance Ship and Craft Symposium.* Everett, WA.

McCartney, N., Heigenhauser, G. J., & Jones, N. L. (1983). Power output and fatigue of human muscle in maximal cycling exercise. *Journal of Applied Physiology*, *55*(1), 218-224.

MIT. (Accessed 2009). *Decavitator history.* `http://lancet.mit.edu/decavitator/History.html`.

Morison, J., Johnson, J., & O'Brien, M. (1953). Experimental studies of forces on piles. In *Coastal Engineering.* Chicago, Illinois.

Morrell, J. (Accessed 2010). *Yale sculling hydrofoil sculling project.* `http://pantheon.yale.edu/~jbm42/Hydrofoil.htm`.

Morton, R. H. (1990). Modelling human power and endurance. *Journal of Mathematical Biology*, *28*, 49-64.

Morton, R. H., & Hodgson, D. J. (1996). The relationship between power output and endurance: a brief review. *European Journal of Applied Physiology*, *73*, 491-502.

Mosier, A. R. (1988, April). *Swim fin having multiple articulating transverse hydrofoil blades.* Patent US 4,944,703.

Muench, C., Ausoni, P., Farhat, M., & Avellan, F. (2007, October). 2d oscillating hydrofoil. In *the proceedings of the* 2^{nd} *IAHR International Meeting of the Workgroup on Cavitation and Dynamic Problems in Hydraulic Machinery and Systems.* Timisoara, Romania.

Murray, M. M., & Howle, L. E. (2003). Spring stiffness influence on an oscillating propulsor. *Journal of Fluids and Structures*, *17*, 915-926.

Newman, J. N. (1977). *Marine hydrodynamics.* The MIT Press.

of Toronto Institute for Aerospace Studies, U. (n.d.). *Human-powered ornithopter project.* `http://hpo.ornithopter.net/`.

Oritsland, T. (1991). Letter to the editor, foil propelled boat. *Human Power*, *9*(2), 3.

Otter, A. (1990). Damping forces on a cylinder oscillating in a viscous fluid. *Applied Ocean Research,*, *12*(3), 153-155.

Ozen, C. A., & Rockwell, D. (2010, February). Control of vortical structures on a flapping wing via a sinusoidal leading-edge. *Physics of Fluids*, *22*.

Pabst, W. (1930). *Theory of the landing impact of seaplanes* (Tech. Rep. No. T.M. No. 580). NACA.

Pacific Blue. (Accessed 2012). *[Pumpabike image].* Retrieved from `http://www.pacificblueasia.com/en/pompabike.html`.

Patnaik, B. S. V., Narayana, P. A. A., & Seetharamu, K. N. (1998, December). Numerical simulation of laminar flow past a transversely vibrating circular cylinder. *Journal of Sound and Vibration*, *228*(3), 459-475.

Payne, P. R. (1981). The virtual mass of a rectangular flat plate of finte aspect ratio. *Ocean Engineering*, *8*(5), 541-545.

Pendergast, D., Zamparo, P., Prampero, P. E. D., Capelli, C., Cerretelli, P., Termin, A., ... Mollendorf, J. (2003). Energy balance of human locomotion in water. *Journal of Applied Physiology*, *90*, 377-386.

Piziali, R. A. (1994, September). *2-D and 3-D oscillating wing aerodynamics for a range of angle of attack including stall* (Tech. Rep. No. TM-4632). NASA.

Platzer, M. F., & Jones, K. D. (2000, September). The unsteady aerodynamics of flapping-foil propellers. In *the proceedings of the* 9^{th} *International Symposium on Unsteady Aerodynamics, Aeronautics and Aeroelasticity of Turbomachines.* Ecole Centrale de Lyon, Lyon, France.

Prempraneerach, P., Hover, F. S., & Triantafyllou, M. S. (2003, August). The effect of chordwise flexibility on the thrust and effeciency of a flapping foil. In *the proceedings of the* 13^{th} *International Symposium Unmanned Untethered Submersible Technology Proceedings.* Durham.

Prud'homme, R. (2010). *Flows of reactive fluids.* Springer.

Pumpabike. (Accessed 2008). *Pumpabike.* `http://www.pumpabike.com/Site1/`.

Puzey, M. (1997, August). *Water vehicle.* Patent WO 97/29010.

Puzey, M. (2000, August). *Water vehicle.* Patent US 6,099,369.

Randall, D. J., Conte, F. P., & Hoar, W. S. (2001). *Tuna: Physiology, ecology and evolution* (Vol. 19). Academic Press.

Rashid, F., Vartdal, M., & Grue, J. (2011). Oscillating cylinder in viscous fluid: calculation of flow patterns and forces. *Journal of Engineering Mathematics*, *70*, 281-295.

Read, D. A., Hover, F. S., & Triantafyllou, M. S. (2003). Forces on oscillating foils for propulsion and maneuvering. *Journal of Fluids and Structures*, *17*, 163-183.

Reuss, R. L., Hoffmann, M. J., & Gregorek, G. M. (1995, December). *Effects of surface roughnessand vortex generators on the naca 4415 airfoil* (Tech. Rep. No. NREL/TP-442-6472). Columbus, Ohio: The Ohio State University.

Rostami, M., Ardeshir, A., Ahmadi, G., & Thomas, P. J. (2006). Can the history force be neglected for the motion of particles at high subcritical reynolds number range? *IJE Transactions B: Applications*, *19*(1), 23-34.

Sahin, M., Sankar, L. N., Chandrasekhara, M. S., & Tung, C. (2003, January-February). Dynamic stall alleviation using a deformable leading edge concepta numerical study. *Journal of Aircraft*, *40*(1), 77-85.

Sahlin, A. (1998, January). *Swedish design database.* Registration number 64539.

Sajonia, C. B. (1988). *Random wave forces on a free-to-surge vertical cylinder.* Unpublished master's thesis, Texas A&M University.

Samek, A., & Latacz, M. (2007). *A method for generating wave motion of watercraft.* Patent WO 2007/139408 A2.

Sarpkaya, T. (1976, February). *Vortex shedding and resistance in harmonic flow about smooth and rough circular cylinders at high reynolds numbers* (Tech. Rep. No. NPS-59SL76021). Monterey, California: Naval Postgraduate School.

Sarpkaya, T. (1986). Forces on a circular cylinder in viscous oscillating flow at low keulegan-carpenter numbers. *Journal of Fluid Mechanics*, *165*, 61-71.

Sarpkaya, T. (2005). On the parameter $\beta = \mathrm{Re/KC} = \mathrm{D}^2/\nu\mathrm{T}$. *Journal of Fluids and Structures*, *21*, 435-440.

Sarpkaya, T., & Garrison, C. J. (1963, March). Vortex formation and resistance in unsteady flow. *Journal of Applied Mechanics*, *30*.

Sarpkaya, T., & Isaacson, M. (1981). *Mechanics of wave forces on offshore structures.* Van Nostrand Reinhold Company Inc.

Scherer, J. O. (1968, May). *Experimental and theoretical investigation of large amplitude oscillating foil propulsion systems* (Tech. Rep. No. 662-1). Hydronautics Incorporated.

Schmidt, W. (1965a). Der wellpropeller, ein neuer antrieb fr wasser- land- und luftfahrzeuge. *Z. Flugwiss*, *13*, 472-479.

Schmidt, W. (1965b). *Driving arrangement for land-,water- and aircraft.* Patent 3,215,371.

Schmidt-Nielsen, K. (1972, July). Locomotion: Cost of swimming, flying and running. *Science*, *177*, 222-228.

Schnipper, T., Andersen, A., & Bohr, T. (2009). Vortex wakes of a flapping foil. *Journal of Fluid Mechanics*, *633*, 411-423.

Shafiee-far, M., Massie, W. W., & Vugts, J. H. (1996, May). The validity of morison equation extensions. In *Offshore Technology Conference.* Houston, Texas.

Siekmann, J. (1962). Theoretical studies of sea animal locomotion, part 1. *Archive of Applied Mechanics*, *31*(1), 214-228.

Siekmann, J. (1963). Theoretical studies of sea animal locomotion, part 2. *Archive of Applied Mechanics*, *32*(1), 40-50.

Sivertsen, D. (1990a). *[The Mutiny on the Boundary Layer, foilboure, ridden by the author].* Hydrofoil boats with flapping-wing propulsion. Human Power, 8(1), 9-16.

Sivertsen, D. (1990b). *[The Mutiny on the Boundary Layer, on the dock at Puddingstone Lake, CA].* Hydrofoil boats with flapping-wing propulsion. Human Power, 8(1), 9-16.

Smith Aerospace Corp. (2012). *Smith Aerospace Corp. website.* `http://smithaerospace.us`.

Sofge, E. (2009, October). Navy seals could turn superhuman with pentagon's powerswim. *Popular Mechanics*.

Stanway, J. (2008). The turtle and the robot. *Oceanus Magazine*, *47*(1), 22-25.

Stokes, G. G. (1851). On the effect of internal friction of fluids on the motion of pendulums. *Transactions of the Cambridge Philosophical Society*, *9*, 8-106.

Suthon, P., & Dalton, C. (2012). Observations on the honji instability. *Journal of Fluids and Structures*, *32*, 27-36.

Tagesschau. (1953). *[Wasserläufer photos].* Frames from the video "Der Wasserläufer".

Tatsuno, M., & Bearman, P. W. (1990). A visual study of the flow around an oscillating circular cylinder at low keulegancarpenter numbers and low stokes numbers. *Journal of Fluid Mechanics*, *211*, 157-182.

Tay, W. B., & Lim, K. B. (2009, August). Analysis of non-symmetrical flapping airfoils. *Acta Mechanica Sinica*, *25*(4), 433-450.

Taylor, G. K., Nudds, R. L., & Thomas, A. L. R. (2003, October). Flying and swimming animals cruise at a strouhal numbers tuned to high power efficiency. *Nature*, *425*, 707-711.

Terao, Y. (2009, May-June). Wave devouring propulsion system - from concept to trans-pacific voyage. In *the proceedings of the ASME* 28^{th} *International Conference on Ocean, Offshore and Arctic Engineering.* Honolulu, Hawaii, USA.

Theodorsen, T. (1935). *General theory of aerodynamic instability and the mechanism of flutter* (Tech. Rep. No. NACA-TR-496). National Advisory Committee for Aeronautics.

Trampofoil. (Accessed 2009). `http://www.trampofoil.com`.

Trampofoil info. (Accessed 2009). `http://www.trampofoil.info/indexen.html`.

[Trampofoil photo]. (Accessed 2012). Retrieved from `http://www.wind-water.nl/trampo_0.htm`.

Triantafyllou, G. S., Triantafyllou, M. S., & Grosenbaugh, M. A. (1993). Optimal thrust development in oscillating foils with applicaiton to fish propulsion. *Journal of Fluids and Structures*, *7*, 205-224.

Triantafyllou, M. S. (1995, March). *Propulsion mechanism employing flapping foils.* Patent US 5,401,196.

Triantafyllou, M. S. (1998, September). *Propulsion mechanism employing flapping foils.* Patent EP 0,728,009.

Triantafyllou, M. S. (1999, December). *Human powed marine vehicle and method for the operation thereof.* Patent US 5,997,369.

Triantafyllou, M. S., Hover, F. S., Techet, A. H., & Yue, D. K. P. (2005, July). Review of hydrodynamic scaling laws in aquatic locomotion and fishlike swimming. *Applied Mechanics Reviews*, *58*, 226-237.

Triantafyllou, M. S., Techet, A. H., Zhu, Q., Beal, D. N., Hover, F. S., & Yue, D. K. (2002). Vorticity control in fish-like propulsion and maneuvering. *Integrative and Comparative Biology*, *42*, 1026-1031.

Triantafyllou, M. S., & Triantafyllou, G. S. (1995, March). An efficient swimming machine. *Scientific American*, *272*(3), 64-70.

Triantafyllou, M. S., Triantafyllou, G. S., & Gopalkrishnan, R. (1991, December). Wake mechanics for thrust generation in ocsillating foils. *American Institute of Physics, Physics of Fluids A*, *3*(12), 2835-2837.

Triantafyllou, M. S., Triantafyllou, G. S., & Yue, D. K. P. (2000). Hydrodynamics of fishlike swimming. *Annual Review of Fluid Mechanics*, *32*, 33-53.

Troesch, A. W., & Kim, A. K. (1991). Hydrodynamic forces acting on cylinders oscillating at small amplitudes. *Journal of Fluids and Structures*, *5*, 113-126.

Tuncer, I. H., Walz, R., & Platzer, M. F. (1998). A computational study on the dynamic stall of a flapping airfoil. In *the proceedings of the* 16^{th} *Applied Aerodynamics Conference.*

Ulrich, K. T. (2006, July). *The environmental paradox of bicycling.* (Available at SSRN: `http://ssrn.com/abstract=1335210orhttp://dx.doi.org/10.2139/ssrn.1335210`)

Umar, F., Hamdani, H. R., ul Haque, A., Chaudhry, S. R., & Parvez, K. (2009). CFD analysis of an oscillating wing at various reduced frequencies. *The International*

Journal of Numerical Methods in Fluids, *59*, 173-194.

Vandenberghe, N., Childress, S., & Zhang, J. (2006). On unidirectional flight of a free flapping wing. *Physics of Fluids*, *18*, 014102.

Videler, J., & Kamermans, P. (1985, June). Differences between upstroke and downstroke in swimming dolphins. *The Journal of Experimental Biology*, *119*, 268-274.

Visbal, M. R. (2009). High-fidelity simulation of transitional flows past a plunging airfoil. *AIAA Journal*, *47*(11), 2685-2699.

von Kármán, T., & Sears, W. R. (1938, August). Airfoil theory for non-uniform motion. *Journal of Aeronautical Sciences*, *5*(10), 379-390.

VortiSeas Innovations LLC. (2012). *Freedom Fins website.* `http://www.freedomfins.com`.

Wadlin, K. L., Shuford, C. L., & McGehee, J., Jr. (1955). *A theoretical and experimental investigation of the lift and drag characteristics of hydrofoils at subcritical and supercritical speeds* (Tech. Rep. No. T.R. No. 1232). NACA.

Welbergen, E., & Clijsen, L. P. V. M. (1990). The influence of body position on maximal performance in cycling. *European Journal of Applied Science*, *61*, 138-142.

Williamson, C. H. K., & Roshko, A. (1988, July). Vortex formation in the wake of an oscillating cylinder. *Journal of Fluids and Structures*, *2*(4), 355381.

Wilson, D. (1986a). The 1988 delft waterbike regatta. *Human Power*, *7*(3), 11-14.

Wilson, D. (1986b). Wide variety of boats at EXPO-86 IHPVA. *Human Power*, *5*(3), 1-6.

Woodcock, J., Banister, D., Edwards, P., Prentice, A. M., & Roberts, I. (2007, September). Energy and transport. *The Lancet*, *370*(3), 10781088.

Wu, T.-T. (1961). Swimming of a waving plate. *Journal of Fluid Mechanics*, *10*, 321-344.

Wu, T.-T. (1971). Hydromechanics of swimming propulsion, part 2. *Journal of Fluid Mechanics*, *46*, 521-544.

Xiao, Q., & Liao, W. (2010). Numerical investigation of angle of attack profile on propulsion performance of an oscillating foil. *Computers and Fluids*, *39*, 1366-1380.

Xie, T., & Vassalos, D. (2007). Performance analysis of 3D hydrofoil near free surface. *Ocean Engineering*, *34*, 1257-1264.

Yadykin, Y., Tenetov, V., & Levin, D. (2003). The added mass of a flexible plate oscillating in a fluid. *Journal of Fluids and Structures*, *17*, 115-123.

Yamaguchi, H., & Bose, N. (1994, April). Oscillating foils for marine propulsion. In *the proceedings of the Fourth International Offshore and Polar Engineering Conference.* Osaka, Japan.

Yamamoto, I., Terada, Y., Nagamatu, T., & Imaizumi, Y. (1995, January). Propulsion system with flexible/rigid oscillating fin. *IEEE Journal of Oceanic Engineering*, *20*(1), 23-30.

Yang, C., & Lee, Y. (2006). Vortex flow patterns of a heaving foil. *Journal of Visualization*, *9*(1), 13-21.

Yasko, M. (1988). Boundary element method for a hydrofoil near the free surface. *Engineering Analysis with Boundary Elements*, *21*, 191-194.

Young, J., & Lai, J. C. S. (2001, December). Frequency and amplitude effects in the wake of a plunging airfoil. In *the proceedings of the* 14^{th} *Australasian Mechanics Conference Proceedings* (p. 163-166). Adelaide University, Adelaide, Australia.

Yu, Y.-T. (1945, November). Virtual masses of rectangular plates and parallelepipeds in water. *Journal of Applied Physics*, *16*, 724-729.

Zamparo, P., Carignani, G., Plaino, L., Sgalmuzzo, B., & Capelli, C. (2008, January). Energy-balance of locomotion with pedal-driven watercraft. *Journal of Sports Sciences*, *26*(1), 75-81.

Zhang, X., min Su, Y., Yang, L., & li Wang, Z. (2010). Hydrodynamic performance of flapping-foil propulsion in the influence of vortices. *Journal of Marine Science and Application*, *9*, 213-219.

Zhang, Y., Song, Y., Yang, J., & Low, K. H. (2008). Numerical and experimental research on modular oscillating fin. *Journal of Bionic Engineering*, *5*, 13-23.

Zhen, L., Beom-soo, H., Moo-rong, K., & Ji-yuan, J. (2008). Experimental and numerical study for hydrodynamic characteristics of an oscillating hydrofoil. *Journal of Hydrodynamics*, *20*(3), 280-287.

Zhu, C., & Fan, L.-S. (1998). *The handbook of fluid dynamics* (R. W. Johnson, Ed.). CRC Press LLC and Springer-Verlag GmbH & Co. KG.

Zhu, Q., Liu, Y., & Yue, D. K. P. (2006, December). Dynamics of a three-dimensional oscillating foil near the free surface. *AAIA Journal*, *44*(12), 2997-3009.

Appendix A

Statistical Uncertainty for Static Measurements Acquired with the Load Cell Assembly

Measurements taken with the load cell assembly in either axis are the sum of four measurements made via the four load cells supporting the respective axis. Since each load cell set is mechanically connected, the individual load cell measurements are considered dependent. Estimating the accuracy of this system via an error analysis of the individual components would be complex so the accuracy was determined via statistical samples instead.

A.1 Single Component Loads

Before samples were taken from the load cell assembly, the gain and offsets were set via hanging calibration weights, the same method executed before any experiment: The offset of the unloaded system was adjusted, and a known load was applied to one axis only while the gain of this axis was calculated. The calibration procedure was repeated to find the gain for the remaining axis. To find the repeatability of the load cell assembly for pure horizontal or vertical loads, 10 different known loads were applied to the load cell assembly parallel to each measurement axis. The loads were applied at the end of the

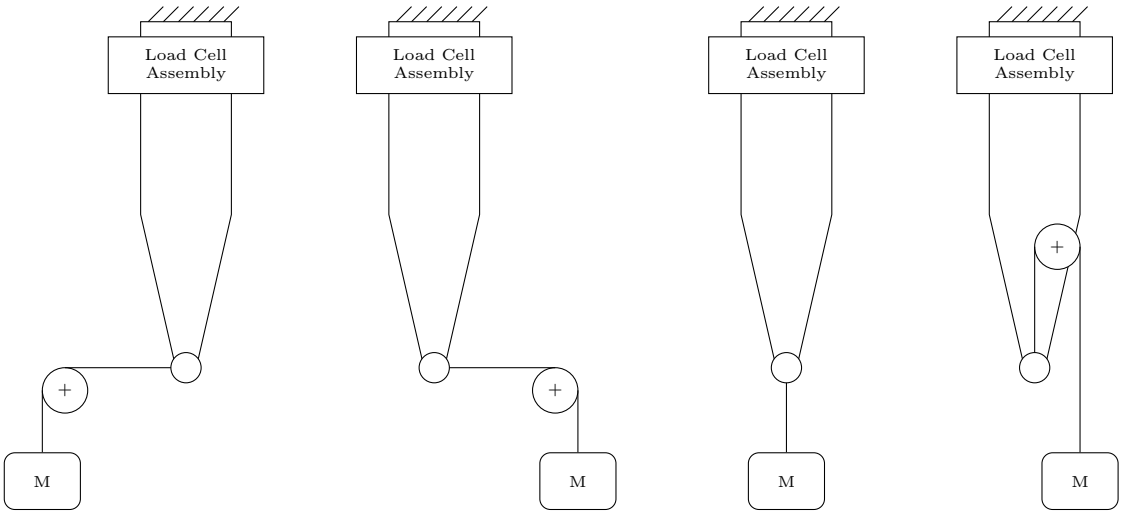

(a) Thrust **(b)** Drag **(c)** Downforce **(d)** Lift

Figure A.1. Arrangement of hanging weights and pulleys to apply load parallel to the two measurement axis in either direction.

struts where the foil would usually be mounted. Fifty of five second samples were recorded for each load.

Loads applied to the load cell assembly were provided by means of hanging weights and pulleys as illustrated in Figure A.1. To apply a load to a single axis, the line of the string must be perfectly parallel to the measurement axis. In practice this is difficult to achieve, which leads to calibration measurement errors. The load cell assembly was very sensitive to the load direction and will therefore sense very small changes in the location of the pulley guiding the string that supports the weight. Since the frame supporting the pulley was not infinitely stiff, there were small deflections in that frame when the load was applied. These deflections resulted in the pulley's position changing, relative to the load cell assembly, when the load was applied.

Measurements were recorded unfiltered so that estimates on typical noise could be made. Masses were hung carefully during the experiment and left to settle. However any remaining small load oscillations added to the spread of the static measurements.

Figures A.2 and A.3 show the means of the 10 repeated load measurements over the full-scale range of the load cell assembly in the surge and heave axis respectively. Due

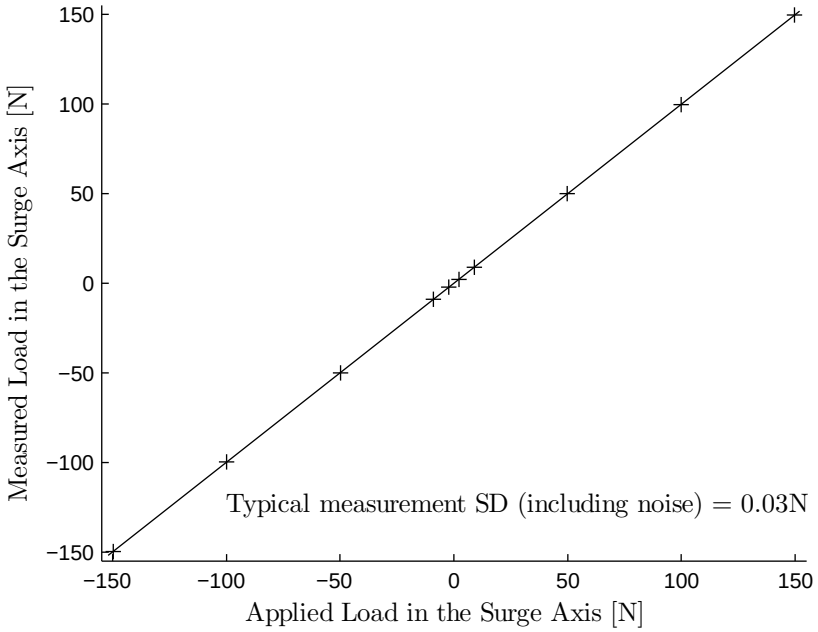

Figure A.2. Applied load versus measured load for the surge axis of the load cell assembly.

to the large range of load magnitudes, the spread of the data is too small to show on these plots. Figures A.4 and A.5 show the measurement bias (mean error of a sample) with the two standard deviation range from the bias. Figures A.6 and A.7 plot the cross-talk of each axis. The distribution of the repeated measurements for each load case was approximately normal. Statistics presented in Figures A.2 to A.7 are all for unfiltered data. Table A.1 summarizes this data in tabular form. Table A.2 contains the p-values for linear correlation between applied load and either the measurement bias or cross-talk. It also contains p-values for the linear correlation between the absolute applied load and the standard deviation of the measurements. P-values less than 0.05 indicate a statistically significant correlation between the two variables.

Table A.1 shows that filtering the data has no appreciable effect on the measurements bias. However it does significantly affect the spread of the data. Unfiltered data recorded from the unloaded load cell had a typical standard deviation of 0.04 N due to signal noise. This is evident in Table A.1, where unfiltered data has a typical standard deviation of 0.03 N-0.04 N and filtered measurements have typical standard deviations of 0.00 N in

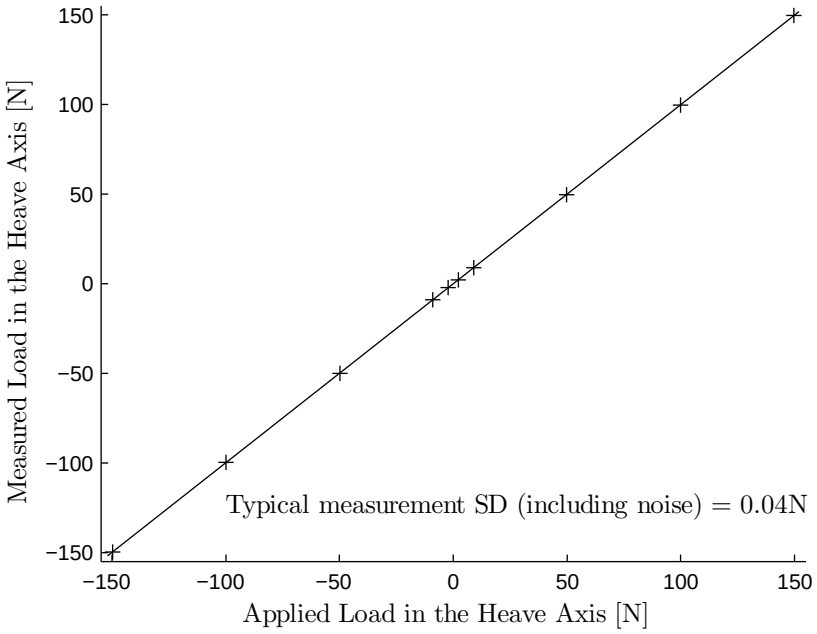

Figure A.3. Applied load versus measured load for the heave axis of the load cell assembly.

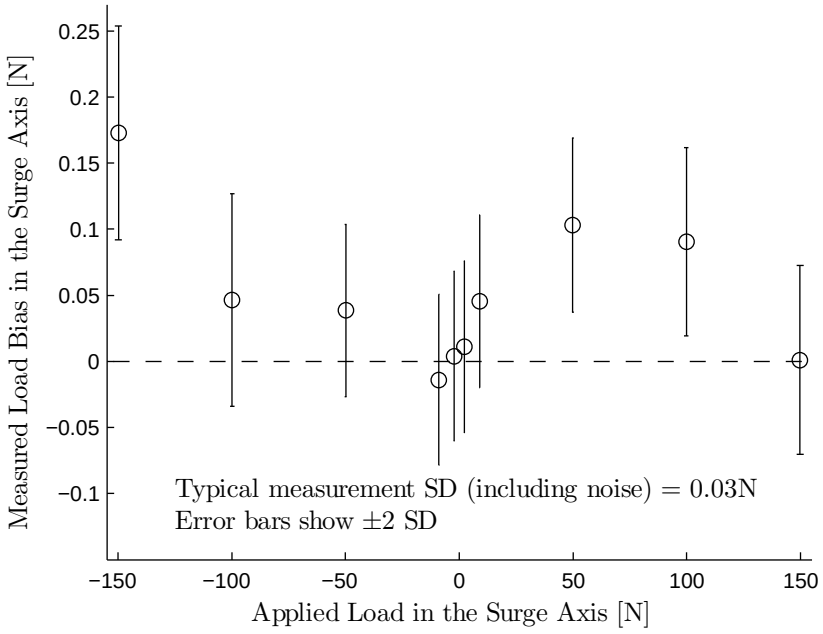

Figure A.4. Applied load versus error in the measured load for the surge axis of the load cell assembly.

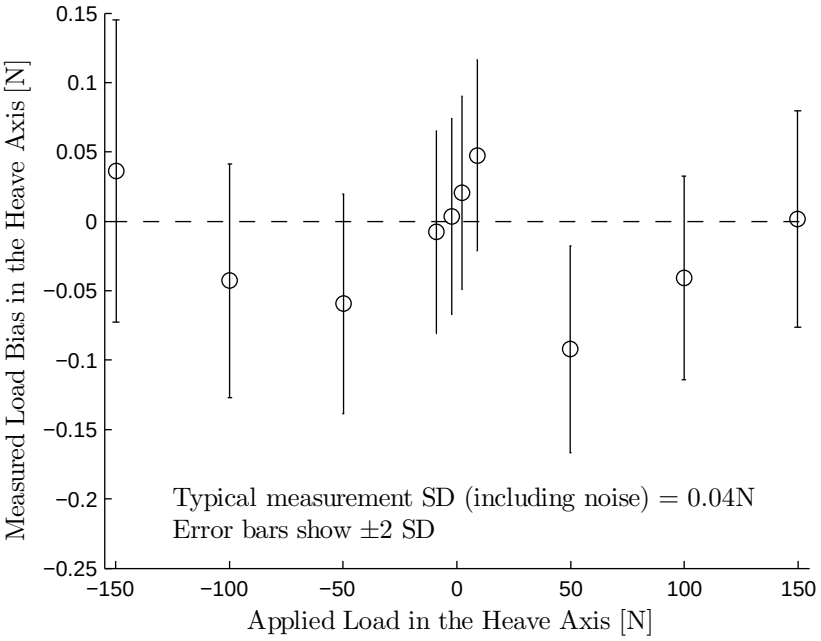

Figure A.5. Applied load versus error in the measured load for the heave axis of the load cell assembly.

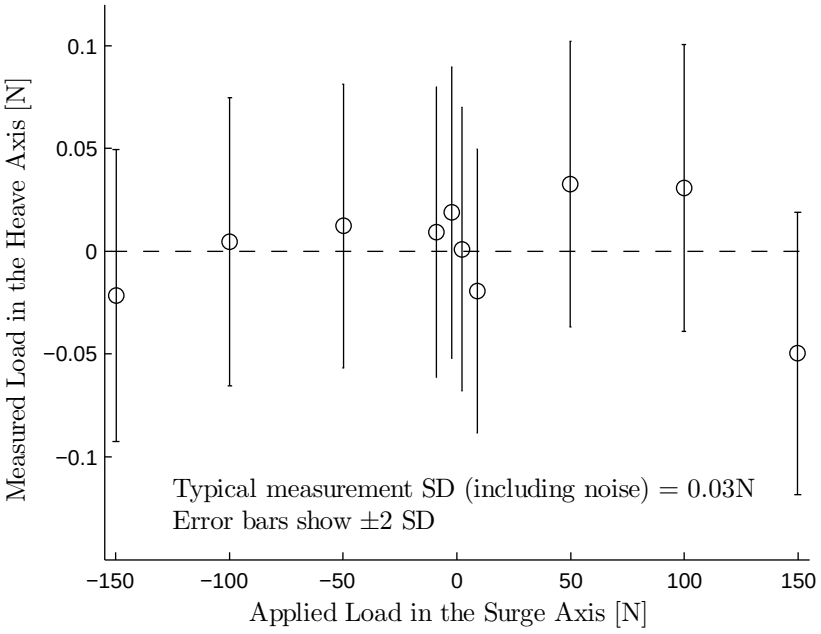

Figure A.6. Applied load in the surge axis versus measured load in the heave axis of the load cell assembly.

Table A.1. Mean bias and standard deviation of repeated force measurements using the load cell assembly *Unfiltered data (Filtered data)*

	Nominal Mass [kg]	Nominal Force [N]		Measurement Bias [N]				Measurement SD [N]			
		Surge	Heave	Surge		Heave		Surge		Heave	
Drag	0.230	2.26	0.00	0.01	(0.01)	0.00	(0.00)	0.03	(0.00)	0.03	(0.00)
	0.911	8.94	0.00	0.05	(0.05)	-0.02	(-0.02)	0.03	(0.01)	0.03	(0.00)
	5.092	49.95	0.00	0.10	(0.10)	0.03	(0.03)	0.03	(0.06)	0.03	(0.00)
	10.177	99.84	0.00	0.09	(0.09)	0.03	(0.03)	0.04	(0.13)	0.03	(0.00)
	15.279	149.89	0.00	0.00	(-0.00)	-0.05	(-0.05)	0.04	(0.19)	0.03	(0.00)
Thrust	0.230	-2.26	0.00	0.00	(0.00)	0.02	(0.02)	0.03	(0.00)	0.04	(0.00)
	0.911	-8.94	0.00	-0.01	(-0.01)	0.01	(0.01)	0.03	(0.01)	0.04	(0.01)
	5.092	-49.95	0.00	0.04	(0.04)	0.01	(0.01)	0.03	(0.06)	0.03	(0.00)
	10.177	-99.84	0.00	0.05	(0.05)	0.00	(0.00)	0.04	(0.13)	0.04	(0.00)
	15.279	-149.89	0.00	0.17	(0.18)	-0.02	(-0.02)	0.04	(0.19)	0.04	(0.01)
Lift	0.230	0.00	2.26	0.09	(0.09)	0.02	(0.02)	0.03	(0.00)	0.03	(0.00)
	0.911	0.00	8.94	0.07	(0.07)	0.05	(0.05)	0.03	(0.00)	0.03	(0.01)
	5.092	0.00	49.95	-0.05	(-0.05)	-0.09	(-0.09)	0.04	(0.00)	0.04	(0.07)
	10.177	0.00	99.84	-0.17	(-0.17)	-0.04	(-0.04)	0.03	(0.00)	0.04	(0.13)
	15.279	0.00	149.89	-0.05	(-0.05)	0.00	(0.00)	0.04	(0.00)	0.04	(0.19)
Downforce	0.230	0.00	-2.26	0.00	(0.00)	0.00	(0.00)	0.03	(0.00)	0.04	(0.01)
	0.911	0.00	-8.94	-0.00	(-0.00)	-0.01	(-0.01)	0.04	(0.01)	0.04	(0.02)
	5.092	0.00	-49.95	-0.02	(-0.02)	-0.06	(-0.06)	0.04	(0.03)	0.04	(0.07)
	10.177	0.00	-99.84	-0.05	(-0.05)	-0.04	(-0.04)	0.05	(0.03)	0.04	(0.13)
	15.279	0.00	-149.89	-0.18	(-0.18)	0.04	(0.04)	0.05	(0.04)	0.05	(0.20)

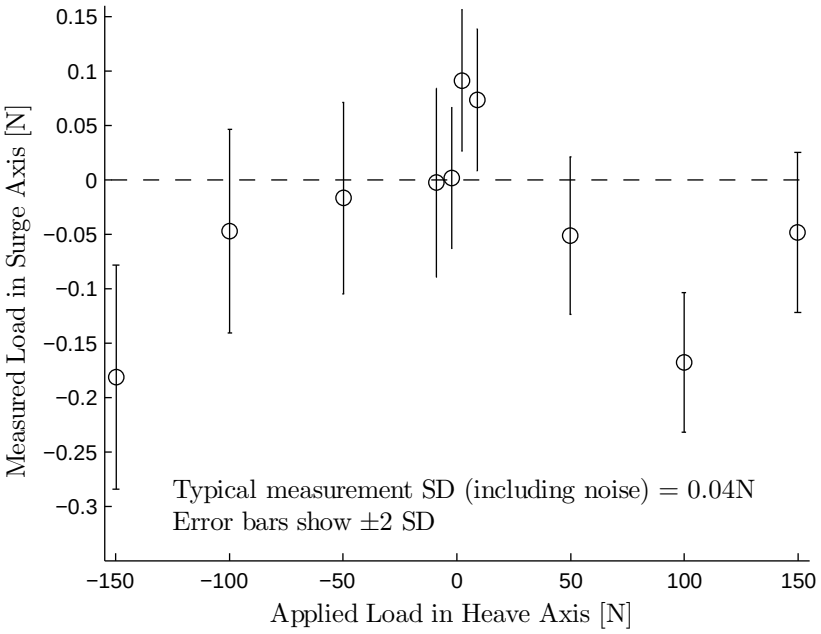

Figure A.7. Applied load in the heave axis versus measured load in the surge axis of the load cell assembly.

Table A.2. P-values for linear correlation between the applied load and measurement bias or measured cross-talk for single component loads
Unfiltered data (Filtered data)

Applied Load Direction	Drag	Thrust	Lift	Downforce
Measurement Bias	0.907 (0.867)	0.025 (0.026)	0.635 (0.633)	0.671 (0.616)
Measurement Cross-talk	0.623 (0.622)	0.040 (0.041)	0.162 (0.162)	0.031 (0.029)
Measurement SD	0.014 (0.000)	0.023 (0.000)	0.032 (0.000)	0.014 (0.000)
Cross-talk SD	0.611 (0.159)	0.851 (0.491)	0.353 (0.980)	0.074 (0.022)

the unloaded axis. Table A.1 also shows that filtered data has some non-zero standard deviation in the loaded axis, which increases in proportion to the applied load. The low p-value for the measurement standard deviation with the applied load in Table A.2 suggests that this relationship is linear. It can be shown that for a simple pendulum, the oscillation amplitude of the tension in the supporting string is proportional to the mass of the pendulum for a constant displacement amplitude. This suggests that the dependence of the standard deviation on the applied load is most likely due to the calibration mass not hanging perfectly still as mentioned earlier.

When a drag, thrust or lift load was applied, there was no correlation between the applied load and the cross-talk standard deviation (Refer to Tables A.1 and A.2). However for the downforce a linear correlation exists. This was because for the cases of drag, thrust, and lift, a pulley was required to guide the string supporting hanging weight to change the direction of the load (see Figure A.1). The pulley ensures that the direction of the applied load was constant for all loads, assuming that the defections of the load cell and the frame positioning the pulley are small. When applying a downforce load, there was no need for a guide pulley, and consequently if the weight was not hanging perfectly still, the direction of the supporting string may not be constant. If this was the case, the increasing cross-talk standard deviation for loads applied in the downforce direction were due to the load cell measuring the component of tension in the supporting string parallel to the surge axis as the weight swung.

To confirm the two previous errors a mass was hung from the load cell and allowed to settle over a period of two minutes before a sample was recorded. This test revealed that the above hypotheses were correct and the standard deviation of any sample, regardless of the load applied, is approximately 0.04 N for unfiltered data and 0.00 N for data with the low pass filter applied (see Section 4.7).

The p-values in Tables A.2 suggest that there is a linear correlation between the applied load and the thrust bias, the thrust cross-talk and the downforce cross-talk. Since the thrust bias and cross-talk are both proportional to the applied load, this is likely to be an error related to the alignment of the applied load to the true thrust axis. Figures A.4 and A.6 show that the mean bias and cross-talk is small over the load range and so this error

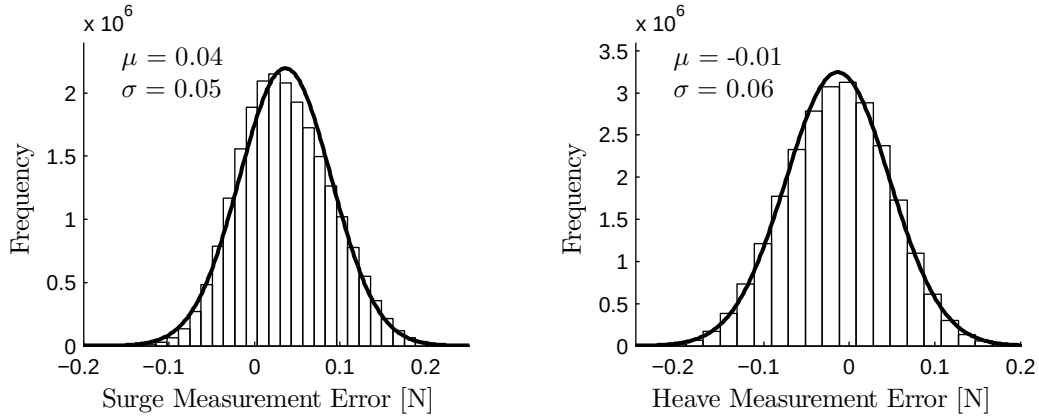

Figure A.8. Repeatability distributions for unfiltered measurements in the surge and heave axis of the load cell assembly.

can be neglected. Similarly the correlation between the applied load and the downforce cross-talk may be due to the alignment of the applied load. Figure A.7 shows that the magnitude of downforce cross-talk error is small over the load range and so this correlation will also be neglected.

Figure A.8 shows the distribution of the sample errors in the surge and heave axis. Samples taken at the maximum thrust load have been omitted from this distribution due to the suspected load alignment error discussed previously. Note that the surge bias is larger that the heave bias. However, the heave error distribution has a larger spread. Table A.3 summarizes the error distribution for both the surge, and heave axes. Since both axes had a similar error distribution, one conservative uncertainty can be applied to measurements made in either axis. The surge and heave axis maximum absolute 95 % confidence interval bounds were 0.14 N and 0.13 N, respectively. Applying the greater of the two symmetrically around future samples, means future measurements would have a 95 % confidence interval of ±0.14 N associated with them. Taking the uncertainty of a measurement due to repeatability to be approximately equal to the standard deviation, future measurements would have a symmetric repeatability uncertainty of 0.07 N.

Table A.3. Error distribution of the load cell assembly

Measurement Axis	Surge	Heave
Mean Error	0.04	-0.01
Standard Deviation	0.06	0.06
95 % CI Lower Bound	-0.07	-0.13
95 % CI Upper Bound	0.14	0.11

A.2 Two-Component Loads

Similarly to the proceeding single component load repeatability study, the repeatability for two-component loads was investigated. Two-component loads were applied to the load cell assembly by applying a known load parallel to each measurement axis as pictured in Figure A.9. Two-component loads were only applied to the thrust/downforce quadrature of the load cell assembly. The load cell performance in the other quadratures is assumed to be similar to the tested quadrature due the symmetry of the load cell assembly. Ten of five second samples of each two-component load were recorded for each of 15 different load cases.

Consistent with the single component load samples, the sample error distribution for each two-component load case was near normal. Table A.4 presents the measurement bias and error standard deviation for each two-component load case. Table A.5 contains p-values for linear correlation between the applied load and the measurement bias and error distribution.

As in the single component load cases, a linear correlation exists between the applied downforce loads, and the force measurement error distributions (refer to Table A.5). As previously discussed this is due to the hanging mass not hanging perfectly still while the measurements were taken. The p-values in Table A.5 also suggest that there is a linear correlation between the applied thrust and the downforce measurement bias, and also between the applied downforce, and thrust measurement bias. Figure A.10 illustrates an explanation for why the measurement biases were larger when two loads were applied, using the method depicted in Figure A.9. F_s and F_h represent the applied load to the undeflected load cell while F_s' and F_h' represent the applied load to the deflected load cell.

Figure A.11 is the vector diagram for this calibration error showing the applied thrust,

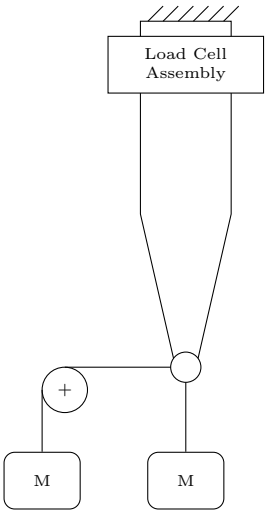

Figure A.9. Arrangement of hanging weights and pulleys to apply two-component loads to the thrust/downforce quadrature of the load cell assembly.

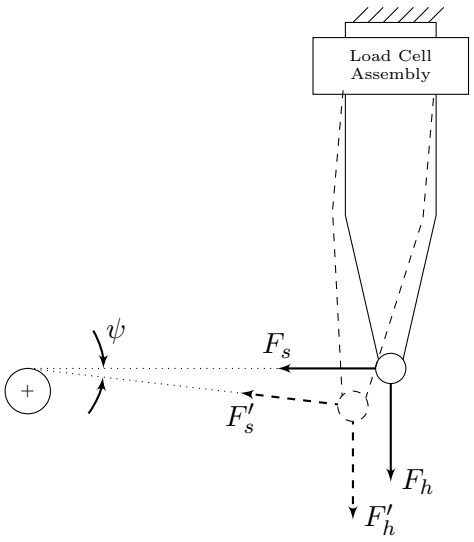

Figure A.10. An illustration of the two-component calibration error due to fixed pulley placement.

Table A.4. Mean bias and standard deviation of repeated two-component force measurements using the load cell assembly *Unfiltered data (Filtered data)*

Nominal Mass [kg]		Nominal Force [N]		Measurement Bias [N]				Measurement SD [N]			
Surge	Heave	Surge	Heave	Surge		Heave		Surge		Heave	
0.230	0.230	-2.26	-2.26	-0.02	(-0.02)	-0.00	(-0.00)	0.04	(0.01)	0.04	(0.01)
0.230	0.911	-2.26	-8.94	0.04	(0.04)	0.02	(0.02)	0.04	(0.02)	0.04	(0.01)
0.230	5.092	-2.26	-49.95	0.06	(0.06)	-0.04	(-0.04)	0.05	(0.03)	0.04	(0.02)
0.230	10.177	-2.26	-99.84	0.10	(0.09)	-0.08	(-0.08)	0.08	(0.05)	0.08	(0.08)
0.911	0.230	-8.94	-2.26	0.05	(0.05)	0.02	(0.02)	0.03	(0.01)	0.04	(0.01)
0.911	0.911	-8.94	-8.94	0.05	(0.05)	0.02	(0.02)	0.04	(0.02)	0.04	(0.01)
0.911	5.092	-8.94	-49.95	0.07	(0.07)	-0.04	(-0.04)	0.04	(0.02)	0.05	(0.04)
0.911	10.177	-8.94	-99.84	0.11	(0.12)	-0.04	(-0.03)	0.08	(0.05)	0.06	(0.06)
5.092	0.230	-49.95	-2.26	0.05	(0.05)	0.02	(0.02)	0.03	(0.01)	0.04	(0.01)
5.092	0.911	-49.95	-8.94	0.07	(0.07)	0.02	(0.02)	0.03	(0.01)	0.04	(0.01)
5.092	5.092	-49.95	-49.95	0.14	(0.14)	0.06	(0.06)	0.04	(0.02)	0.05	(0.04)
5.092	10.177	-49.95	-99.84	0.29	(0.30)	0.17	(0.17)	0.07	(0.06)	0.11	(0.10)
10.177	0.230	-99.84	-2.26	-0.01	(-0.01)	0.09	(0.09)	0.04	(0.01)	0.04	(0.01)
10.177	0.911	-99.84	-8.94	0.08	(0.08)	0.14	(0.14)	0.04	(0.01)	0.04	(0.00)
10.177	5.092	-99.84	-49.95	0.29	(0.29)	0.22	(0.22)	0.05	(0.03)	0.05	(0.03)
10.177	10.177	-99.84	-99.84	0.31	(0.30)	0.53	(0.53)	0.06	(0.04)	0.10	(0.01)

Table A.5. P-values for linear correlation between the applied load and measurement bias or measured cross-talk for two-component loads
Unfiltered data (Filtered data)

Applied Load Direction	Thrust	Downforce
Thrust Measurement Bias	0.214 (0.222)	0.011 (0.010)
Downforce Measurement Bias	0.000 (0.000)	0.767 (0.770)
Thrust Bias SD	0.473 (0.541)	0.000 (0.000)
Downforce Bias SD	0.684 (0.609)	0.000 (0.000)

F'_s, and downforce, F'_h, the translation of the object attachment point due to deflection of the load cell and the struts, Δx and Δy, and the resulting true horizontal and vertical loads applied to the load cell, F_x and F_y, respectively. Equation A.1 equates the applied loads F'_s and F'_h to the loads felt by each measurement axis of the load cell F_x and F_y. Given that the magnitudes of F'_s and F'_h are equal to those of F_s and F_h respectively, Equation A.2 and A.3 defines the magnitudes of F_x and F_y respectively in terms of F_s and F_h and angle ψ. Equation A.4 defines ψ as a function of the deflection at the end of the struts Δx and Δy.

Equation A.5 defines the measurement bias from error of method B_e as the difference between intended applied loads F_s and F_h and the actual applied loads F_x and F_y. Now assuming that the load cell and strut system deflection is linear with the applied load, the deflections Δx and Δy can be given by Equation A.6, where C_x and C_y are the compliance constants of the measurement axes. To predict the bias due to error of method with Equation A.5, first Equations A.4 and A.6 must be combined and the resulting expression solved for ψ. Alternatively, given that $\Delta x << d$, and approximating the trigonometric functions as $sin(x) \approx x$, $tan^{-1}(x) \approx x$ and $cos(x) \approx 1 - x$ for small values of x, Equation A.5 simplifies to Equation A.7.

$$\hat{F}'_s + \hat{F}'_h = \hat{F}_x + \hat{F}_y \tag{A.1}$$

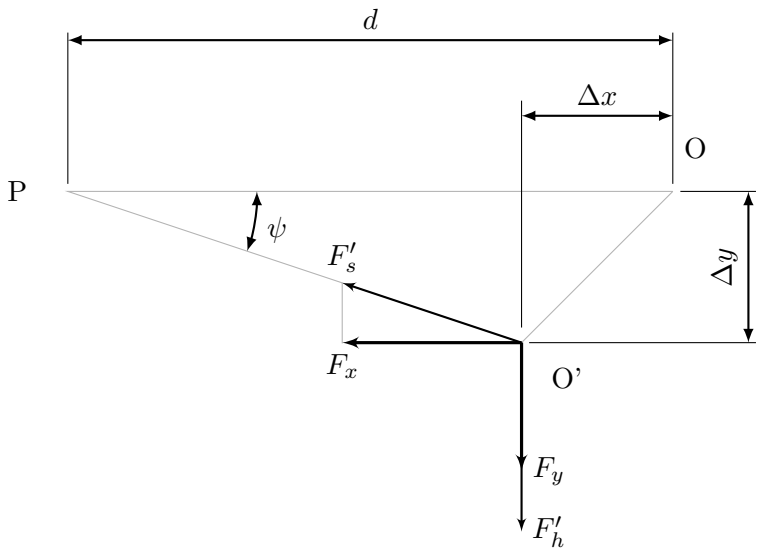

Figure A.11. A vector diagram of the two-component calibration error due to fixed pulley placement.

$$|\hat{F_x}| = |\hat{F_s}|cos(\psi) \tag{A.2}$$

$$|\hat{F_y}| = |\hat{F_h}| - |\hat{F_s}|sin(\psi) \tag{A.3}$$

$$\psi = tan^{-1}\left(\frac{\Delta y}{d - \Delta x}\right) \tag{A.4}$$

$$\hat{B_e} = \begin{bmatrix} |\hat{F_x}| - |\hat{F_s}| \\ |\hat{F_y}| - |\hat{F_h}| \end{bmatrix} = \begin{bmatrix} |\hat{F_s}|\,(cos(\psi) - 1) \\ -|\hat{F_s}|sin(\psi) \end{bmatrix} \tag{A.5}$$

$$\begin{bmatrix} \Delta x \\ \Delta y \end{bmatrix} = \begin{bmatrix} C_x|\hat{F_x}| \\ C_y|\hat{F_y}| \end{bmatrix} = \begin{bmatrix} C_x|\hat{F_s}|cos(\psi) \\ C_y(|\hat{F_h}| - |\hat{F_s}|sin(\psi)) \end{bmatrix} \tag{A.6}$$

$$\hat{B_e} \approx \frac{C_y}{d}\begin{bmatrix} -|\hat{F_s}||\hat{F_h}| \\ -|\hat{F_s}||\hat{F_h}| \end{bmatrix} \tag{A.7}$$

Figures A.12 and A.13 visually confirm a linear relationship between the drag and lift

Table A.6. Error distribution of the load cell assembly

Measurement Axis	Surge	Heave
Mean Error	0.00	0.00
Standard Deviation	0.07	0.08
95 % CI Lower Bound	-0.13	-0.16
95 % CI Upper Bound	0.13	0.16

measurement bias and the product of the applied loads $|\hat{F}_s||\hat{F}_h|$ respectively. The p-values for the linear correlations between either the drag or lift bias and $|\hat{F}_s||\hat{F}_h|$ are 1.65×10^{-6} and 3.50×10^{-7} respectively. The magnitude of these p-values indicates that error bias is very likely proportional to $|\hat{F}_s||\hat{F}_h|$ as expressed in Equation A.7.

Taking the average of the gradient from the two lines of best fit (from Figures A.12 and A.13), C_y/d from the load cell assembly is estimated to be 4.11×10^{-5}. Adjusting the calibration data for this systematic error, due to the fixed pulley position, allows the results of the two-component repeatability study to be compared fairly to the single component repeatability study results. Figure A.14 shows the distribution of the adjusted errors and Table A.6 summarises the error distribution for both surge and heave axis under two-component loads. When comparing Table A.6 to Table A.3, the error distribution in the surge and heave axes have similar spreads for single component and two-component loads. Again referring to Table A.6, the mean error in the surge and heave axes is also similar. Therefore, a conservative estimate of the load cell's error would be to apply the larger of the two biases and standard deviations to future measurements. This means that 95 % of all future measurement will fall between plus or minus the sum of the mean error and two standard deviations i.e. ± 0.20 N. Now taking the uncertainty of a measurement due to repeatability to be approximately equal to the standard deviation (Castrup & Castrup, 2010), future two-component measurements will have a symmetric repeatability uncertainty of 0.10 N.

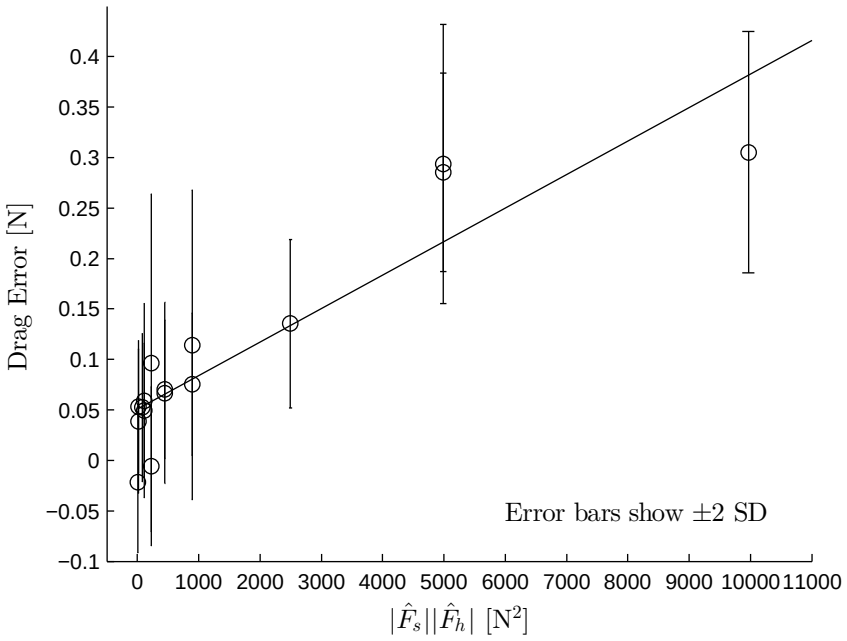

Figure A.12. Drag calibration error plotted against the product of the applied drag and lift loads.

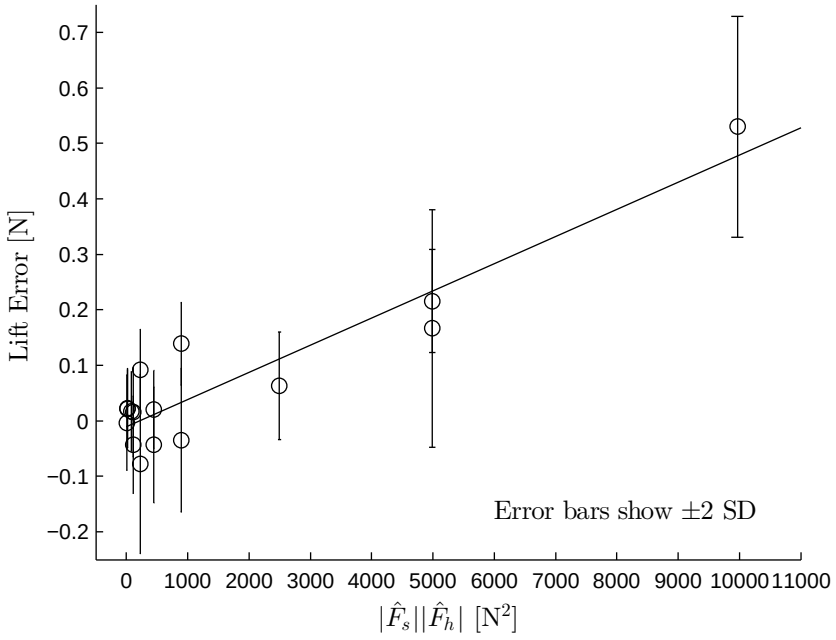

Figure A.13. Lift calibration error plotted against the product of the applied drag and lift loads.

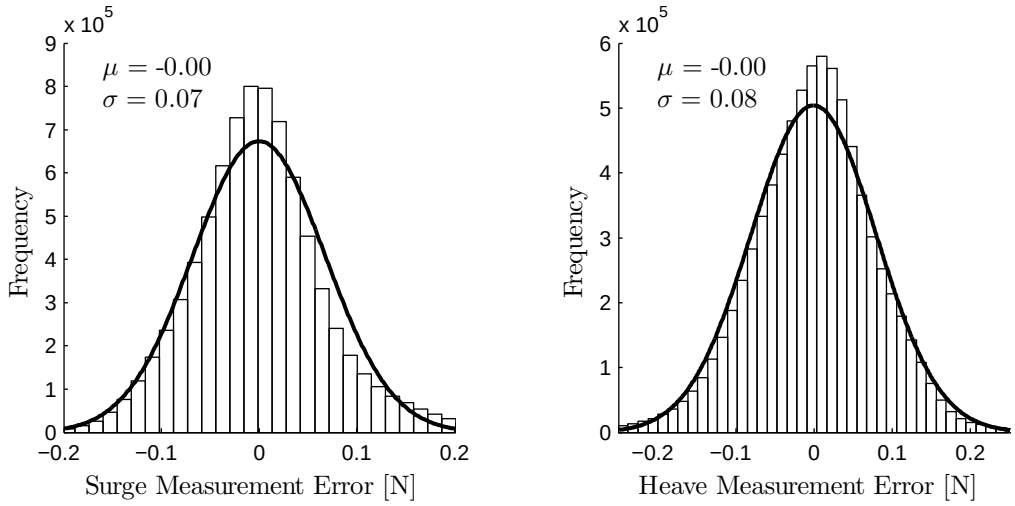

Figure A.14. Adjusted error distributions for unfiltered measurements of two-component loads with the load cell assembly.

Appendix B

Uncertainty of Dynamic Measurements Acquired with the Load Cell Assembly

Dynamic measurements present difficulties additional to those of static measurements, due their time dependence. Now the phase and frequency of the measured signal becomes important as well as the measurement amplitude. In this Appendix, suitability of the test equipment for recording dynamic force measurements is evaluated.

Consider an object of mass m mounted to the struts of the test equipment described in Section 4. Since the components of the test equipment are made from aluminium alloy and steel, internal damping is negligible, and so the equipment may be modelled by the spring mass system shown in Figure B.1. Here, the load cell assembly is represented by a spring of stiffness k. The free body diagram in Figure B.1 shows the forces on the mass when the equipment is oscillating. These forces are; the mass's own weight mg and inertia $m\ddot{y}$, any hydrodynamic force in the heave axis F_h, and the reaction of the load cell F_{lc}.

Ideally, the forces on the object would be measured proportional to its heaving motion. However, due to the test equipment having a limited stiffness, the displacement of the mass y may not be equal to the driving displacement h. Lack of stiffness in the test rig is predominantly due to the load cell assembly, which requires a certain compliance to

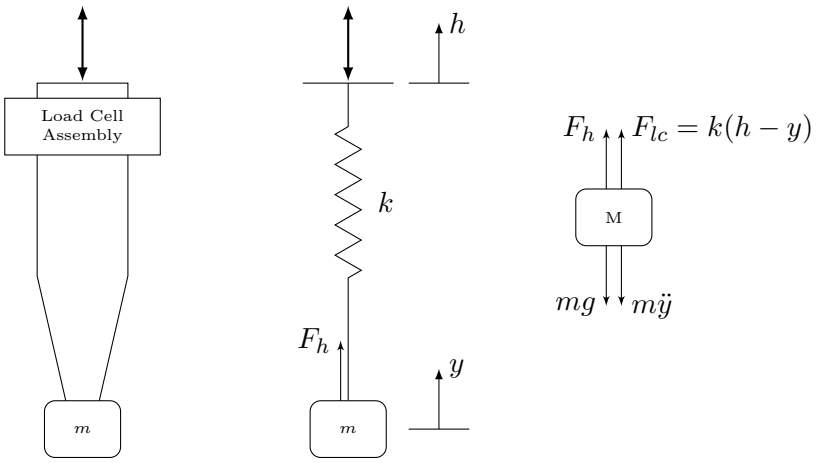

Figure B.1. Mass mounted to the struts to measure inertia forces in air.

operate. Equating the forces on the mass undergoing forced oscillations results in Equation B.1. Here the measured inertial force is a function of the objects mass, and the unknown acceleration $\ddot{y}$.

$$F_{lc} = m(\ddot{y} + g) - F_h \tag{B.1}$$

If the load cell assembly was infinitely stiff, the displacement response of the mass y would equal the forcing heaving profile h. In this case the force on the load cell assembly would equate to hydrodynamic heaving forces in addition to the mass's weight and inertia proportional to m and $\ddot{h}$. However, in this scenario the load cell assembly would have zero output due to its infinite stiffness. Hence, measuring the forces on the object, via strain based measurements, introduces some error proportional to $m(\ddot{y} - \ddot{h})$.

To minimise this error, the stiffness of the load cell can be increased, to minimise the difference between h and y. However, as mentioned above, increasing the stiffness of the load cell reduces its sensitivity. Reducing the oscillating mass will also reduce the error in the force measurements. To reduce the weight of the test objects while maintaining stiffness, the majority were constructed from from carbon fibre (see Section 4.3).

Before continuing, it is important to make clear the term 'error' in this context. The load cell assembly is subject to an oscillating load due to the test object inertia in sub-

sequent results. The load cycle measured by the load cell is the true load cycle that it experiences, to the accuracy of the static measurements as described in Appendix A. However, due to limited stiffness of the equipment, this load cycle differs from the load cycle the load cell assembly would experience if the equipment, and the load cell assembly, were rigid. Since the measured load cycles are compared to the heaving cycles (in the results chapters of this thesis), the load cycles ideally would be measured with no phase difference, or change in amplitude response with respect to the heaving motion. However, due to the stiffness limitations of the strain based force sensors, this is difficult to achieve. To sum up, the term 'dynamic measurement error' in this appendix does not refer to a random measurement error, but refers to the systematic difference between the desired measurement and the measurement that has been recorded. This difference is due to the stiffness limitation of the force sensing elements.

To check that the stiffness of the load cell assembly was sufficiently high, so that $\ddot{y} \approx \ddot{h}$, the inertia of a mass was recorded in air as illustrated in Figure B.1. The mounted mass was chosen large enough to represent the mass of a test object, end plates, and added mass (in-phase components on F_h) acting on the load cell assembly. The test procedure involved firstly statically calibrating the load cell assembly gain and offset, and recording the inertia of the oscillating struts alone. Secondly, the inertial forces of the oscillating struts with the mass m fixed to them was recorded. Finally, the inertial forces of the struts were subtracted from the force measurements with the mounted mass. The remaining forces should be approximately equal to the weight and the inertia of the mounted mass (i.e. $m\ddot{h} - mg$). All tests were conducted with a heave amplitude of 0.45 mm.

Aerodynamic forces on the object while oscillating in air were considered negligible compared to the measured inertial forces. Therefore, the dynamic measurement error ϵ_d is the difference between the measured heaving force F_h and the expected inertia force based on the heaving acceleration $m\ddot{h}$ (Equation B.2). In the following analysis ϵ_d in calculated on a point-wise basis (see Figure B.7).

$$\epsilon_d = F_h - m\ddot{h} \tag{B.2}$$

Figures B.2 to B.4 show the measured inertia forces, at various frequencies, for three

different masses mounted to the struts. Figure B.2 shows inertia measurements with the flat plate and end plates of 5.3 chord diameter mounted to the struts. This is the heaviest combination of objects ever mounted to the struts in the experiments published in this thesis. In each figure, the measured inertia forces (in red) are compared to the calculated inertia forces that would be measured by rigid equipment ($m\ddot{h}$, in black). The difference between the two cycles is due to the compliance of the current test rig as discussed above. Figure B.5 shows the mean dynamic measurement error with the error spread over the working range of oscillating frequencies.

Cycles plotted in Figures B.2 to B.4 show that the point-wise dynamic measurement error is largest at the turning points of the cycle (i.e. either at top dead centre or bottom dead centre). At these locations, the heave acceleration is largest and so inertial effects are most prominent. The force measurement not only varies in amplitude from the $m\ddot{h}$ cycle, but also has a phase shift. Surprisingly the phase of the force measurement maximum lags the $m\ddot{h}$ cycle cycle maximum, but the force measurement minimum leads the $m\ddot{h}$ cycle minimum at low frequencies. This illustrates that the response of the compliant measurement system distorts the measured force cycle profiles with respect to the $m\ddot{h}$ cycle.

Referring to Figure B.5, the point-wise dynamic measurement error is similar for all the tested masses. Figures B.2 to B.4 show that the force measurements tend to evenly underestimate and overestimate the $m\ddot{h}$ cycle throughout a single period. This is also evident in Figure B.5 where the point-wise dynamic mean is near zero. The spread of the dynamic measurement error is largest at low oscillating frequencies. However, the measurement uncertainty is also large at low oscillating frequencies, and so the $m\ddot{h}$ cycle stays within the measurement ± 2 SD bounds. Figure B.6 shows that the absolute spread of data is relatively insensitive to the oscillating frequency and the magnitude of the heaving forces. So as the heaving forces increase in magnitude, the measurement uncertainty decreases relative to the cycle amplitude. Consequently, at high oscillating frequency the $m\ddot{h}$ cycle escapes the ± 2 SD bounds of the measurement. This clearly shows that the ± 2 SD measurement uncertainty adequately includes the effects of dynamic error at low oscillating frequencies, but not at high oscillating frequencies.

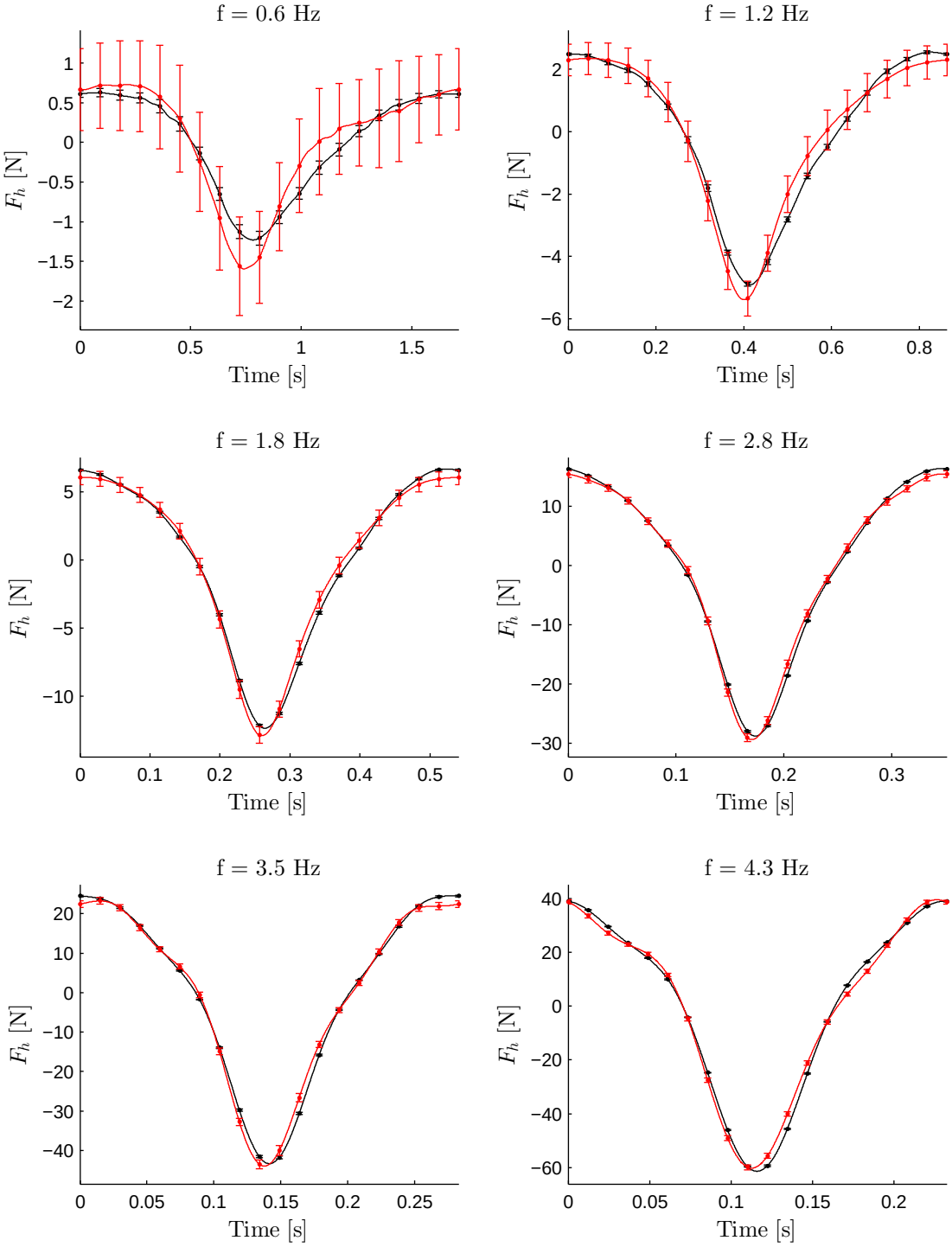

Figure B.2. Comparison of the measured inertia of the flat plate with 5.3 chord length diameter end plates (total mass: 1.373 kg), and the mass multiplied by the heaving acceleration, $m\ddot{h}$.

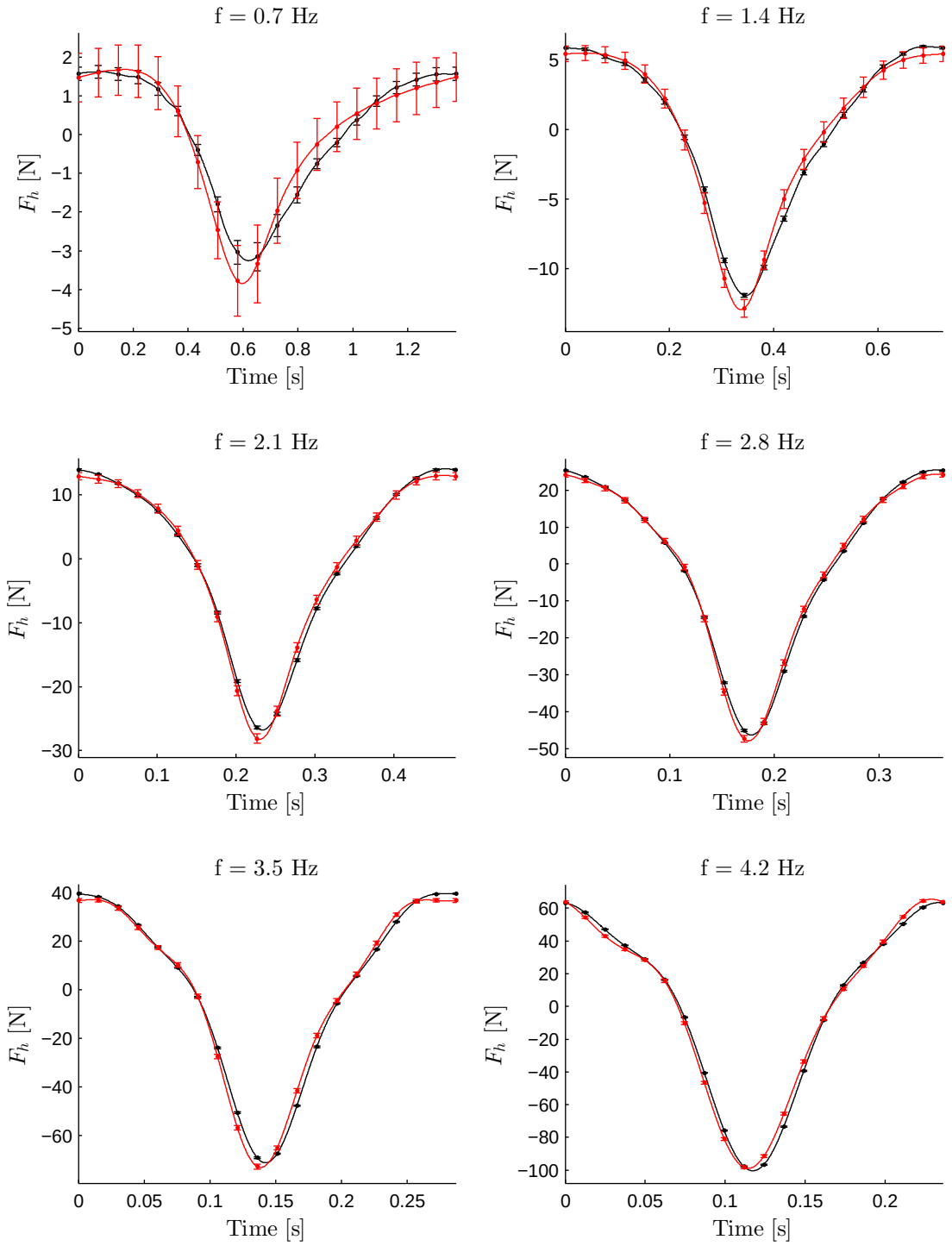

Figure B.3. Comparison of the measured inertia of a 2.292 kg mass mounted to the struts, and the mass multiplied by the heaving acceleration, $m\ddot{h}$.

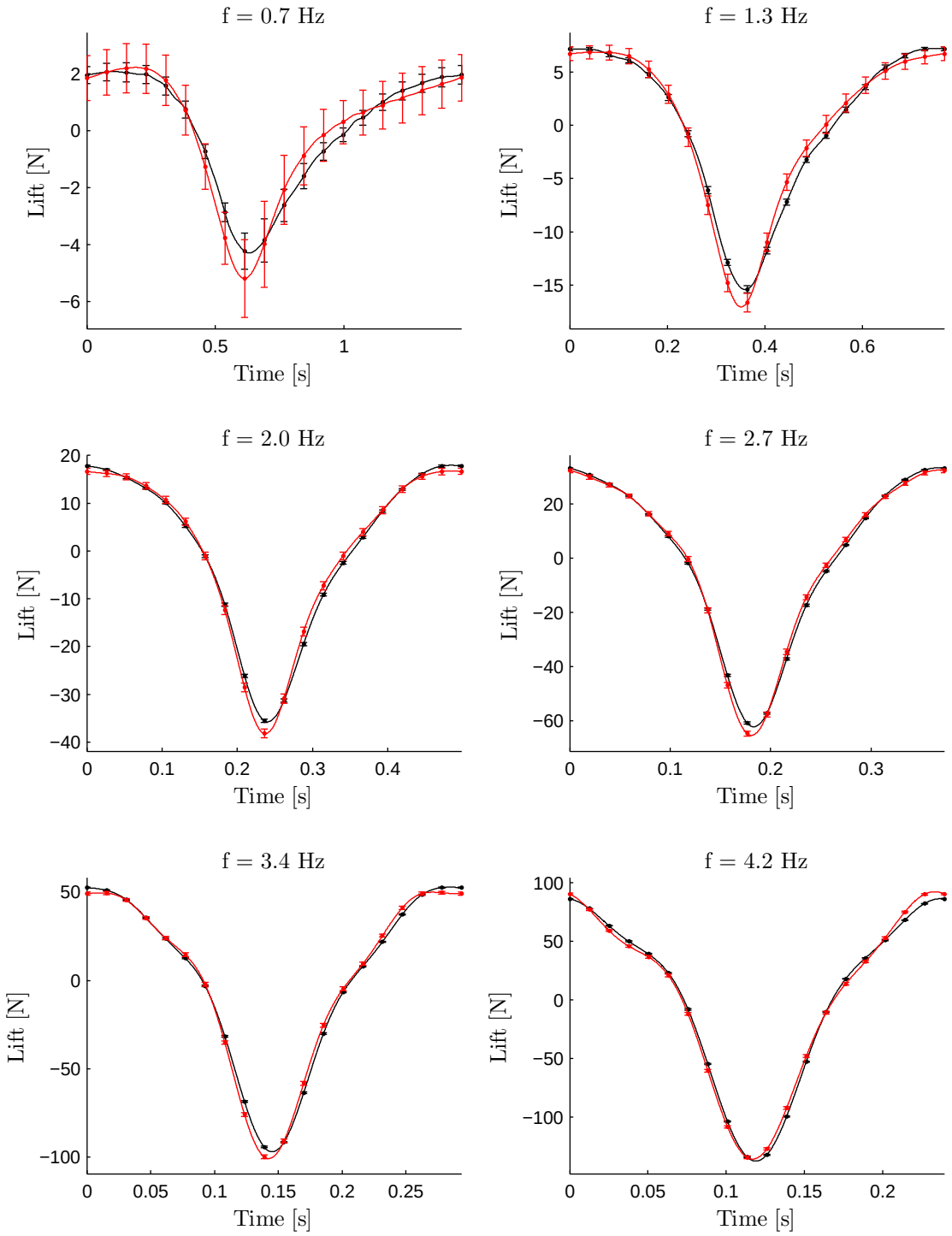

Figure B.4. Comparison of the measured inertia of a 3.208 kg mass mounted to the struts, and the mass multiplied by the heaving acceleration, $m\ddot{h}$.

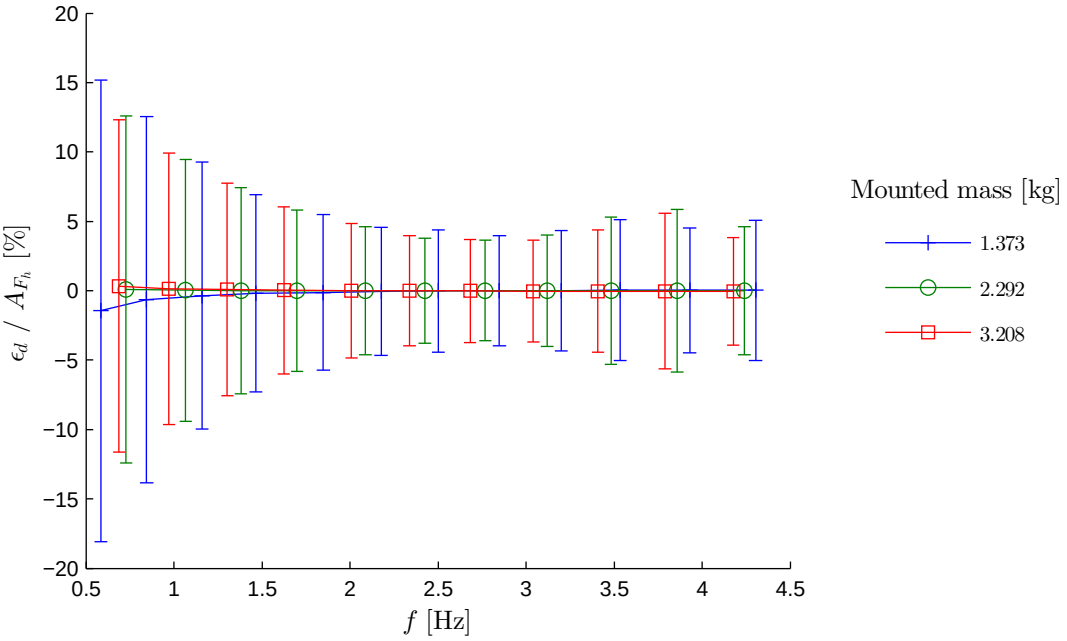

Figure B.5. Mean point-wise force measurement dynamic error normalised by the range of $m\ddot{h}$ plotted over the working frequency domain. Error bars represent ± 2 standard deviations.

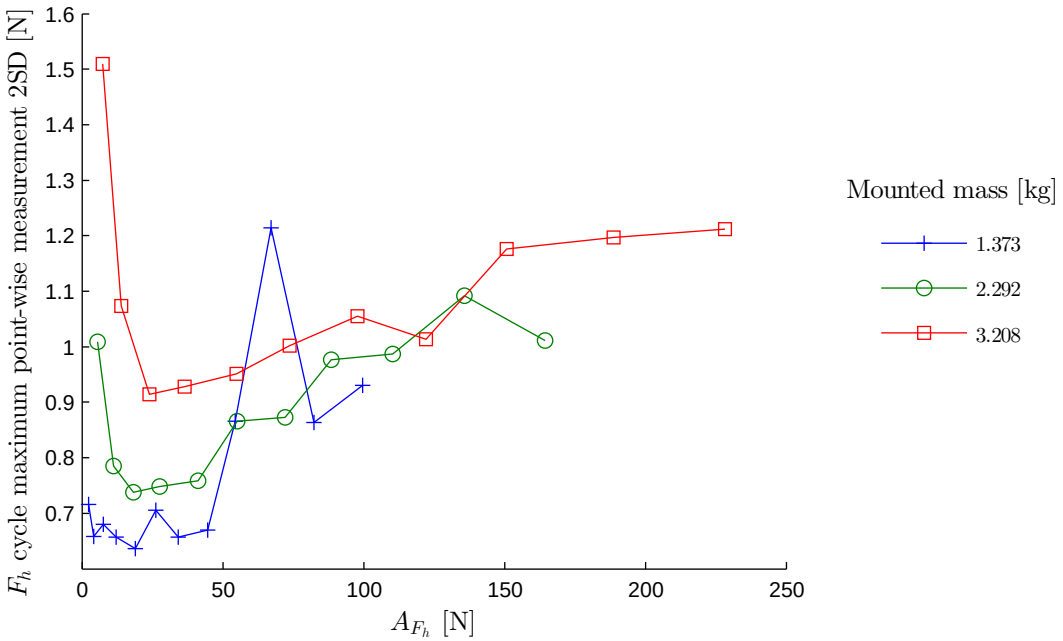

Figure B.6. Maximum point-wise heave force 2 SD versus the heave force range.

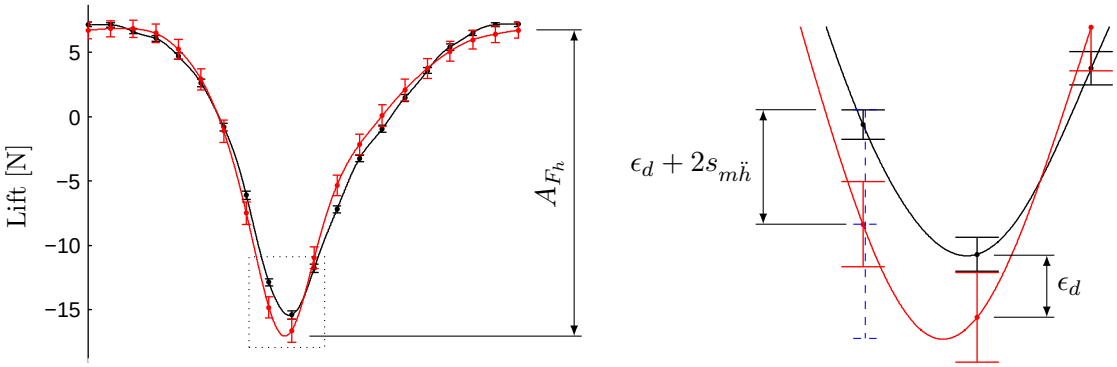

Figure B.7. Quantities used to estimate the dynamic uncertainty gain.

B.1 Dynamic Uncertainty Bounds

To express the dynamic error of measurements, an interval around the mean heave force cycle where the true (free from dynamic error), in-phase heave force cycle should be shown. This interval will be referred to as the dynamic uncertainty bounds. Unlike in dry tests, the virtual mass (sum of the dry mass and added mass of a test object) during hydrodynamic tests is not a known and so can not be used to estimate the dynamic uncertainty bounds. Instead the heave force cycle range A_{F_h} (see Figure B.7) will be used as a conservative predictor for the size of the dynamic uncertainty bounds.

The data displayed in Figures B.2 to B.4 has been used to estimate how large the dynamic confidence bounds should be. Consider the heave force measurement in Figure B.7. If the ±2 SD uncertainty bound of the measurement was extended symmetrically to include the entire ±2 SD bounds of the expected inertia measurement (dashed blue error bar in Figure B.7), approximately 97.5 % of the $m\ddot{h}$ cycle would be expected to fall within these bounds. The magnitude of these bounds was calculated on a point-wise basis (using Equation B.3) to provide estimates $\hat{u}_d$ of the dynamic uncertainty bound magnitude.

$$\hat{u}_d = \epsilon_d + 2s_{m\ddot{h}} \tag{B.3}$$

Figure B.8 shows the sum of the mean dynamic uncertainty bounds estimator $\hat{u}_d$ and 2 standard deviations as a function of A_{F_h}. There exists significant linear correlation between

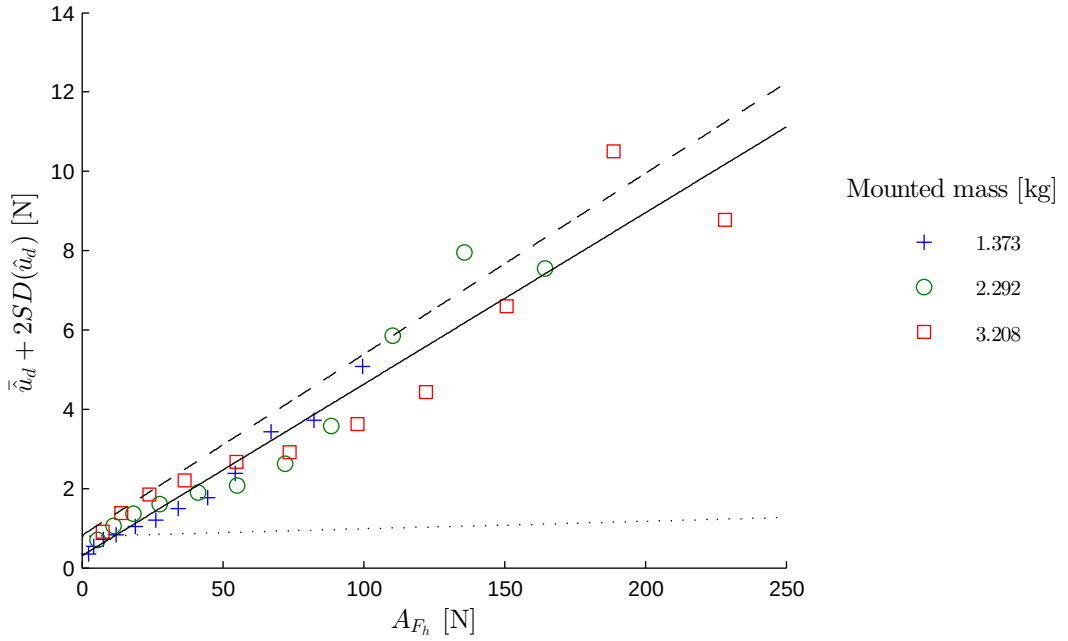

Figure B.8. Dynamic uncertainty estimate plus 2 standard deviations versus the heave force range. The line of best fit (Equation B.4) is shown with its 95 % upper prediction bound (dashed line). The maximum measurement 2 SD magnitude (dotted line) is also shown for comparison.

these two quantities ($p < 4.07 \times 10^{-20}$), the relationship of which is given by Equation B.4. Figure B.8 shows that for low amplitude heave force cycles the measurement uncertainty is large enough to include dynamic measurement errors as seen in Figures B.2 to B.4. However, once the heave force range exceeds approximately 12 N dynamic error becomes larger than the measurement uncertainty.

$$u_d = 0.043 A_{F_h} + 0.302 \tag{B.4}$$

$$u_d = 0.047 A_{F_h} + 0.817 \tag{B.5}$$

If the correlation shown in Figure B.8 was perfectly linear, uncertainty bounds of a magnitude predicted with Equation B.4 would mean that approximately 97.5 % of the mean $m\ddot{h}$ cycle should fall within these bounds 97.5 % of the time on a point-wise basis.

Hence, the dynamic uncertainty bounds would estimate the point-wise range where the true heave force cycle, unaffected by dynamic measurement error, would lie with approximately 95 % confidence. However, the correlation in Figure B.8 is not perfectly linear, and so this confidence is overestimated due to some observations falling above the line of best fit.

Taking the 95 % prediction bound of the correlation in Figure B.8 leads to Equation B.5. Using Equation B.5 to predict the size of the dynamic uncertainty bounds, means that confidence of the mean true heave force lying within the dynamic uncertainty bounds is approximately 92.7 %.

Figures B.5 shows evidence of structural resonance with a increasing spread of relative dynamic error between 3.5 Hz and 4.1 Hz. This increase in dynamic error is also evident in Figure B.8 with two outliers peaking above the 95 % prediction bound late in the A_{F_h} range. Taking these exceptional errors into account, it would be reasonable to maintain a 92 % confidence associated with the dynamic uncertainty bounds for oscillating frequencies less than 3.5 Hz.

Over predicted dynamic uncertainty bounds would lead to a conservative estimate of the dynamic uncertainty, which may unnecessarily imply inaccurate data. Worse still, under predicted bounds would not fully capture where the true heave force cycle lies. To confirm the estimate of confidence in the dynamic uncertainty bounds, independent data was recorded with dry mass mounted with the NACA4415 and ⌀120 mm end plates. The proportion of a cycle where the mean $m\ddot{h}$ fell within the dynamic uncertainty bounds was calculated. Figure B.10 shows the results of this test and Figure B.9 shows two example heaving force cycles with the measurement ± 2 SD bounds (inner error bars) and the dynamic measurement confidence bounds marked.

As expected, the dynamic measurement confidence interval is substantially larger than the measurement uncertainty for high oscillating frequencies. This indicates that measured force cycles with a high oscillation frequency are very consistent (having low relative uncertainty). However, they have a relatively large systematic, dynamic measurement error. Nevertheless, the $m\ddot{h}$ cycle appears to stay within the dynamic uncertainty bounds for most of the cycle period. Figure B.9b shows how structural resonance distorts the

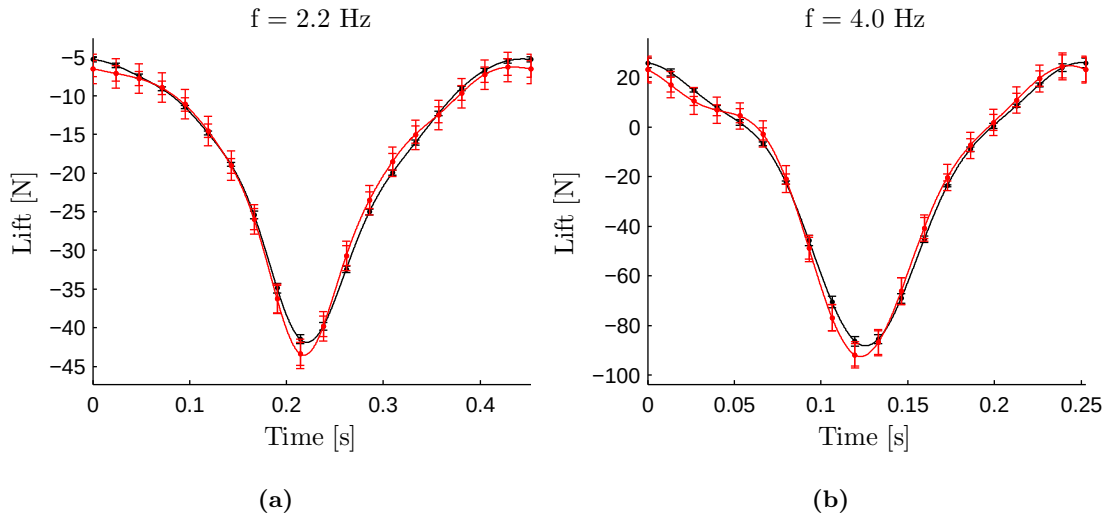

(a) **(b)**

Figure B.9. Example dynamic measurement confidence bounds.

measured heave profile at an oscillating frequency of 4 Hz leading to some under predicted dynamic uncertainty bounds.

As observed, the proportion of the measured heave cycle where the measurement uncertainty includes dynamic measurement error declines as the oscillating frequency and heave force range increase. The dynamic confidence interval adequately represents the range where the true heave force cycle lies with 92 % confidence, until the oscillating frequency reaches approximately 3.2 Hz. Above 3.2 Hz structural resonance increases the dynamic measurement error and confidence in the dynamic uncertainty bounds may drop as low as 75 %. As long as the reader is aware of this limitation, predicting the size of the dynamic uncertainty bounds with Equation B.5 is deemed adequate to express the dynamic error of measurements.

B.2 Conclusion

The data presented in this appendix verifies that the measurements do contain systematic errors due to the compliance of the experimental equipment. However, this error is sufficiently small, and consequently, the results presented in this thesis are of adequate accuracy for design purposes.

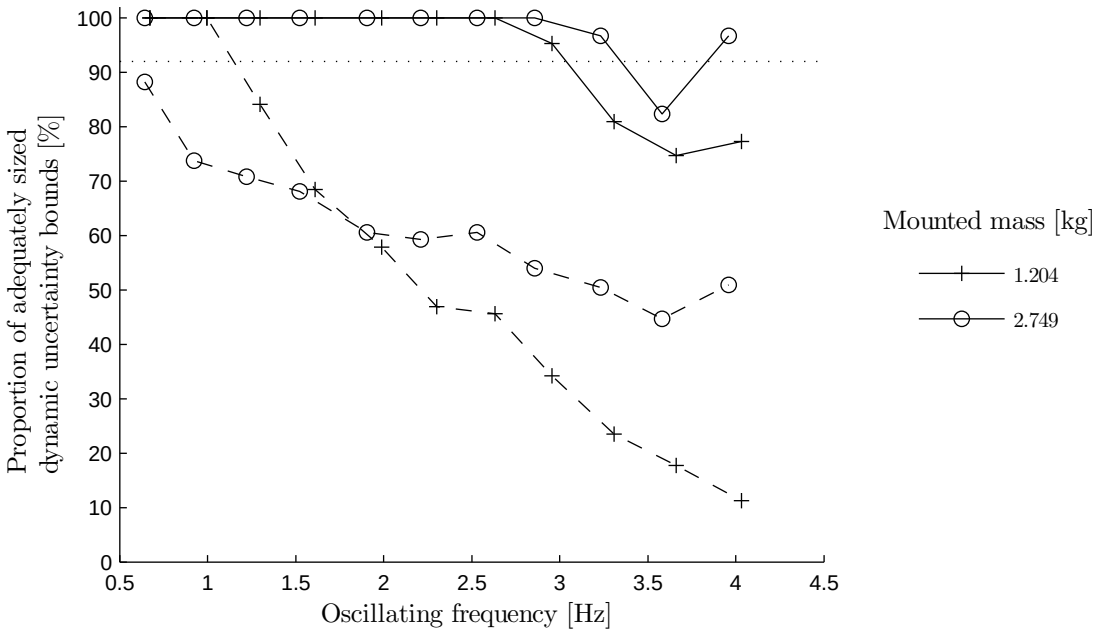

Figure B.10. The proportion of dynamic confidence bounds that capture mean true heave force cycle (solid lines). Dashed lines show the proportion of the mean true heave force cycle that falls within the measurement $\pm 2\,\mathrm{SD}$ bounds.

To estimate the affect in-phase hydrodynamic forces would have on dynamic measurement errors, inertia forces on some oscillating dry mass were measured and compared to calculated inertia forces based on heaving acceleration. Changes in oscillating dry mass did not significantly change the relative dynamic measurement error, and so the effects of in-phase hydrodynamic forces are not expected to significantly degrade the accuracy of the hydrodynamic measurements either. The affect of out-of-phase hydrodynamic forces was not investigated for two reasons; Firstly, applying known out-of-phase forces to the test equipment was considered too difficult, and secondly, in-phase hydrodynamic force contributions were expected to dominate measured heave forces because of the small heave-to-chord ratios ($h_0/c \leq 1$).

The dynamic measurement error has a linear dependence on the magnitude of the heave force cycle. Hence, the heave force cycle range was used to predict the size of the dynamic uncertainty bounds. The true in-phase heaving force cycle is expected to lie within these bounds with 92 % confidence when the oscillating frequency is less than 3.2 Hz. At oscillating frequencies higher than 3.2 Hz, the certainty that the true heave force cycle lies within the dynamic measurement bounds may be reduced to 75 % due to structural resonance of the equipment under high in-phase loads.

Appendix C

Measurement Repeatability Examples

Figures C.1 to C.3 show repeated measurements of the forces on a NACA4415 foil oscillating at three different states. The actual oscillating frequency, translational velocity and Strouhal number for each measurement is shown in Table C.1. All runs had a heave-to-chord ratio of 0.75.

Table C.1. Parameters for runs investigating the repeatability of the force measurements.

Test No.	Figure No.	f [Hz]	u [$\mathrm{m\,s^{-1}}$]	St
		2.67	2.00	0.12
1	Figure C.1	2.70	2.00	0.12
		2.70	2.00	0.12
		2.74	1.50	0.16
2	Figure C.2	2.75	1.50	0.17
		2.77	1.50	0.17
		2.83	0.99	0.26
3	Figure C.3	2.85	0.99	0.26
		2.86	0.99	0.26

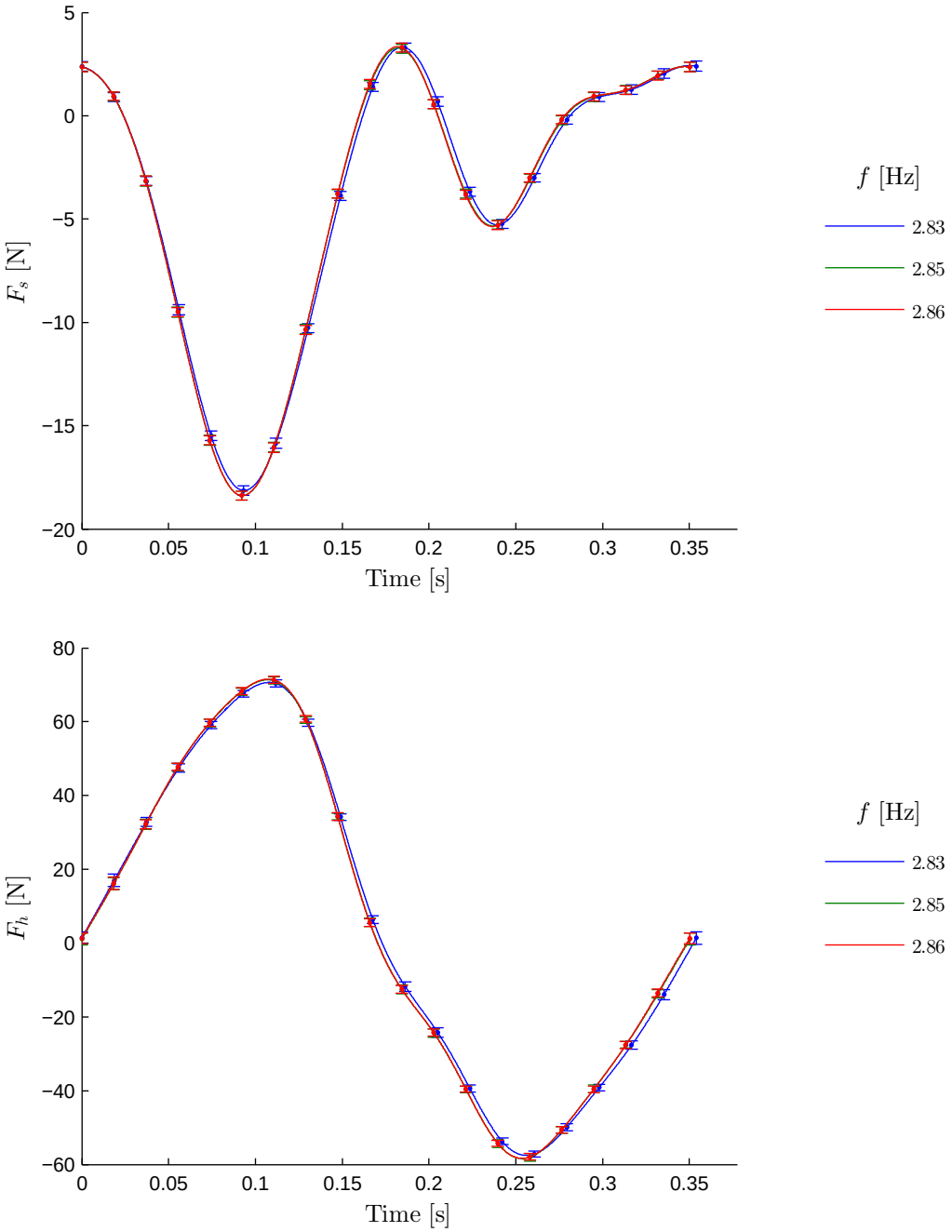

Figure C.1. Repeated measurements of the forces on a oscillating NACA5514 at: u=1.0 m s^{-1}, h_0/c=0.75

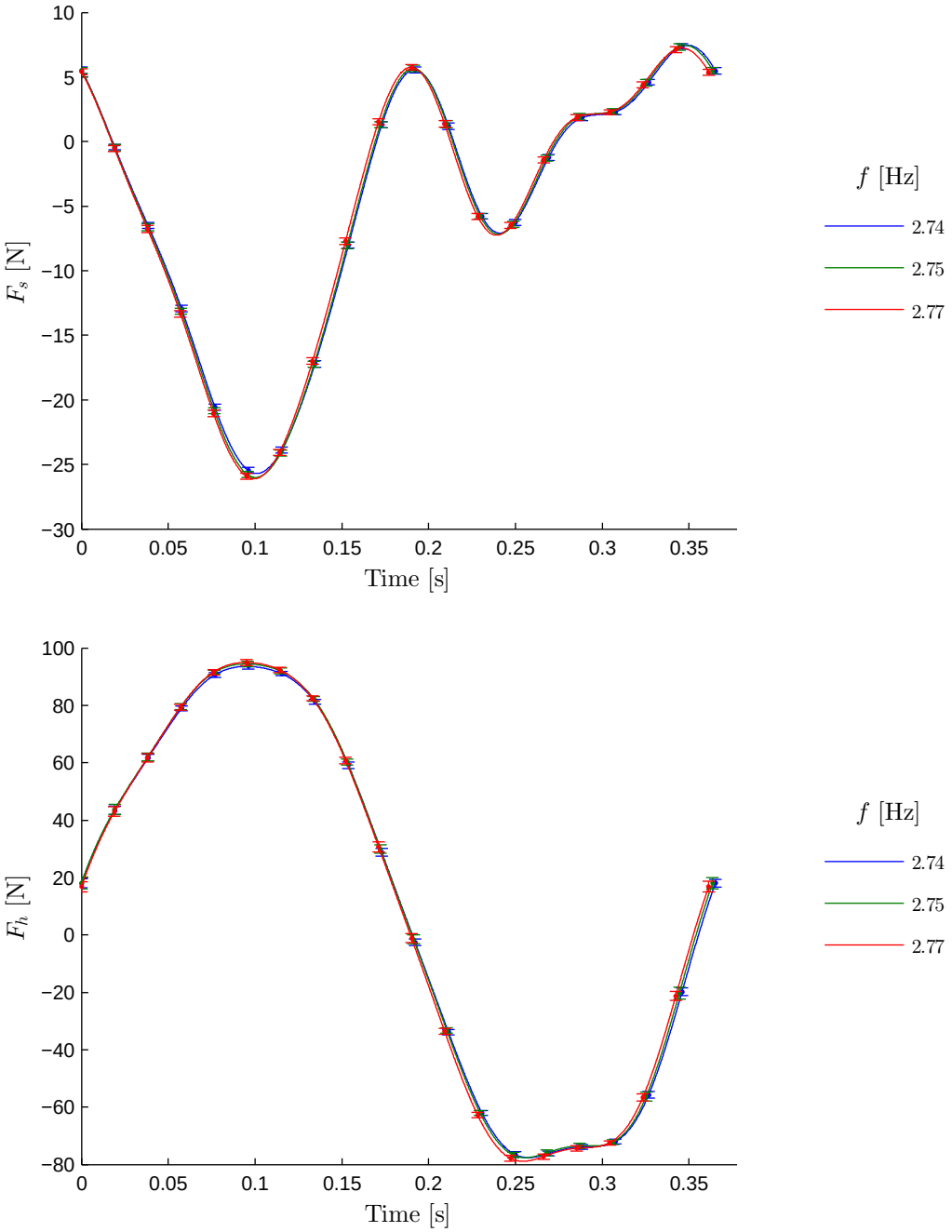

Figure C.2. Repeated measurements of the forces on a oscillating NACA5514 at: u=1.5 m s^{-1}, h_0/c=0.75

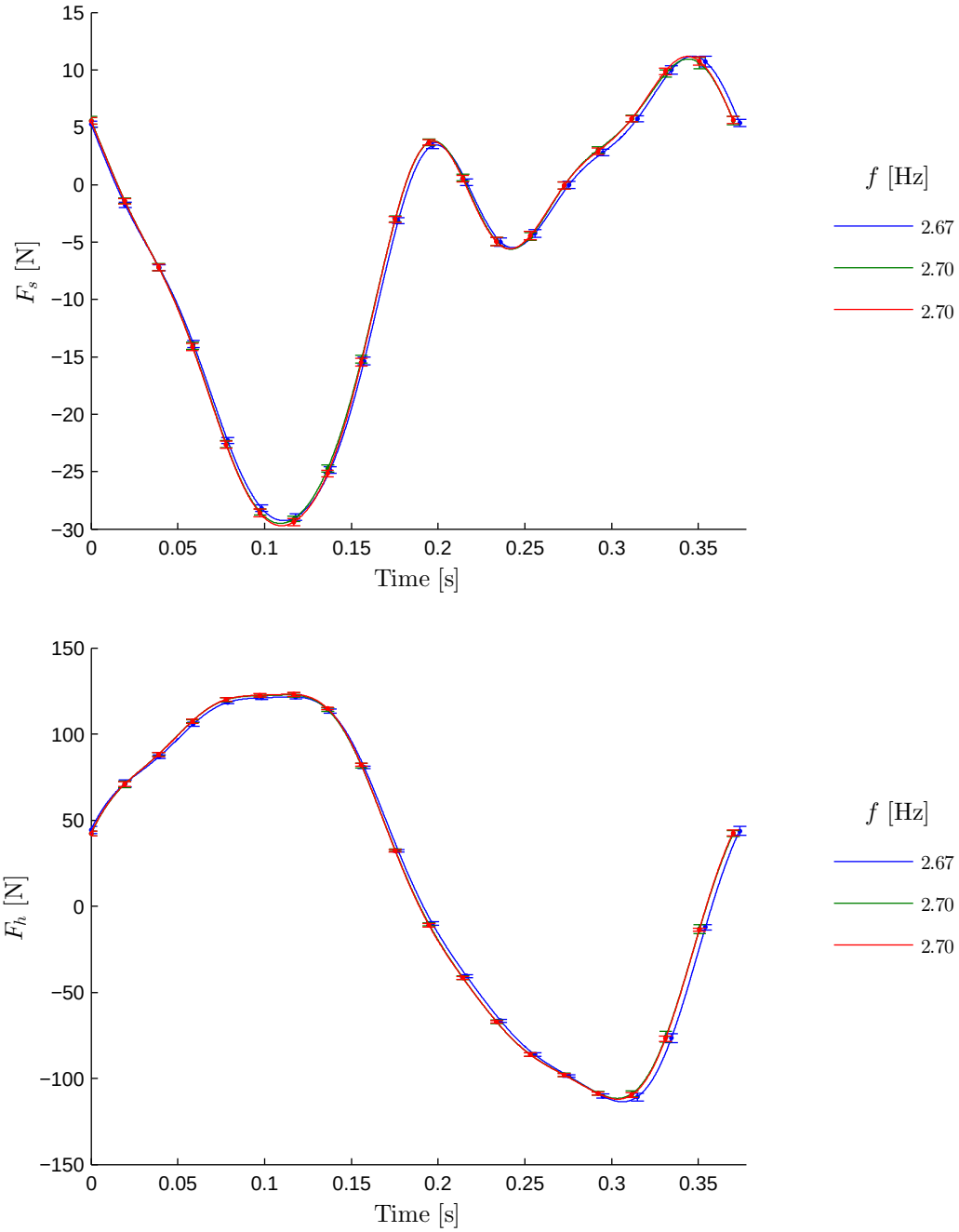

Figure C.3. Repeated measurements of the forces on a oscillating NACA5514 at: u=2.0 m s^{-1}, h_0/c=0.75

Appendix D

Crank and Connecting Rod Heaving Profiles

In the majority of the literature the pitching and plunging motions of a oscillating foil are sinusoidal. However, Read et al. (2003) showed that small changes in a heaving profile can drastically change the angle of attack profile, due to the arctan(x) component of the heave-induced angle of attack. Hover et al. (2004) studied a number of alternative heaving profiles as a way of varying the angle of attack profile (See Section 3.5.1 for more details). They showed that the desired near cosine angle of attack function was achievable at low Strouhal numbers through sinusoidal heaving motions. However, as the Strouhal number increases, the heave-induced angle of attack degrades the angle of attack profile. In this appendix, the oscillating linear motion provided by a crank and connecting rod mechanism is compared to that of a scotch yoke. Furthermore, the angle of attack profile of a foil undergoing pure heaving, driven by a crank and connecting rod mechanism is investigated, and qualitative estimates on its propulsive efficiency are made with respect to the Strouhal number and the connecting rod to crank length ratio.

Assuming a sinusoidal heaving profile, and then substituting the heave velocity profile into Equation 3.21, and simplifying this expression with Equation 3.25, leads to Equation D.1. This equation shows that at low Strouhal numbers, the angle of attack function will be near sinusoidal due to $tan^{-1}(x) \approx x$ when x is small. At high Strouhal numbers the

heave-induced angle of attack will be distorted by the *tan* function.

$$\alpha_h = tan^{-1}\left(\pi St cos(\omega t)\right) \tag{D.1}$$

Sinusoidal heaving can be achieved with a scotch-yoke mechanism (Figure D.1a), or any other linear motion mechanism driven under closed loop control. In the present experiments, the motor driving the heaving motion is under open loop control. Open loop control was chosen over closed loop control since it more accurately represents a person producing shaft power via pedalling. Other common sources of shaft power such as internal combustion engines also work under open loop control, providing relatively constant power and drive shaft velocities.

Cranks in combination with connecting rods (con-rods), and some form of linear guide, are a common robust mechanism for converting rotary motion into oscillating linear motion. Figure D.1b shows a schematic for a crank and con-rod mechanism. A crank and con-rod arrangement was used in the current experimental equipment to drive the heaving motion. To achieve sinusoidal linear oscillations with a crank and con-rod, either the motor driving the crankshaft must be under closed loop control, or the mechanism must have an infinite con-rod to crank length ratio. Obviously, the latter of these two options is impractical. In this appendix, the consequence of a finite con-rod to crank length ratio on heaving velocity and acceleration is discussed.

The heave position of the slider h, driven by a crank and con-rod mechanism, can be calculated with Equation D.2 if the crank angle θ_c, the con-rod length, l_r and the crank length l_c, are known. Furthermore, by normalising the slider position h, and the connecting rod length l_r, with the crank length l_c, Equation D.2 can be simplified to

Equation D.3. S and L are the normalised slider position, and con-rod length respectively. The first term of this equation is the sinusoidal component of the heaving position profile (i.e. the heaving position profile achieved with a scotch yoke). The second term is the heave position deviation from the sinusoidal profile. At the extremities of the slider motion (θ_c =90° and θ_c =270°), the second term of Equation D.2 equates to zero. These are the only two points in the slider position cycle that are coincident with a sinusoidal heaving profile. Again referring to Equation D.3, the frequency response of

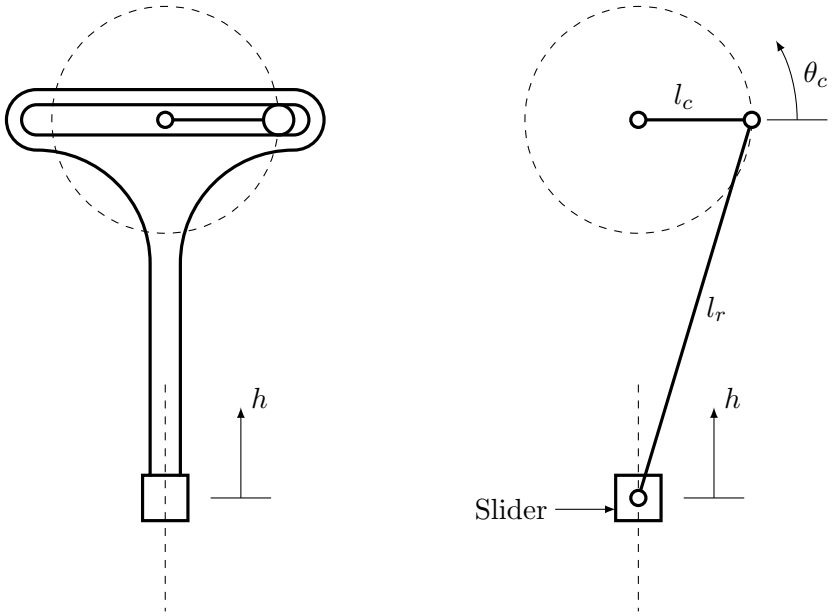

(a) Scotch yoke **(b)** Crank and connecting rod

Figure D.1. Mechanisms for converting continuous rotary motion to oscillating linear motion.

the slider motion has two components. One proportional to the crank frequency and one twice the crank frequency. This significantly affects the slider velocity profile, and hence the heave-induced angle of a attack profile (refer to Equation 3.21).

$$h = l_c sin\theta_c + l_r sin\left(cos^{-1}\left(\frac{l_c cos\theta_c}{l_r}\right)\right) \tag{D.2}$$

$$S = sin\theta_c + \sqrt{L^2 - cos^2\theta_c} \tag{D.3}$$

D.1 Heaving Symmetry

Figure D.2 illustrates the effect of the connecting rod to crank length ratio on the heave position profile of the slider. Note that as the crank to connecting rod length ratio changes the Koochesfahani's (1989) symmetry parameter (see Section 3.5.6) remains constant. However, there is a bias towards the time spent in the negative heave range. To describe this bias, we define the position based symmetry parameter S_h, given by EquationD.4. The position based symmetry parameter is the ratio between the time spent in positive heave during a cycle, to the total period of the cycle. Figure D.3 illustrates the difference between the position based symmetry parameter, and Koochesfahani's (1989) velocity based symmetry parameter. Figure D.4 shows how the con-rod to crank length ratio affects the symmetry of a heaving position cycle.

$$S_h = \frac{T_{h>0}}{T} \tag{D.4}$$

D.2 Heaving Velocity and Acceleration Profiles

Figure D.5 shows how the heave position bias affects the heaving velocity, and acceleration profiles, respectively assuming a constant crank shaft speed. This bias in turn affects the symmetry of the heave-induced angle of attack profile, and its first derivative with respect to time, as shown by Figures D.8 and D.9. Figure D.5 shows that both the heave velocity and acceleration tend toward sinusoidal profiles with large con-rod to crank length

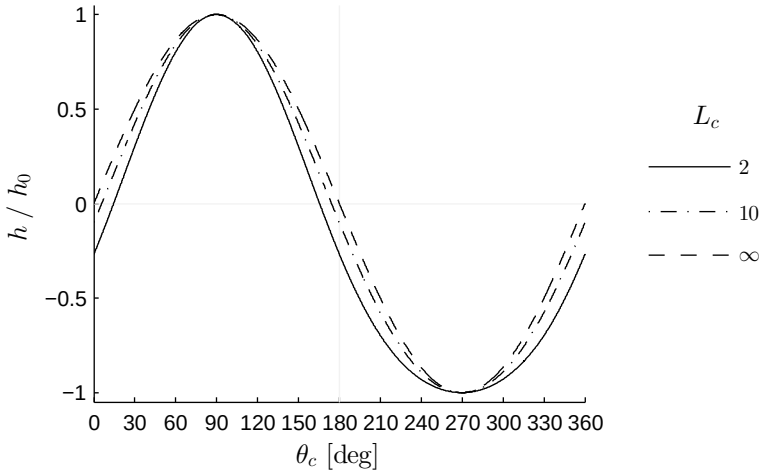

Figure D.2. Heaving profiles for various connecting rod to crank length ratios.

ratios. When L_c is small the heave velocity (Figure D.5a) maintains a smooth compressed sinusoidal shape for the positive heave portion of the cycle. However, the negative heave section forms a small inflection as the con-rod to crank ratio becomes small. This change in shape is more prominent in the heaving acceleration profile (Figure D.5b). The small inflection in the velocity profile corresponds to a more obvious double peak in the heave acceleration profile (L_c< 3.0288).

All these heave profile alterations are consequences of the harmonic heave error introduced by the second term in Equation D.3. This term has a frequency of twice the crank frequency f_c due to the cos^2 function. The contribution of this term is relatively small in the heave position profile. However, its contribution becomes larger in the heave velocity and acceleration profiles. Figure D.6 shows that the heave velocity and acceleration profile's power density spectrums may comprise up to 6.5 % and 22 % of this term respectively (L_c=2).

Figure D.7 shows how L_c affects the absolute magnitude of the peak heave accelerations. It shows how the maximum and minimum heave accelerations become weaker and stronger respectively when L_c is decreased (also seen in Figure D.5b). When L_c is decreased to approximately 2.5, peak heave acceleration becomes negatively bias with the peak negative acceleration being approximately twice the magnitude of the peak positive acceleration. With the mechanism orientation shown in Figure D.1b, i.e. the crank posi-

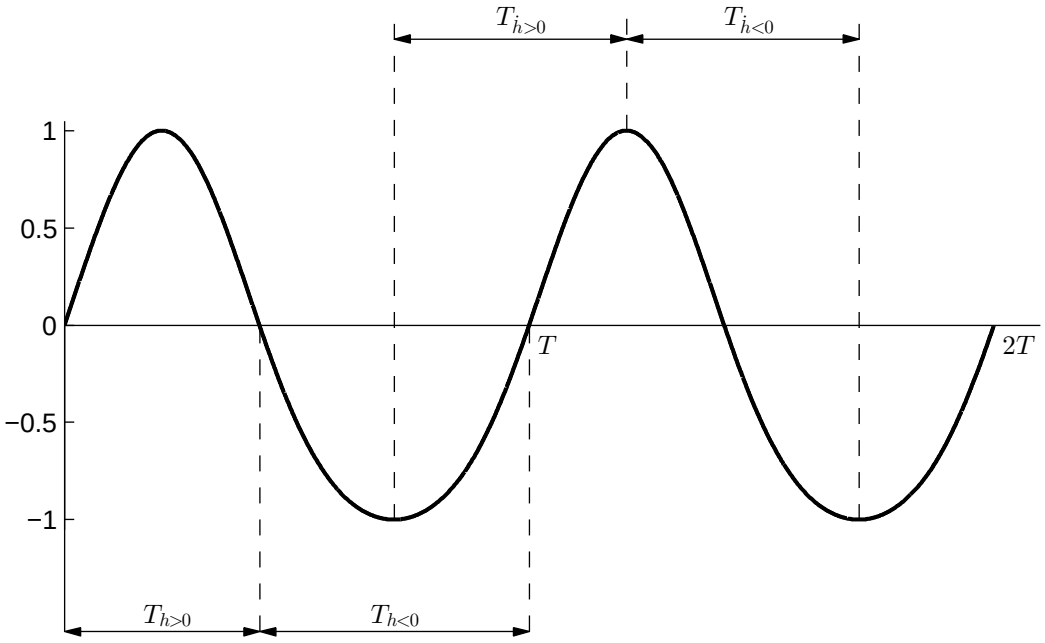

Figure D.3. The proportions of a near sinusoidal cycle that affect the position based and velocity based symmetry parameters.

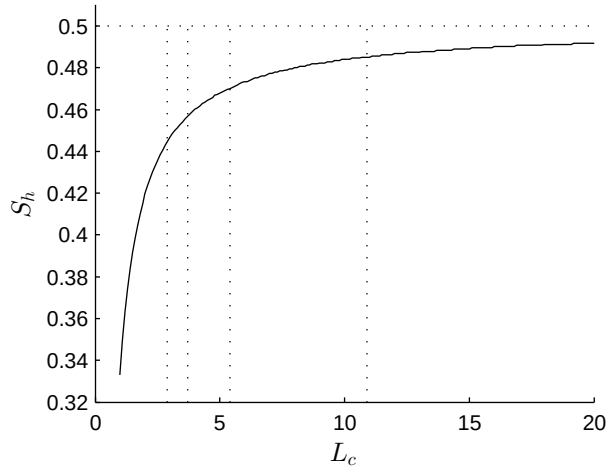

Figure D.4. Heave position based symmetry parameter for various connecting rod to crank length ratios. Vertical dotted lines mark the values of L_c used for the heave amplitude study in Section 5.4.

tioned above the slider, this corresponds to decreased inertial forces as the crank goes past bottom dead centre, and increased inertial forces as the crank goes past top dead centre.

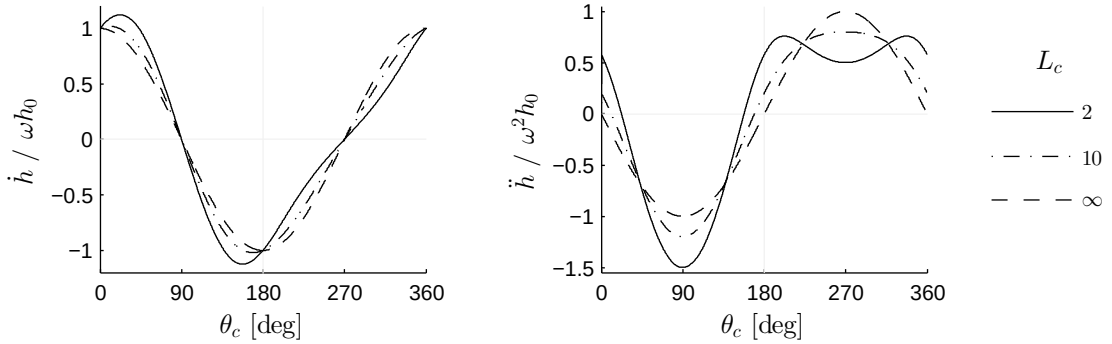

(a) **(b)**

Figure D.5. Normalised heave velocity and heave accelerations profiles for various connecting rod to crank length ratios.

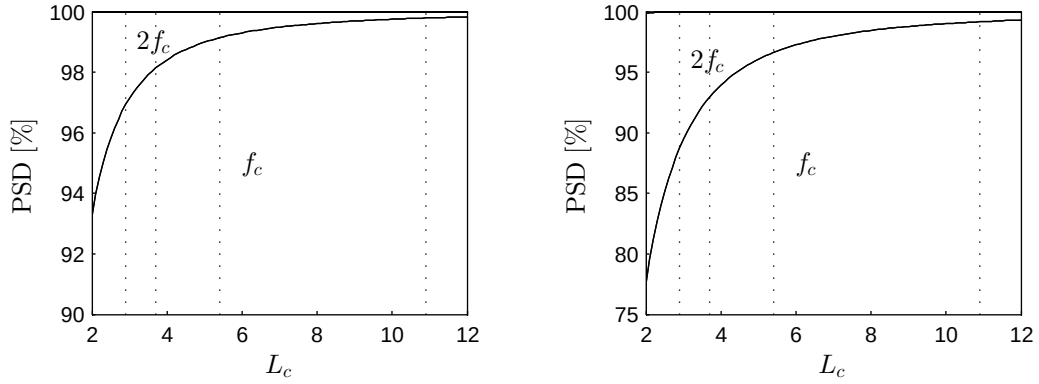

(a) **(b)**

Figure D.6. Power spectral density of (a) the heaving velocity and (b) the heaving acceleration profiles for small connecting rod to crank length ratios. Vertical dotted lines mark the values of L_c used for the heave amplitude study in Section 5.4.

D.3 Angle of Attack Profiles

The angle of attack, and angle of attack rate, suffer similar profile distortion characteristics as the heave velocity and heave acceleration profiles respectively when L_c is small (Figures D.8 and D.9). At large Strouhal numbers, distortion of the heaving profile from use of a crank and con-rod mechanism have little significance since the angle of attack function tends to a square wave of $\pm 90^\circ$ amplitude. In this case, the foil will be operating

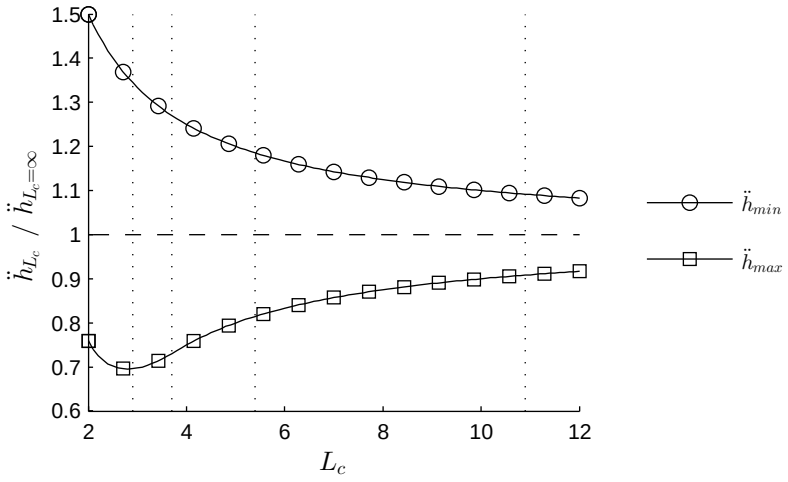

Figure D.7. The affect of the connecting rod to crank length ratio on maximum and minimum heaving accelerations. Vertical dotted lines mark the values of L_c used for the heave amplitude study in Section 5.4.

in piston mode and so is expected to have a low efficiency (Anderson et al., 1998). At low Strouhal numbers, small con-rod to crank length ratios cause a double peak in the angle of attack rate profile (see Figure D.9a). Assuming that vortices are shed at turning points in the angle of attack rate cycle (Anderson, 1996; Hover et al., 2004), the profile in Figure D.9a would create a $1S + 1P$ wake as opposed to the $2S$ wake $L_c{=}\infty$ (Figure D.9b). According to Koochesfahani (1989), the single vortex would be shed during the fast angle of attack stroke ($20 < \theta_c < 160$ in Figure D.8a) and the vortex pair on the slow angle of attack stroke ($160 < \theta_c < 360$ in Figure D.8a). The extra vortices shed with a low con-rod to crank length ratio would likely corrupt the thrust wake and reduce thrust efficiency (Hover et al., 2004).

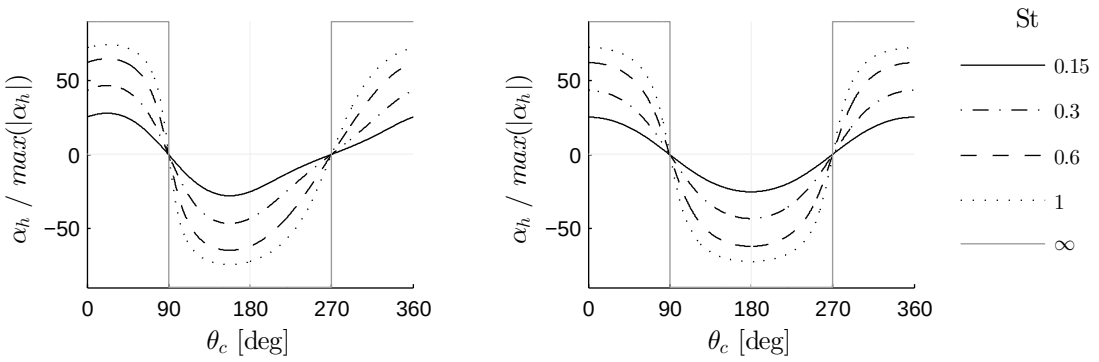

(a) **(b)**

Figure D.8. Heave induced angle of attack profiles for (a) a connecting rod to crank length ratio of 2 and (b) for an infinite connecting rod to crank length ratio.

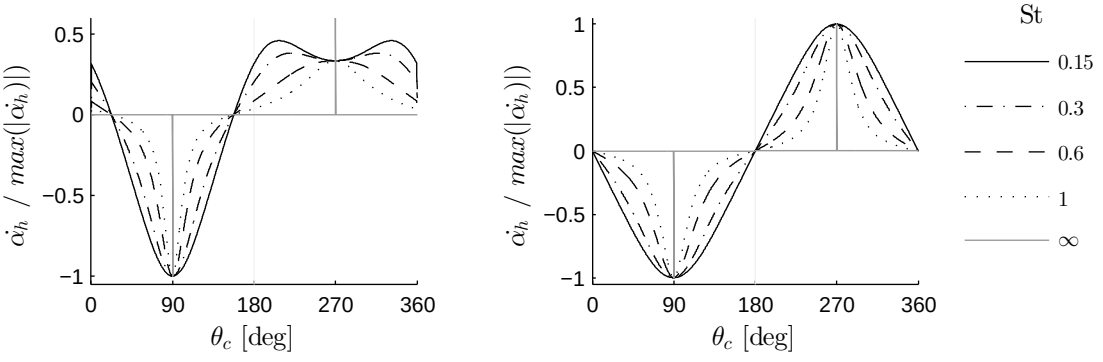

(a) **(b)**

Figure D.9. Heave induced angle of attack rate profiles for (a) a connecting rod to crank length ratio of 2 and (b) for an infinite connecting rod to crank length ratio.

Appendix E

Measured Hydrodynamic Force Cycles on a Heaving Cylinder

The figures included in this appendix show measured hydrodynamic forces on a cylinder undergoing a heaving motion with no forward velocity. All the measurements presented in this appendix were recorded with a heave-to-chord ratio of $h^* = 0.75$ and circular end plates of size $\varnothing 320\,\text{mm}$ ($\varnothing 5.3c$) fitted. The dimensions of the cylinder cross-section are shown in Figure E.1. Refer to Table 4.1 for a comparison between the cylinder and the other test objects.

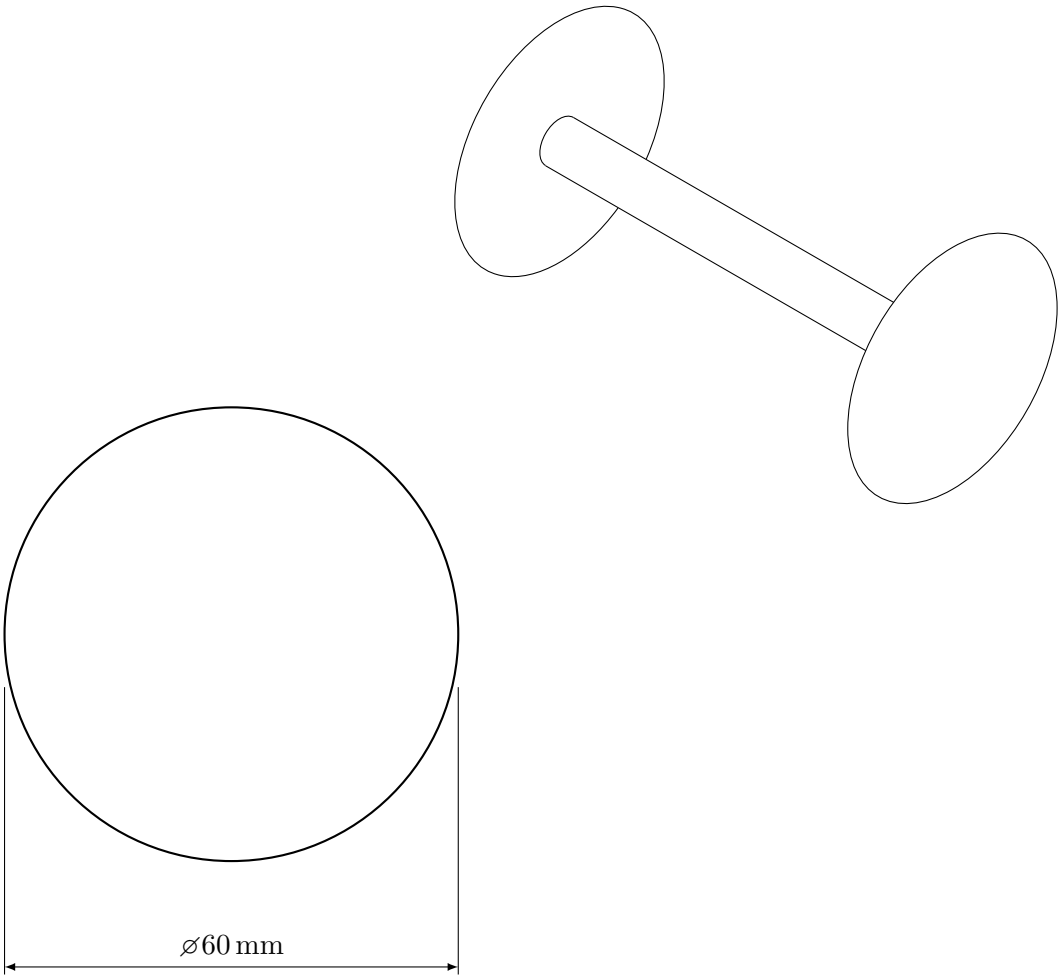

Figure E.1. Dimensions of the cylinder cross-section (scale 1:1) and an isometric of the cylinder with end plates attached (scale 1:5).

Object: Cylinder		Motion	Water
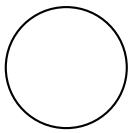	$c = 0.060\,\mathrm{m}$ $L = 0.600\,\mathrm{m}$	$h_0 = 0.045\,\mathrm{m}$ $h^* = 0.75$ $f = 0.79\,\mathrm{Hz}$ $u = 0.00\,\mathrm{m\,s^{-1}}$	$T_w = 11.8\,^\circ\mathrm{C}$ $\rho = 999\,\mathrm{kg\,m^{-3}}$

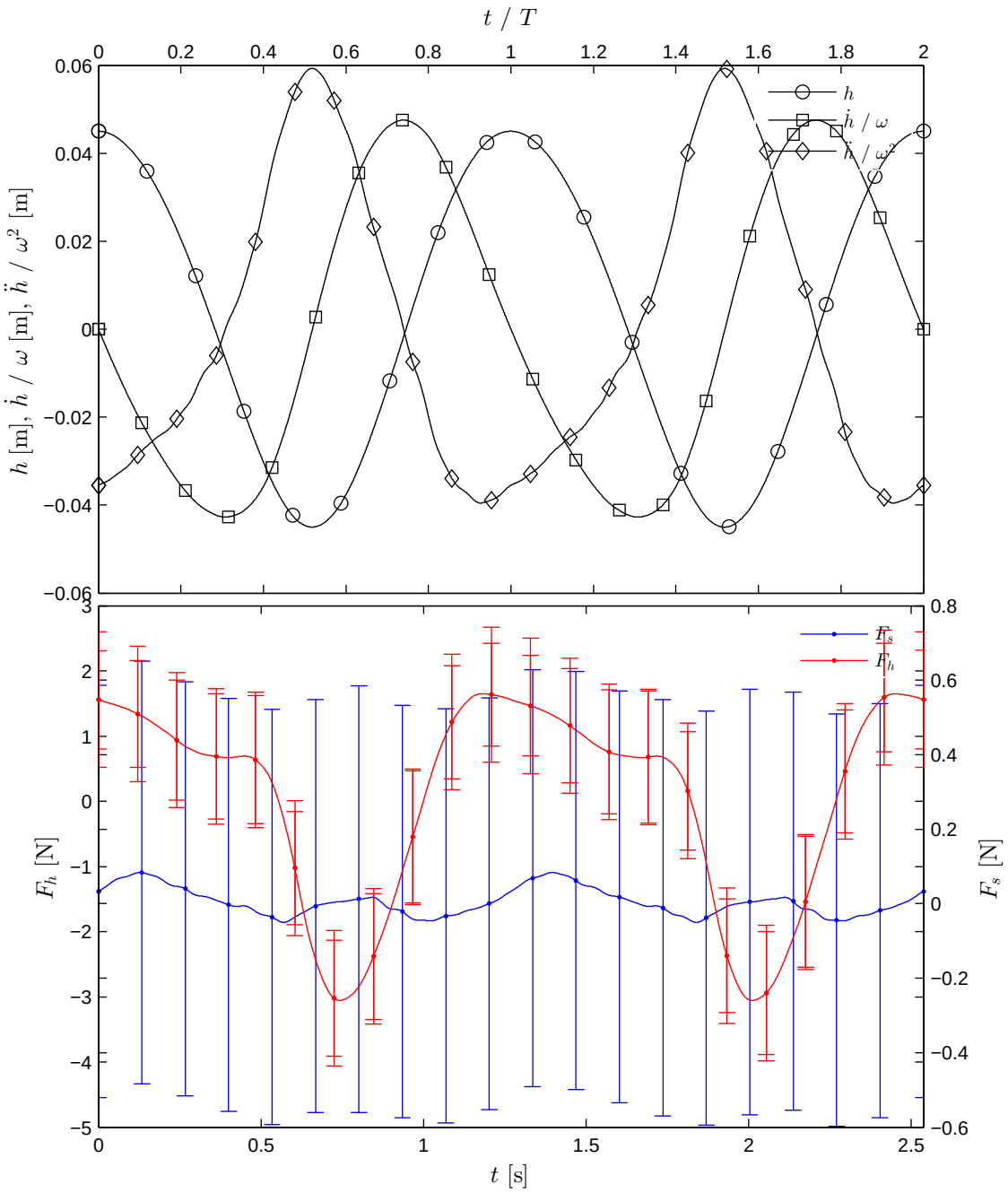

Object: Cylinder		Motion	Water
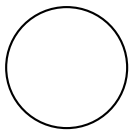	$c = 0.060\,\mathrm{m}$ $L = 0.600\,\mathrm{m}$	$h_0 = 0.045\,\mathrm{m}$ $h^* = 0.75$ $f = 1.32\,\mathrm{Hz}$ $u = 0.00\,\mathrm{m\,s^{-1}}$	$T_w = 11.8\,^\circ\mathrm{C}$ $\rho = 999\,\mathrm{kg\,m^{-3}}$

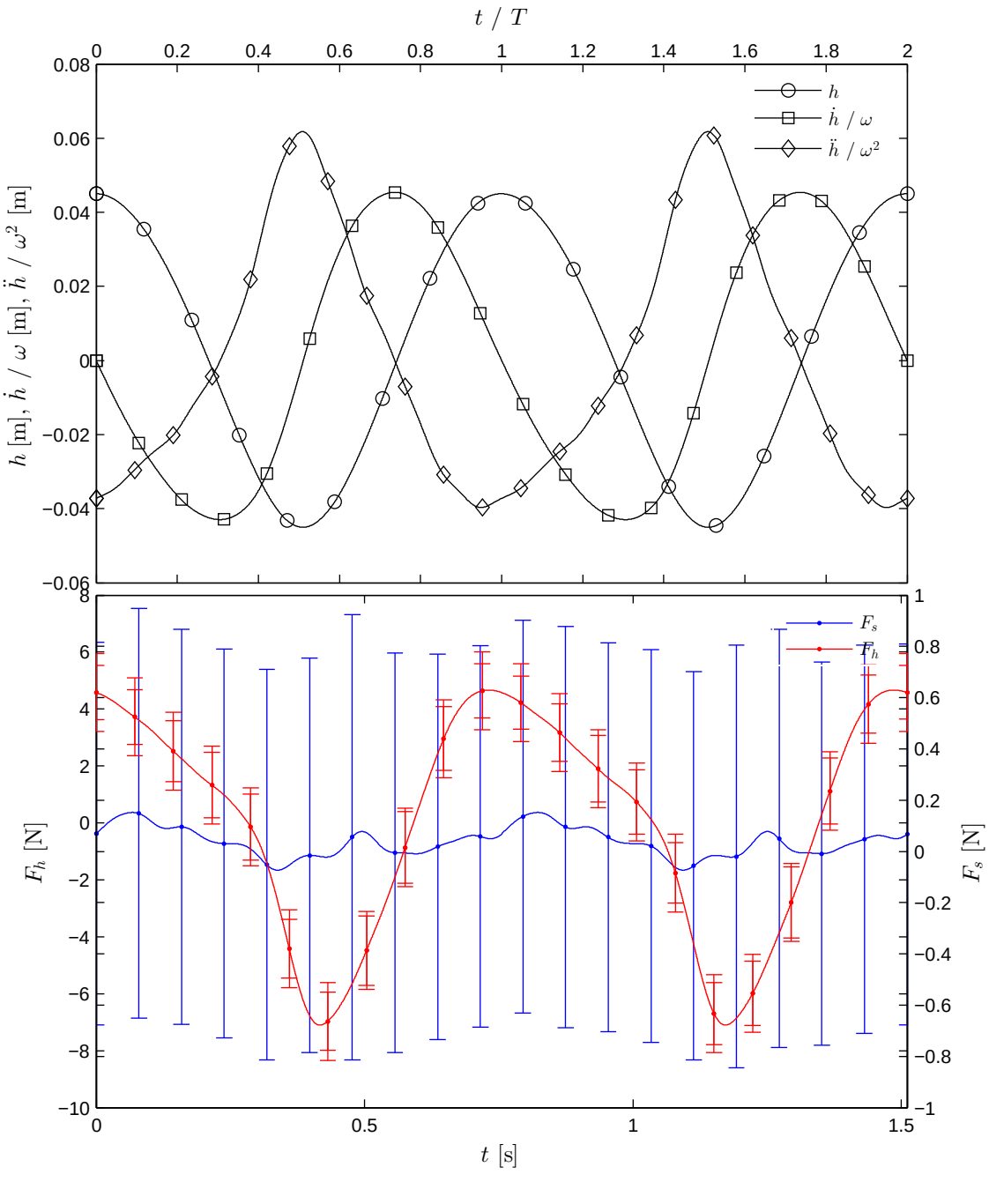

Object: Cylinder		Motion	Water
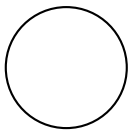	$c = 0.060\,\mathrm{m}$ $L = 0.600\,\mathrm{m}$	$h_0 = 0.045\,\mathrm{m}$ $h^* = 0.75$ $f = 1.83\,\mathrm{Hz}$ $u = 0.00\,\mathrm{m\,s^{-1}}$	$T_w = 11.8\,^\circ\mathrm{C}$ $\rho = 999\,\mathrm{kg\,m^{-3}}$

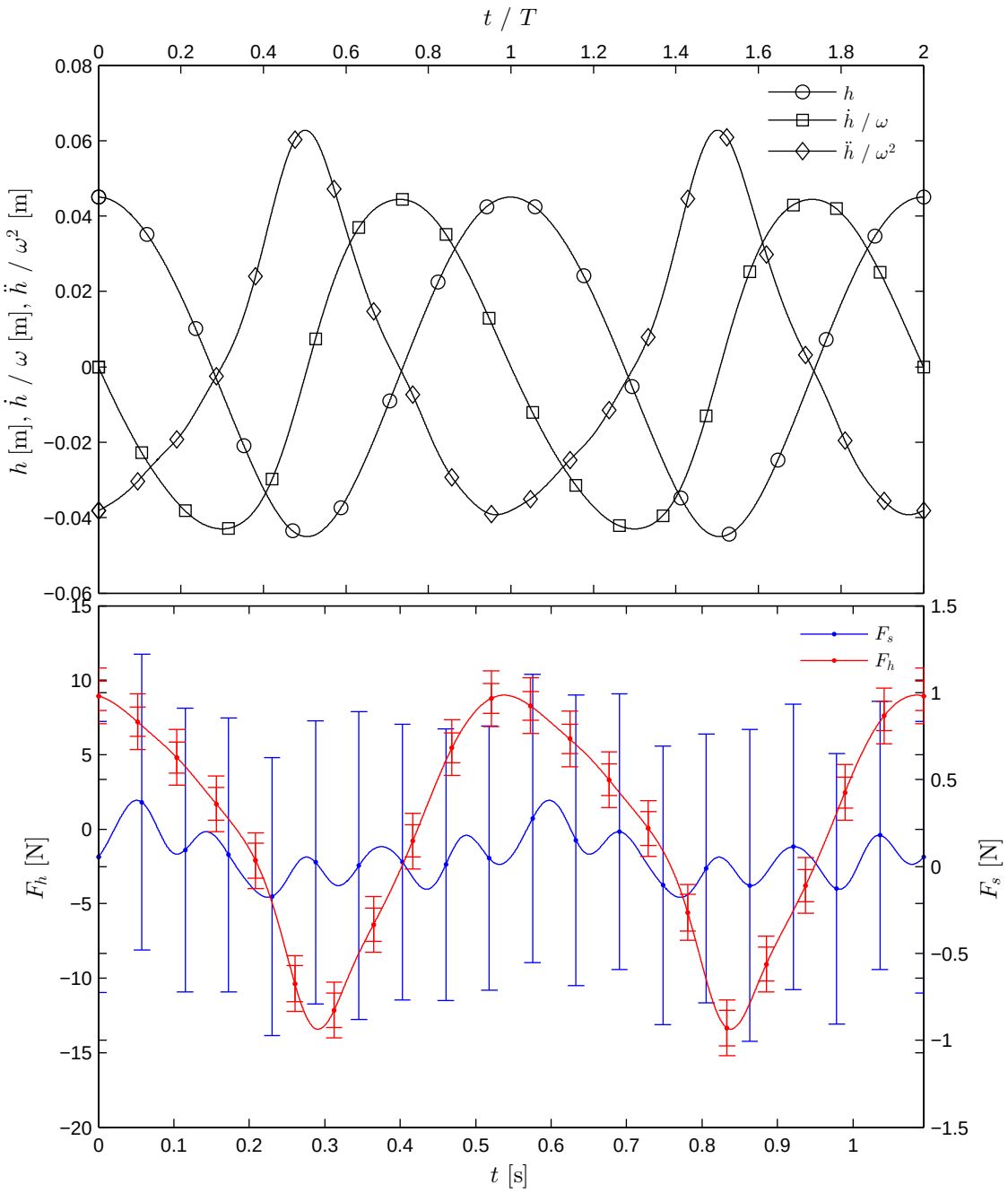

Object: Cylinder		Motion	Water
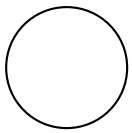	$c = 0.060\,\mathrm{m}$ $L = 0.600\,\mathrm{m}$	$h_0 = 0.045\,\mathrm{m}$ $h^* = 0.75$ $f = 2.27\,\mathrm{Hz}$ $u = 0.00\,\mathrm{m\,s^{-1}}$	$T_w = 11.8\,^\circ\mathrm{C}$ $\rho = 999\,\mathrm{kg\,m^{-3}}$

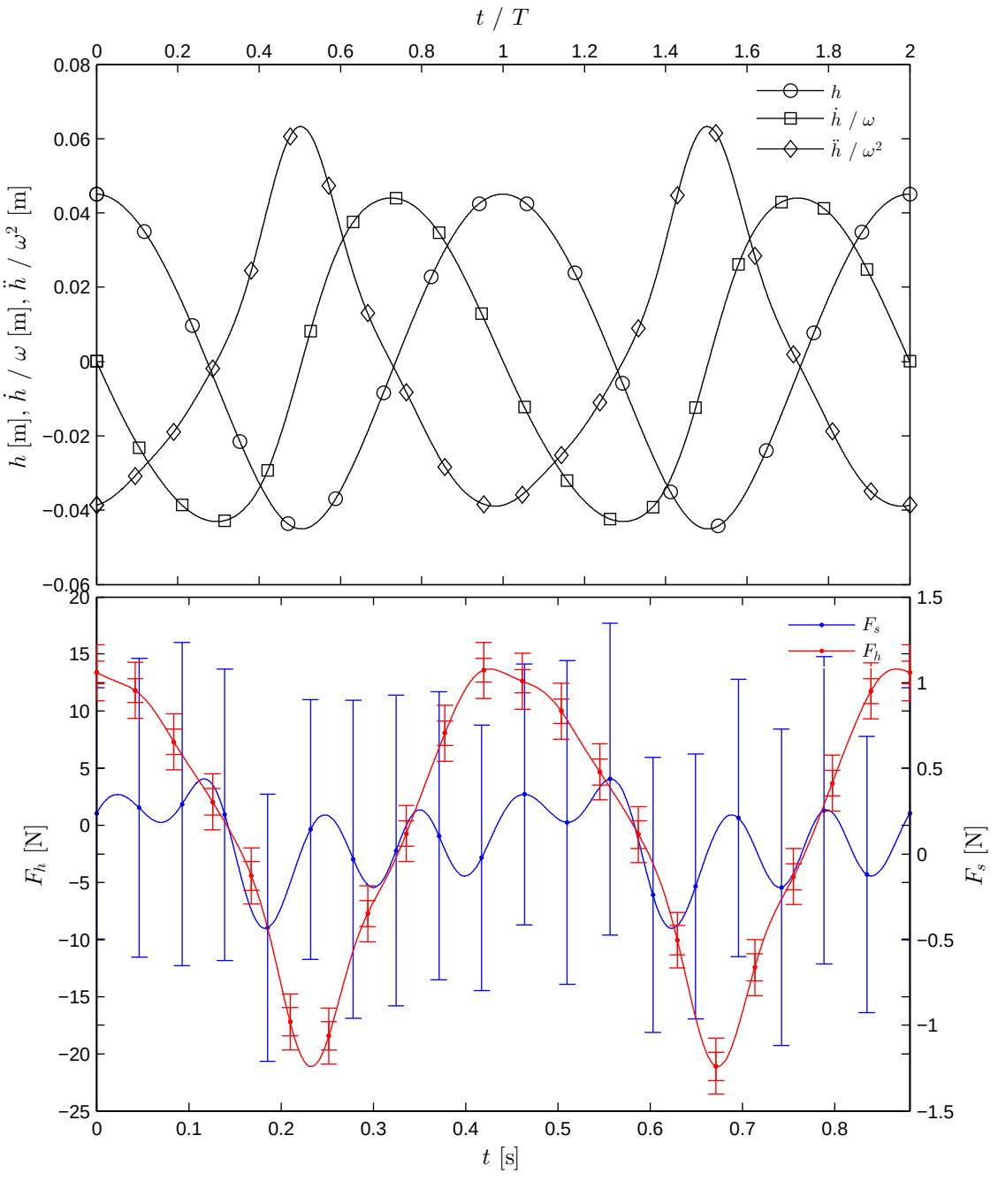

Object: Cylinder		Motion	Water
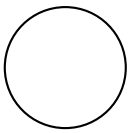	$c = 0.060\,\mathrm{m}$ $L = 0.600\,\mathrm{m}$	$h_0 = 0.045\,\mathrm{m}$ $h^* = 0.75$ $f = 2.82\,\mathrm{Hz}$ $u = 0.00\,\mathrm{m\,s^{-1}}$	$T_w = 11.8\,^\circ\mathrm{C}$ $\rho = 999\,\mathrm{kg\,m^{-3}}$

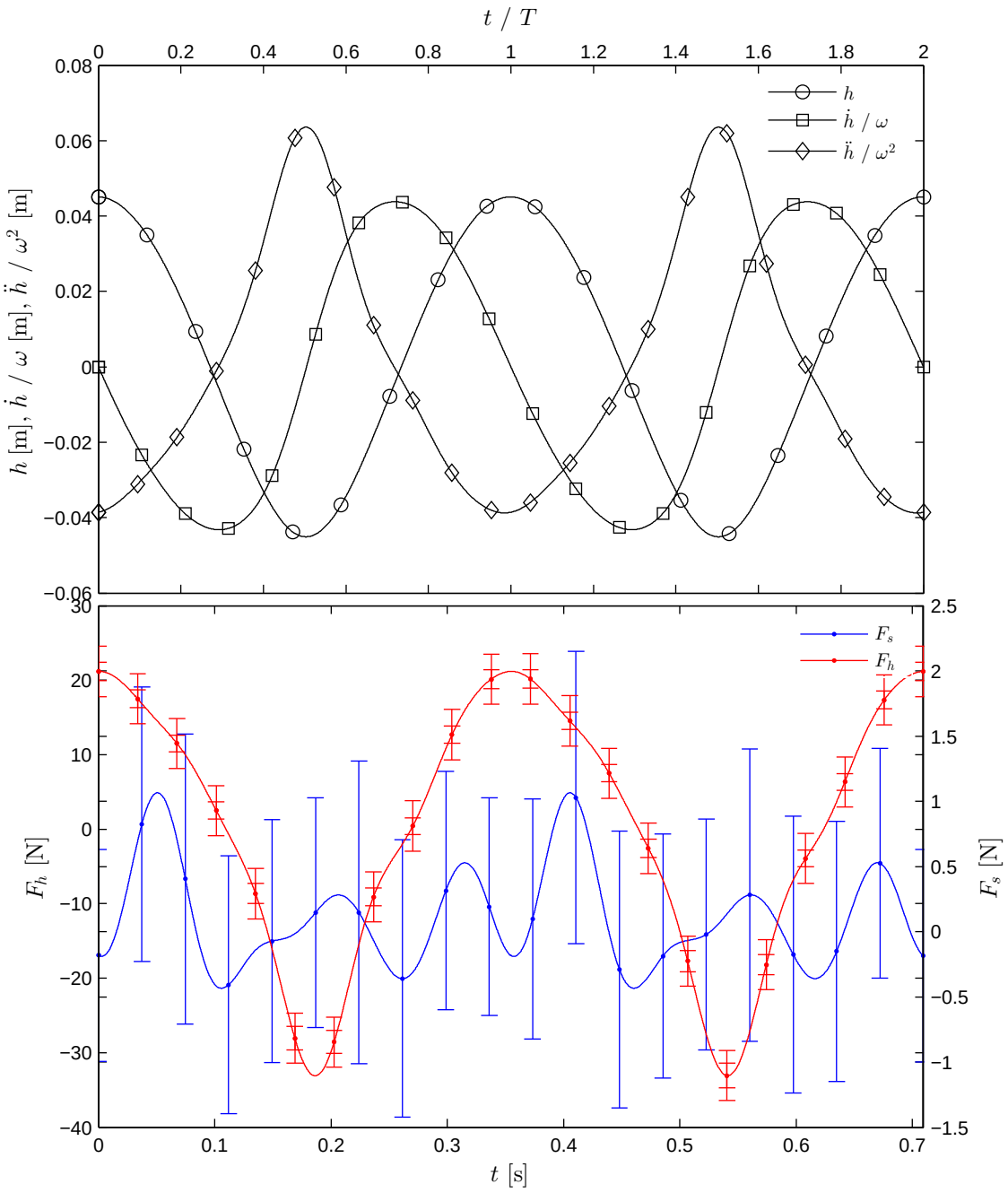

Object: Cylinder		Motion	Water
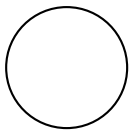	$c = 0.060\,\mathrm{m}$ $L = 0.600\,\mathrm{m}$	$h_0 = 0.045\,\mathrm{m}$ $h^* = 0.75$ $f = 3.34\,\mathrm{Hz}$ $u = 0.00\,\mathrm{m\,s^{-1}}$	$T_w = 11.8\,^\circ\mathrm{C}$ $\rho = 999\,\mathrm{kg\,m^{-3}}$

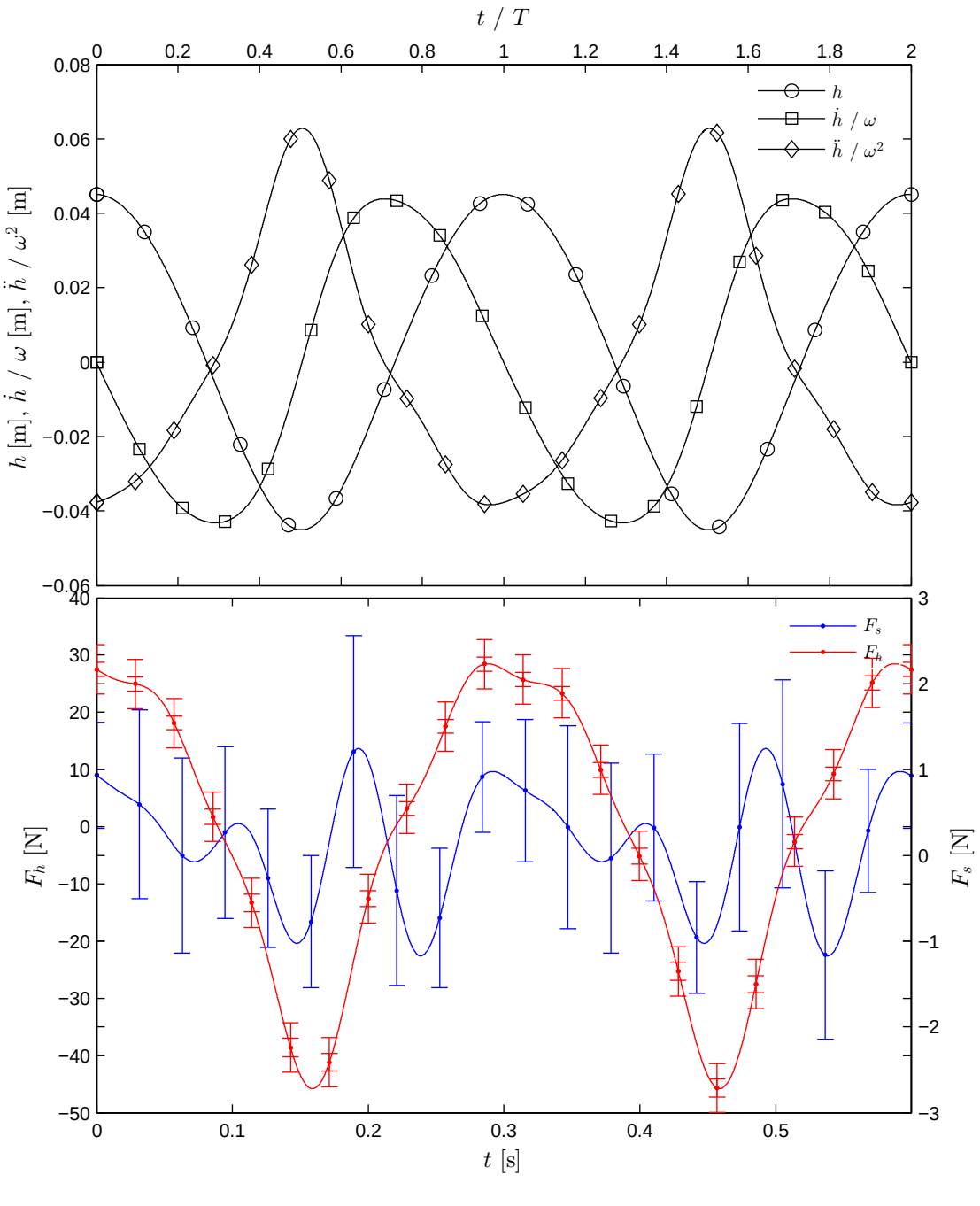

Object: Cylinder		Motion	Water
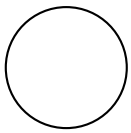	$c = 0.060\,\mathrm{m}$ $L = 0.600\,\mathrm{m}$	$h_0 = 0.045\,\mathrm{m}$ $h^* = 0.75$ $f = 3.77\,\mathrm{Hz}$ $u = 0.00\,\mathrm{m\,s^{-1}}$	$T_w = 11.8\,^\circ\mathrm{C}$ $\rho = 999\,\mathrm{kg\,m^{-3}}$

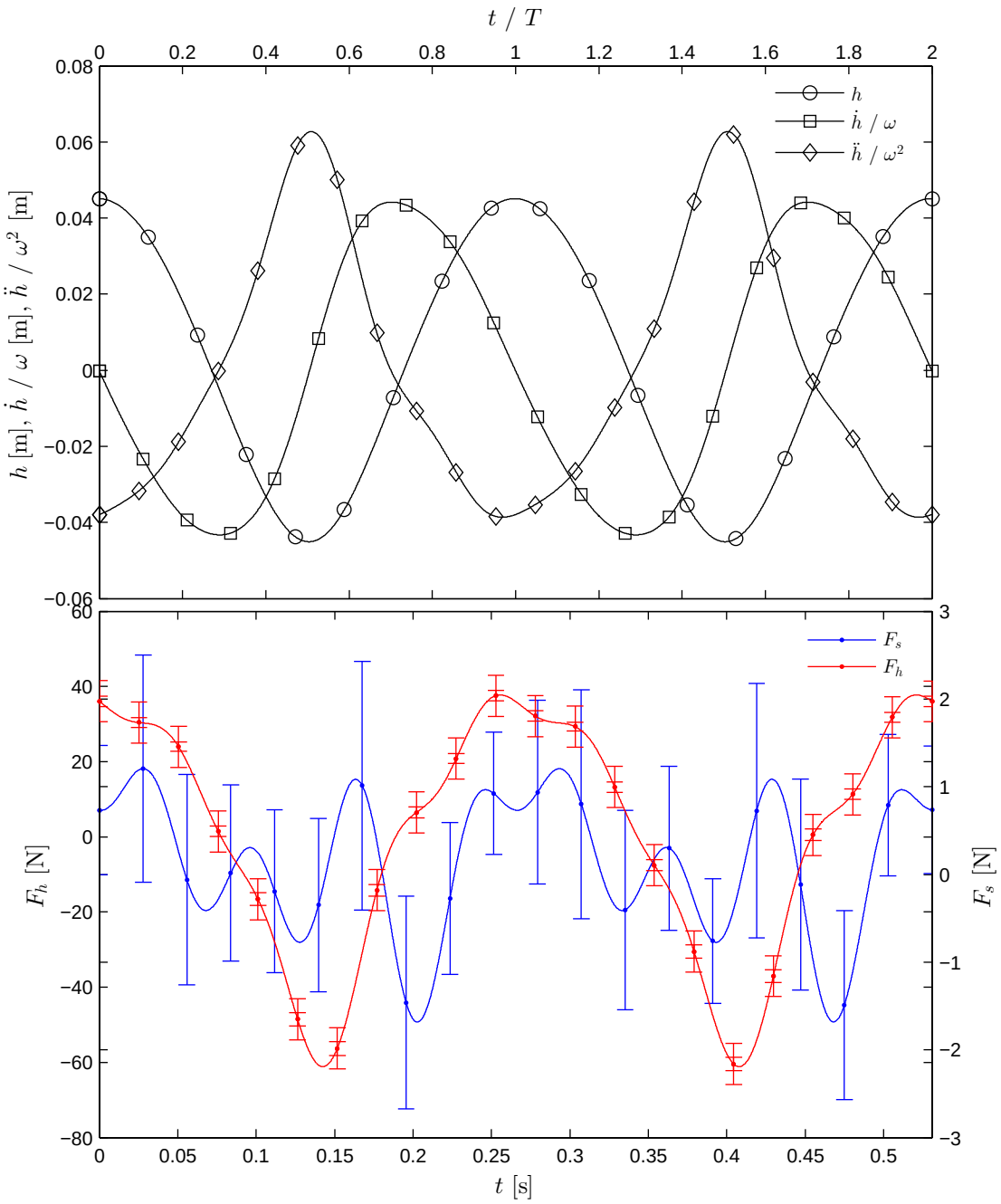

Object: Cylinder		Motion	Water
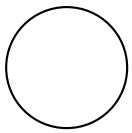	$c = 0.060\,\mathrm{m}$ $L = 0.600\,\mathrm{m}$	$h_0 = 0.045\,\mathrm{m}$ $h^* = 0.75$ $f = 1.58\,\mathrm{Hz}$ $u = 0.52\,\mathrm{m\,s^{-1}}$	$T_w = 10.9\,^\circ\mathrm{C}$ $\rho = 1000\,\mathrm{kg\,m^{-3}}$

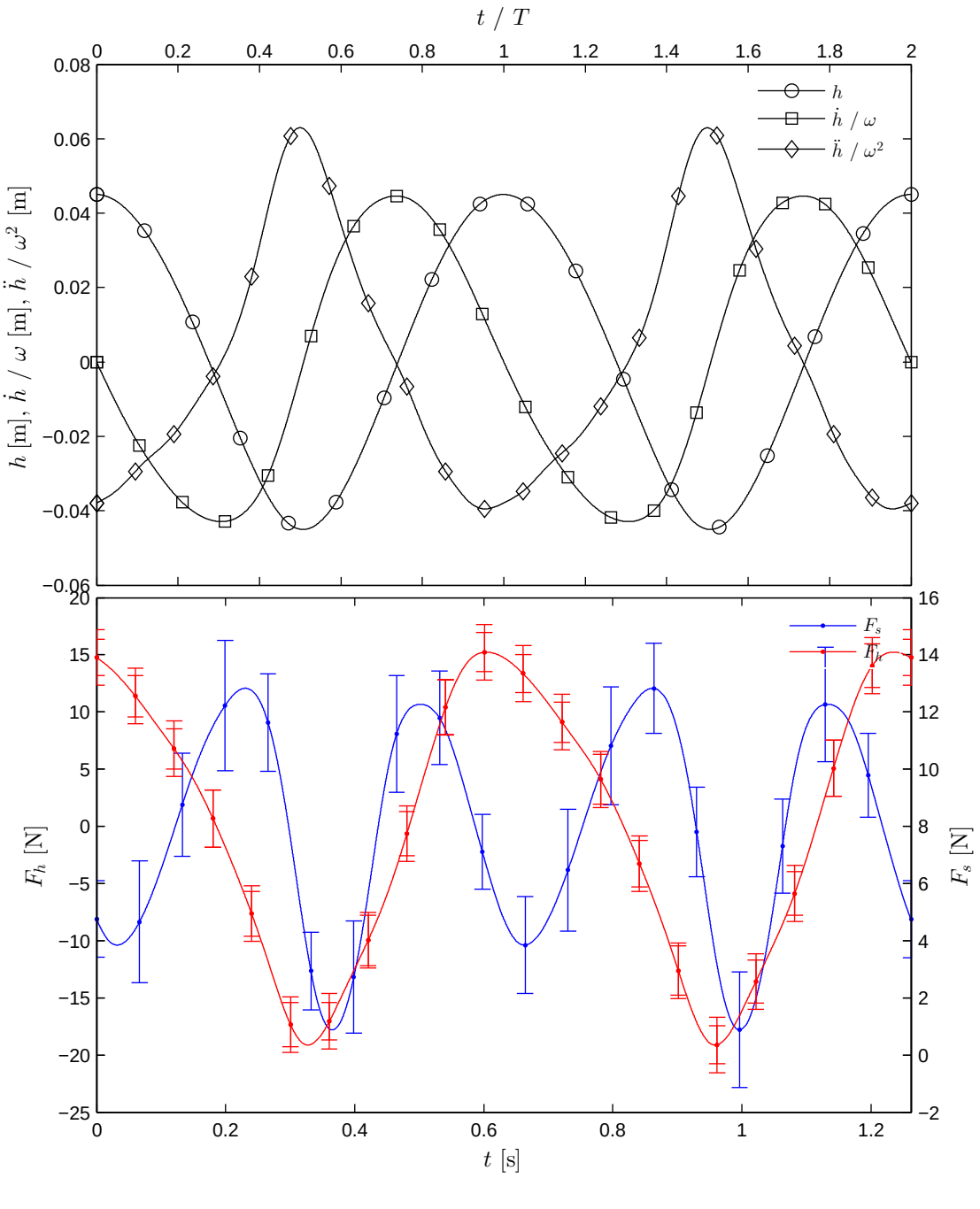

Object: Cylinder		Motion	Water
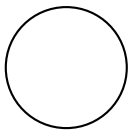	$c = 0.060\,\mathrm{m}$ $L = 0.600\,\mathrm{m}$	$h_0 = 0.045\,\mathrm{m}$ $h^* = 0.75$ $f = 1.57\,\mathrm{Hz}$ $u = 0.99\,\mathrm{m\,s^{-1}}$	$T_w = 10.9\,^\circ\mathrm{C}$ $\rho = 1000\,\mathrm{kg\,m^{-3}}$

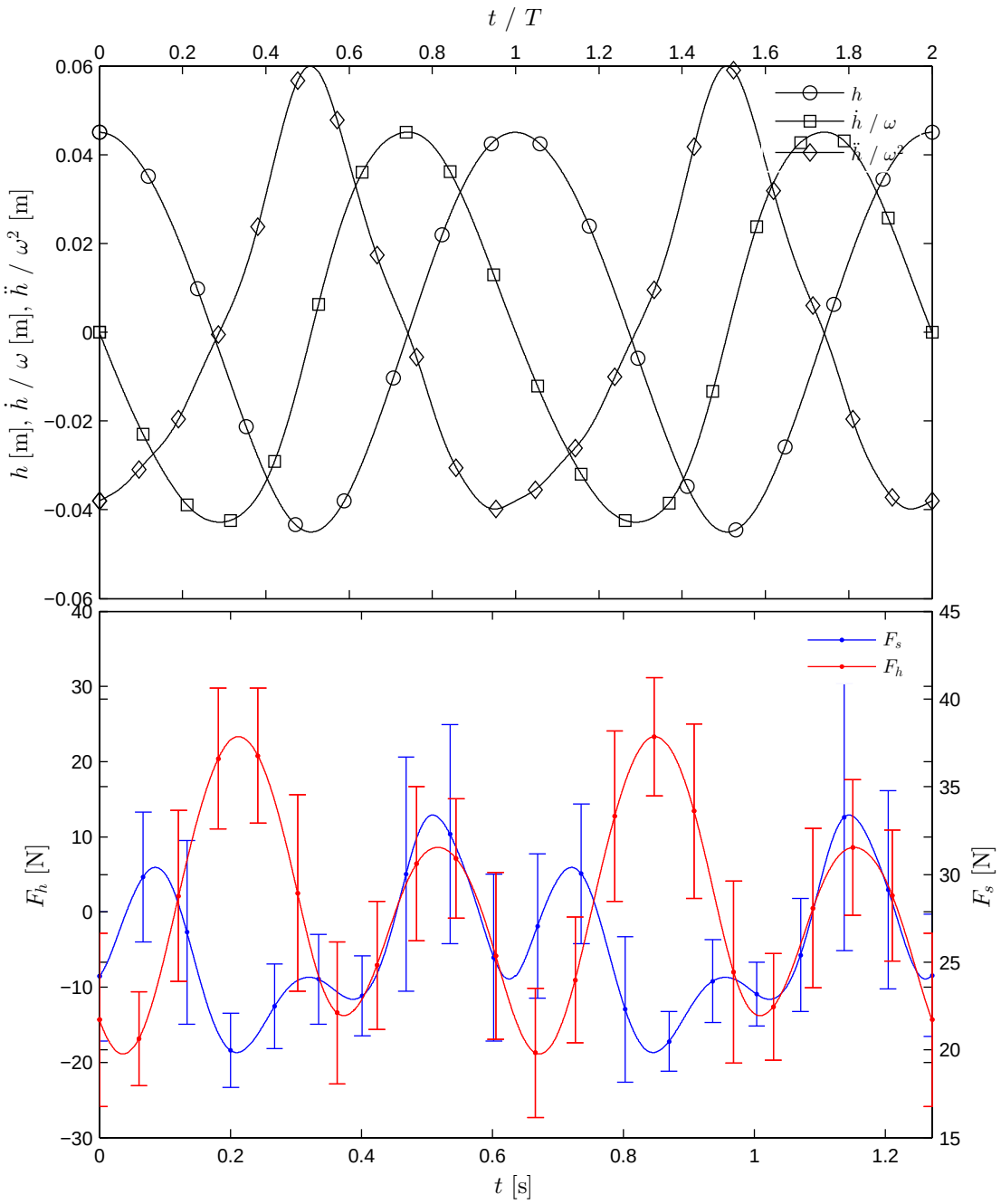

Object: Cylinder		Motion	Water
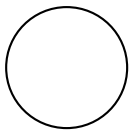	$c = 0.060\,\mathrm{m}$ $L = 0.600\,\mathrm{m}$	$h_0 = 0.045\,\mathrm{m}$ $h^* = 0.75$ $f = 1.57\,\mathrm{Hz}$ $u = 1.49\,\mathrm{m\,s^{-1}}$	$T_w = 10.9\,^\circ\mathrm{C}$ $\rho = 1000\,\mathrm{kg\,m^{-3}}$

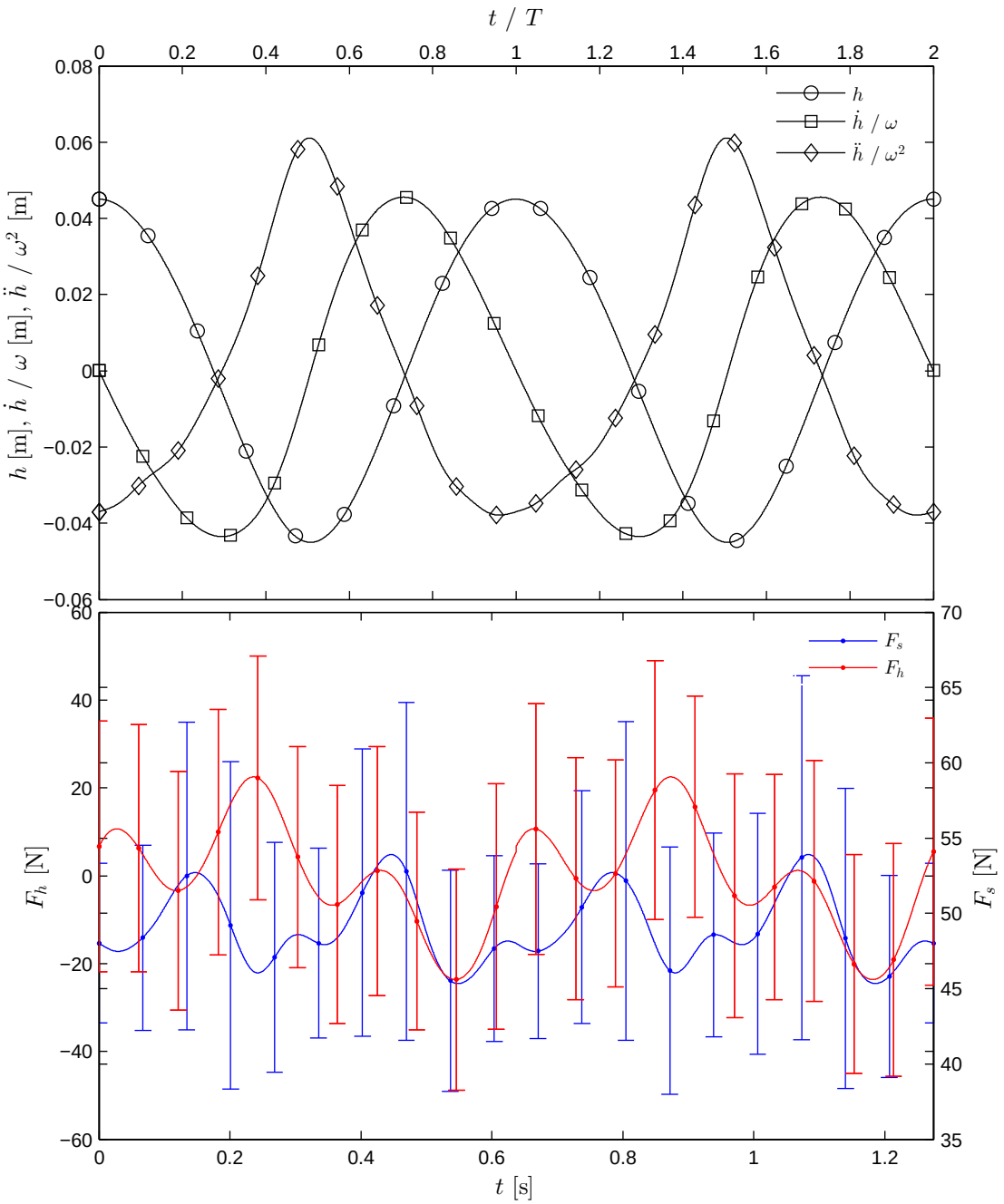

Object: Cylinder		Motion	Water
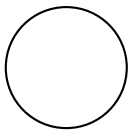	$c = 0.060\,\mathrm{m}$ $L = 0.600\,\mathrm{m}$	$h_0 = 0.045\,\mathrm{m}$ $h^* = 0.75$ $f = 1.57\,\mathrm{Hz}$ $u = 1.94\,\mathrm{m\,s^{-1}}$	$T_w = 10.9\,^\circ\mathrm{C}$ $\rho = 1000\,\mathrm{kg\,m^{-3}}$

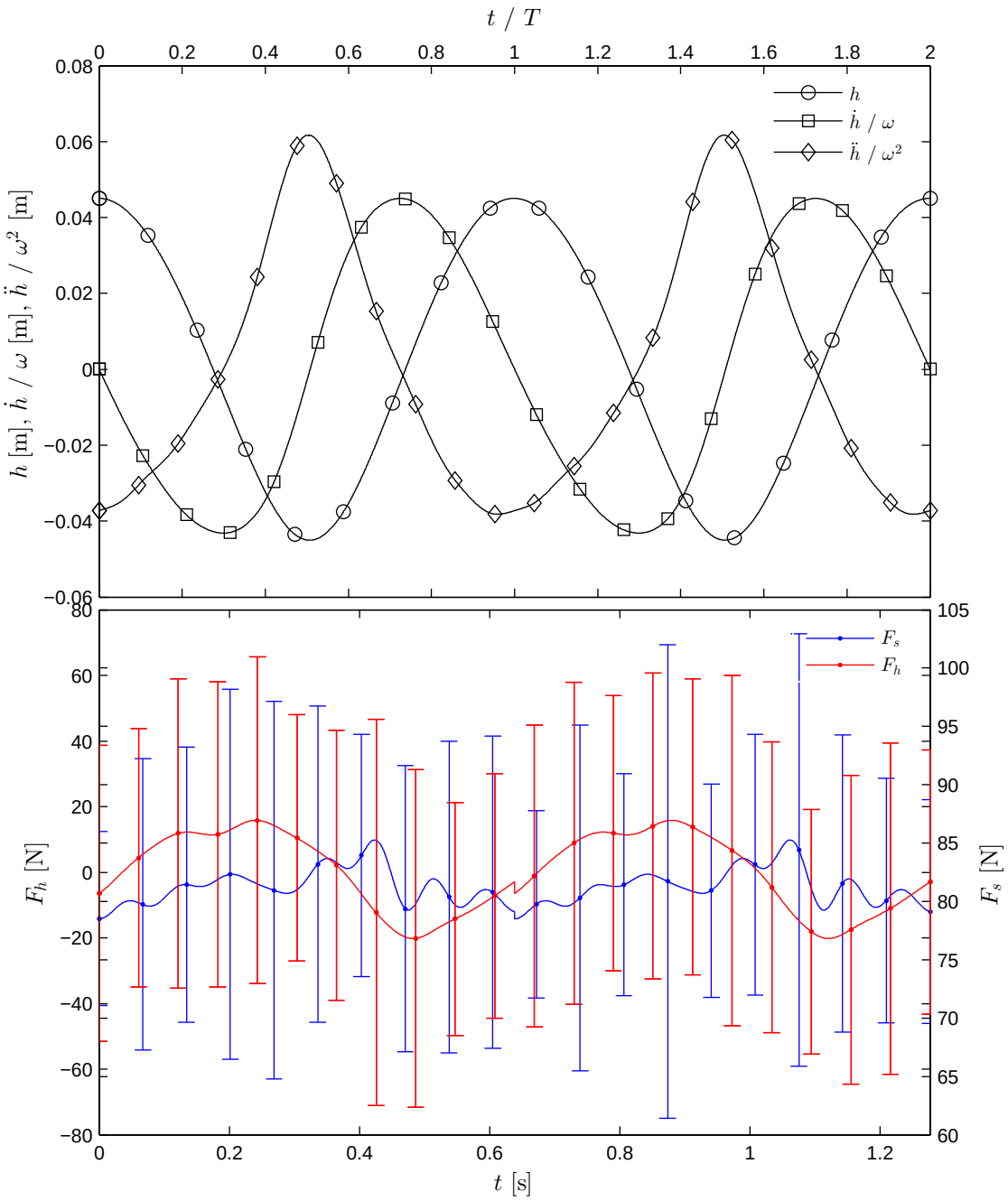

Object: Cylinder		Motion	Water
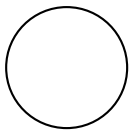	$c = 0.060\,\mathrm{m}$ $L = 0.600\,\mathrm{m}$	$h_0 = 0.045\,\mathrm{m}$ $h^* = 0.75$ $f = 2.16\,\mathrm{Hz}$ $u = 0.52\,\mathrm{m\,s^{-1}}$	$T_w = 10.9\,^\circ\mathrm{C}$ $\rho = 1000\,\mathrm{kg\,m^{-3}}$

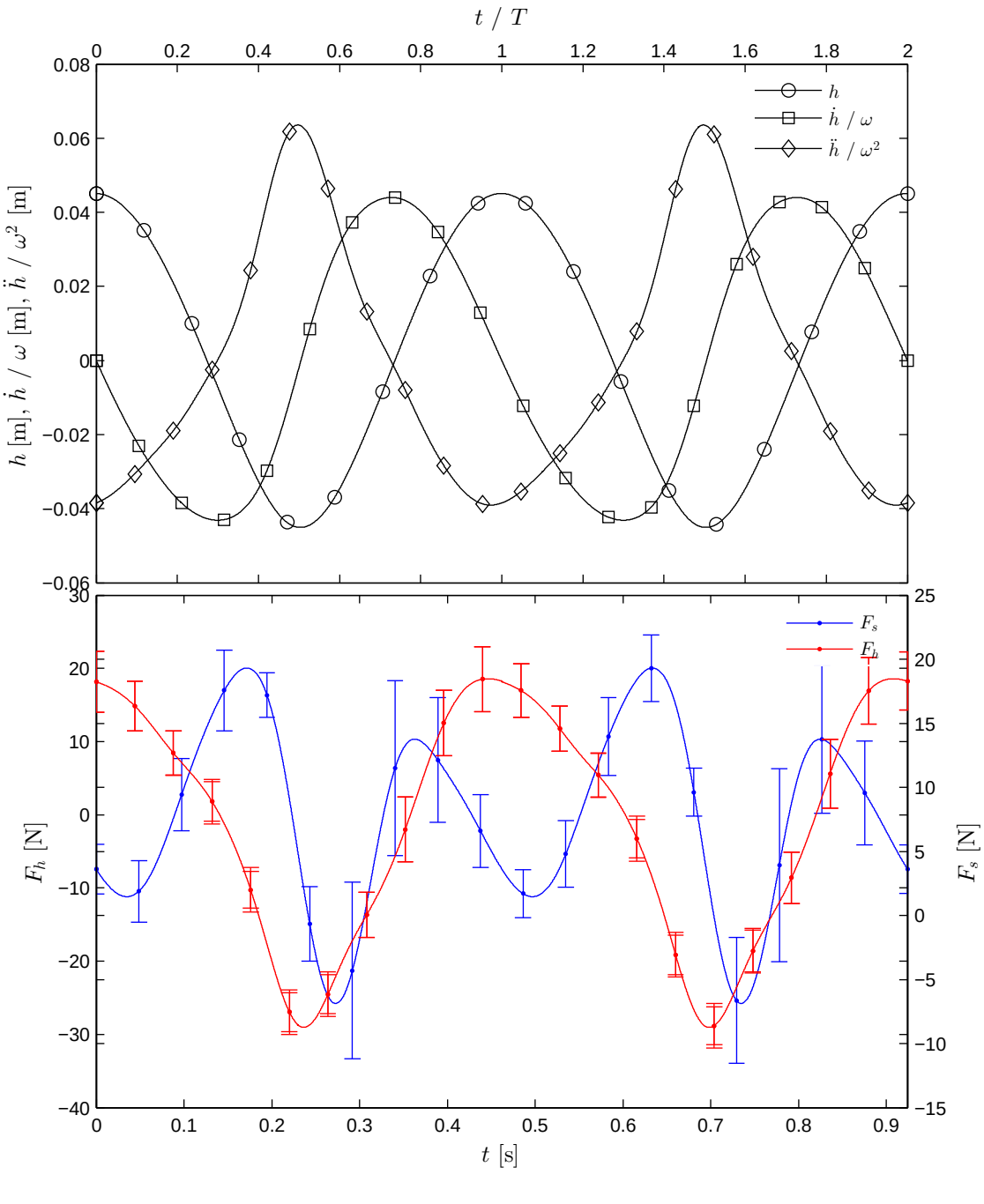

Object: Cylinder		Motion	Water
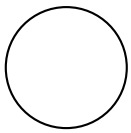	$c = 0.060\,\mathrm{m}$ $L = 0.600\,\mathrm{m}$	$h_0 = 0.045\,\mathrm{m}$ $h^* = 0.75$ $f = 2.15\,\mathrm{Hz}$ $u = 0.99\,\mathrm{m\,s^{-1}}$	$T_w = 10.9\,^\circ\mathrm{C}$ $\rho = 1000\,\mathrm{kg\,m^{-3}}$

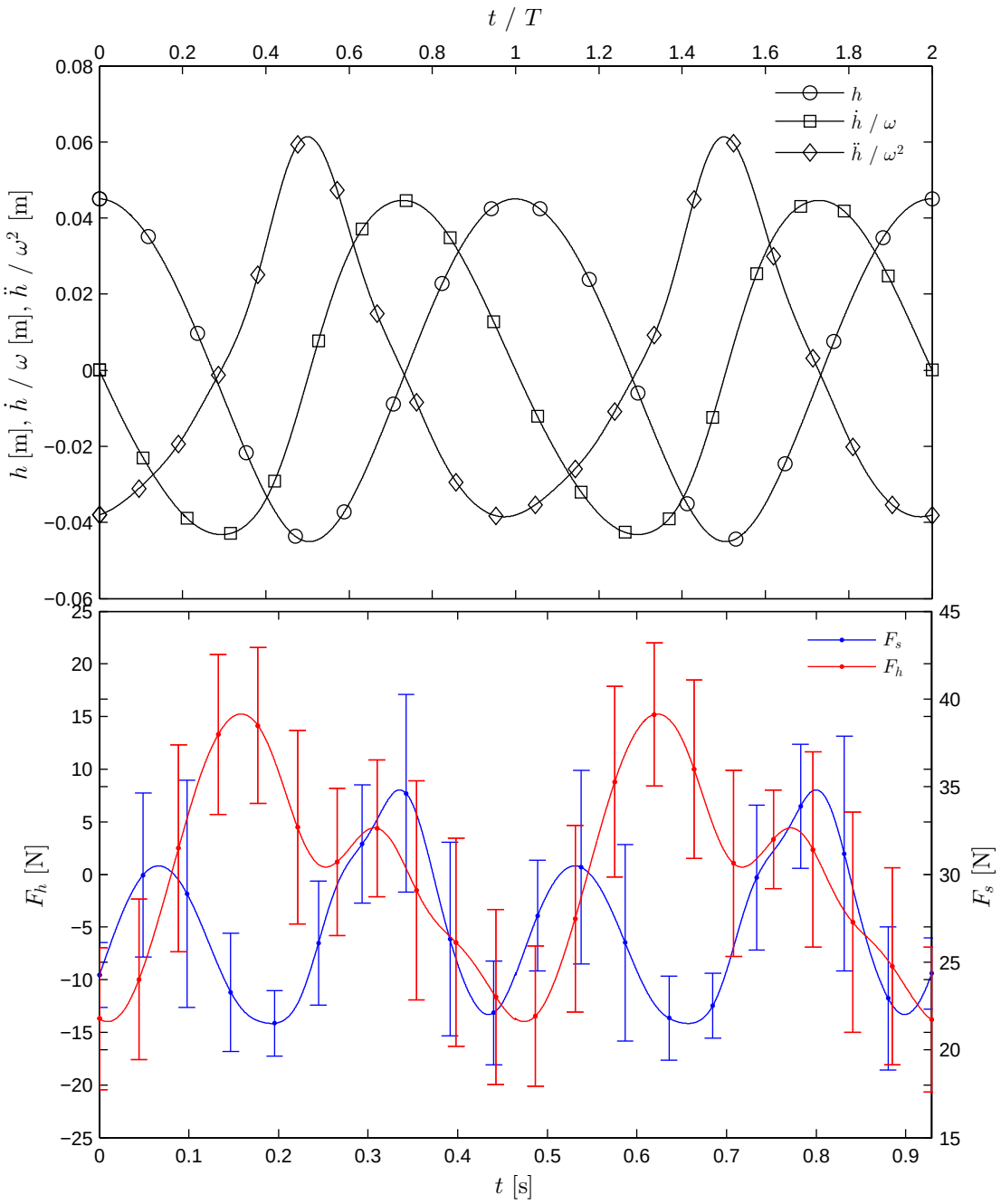

Object: Cylinder		Motion	Water
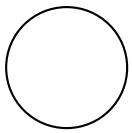	$c = 0.060\,\mathrm{m}$ $L = 0.600\,\mathrm{m}$	$h_0 = 0.045\,\mathrm{m}$ $h^* = 0.75$ $f = 2.16\,\mathrm{Hz}$ $u = 1.49\,\mathrm{m\,s^{-1}}$	$T_w = 10.9\,^\circ\mathrm{C}$ $\rho = 1000\,\mathrm{kg\,m^{-3}}$

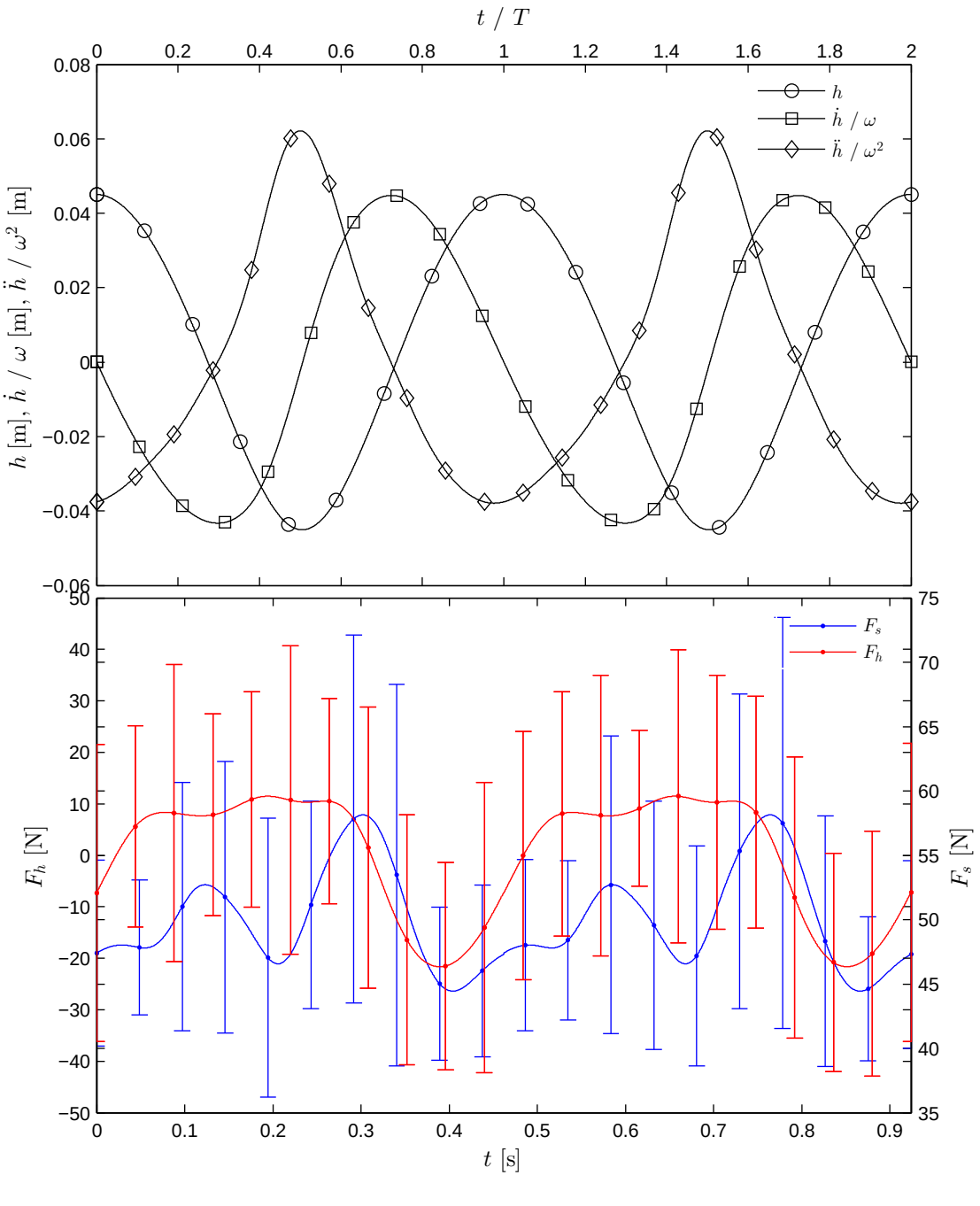

Object: Cylinder		Motion	Water
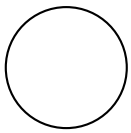	$c = 0.060\,\mathrm{m}$ $L = 0.600\,\mathrm{m}$	$h_0 = 0.045\,\mathrm{m}$ $h^* = 0.75$ $f = 2.14\,\mathrm{Hz}$ $u = 1.95\,\mathrm{m\,s^{-1}}$	$T_w = 10.9\,^\circ\mathrm{C}$ $\rho = 1000\,\mathrm{kg\,m^{-3}}$

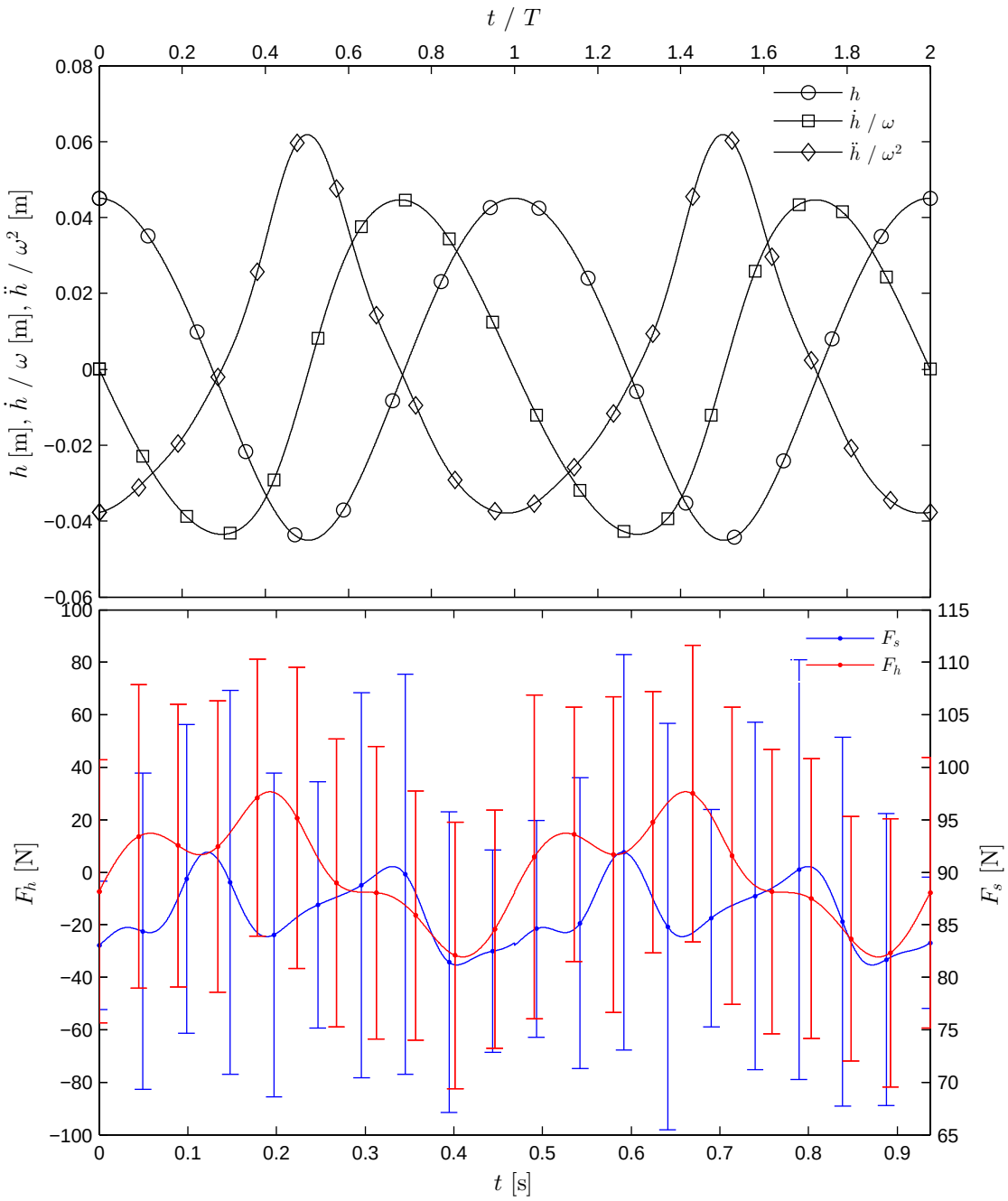

Object: Cylinder		Motion	Water
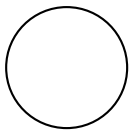	$c = 0.060\,\mathrm{m}$ $L = 0.600\,\mathrm{m}$	$h_0 = 0.045\,\mathrm{m}$ $h^* = 0.75$ $f = 2.76\,\mathrm{Hz}$ $u = 0.52\,\mathrm{m\,s^{-1}}$	$T_w = 10.9\,^\circ\mathrm{C}$ $\rho = 1000\,\mathrm{kg\,m^{-3}}$

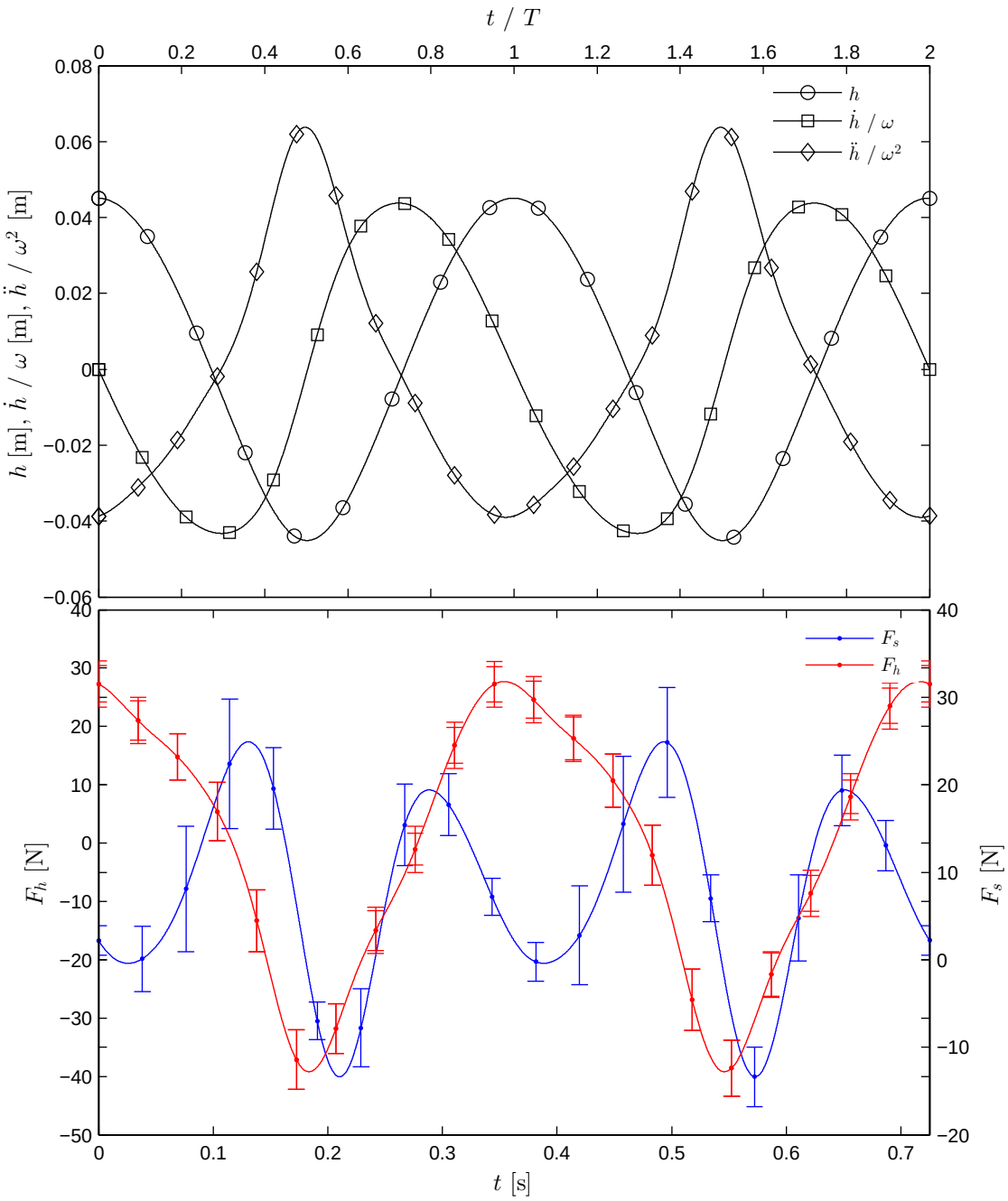

Object: Cylinder		Motion	Water
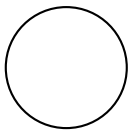	$c = 0.060\,\mathrm{m}$ $L = 0.600\,\mathrm{m}$	$h_0 = 0.045\,\mathrm{m}$ $h^* = 0.75$ $f = 2.76\,\mathrm{Hz}$ $u = 0.99\,\mathrm{m\,s^{-1}}$	$T_w = 10.9\,^\circ\mathrm{C}$ $\rho = 1000\,\mathrm{kg\,m^{-3}}$

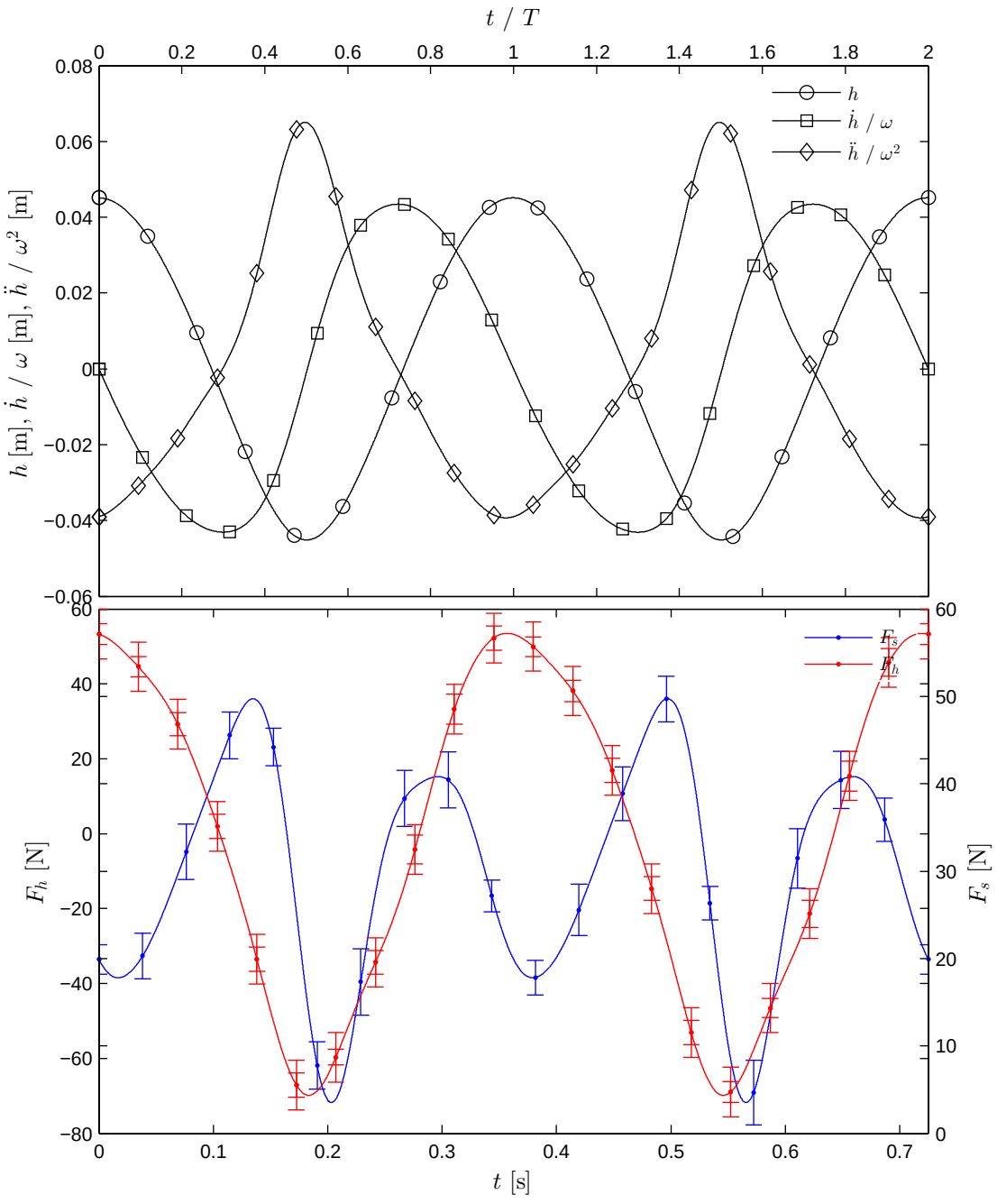

Object: Cylinder		Motion	Water
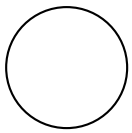	$c = 0.060\,\mathrm{m}$ $L = 0.600\,\mathrm{m}$	$h_0 = 0.045\,\mathrm{m}$ $h^* = 0.75$ $f = 2.84\,\mathrm{Hz}$ $u = 1.49\,\mathrm{m\,s^{-1}}$	$T_w = 10.9\,^\circ\mathrm{C}$ $\rho = 1000\,\mathrm{kg\,m^{-3}}$

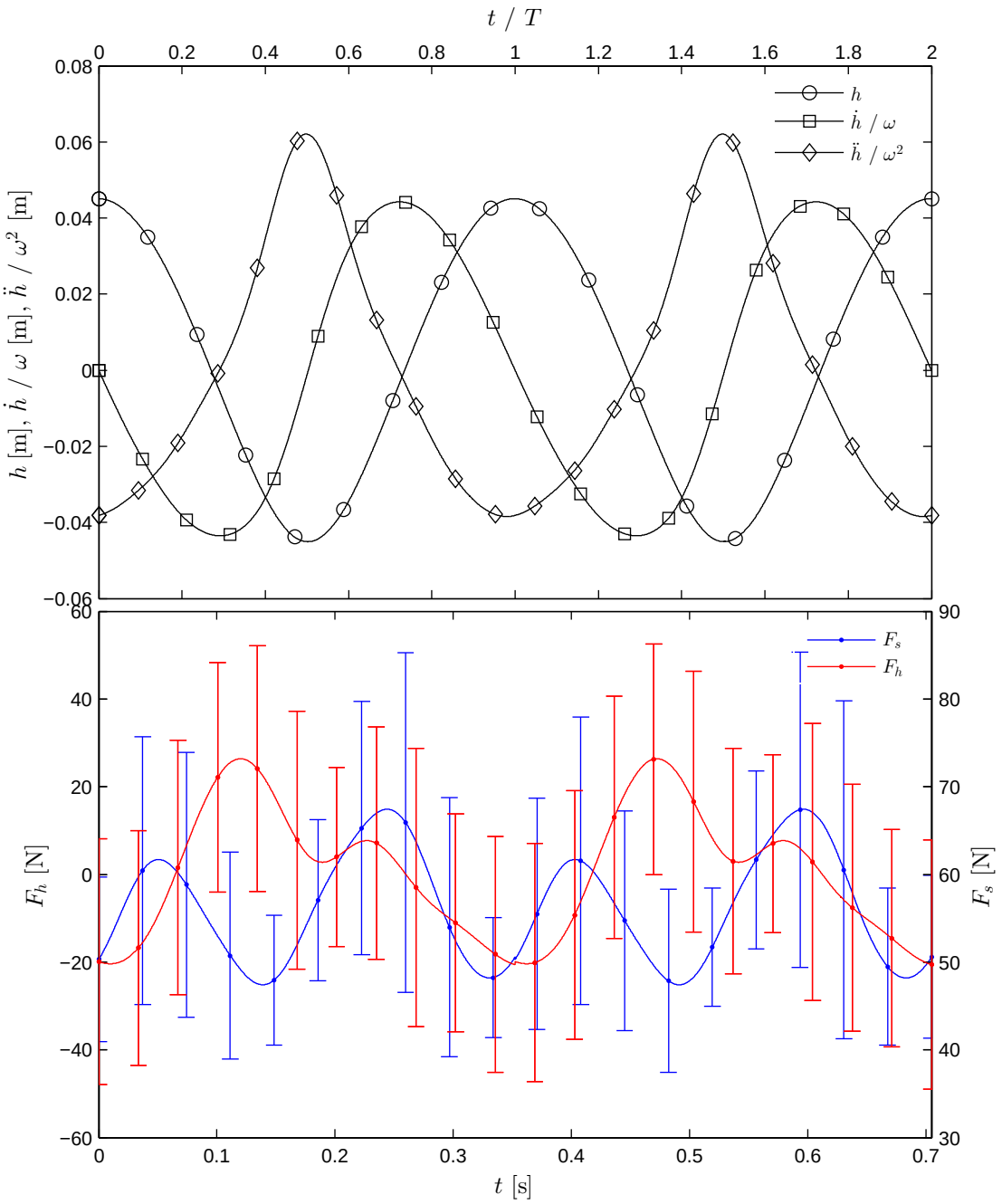

Object: Cylinder		Motion	Water
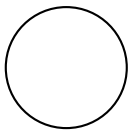	$c = 0.060\,\mathrm{m}$ $L = 0.600\,\mathrm{m}$	$h_0 = 0.045\,\mathrm{m}$ $h^* = 0.75$ $f = 2.73\,\mathrm{Hz}$ $u = 1.95\,\mathrm{m\,s^{-1}}$	$T_w = 10.9\,^\circ\mathrm{C}$ $\rho = 1000\,\mathrm{kg\,m^{-3}}$

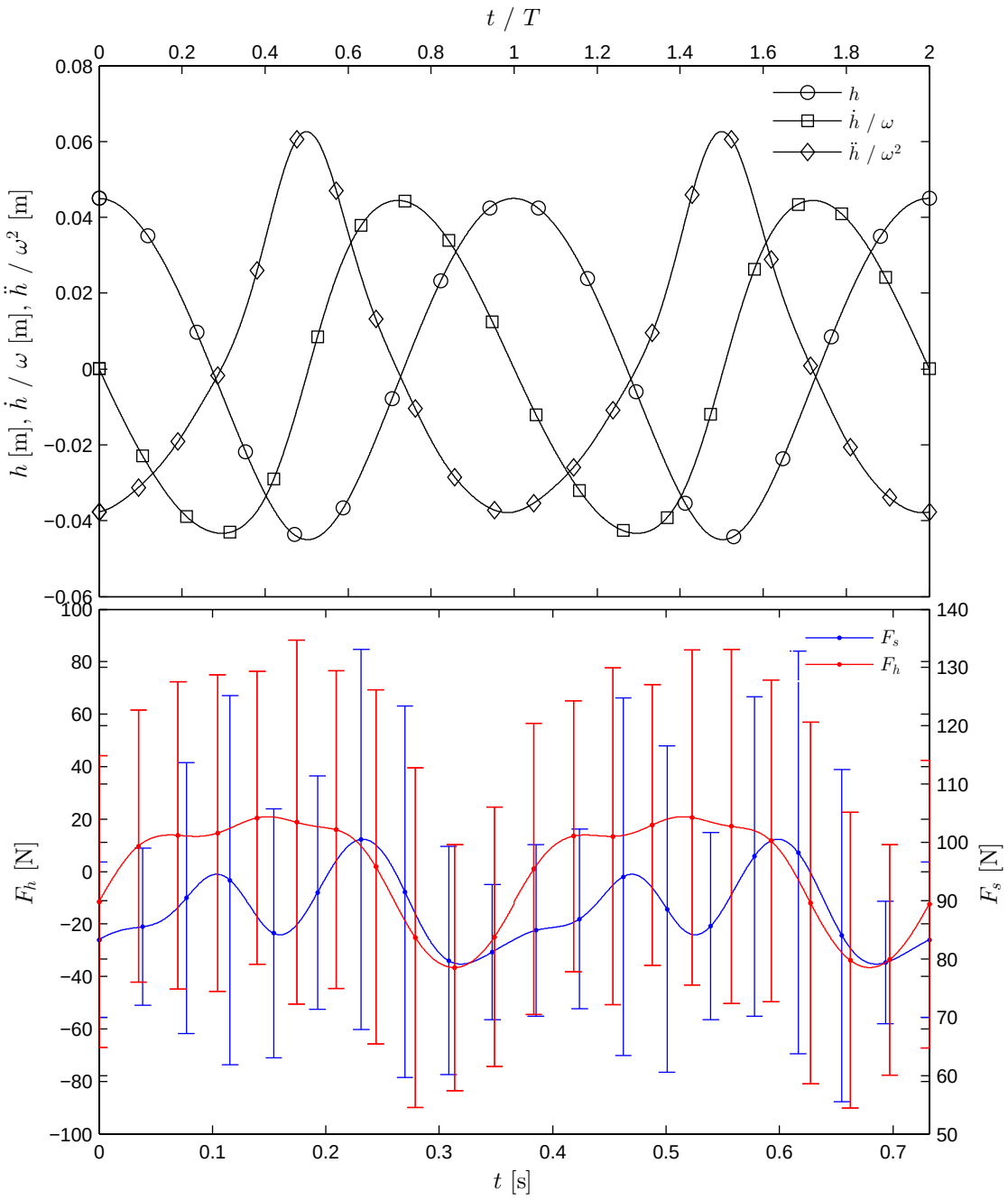

Object: Cylinder		Motion	Water
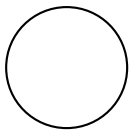	$c = 0.060\,\mathrm{m}$ $L = 0.600\,\mathrm{m}$	$h_0 = 0.045\,\mathrm{m}$ $h^* = 0.75$ $f = 3.32\,\mathrm{Hz}$ $u = 0.52\,\mathrm{m\,s^{-1}}$	$T_w = 10.9\,^\circ\mathrm{C}$ $\rho = 1000\,\mathrm{kg\,m^{-3}}$

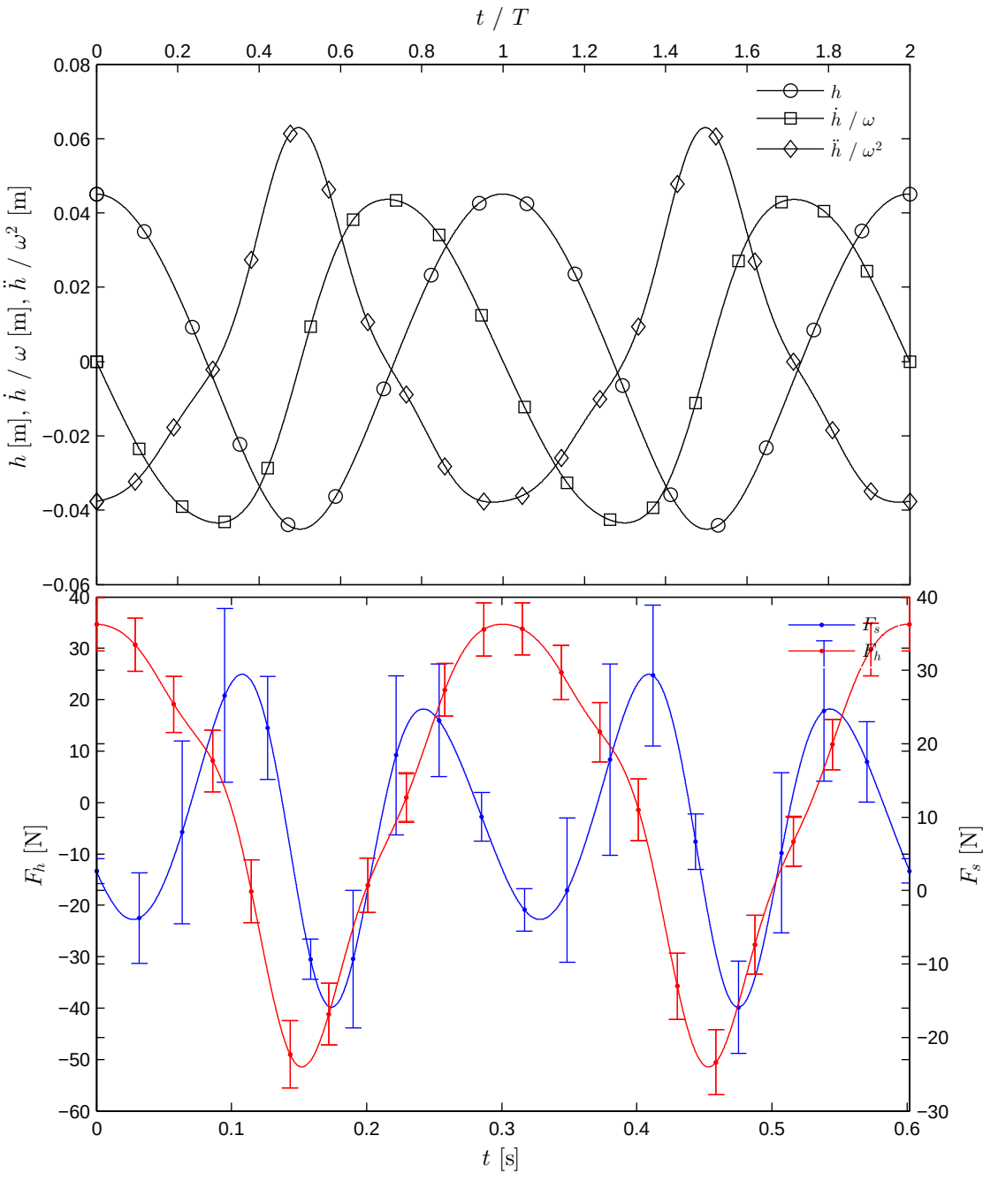

Object: Cylinder		Motion	Water
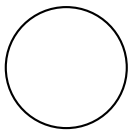	$c = 0.060\,\mathrm{m}$ $L = 0.600\,\mathrm{m}$	$h_0 = 0.045\,\mathrm{m}$ $h^* = 0.75$ $f = 3.34\,\mathrm{Hz}$ $u = 0.99\,\mathrm{m\,s^{-1}}$	$T_w = 10.9\,^\circ\mathrm{C}$ $\rho = 1000\,\mathrm{kg\,m^{-3}}$

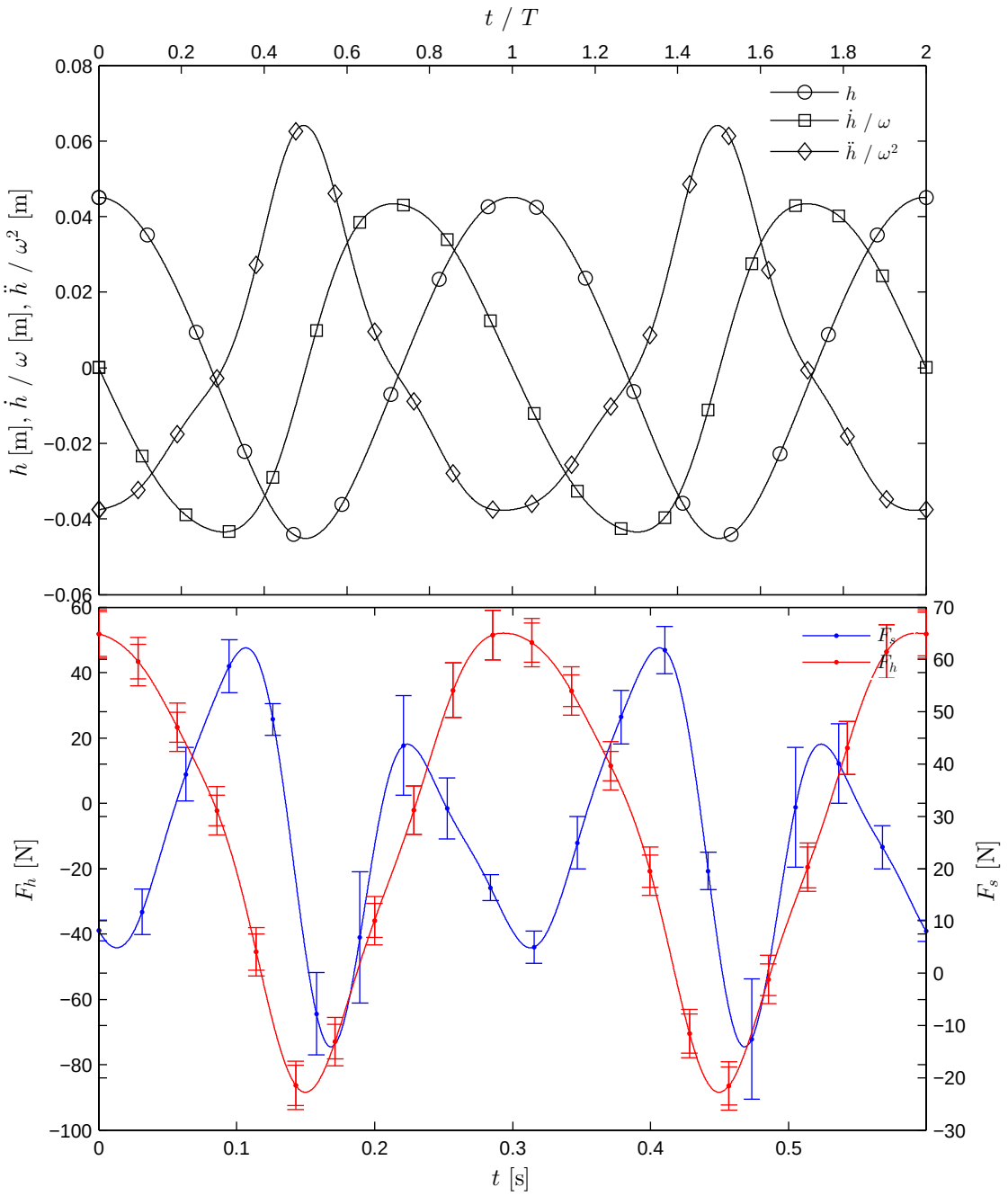

Object: Cylinder		Motion	Water
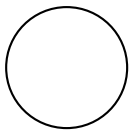	$c = 0.060\,\mathrm{m}$ $L = 0.600\,\mathrm{m}$	$h_0 = 0.045\,\mathrm{m}$ $h^* = 0.75$ $f = 3.48\,\mathrm{Hz}$ $u = 1.49\,\mathrm{m\,s^{-1}}$	$T_w = 10.9\,^\circ\mathrm{C}$ $\rho = 1000\,\mathrm{kg\,m^{-3}}$

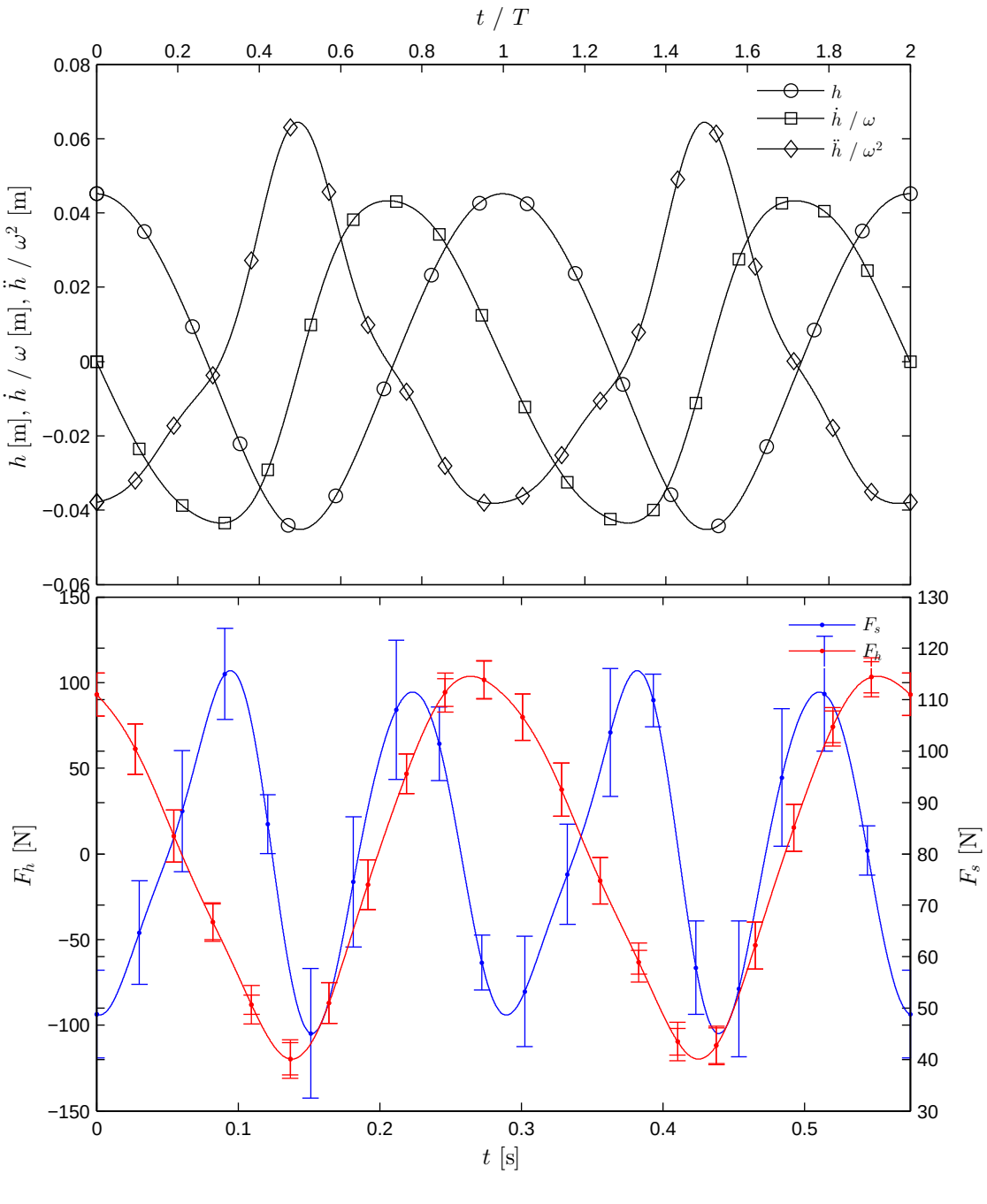

Object: Cylinder		Motion	Water
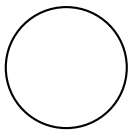	$c = 0.060\,\mathrm{m}$ $L = 0.600\,\mathrm{m}$	$h_0 = 0.045\,\mathrm{m}$ $h^* = 0.75$ $f = 3.30\,\mathrm{Hz}$ $u = 1.96\,\mathrm{m\,s^{-1}}$	$T_w = 10.9\,^\circ\mathrm{C}$ $\rho = 1000\,\mathrm{kg\,m^{-3}}$

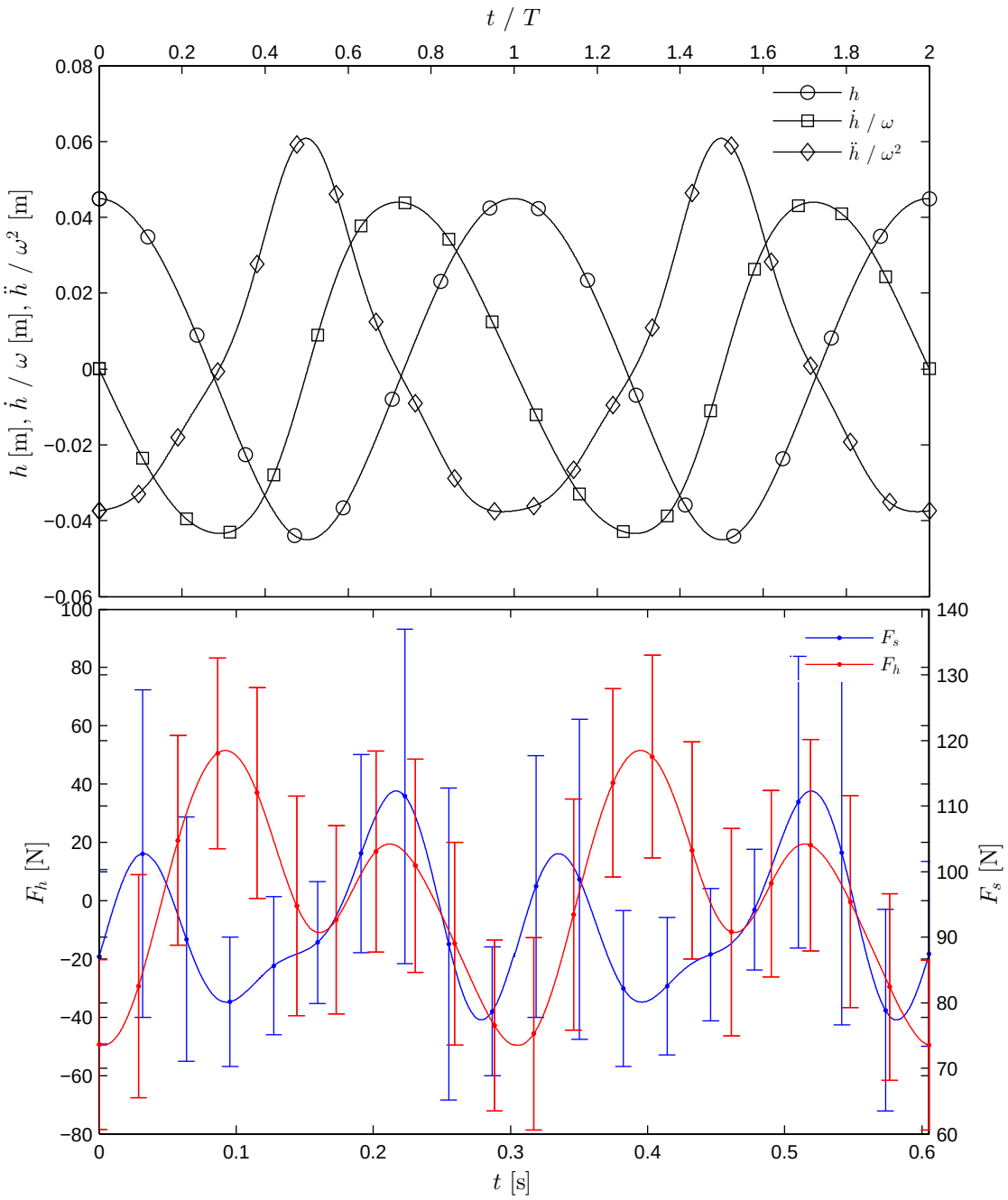

Object: Cylinder		Motion	Water
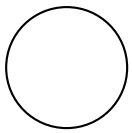	$c = 0.060\,\mathrm{m}$ $L = 0.600\,\mathrm{m}$	$h_0 = 0.045\,\mathrm{m}$ $h^* = 0.75$ $f = 3.87\,\mathrm{Hz}$ $u = 0.52\,\mathrm{m\,s^{-1}}$	$T_w = 10.9\,^\circ\mathrm{C}$ $\rho = 1000\,\mathrm{kg\,m^{-3}}$

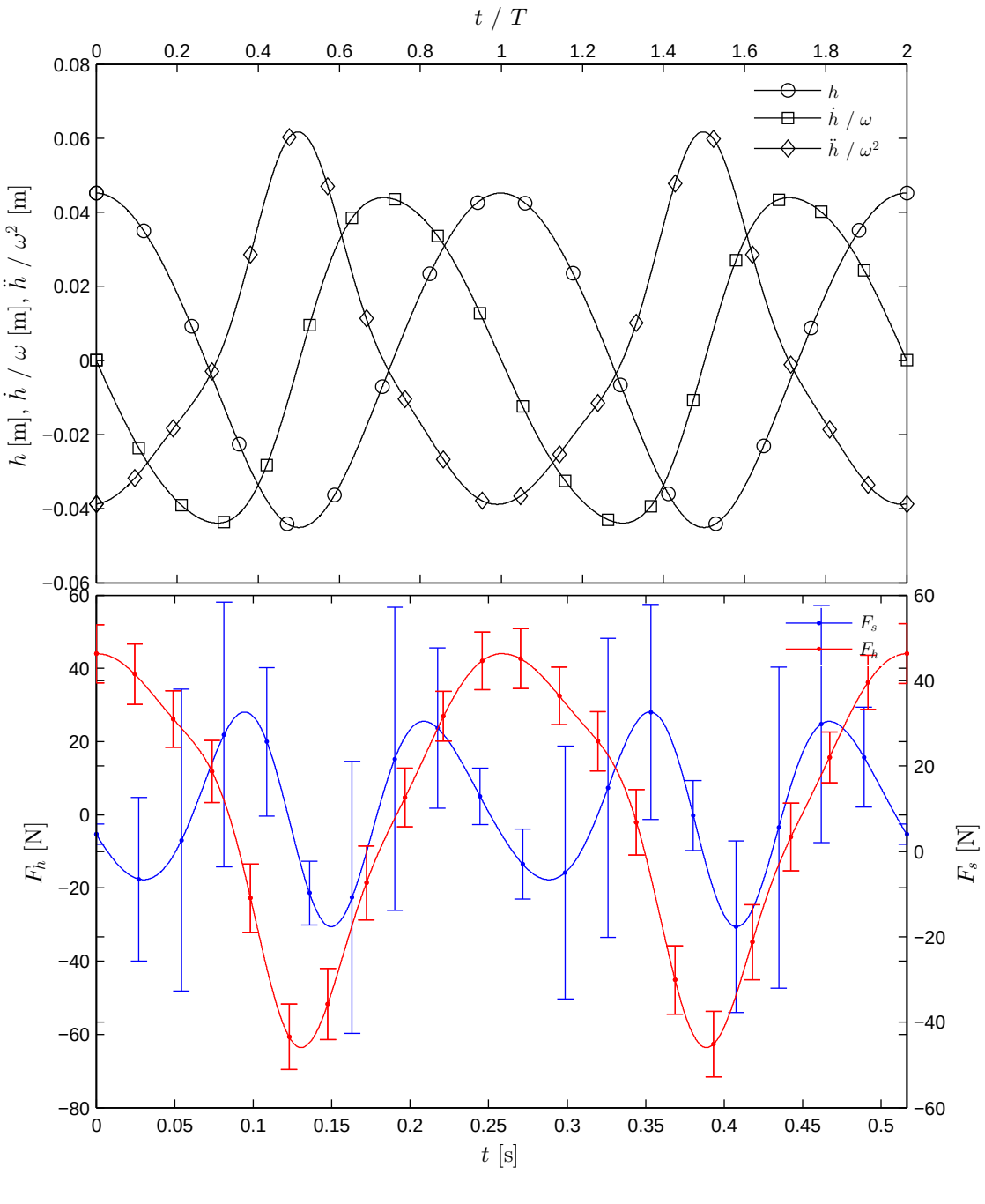

Object: Cylinder		Motion	Water
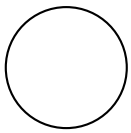	$c = 0.060\,\mathrm{m}$ $L = 0.600\,\mathrm{m}$	$h_0 = 0.045\,\mathrm{m}$ $h^* = 0.75$ $f = 3.89\,\mathrm{Hz}$ $u = 0.99\,\mathrm{m\,s^{-1}}$	$T_w = 10.9\,^\circ\mathrm{C}$ $\rho = 1000\,\mathrm{kg\,m^{-3}}$

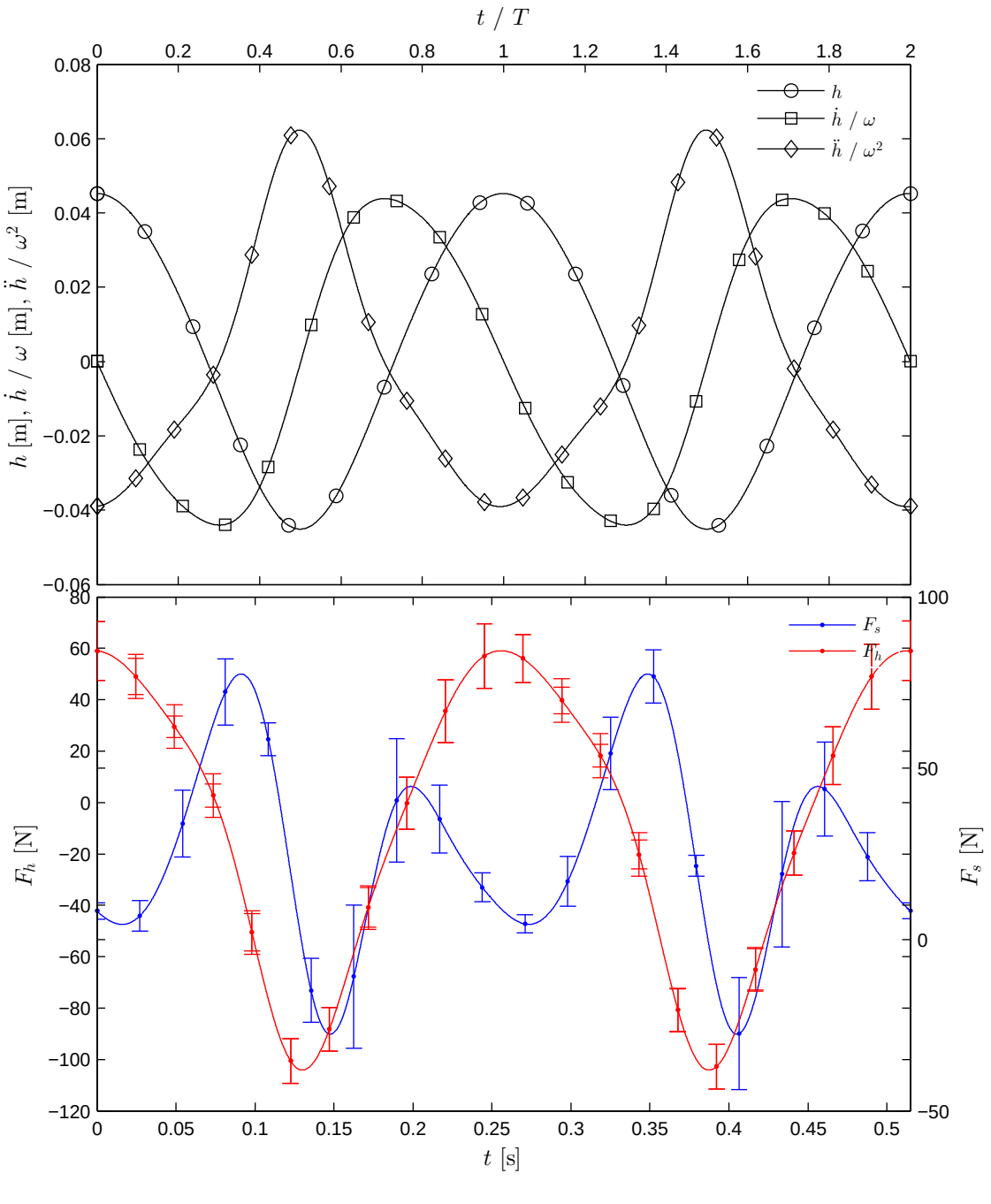

Object: Cylinder		Motion	Water
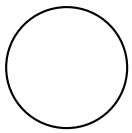	$c = 0.060\,\mathrm{m}$ $L = 0.600\,\mathrm{m}$	$h_0 = 0.045\,\mathrm{m}$ $h^* = 0.75$ $f = 3.87\,\mathrm{Hz}$ $u = 1.49\,\mathrm{m\,s^{-1}}$	$T_w = 10.9\,^\circ\mathrm{C}$ $\rho = 1000\,\mathrm{kg\,m^{-3}}$

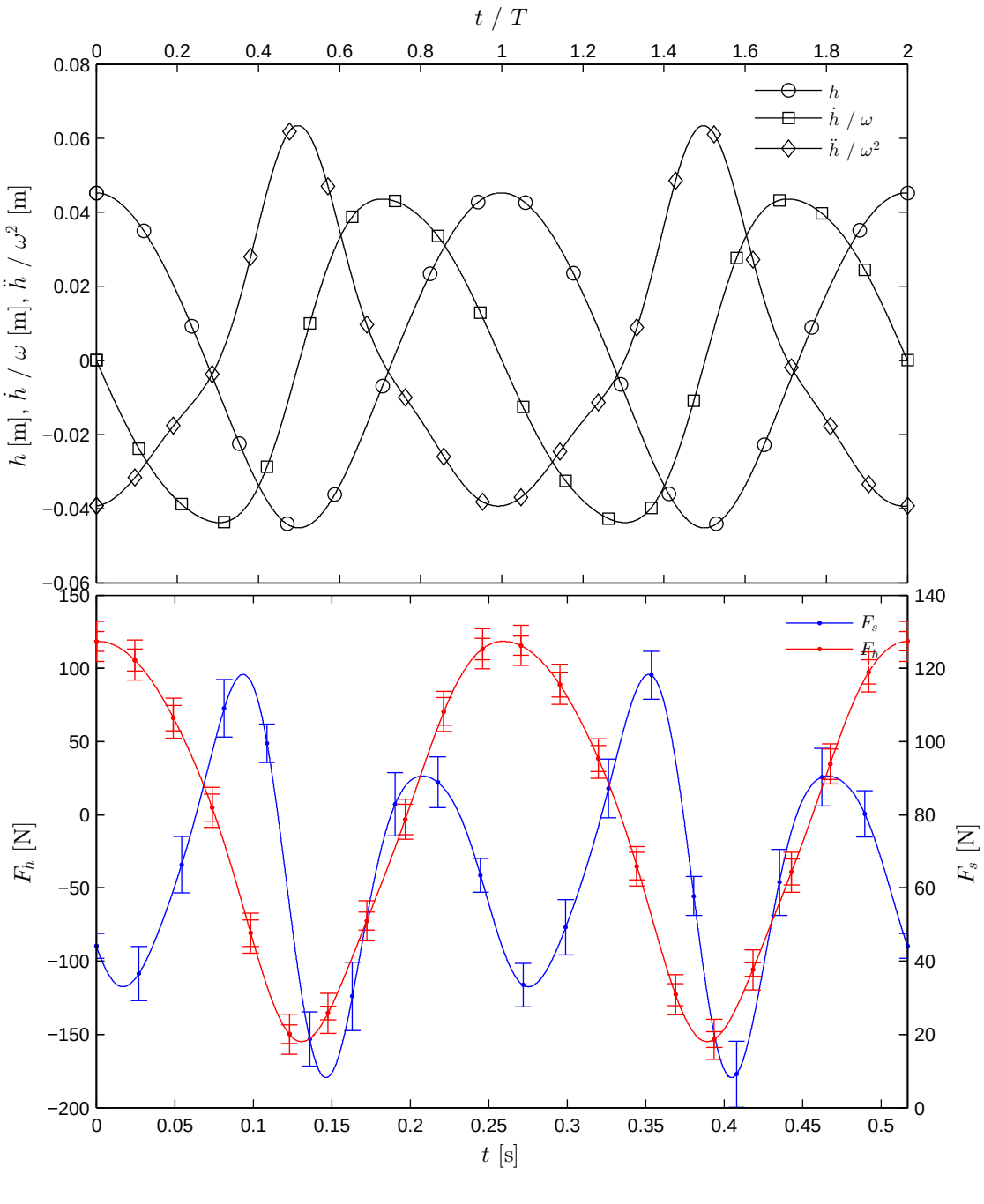

Object: Cylinder		Motion	Water
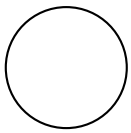	$c = 0.060\,\mathrm{m}$ $L = 0.600\,\mathrm{m}$	$h_0 = 0.045\,\mathrm{m}$ $h^* = 0.75$ $f = 3.92\,\mathrm{Hz}$ $u = 1.96\,\mathrm{m\,s^{-1}}$	$T_w = 10.9\,^\circ\mathrm{C}$ $\rho = 1000\,\mathrm{kg\,m^{-3}}$

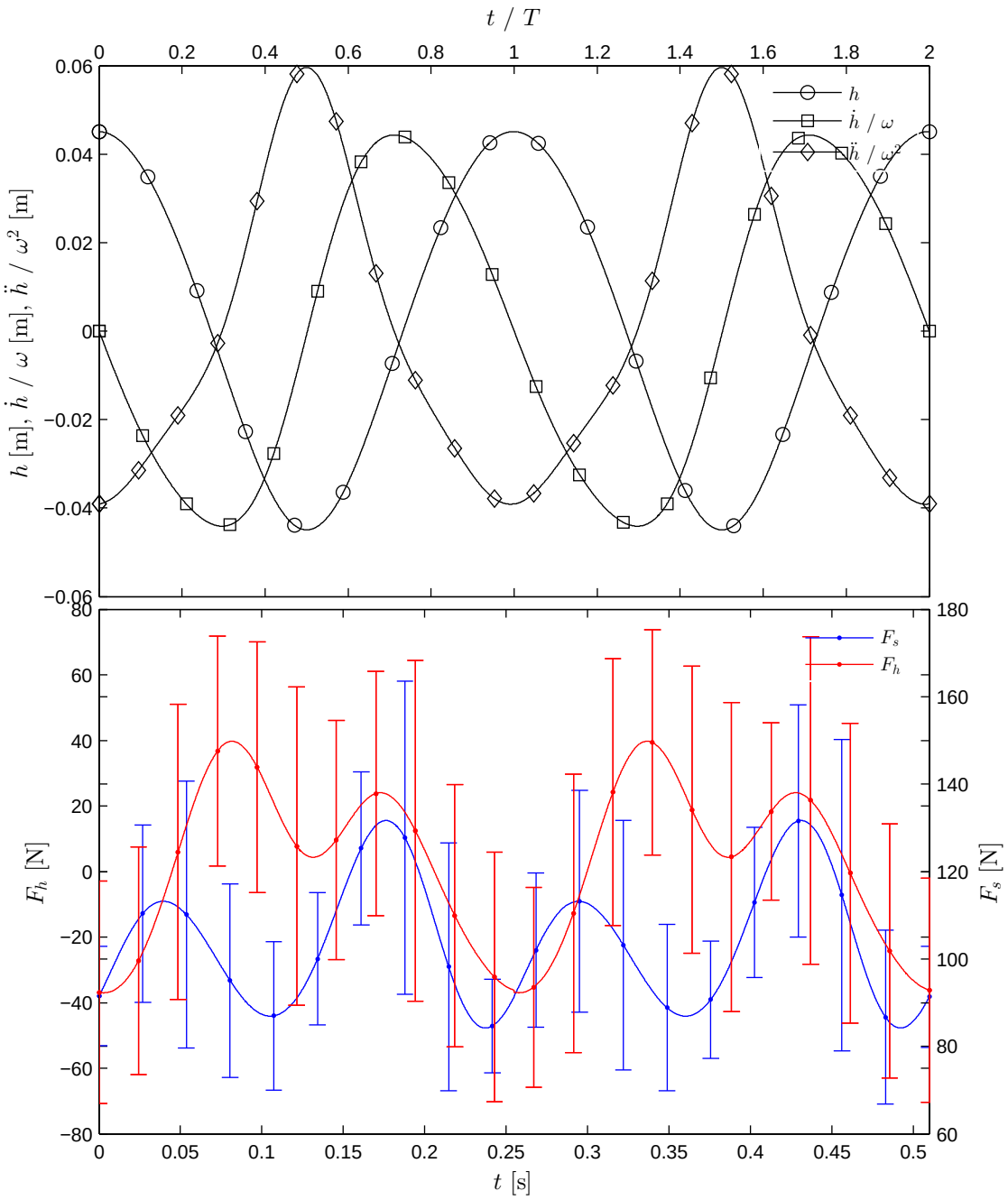

Appendix F

Measured Hydrodynamic Force Cycles on a Heaving Flat Plate

The figures included in this appendix show measured hydrodynamic forces on a flat plate of finite thickness undergoing a heaving motion with no forward velocity. All the measurements presented in this appendix were recorded with a heave-to-chord ratio of $h^* = 0.88$ and circular end plates of size $\varnothing 320\,\text{mm}$ ($\varnothing 6.3c$) fitted. The dimensions of the flat plate cross-section are shown in Figure F.1. Refer to Table 4.1 for a comparison between the flat plate and the other test objects.

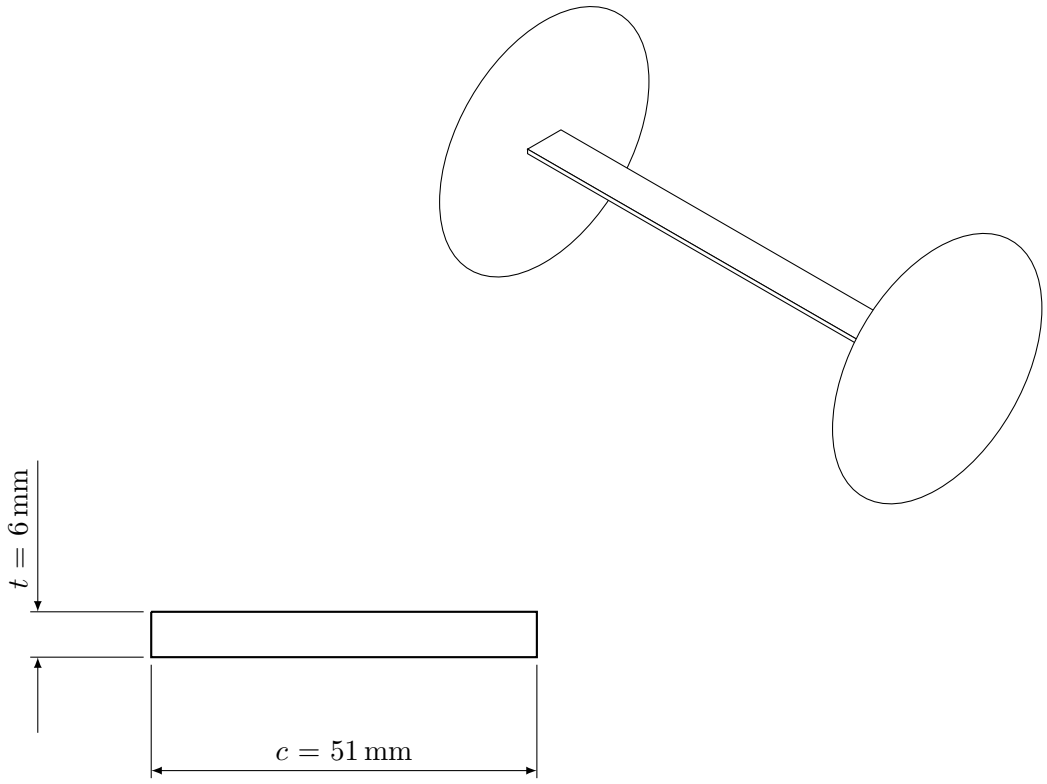

Figure F.1. Dimensions of the flat plate cross-section (scale 1:1) and an isometric of the flat plate with end plates attached (scale 1:5).

Object: Flat Plate		Motion	Water
	$c = 0.051\,\mathrm{m}$ $L = 0.600\,\mathrm{m}$ $t = 0.006\,\mathrm{m}$ $\theta = 0°$	$h_0 = 0.045\,\mathrm{m}$ $h^* = 0.88$ $f = 0.80\,\mathrm{Hz}$ $u = 0.00\,\mathrm{m\,s^{-1}}$	$T_w = 11.9\,°\mathrm{C}$ $\rho = 999\,\mathrm{kg\,m^{-3}}$

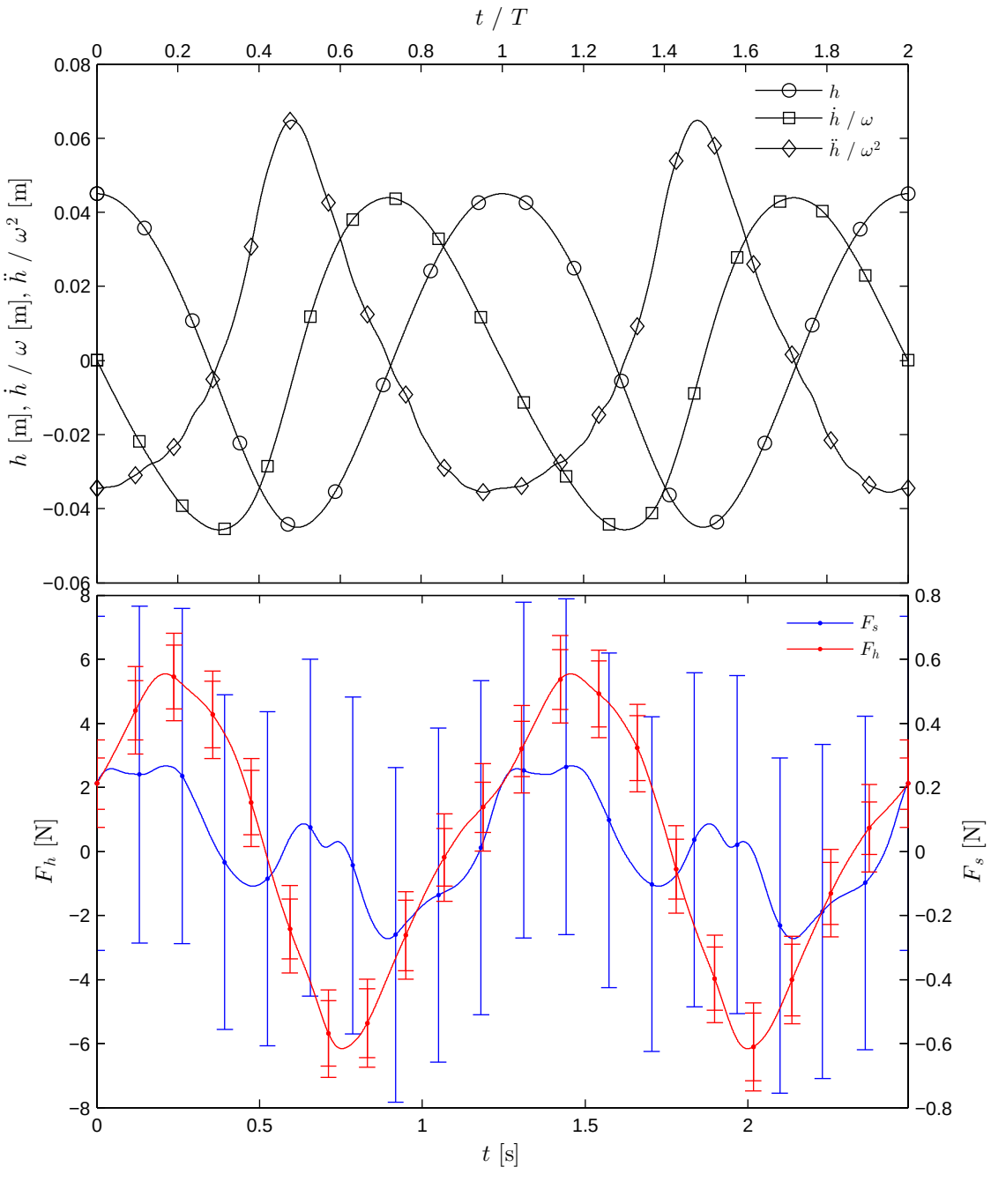

Object: Flat Plate		Motion	Water
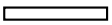	$c = 0.051\,\mathrm{m}$ $L = 0.600\,\mathrm{m}$ $t = 0.006\,\mathrm{m}$ $\theta = 0°$	$h_0 = 0.045\,\mathrm{m}$ $h^* = 0.88$ $f = 1.32\,\mathrm{Hz}$ $u = 0.00\,\mathrm{m\,s^{-1}}$	$T_w = 11.9\,°\mathrm{C}$ $\rho = 999\,\mathrm{kg\,m^{-3}}$

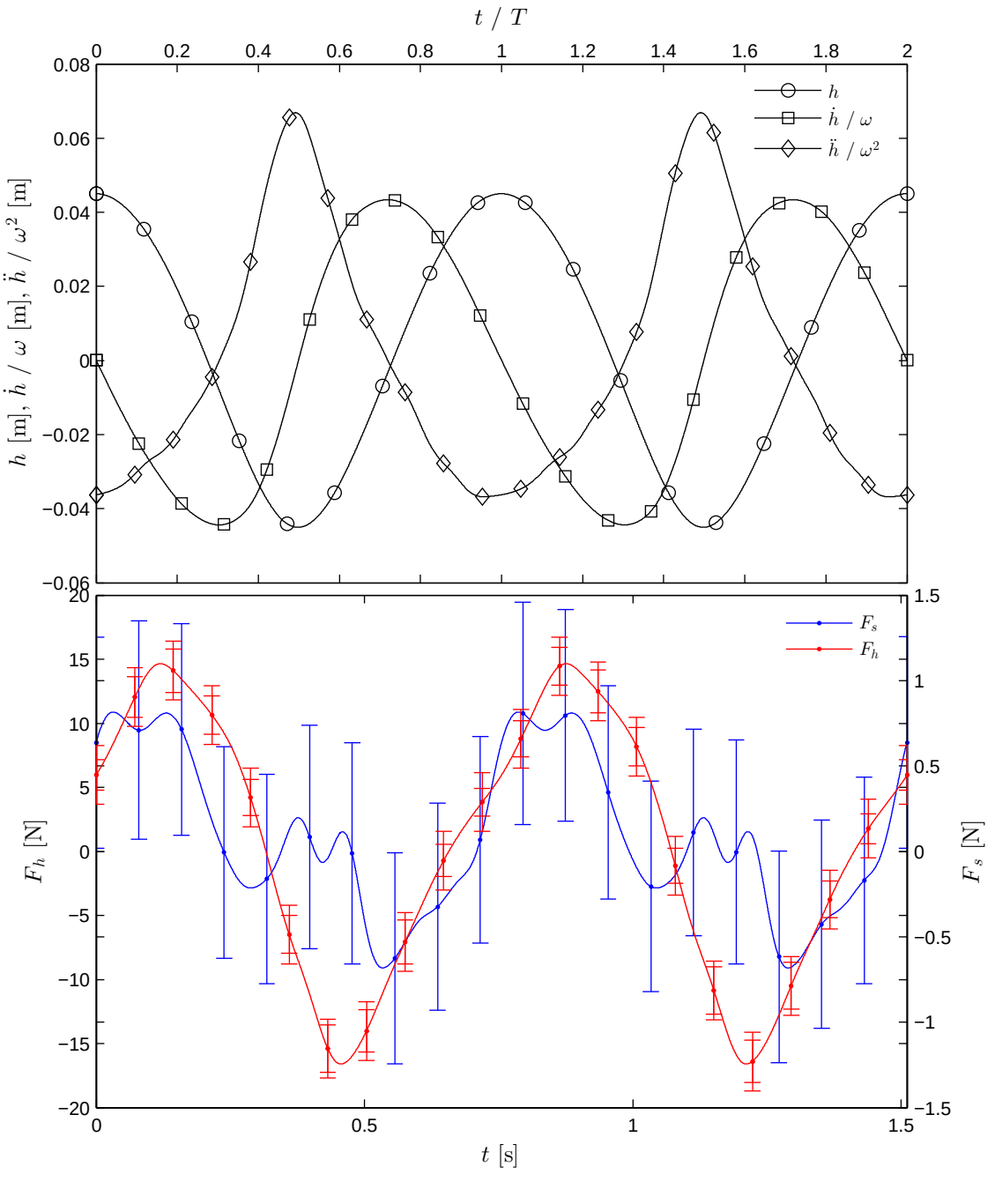

Object: Flat Plate		Motion	Water
	$c = 0.051\,\mathrm{m}$ $L = 0.600\,\mathrm{m}$ $t = 0.006\,\mathrm{m}$ $\theta = 0°$	$h_0 = 0.045\,\mathrm{m}$ $h^* = 0.88$ $f = 1.84\,\mathrm{Hz}$ $u = 0.00\,\mathrm{m\,s^{-1}}$	$T_w = 11.9\,°\mathrm{C}$ $\rho = 999\,\mathrm{kg\,m^{-3}}$

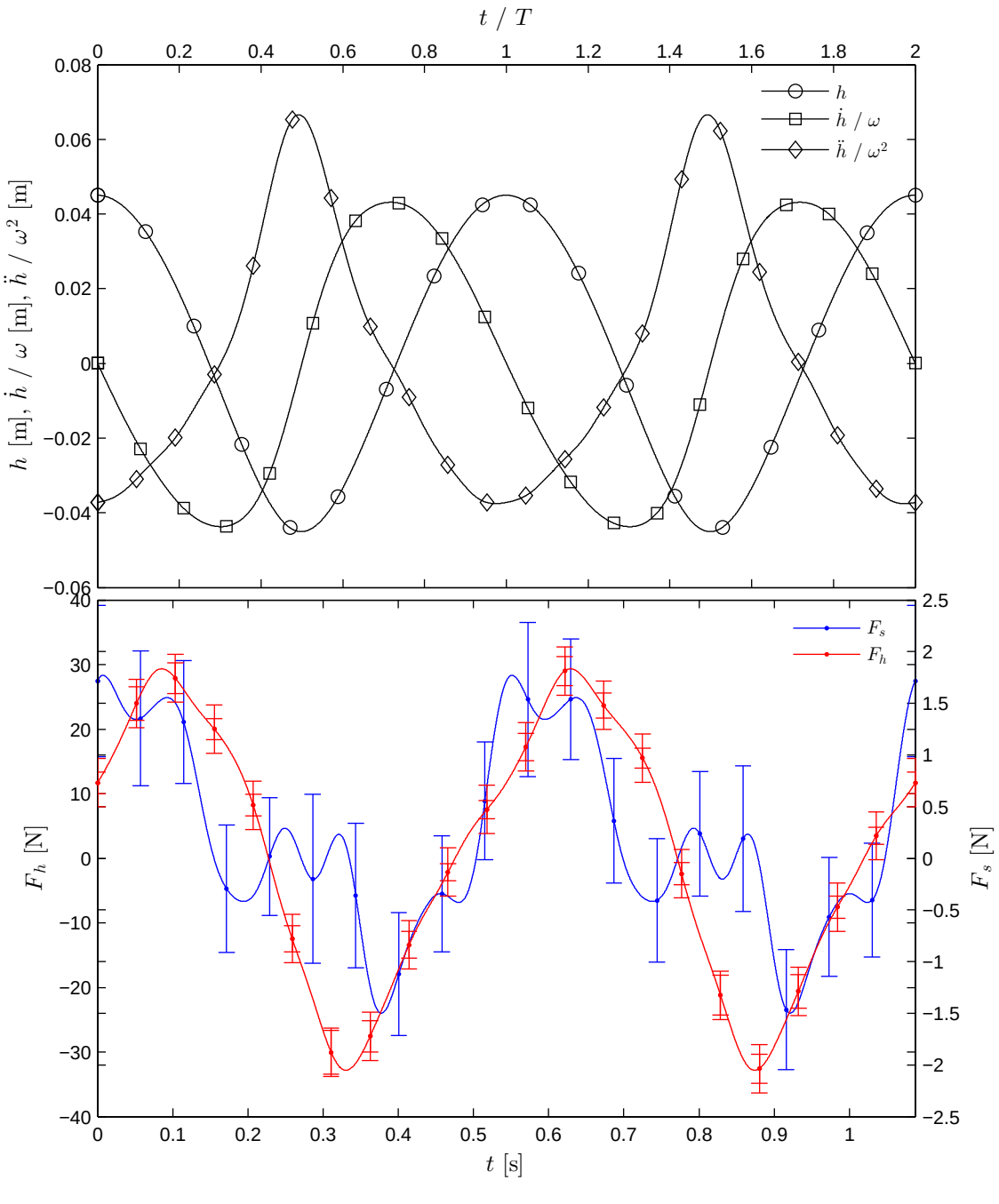

Object: Flat Plate		Motion	Water
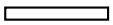	$c = 0.051\,\mathrm{m}$ $L = 0.600\,\mathrm{m}$ $t = 0.006\,\mathrm{m}$ $\theta = 0°$	$h_0 = 0.045\,\mathrm{m}$ $h^* = 0.88$ $f = 2.31\,\mathrm{Hz}$ $u = 0.00\,\mathrm{m\,s^{-1}}$	$T_w = 11.9\,°\mathrm{C}$ $\rho = 999\,\mathrm{kg\,m^{-3}}$

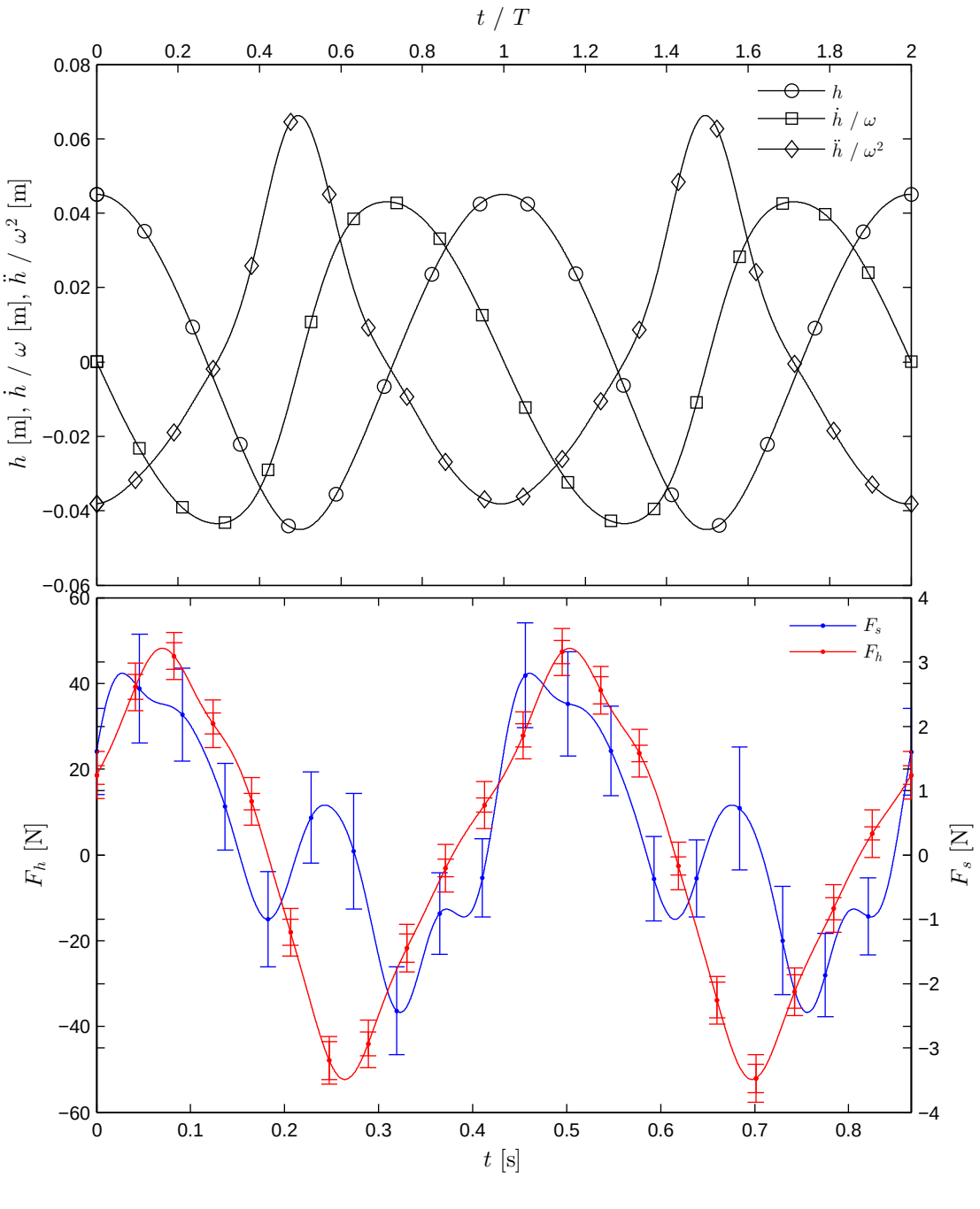

Object: Flat Plate		Motion	Water
	$c = 0.051\,\mathrm{m}$ $L = 0.600\,\mathrm{m}$ $t = 0.006\,\mathrm{m}$ $\theta = 0°$	$h_0 = 0.045\,\mathrm{m}$ $h^* = 0.88$ $f = 2.78\,\mathrm{Hz}$ $u = 0.00\,\mathrm{m\,s^{-1}}$	$T_w = 11.9\,°\mathrm{C}$ $\rho = 999\,\mathrm{kg\,m^{-3}}$

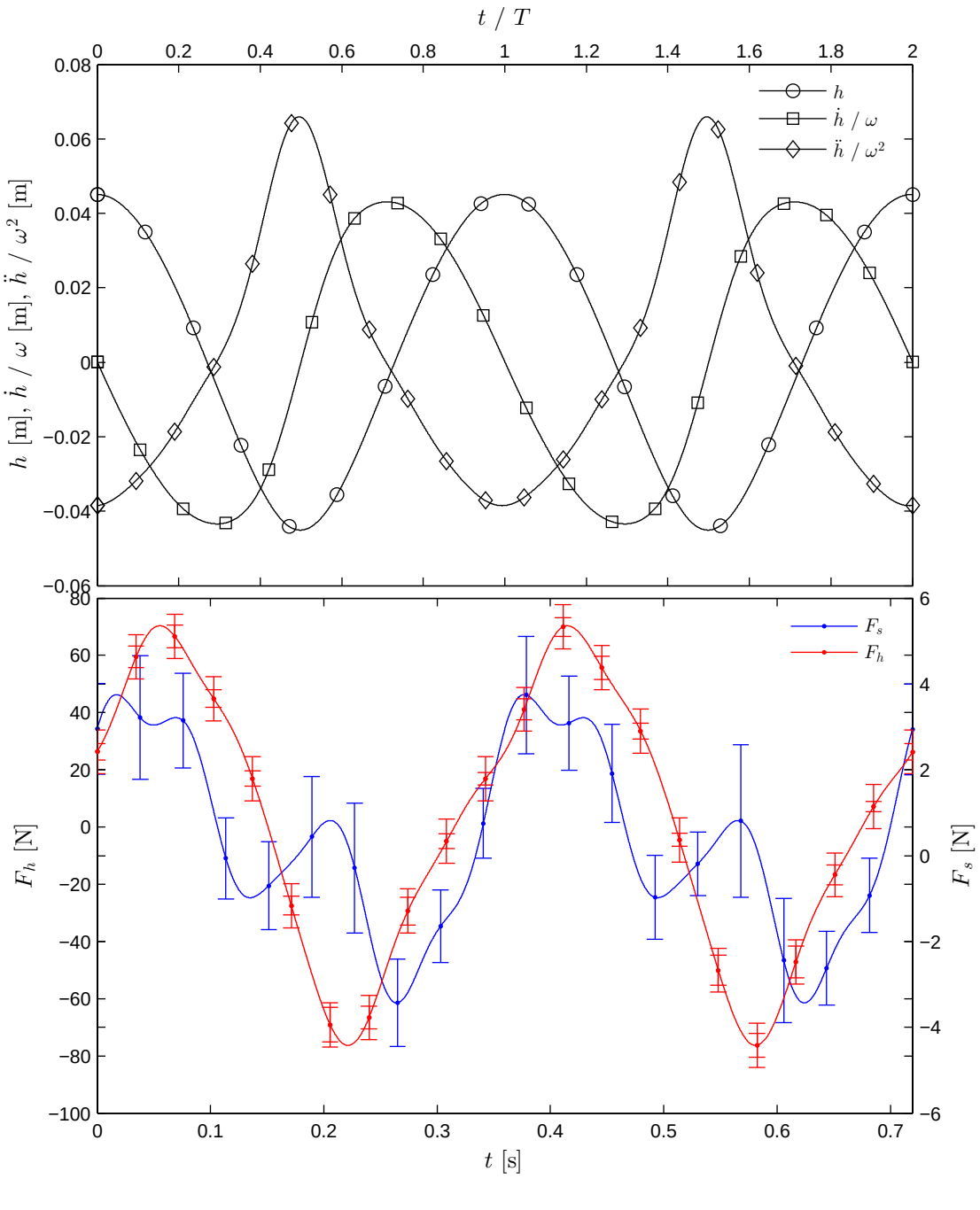

Object: Flat Plate		Motion	Water
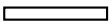	$c = 0.051\,\mathrm{m}$ $L = 0.600\,\mathrm{m}$ $t = 0.006\,\mathrm{m}$ $\theta = 0°$	$h_0 = 0.045\,\mathrm{m}$ $h^* = 0.88$ $f = 3.30\,\mathrm{Hz}$ $u = 0.00\,\mathrm{m\,s^{-1}}$	$T_w = 11.9\,°\mathrm{C}$ $\rho = 999\,\mathrm{kg\,m^{-3}}$

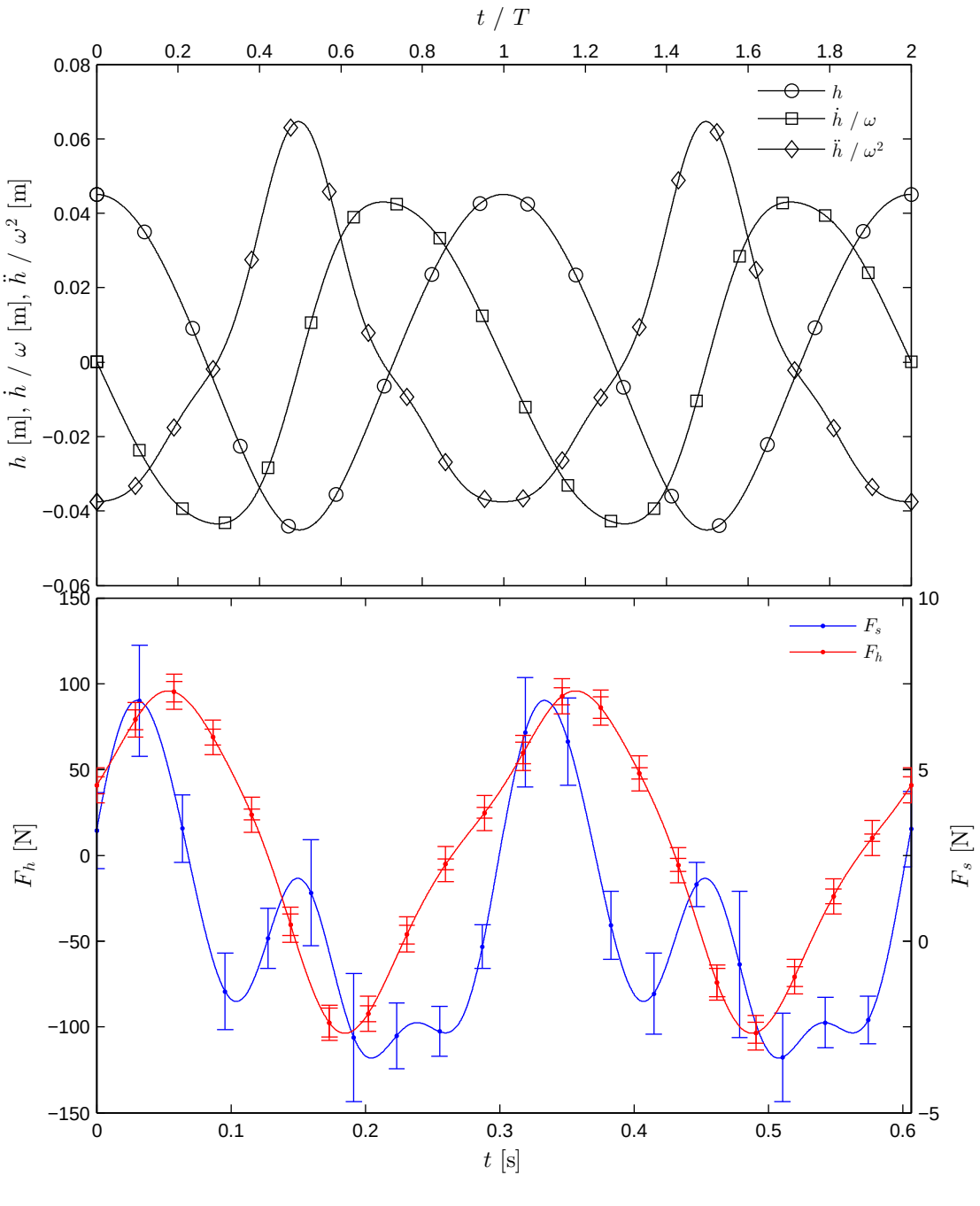

Object: Flat Plate		Motion	Water
	$c = 0.051\,\mathrm{m}$ $L = 0.600\,\mathrm{m}$ $t = 0.006\,\mathrm{m}$ $\theta = 0°$	$h_0 = 0.045\,\mathrm{m}$ $h^* = 0.88$ $f = 3.77\,\mathrm{Hz}$ $u = 0.00\,\mathrm{m\,s^{-1}}$	$T_w = 11.9\,°\mathrm{C}$ $\rho = 999\,\mathrm{kg\,m^{-3}}$

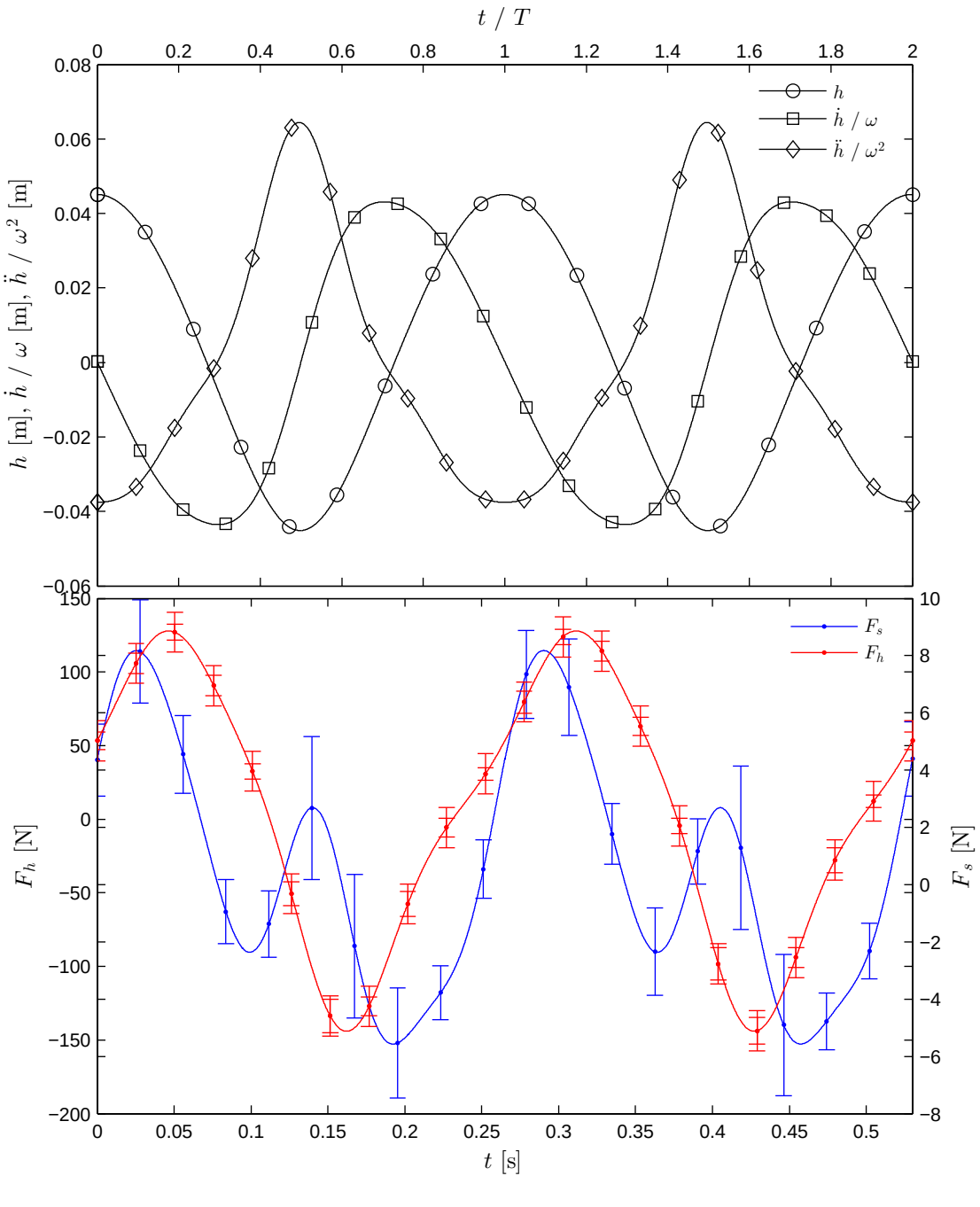

Object: Flat Plate		Motion	Water
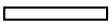	$c = 0.051\,\mathrm{m}$ $L = 0.600\,\mathrm{m}$ $t = 0.006\,\mathrm{m}$ $\theta = 10°$	$h_0 = 0.045\,\mathrm{m}$ $h^* = 0.88$ $f = 0.82\,\mathrm{Hz}$ $u = 0.00\,\mathrm{m\,s^{-1}}$	$T_w = 9.7\,°\mathrm{C}$ $\rho = 1000\,\mathrm{kg\,m^{-3}}$

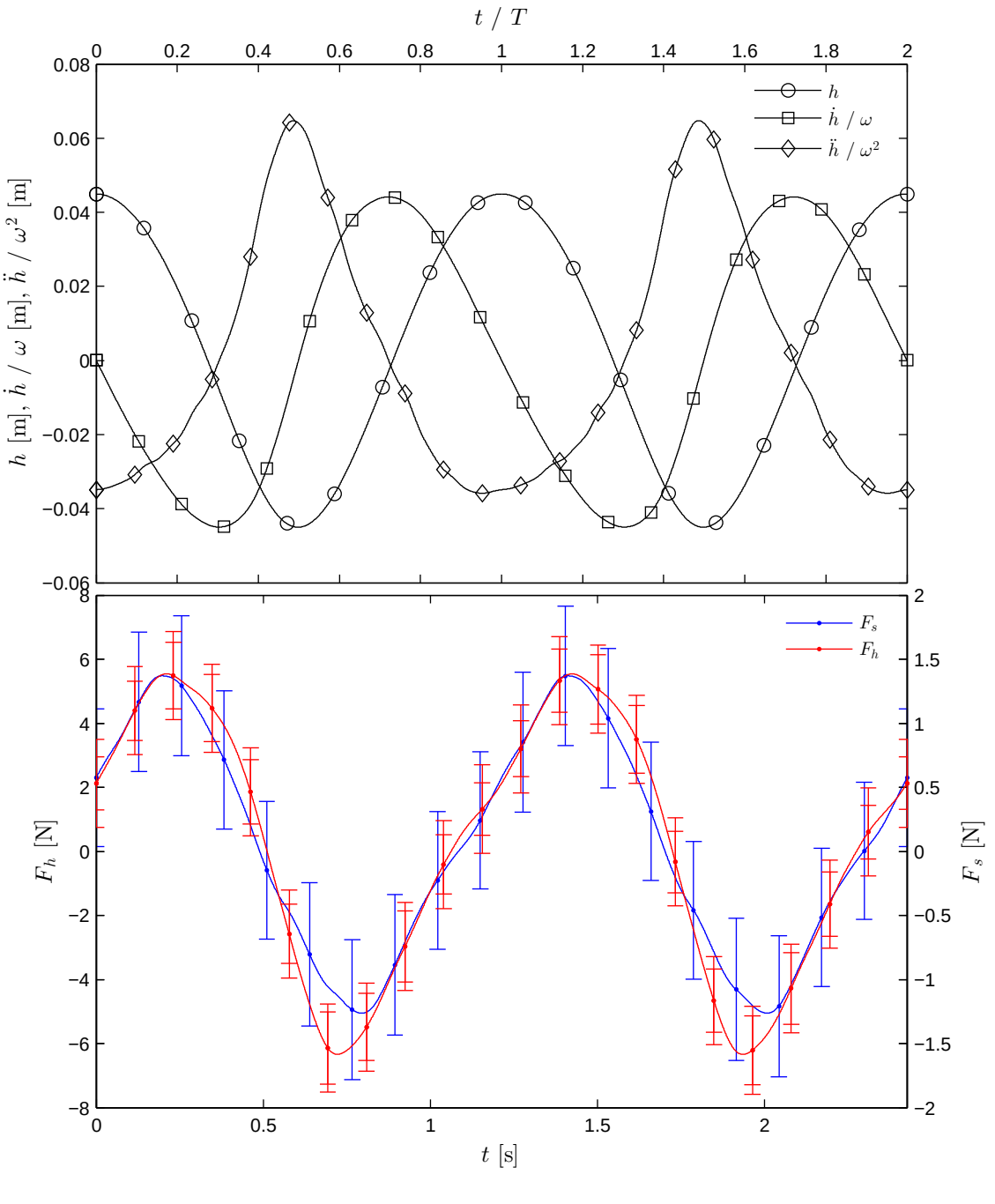

Object: Flat Plate		Motion	Water
	$c = 0.051\,\mathrm{m}$ $L = 0.600\,\mathrm{m}$ $t = 0.006\,\mathrm{m}$ $\theta = 10°$	$h_0 = 0.045\,\mathrm{m}$ $h^* = 0.88$ $f = 1.31\,\mathrm{Hz}$ $u = 0.00\,\mathrm{m\,s^{-1}}$	$T_w = 9.7\,°\mathrm{C}$ $\rho = 1000\,\mathrm{kg\,m^{-3}}$

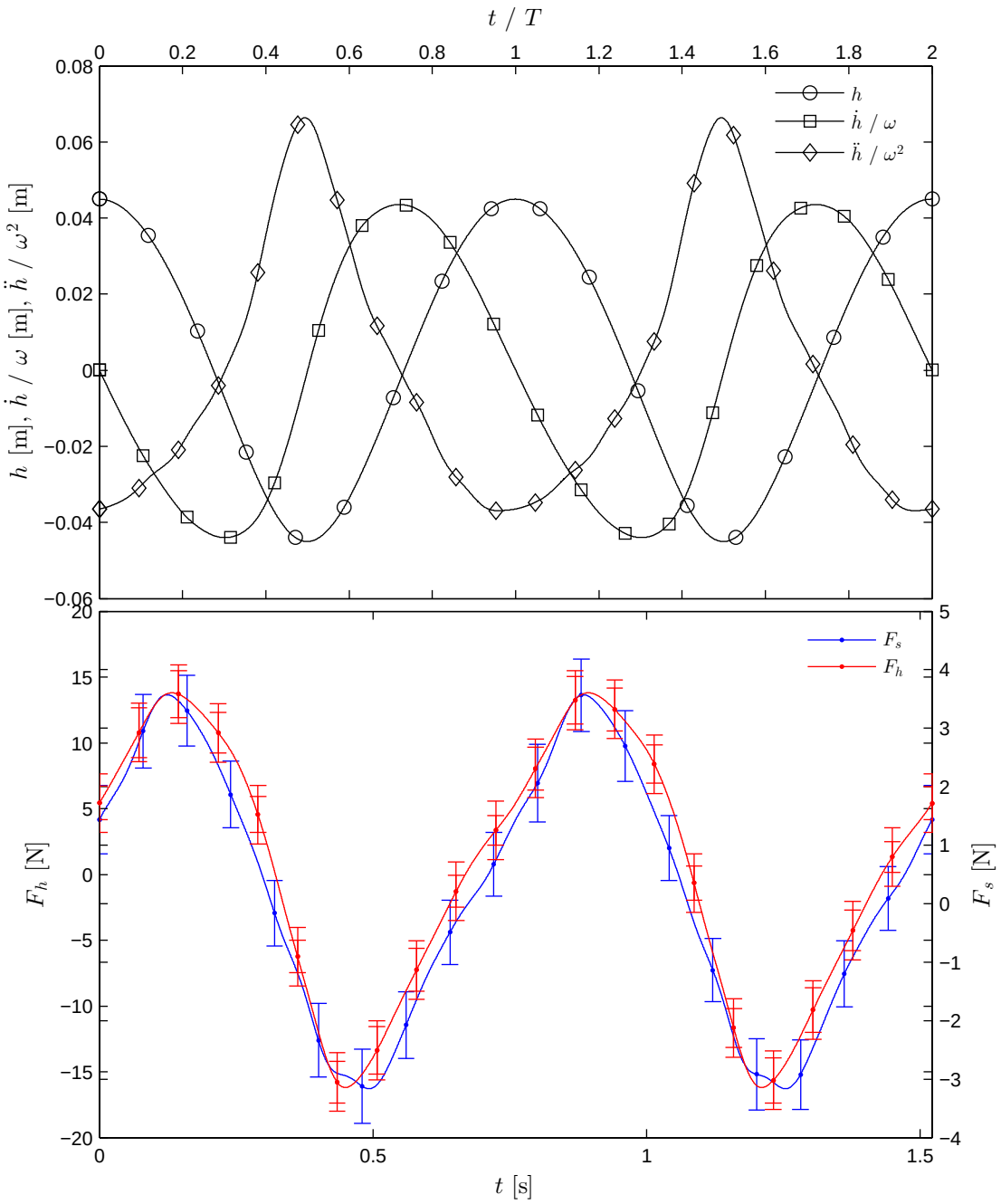

Object: Flat Plate		Motion	Water
	$c = 0.051\,\mathrm{m}$ $L = 0.600\,\mathrm{m}$ $t = 0.006\,\mathrm{m}$ $\theta = 10°$	$h_0 = 0.045\,\mathrm{m}$ $h^* = 0.88$ $f = 1.84\,\mathrm{Hz}$ $u = 0.00\,\mathrm{m\,s^{-1}}$	$T_w = 9.7\,°\mathrm{C}$ $\rho = 1000\,\mathrm{kg\,m^{-3}}$

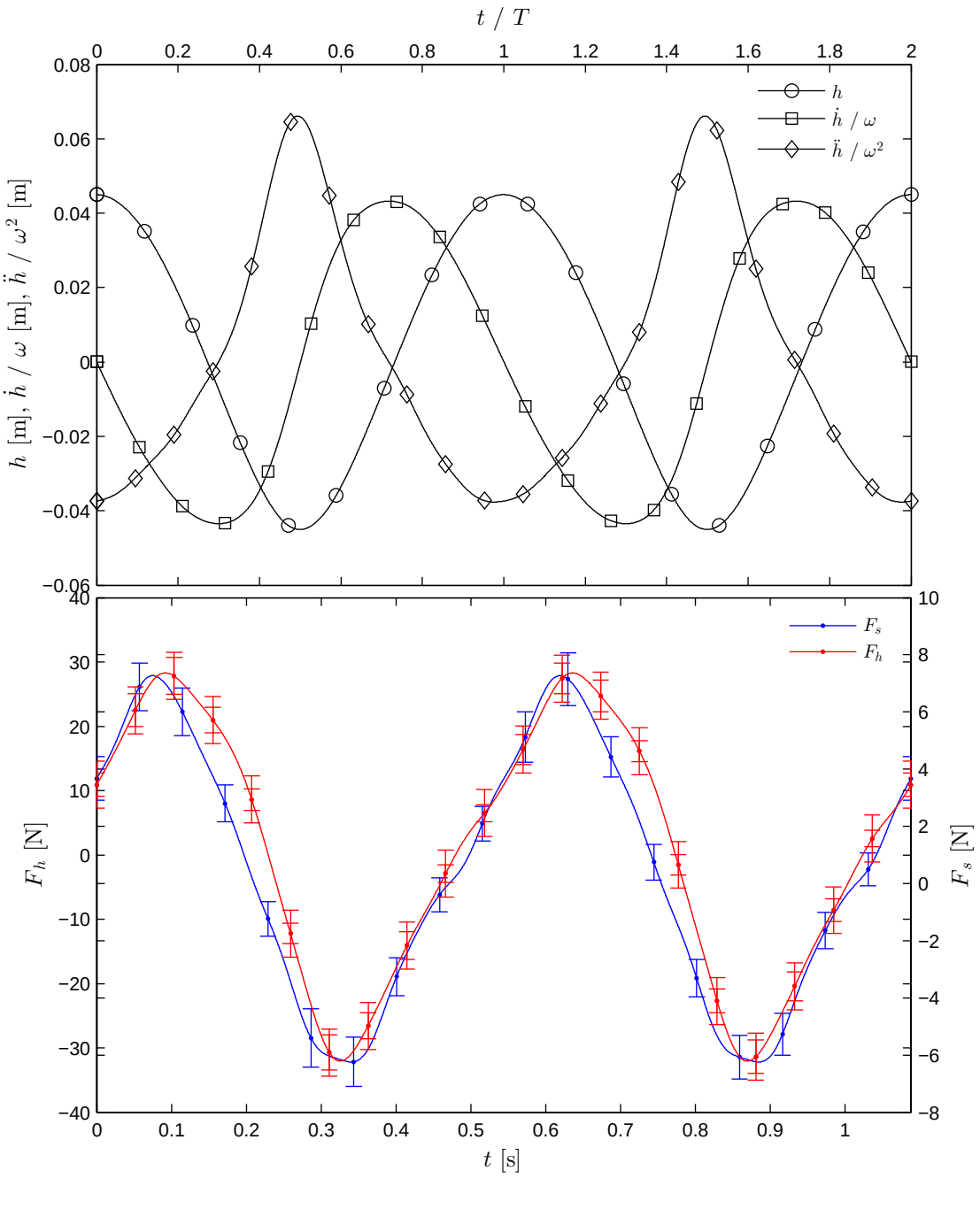

Object: Flat Plate		Motion	Water
	$c = 0.051\,\mathrm{m}$ $L = 0.600\,\mathrm{m}$ $t = 0.006\,\mathrm{m}$ $\theta = 10°$	$h_0 = 0.045\,\mathrm{m}$ $h^* = 0.88$ $f = 2.28\,\mathrm{Hz}$ $u = 0.00\,\mathrm{m\,s^{-1}}$	$T_w = 9.7\,°\mathrm{C}$ $\rho = 1000\,\mathrm{kg\,m^{-3}}$

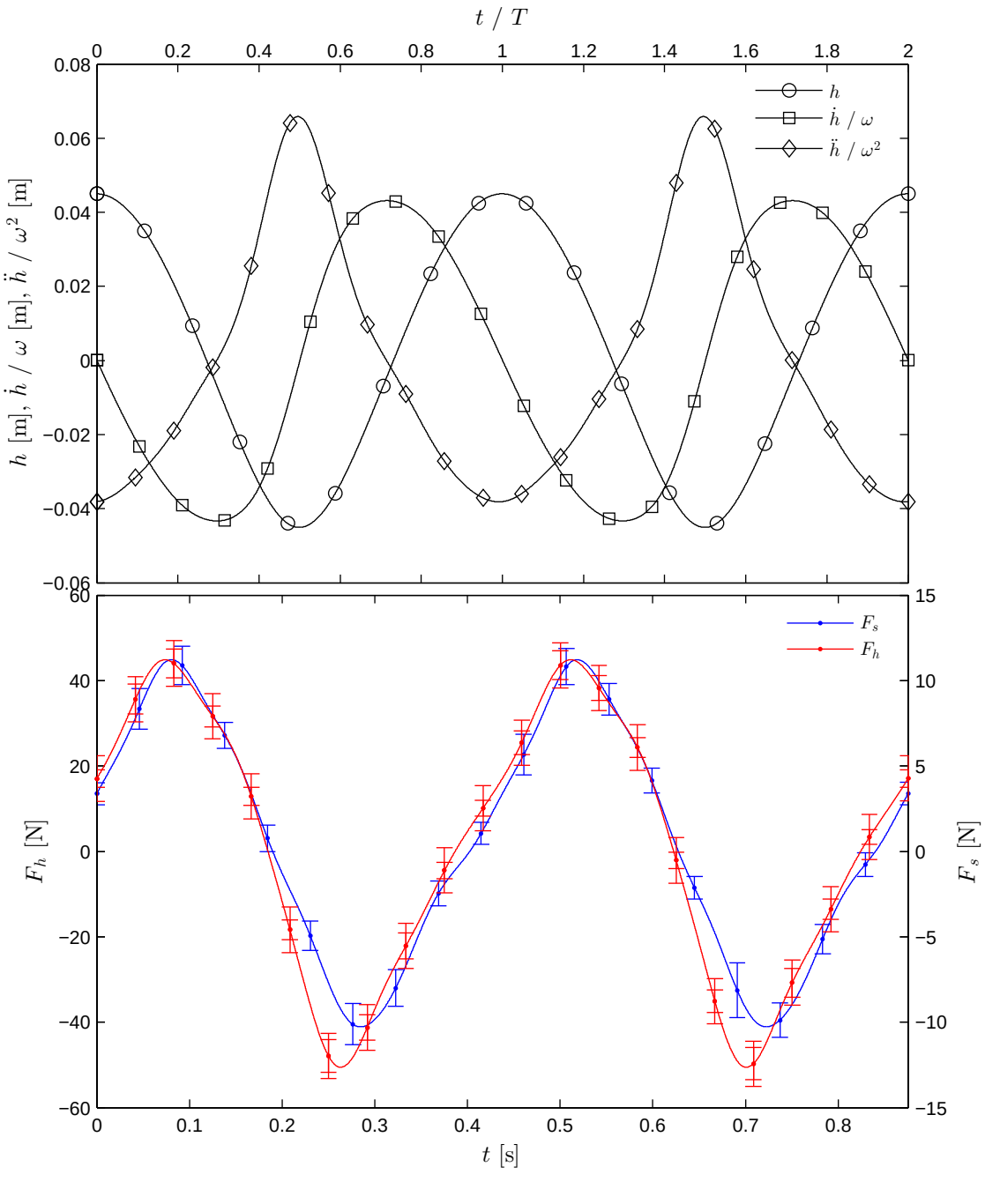

Object: Flat Plate		Motion	Water
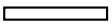	$c = 0.051\,\mathrm{m}$ $L = 0.600\,\mathrm{m}$ $t = 0.006\,\mathrm{m}$ $\theta = 10°$	$h_0 = 0.045\,\mathrm{m}$ $h^* = 0.88$ $f = 2.86\,\mathrm{Hz}$ $u = 0.00\,\mathrm{m\,s^{-1}}$	$T_w = 9.7\,°\mathrm{C}$ $\rho = 1000\,\mathrm{kg\,m^{-3}}$

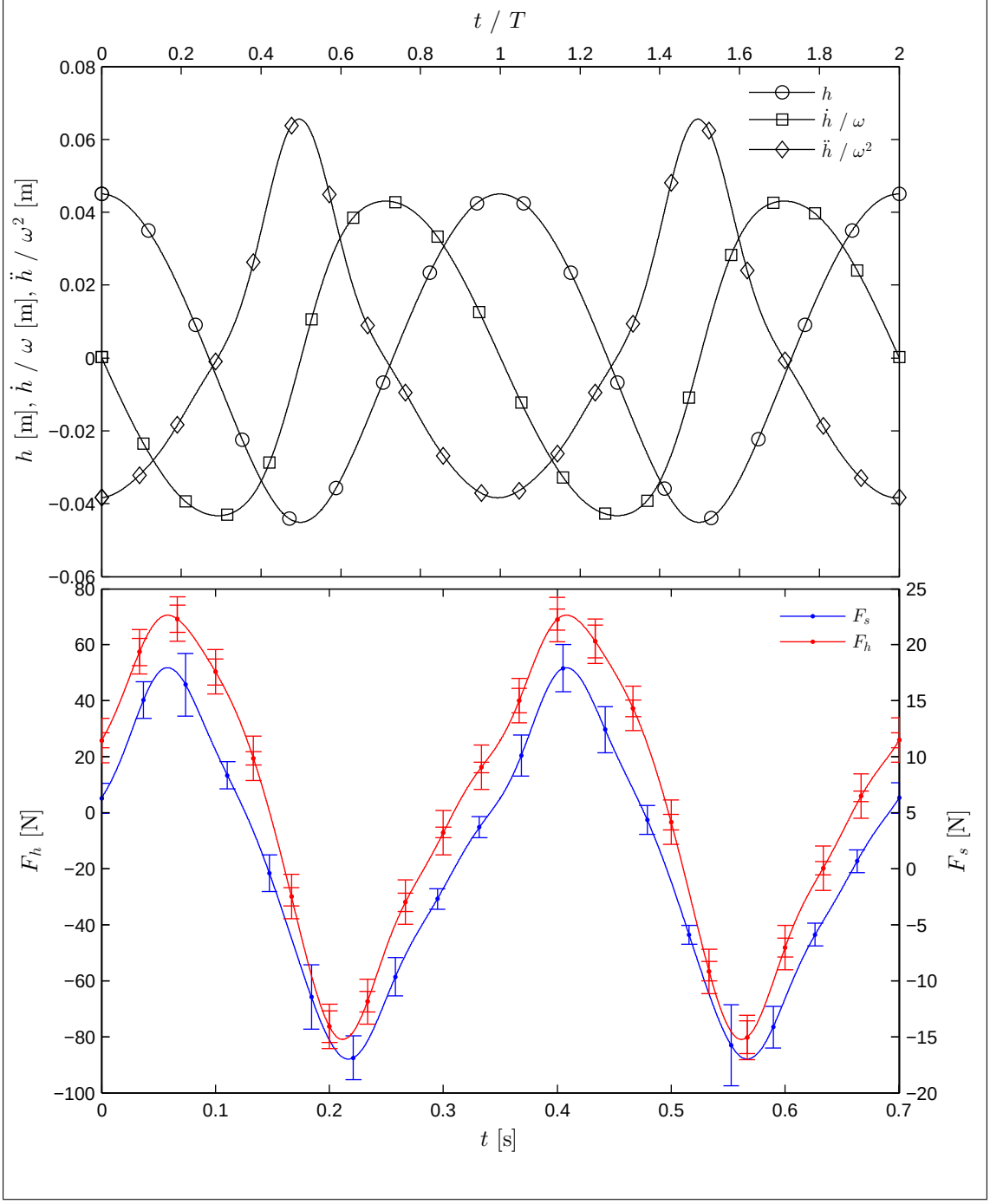

Object: Flat Plate		Motion	Water
	$c = 0.051\,\mathrm{m}$ $L = 0.600\,\mathrm{m}$ $t = 0.006\,\mathrm{m}$ $\theta = 10°$	$h_0 = 0.045\,\mathrm{m}$ $h^* = 0.88$ $f = 3.32\,\mathrm{Hz}$ $u = 0.00\,\mathrm{m\,s^{-1}}$	$T_w = 9.7\,°\mathrm{C}$ $\rho = 1000\,\mathrm{kg\,m^{-3}}$

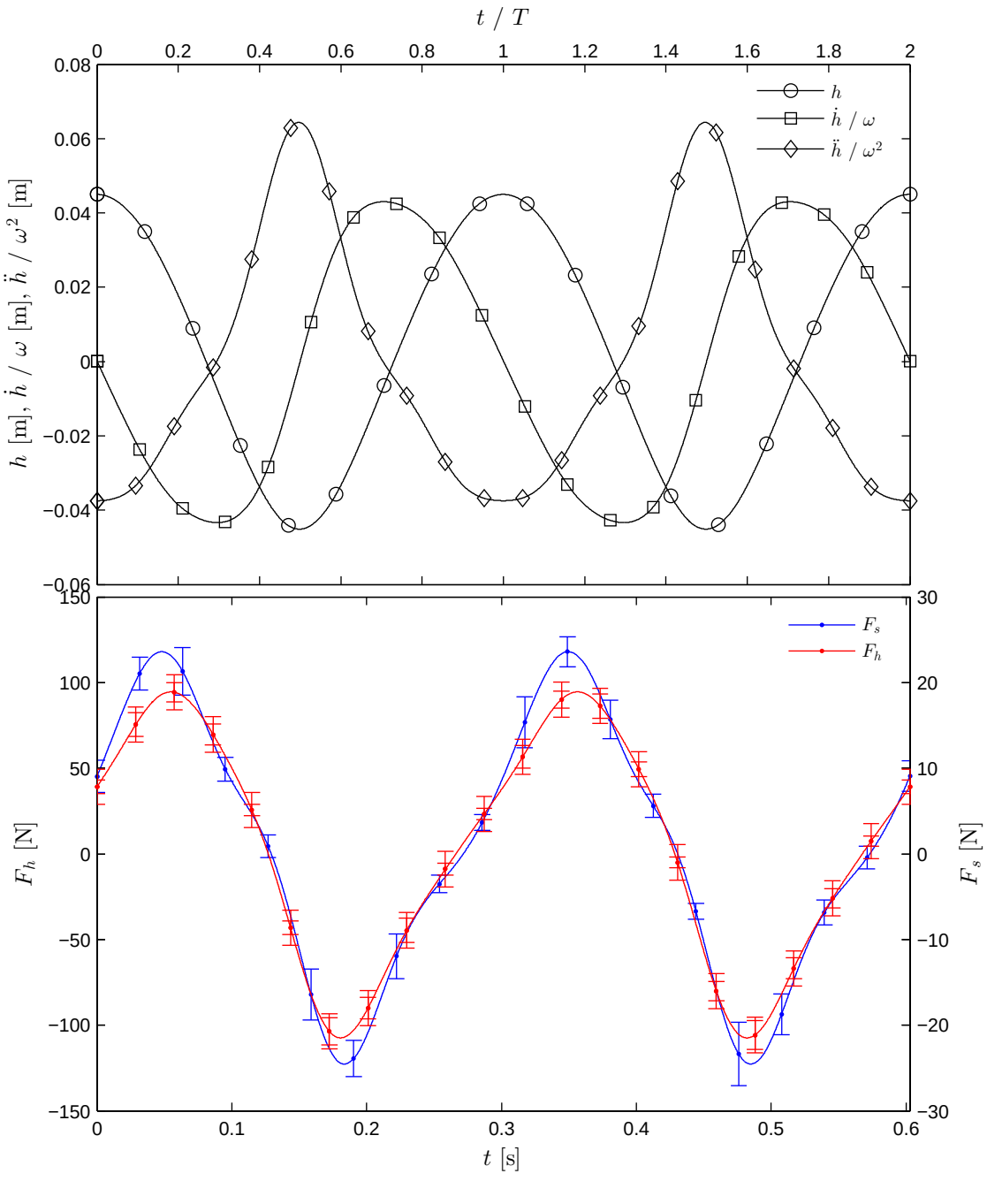

Object: Flat Plate		Motion	Water
	$c = 0.051\,\mathrm{m}$ $L = 0.600\,\mathrm{m}$ $t = 0.006\,\mathrm{m}$ $\theta = 10°$	$h_0 = 0.045\,\mathrm{m}$ $h^* = 0.88$ $f = 3.82\,\mathrm{Hz}$ $u = 0.00\,\mathrm{m\,s^{-1}}$	$T_w = 9.7\,°\mathrm{C}$ $\rho = 1000\,\mathrm{kg\,m^{-3}}$

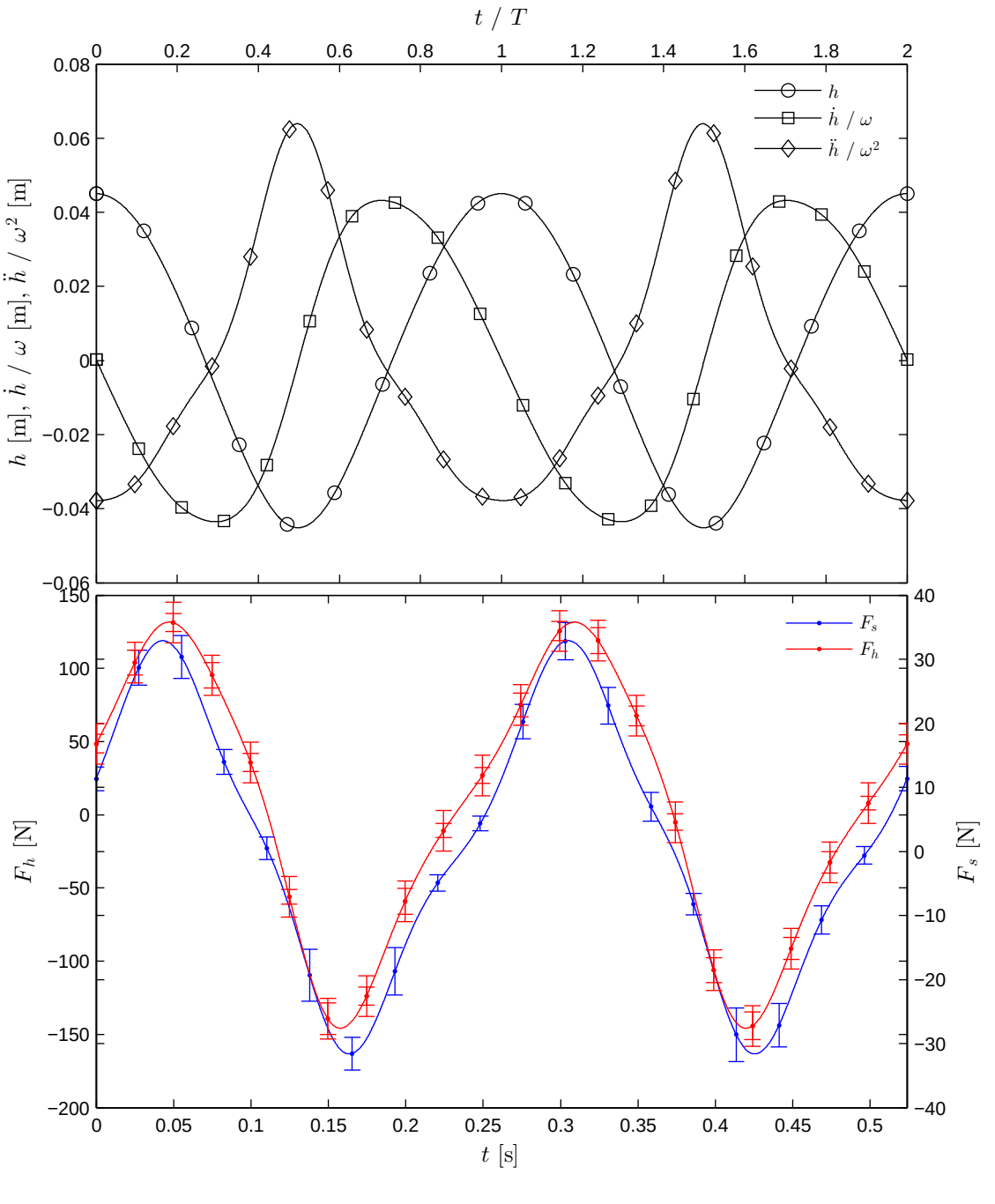

Object: Flat Plate		Motion	Water
	$c = 0.051\,\mathrm{m}$ $L = 0.600\,\mathrm{m}$ $t = 0.006\,\mathrm{m}$ $\theta = 40°$	$h_0 = 0.045\,\mathrm{m}$ $h^* = 0.88$ $f = 0.84\,\mathrm{Hz}$ $u = 0.00\,\mathrm{m\,s^{-1}}$	$T_w = 9.7\,°\mathrm{C}$ $\rho = 1000\,\mathrm{kg\,m^{-3}}$

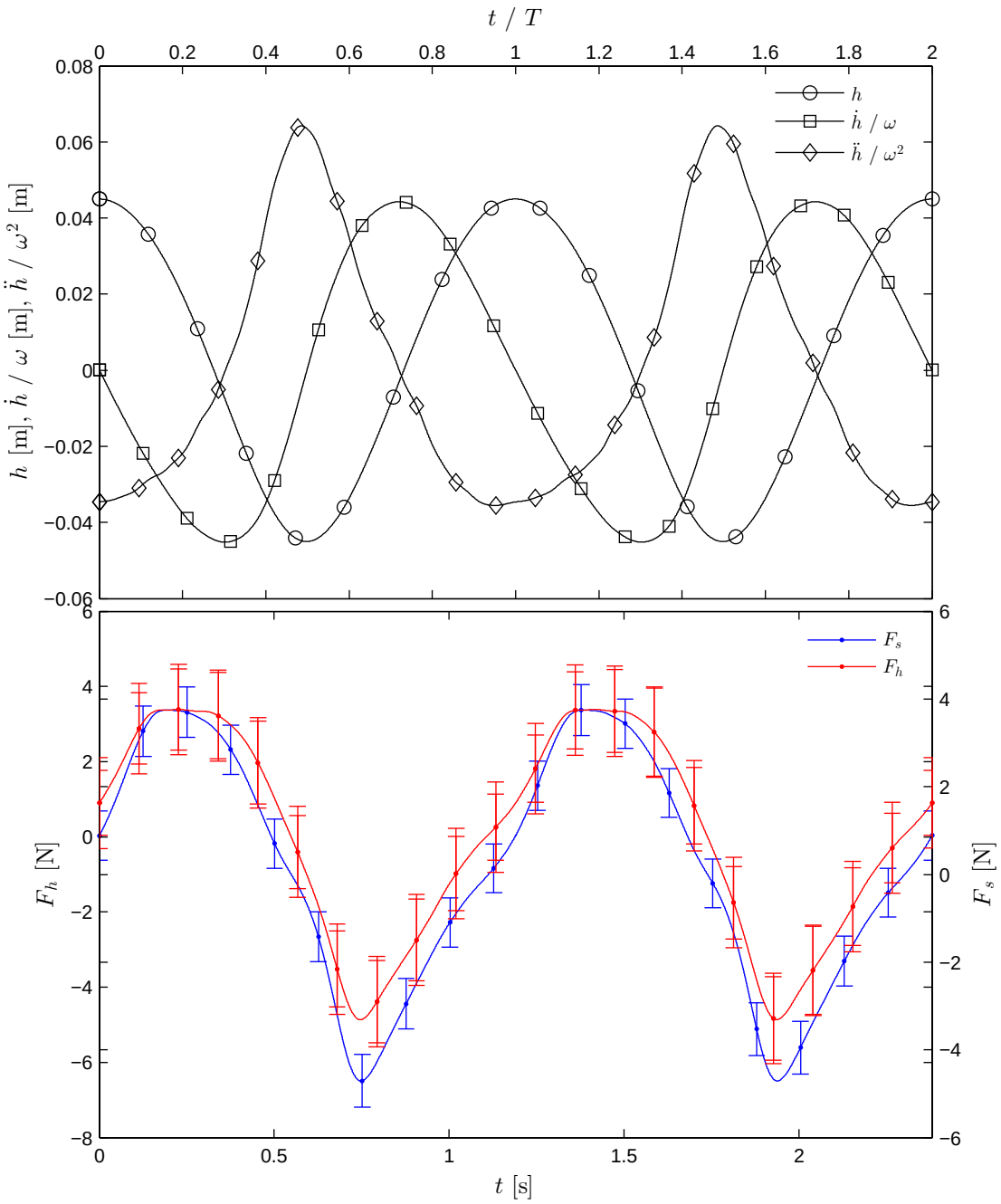

Object: Flat Plate		Motion	Water
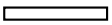	$c = 0.051\,\mathrm{m}$ $L = 0.600\,\mathrm{m}$ $t = 0.006\,\mathrm{m}$ $\theta = 40°$	$h_0 = 0.045\,\mathrm{m}$ $h^* = 0.88$ $f = 1.32\,\mathrm{Hz}$ $u = 0.00\,\mathrm{m\,s^{-1}}$	$T_w = 9.7\,°\mathrm{C}$ $\rho = 1000\,\mathrm{kg\,m^{-3}}$

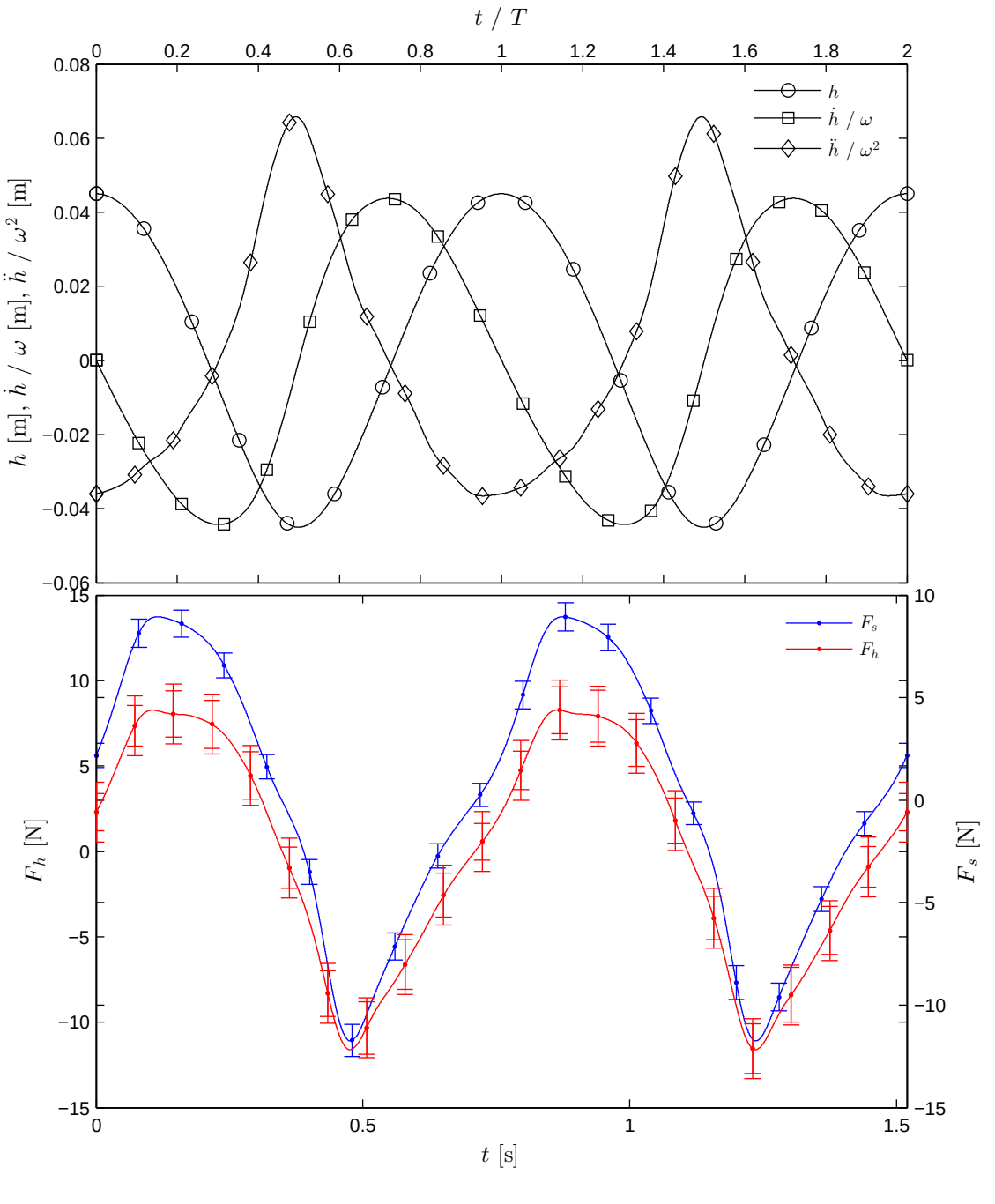

Object: Flat Plate		Motion	Water
	$c = 0.051\,\mathrm{m}$ $L = 0.600\,\mathrm{m}$ $t = 0.006\,\mathrm{m}$ $\theta = 40°$	$h_0 = 0.045\,\mathrm{m}$ $h^* = 0.88$ $f = 1.86\,\mathrm{Hz}$ $u = 0.00\,\mathrm{m\,s^{-1}}$	$T_w = 9.7\,°\mathrm{C}$ $\rho = 1000\,\mathrm{kg\,m^{-3}}$

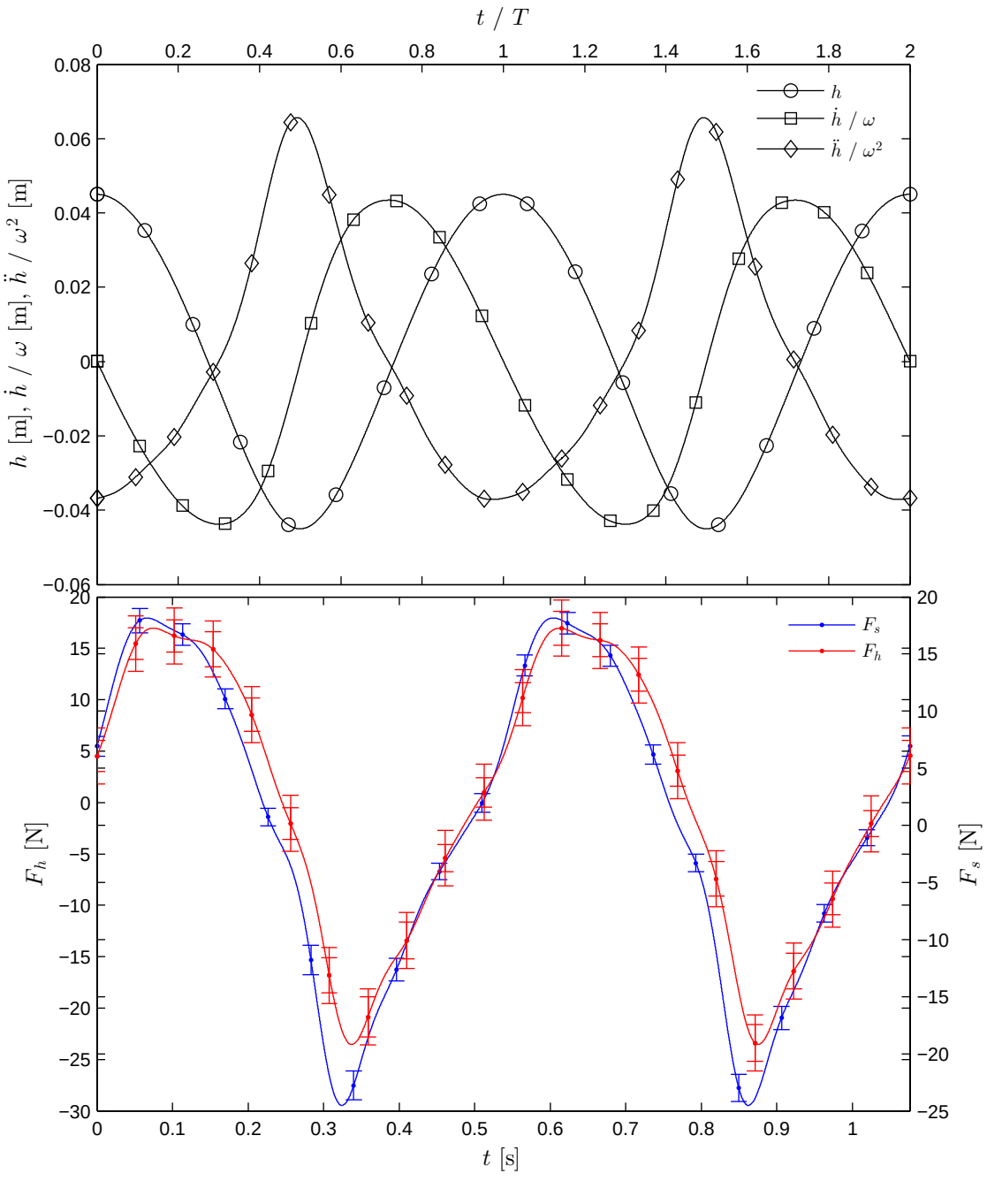

Object: Flat Plate		Motion	Water
	$c = 0.051\,\mathrm{m}$ $L = 0.600\,\mathrm{m}$ $t = 0.006\,\mathrm{m}$ $\theta = 40°$	$h_0 = 0.045\,\mathrm{m}$ $h^* = 0.88$ $f = 2.29\,\mathrm{Hz}$ $u = 0.00\,\mathrm{m\,s^{-1}}$	$T_w = 9.7\,°\mathrm{C}$ $\rho = 1000\,\mathrm{kg\,m^{-3}}$

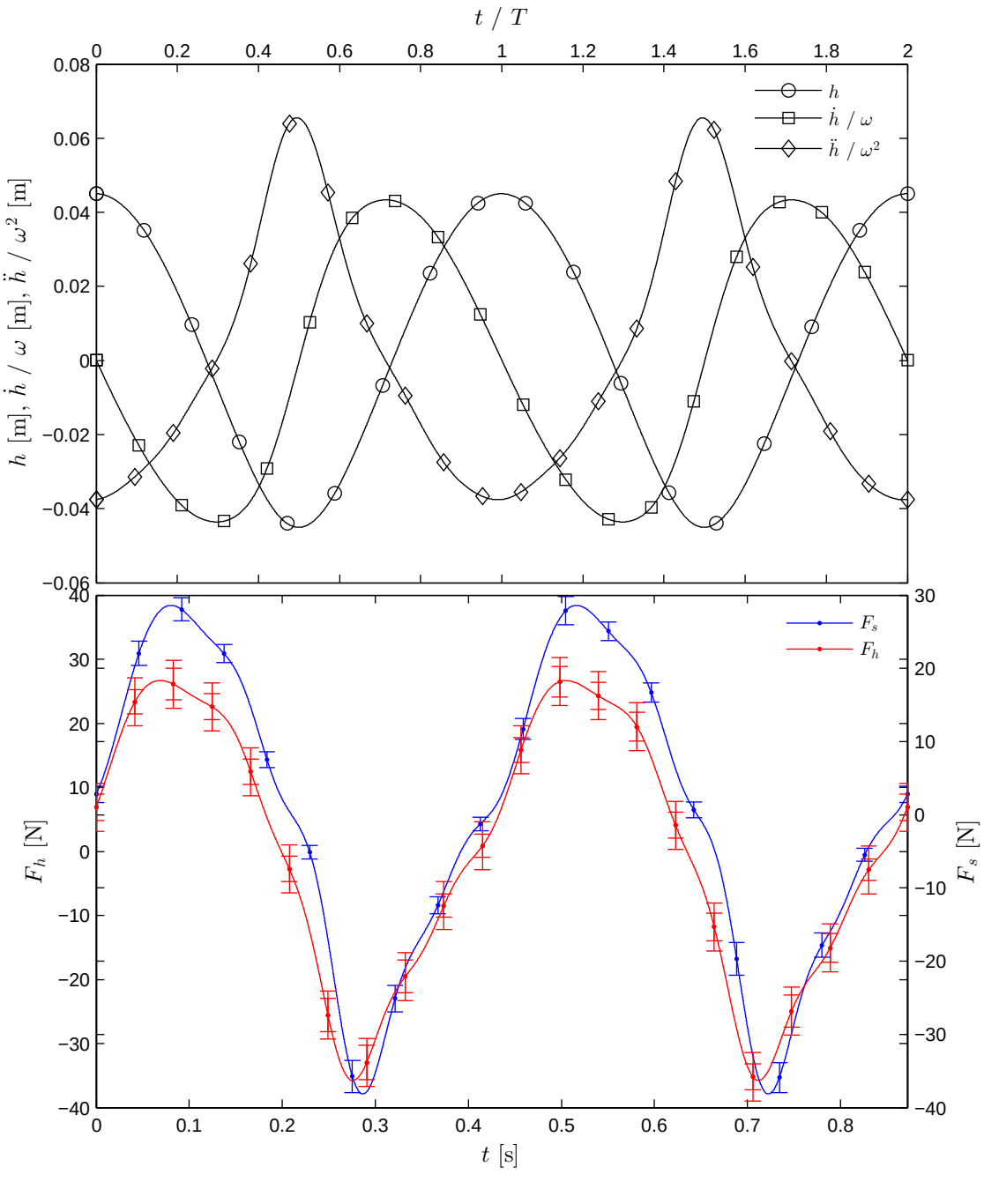

Object: Flat Plate		Motion	Water
	$c = 0.051\,\mathrm{m}$ $L = 0.600\,\mathrm{m}$ $t = 0.006\,\mathrm{m}$ $\theta = 40°$	$h_0 = 0.045\,\mathrm{m}$ $h^* = 0.88$ $f = 2.76\,\mathrm{Hz}$ $u = 0.00\,\mathrm{m\,s^{-1}}$	$T_w = 9.7\,°\mathrm{C}$ $\rho = 1000\,\mathrm{kg\,m^{-3}}$

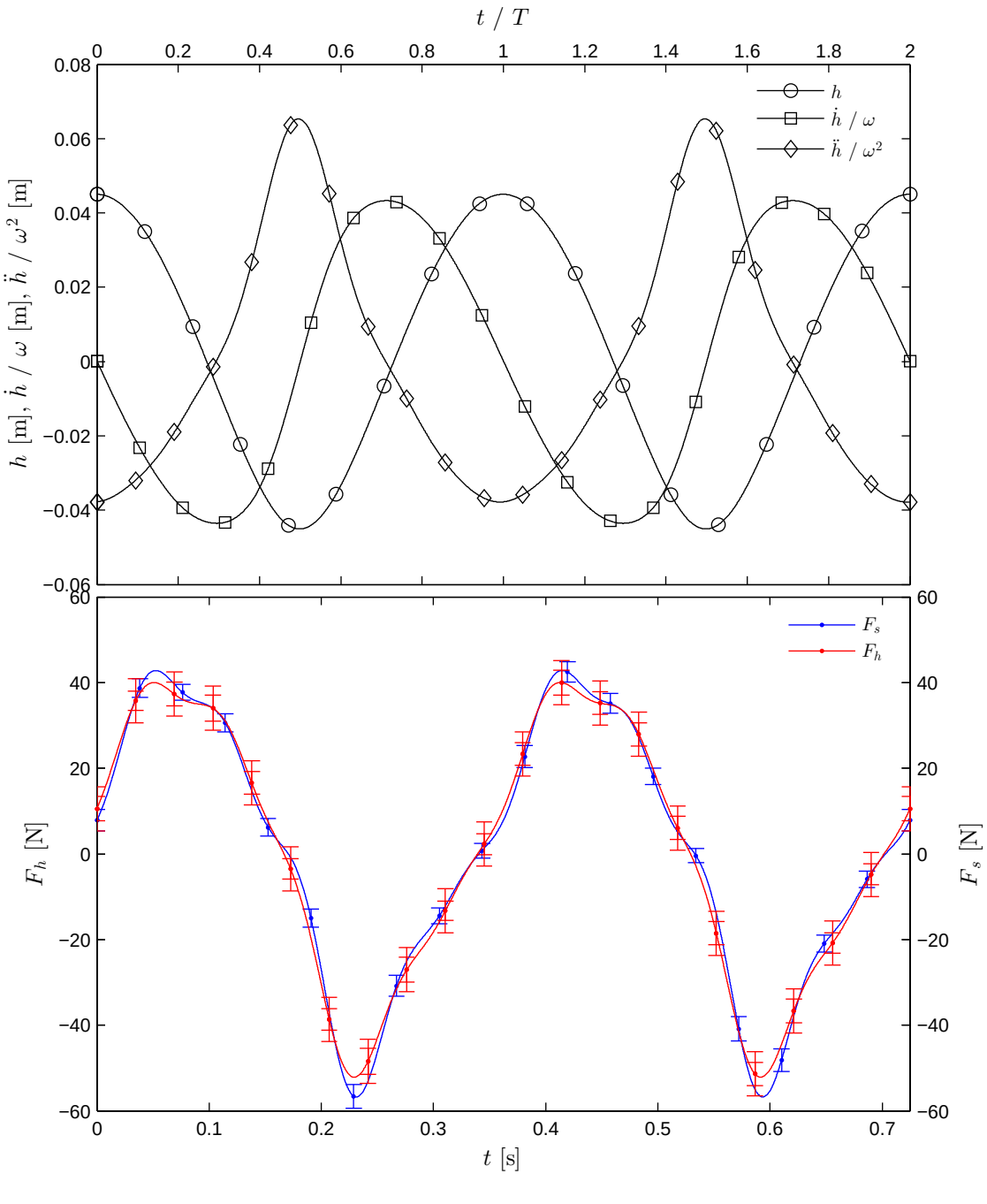

Object: Flat Plate		Motion	Water
	$c = 0.051\,\mathrm{m}$ $L = 0.600\,\mathrm{m}$ $t = 0.006\,\mathrm{m}$ $\theta = 40°$	$h_0 = 0.045\,\mathrm{m}$ $h^* = 0.88$ $f = 3.34\,\mathrm{Hz}$ $u = 0.00\,\mathrm{m\,s^{-1}}$	$T_w = 9.7\,°\mathrm{C}$ $\rho = 1000\,\mathrm{kg\,m^{-3}}$

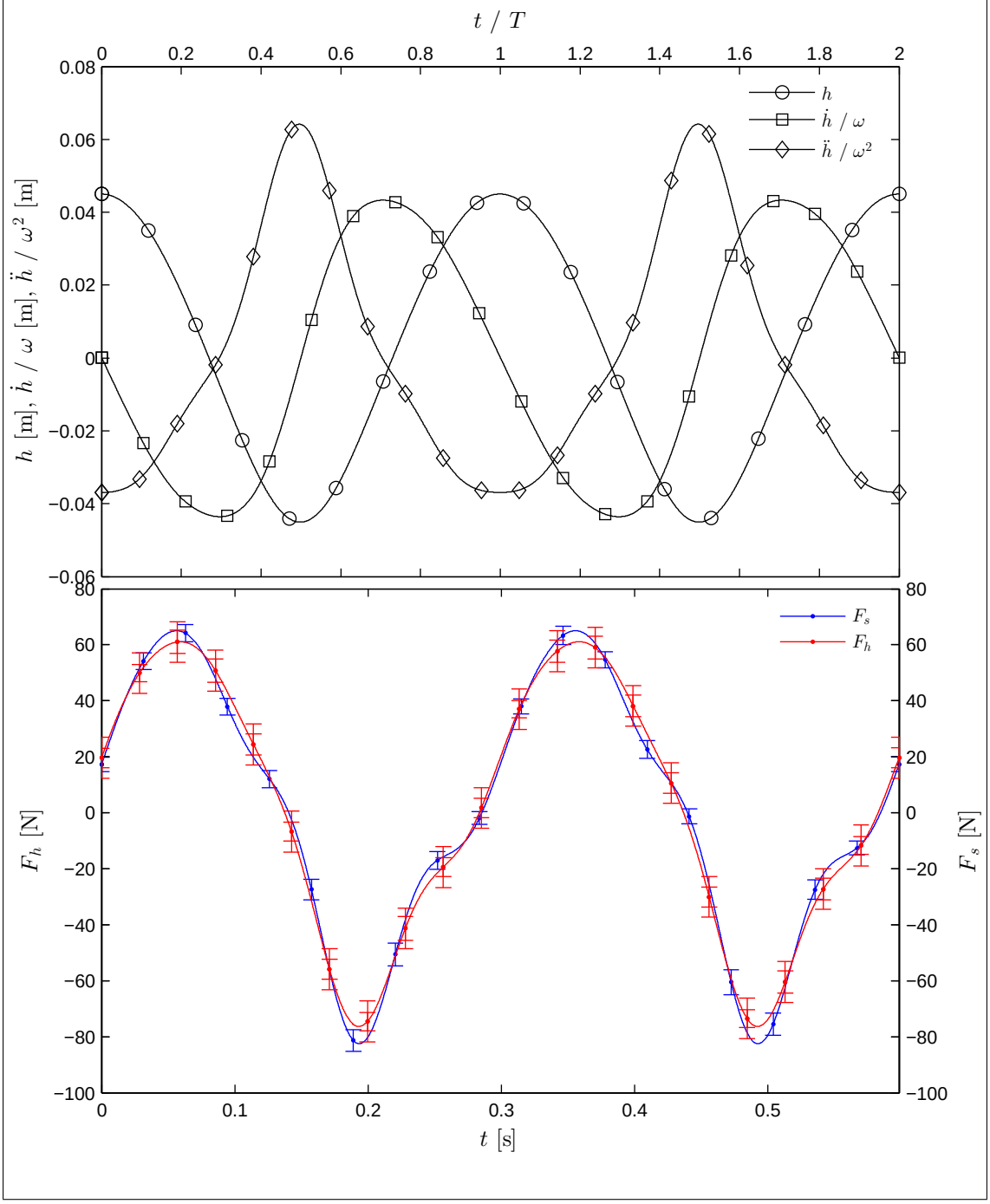

Object: Flat Plate		Motion	Water
	$c = 0.051\,\mathrm{m}$ $L = 0.600\,\mathrm{m}$ $t = 0.006\,\mathrm{m}$ $\theta = 40°$	$h_0 = 0.045\,\mathrm{m}$ $h^* = 0.88$ $f = 3.73\,\mathrm{Hz}$ $u = 0.00\,\mathrm{m\,s^{-1}}$	$T_w = 9.7\,°\mathrm{C}$ $\rho = 1000\,\mathrm{kg\,m^{-3}}$

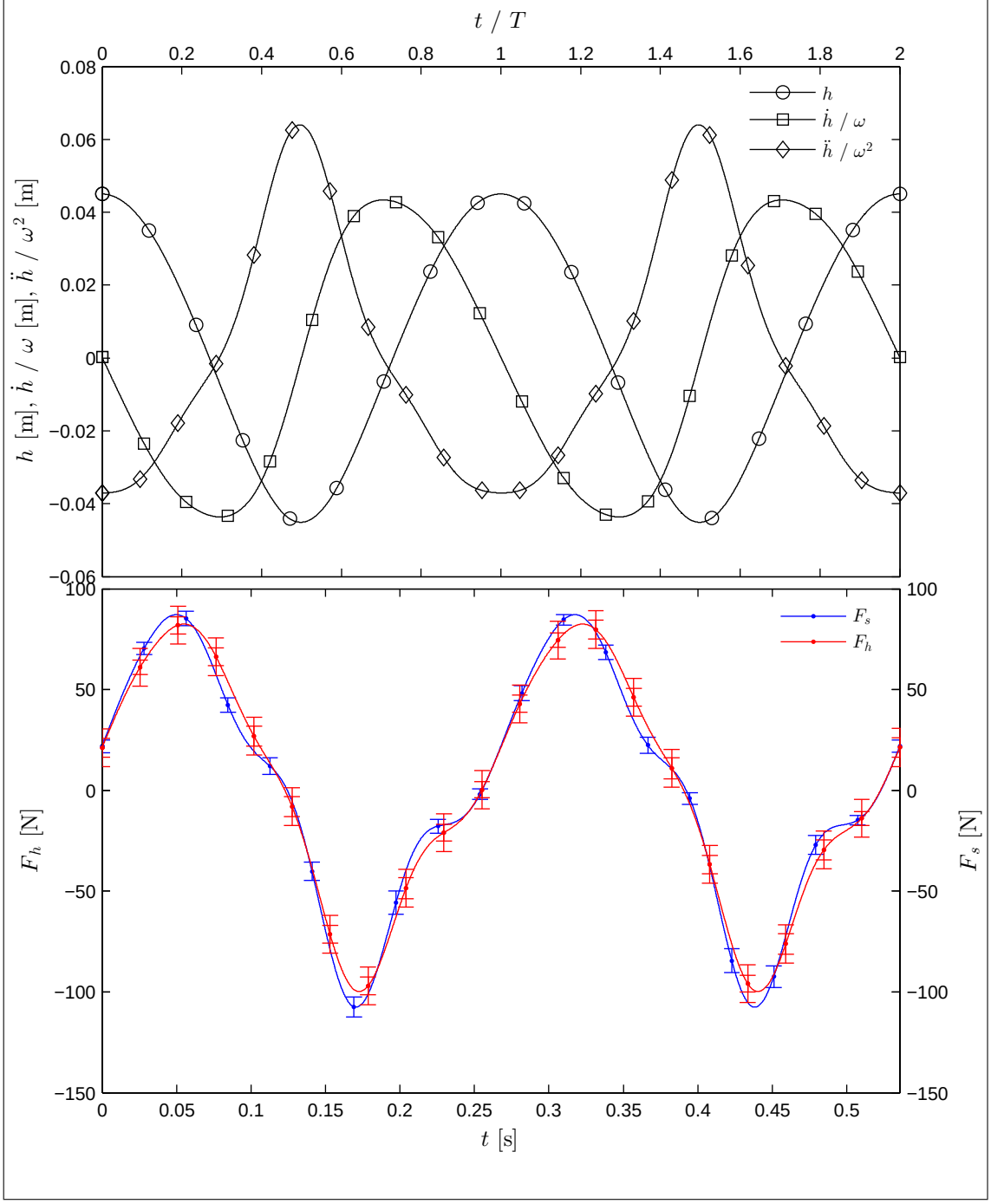

Object: Flat Plate		Motion	Water
	$c = 0.051\,\mathrm{m}$ $L = 0.600\,\mathrm{m}$ $t = 0.006\,\mathrm{m}$ $\theta = 0°$	$h_0 = 0.045\,\mathrm{m}$ $h^* = 0.88$ $f = 1.56\,\mathrm{Hz}$ $u = 0.52\,\mathrm{m\,s^{-1}}$	$T_w = 9.7\,°\mathrm{C}$ $\rho = 1000\,\mathrm{kg\,m^{-3}}$

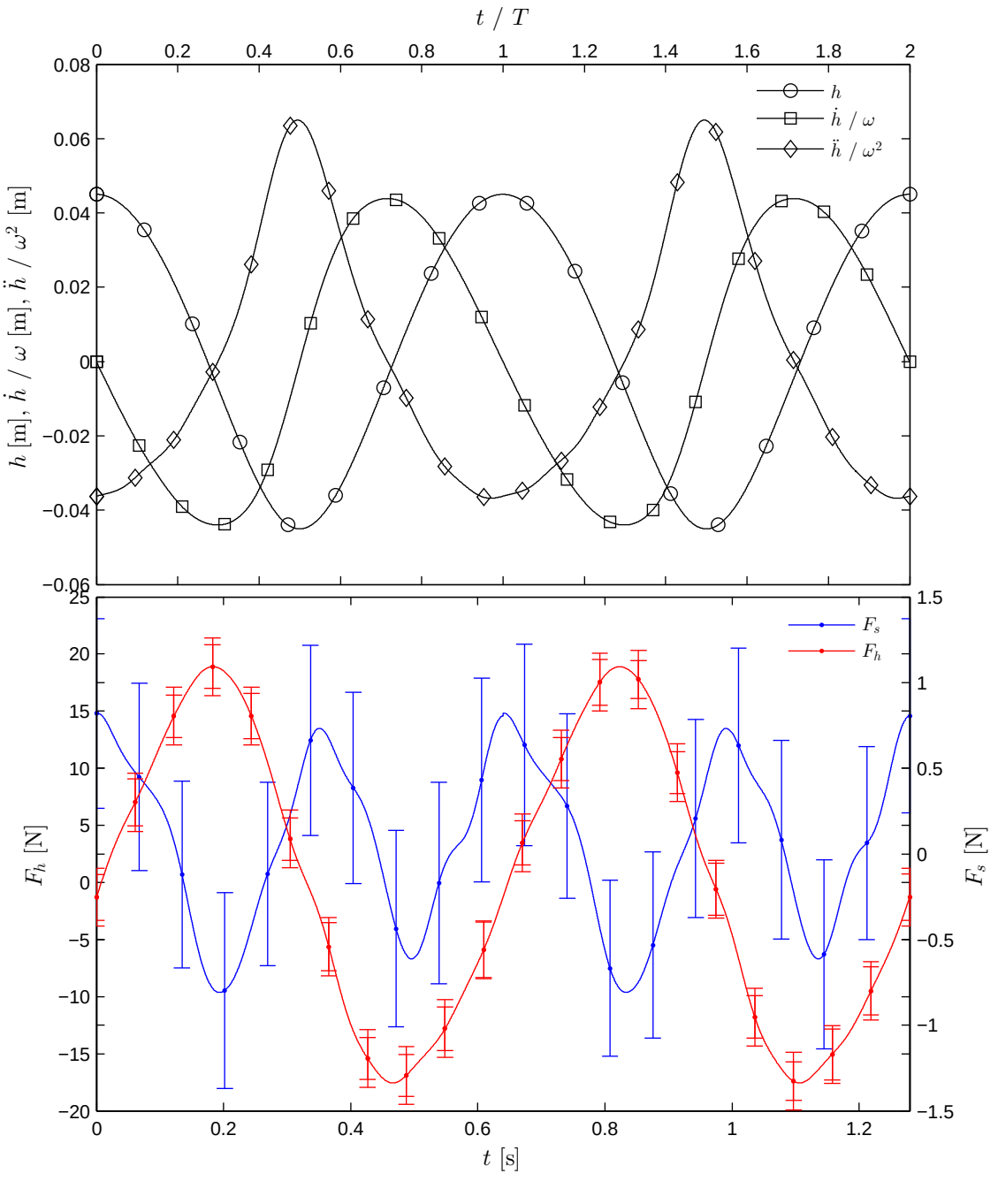

Object: Flat Plate		Motion	Water
	$c = 0.051\,\mathrm{m}$ $L = 0.600\,\mathrm{m}$ $t = 0.006\,\mathrm{m}$ $\theta = 0°$	$h_0 = 0.045\,\mathrm{m}$ $h^* = 0.88$ $f = 1.55\,\mathrm{Hz}$ $u = 0.99\,\mathrm{m\,s^{-1}}$	$T_w = 9.7\,°\mathrm{C}$ $\rho = 1000\,\mathrm{kg\,m^{-3}}$

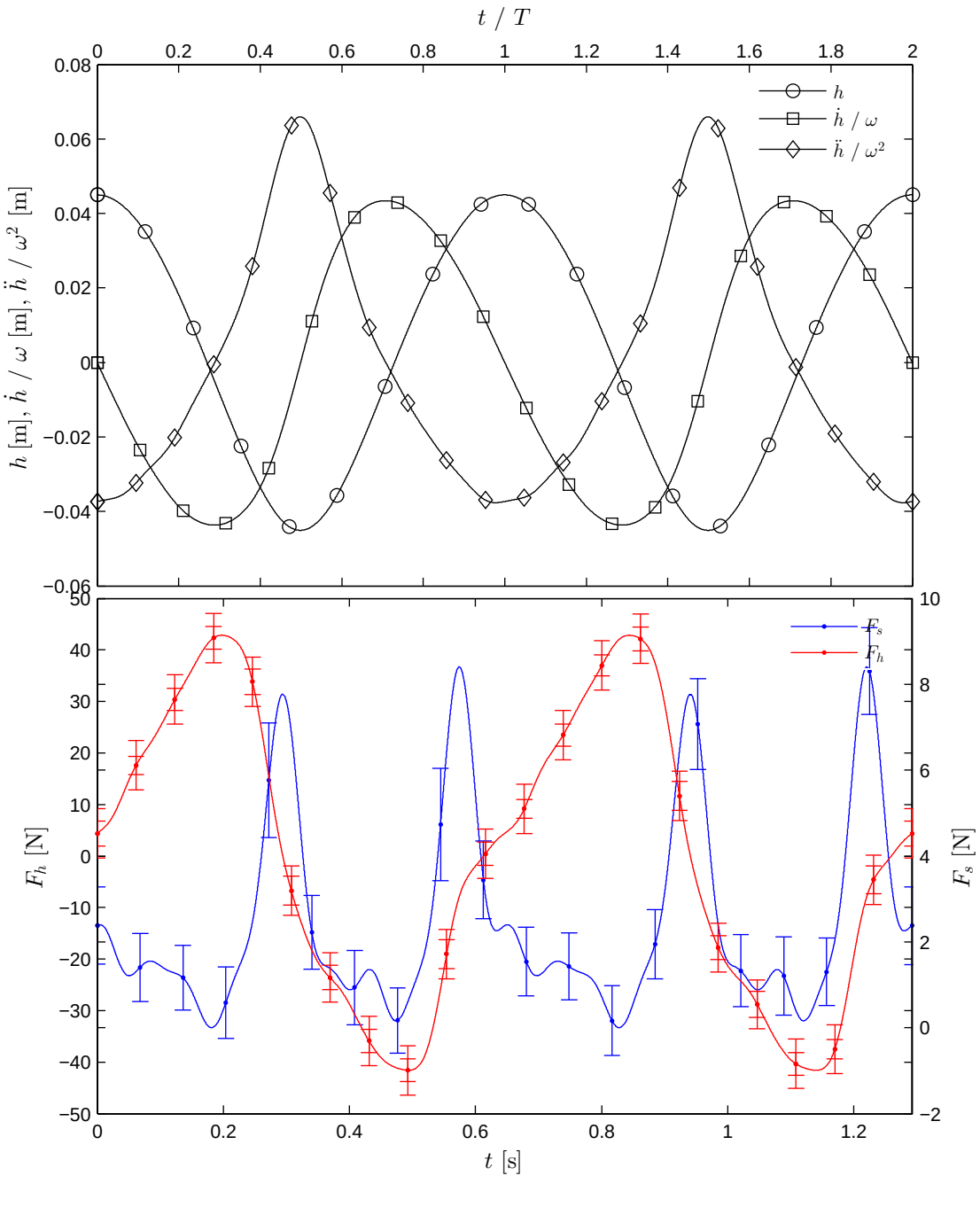

Object: Flat Plate		Motion	Water
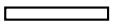	$c = 0.051\,\mathrm{m}$ $L = 0.600\,\mathrm{m}$ $t = 0.006\,\mathrm{m}$ $\theta = 0°$	$h_0 = 0.045\,\mathrm{m}$ $h^* = 0.88$ $f = 1.53\,\mathrm{Hz}$ $u = 1.50\,\mathrm{m\,s^{-1}}$	$T_w = 9.7\,°\mathrm{C}$ $\rho = 1000\,\mathrm{kg\,m^{-3}}$

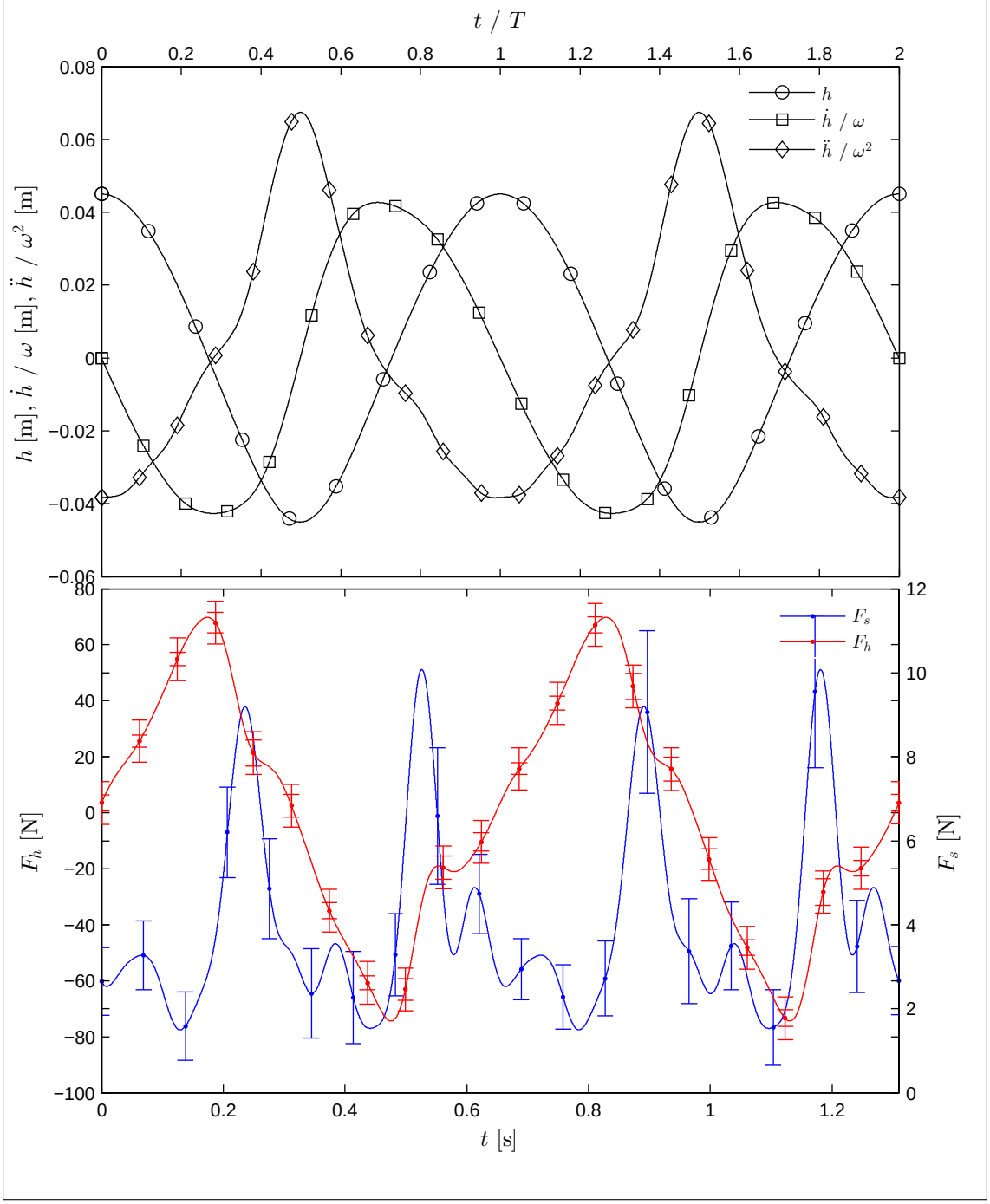

Object: Flat Plate		Motion	Water
	$c = 0.051\,\mathrm{m}$ $L = 0.600\,\mathrm{m}$ $t = 0.006\,\mathrm{m}$ $\theta = 0°$	$h_0 = 0.045\,\mathrm{m}$ $h^* = 0.88$ $f = 1.48\,\mathrm{Hz}$ $u = 1.98\,\mathrm{m\,s^{-1}}$	$T_w = 9.7\,°\mathrm{C}$ $\rho = 1000\,\mathrm{kg\,m^{-3}}$

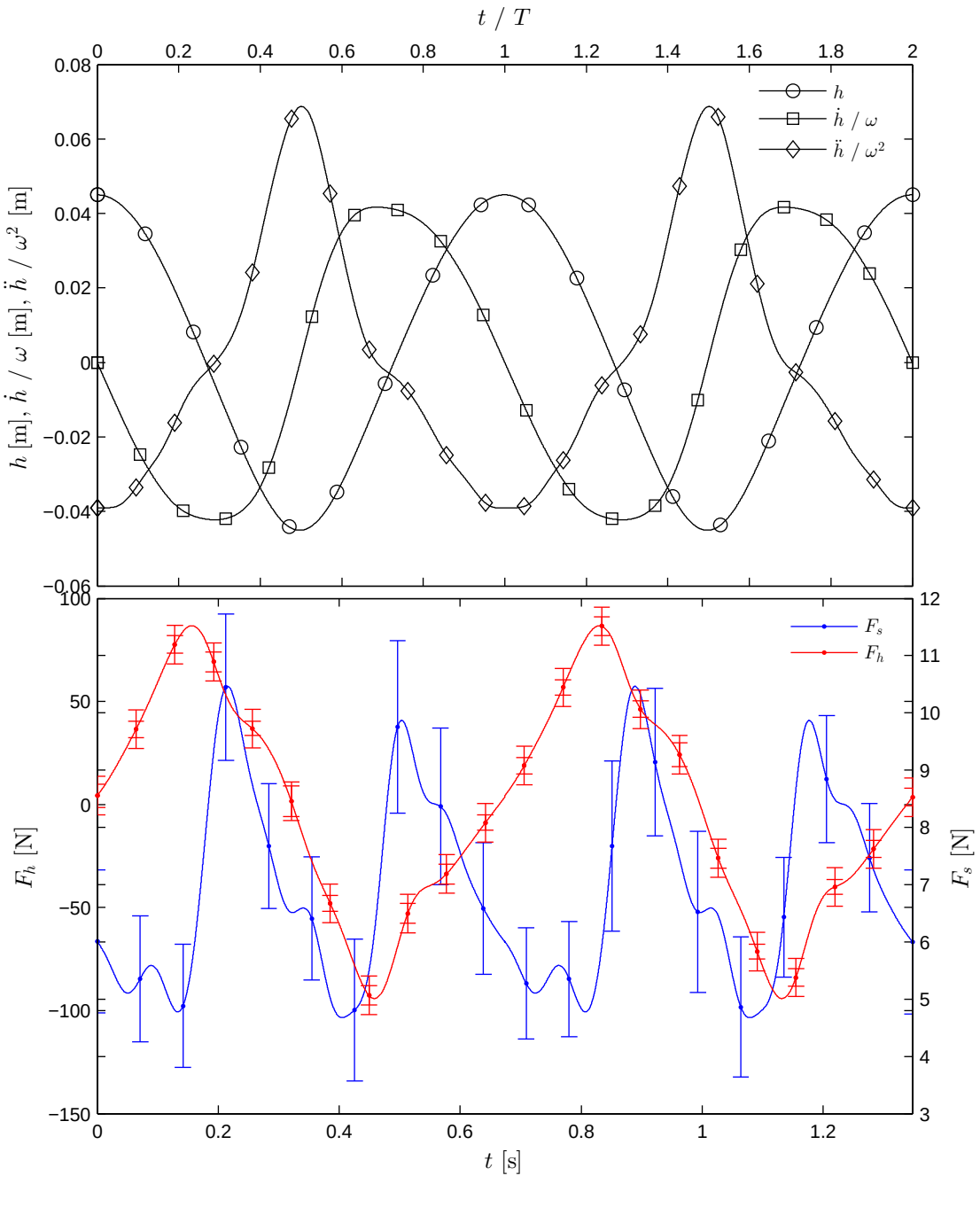

Object: Flat Plate		Motion	Water
	$c = 0.051\,\mathrm{m}$ $L = 0.600\,\mathrm{m}$ $t = 0.006\,\mathrm{m}$ $\theta = 0°$	$h_0 = 0.045\,\mathrm{m}$ $h^* = 0.88$ $f = 2.12\,\mathrm{Hz}$ $u = 0.52\,\mathrm{m\,s^{-1}}$	$T_w = 9.7\,°\mathrm{C}$ $\rho = 1000\,\mathrm{kg\,m^{-3}}$

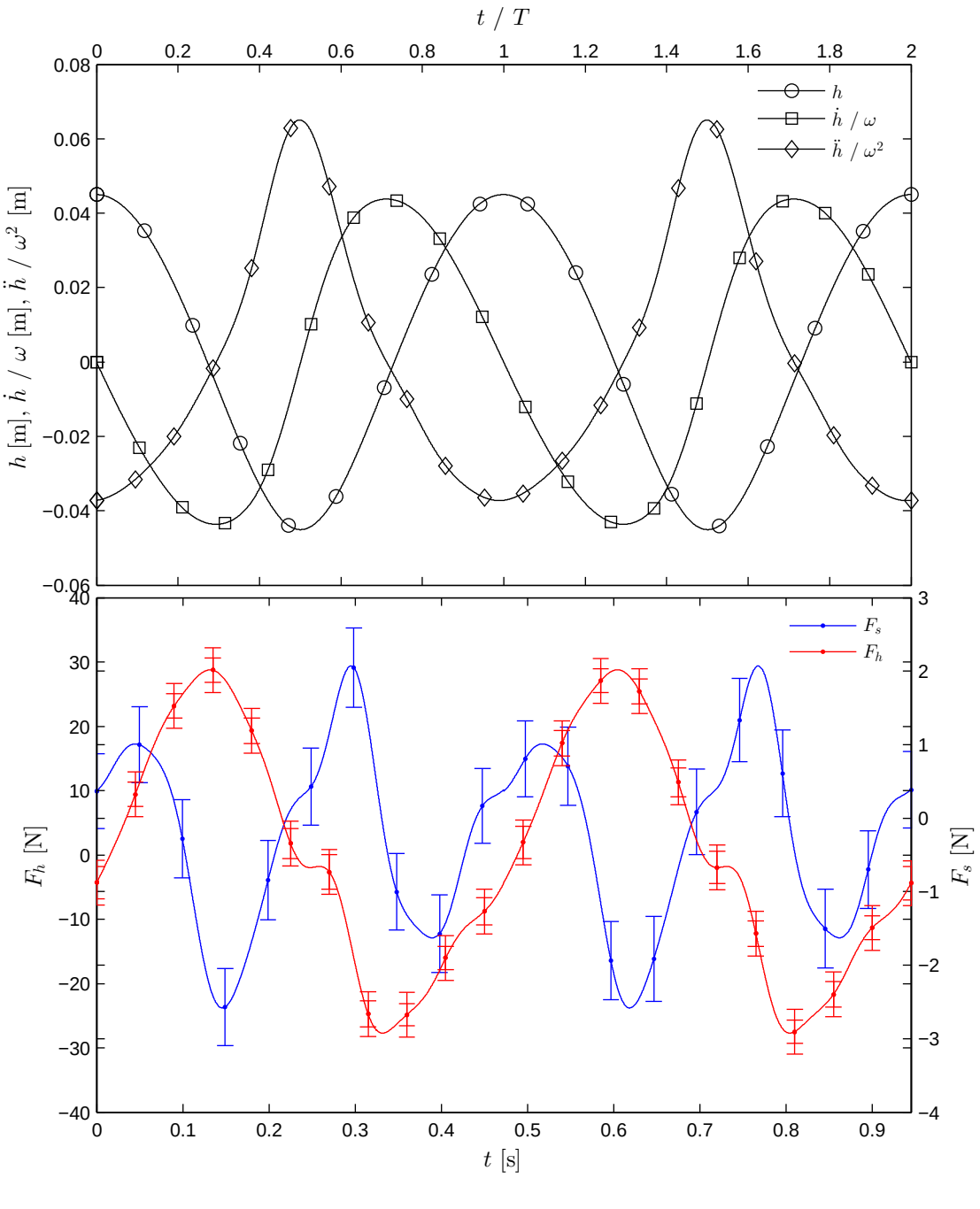

Object: Flat Plate		Motion	Water
	$c = 0.051\,\mathrm{m}$ $L = 0.600\,\mathrm{m}$ $t = 0.006\,\mathrm{m}$ $\theta = 0°$	$h_0 = 0.045\,\mathrm{m}$ $h^* = 0.88$ $f = 2.07\,\mathrm{Hz}$ $u = 0.99\,\mathrm{m\,s^{-1}}$	$T_w = 9.7\,°\mathrm{C}$ $\rho = 1000\,\mathrm{kg\,m^{-3}}$

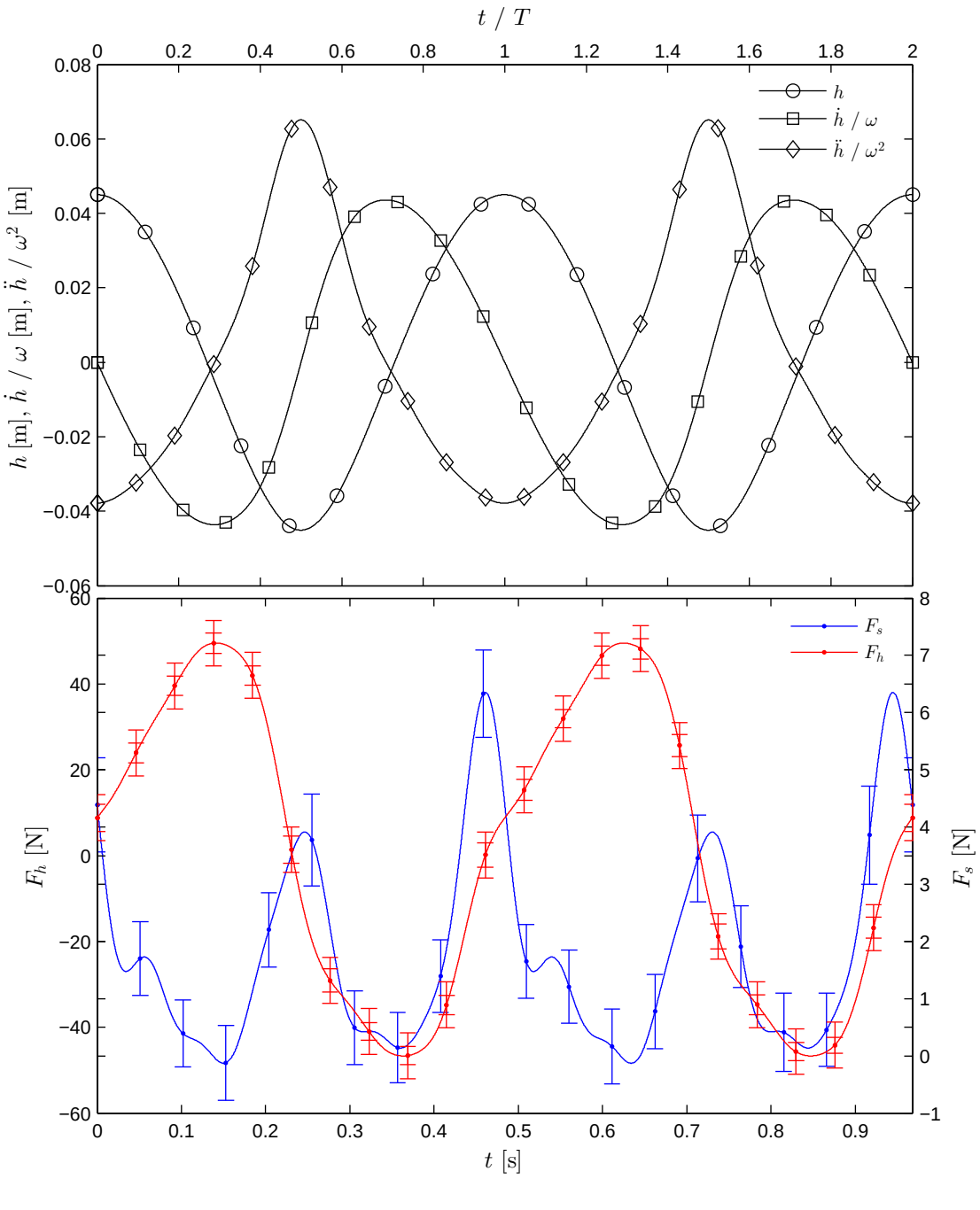

Object: Flat Plate		Motion	Water
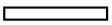	$c = 0.051\,\mathrm{m}$ $L = 0.600\,\mathrm{m}$ $t = 0.006\,\mathrm{m}$ $\theta = 0°$	$h_0 = 0.045\,\mathrm{m}$ $h^* = 0.88$ $f = 2.01\,\mathrm{Hz}$ $u = 1.50\,\mathrm{m\,s^{-1}}$	$T_w = 9.7\,°\mathrm{C}$ $\rho = 1000\,\mathrm{kg\,m^{-3}}$

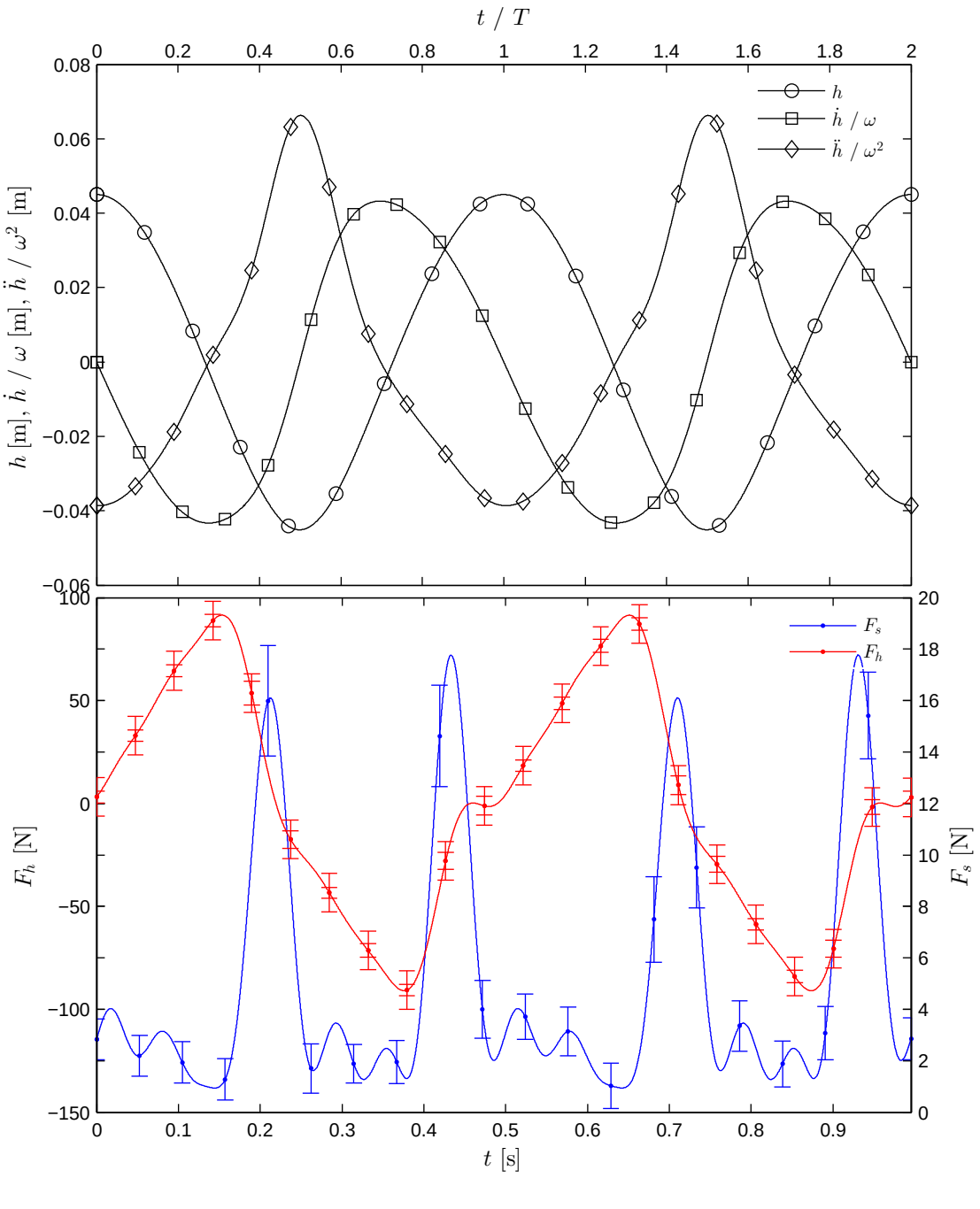

Object: Flat Plate		Motion	Water
	$c = 0.051\,\mathrm{m}$ $L = 0.600\,\mathrm{m}$ $t = 0.006\,\mathrm{m}$ $\theta = 0°$	$h_0 = 0.045\,\mathrm{m}$ $h^* = 0.88$ $f = 1.96\,\mathrm{Hz}$ $u = 1.97\,\mathrm{m\,s^{-1}}$	$T_w = 9.7\,°\mathrm{C}$ $\rho = 1000\,\mathrm{kg\,m^{-3}}$

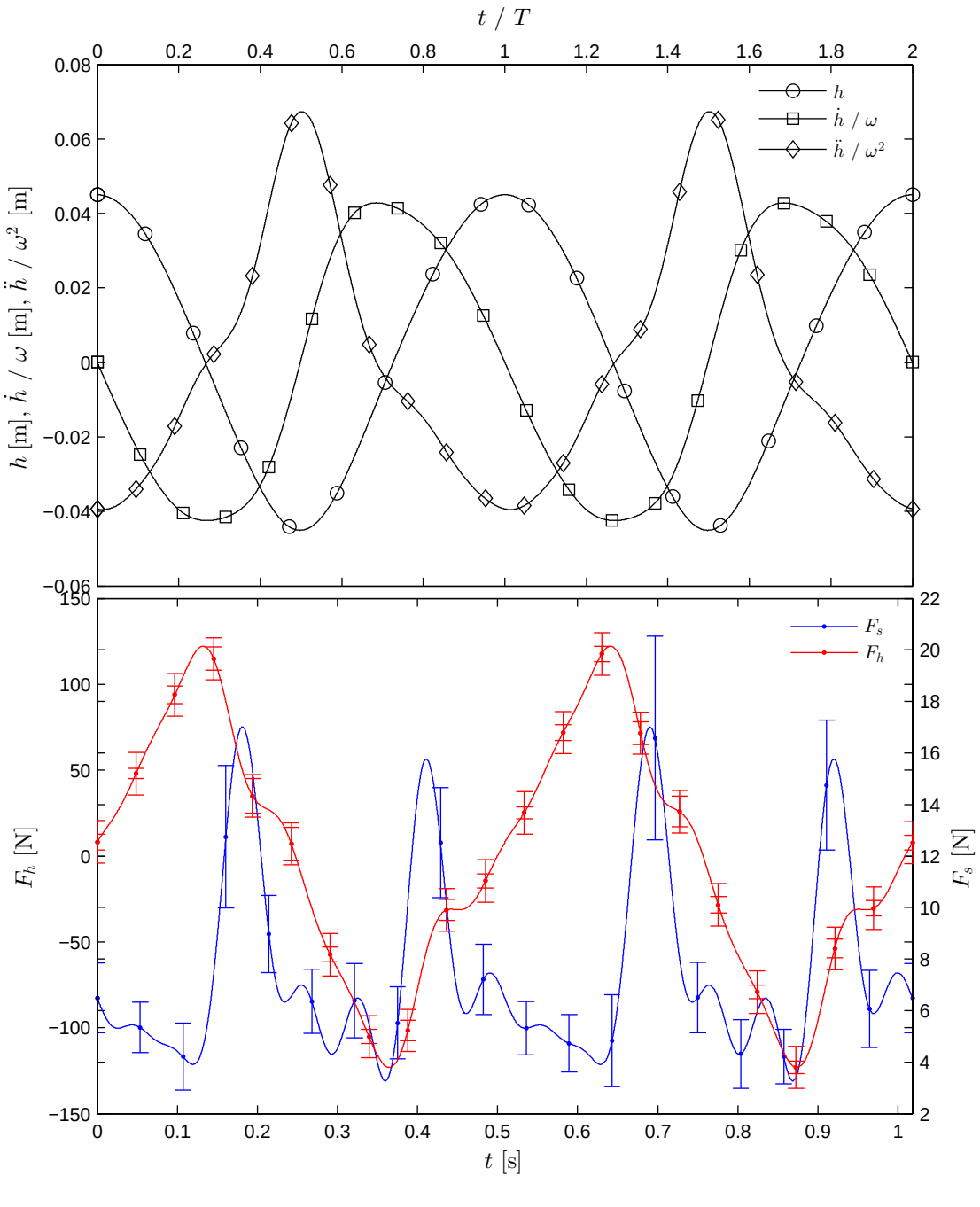

Object: Flat Plate		Motion	Water
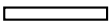	$c = 0.051\,\mathrm{m}$ $L = 0.600\,\mathrm{m}$ $t = 0.006\,\mathrm{m}$ $\theta = 0°$	$h_0 = 0.045\,\mathrm{m}$ $h^* = 0.88$ $f = 2.67\,\mathrm{Hz}$ $u = 0.52\,\mathrm{m\,s^{-1}}$	$T_w = 9.7\,°\mathrm{C}$ $\rho = 1000\,\mathrm{kg\,m^{-3}}$

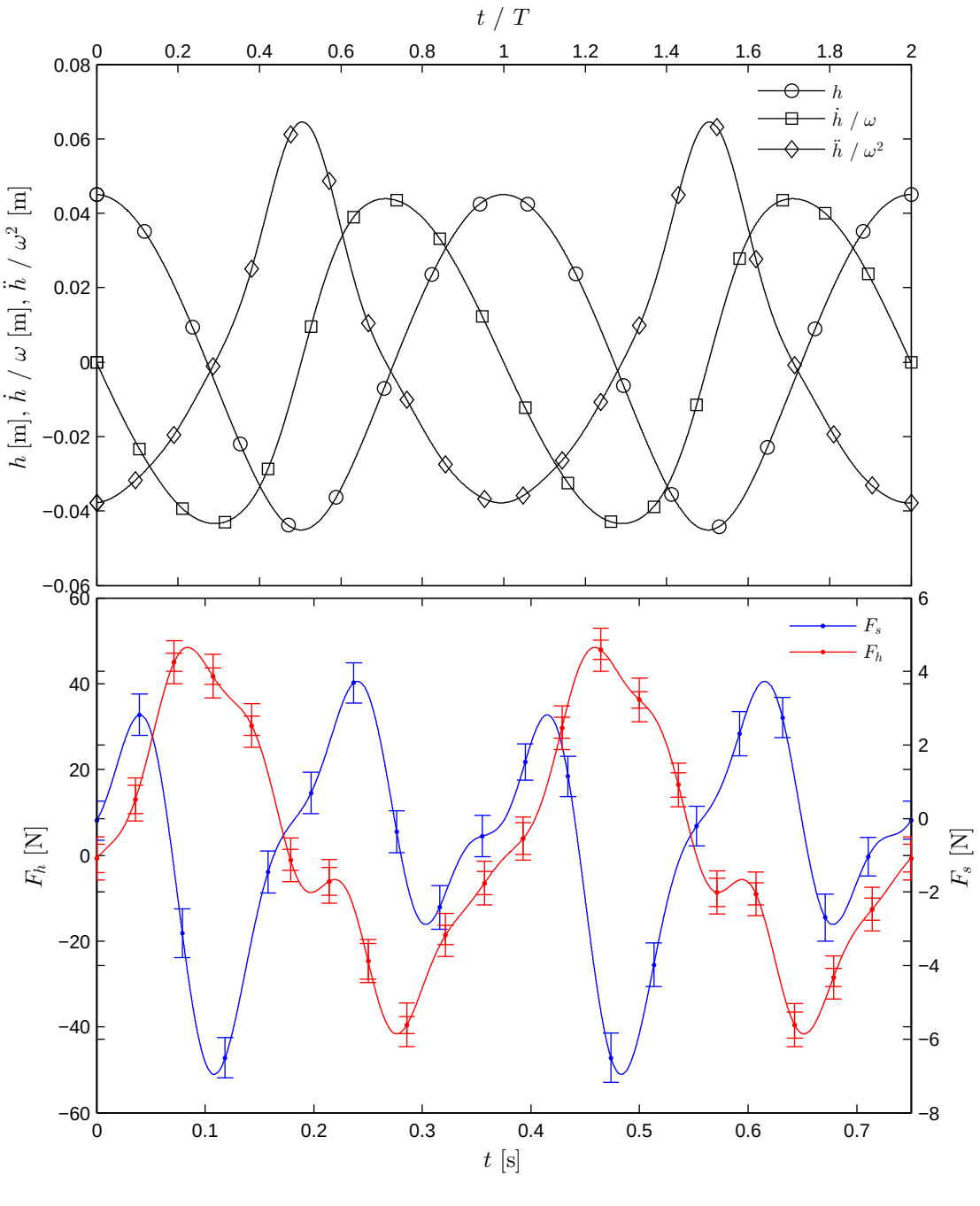

Object: Flat Plate		Motion	Water
	$c = 0.051\,\mathrm{m}$ $L = 0.600\,\mathrm{m}$ $t = 0.006\,\mathrm{m}$ $\theta = 0°$	$h_0 = 0.045\,\mathrm{m}$ $h^* = 0.88$ $f = 2.62\,\mathrm{Hz}$ $u = 0.99\,\mathrm{m\,s^{-1}}$	$T_w = 9.7\,°\mathrm{C}$ $\rho = 1000\,\mathrm{kg\,m^{-3}}$

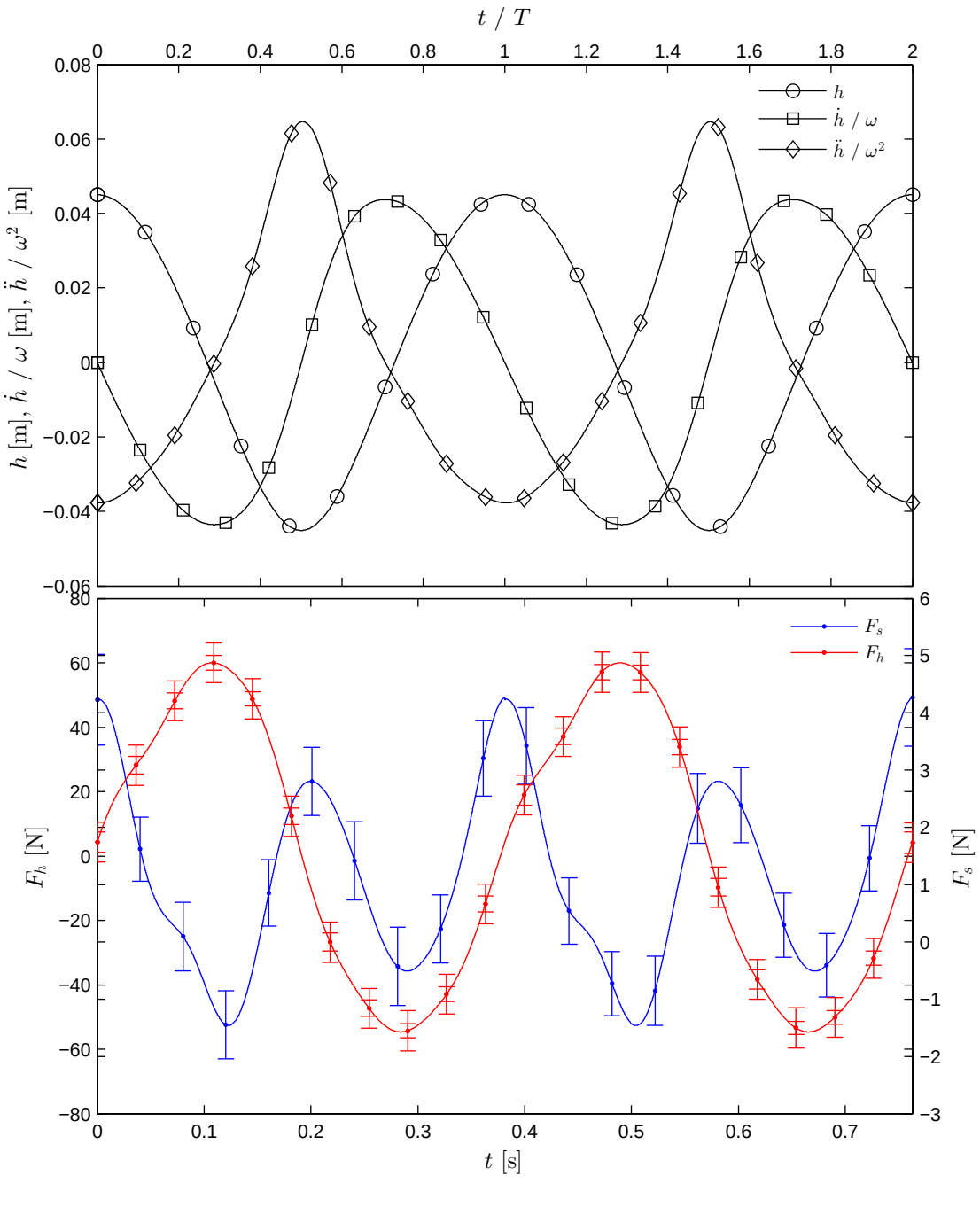

Object: Flat Plate		Motion	Water
	$c = 0.051\,\mathrm{m}$ $L = 0.600\,\mathrm{m}$ $t = 0.006\,\mathrm{m}$ $\theta = 0°$	$h_0 = 0.045\,\mathrm{m}$ $h^* = 0.88$ $f = 2.53\,\mathrm{Hz}$ $u = 1.50\,\mathrm{m\,s^{-1}}$	$T_w = 9.7\,°\mathrm{C}$ $\rho = 1000\,\mathrm{kg\,m^{-3}}$

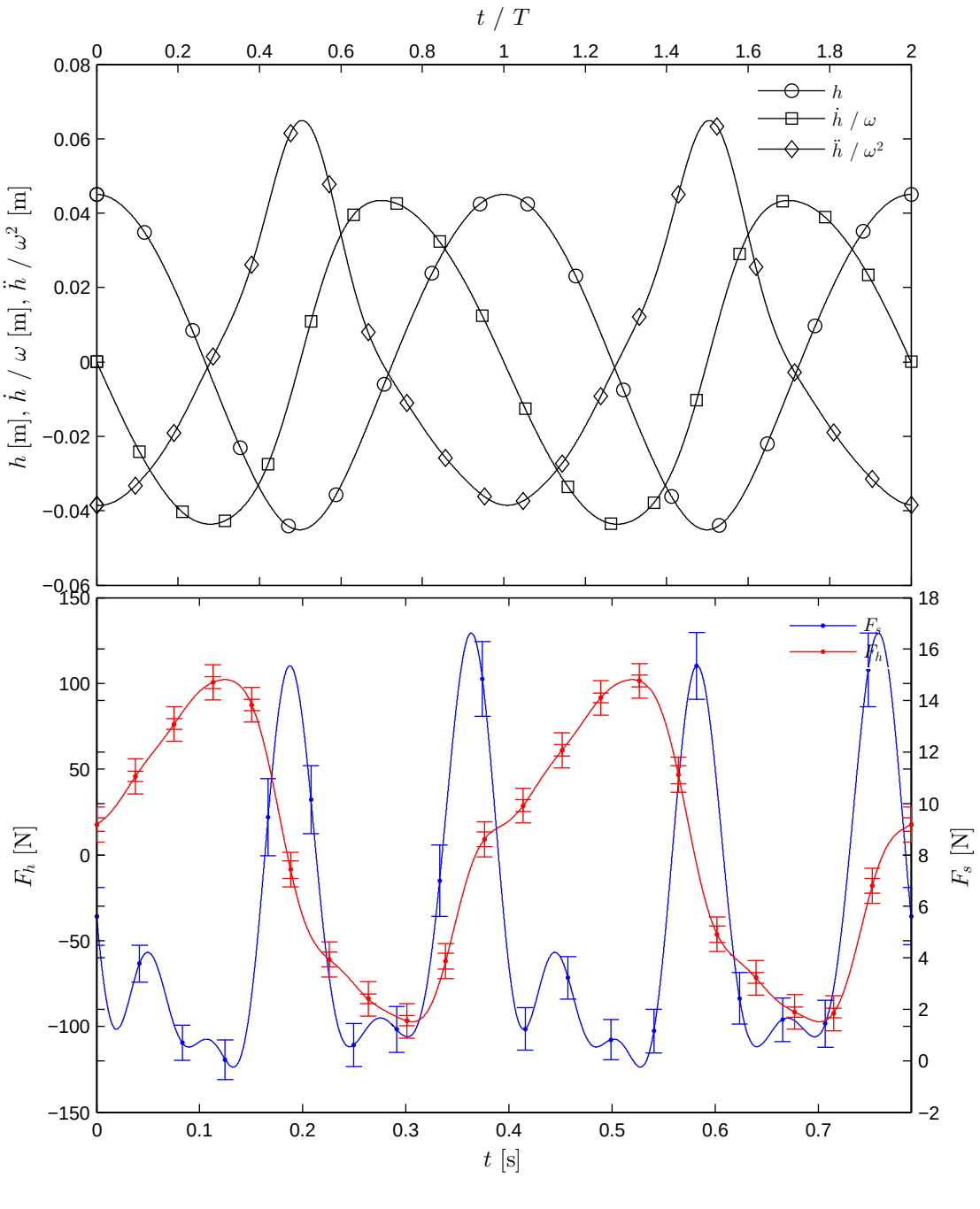

Object: Flat Plate		Motion	Water
	$c = 0.051\,\mathrm{m}$ $L = 0.600\,\mathrm{m}$ $t = 0.006\,\mathrm{m}$ $\theta = 0°$	$h_0 = 0.045\,\mathrm{m}$ $h^* = 0.88$ $f = 2.45\,\mathrm{Hz}$ $u = 1.98\,\mathrm{m\,s^{-1}}$	$T_w = 9.7\,°\mathrm{C}$ $\rho = 1000\,\mathrm{kg\,m^{-3}}$

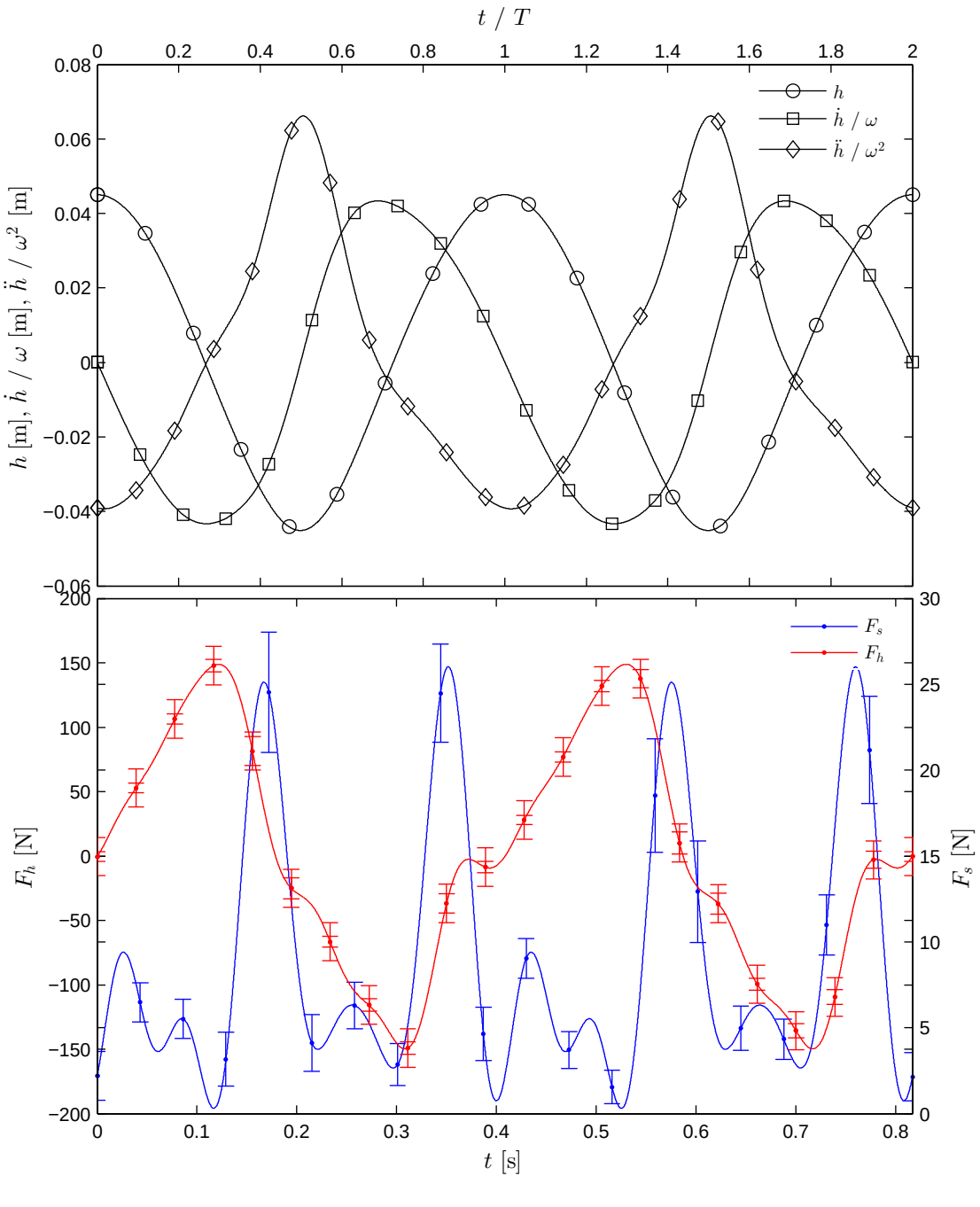

Object: Flat Plate		Motion	Water
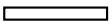	$c = 0.051\,\mathrm{m}$ $L = 0.600\,\mathrm{m}$ $t = 0.006\,\mathrm{m}$ $\theta = 0°$	$h_0 = 0.045\,\mathrm{m}$ $h^* = 0.88$ $f = 3.19\,\mathrm{Hz}$ $u = 0.52\,\mathrm{m\,s^{-1}}$	$T_w = 9.7\,°\mathrm{C}$ $\rho = 1000\,\mathrm{kg\,m^{-3}}$

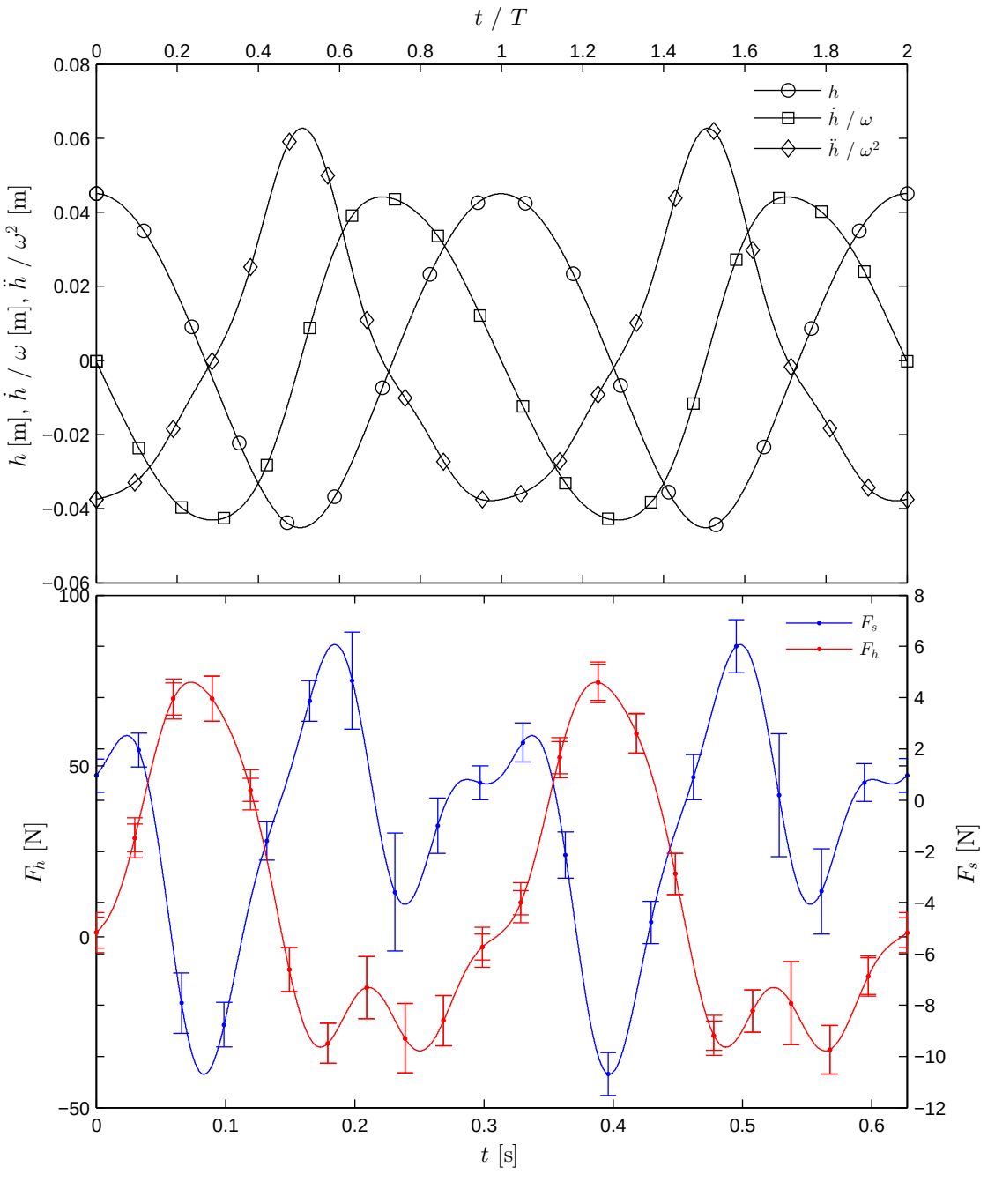

Object: Flat Plate		Motion	Water
	$c = 0.051\,\mathrm{m}$ $L = 0.600\,\mathrm{m}$ $t = 0.006\,\mathrm{m}$ $\theta = 0°$	$h_0 = 0.045\,\mathrm{m}$ $h^* = 0.88$ $f = 3.13\,\mathrm{Hz}$ $u = 0.99\,\mathrm{m\,s^{-1}}$	$T_w = 9.7\,°\mathrm{C}$ $\rho = 1000\,\mathrm{kg\,m^{-3}}$

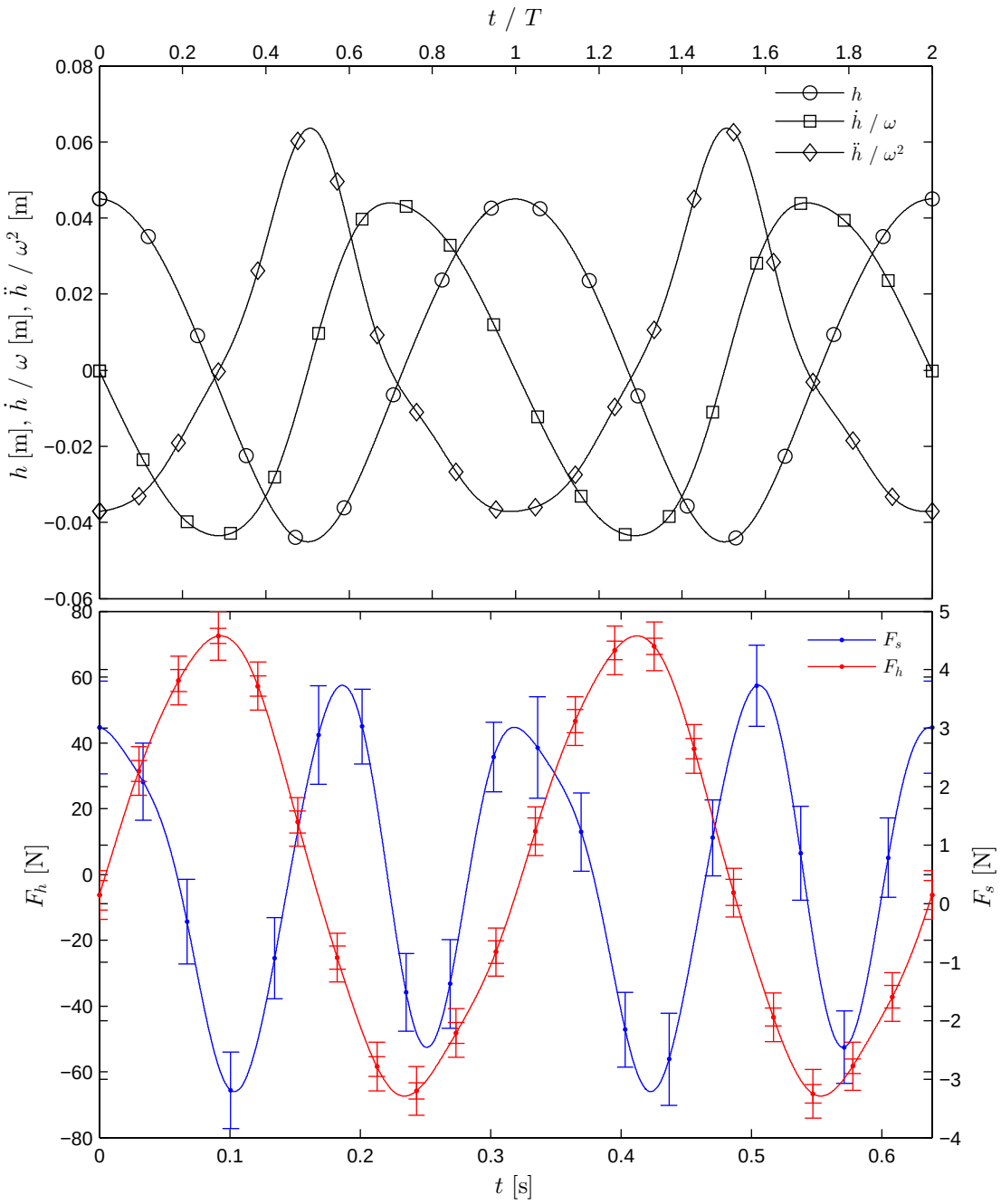

Object: Flat Plate		Motion	Water
	$c = 0.051\,\mathrm{m}$ $L = 0.600\,\mathrm{m}$ $t = 0.006\,\mathrm{m}$ $\theta = 0°$	$h_0 = 0.045\,\mathrm{m}$ $h^* = 0.88$ $f = 3.01\,\mathrm{Hz}$ $u = 1.50\,\mathrm{m\,s^{-1}}$	$T_w = 9.7\,°\mathrm{C}$ $\rho = 1000\,\mathrm{kg\,m^{-3}}$

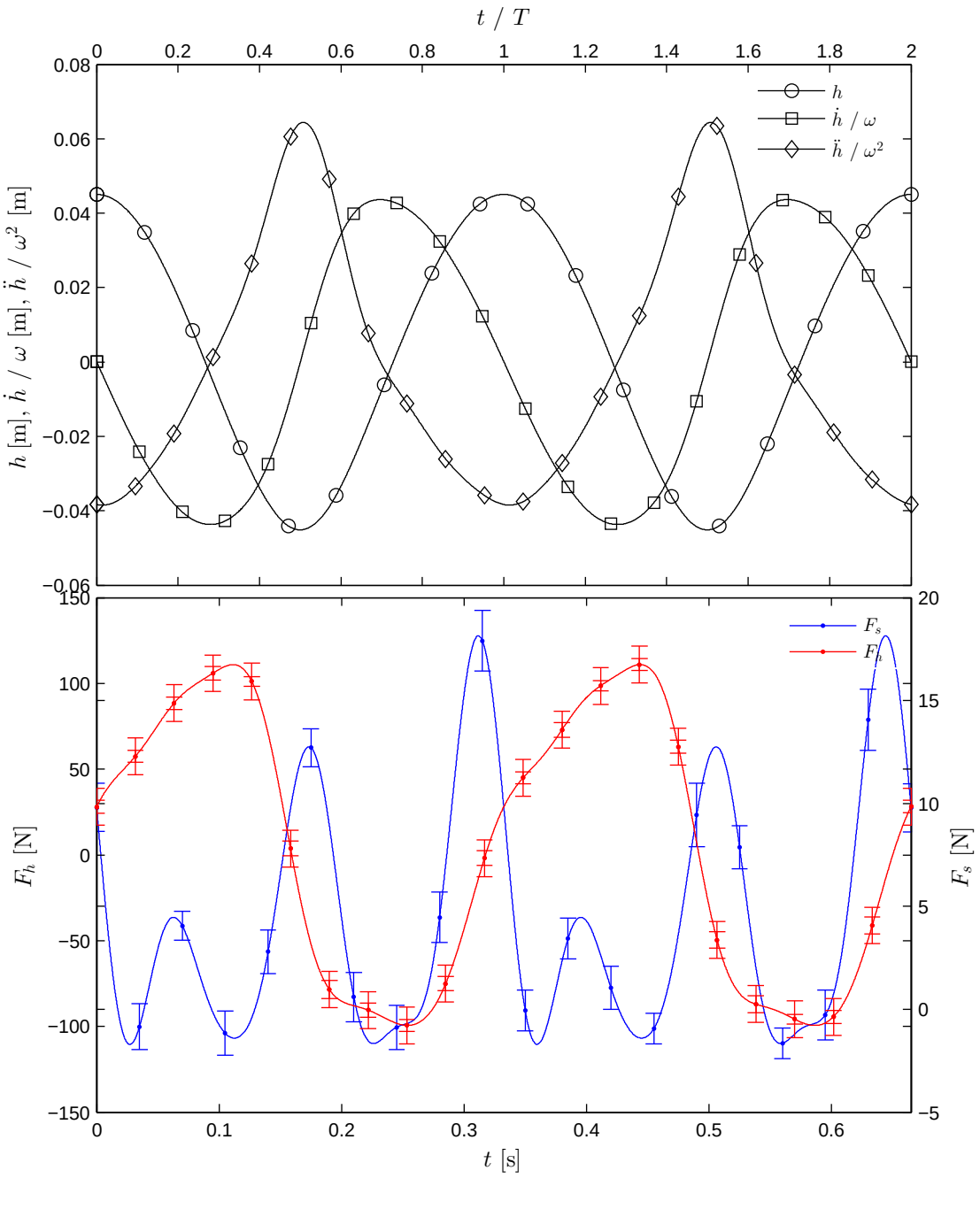

Object: Flat Plate		Motion	Water
	$c = 0.051\,\mathrm{m}$ $L = 0.600\,\mathrm{m}$ $t = 0.006\,\mathrm{m}$ $\theta = 0°$	$h_0 = 0.045\,\mathrm{m}$ $h^* = 0.88$ $f = 2.87\,\mathrm{Hz}$ $u = 1.98\,\mathrm{m\,s^{-1}}$	$T_w = 9.7\,°\mathrm{C}$ $\rho = 1000\,\mathrm{kg\,m^{-3}}$

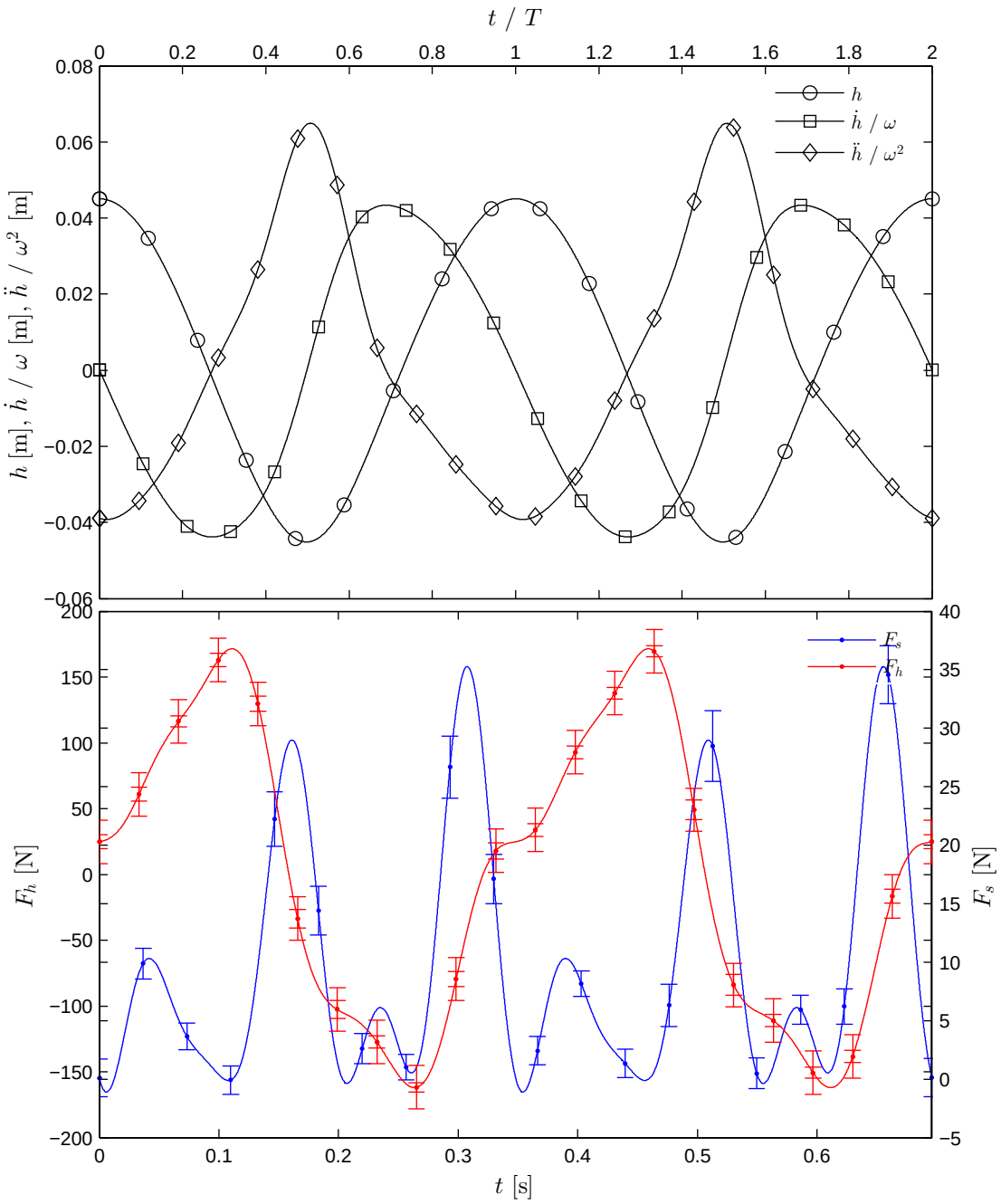

Object: Flat Plate		Motion	Water
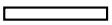	$c = 0.051\,\mathrm{m}$ $L = 0.600\,\mathrm{m}$ $t = 0.006\,\mathrm{m}$ $\theta = 0°$	$h_0 = 0.045\,\mathrm{m}$ $h^* = 0.88$ $f = 3.64\,\mathrm{Hz}$ $u = 0.52\,\mathrm{m\,s^{-1}}$	$T_w = 9.7\,°\mathrm{C}$ $\rho = 1000\,\mathrm{kg\,m^{-3}}$

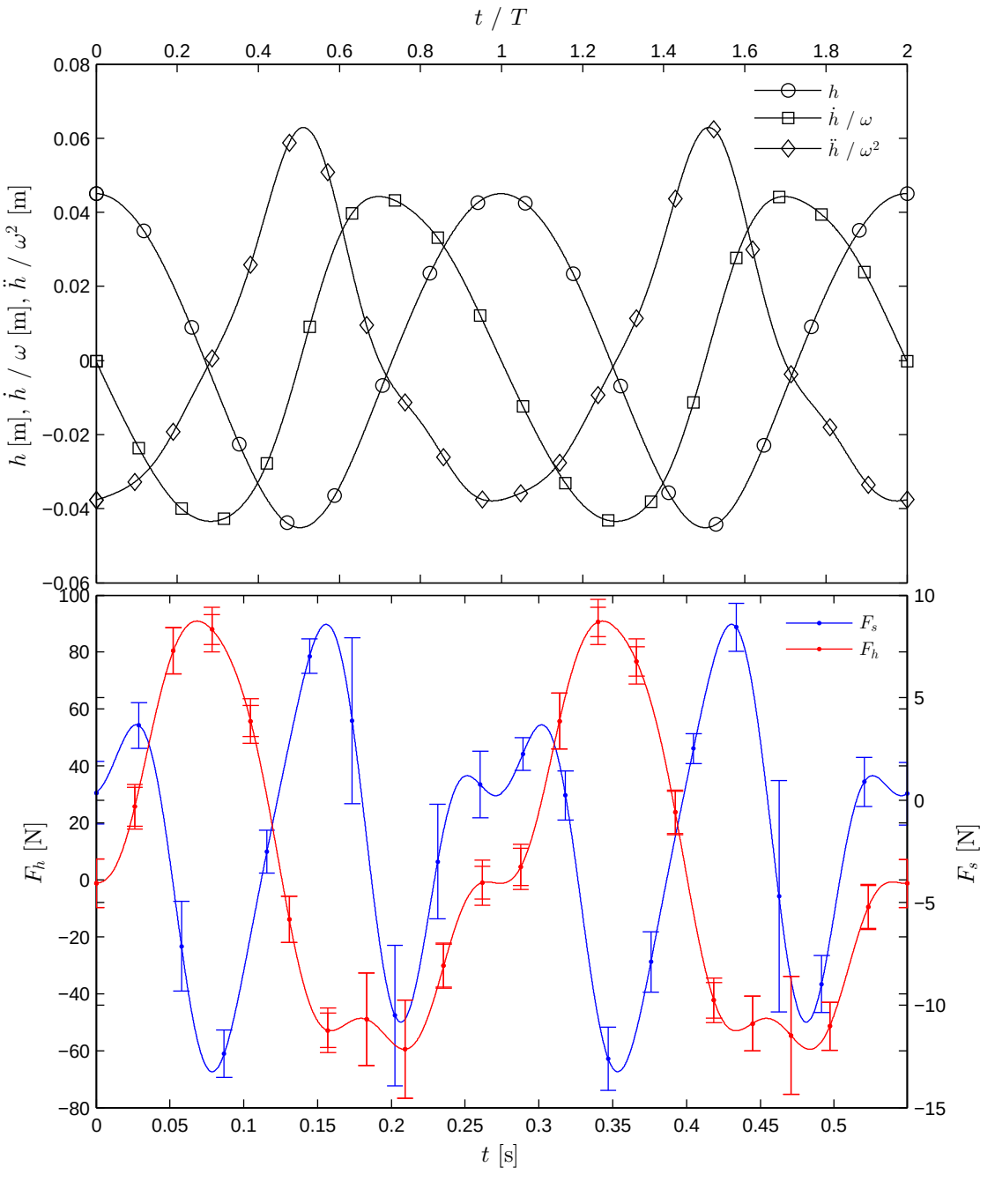

Object: Flat Plate		Motion	Water
	$c = 0.051\,\mathrm{m}$ $L = 0.600\,\mathrm{m}$ $t = 0.006\,\mathrm{m}$ $\theta = 0°$	$h_0 = 0.045\,\mathrm{m}$ $h^* = 0.88$ $f = 3.61\,\mathrm{Hz}$ $u = 0.99\,\mathrm{m\,s^{-1}}$	$T_w = 9.7\,°\mathrm{C}$ $\rho = 1000\,\mathrm{kg\,m^{-3}}$

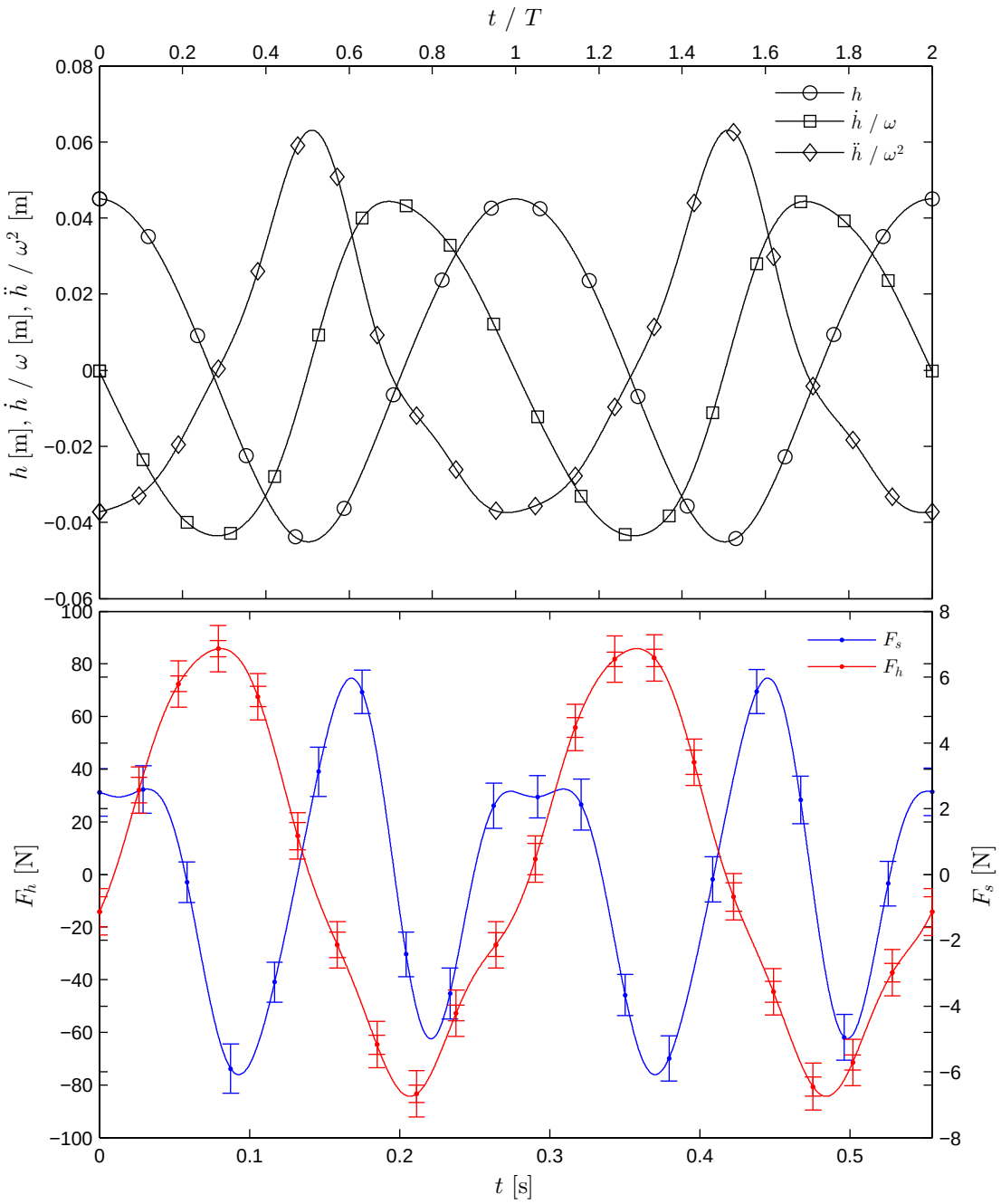

Object: Flat Plate		Motion	Water
	$c = 0.051\,\mathrm{m}$ $L = 0.600\,\mathrm{m}$ $t = 0.006\,\mathrm{m}$ $\theta = 0°$	$h_0 = 0.045\,\mathrm{m}$ $h^* = 0.88$ $f = 3.48\,\mathrm{Hz}$ $u = 1.49\,\mathrm{m\,s^{-1}}$	$T_w = 9.7\,°\mathrm{C}$ $\rho = 1000\,\mathrm{kg\,m^{-3}}$

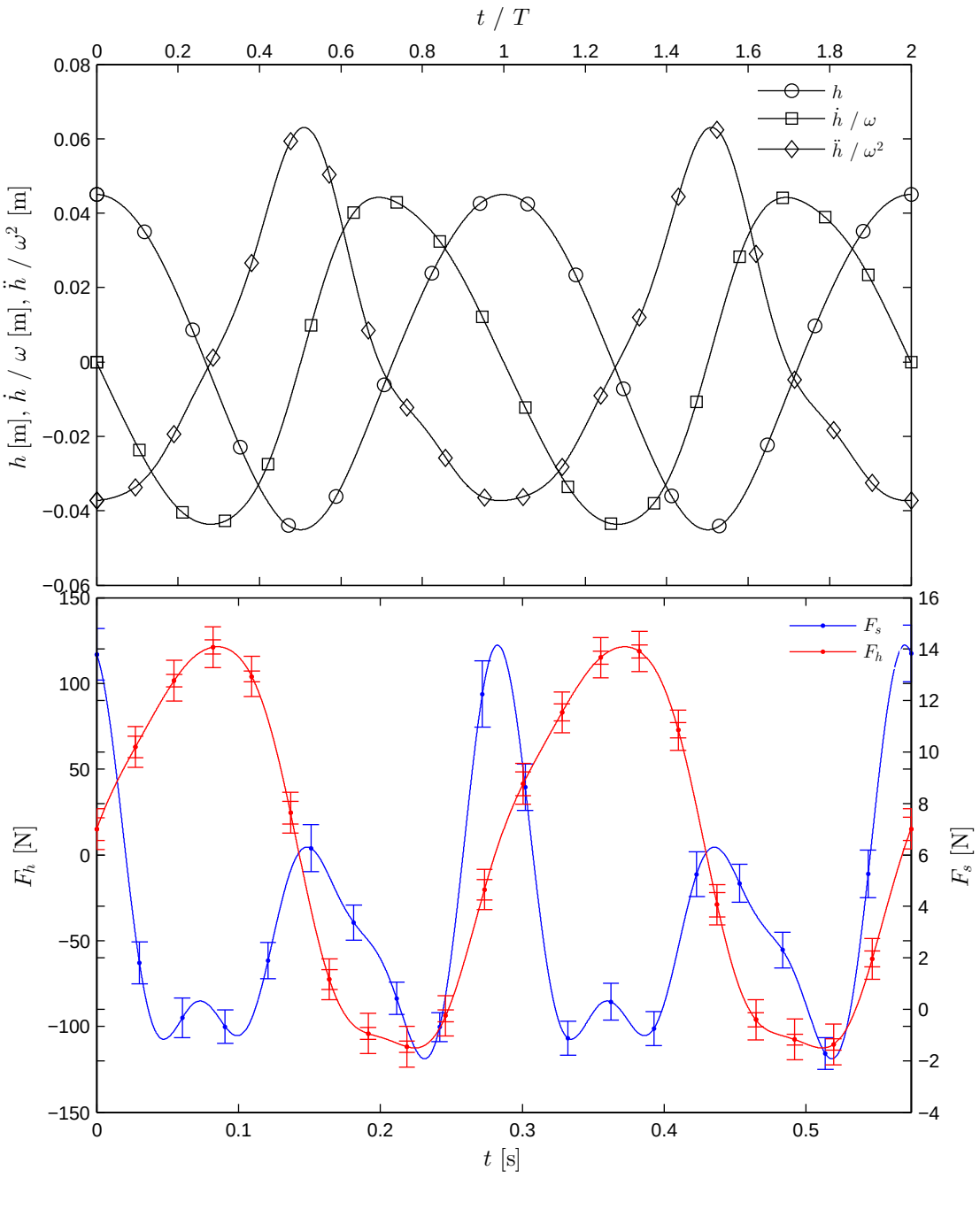

Object: Flat Plate		Motion	Water
	$c = 0.051\,\mathrm{m}$ $L = 0.600\,\mathrm{m}$ $t = 0.006\,\mathrm{m}$ $\theta = 0°$	$h_0 = 0.045\,\mathrm{m}$ $h^* = 0.88$ $f = 3.33\,\mathrm{Hz}$ $u = 1.98\,\mathrm{m\,s^{-1}}$	$T_w = 9.7\,°\mathrm{C}$ $\rho = 1000\,\mathrm{kg\,m^{-3}}$

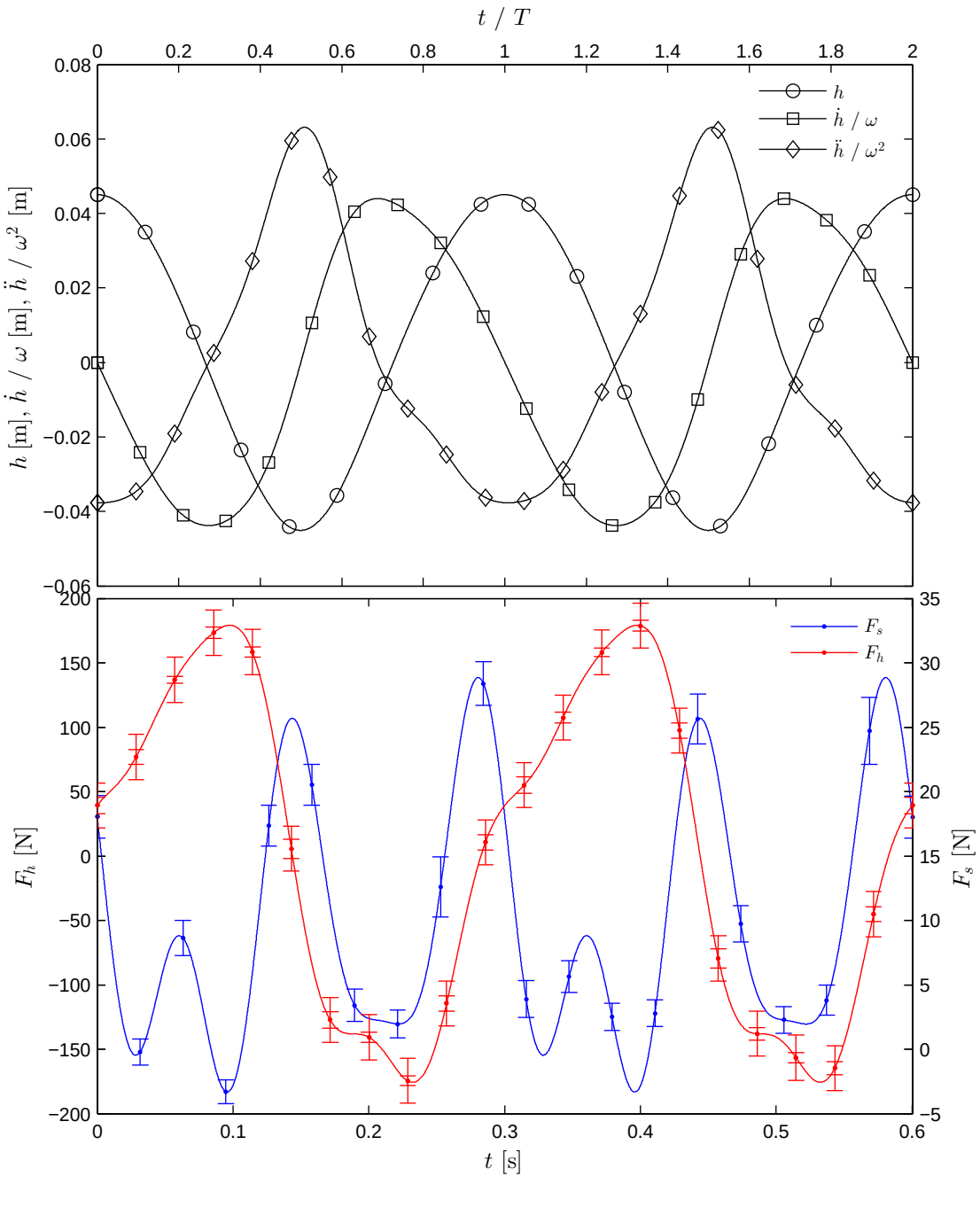

Appendix G

Measured Hydrodynamic Force Cycles on a Heaving NACA0012

The figures included in this appendix show measured hydrodynamic forces on a NACA0012 undergoing a heaving motion with no forward velocity. All the measurements presented in this appendix were recorded with a heave-to-chord ratio of $h^* = 0.75$ and circular end plates of size $\varnothing 320\,\text{mm}$ ($\varnothing 5.3c$) fitted. The dimensions of the NACA0012 cross-section are shown in Figure G.1. Refer to Table 4.1 for a comparison between the NACA0012 and the other test objects.

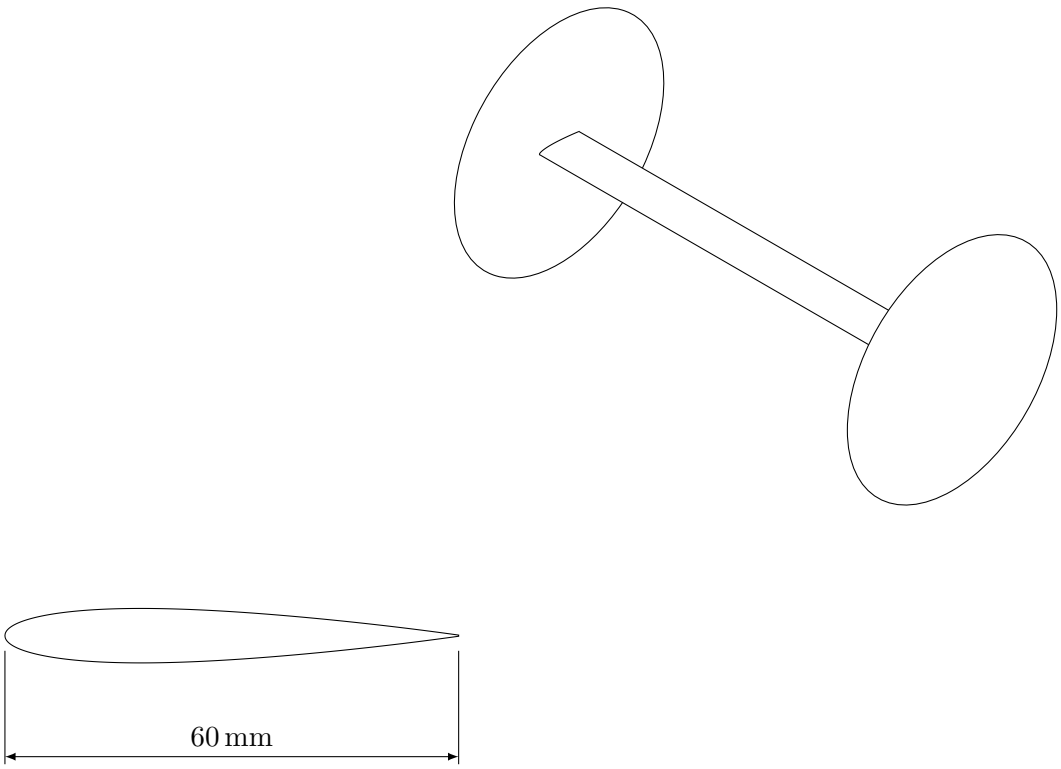

Figure G.1. Dimensions of the NACA0012 cross-section (scale 1:1) and an isometric of the NACA0012 with end plates attached (scale 1:5).

Object: NACA0012		Motion	Water
	$c = 0.060\,\mathrm{m}$ $L = 0.600\,\mathrm{m}$ $\theta = 0°$	$h_0 = 0.045\,\mathrm{m}$ $h^* = 0.75$ $f = 0.79\,\mathrm{Hz}$ $u = 0.00\,\mathrm{m\,s^{-1}}$	$T_w = 12.7\,°\mathrm{C}$ $\rho = 999\,\mathrm{kg\,m^{-3}}$

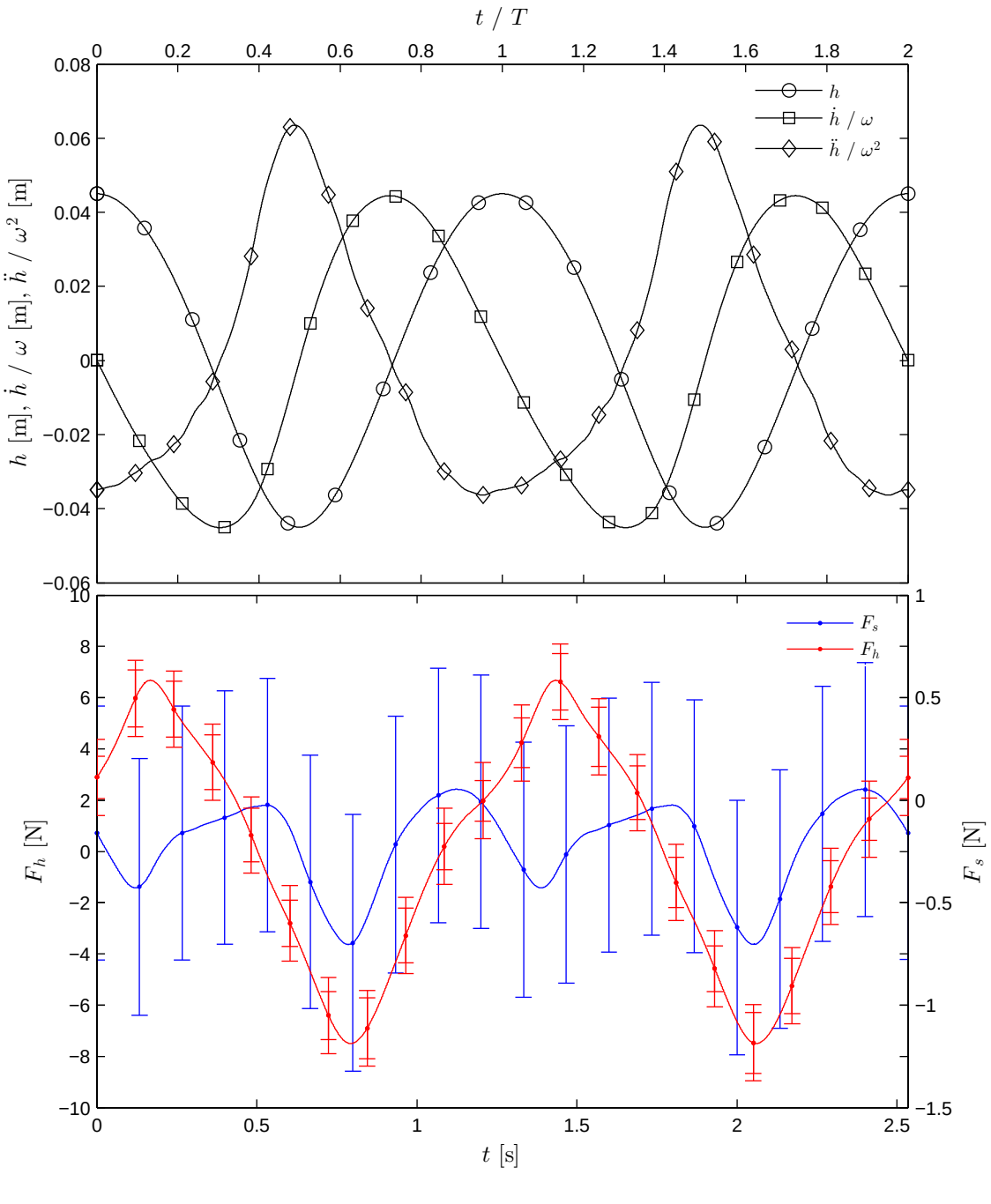

Object: NACA0012		Motion	Water
	$c = 0.060\,\mathrm{m}$ $L = 0.600\,\mathrm{m}$ $\theta = 0°$	$h_0 = 0.045\,\mathrm{m}$ $h^* = 0.75$ $f = 1.30\,\mathrm{Hz}$ $u = 0.00\,\mathrm{m\,s^{-1}}$	$T_w = 12.7\,°\mathrm{C}$ $\rho = 999\,\mathrm{kg\,m^{-3}}$

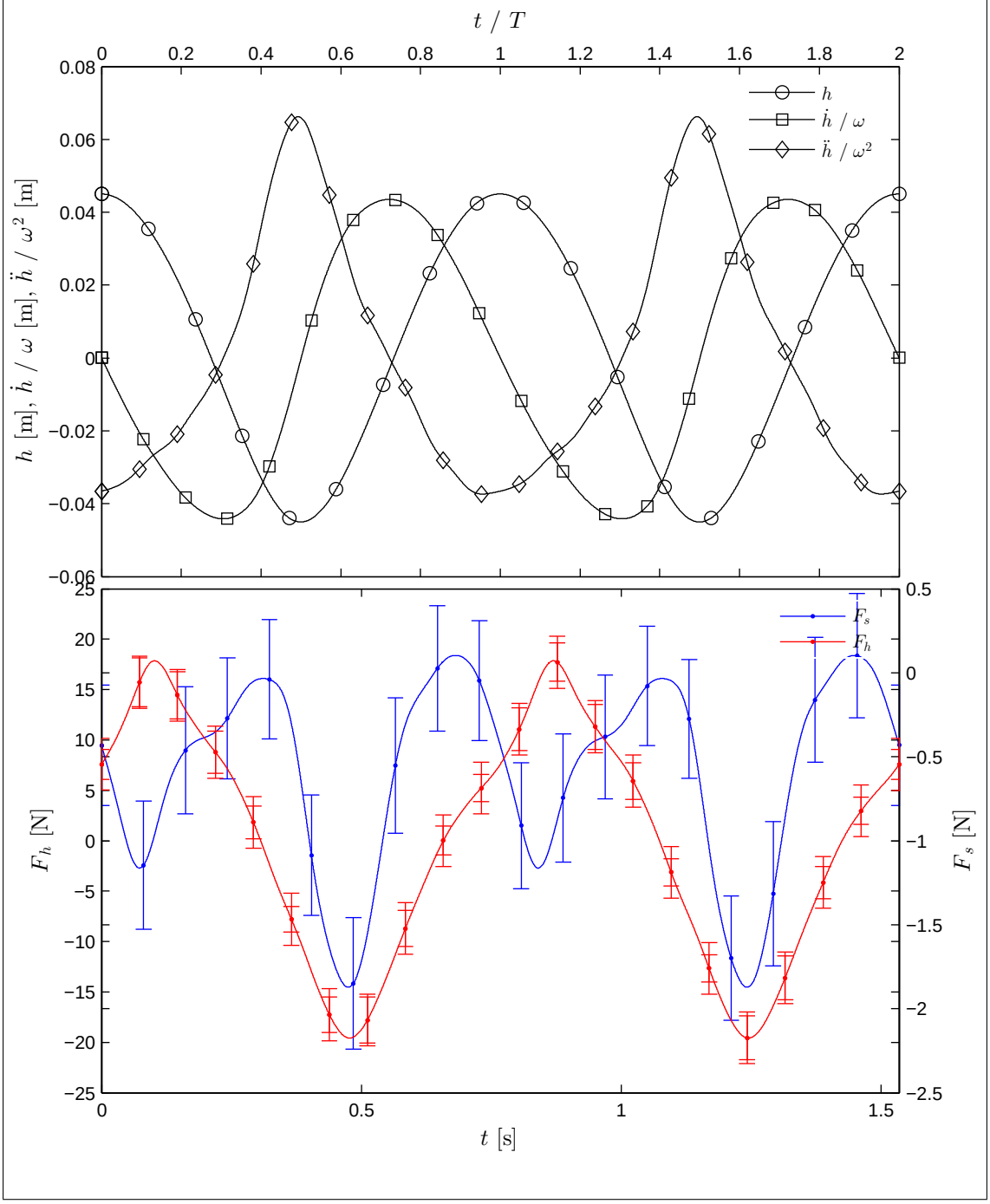

Object: NACA0012		Motion	Water
	$c = 0.060\,\mathrm{m}$ $L = 0.600\,\mathrm{m}$ $\theta = 0°$	$h_0 = 0.045\,\mathrm{m}$ $h^* = 0.75$ $f = 1.79\,\mathrm{Hz}$ $u = 0.00\,\mathrm{m\,s^{-1}}$	$T_w = 12.7\,°\mathrm{C}$ $\rho = 999\,\mathrm{kg\,m^{-3}}$

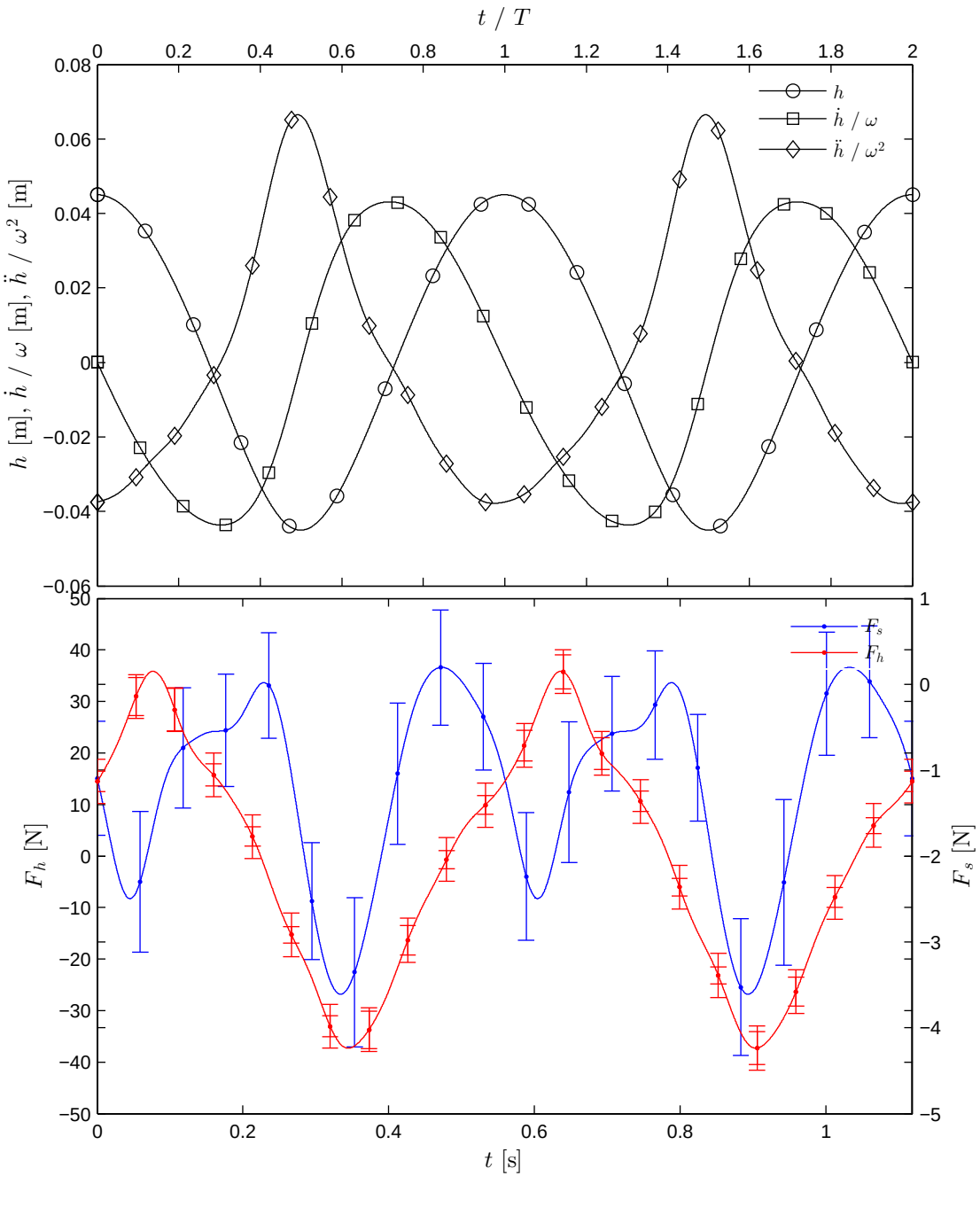

Object: NACA0012		Motion	Water
	$c = 0.060\,\mathrm{m}$ $L = 0.600\,\mathrm{m}$ $\theta = 0°$	$h_0 = 0.045\,\mathrm{m}$ $h^* = 0.75$ $f = 2.30\,\mathrm{Hz}$ $u = 0.00\,\mathrm{m\,s^{-1}}$	$T_w = 12.7\,°\mathrm{C}$ $\rho = 999\,\mathrm{kg\,m^{-3}}$

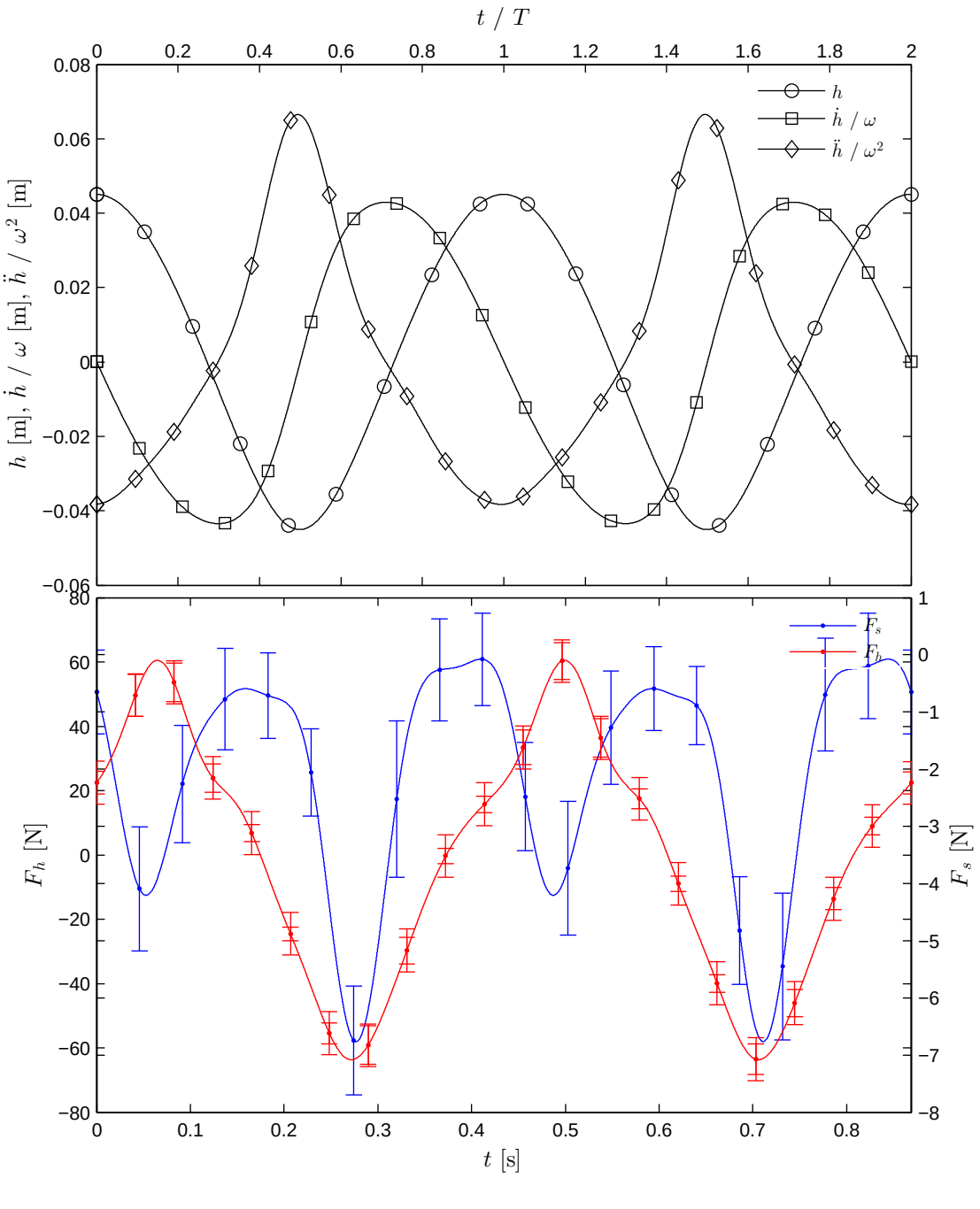

Object: NACA0012		Motion	Water
	$c = 0.060\,\mathrm{m}$ $L = 0.600\,\mathrm{m}$ $\theta = 0°$	$h_0 = 0.045\,\mathrm{m}$ $h^* = 0.75$ $f = 2.80\,\mathrm{Hz}$ $u = 0.00\,\mathrm{m\,s^{-1}}$	$T_w = 12.7\,°\mathrm{C}$ $\rho = 999\,\mathrm{kg\,m^{-3}}$

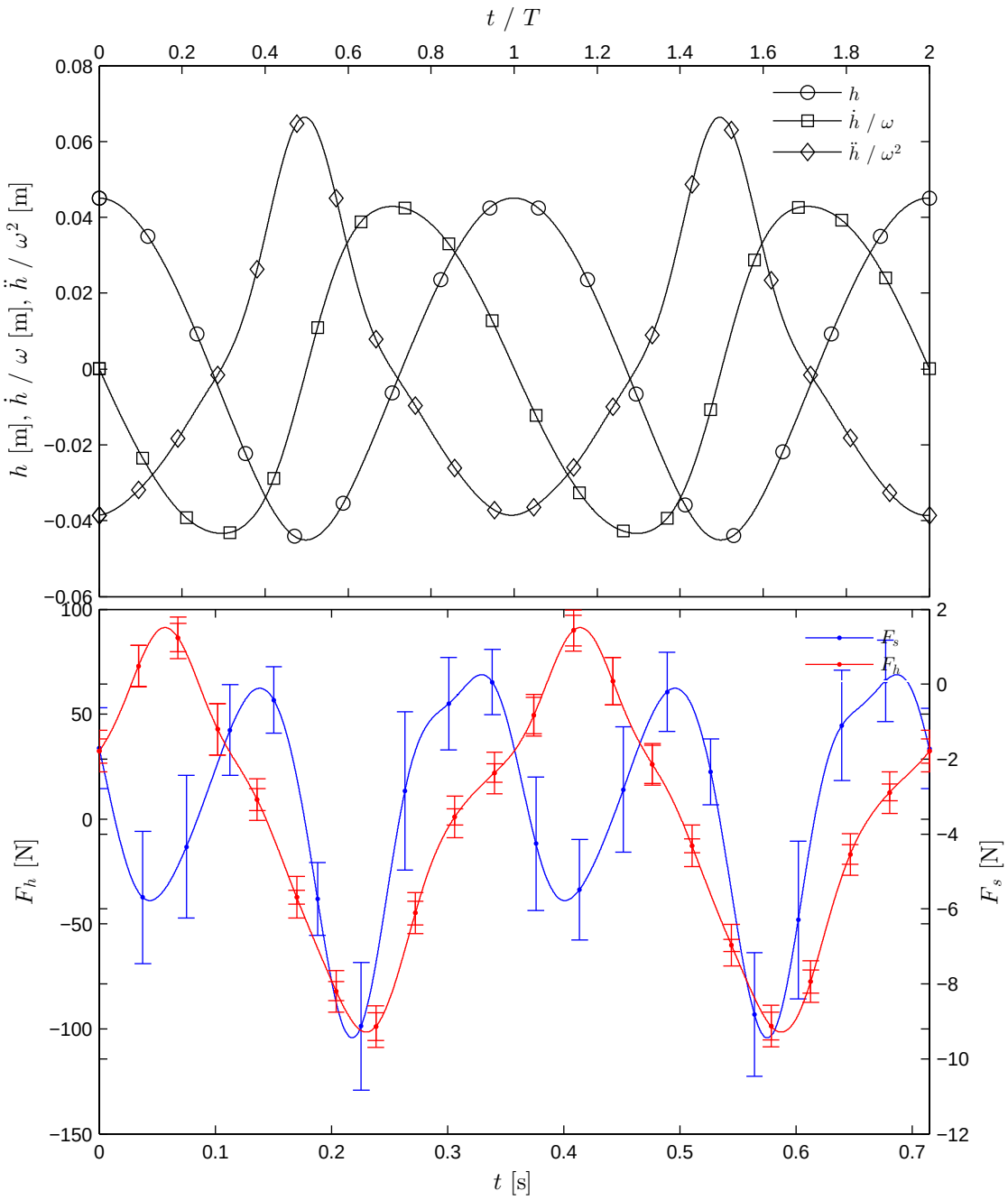

Object: NACA0012		Motion	Water
	$c = 0.060\,\mathrm{m}$ $L = 0.600\,\mathrm{m}$ $\theta = 0°$	$h_0 = 0.045\,\mathrm{m}$ $h^* = 0.75$ $f = 3.29\,\mathrm{Hz}$ $u = 0.00\,\mathrm{m\,s^{-1}}$	$T_w = 12.7\,°\mathrm{C}$ $\rho = 999\,\mathrm{kg\,m^{-3}}$

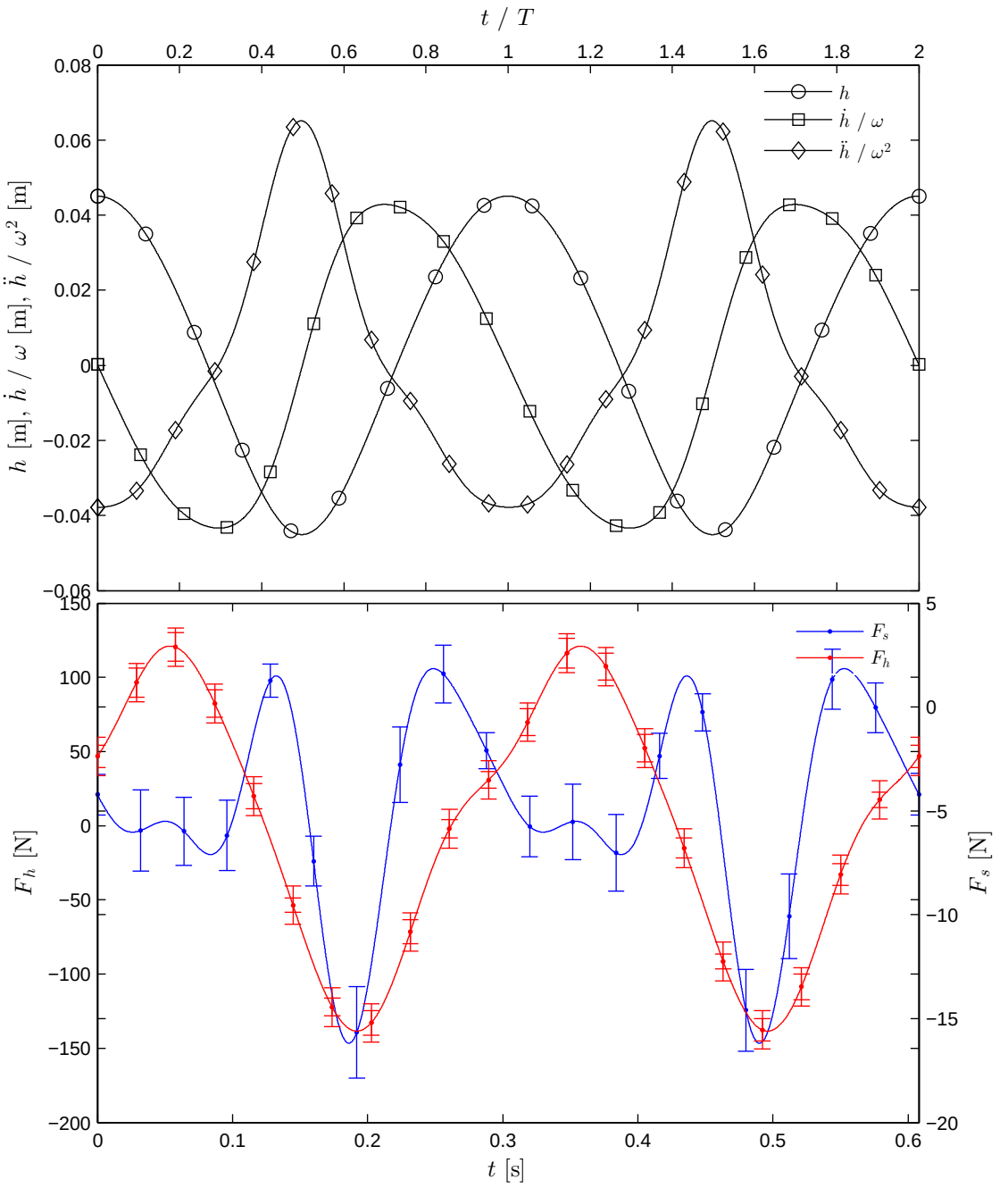

Object: NACA0012		Motion	Water
	$c = 0.060\,\mathrm{m}$ $L = 0.600\,\mathrm{m}$ $\theta = 0°$	$h_0 = 0.045\,\mathrm{m}$ $h^* = 0.75$ $f = 3.73\,\mathrm{Hz}$ $u = 0.00\,\mathrm{m\,s^{-1}}$	$T_w = 12.7\,°\mathrm{C}$ $\rho = 999\,\mathrm{kg\,m^{-3}}$

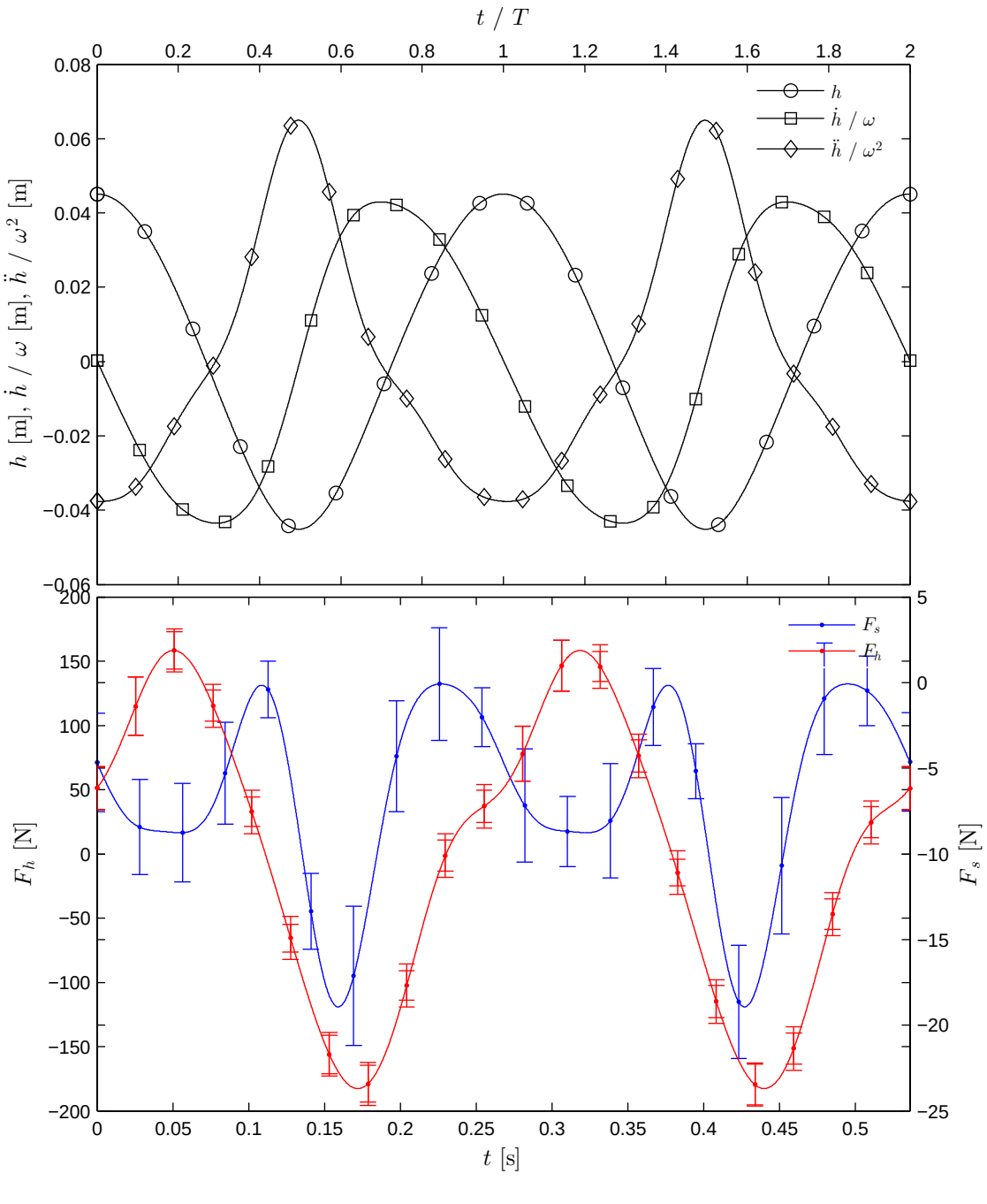

Object: NACA0012		Motion	Water
	$c = 0.060\,\mathrm{m}$ $L = 0.600\,\mathrm{m}$ $\theta = 10°$	$h_0 = 0.045\,\mathrm{m}$ $h^* = 0.75$ $f = 0.82\,\mathrm{Hz}$ $u = 0.00\,\mathrm{m\,s^{-1}}$	$T_w = 9.5\,°\mathrm{C}$ $\rho = 1000\,\mathrm{kg\,m^{-3}}$

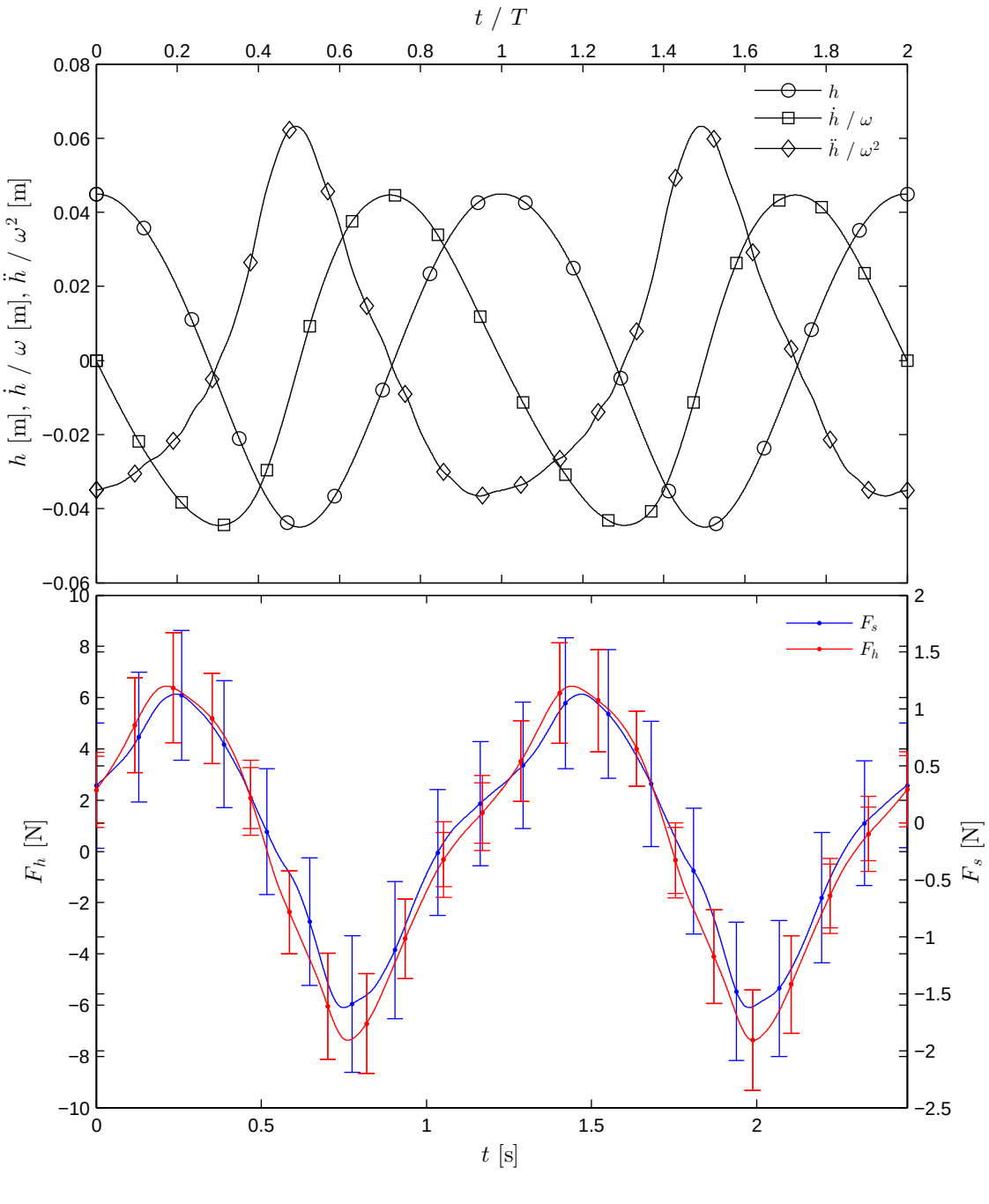

Object: NACA0012		Motion	Water
	$c = 0.060\,\mathrm{m}$ $L = 0.600\,\mathrm{m}$ $\theta = 10°$	$h_0 = 0.045\,\mathrm{m}$ $h^* = 0.75$ $f = 1.34\,\mathrm{Hz}$ $u = 0.00\,\mathrm{m\,s^{-1}}$	$T_w = 9.5\,°\mathrm{C}$ $\rho = 1000\,\mathrm{kg\,m^{-3}}$

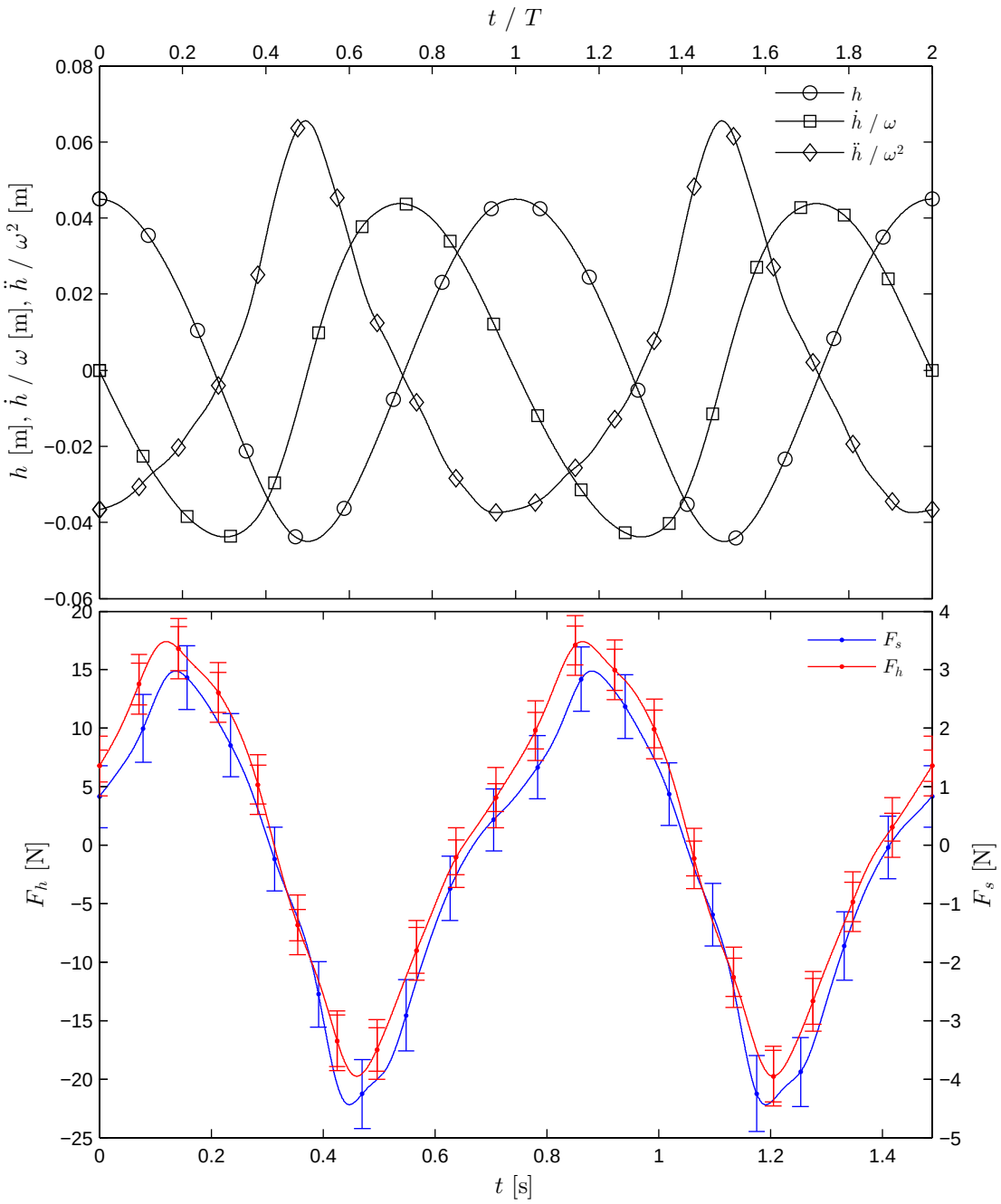

Object: NACA0012		Motion	Water
	$c = 0.060\,\mathrm{m}$ $L = 0.600\,\mathrm{m}$ $\theta = 10°$	$h_0 = 0.045\,\mathrm{m}$ $h^* = 0.75$ $f = 1.88\,\mathrm{Hz}$ $u = 0.00\,\mathrm{m\,s^{-1}}$	$T_w = 9.5\,°\mathrm{C}$ $\rho = 1000\,\mathrm{kg\,m^{-3}}$

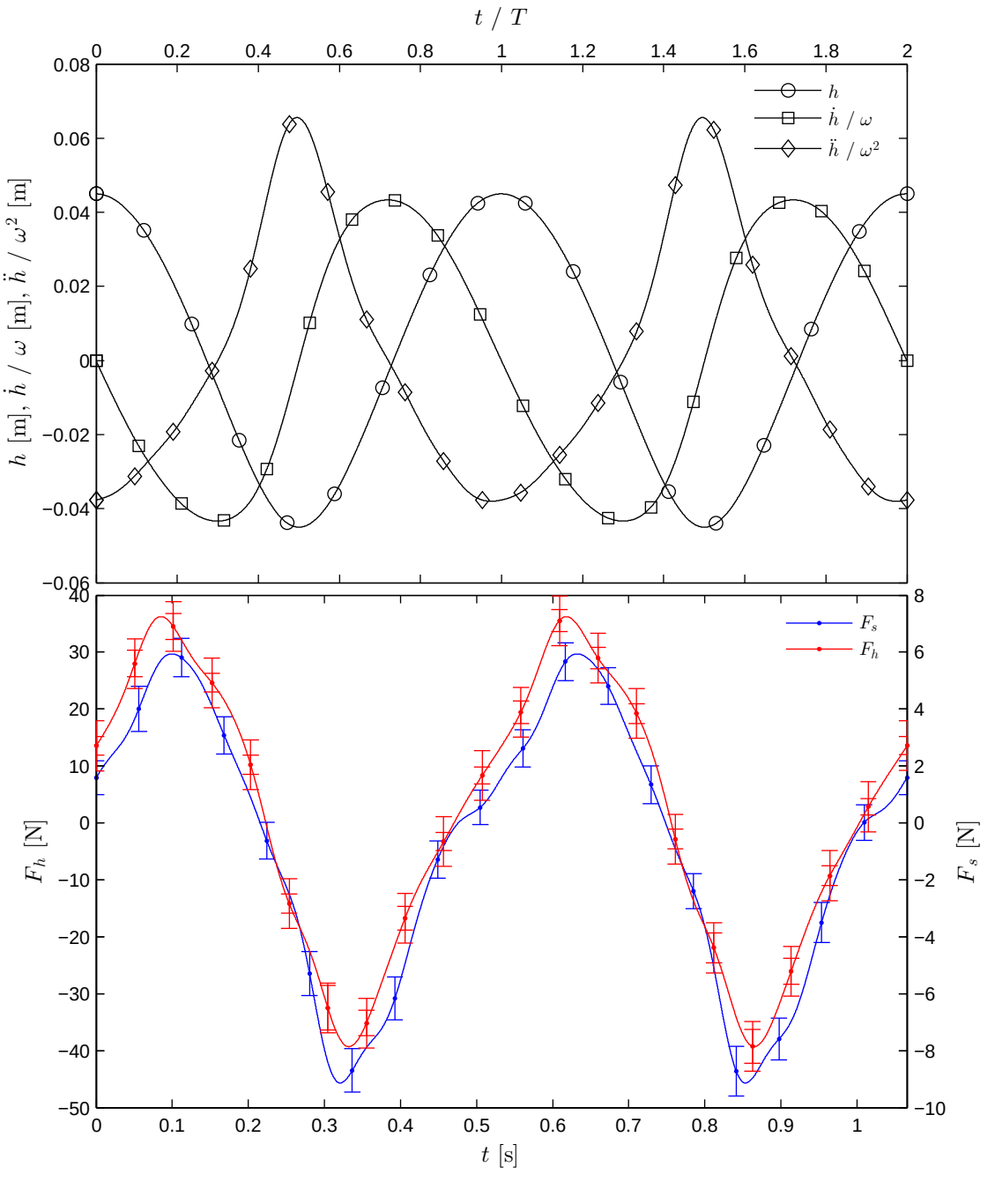

Object: NACA0012		Motion	Water
	$c = 0.060\,\mathrm{m}$ $L = 0.600\,\mathrm{m}$ $\theta = 10°$	$h_0 = 0.045\,\mathrm{m}$ $h^* = 0.75$ $f = 2.33\,\mathrm{Hz}$ $u = 0.00\,\mathrm{m\,s^{-1}}$	$T_w = 9.5\,°\mathrm{C}$ $\rho = 1000\,\mathrm{kg\,m^{-3}}$

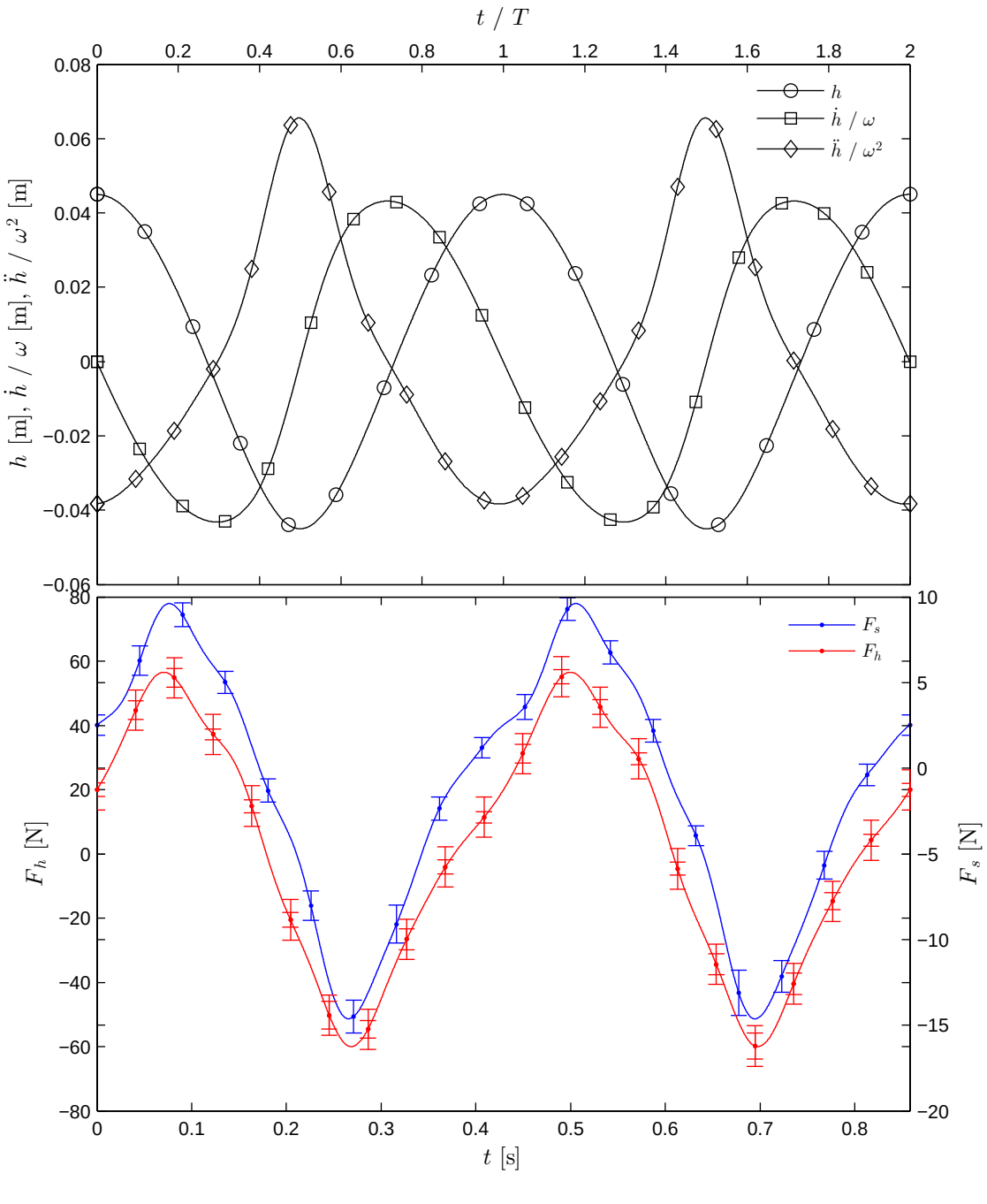

Object: NACA0012		Motion	Water
	$c = 0.060\,\mathrm{m}$ $L = 0.600\,\mathrm{m}$ $\theta = 10°$	$h_0 = 0.045\,\mathrm{m}$ $h^* = 0.75$ $f = 2.80\,\mathrm{Hz}$ $u = 0.00\,\mathrm{m\,s^{-1}}$	$T_w = 9.5\,°\mathrm{C}$ $\rho = 1000\,\mathrm{kg\,m^{-3}}$

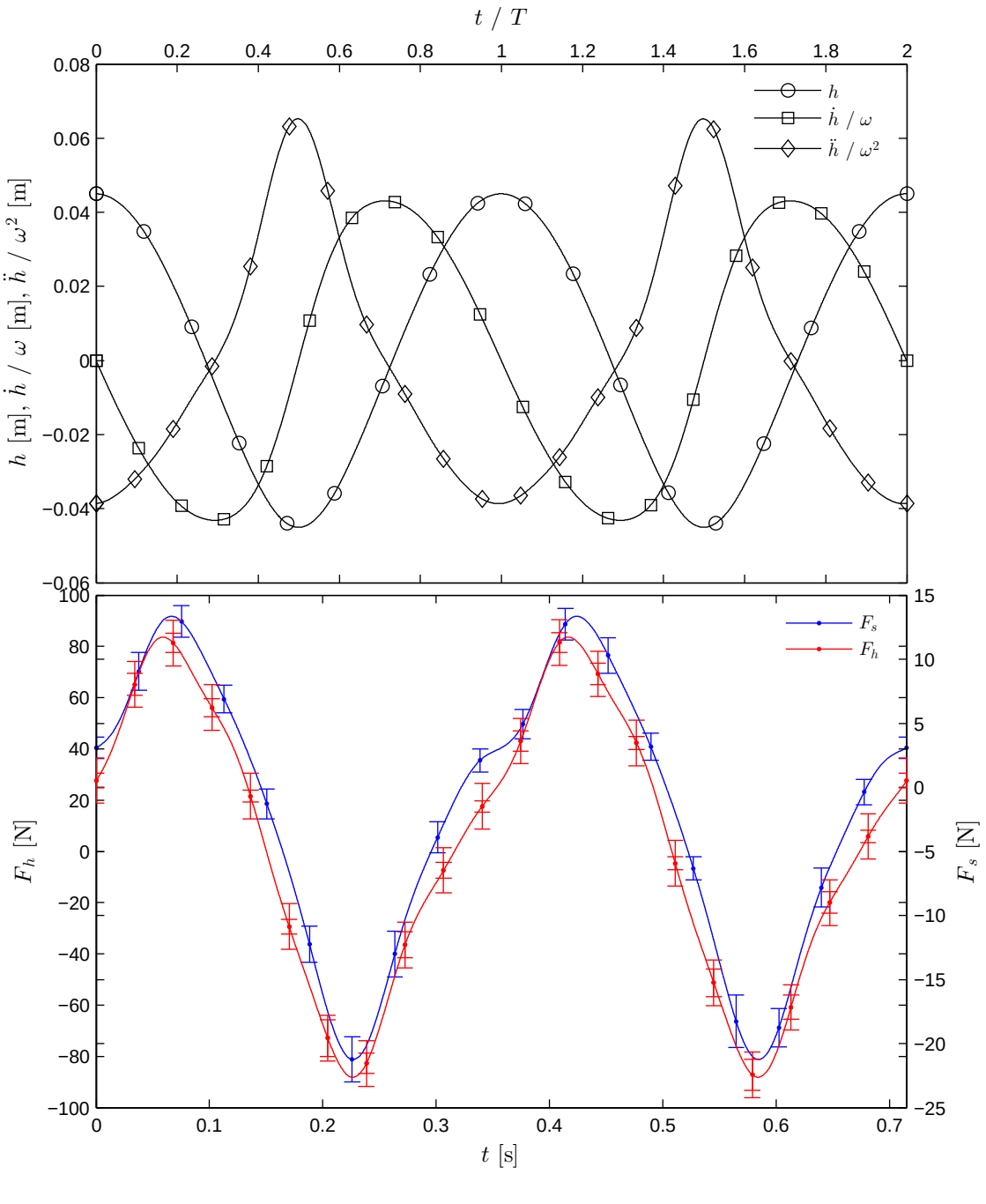

Object: NACA0012		Motion	Water
	$c = 0.060\,\mathrm{m}$ $L = 0.600\,\mathrm{m}$ $\theta = 10°$	$h_0 = 0.045\,\mathrm{m}$ $h^* = 0.75$ $f = 3.29\,\mathrm{Hz}$ $u = 0.00\,\mathrm{m\,s^{-1}}$	$T_w = 9.5\,°\mathrm{C}$ $\rho = 1000\,\mathrm{kg\,m^{-3}}$

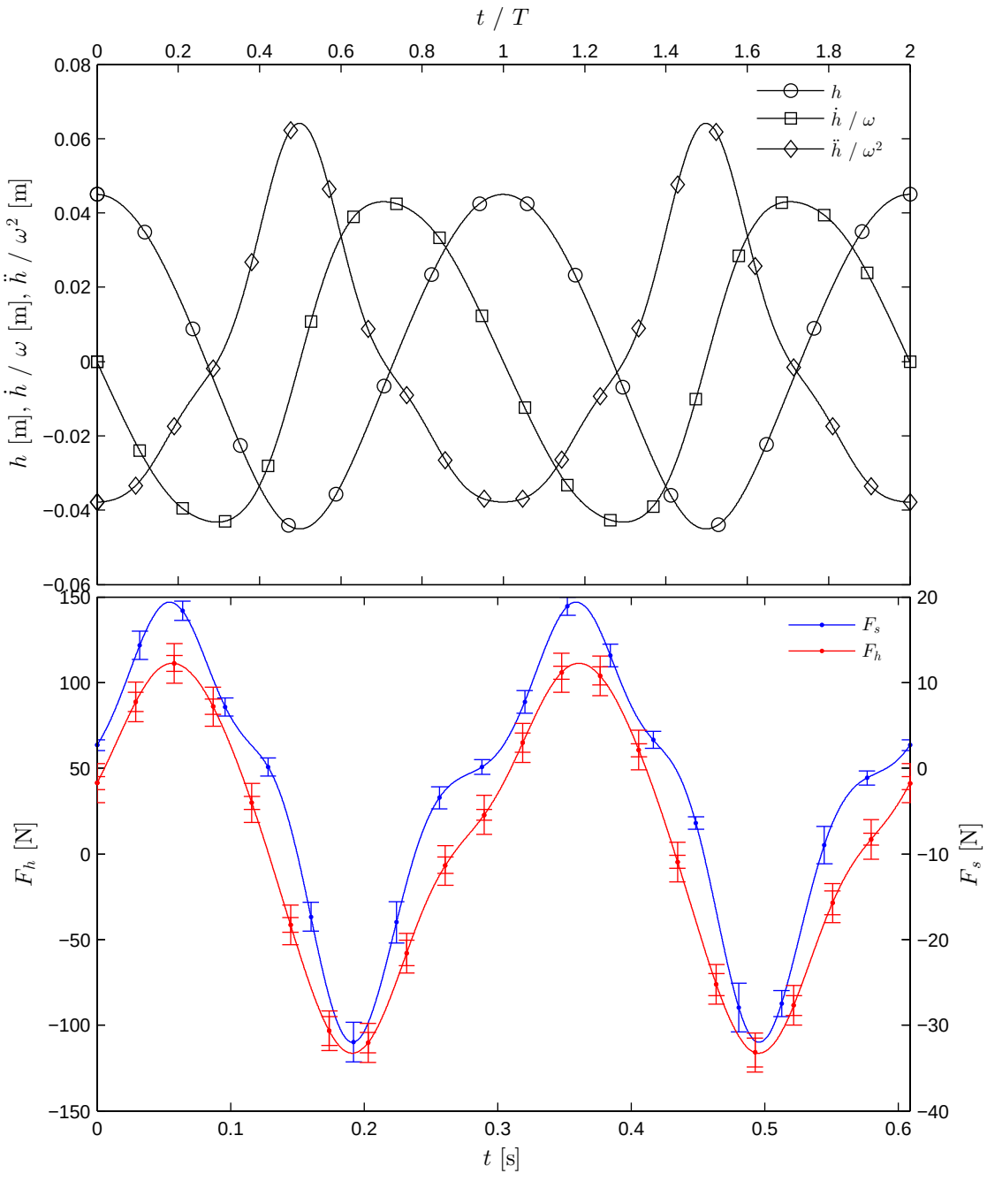

Object: NACA0012		Motion	Water
	$c = 0.060\,\mathrm{m}$ $L = 0.600\,\mathrm{m}$ $\theta = 10°$	$h_0 = 0.045\,\mathrm{m}$ $h^* = 0.75$ $f = 3.76\,\mathrm{Hz}$ $u = 0.00\,\mathrm{m\,s^{-1}}$	$T_w = 9.5\,°\mathrm{C}$ $\rho = 1000\,\mathrm{kg\,m^{-3}}$

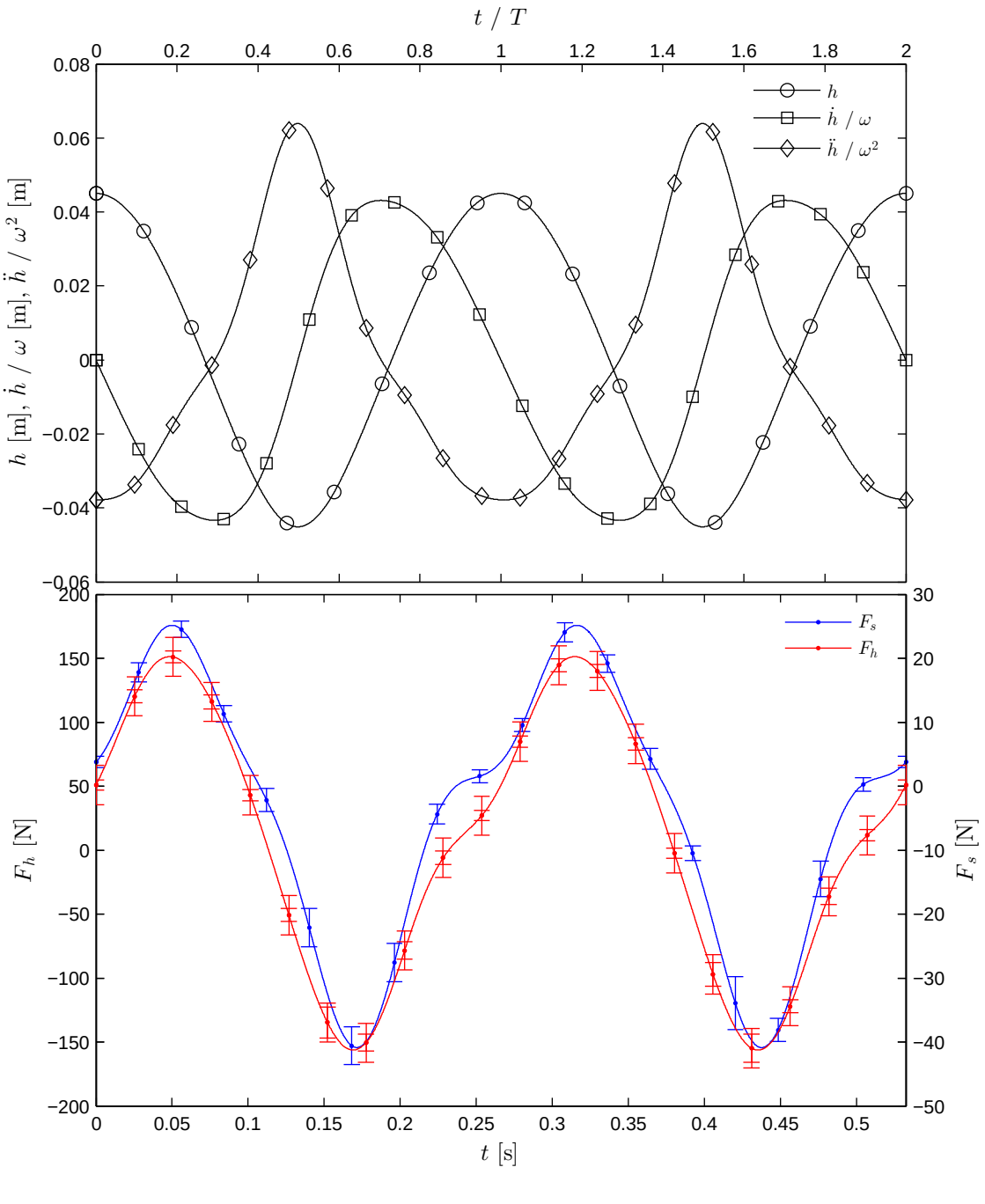

Object: NACA0012		Motion	Water
	$c = 0.060\,\mathrm{m}$ $L = 0.600\,\mathrm{m}$ $\theta = 40°$	$h_0 = 0.045\,\mathrm{m}$ $h^* = 0.75$ $f = 0.85\,\mathrm{Hz}$ $u = 0.00\,\mathrm{m\,s^{-1}}$	$T_w = 9.5\,°\mathrm{C}$ $\rho = 1000\,\mathrm{kg\,m^{-3}}$

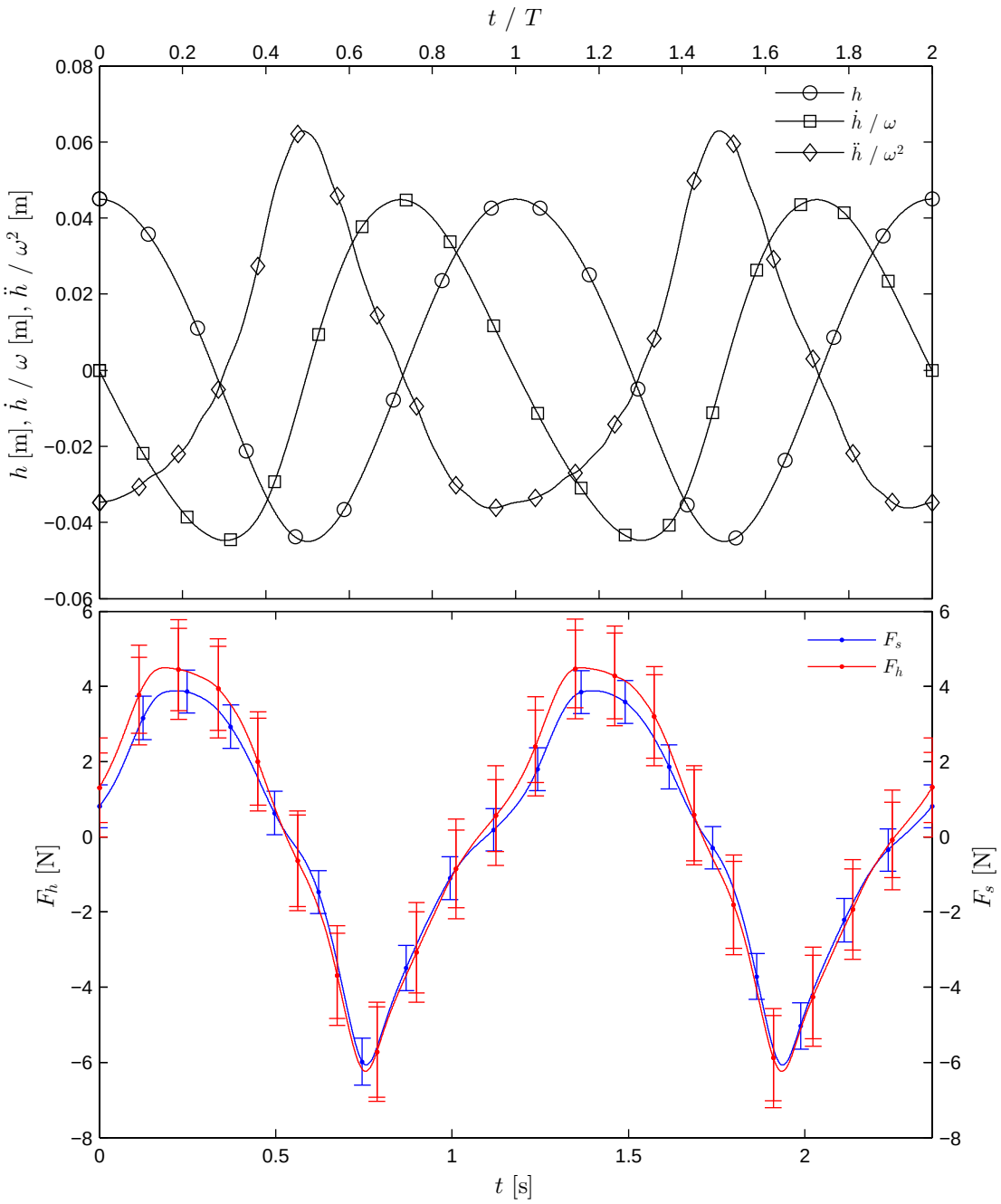

Object: NACA0012		Motion	Water
	$c = 0.060\,\mathrm{m}$ $L = 0.600\,\mathrm{m}$ $\theta = 40°$	$h_0 = 0.045\,\mathrm{m}$ $h^* = 0.75$ $f = 1.34\,\mathrm{Hz}$ $u = 0.00\,\mathrm{m\,s^{-1}}$	$T_w = 9.5\,°\mathrm{C}$ $\rho = 1000\,\mathrm{kg\,m^{-3}}$

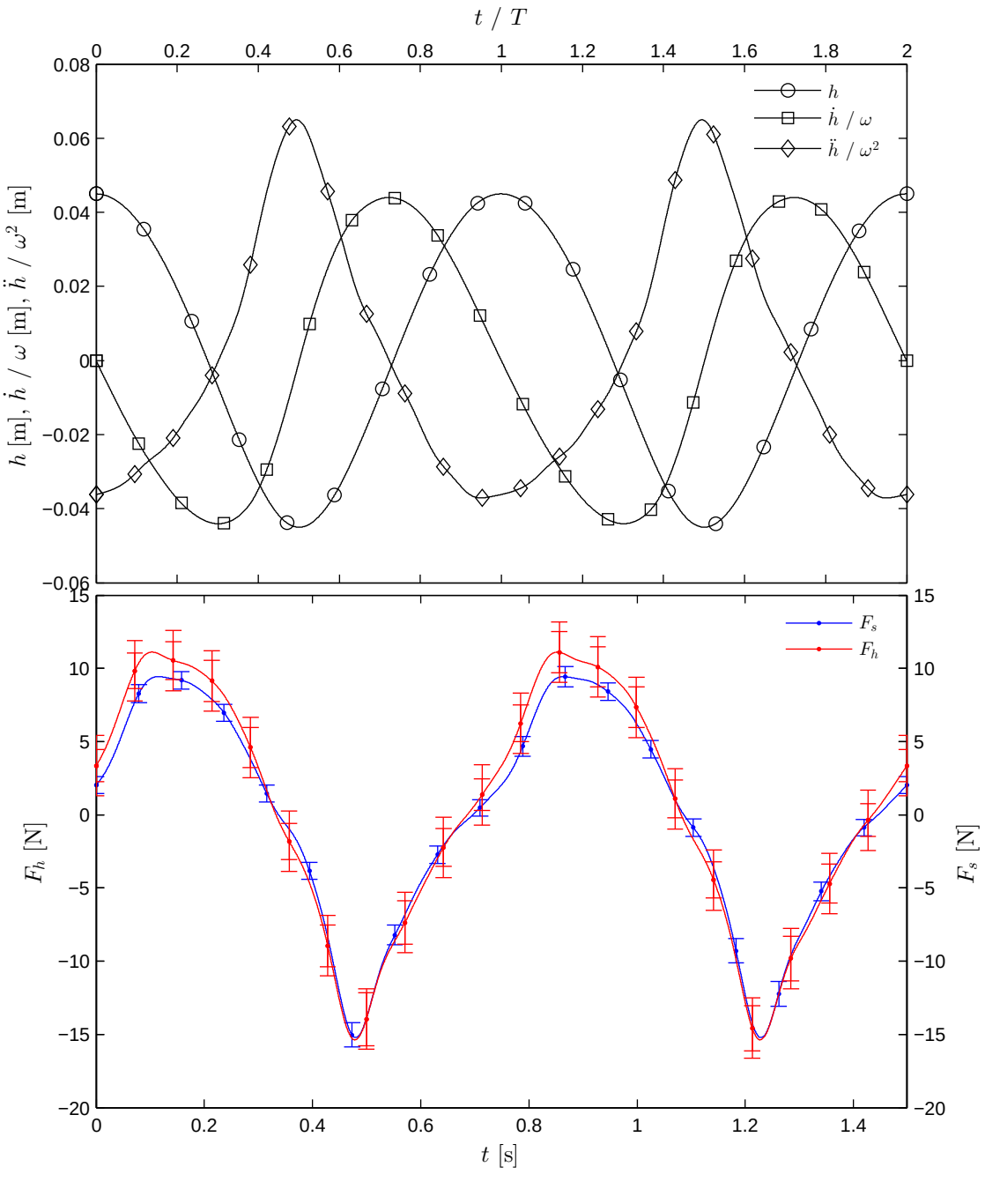

Object: NACA0012		Motion	Water
	$c = 0.060\,\mathrm{m}$ $L = 0.600\,\mathrm{m}$ $\theta = 40°$	$h_0 = 0.045\,\mathrm{m}$ $h^* = 0.75$ $f = 1.87\,\mathrm{Hz}$ $u = 0.00\,\mathrm{m\,s^{-1}}$	$T_w = 9.5\,°\mathrm{C}$ $\rho = 1000\,\mathrm{kg\,m^{-3}}$

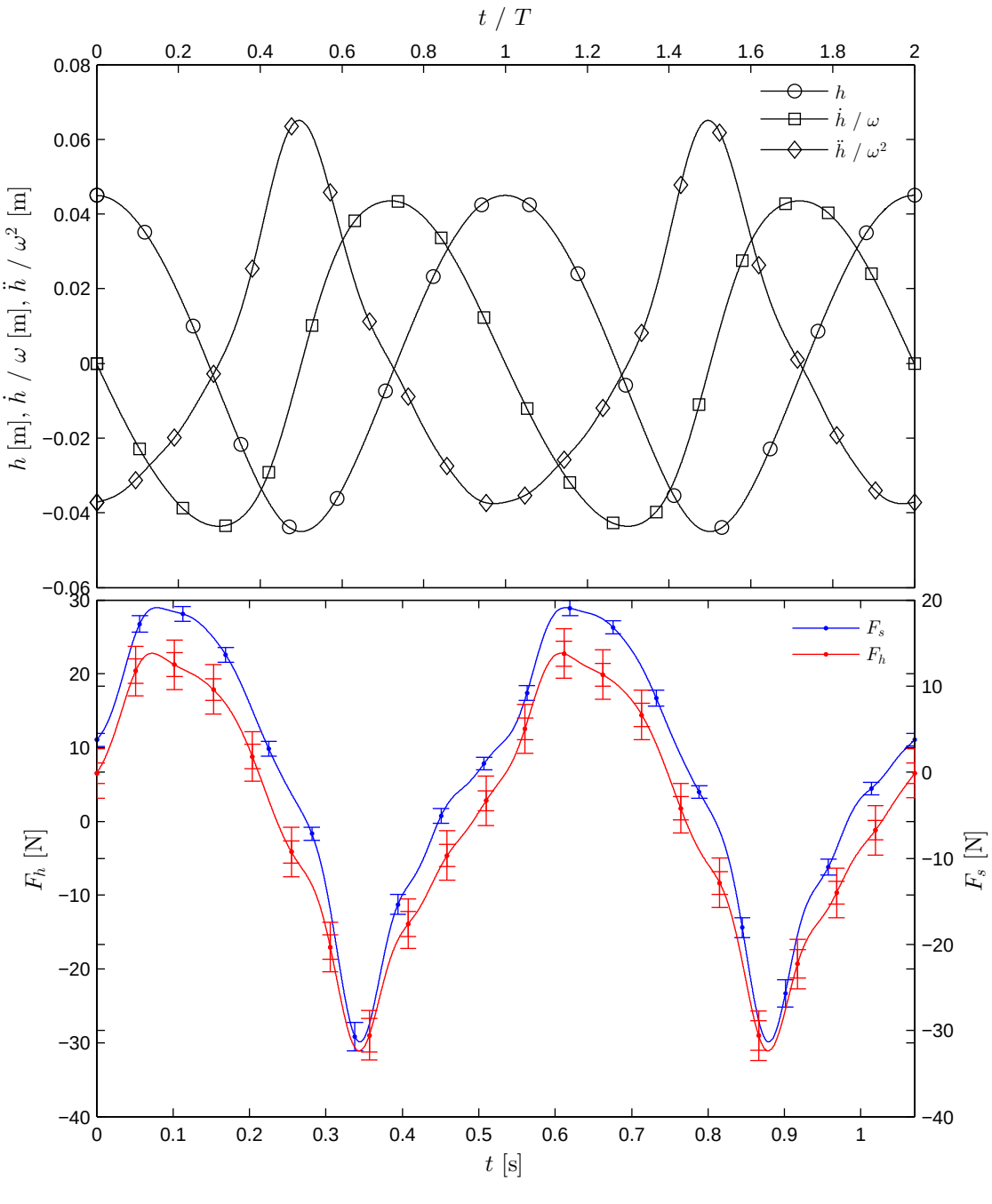

Object: NACA0012		Motion	Water
	$c = 0.060\,\mathrm{m}$ $L = 0.600\,\mathrm{m}$ $\theta = 40°$	$h_0 = 0.045\,\mathrm{m}$ $h^* = 0.75$ $f = 2.31\,\mathrm{Hz}$ $u = 0.00\,\mathrm{m\,s^{-1}}$	$T_w = 9.5\,°\mathrm{C}$ $\rho = 1000\,\mathrm{kg\,m^{-3}}$

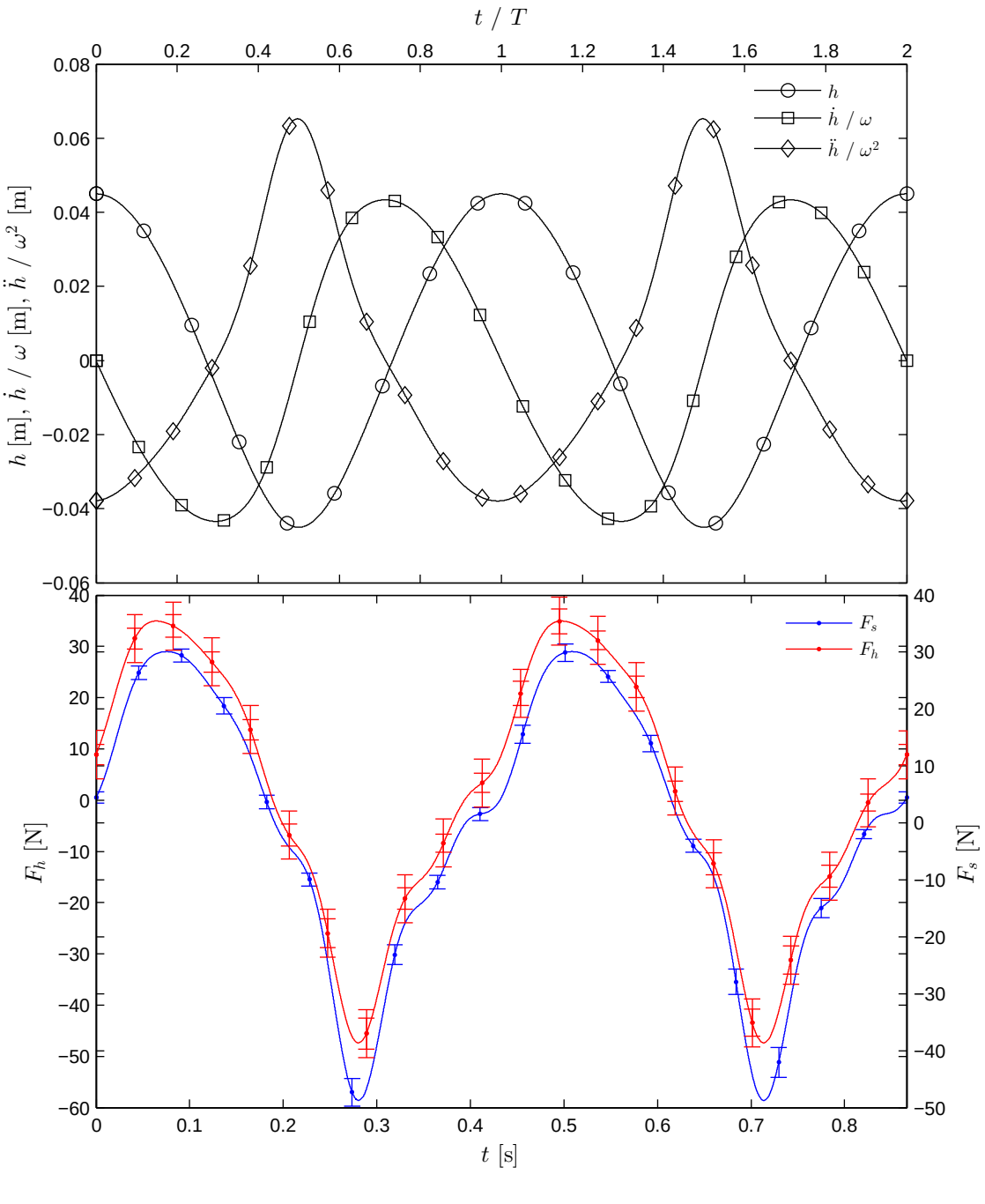

Object: NACA0012		Motion	Water
	$c = 0.060\,\mathrm{m}$ $L = 0.600\,\mathrm{m}$ $\theta = 40°$	$h_0 = 0.045\,\mathrm{m}$ $h^* = 0.75$ $f = 2.77\,\mathrm{Hz}$ $u = 0.00\,\mathrm{m\,s^{-1}}$	$T_w = 9.5\,°\mathrm{C}$ $\rho = 1000\,\mathrm{kg\,m^{-3}}$

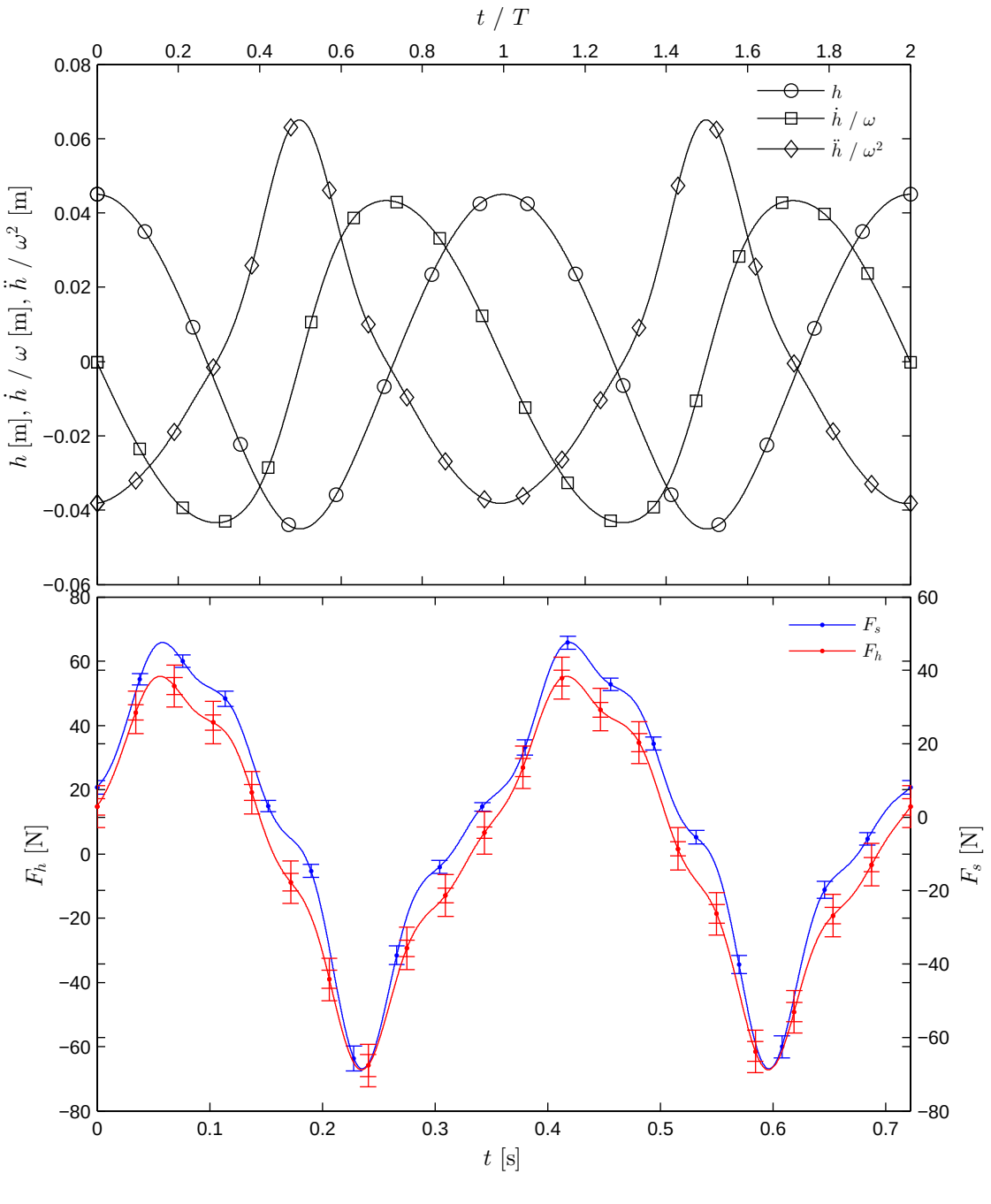

Object: NACA0012		Motion	Water
	$c = 0.060\,\mathrm{m}$ $L = 0.600\,\mathrm{m}$ $\theta = 40°$	$h_0 = 0.045\,\mathrm{m}$ $h^* = 0.75$ $f = 3.25\,\mathrm{Hz}$ $u = 0.00\,\mathrm{m\,s^{-1}}$	$T_w = 9.5\,°\mathrm{C}$ $\rho = 1000\,\mathrm{kg\,m^{-3}}$

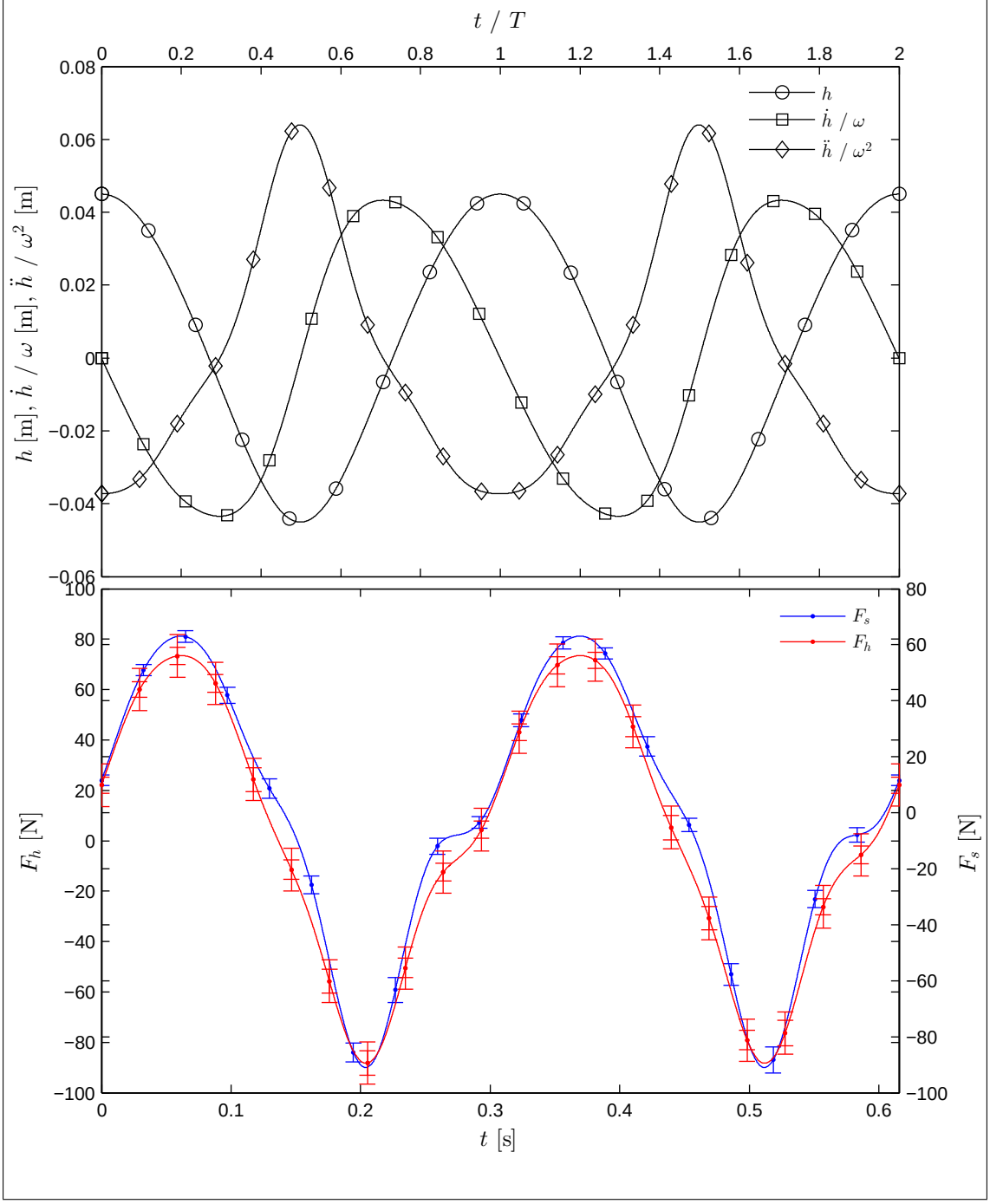

Object: NACA0012		Motion	Water
	$c = 0.060\,\mathrm{m}$ $L = 0.600\,\mathrm{m}$ $\theta = 40°$	$h_0 = 0.045\,\mathrm{m}$ $h^* = 0.75$ $f = 3.85\,\mathrm{Hz}$ $u = 0.00\,\mathrm{m\,s^{-1}}$	$T_w = 9.5\,°\mathrm{C}$ $\rho = 1000\,\mathrm{kg\,m^{-3}}$

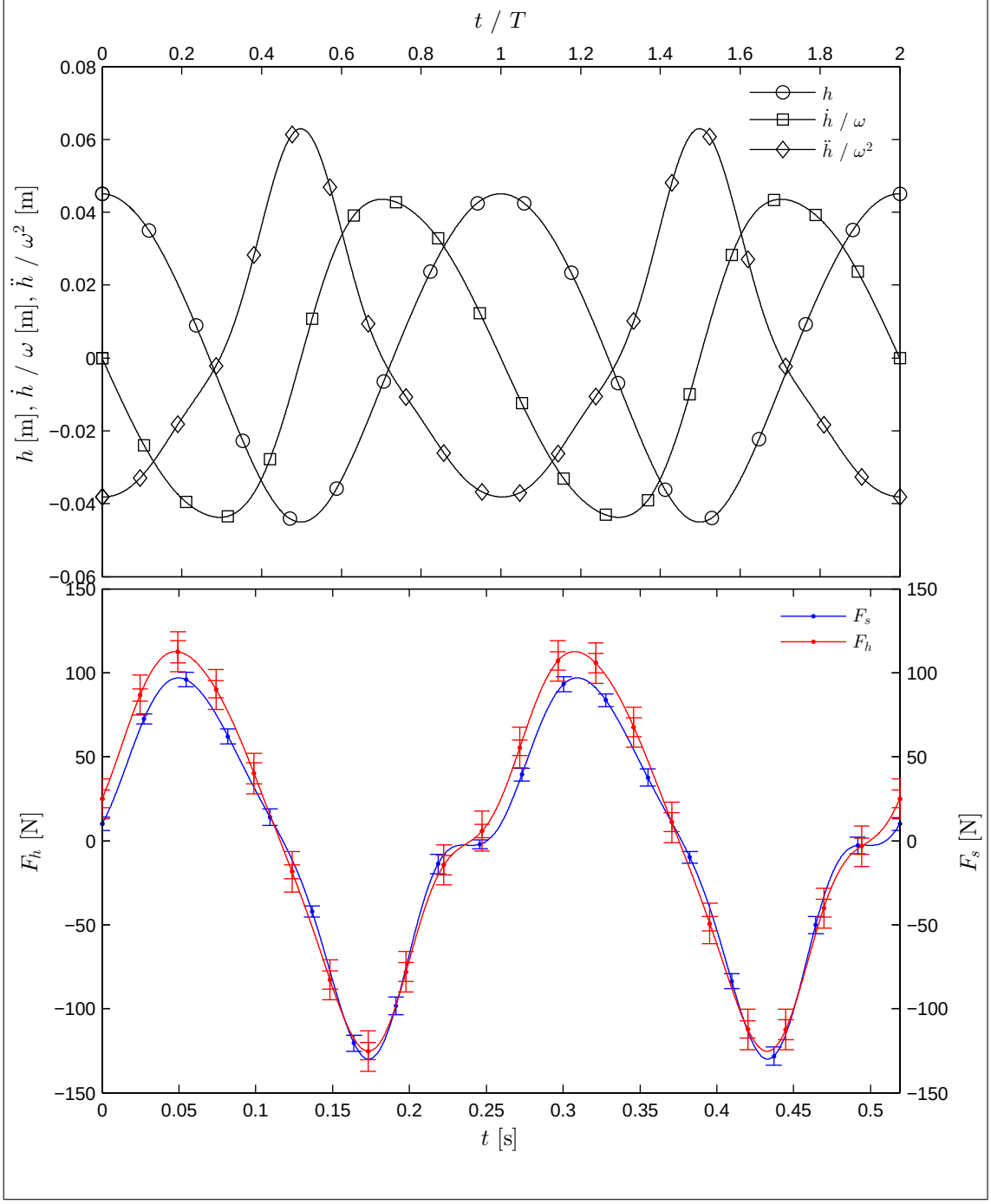

Object: NACA0012		Motion	Water
	$c = 0.060\,\mathrm{m}$ $L = 0.600\,\mathrm{m}$ $\theta = 0°$	$h_0 = 0.045\,\mathrm{m}$ $h^* = 0.75$ $f = 1.62\,\mathrm{Hz}$ $u = 0.52\,\mathrm{m\,s^{-1}}$	$T_w = 9.5\,°\mathrm{C}$ $\rho = 1000\,\mathrm{kg\,m^{-3}}$

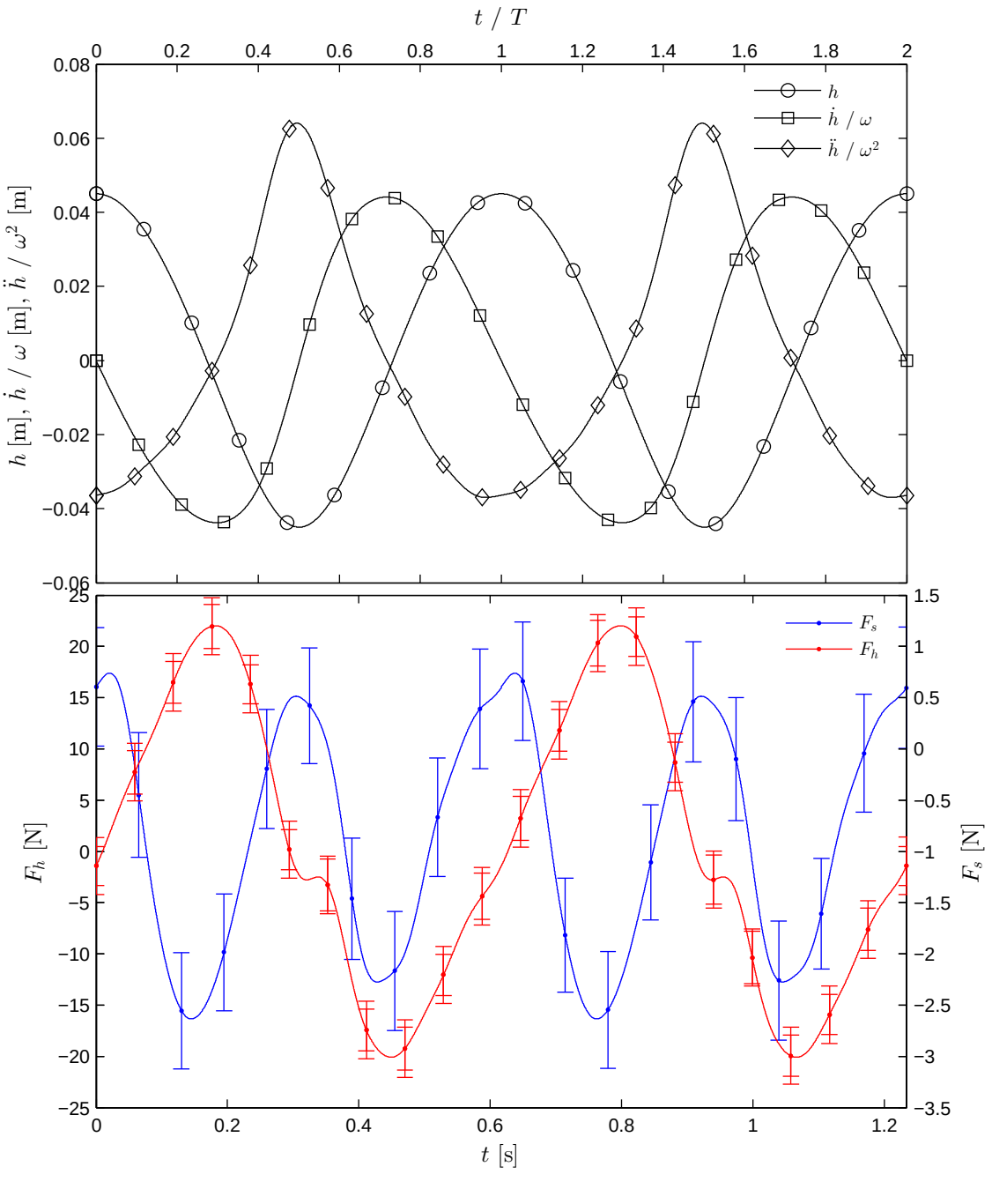

Object: NACA0012		Motion	Water
	$c = 0.060\,\mathrm{m}$ $L = 0.600\,\mathrm{m}$ $\theta = 0°$	$h_0 = 0.045\,\mathrm{m}$ $h^* = 0.75$ $f = 1.59\,\mathrm{Hz}$ $u = 0.99\,\mathrm{m\,s^{-1}}$	$T_w = 9.5\,°\mathrm{C}$ $\rho = 1000\,\mathrm{kg\,m^{-3}}$

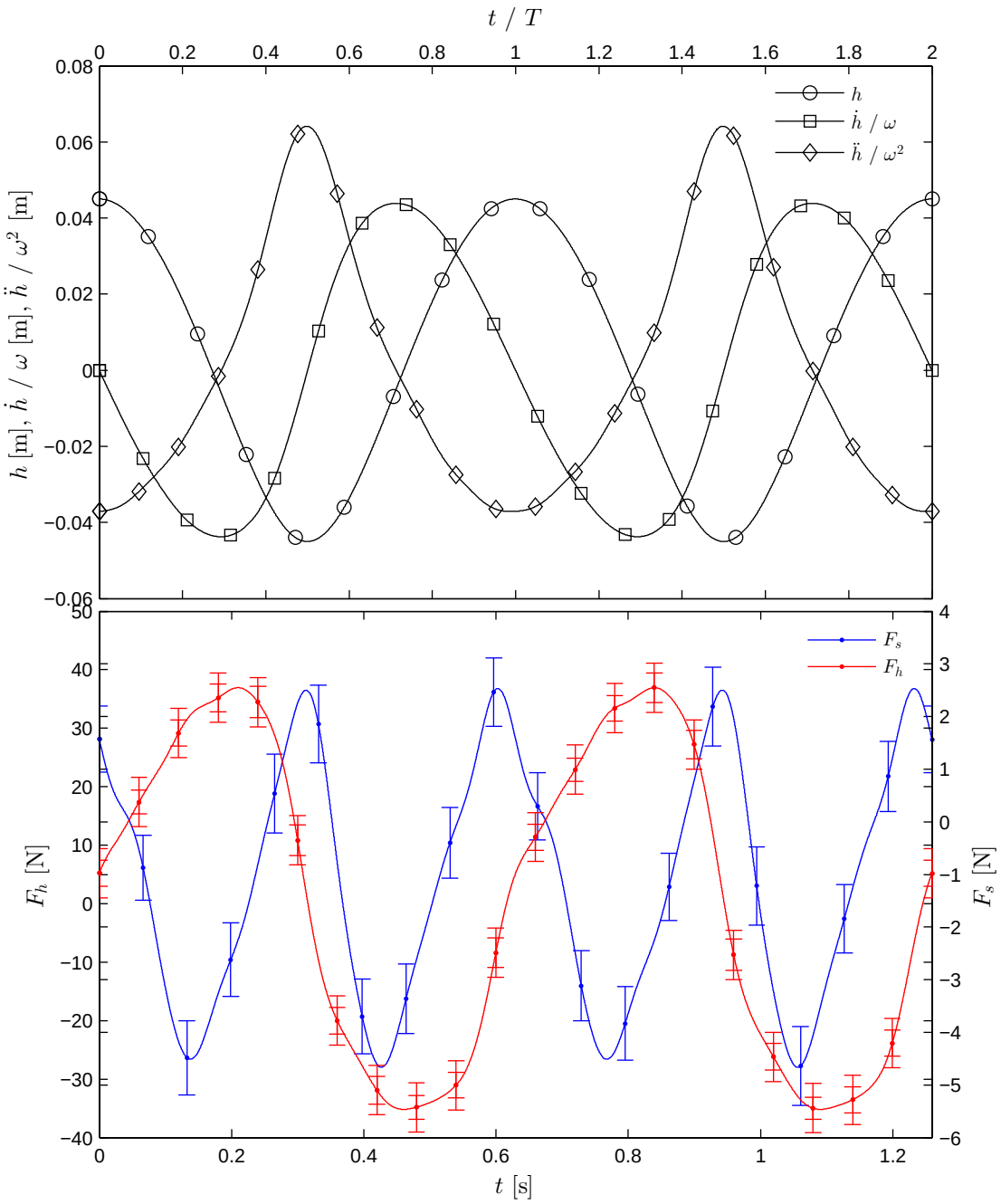

Object: NACA0012		Motion	Water
	$c = 0.060\,\mathrm{m}$ $L = 0.600\,\mathrm{m}$ $\theta = 0°$	$h_0 = 0.045\,\mathrm{m}$ $h^* = 0.75$ $f = 1.56\,\mathrm{Hz}$ $u = 1.50\,\mathrm{m\,s^{-1}}$	$T_w = 9.5\,°\mathrm{C}$ $\rho = 1000\,\mathrm{kg\,m^{-3}}$

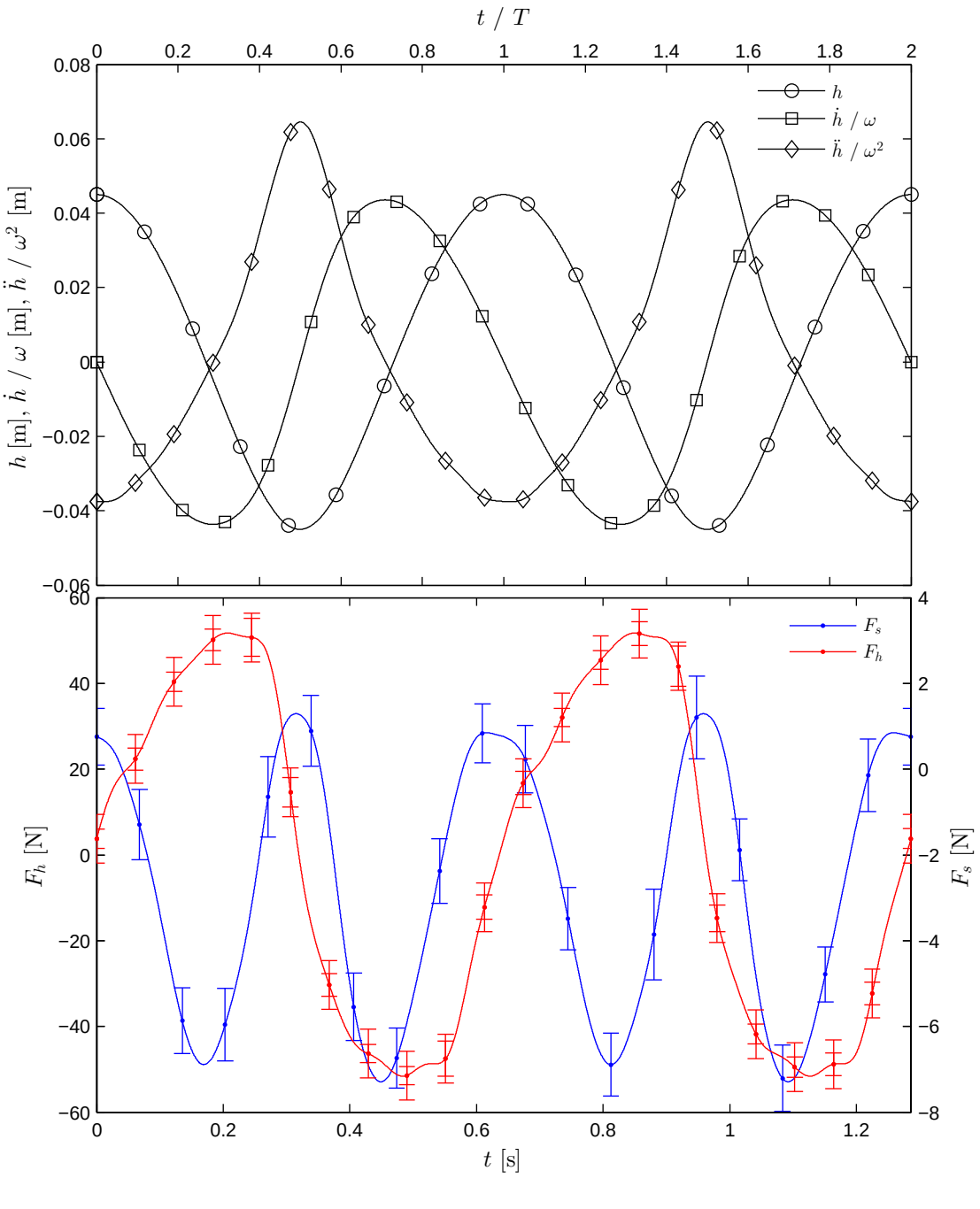

Object: NACA0012		Motion	Water
	$c = 0.060\,\mathrm{m}$ $L = 0.600\,\mathrm{m}$ $\theta = 0°$	$h_0 = 0.045\,\mathrm{m}$ $h^* = 0.75$ $f = 1.53\,\mathrm{Hz}$ $u = 1.97\,\mathrm{m\,s^{-1}}$	$T_w = 9.5\,°\mathrm{C}$ $\rho = 1000\,\mathrm{kg\,m^{-3}}$

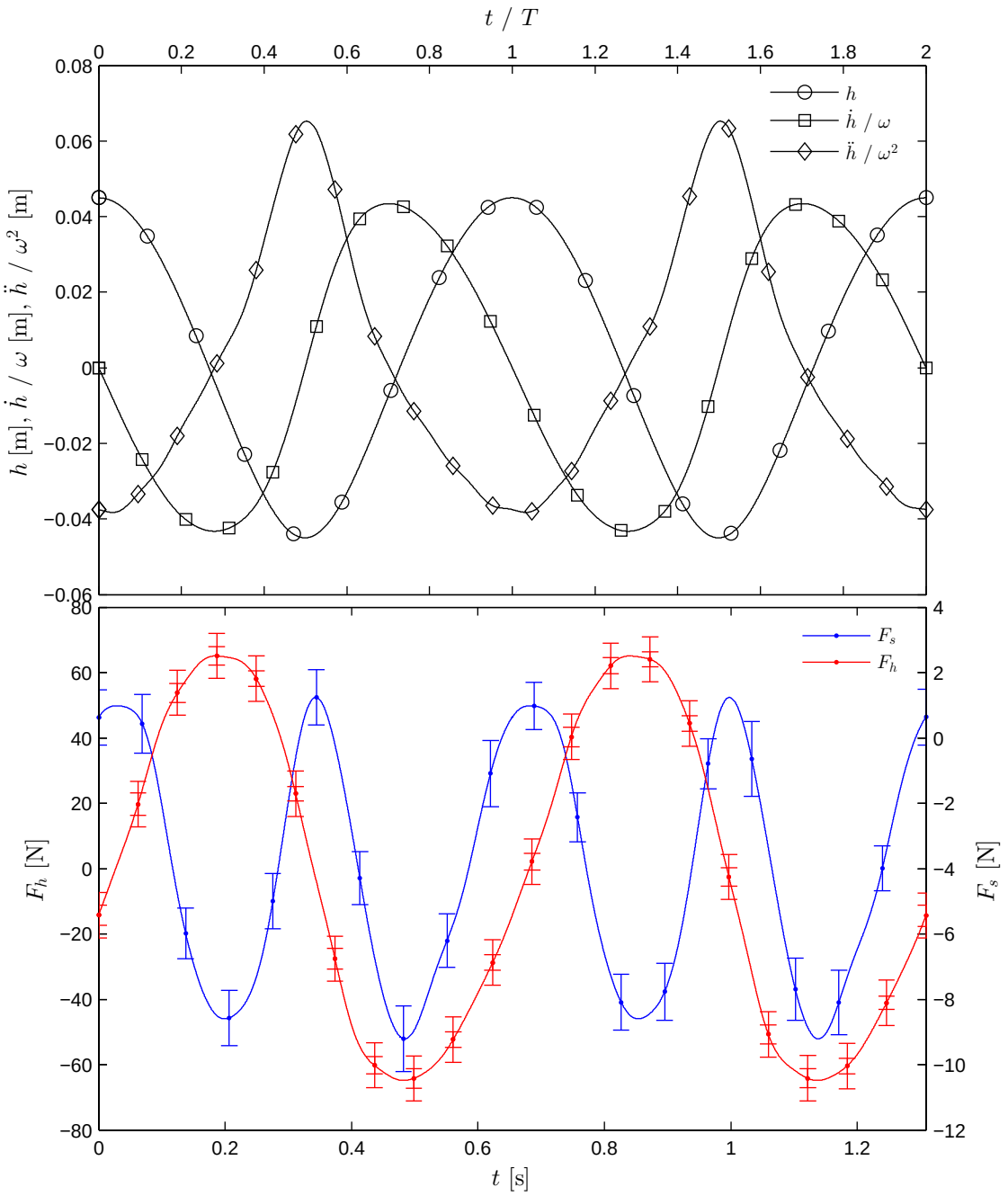

Object: NACA0012		Motion	Water
	$c = 0.060\,\mathrm{m}$ $L = 0.600\,\mathrm{m}$ $\theta = 0°$	$h_0 = 0.045\,\mathrm{m}$ $h^* = 0.75$ $f = 2.18\,\mathrm{Hz}$ $u = 0.52\,\mathrm{m\,s^{-1}}$	$T_w = 9.5\,°\mathrm{C}$ $\rho = 1000\,\mathrm{kg\,m^{-3}}$

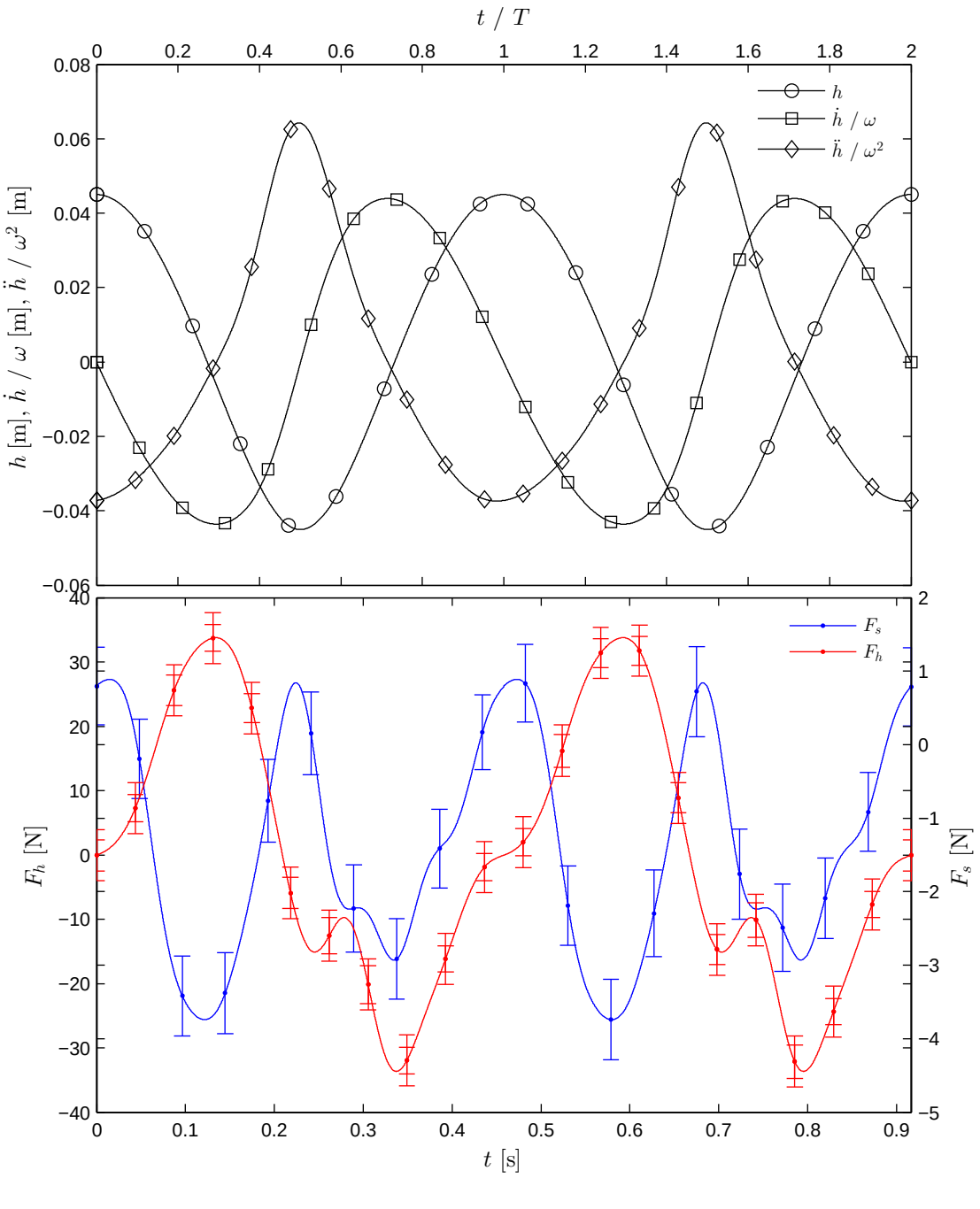

Object: NACA0012		Motion	Water
	$c = 0.060\,\mathrm{m}$ $L = 0.600\,\mathrm{m}$ $\theta = 0°$	$h_0 = 0.045\,\mathrm{m}$ $h^* = 0.75$ $f = 2.13\,\mathrm{Hz}$ $u = 0.99\,\mathrm{m\,s^{-1}}$	$T_w = 9.5\,°\mathrm{C}$ $\rho = 1000\,\mathrm{kg\,m^{-3}}$

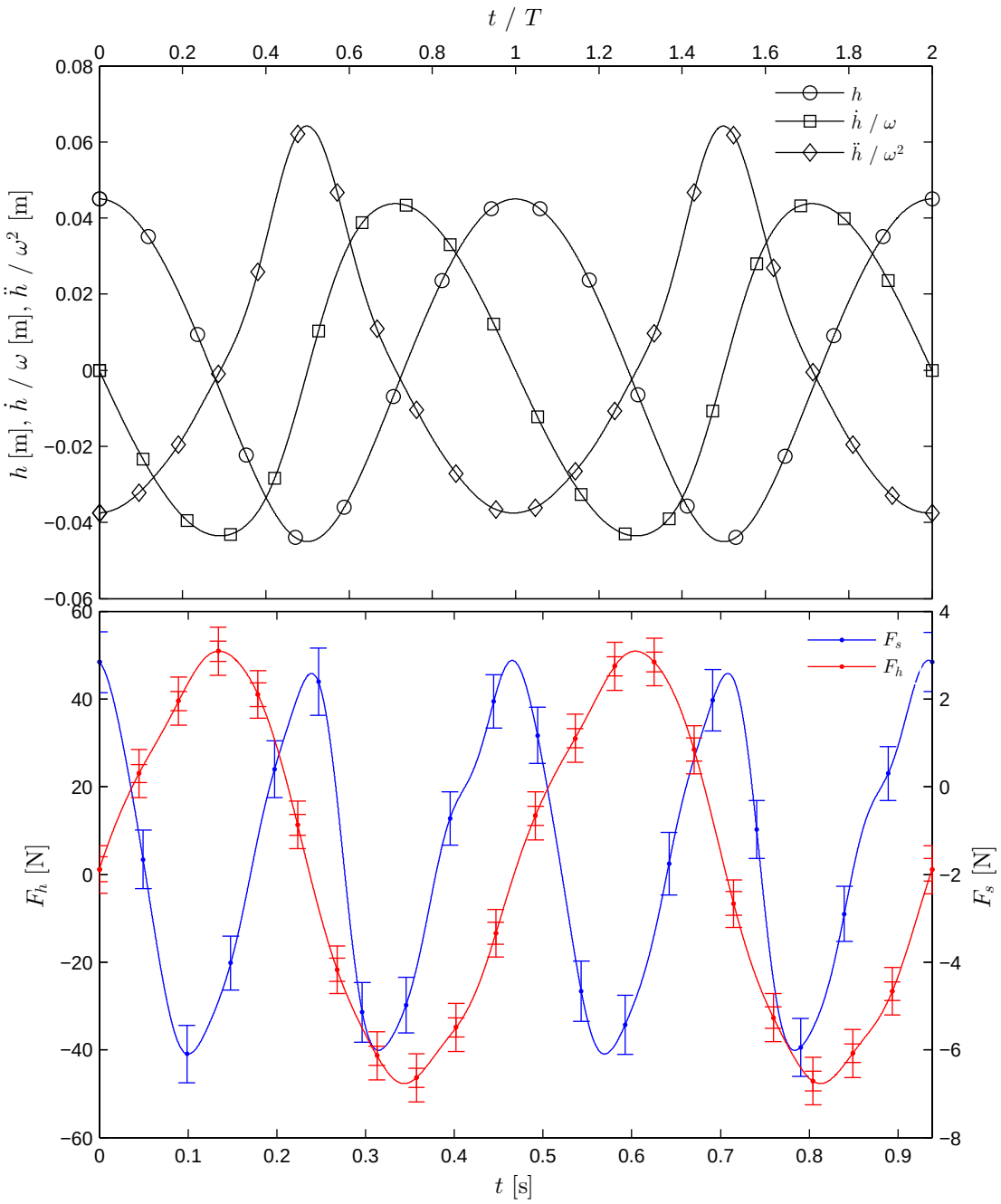

Object: NACA0012		Motion	Water
	$c = 0.060\,\mathrm{m}$ $L = 0.600\,\mathrm{m}$ $\theta = 0°$	$h_0 = 0.045\,\mathrm{m}$ $h^* = 0.75$ $f = 2.07\,\mathrm{Hz}$ $u = 1.50\,\mathrm{m\,s^{-1}}$	$T_w = 9.5\,°\mathrm{C}$ $\rho = 1000\,\mathrm{kg\,m^{-3}}$

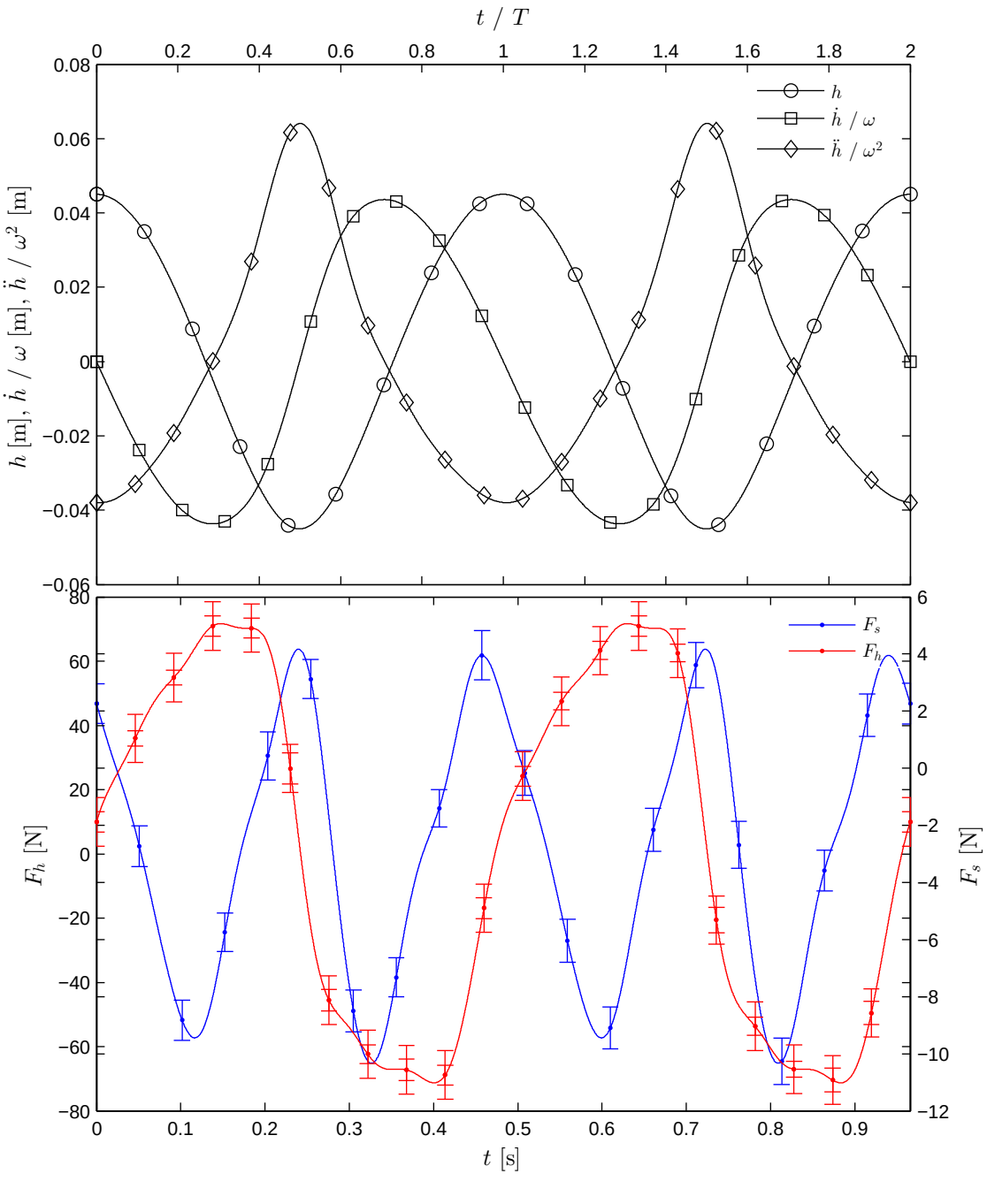

Object: NACA0012		Motion	Water
	$c = 0.060\,\mathrm{m}$ $L = 0.600\,\mathrm{m}$ $\theta = 0°$	$h_0 = 0.045\,\mathrm{m}$ $h^* = 0.75$ $f = 2.06\,\mathrm{Hz}$ $u = 1.97\,\mathrm{m\,s^{-1}}$	$T_w = 9.5\,°\mathrm{C}$ $\rho = 1000\,\mathrm{kg\,m^{-3}}$

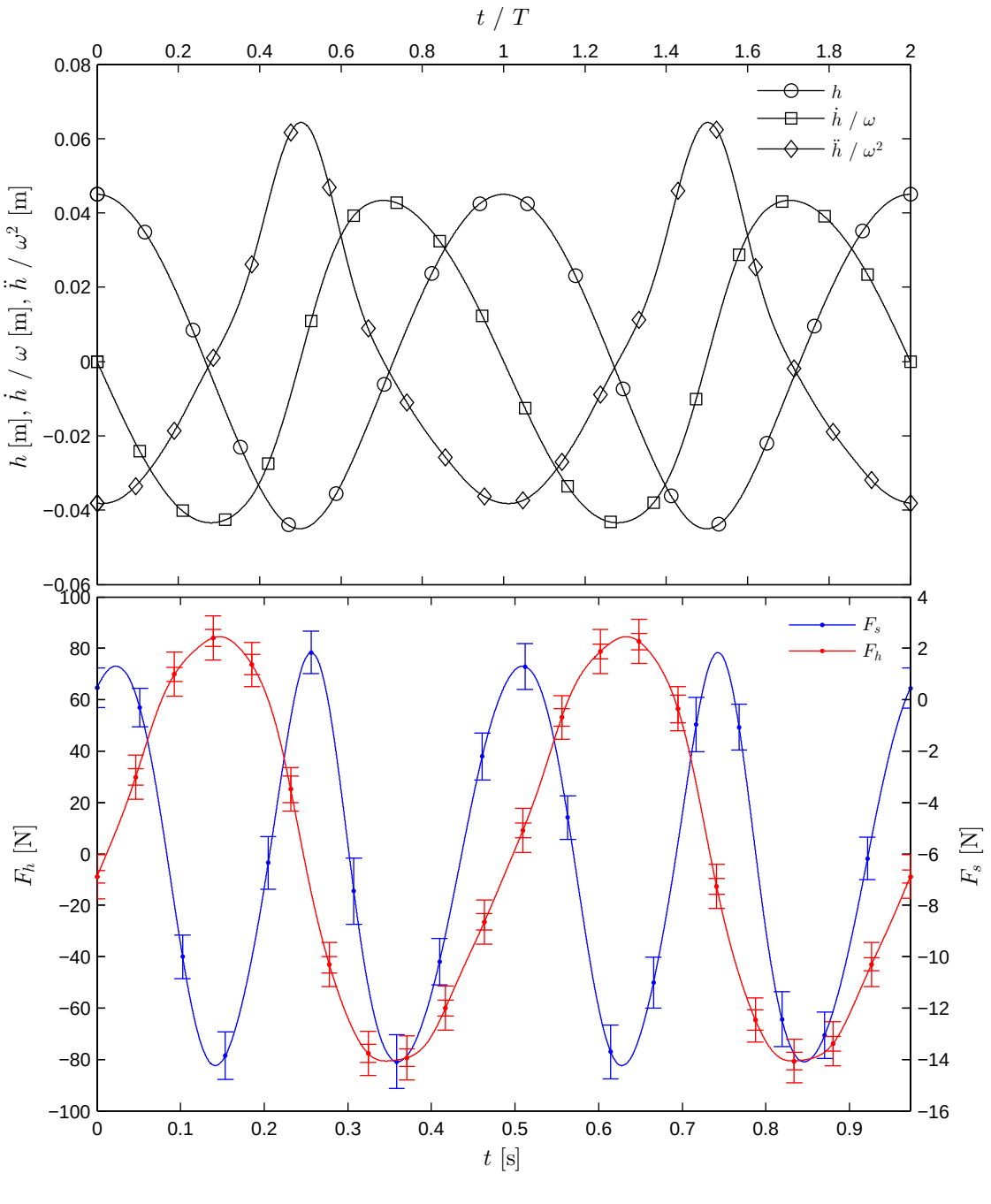

Object: NACA0012		Motion	Water
	$c = 0.060\,\mathrm{m}$ $L = 0.600\,\mathrm{m}$ $\theta = 0°$	$h_0 = 0.045\,\mathrm{m}$ $h^* = 0.75$ $f = 2.75\,\mathrm{Hz}$ $u = 0.52\,\mathrm{m\,s^{-1}}$	$T_w = 9.5\,°\mathrm{C}$ $\rho = 1000\,\mathrm{kg\,m^{-3}}$

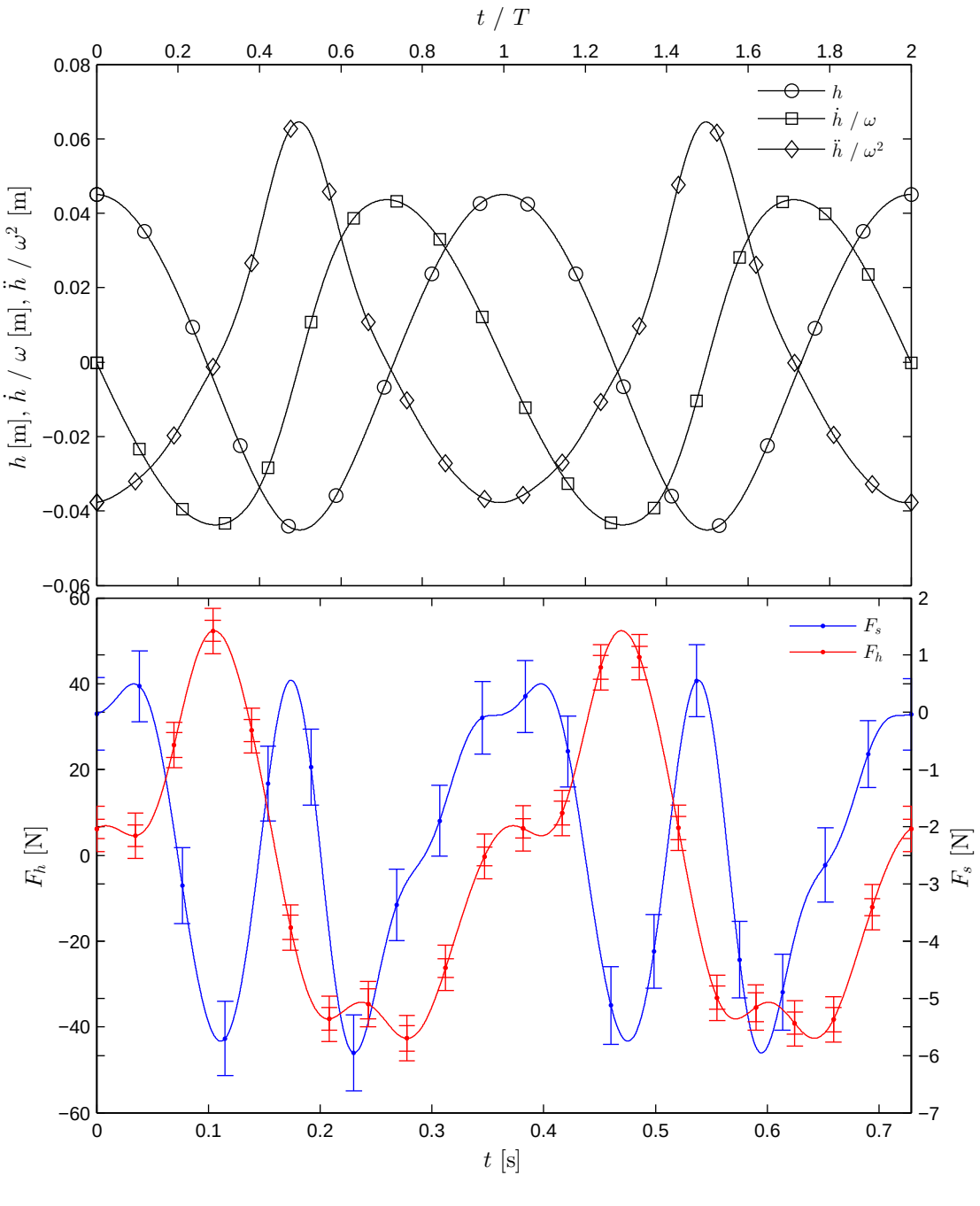

Object: NACA0012		Motion	Water
	$c = 0.060\,\mathrm{m}$ $L = 0.600\,\mathrm{m}$ $\theta = 0°$	$h_0 = 0.045\,\mathrm{m}$ $h^* = 0.75$ $f = 2.70\,\mathrm{Hz}$ $u = 0.99\,\mathrm{m\,s^{-1}}$	$T_w = 9.5\,°\mathrm{C}$ $\rho = 1000\,\mathrm{kg\,m^{-3}}$

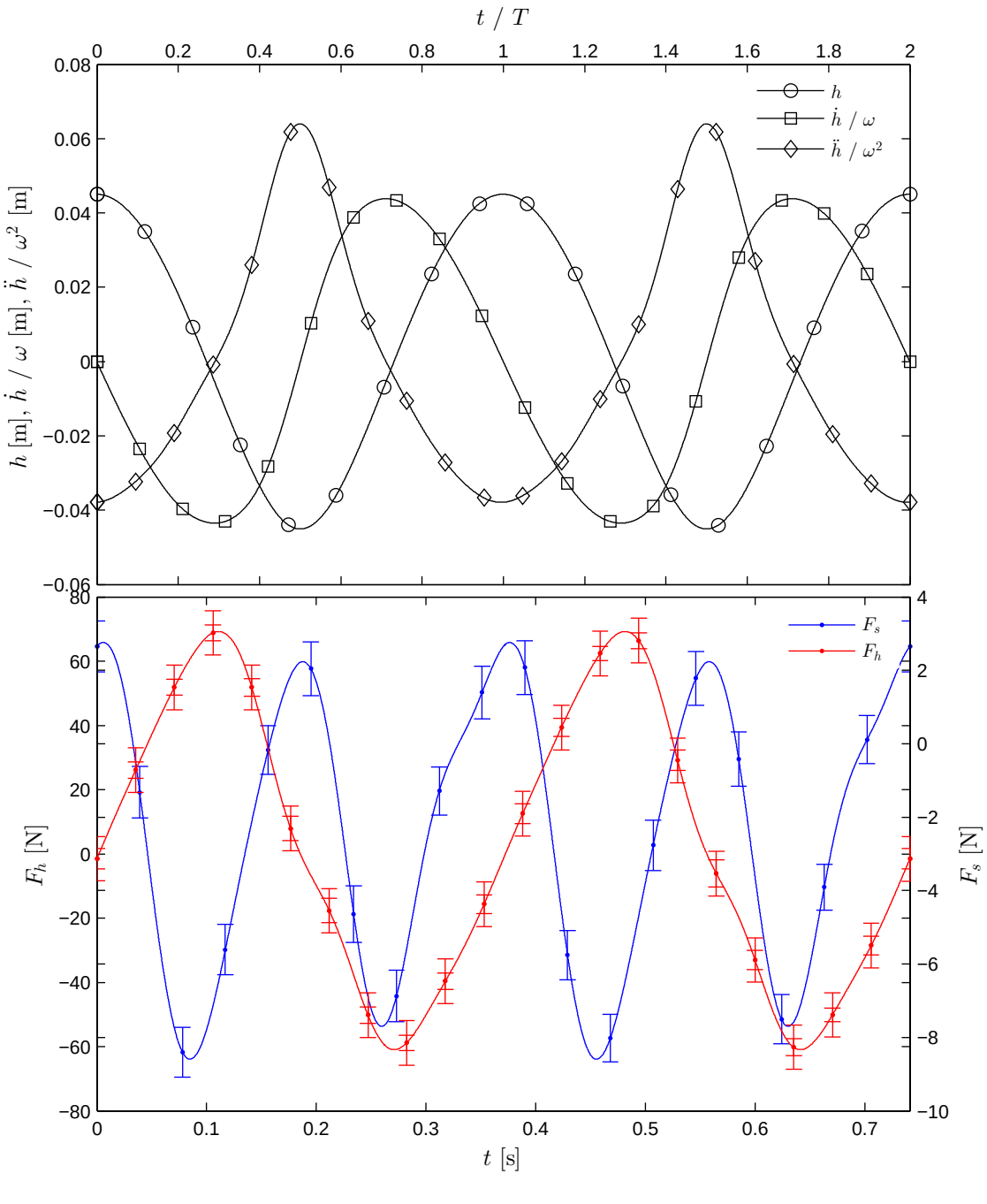

Object: NACA0012		Motion	Water
	$c = 0.060\,\mathrm{m}$ $L = 0.600\,\mathrm{m}$ $\theta = 0°$	$h_0 = 0.045\,\mathrm{m}$ $h^* = 0.75$ $f = 2.61\,\mathrm{Hz}$ $u = 1.50\,\mathrm{m\,s^{-1}}$	$T_w = 9.5\,°\mathrm{C}$ $\rho = 1000\,\mathrm{kg\,m^{-3}}$

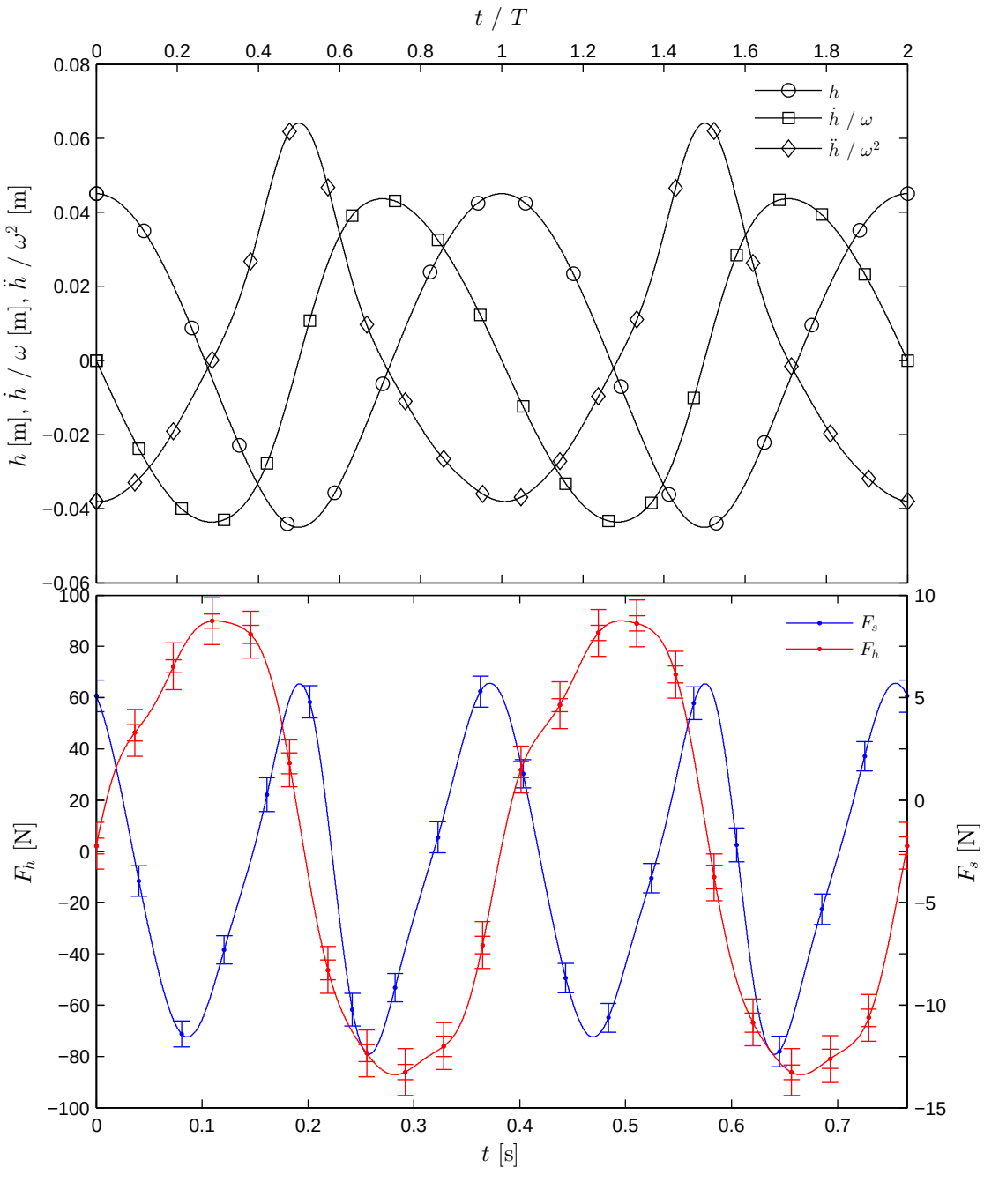

Object: NACA0012		Motion	Water
	$c = 0.060\,\mathrm{m}$ $L = 0.600\,\mathrm{m}$ $\theta = 0°$	$h_0 = 0.045\,\mathrm{m}$ $h^* = 0.75$ $f = 2.55\,\mathrm{Hz}$ $u = 1.98\,\mathrm{m\,s^{-1}}$	$T_w = 9.5\,°\mathrm{C}$ $\rho = 1000\,\mathrm{kg\,m^{-3}}$

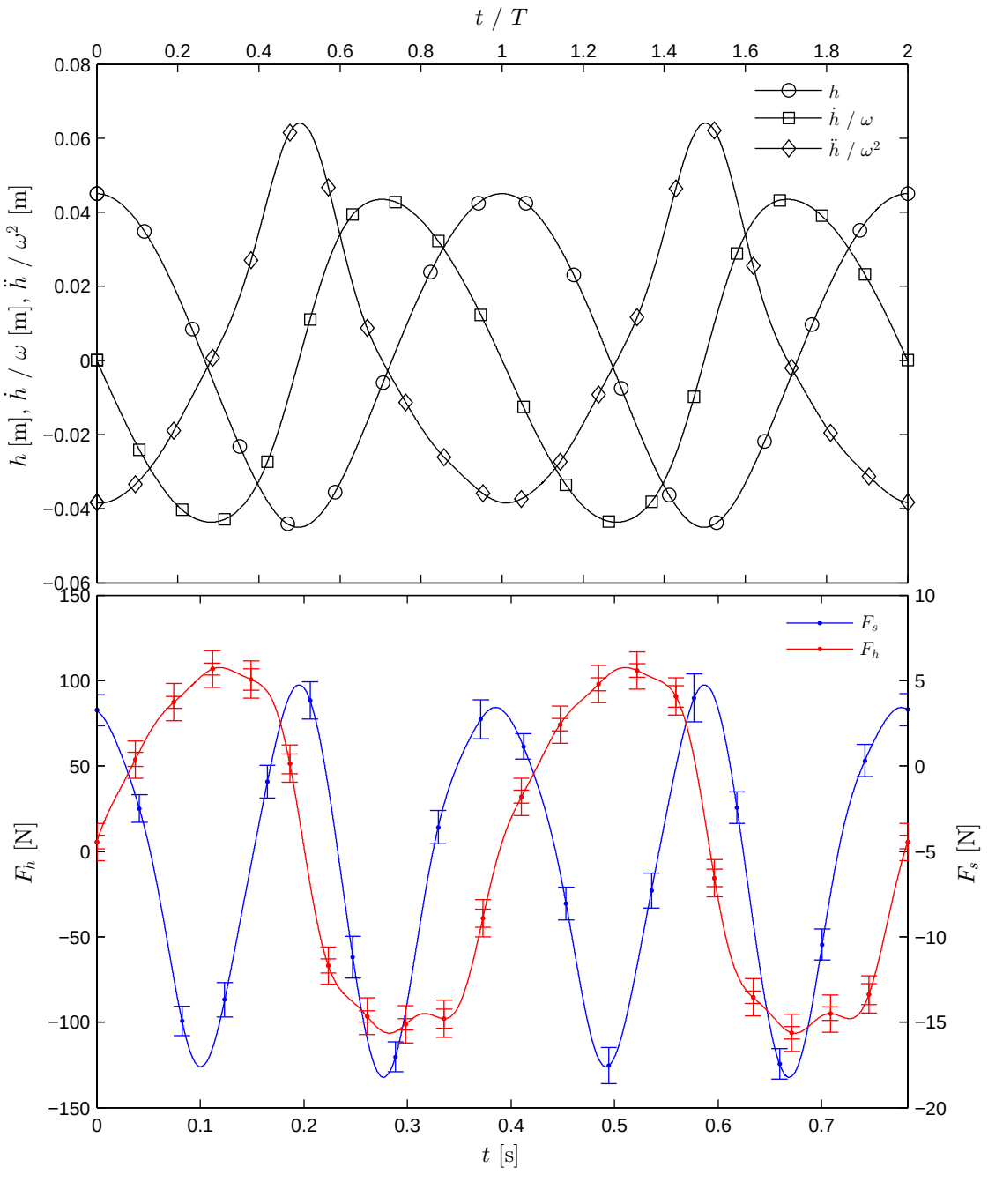

Object: NACA0012		Motion	Water
	$c = 0.060\,\mathrm{m}$ $L = 0.600\,\mathrm{m}$ $\theta = 0°$	$h_0 = 0.045\,\mathrm{m}$ $h^* = 0.75$ $f = 3.26\,\mathrm{Hz}$ $u = 0.52\,\mathrm{m\,s^{-1}}$	$T_w = 9.5\,°\mathrm{C}$ $\rho = 1000\,\mathrm{kg\,m^{-3}}$

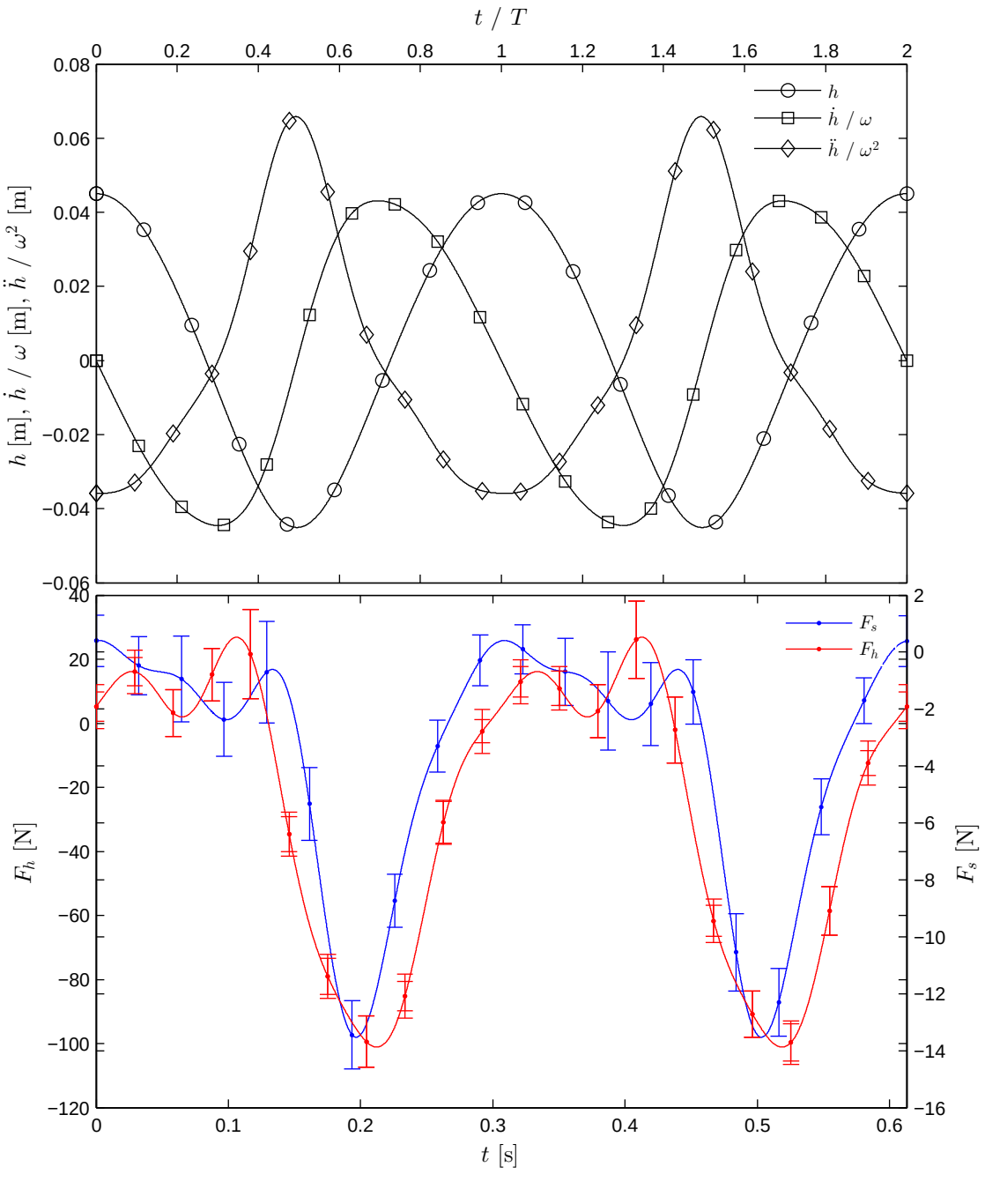

Object: NACA0012		Motion	Water
	$c = 0.060\,\mathrm{m}$ $L = 0.600\,\mathrm{m}$ $\theta = 0°$	$h_0 = 0.045\,\mathrm{m}$ $h^* = 0.75$ $f = 3.21\,\mathrm{Hz}$ $u = 0.99\,\mathrm{m\,s^{-1}}$	$T_w = 9.5\,°\mathrm{C}$ $\rho = 1000\,\mathrm{kg\,m^{-3}}$

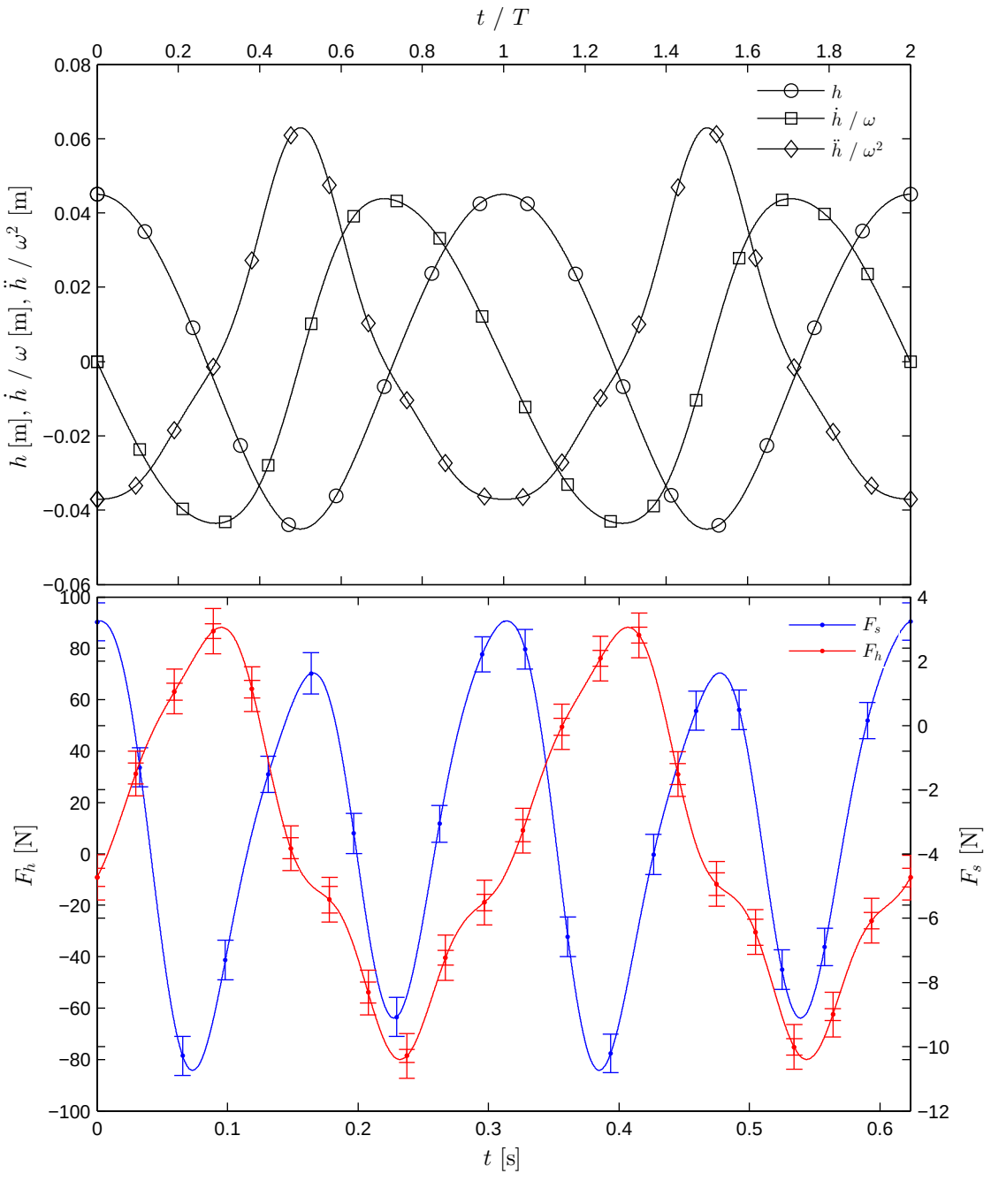

Object: NACA0012		Motion	Water
	$c = 0.060\,\mathrm{m}$ $L = 0.600\,\mathrm{m}$ $\theta = 0°$	$h_0 = 0.045\,\mathrm{m}$ $h^* = 0.75$ $f = 3.10\,\mathrm{Hz}$ $u = 1.49\,\mathrm{m\,s^{-1}}$	$T_w = 9.5\,°\mathrm{C}$ $\rho = 1000\,\mathrm{kg\,m^{-3}}$

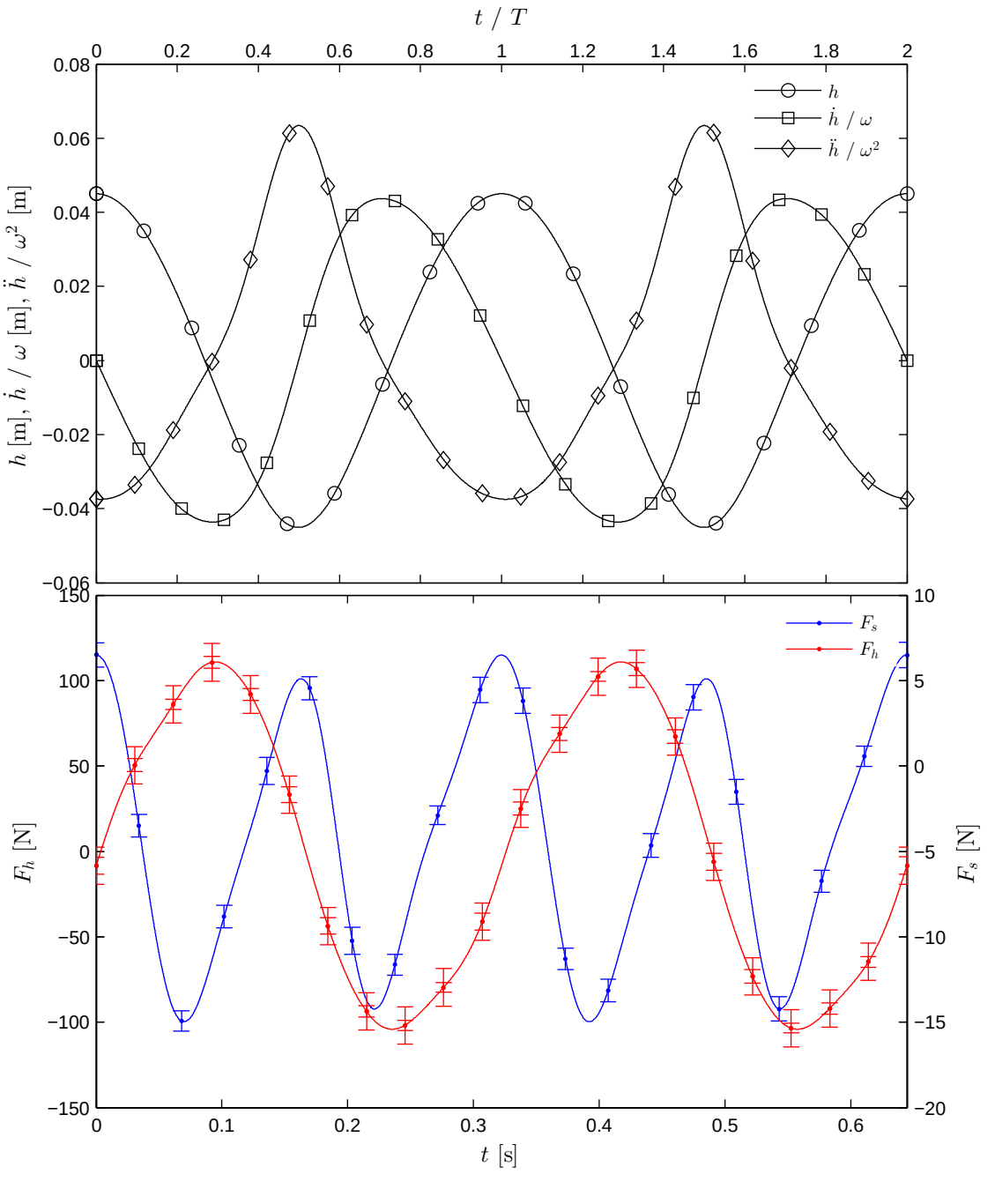

Object: NACA0012		Motion	Water
	$c = 0.060\,\mathrm{m}$ $L = 0.600\,\mathrm{m}$ $\theta = 0°$	$h_0 = 0.045\,\mathrm{m}$ $h^* = 0.75$ $f = 3.00\,\mathrm{Hz}$ $u = 1.97\,\mathrm{m\,s^{-1}}$	$T_w = 9.5\,°\mathrm{C}$ $\rho = 1000\,\mathrm{kg\,m^{-3}}$

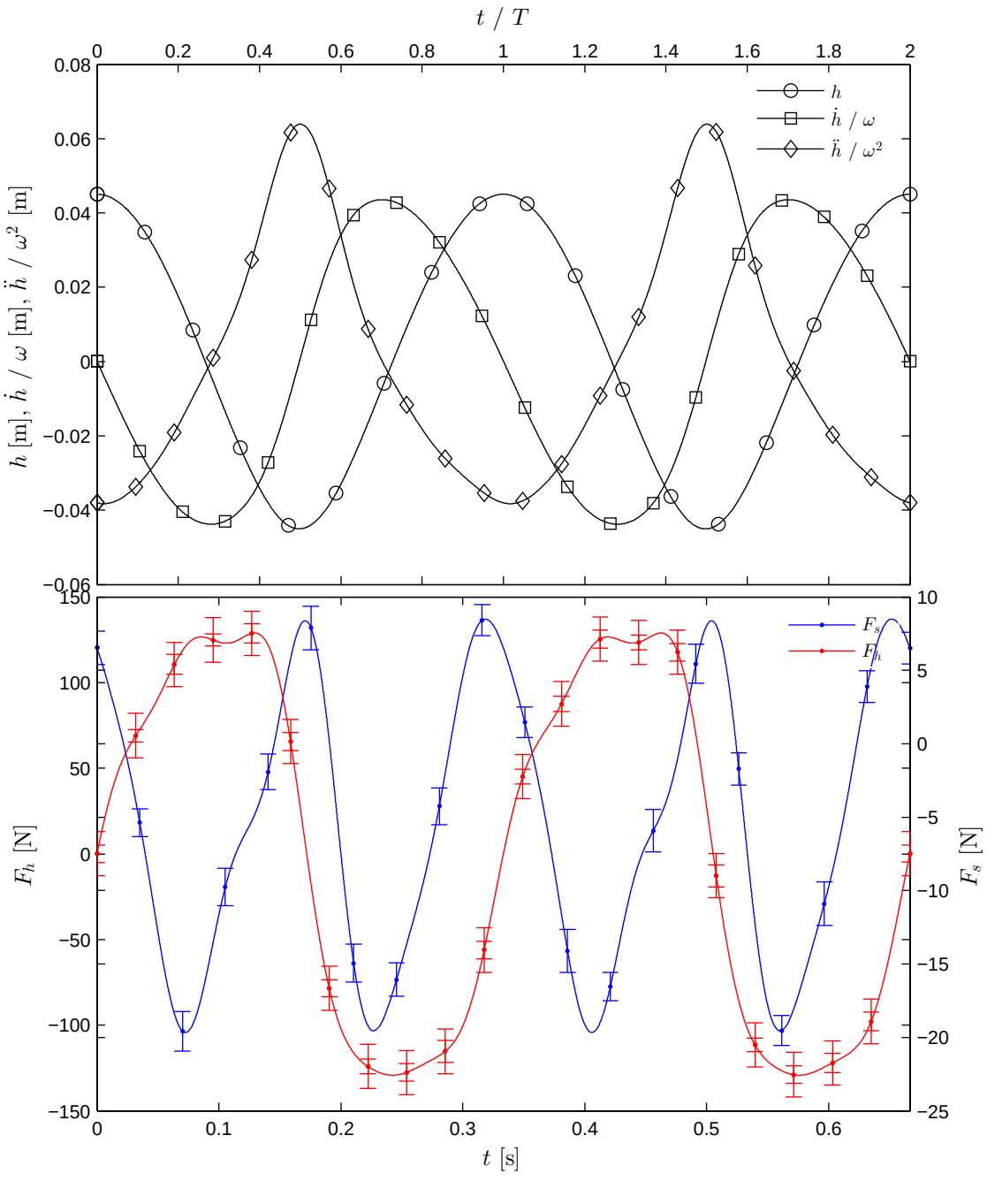

Object: NACA0012		Motion	Water
	$c = 0.060\,\mathrm{m}$ $L = 0.600\,\mathrm{m}$ $\theta = 0°$	$h_0 = 0.045\,\mathrm{m}$ $h^* = 0.75$ $f = 3.70\,\mathrm{Hz}$ $u = 0.52\,\mathrm{m\,s^{-1}}$	$T_w = 9.5\,°\mathrm{C}$ $\rho = 1000\,\mathrm{kg\,m^{-3}}$

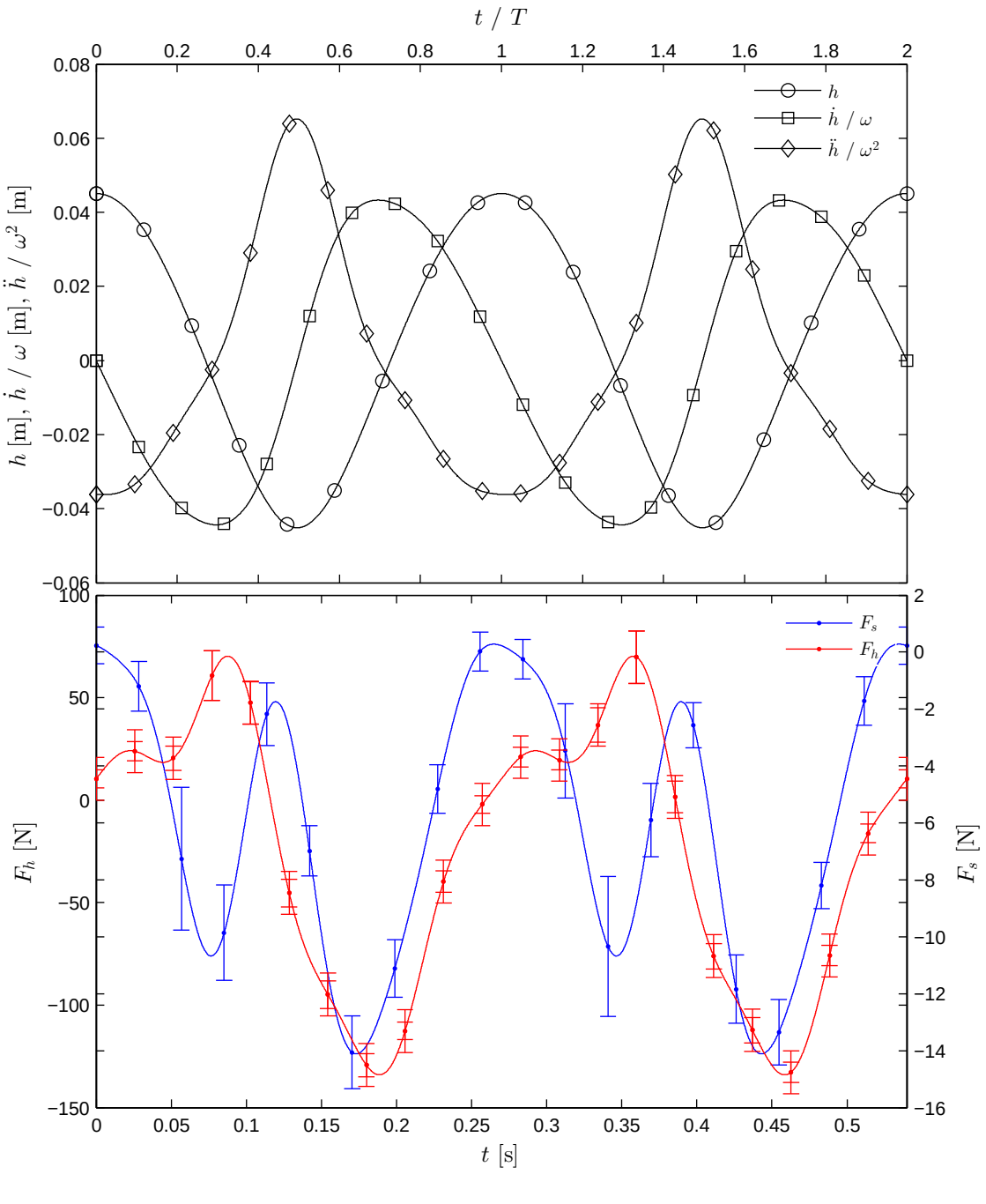

Object: NACA0012		Motion	Water
	$c = 0.060\,\mathrm{m}$ $L = 0.600\,\mathrm{m}$ $\theta = 0°$	$h_0 = 0.045\,\mathrm{m}$ $h^* = 0.75$ $f = 3.73\,\mathrm{Hz}$ $u = 0.99\,\mathrm{m\,s^{-1}}$	$T_w = 9.5\,°\mathrm{C}$ $\rho = 1000\,\mathrm{kg\,m^{-3}}$

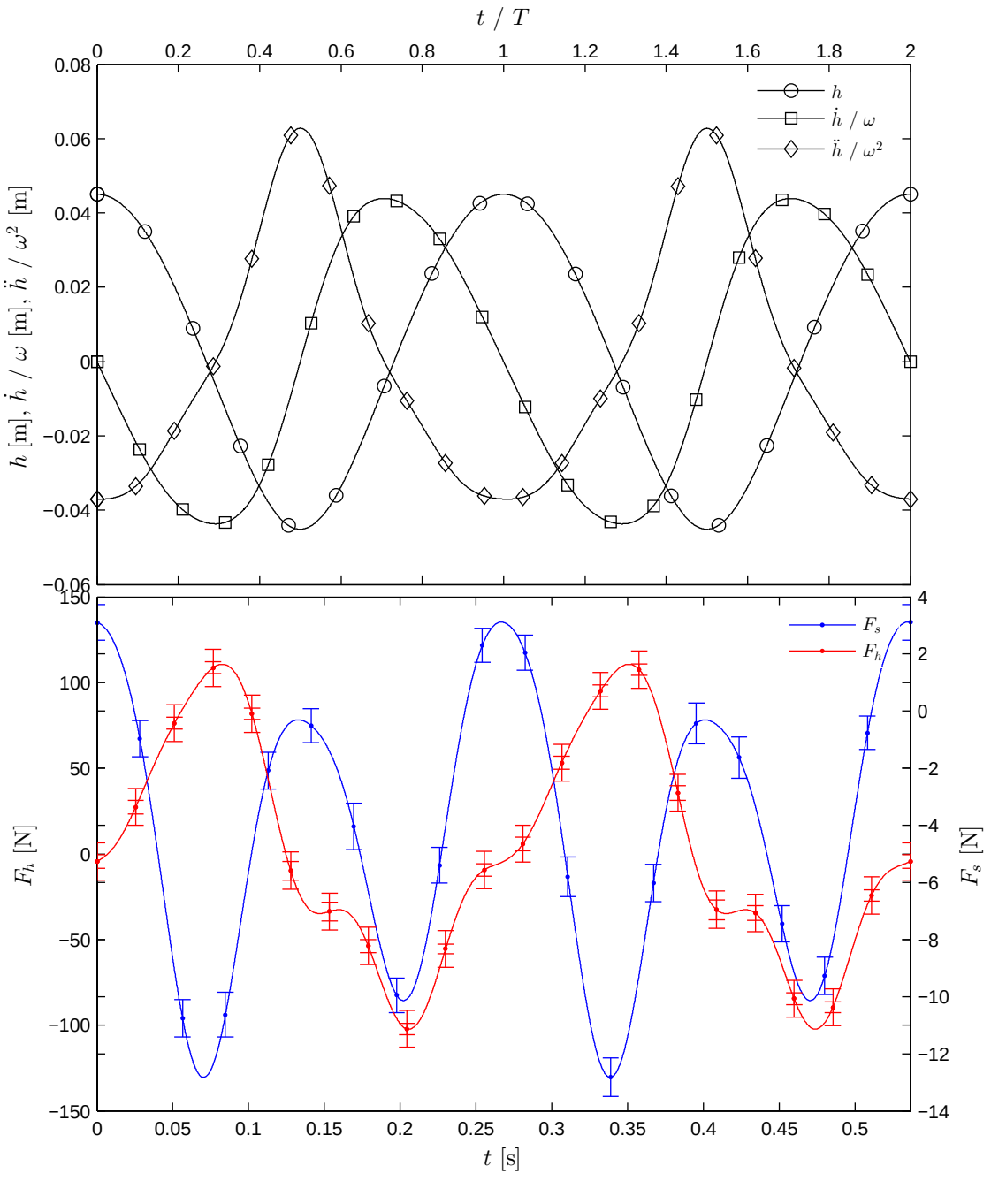

Object: NACA0012		Motion	Water
	$c = 0.060\,\mathrm{m}$ $L = 0.600\,\mathrm{m}$ $\theta = 0°$	$h_0 = 0.045\,\mathrm{m}$ $h^* = 0.75$ $f = 3.60\,\mathrm{Hz}$ $u = 1.49\,\mathrm{m\,s^{-1}}$	$T_w = 9.5\,°\mathrm{C}$ $\rho = 1000\,\mathrm{kg\,m^{-3}}$

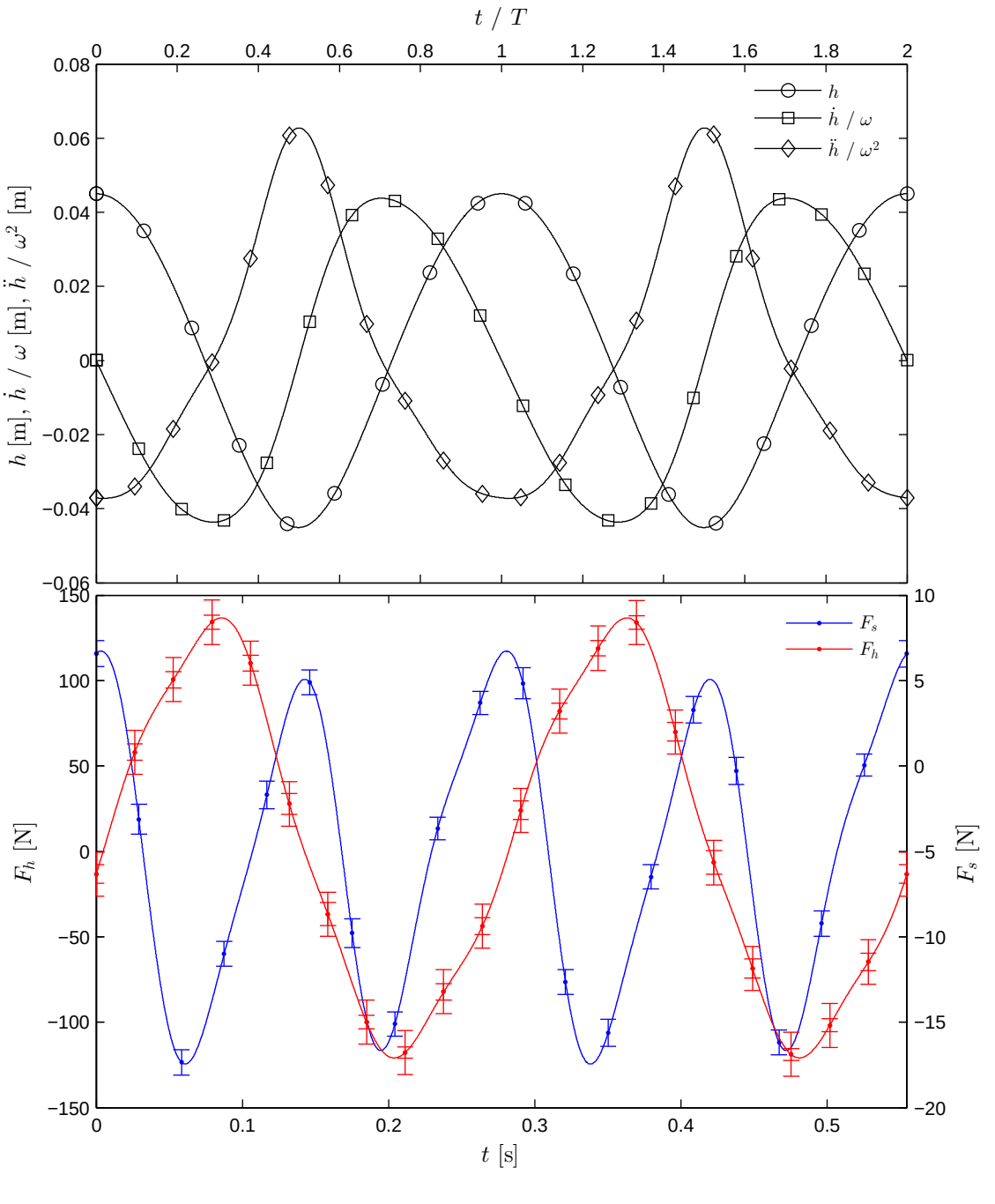

Object: NACA0012		Motion	Water
	$c = 0.060\,\mathrm{m}$ $L = 0.600\,\mathrm{m}$ $\theta = 0°$	$h_0 = 0.045\,\mathrm{m}$ $h^* = 0.75$ $f = 3.49\,\mathrm{Hz}$ $u = 1.97\,\mathrm{m\,s^{-1}}$	$T_w = 9.5\,°\mathrm{C}$ $\rho = 1000\,\mathrm{kg\,m^{-3}}$

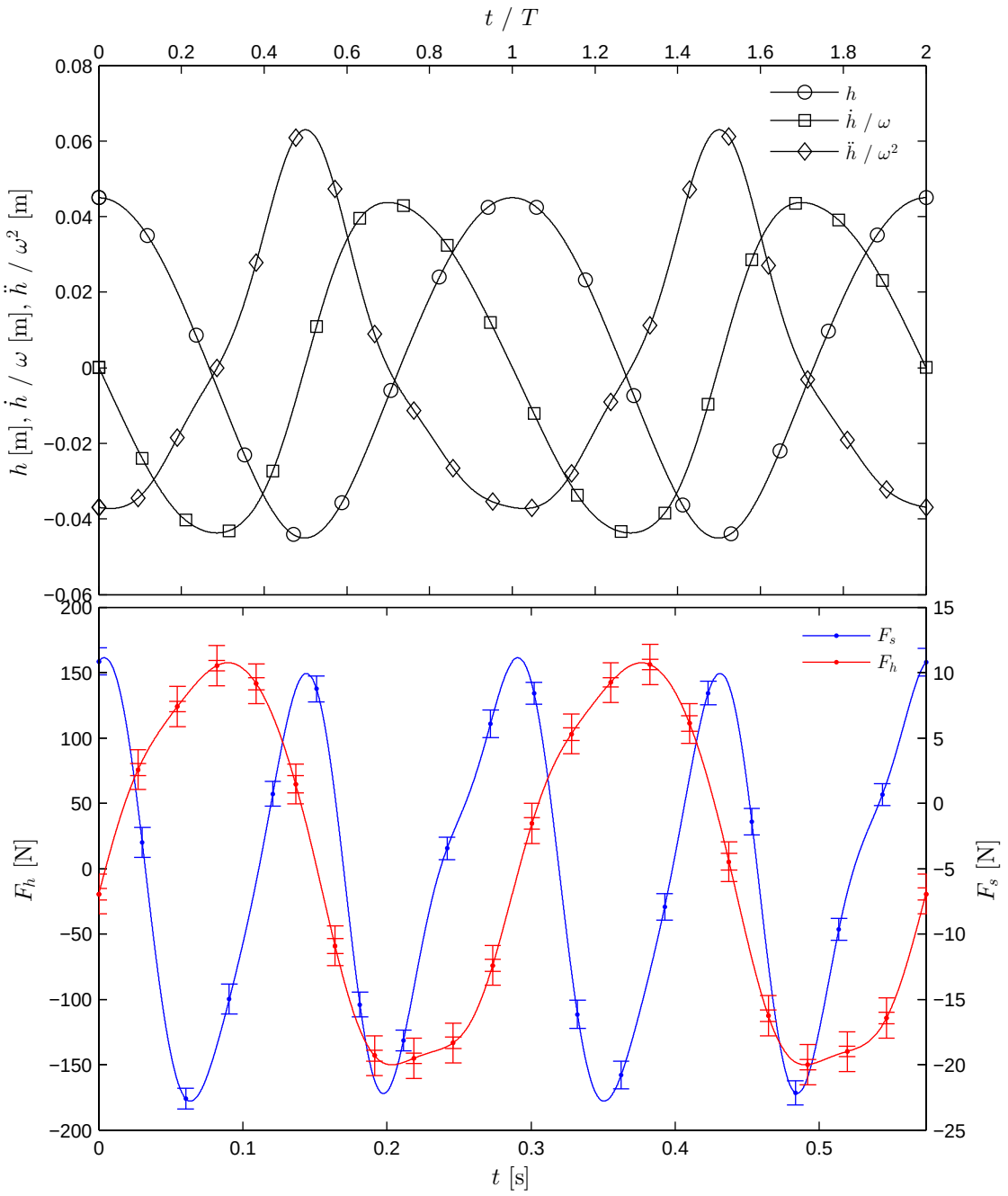

Appendix H

Measured Hydrodynamic Force Cycles on a Heaving NACA4415

The figures included in this appendix show measured hydrodynamic forces on a NACA4415 undergoing a heaving motion with no forward velocity. All the measurements presented in this appendix were recorded with a heave-to-chord ratio of $h^* = 0.75$ and circular end plates of size $\varnothing 320\,\text{mm}$ ($\varnothing 5.3c$) fitted. The dimensions of the NACA4415 cross-section are shown in Figure H.1. Refer to Table 4.1 for a comparison between the NACA4415 and the other test objects.

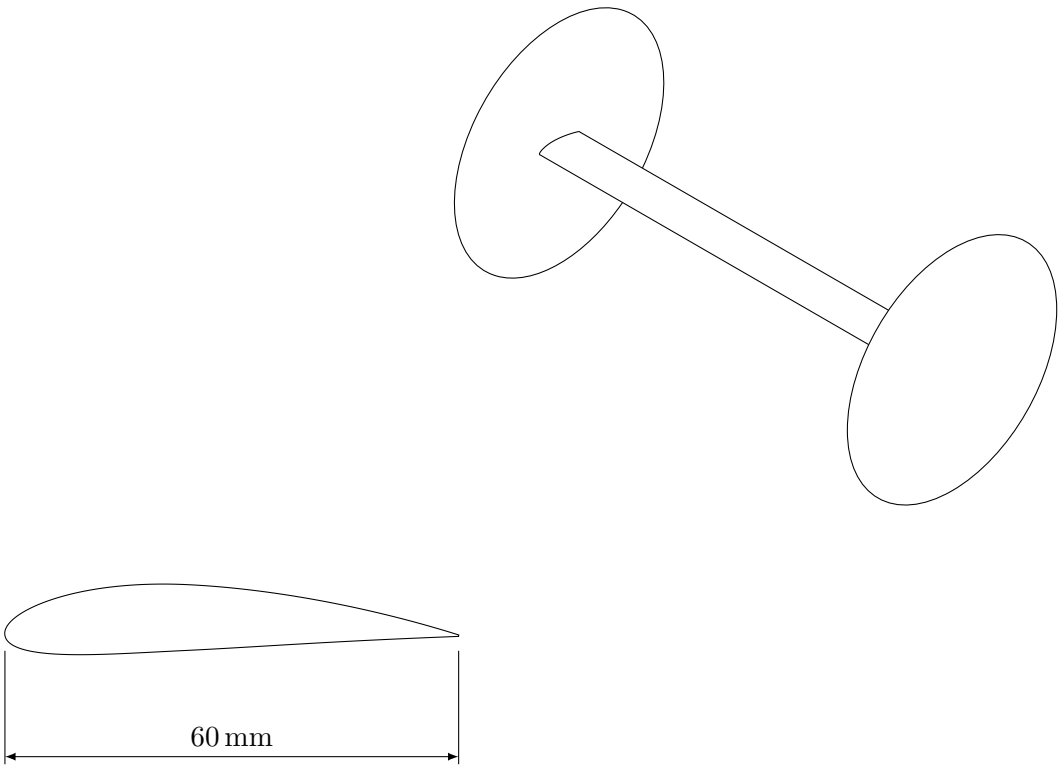

Figure H.1. Dimensions of the NACA4415 cross-section (scale 1:1) and an isometric of the NACA4415 with end plates attached (scale 1:5).

Object: NACA4415		Motion	Water
	$c = 0.060\,\mathrm{m}$ $L = 0.600\,\mathrm{m}$ $\theta = -40°$	$h_0 = 0.045\,\mathrm{m}$ $h^* = 0.75$ $f = 0.77\,\mathrm{Hz}$ $u = 0.00\,\mathrm{m\,s^{-1}}$	$T_w = 7.8\,°\mathrm{C}$ $\rho = 1000\,\mathrm{kg\,m^{-3}}$

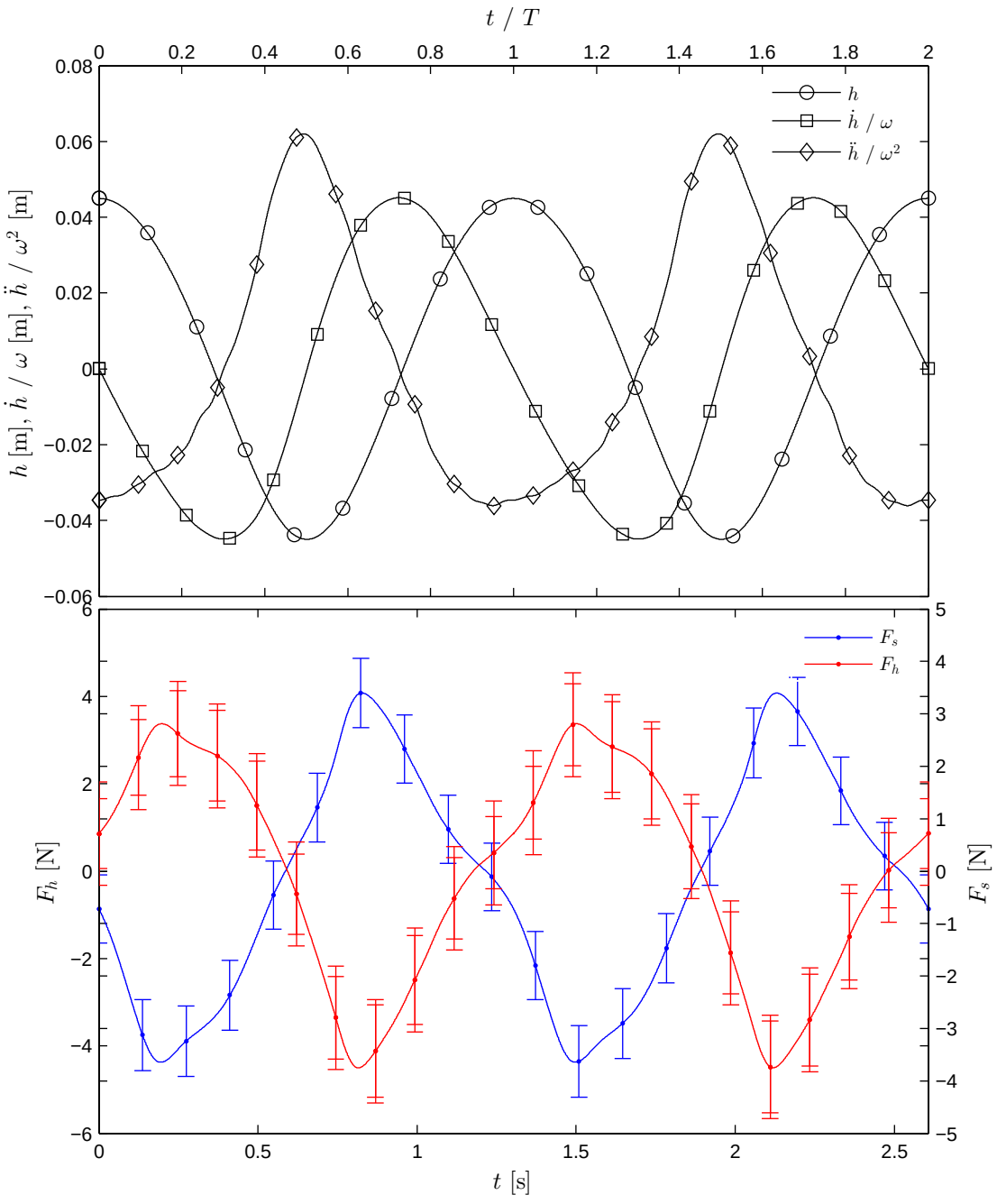

Object: NACA4415		Motion	Water
	$c = 0.060\,\mathrm{m}$ $L = 0.600\,\mathrm{m}$ $\theta = -40°$	$h_0 = 0.045\,\mathrm{m}$ $h^* = 0.75$ $f = 1.36\,\mathrm{Hz}$ $u = 0.00\,\mathrm{m\,s^{-1}}$	$T_w = 7.8\,°\mathrm{C}$ $\rho = 1000\,\mathrm{kg\,m^{-3}}$

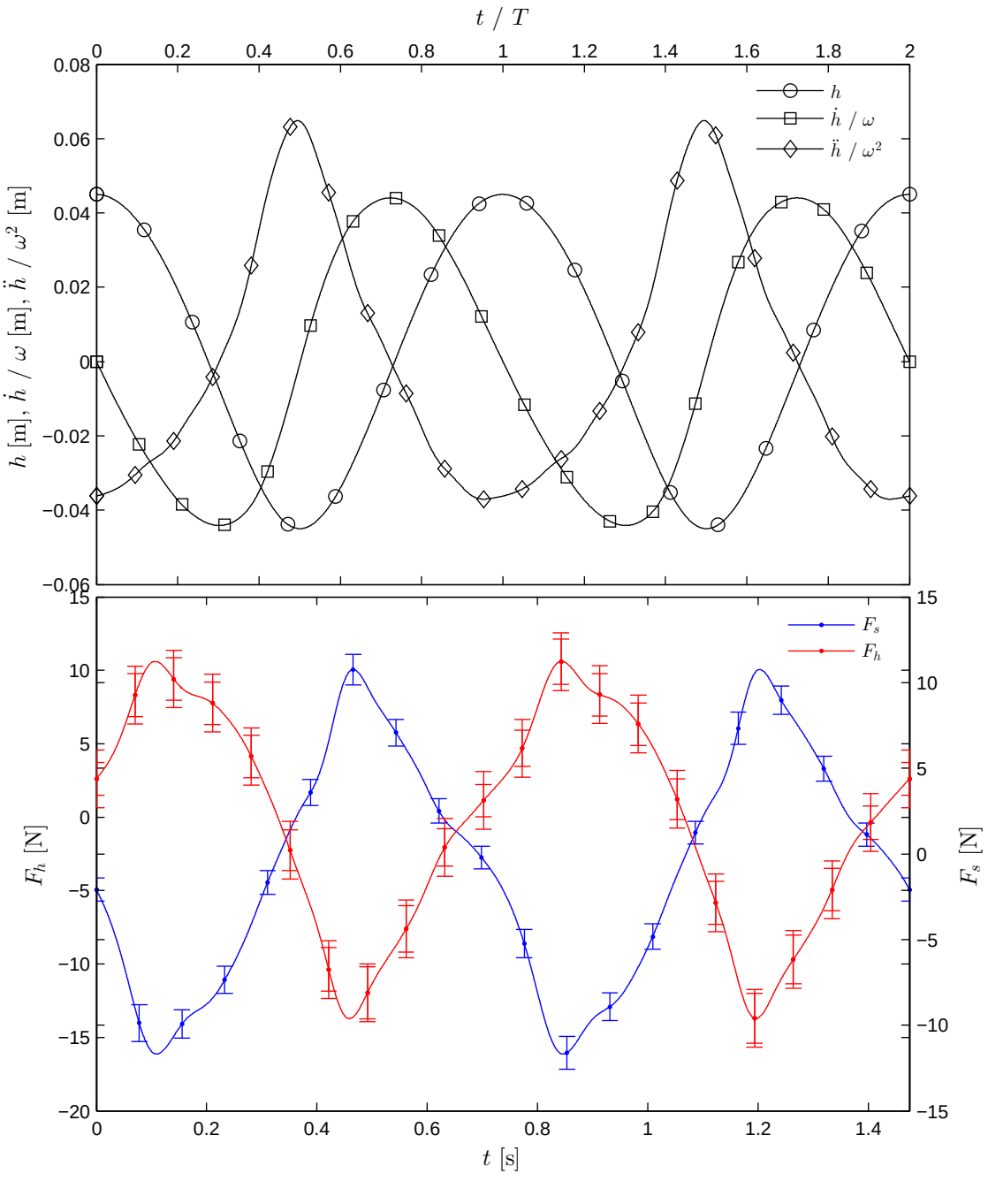

Object: NACA4415		Motion	Water
	$c = 0.060\,\mathrm{m}$ $L = 0.600\,\mathrm{m}$ $\theta = -40°$	$h_0 = 0.045\,\mathrm{m}$ $h^* = 0.75$ $f = 1.73\,\mathrm{Hz}$ $u = 0.00\,\mathrm{m\,s^{-1}}$	$T_w = 7.8\,°\mathrm{C}$ $\rho = 1000\,\mathrm{kg\,m^{-3}}$

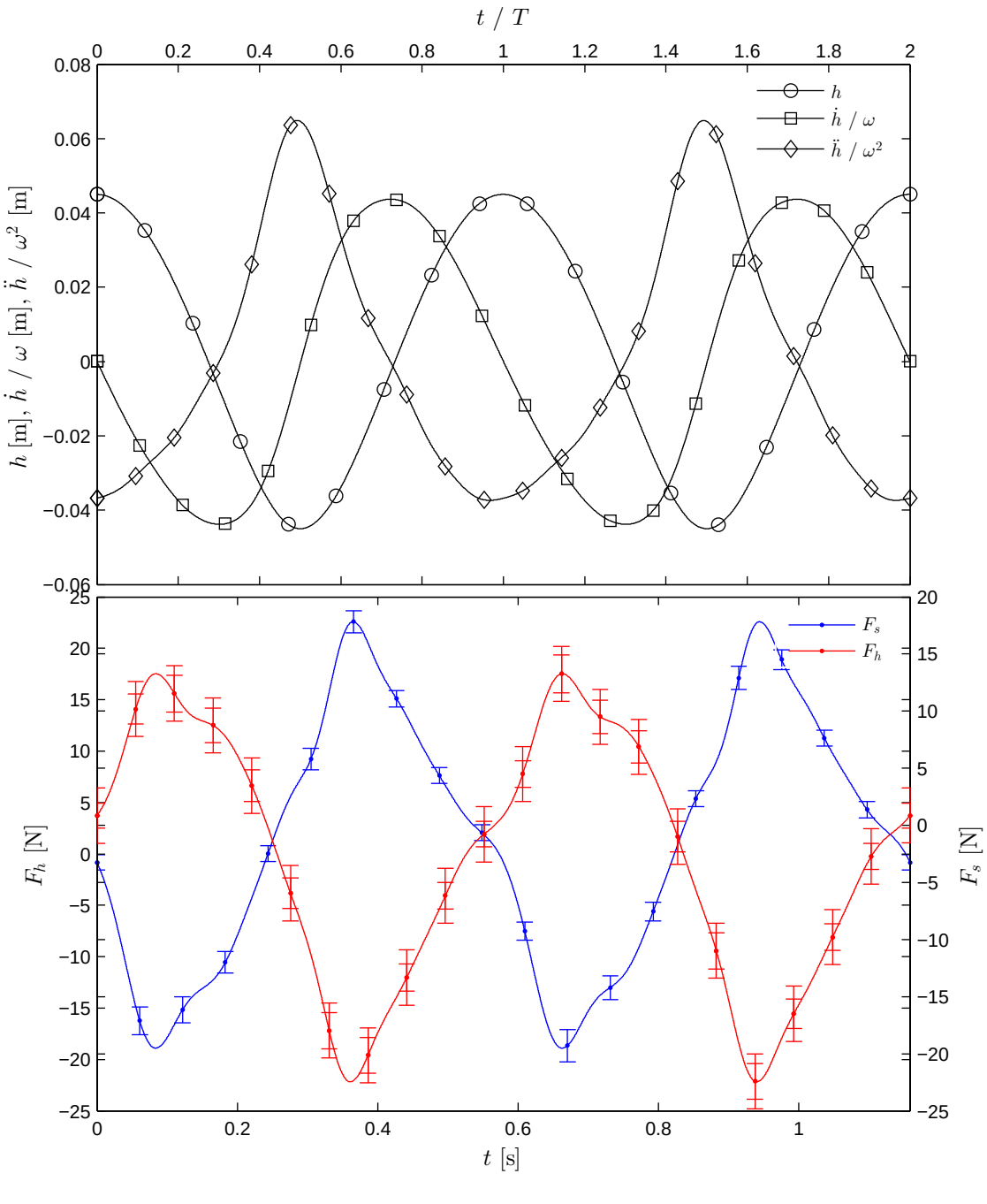

Object: NACA4415		Motion	Water
	$c = 0.060\,\mathrm{m}$ $L = 0.600\,\mathrm{m}$ $\theta = -40°$	$h_0 = 0.045\,\mathrm{m}$ $h^* = 0.75$ $f = 2.28\,\mathrm{Hz}$ $u = 0.00\,\mathrm{m\,s^{-1}}$	$T_w = 7.8\,°\mathrm{C}$ $\rho = 1000\,\mathrm{kg\,m^{-3}}$

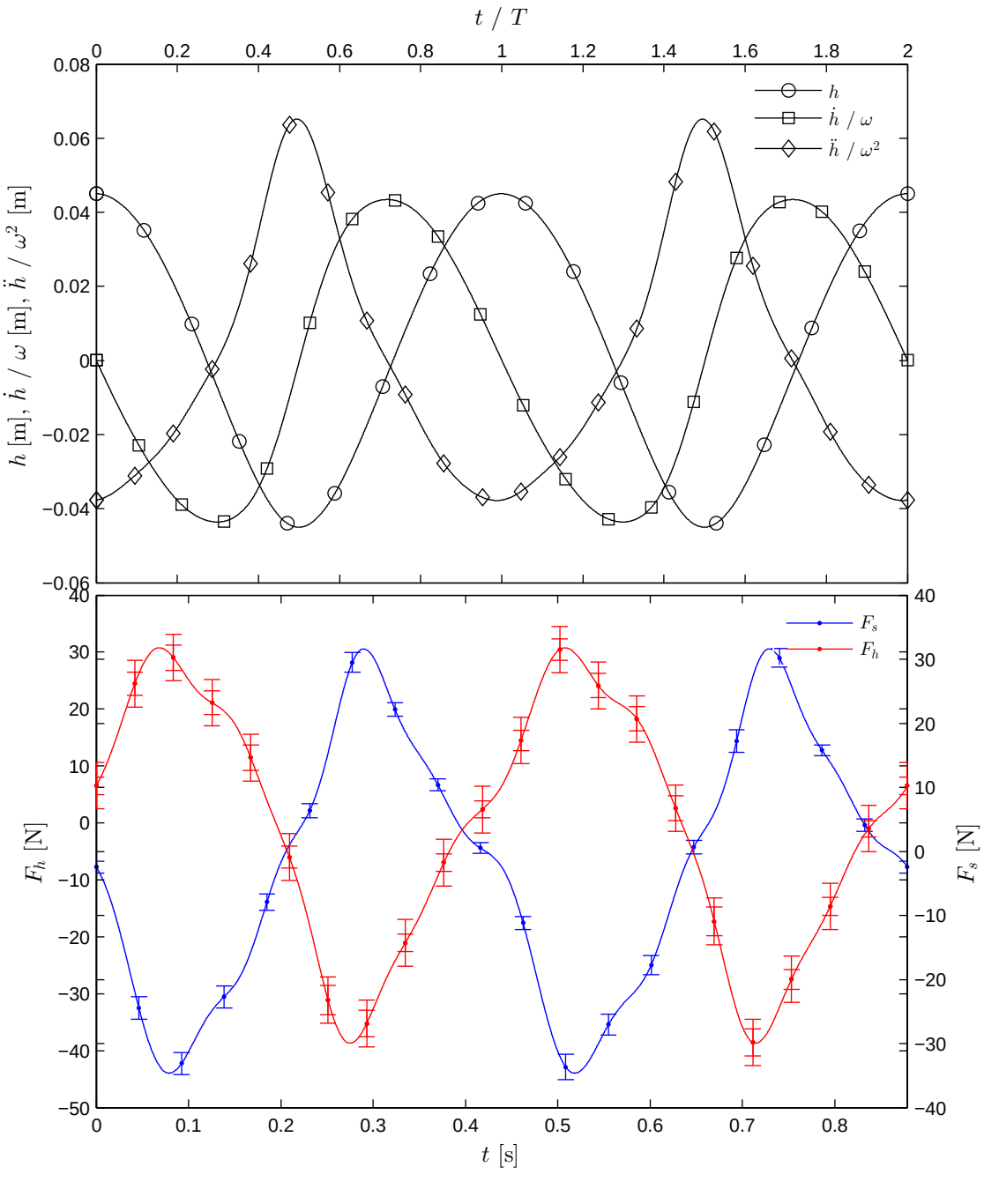

Object: NACA4415		Motion	Water
	$c = 0.060\,\mathrm{m}$ $L = 0.600\,\mathrm{m}$ $\theta = -40°$	$h_0 = 0.045\,\mathrm{m}$ $h^* = 0.75$ $f = 2.78\,\mathrm{Hz}$ $u = 0.00\,\mathrm{m\,s^{-1}}$	$T_w = 7.8\,°\mathrm{C}$ $\rho = 1000\,\mathrm{kg\,m^{-3}}$

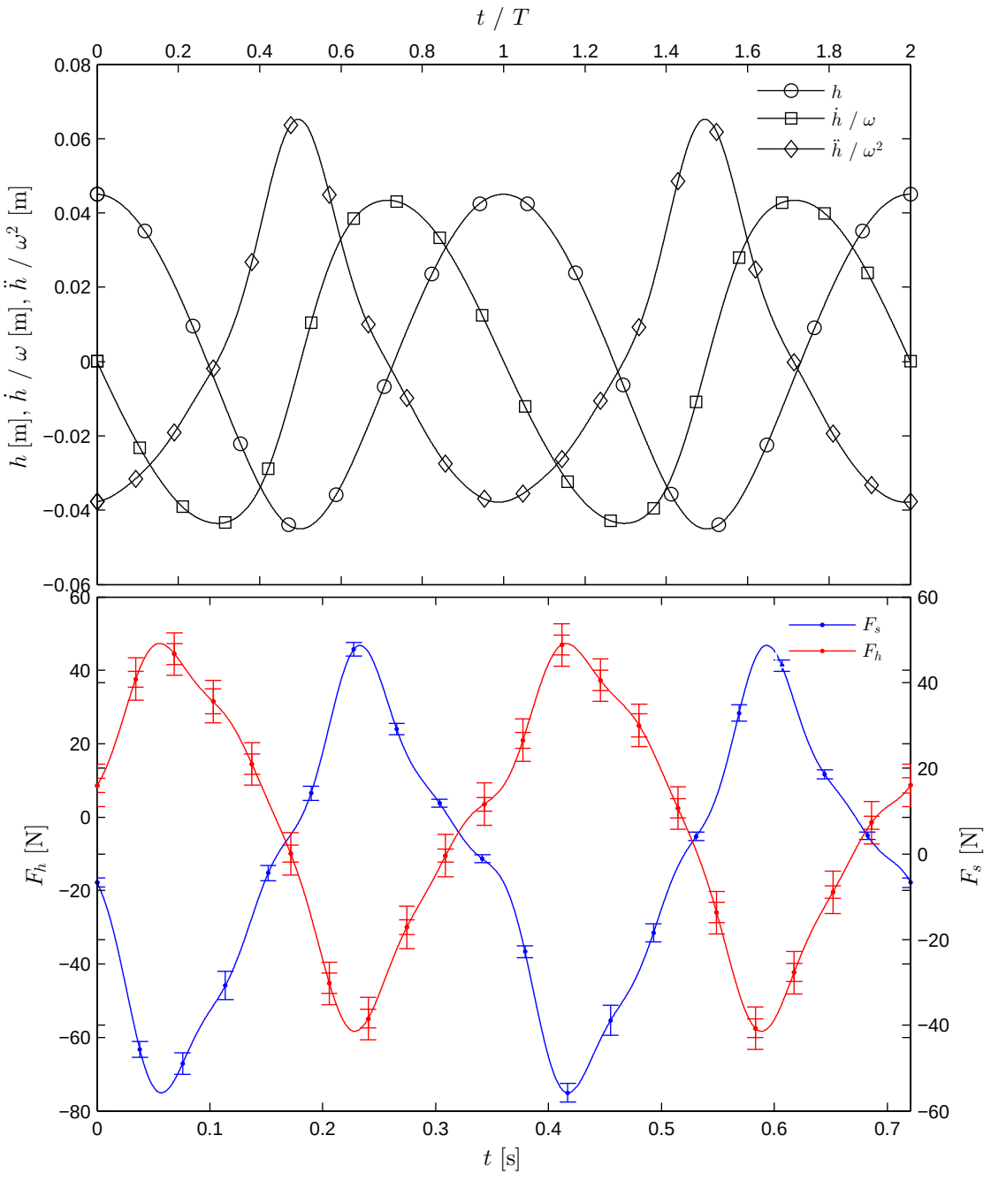

Object: NACA4415		Motion	Water
	$c = 0.060\,\mathrm{m}$ $L = 0.600\,\mathrm{m}$ $\theta = -40°$	$h_0 = 0.045\,\mathrm{m}$ $h^* = 0.75$ $f = 3.29\,\mathrm{Hz}$ $u = 0.00\,\mathrm{m\,s^{-1}}$	$T_w = 7.8\,°\mathrm{C}$ $\rho = 1000\,\mathrm{kg\,m^{-3}}$

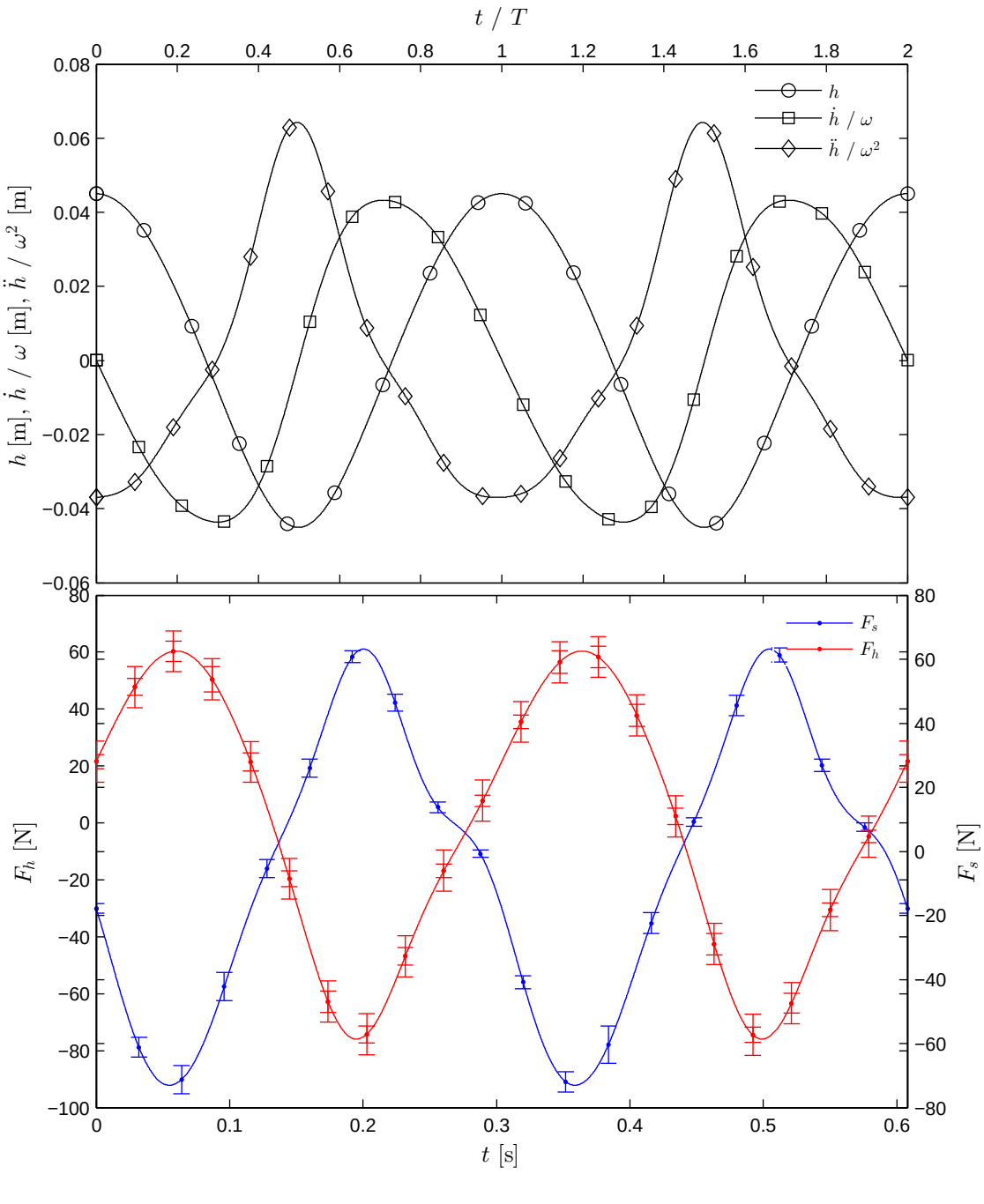

Object: NACA4415		Motion	Water
	$c = 0.060\,\mathrm{m}$ $L = 0.600\,\mathrm{m}$ $\theta = -40°$	$h_0 = 0.045\,\mathrm{m}$ $h^* = 0.75$ $f = 3.78\,\mathrm{Hz}$ $u = 0.00\,\mathrm{m\,s^{-1}}$	$T_w = 7.8\,°\mathrm{C}$ $\rho = 1000\,\mathrm{kg\,m^{-3}}$

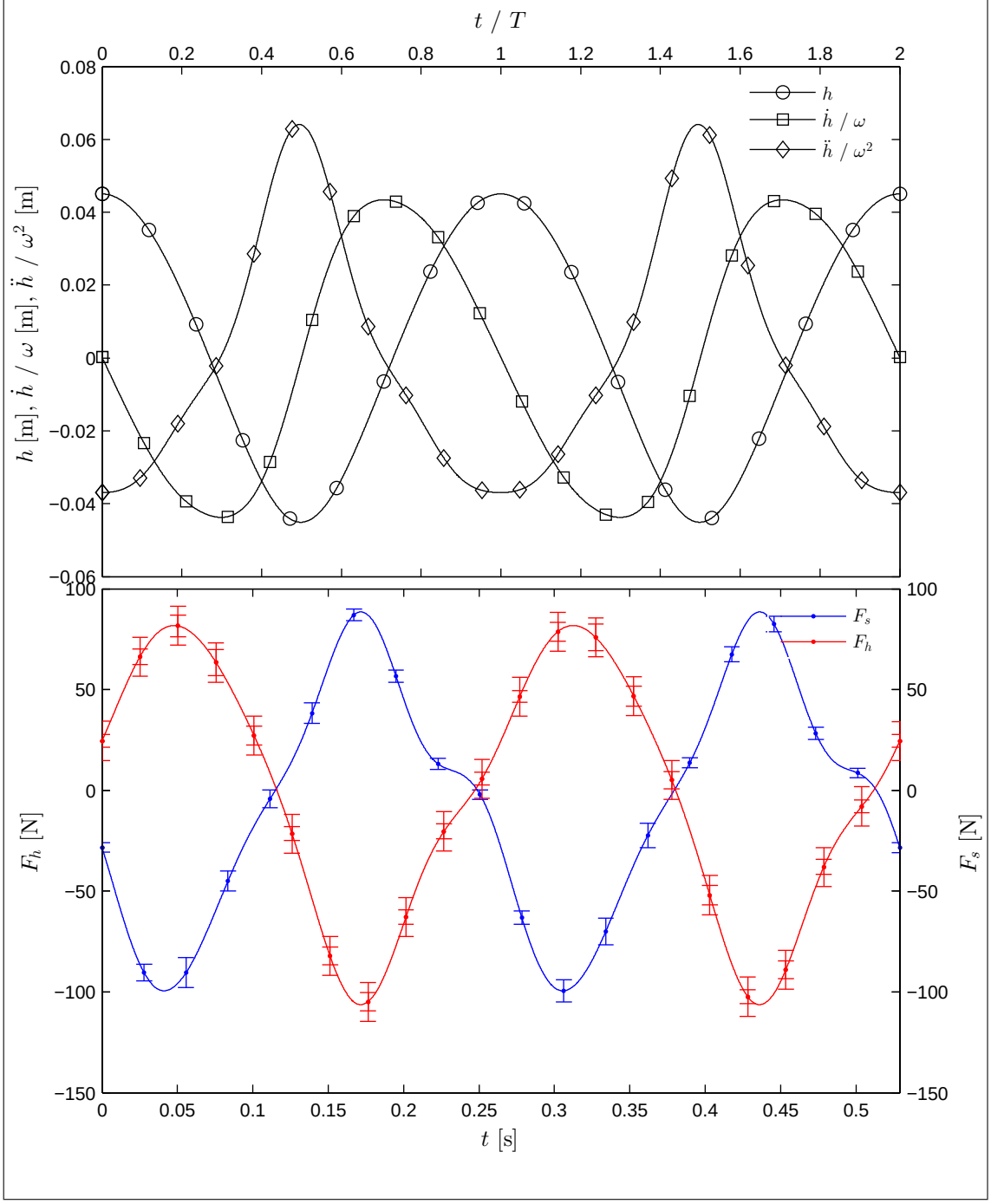

Object: NACA4415		Motion	Water
	$c = 0.060\,\mathrm{m}$ $L = 0.600\,\mathrm{m}$ $\theta = -10°$	$h_0 = 0.045\,\mathrm{m}$ $h^* = 0.75$ $f = 0.75\,\mathrm{Hz}$ $u = 0.00\,\mathrm{m\,s^{-1}}$	$T_w = 7.8\,°\mathrm{C}$ $\rho = 1000\,\mathrm{kg\,m^{-3}}$

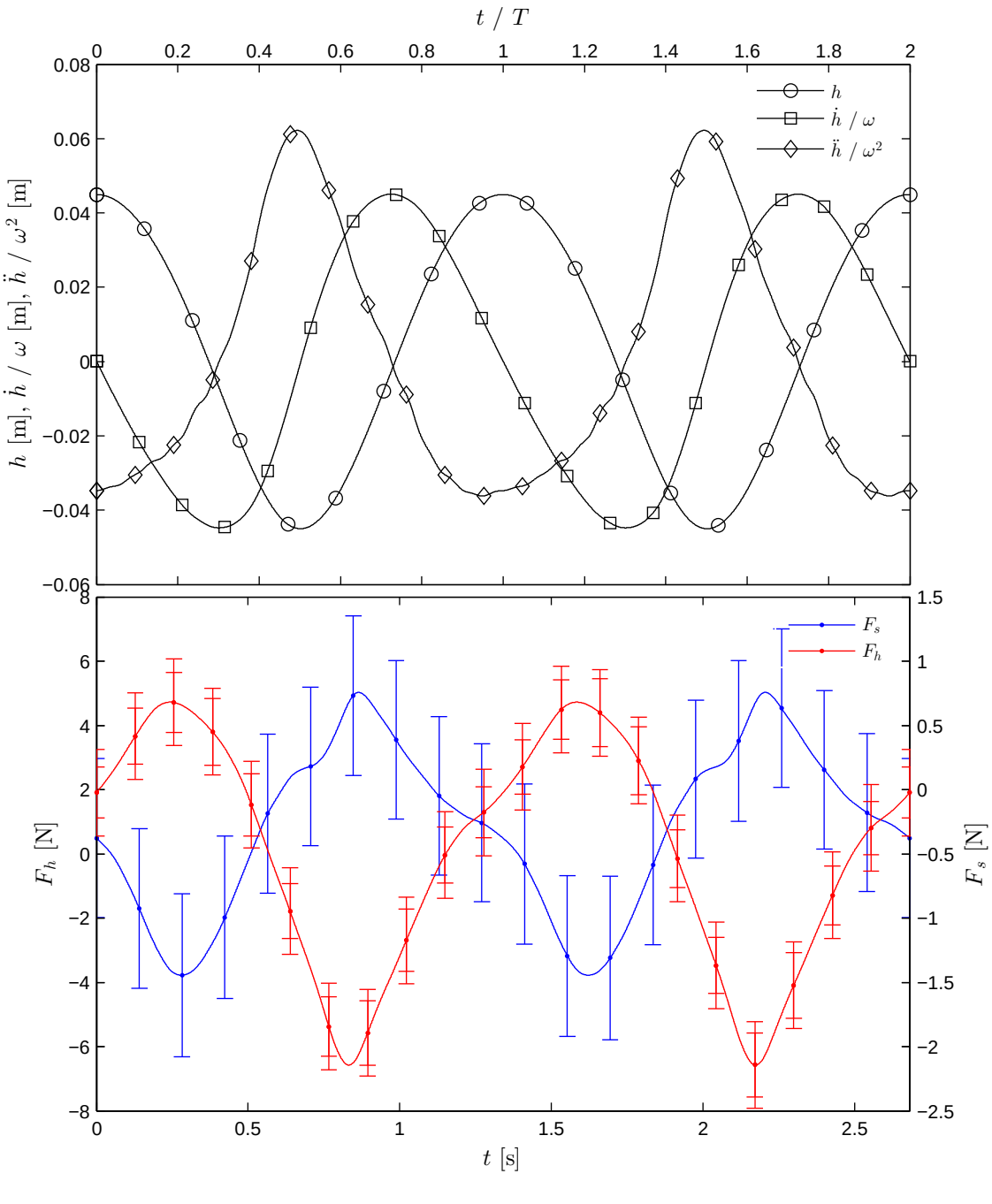

Object: NACA4415		Motion	Water
	$c = 0.060\,\mathrm{m}$ $L = 0.600\,\mathrm{m}$ $\theta = -10°$	$h_0 = 0.045\,\mathrm{m}$ $h^* = 0.75$ $f = 1.34\,\mathrm{Hz}$ $u = 0.00\,\mathrm{m\,s^{-1}}$	$T_w = 7.8\,°\mathrm{C}$ $\rho = 1000\,\mathrm{kg\,m^{-3}}$

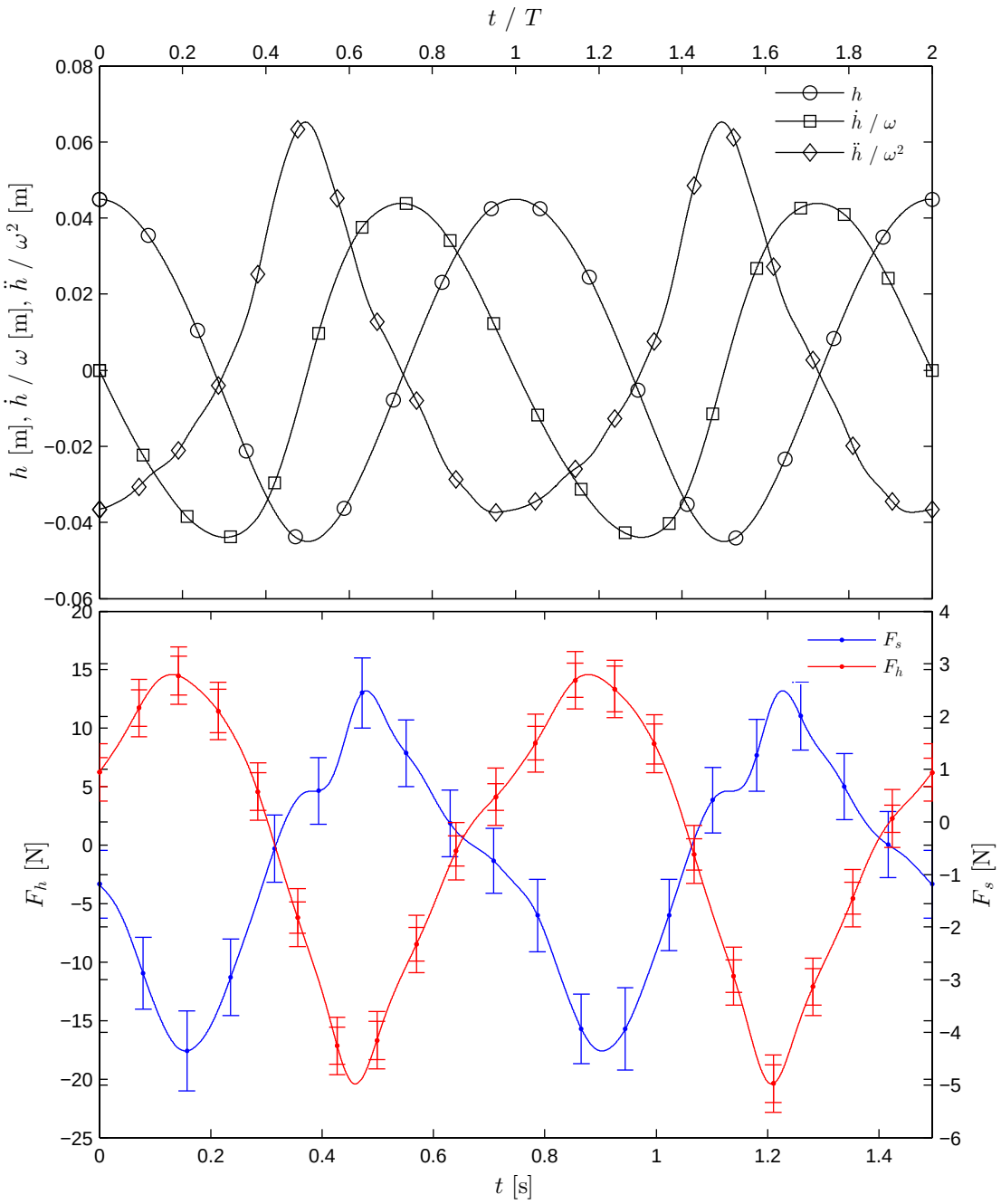

Object: NACA4415		Motion	Water
	$c = 0.060\,\mathrm{m}$ $L = 0.600\,\mathrm{m}$ $\theta = -10°$	$h_0 = 0.045\,\mathrm{m}$ $h^* = 0.75$ $f = 1.87\,\mathrm{Hz}$ $u = 0.00\,\mathrm{m\,s^{-1}}$	$T_w = 7.8\,°\mathrm{C}$ $\rho = 1000\,\mathrm{kg\,m^{-3}}$

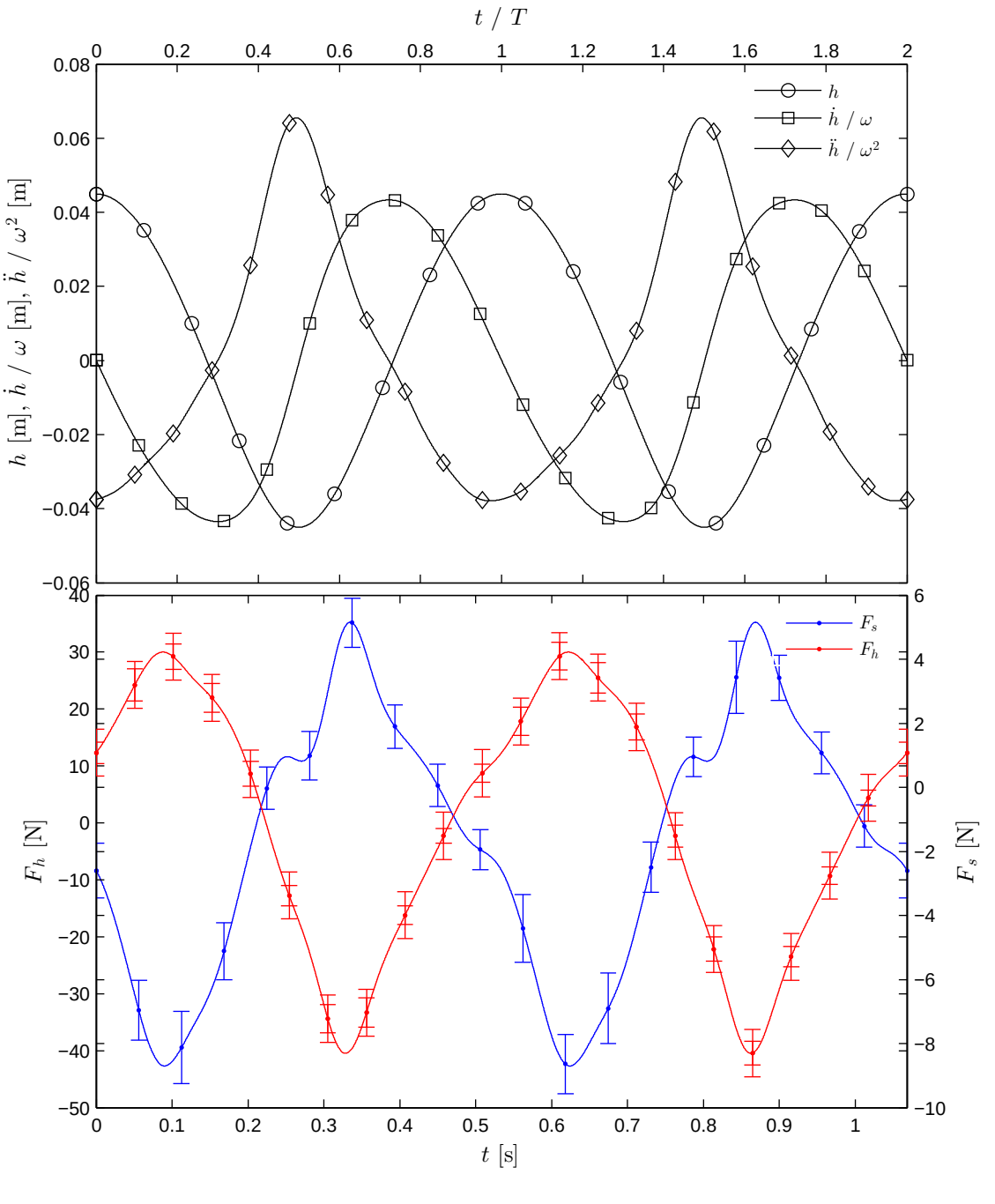

Object: NACA4415		Motion	Water
	$c = 0.060\,\mathrm{m}$ $L = 0.600\,\mathrm{m}$ $\theta = -10°$	$h_0 = 0.045\,\mathrm{m}$ $h^* = 0.75$ $f = 2.33\,\mathrm{Hz}$ $u = 0.00\,\mathrm{m\,s^{-1}}$	$T_w = 7.8\,°\mathrm{C}$ $\rho = 1000\,\mathrm{kg\,m^{-3}}$

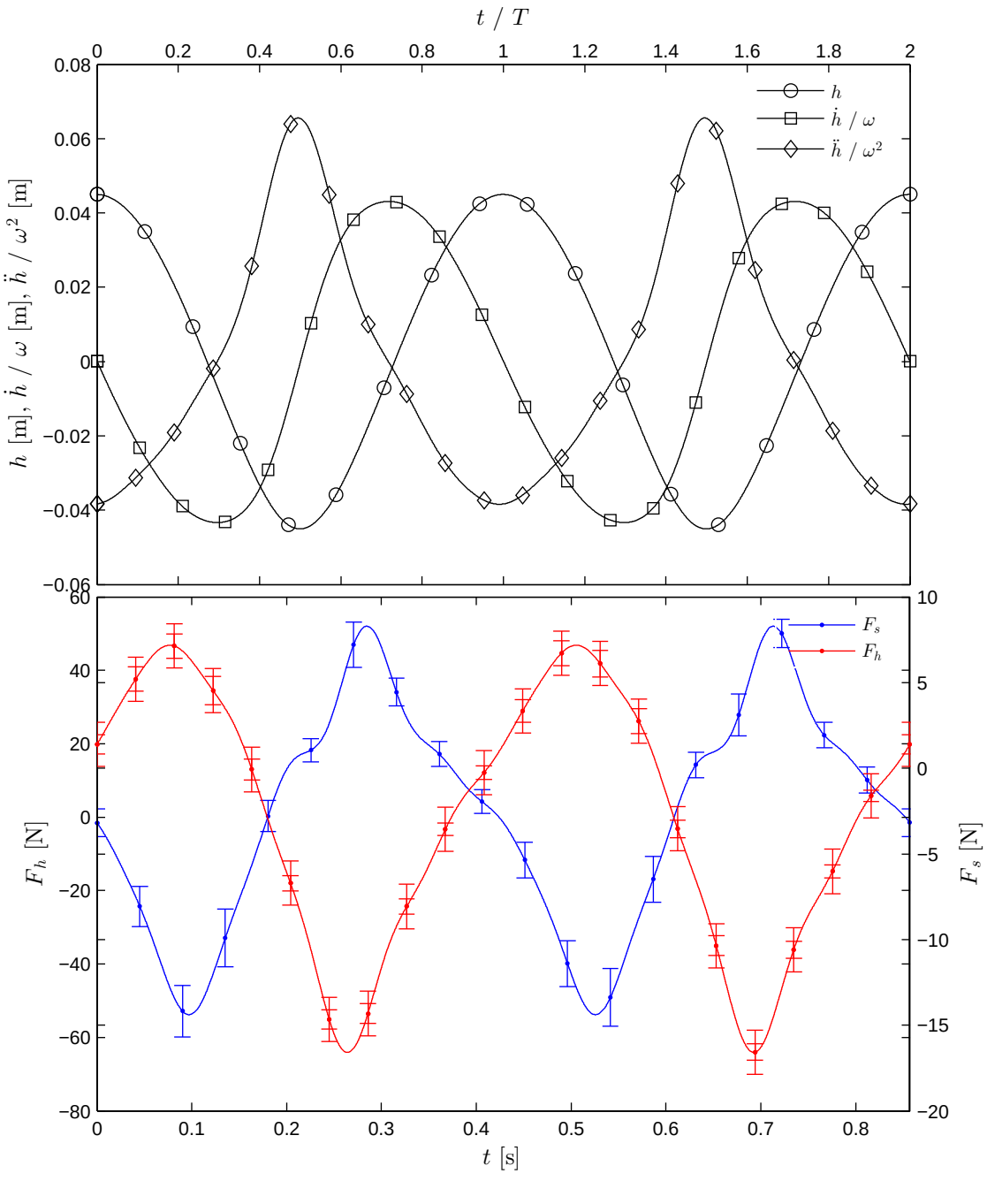

Object: NACA4415		Motion	Water
	$c = 0.060\,\mathrm{m}$ $L = 0.600\,\mathrm{m}$ $\theta = -10°$	$h_0 = 0.045\,\mathrm{m}$ $h^* = 0.75$ $f = 2.81\,\mathrm{Hz}$ $u = 0.00\,\mathrm{m\,s^{-1}}$	$T_w = 7.8\,°\mathrm{C}$ $\rho = 1000\,\mathrm{kg\,m^{-3}}$

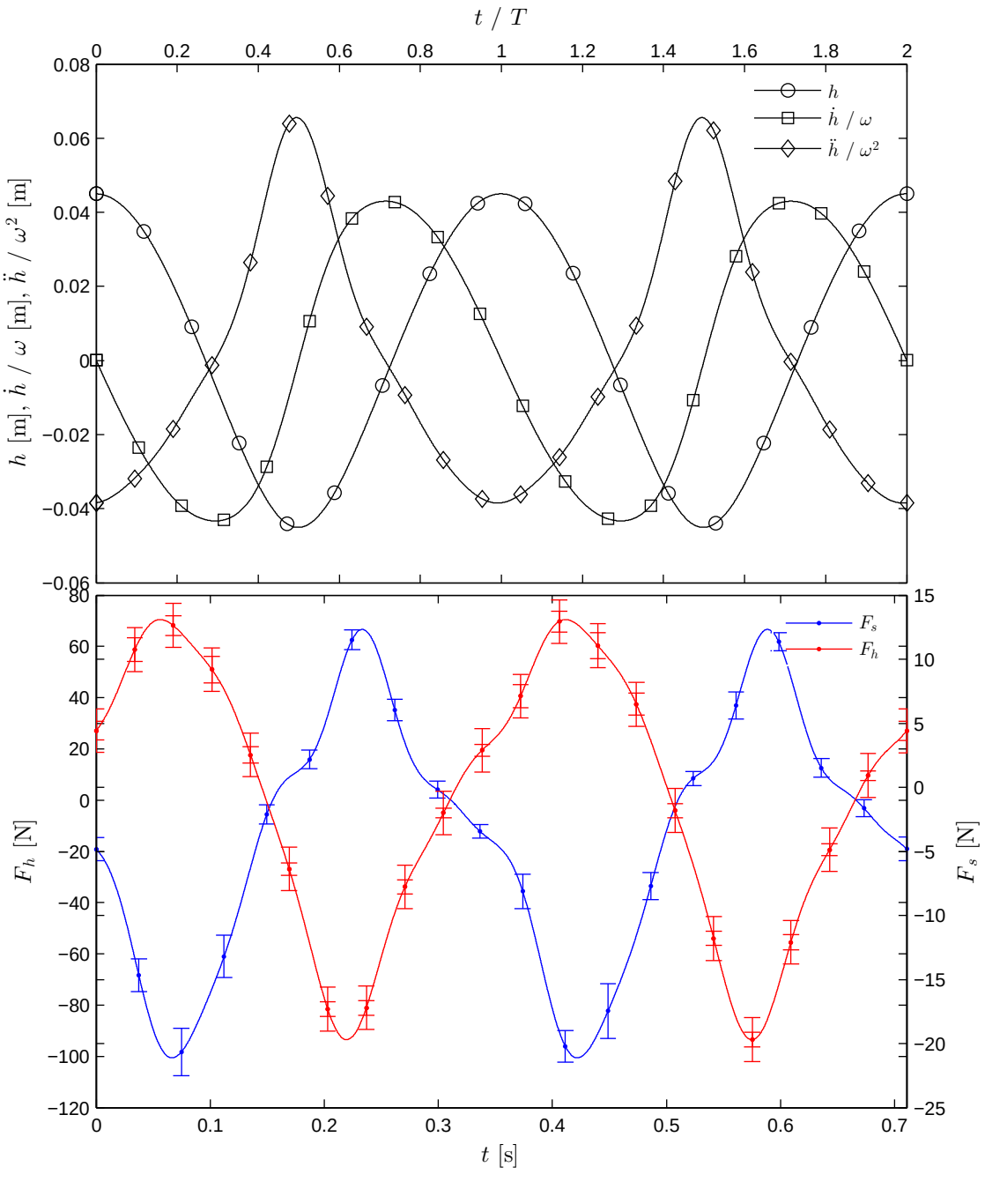

Object: NACA4415		Motion	Water
	$c = 0.060\,\mathrm{m}$ $L = 0.600\,\mathrm{m}$ $\theta = -10°$	$h_0 = 0.045\,\mathrm{m}$ $h^* = 0.75$ $f = 3.29\,\mathrm{Hz}$ $u = 0.00\,\mathrm{m\,s^{-1}}$	$T_w = 7.8\,°\mathrm{C}$ $\rho = 1000\,\mathrm{kg\,m^{-3}}$

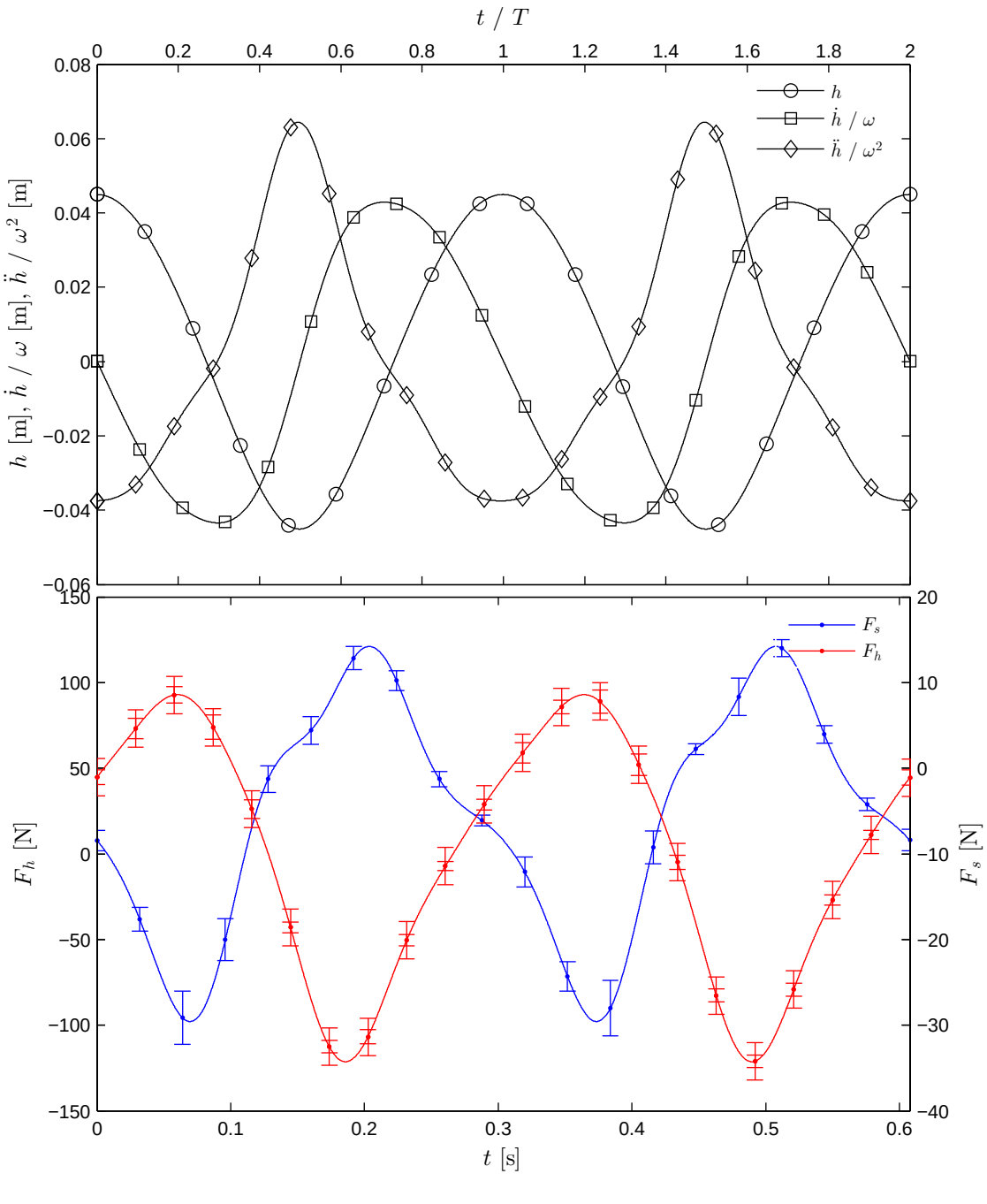

Object: NACA4415		Motion	Water
	$c = 0.060\,\mathrm{m}$ $L = 0.600\,\mathrm{m}$ $\theta = -10°$	$h_0 = 0.045\,\mathrm{m}$ $h^* = 0.75$ $f = 3.77\,\mathrm{Hz}$ $u = 0.00\,\mathrm{m\,s^{-1}}$	$T_w = 7.8\,°\mathrm{C}$ $\rho = 1000\,\mathrm{kg\,m^{-3}}$

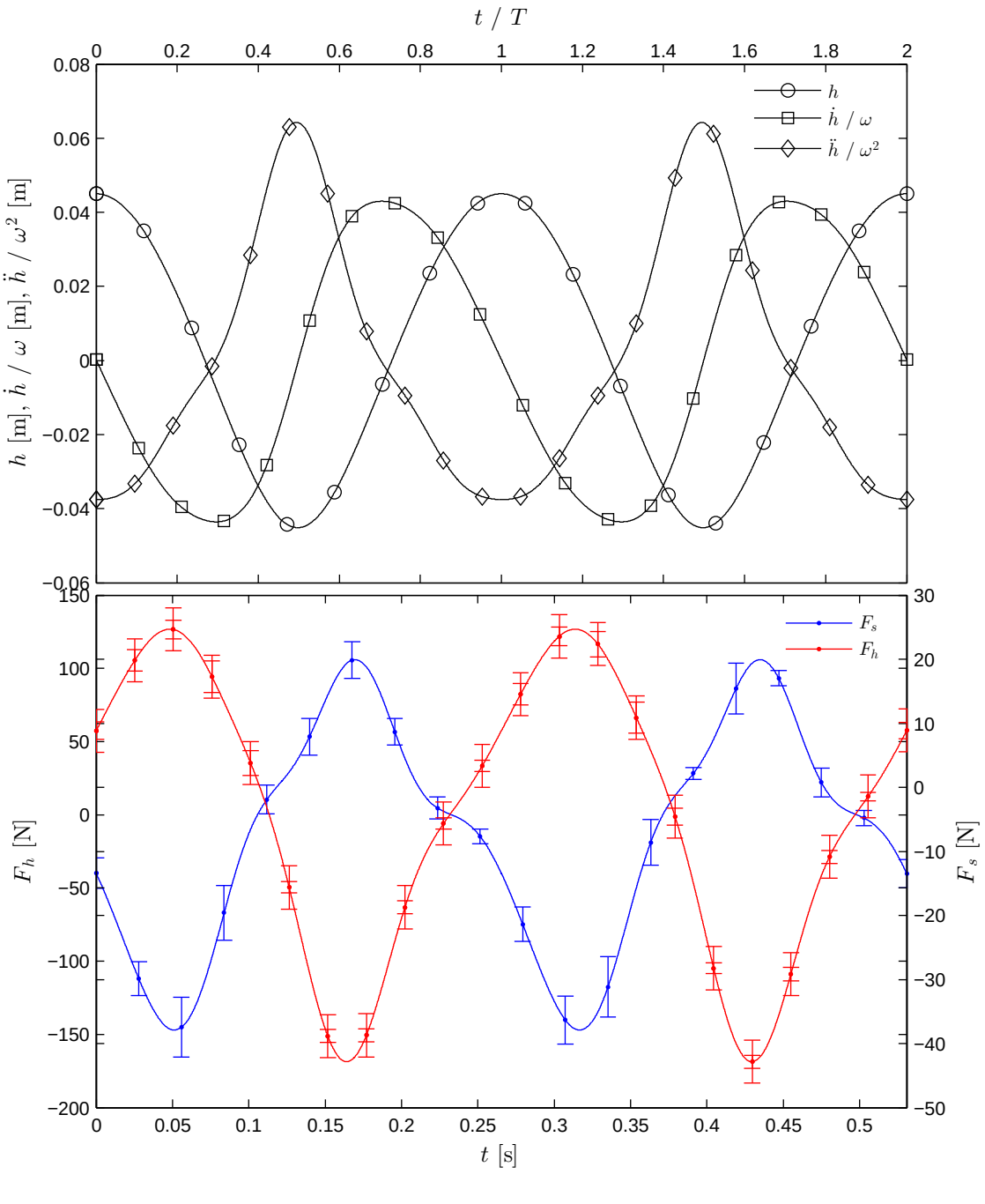

Object: NACA4415		Motion	Water
	$c = 0.060\,\mathrm{m}$ $L = 0.600\,\mathrm{m}$ $\theta = 0°$	$h_0 = 0.045\,\mathrm{m}$ $h^* = 0.75$ $f = 0.80\,\mathrm{Hz}$ $u = 0.00\,\mathrm{m\,s^{-1}}$	$T_w = 14.3\,°\mathrm{C}$ $\rho = 999\,\mathrm{kg\,m^{-3}}$

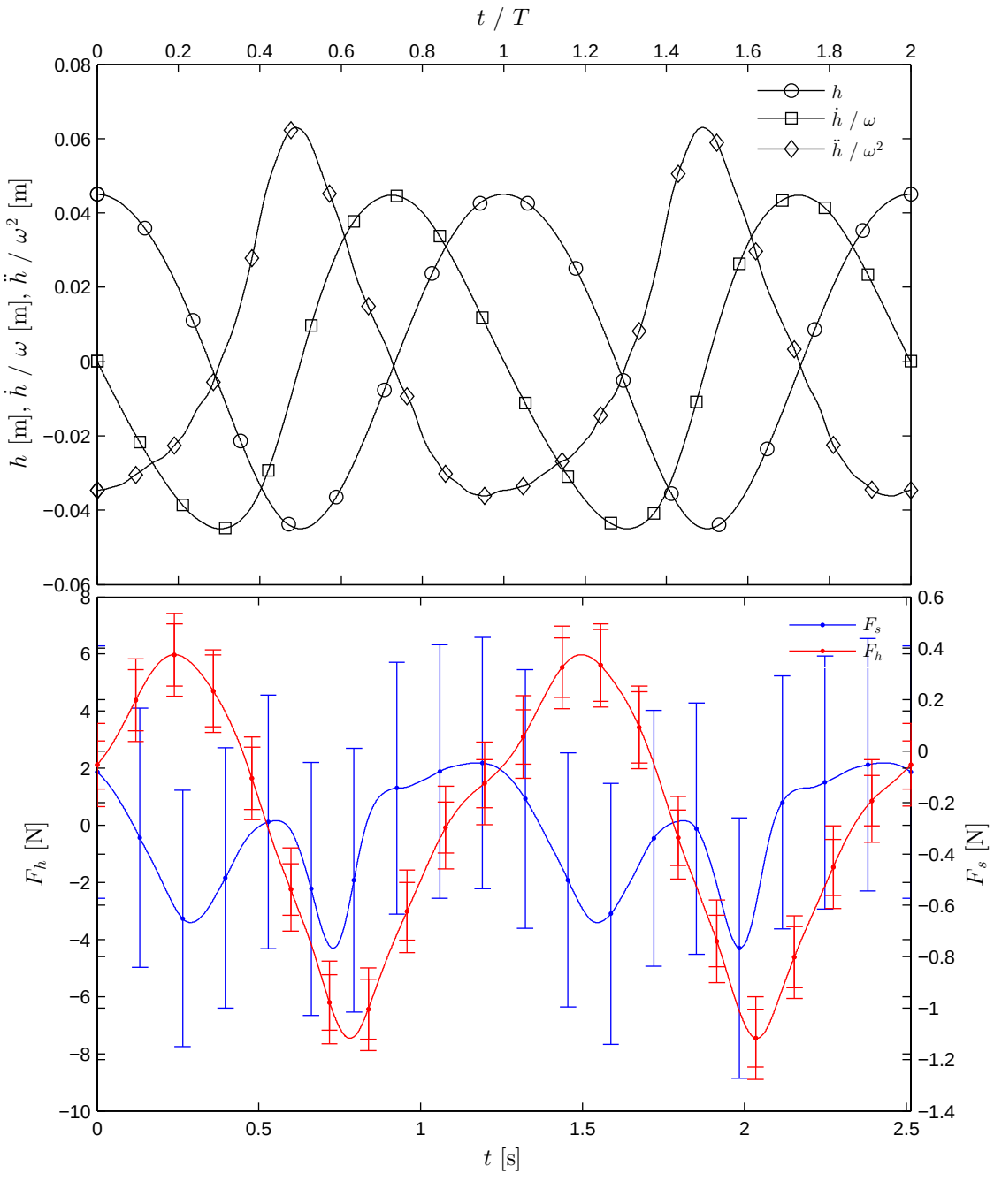

Object: NACA4415		Motion	Water
	$c = 0.060\,\mathrm{m}$ $L = 0.600\,\mathrm{m}$ $\theta = 0°$	$h_0 = 0.045\,\mathrm{m}$ $h^* = 0.75$ $f = 1.32\,\mathrm{Hz}$ $u = 0.00\,\mathrm{m\,s^{-1}}$	$T_w = 14.3\,°\mathrm{C}$ $\rho = 999\,\mathrm{kg\,m^{-3}}$

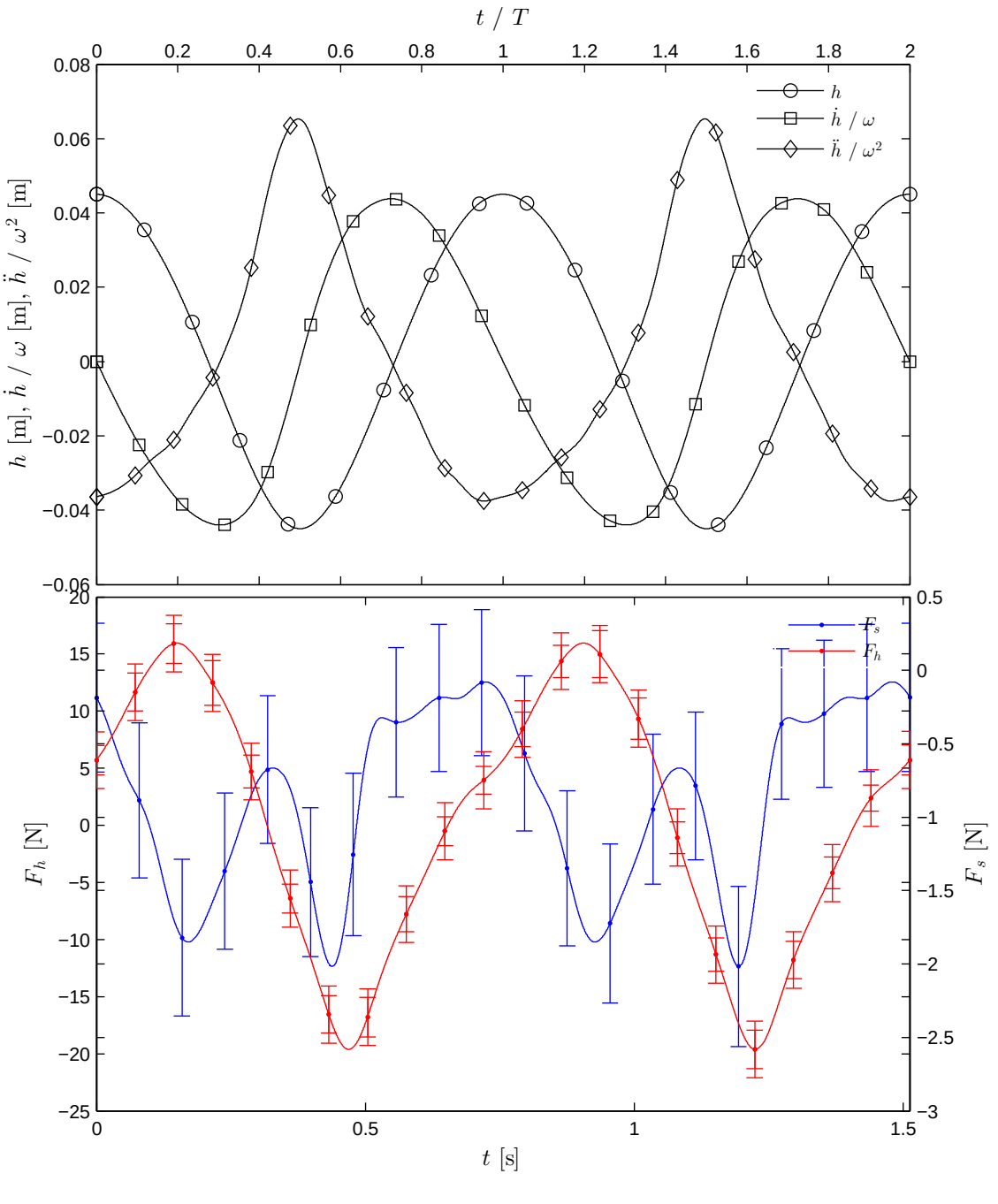

Object: NACA4415		Motion	Water
	$c = 0.060\,\mathrm{m}$ $L = 0.600\,\mathrm{m}$ $\theta = 0°$	$h_0 = 0.045\,\mathrm{m}$ $h^* = 0.75$ $f = 1.80\,\mathrm{Hz}$ $u = 0.00\,\mathrm{m\,s^{-1}}$	$T_w = 14.3\,°\mathrm{C}$ $\rho = 999\,\mathrm{kg\,m^{-3}}$

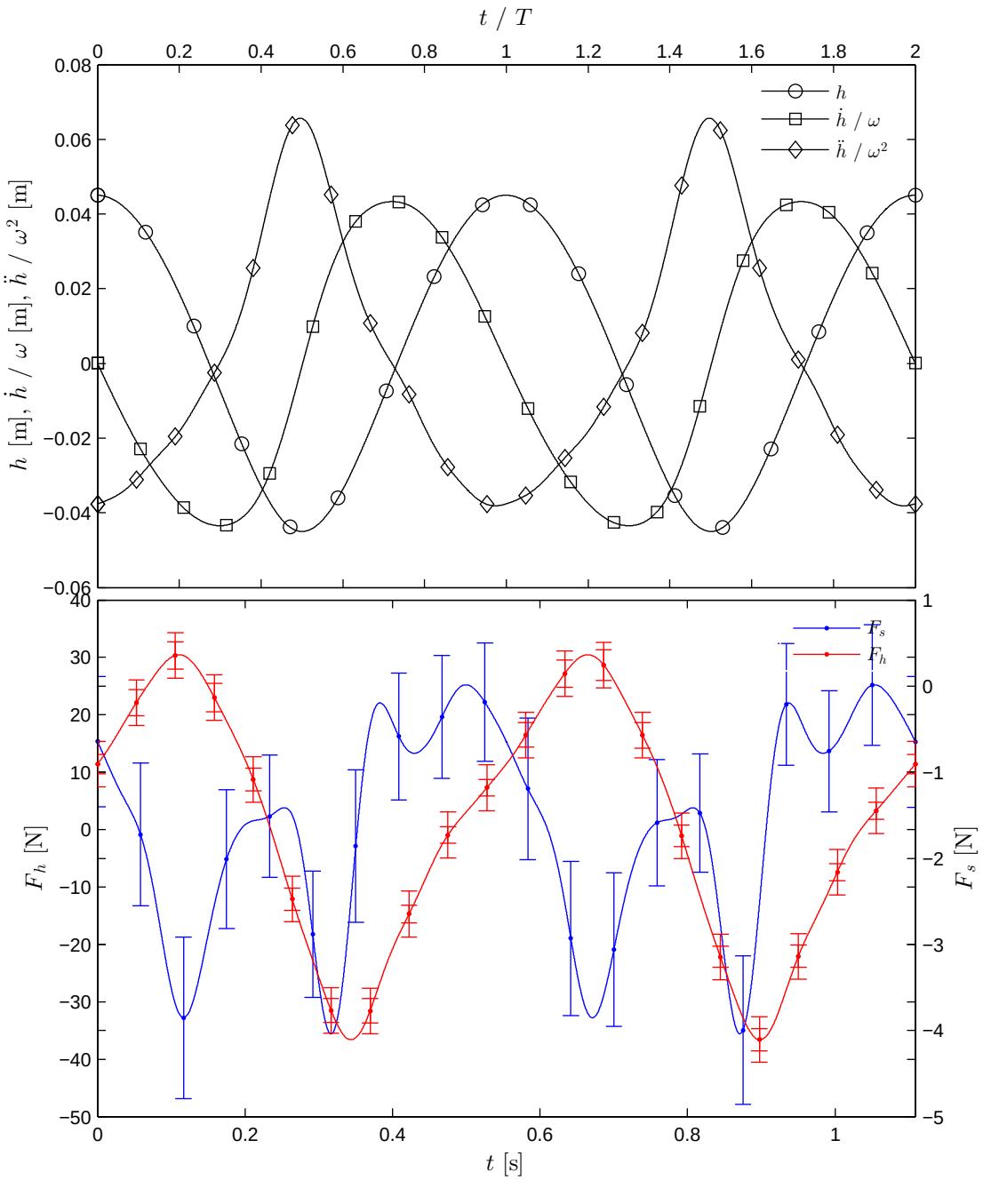

Object: NACA4415		Motion	Water
	$c = 0.060\,\mathrm{m}$ $L = 0.600\,\mathrm{m}$ $\theta = 0°$	$h_0 = 0.045\,\mathrm{m}$ $h^* = 0.75$ $f = 2.29\,\mathrm{Hz}$ $u = 0.00\,\mathrm{m\,s^{-1}}$	$T_w = 14.3\,°\mathrm{C}$ $\rho = 999\,\mathrm{kg\,m^{-3}}$

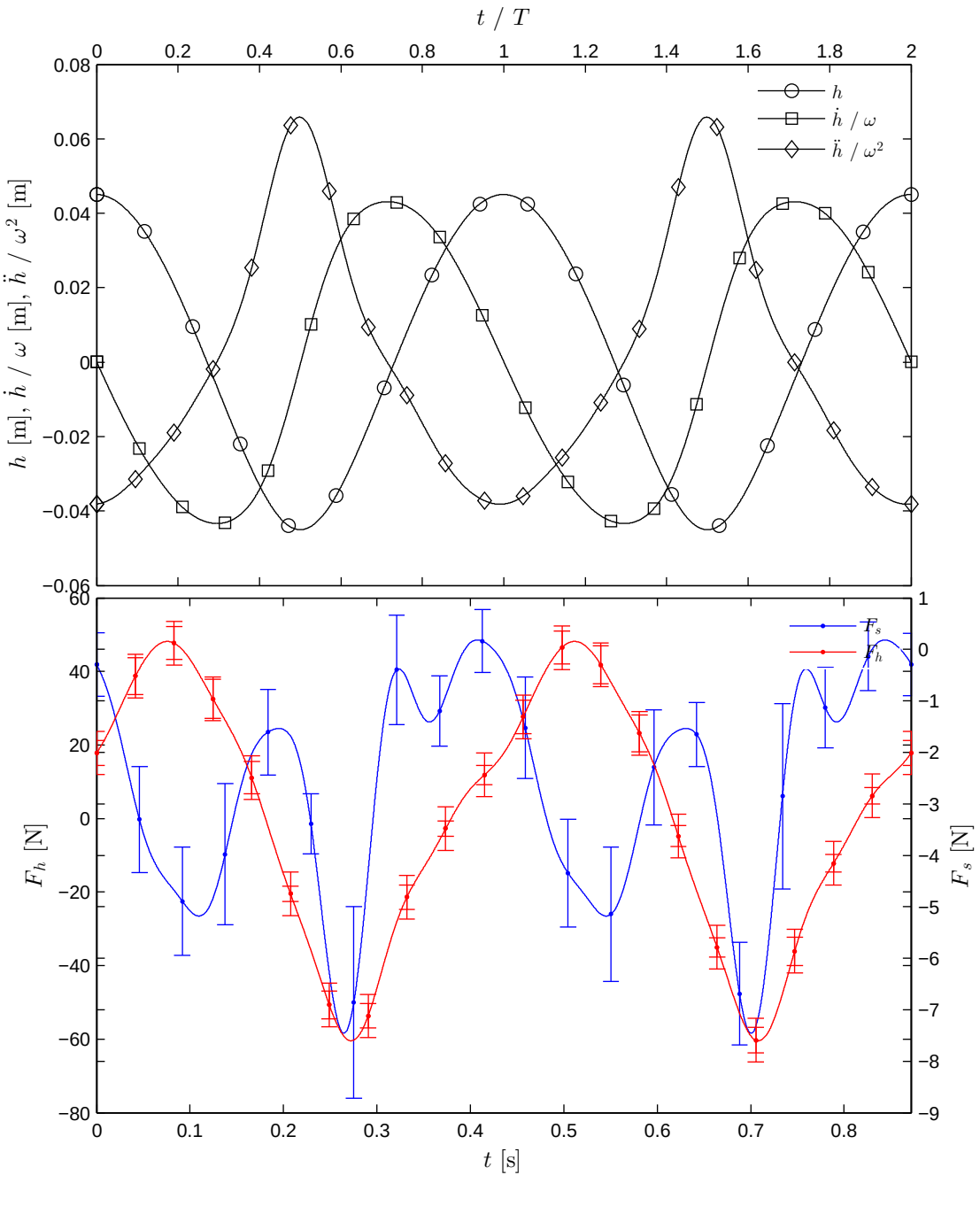

Object: NACA4415		Motion	Water
	$c = 0.060\,\mathrm{m}$ $L = 0.600\,\mathrm{m}$ $\theta = 0°$	$h_0 = 0.045\,\mathrm{m}$ $h^* = 0.75$ $f = 2.78\,\mathrm{Hz}$ $u = 0.00\,\mathrm{m\,s^{-1}}$	$T_w = 14.3\,°\mathrm{C}$ $\rho = 999\,\mathrm{kg\,m^{-3}}$

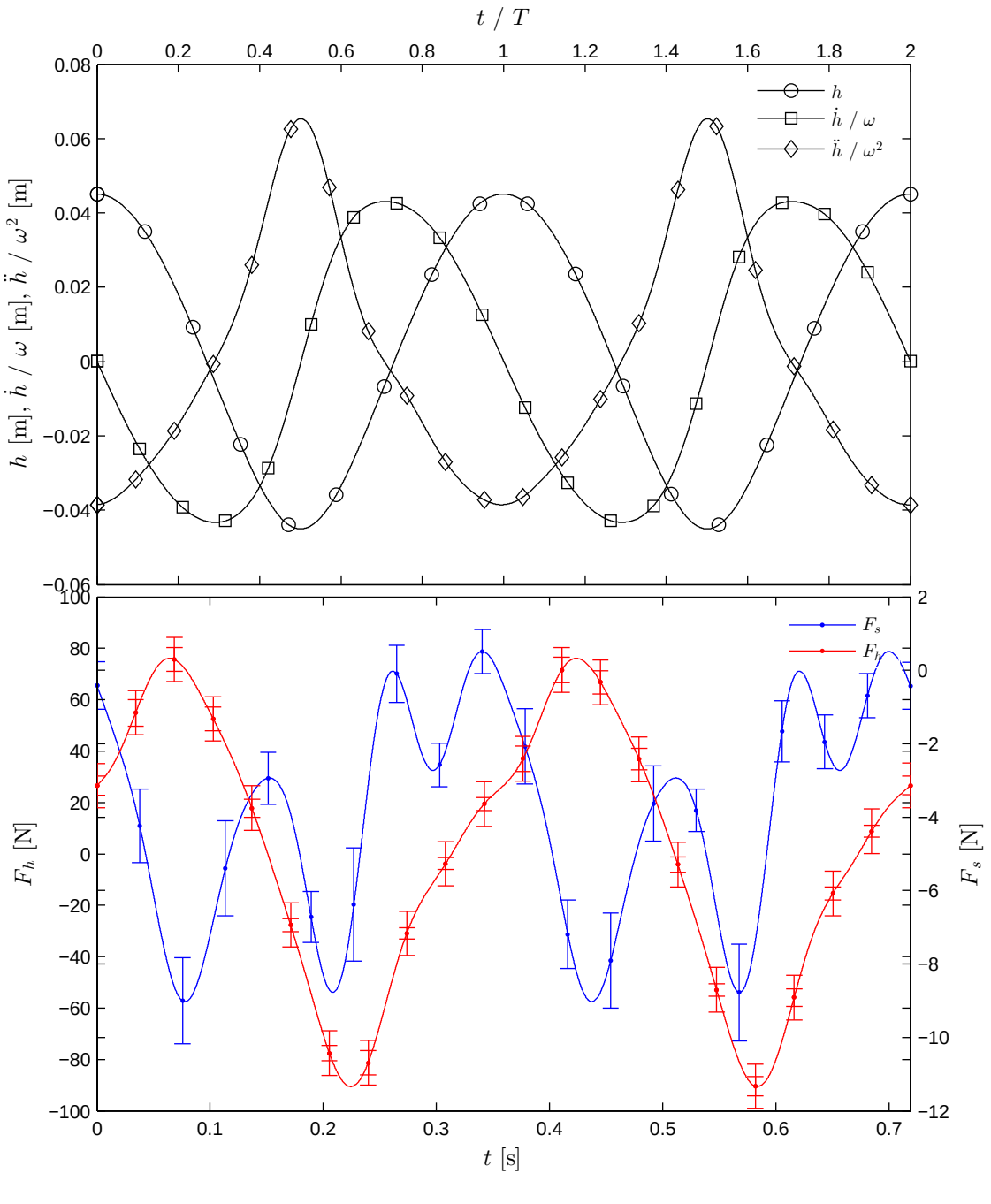

Object: NACA4415		Motion	Water
	$c = 0.060\,\mathrm{m}$ $L = 0.600\,\mathrm{m}$ $\theta = 0°$	$h_0 = 0.045\,\mathrm{m}$ $h^* = 0.75$ $f = 3.31\,\mathrm{Hz}$ $u = 0.00\,\mathrm{m\,s^{-1}}$	$T_w = 14.3\,°\mathrm{C}$ $\rho = 999\,\mathrm{kg\,m^{-3}}$

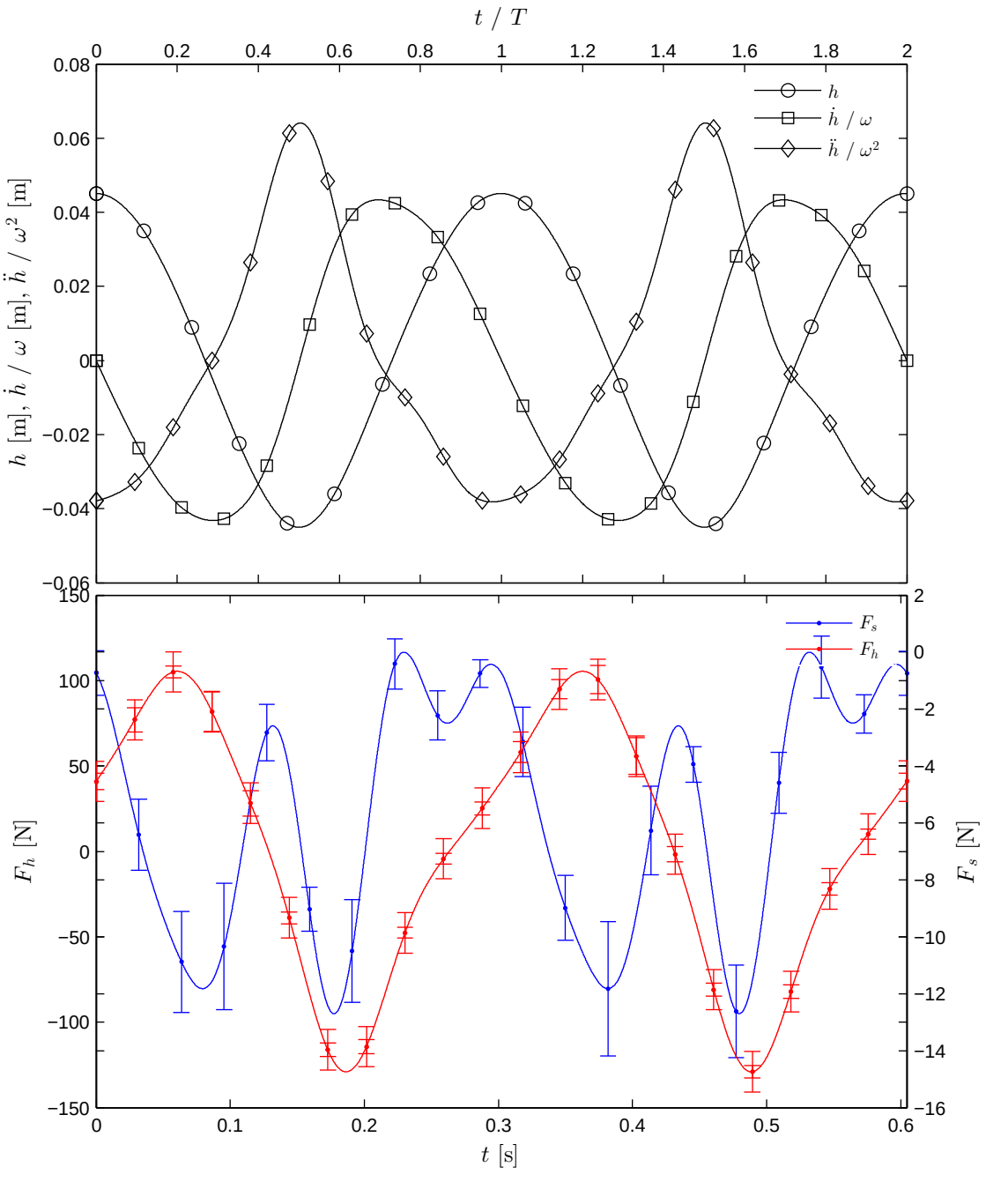

Object: NACA4415		Motion	Water
	$c = 0.060\,\mathrm{m}$ $L = 0.600\,\mathrm{m}$ $\theta = 0°$	$h_0 = 0.045\,\mathrm{m}$ $h^* = 0.75$ $f = 3.82\,\mathrm{Hz}$ $u = 0.00\,\mathrm{m\,s^{-1}}$	$T_w = 14.3\,°\mathrm{C}$ $\rho = 999\,\mathrm{kg\,m^{-3}}$

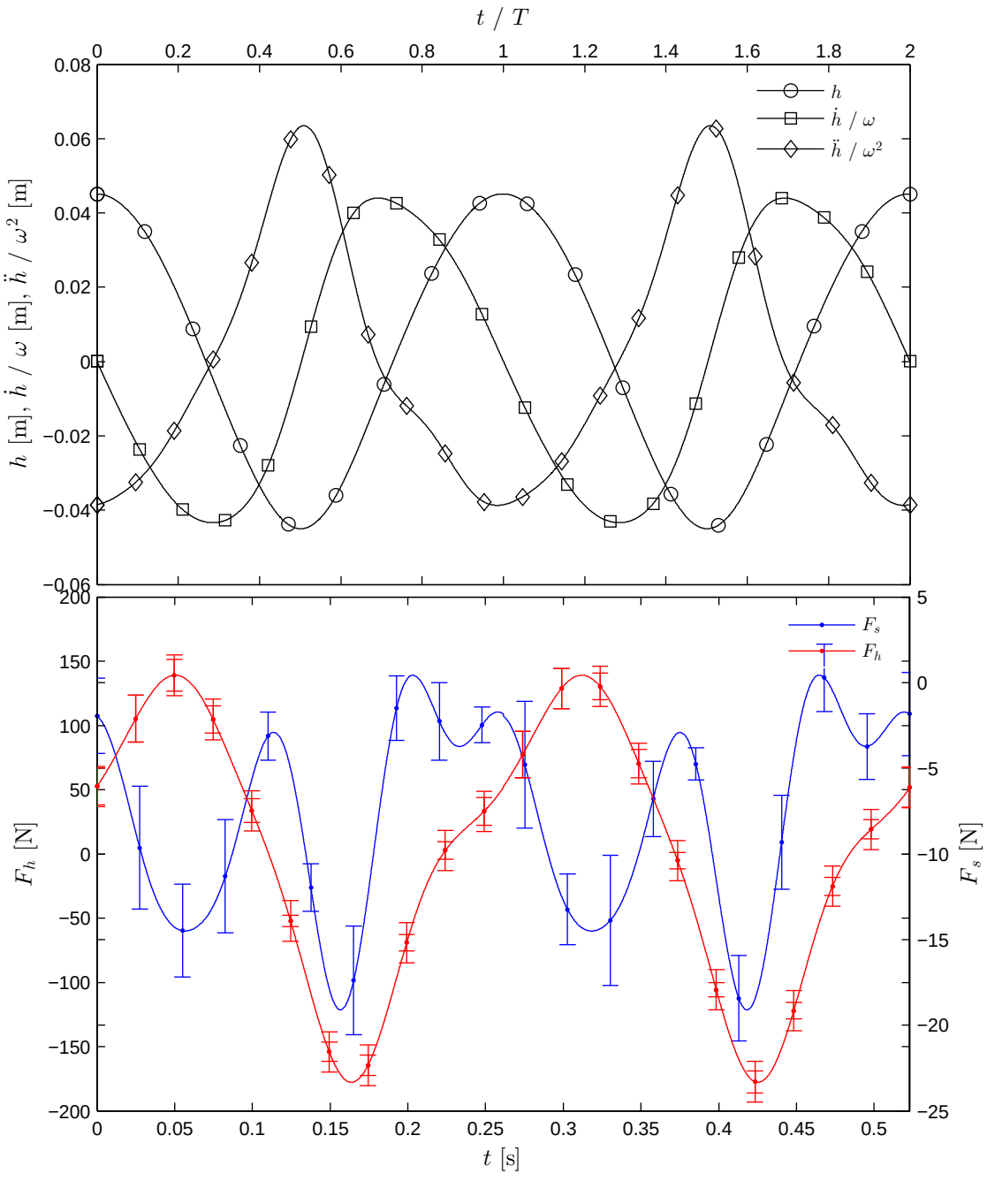

Object: NACA4415		Motion	Water
	$c = 0.060\,\mathrm{m}$ $L = 0.600\,\mathrm{m}$ $\theta = 10°$	$h_0 = 0.045\,\mathrm{m}$ $h^* = 0.75$ $f = 0.78\,\mathrm{Hz}$ $u = 0.00\,\mathrm{m\,s^{-1}}$	$T_w = 7.8\,°\mathrm{C}$ $\rho = 1000\,\mathrm{kg\,m^{-3}}$

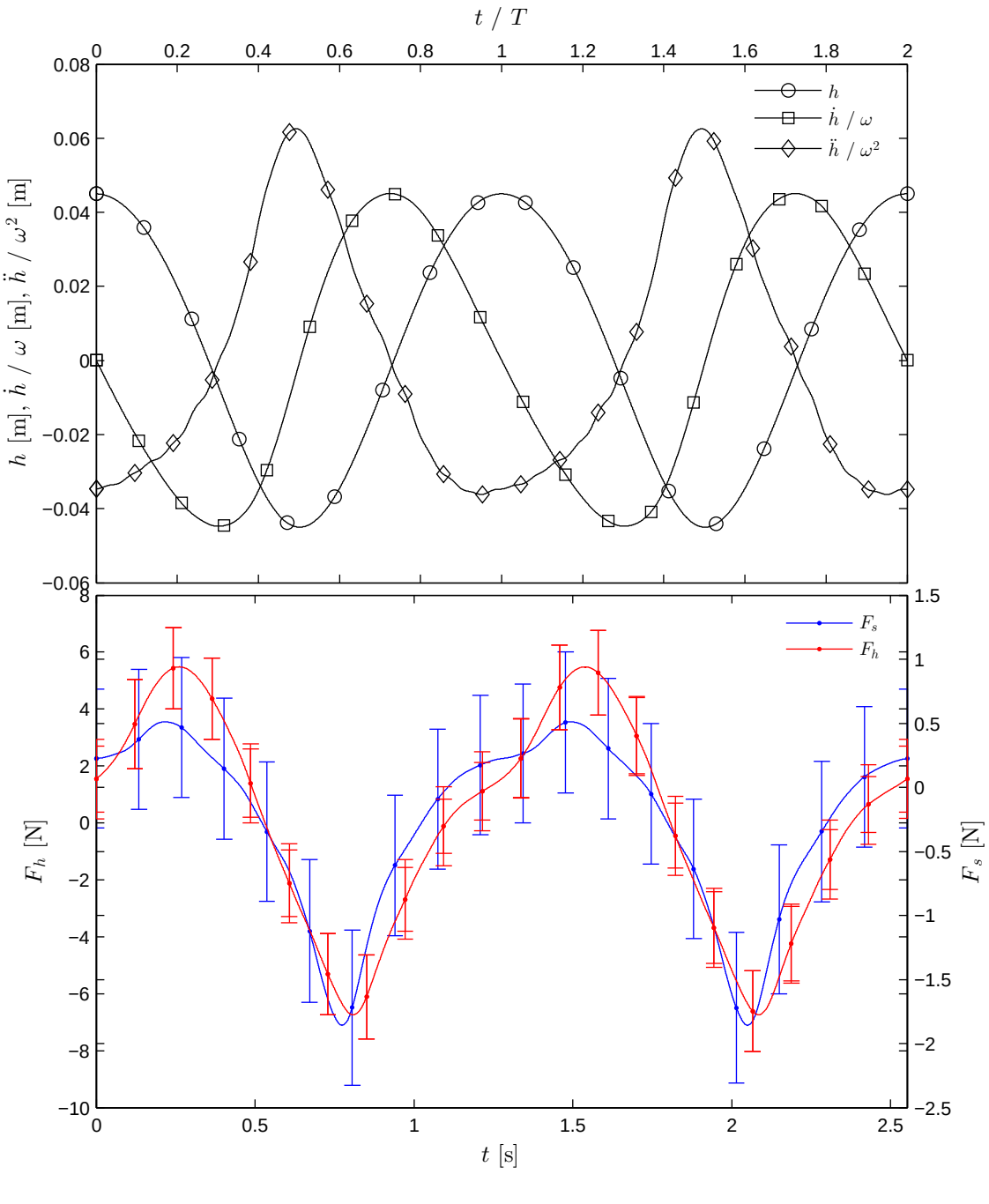

Object: NACA4415		Motion	Water
	$c = 0.060\,\mathrm{m}$ $L = 0.600\,\mathrm{m}$ $\theta = 10°$	$h_0 = 0.045\,\mathrm{m}$ $h^* = 0.75$ $f = 1.29\,\mathrm{Hz}$ $u = 0.00\,\mathrm{m\,s^{-1}}$	$T_w = 7.8\,°\mathrm{C}$ $\rho = 1000\,\mathrm{kg\,m^{-3}}$

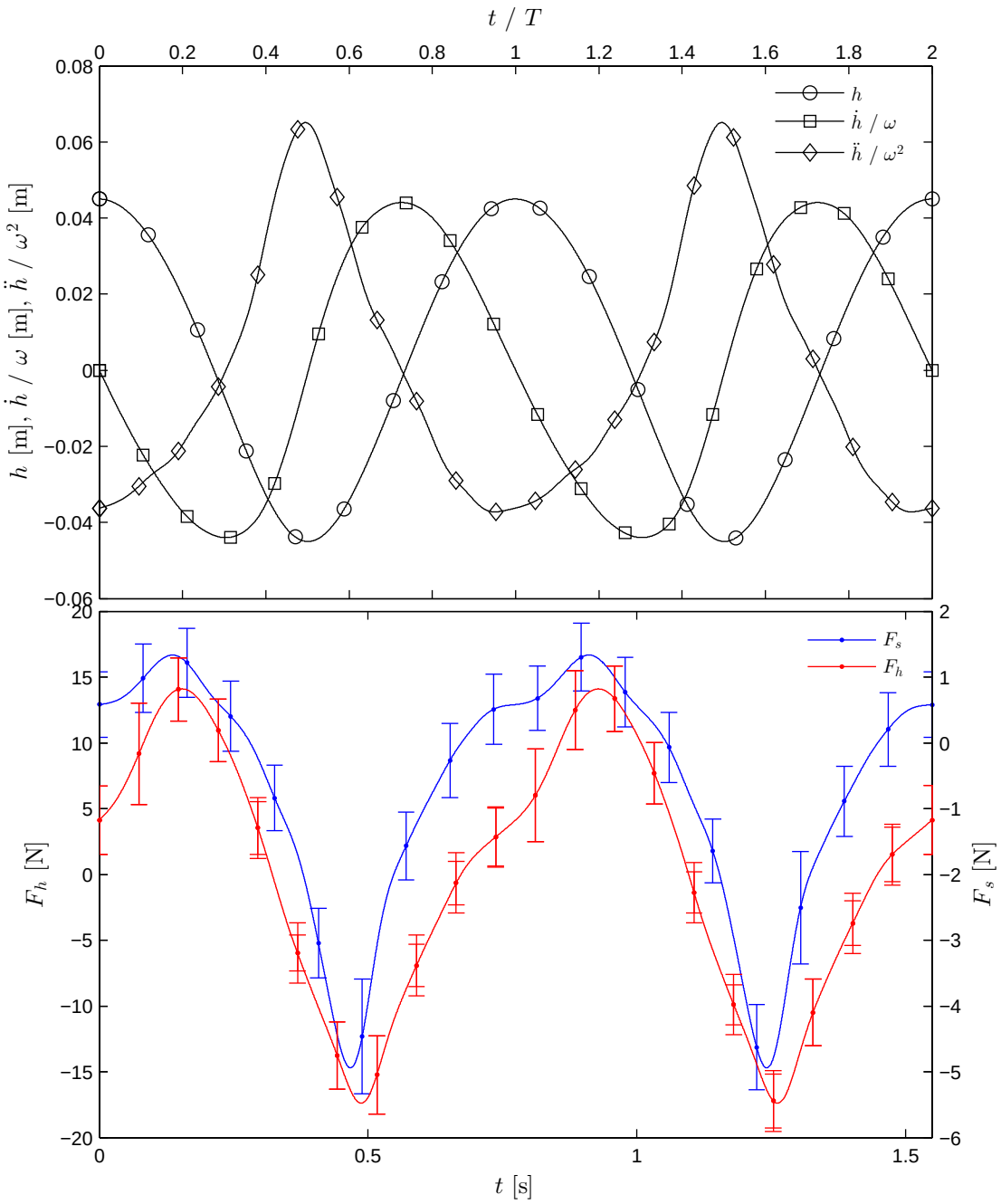

Object: NACA4415		Motion	Water
	$c = 0.060\,\mathrm{m}$ $L = 0.600\,\mathrm{m}$ $\theta = 10°$	$h_0 = 0.045\,\mathrm{m}$ $h^* = 0.75$ $f = 1.83\,\mathrm{Hz}$ $u = 0.00\,\mathrm{m\,s^{-1}}$	$T_w = 7.8\,°\mathrm{C}$ $\rho = 1000\,\mathrm{kg\,m^{-3}}$

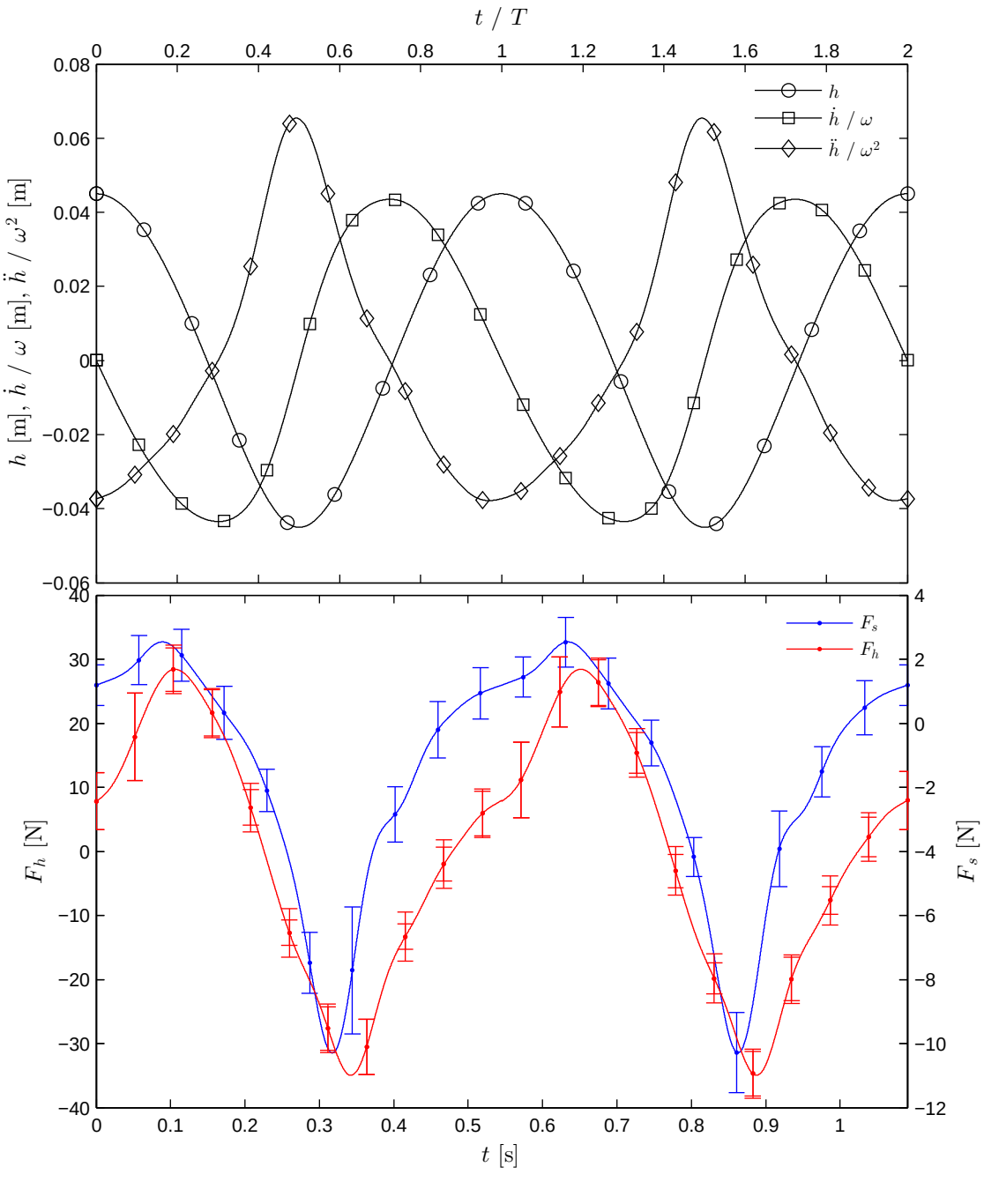

Object: NACA4415		Motion	Water
	$c = 0.060\,\mathrm{m}$ $L = 0.600\,\mathrm{m}$ $\theta = 10°$	$h_0 = 0.045\,\mathrm{m}$ $h^* = 0.75$ $f = 2.30\,\mathrm{Hz}$ $u = 0.00\,\mathrm{m\,s^{-1}}$	$T_w = 7.8\,°\mathrm{C}$ $\rho = 1000\,\mathrm{kg\,m^{-3}}$

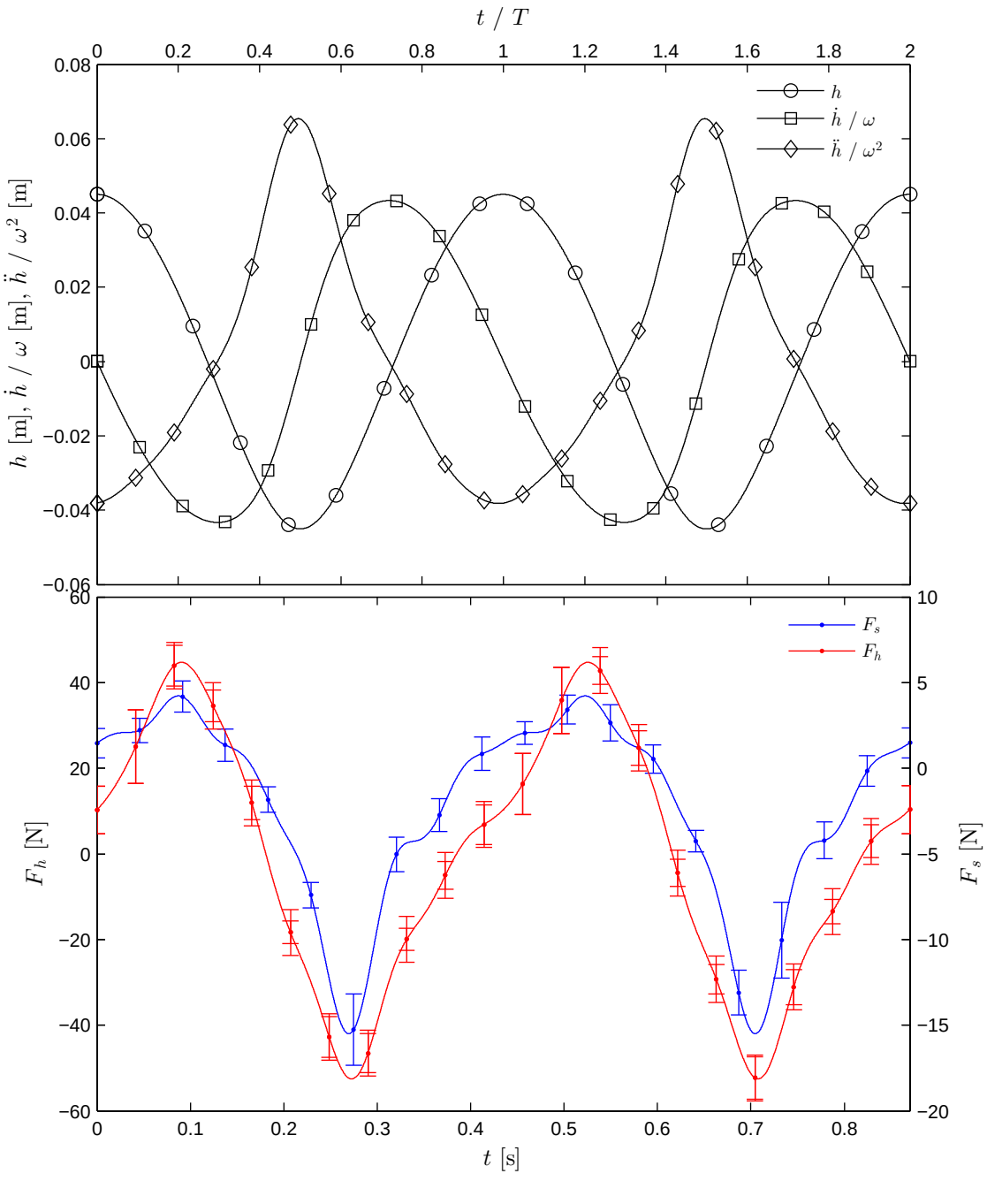

Object: NACA4415		Motion	Water
	$c = 0.060\,\mathrm{m}$ $L = 0.600\,\mathrm{m}$ $\theta = 10°$	$h_0 = 0.045\,\mathrm{m}$ $h^* = 0.75$ $f = 2.77\,\mathrm{Hz}$ $u = 0.00\,\mathrm{m\,s^{-1}}$	$T_w = 7.8\,°\mathrm{C}$ $\rho = 1000\,\mathrm{kg\,m^{-3}}$

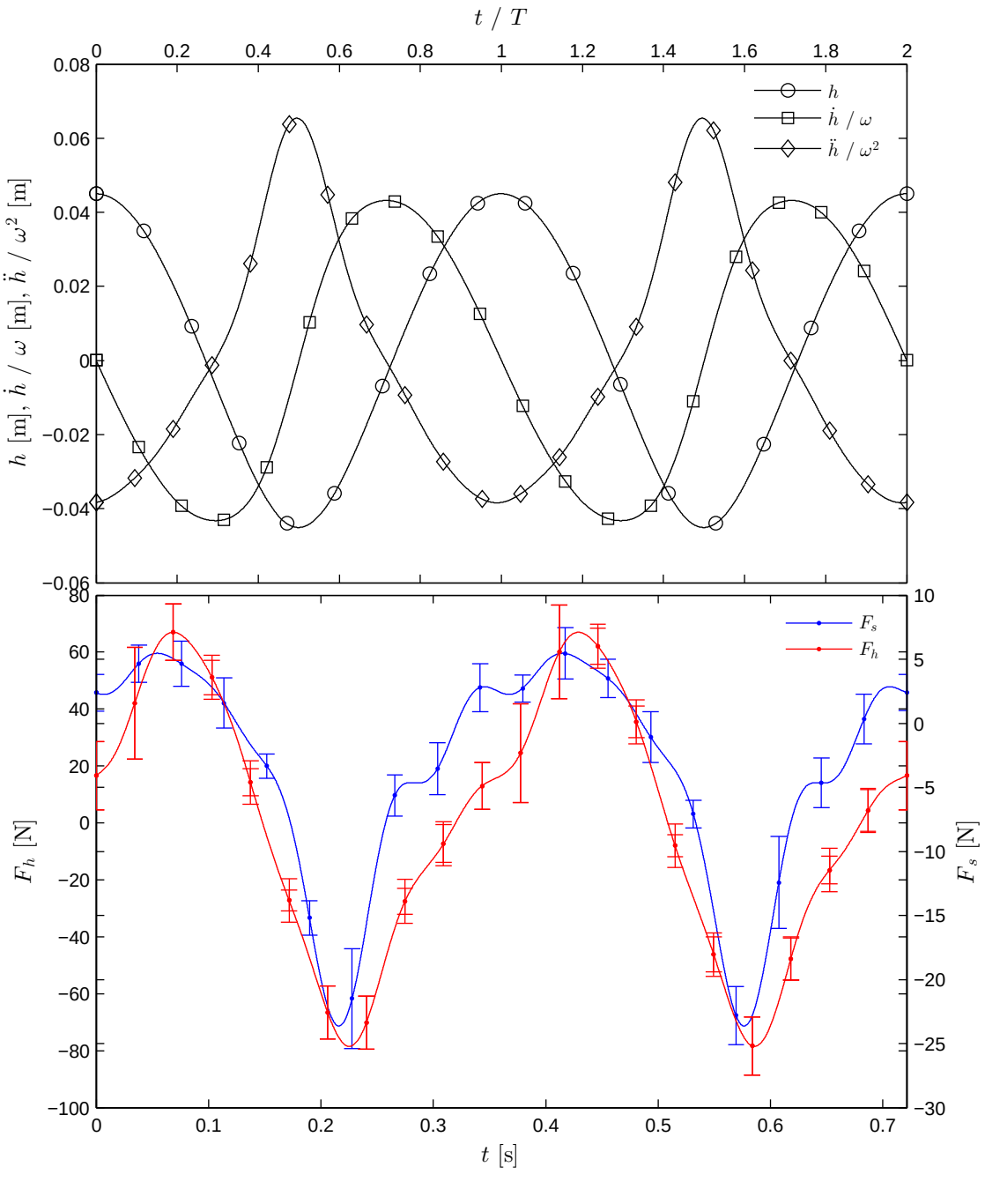

Object: NACA4415		Motion	Water
	$c = 0.060\,\mathrm{m}$ $L = 0.600\,\mathrm{m}$ $\theta = 10°$	$h_0 = 0.045\,\mathrm{m}$ $h^* = 0.75$ $f = 3.27\,\mathrm{Hz}$ $u = 0.00\,\mathrm{m\,s^{-1}}$	$T_w = 7.8\,°\mathrm{C}$ $\rho = 1000\,\mathrm{kg\,m^{-3}}$

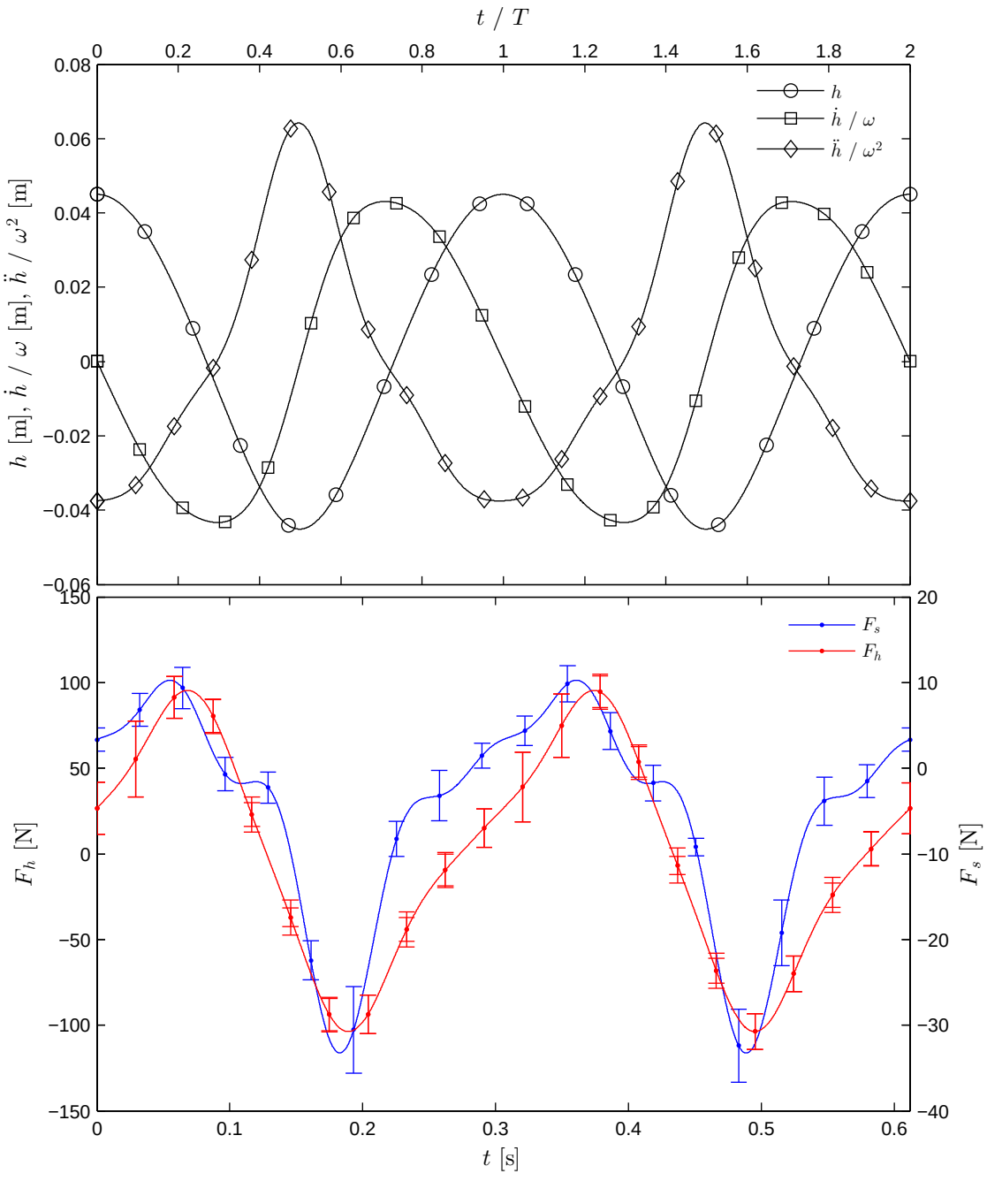

Object: NACA4415		Motion	Water
	$c = 0.060\,\mathrm{m}$ $L = 0.600\,\mathrm{m}$ $\theta = 10°$	$h_0 = 0.045\,\mathrm{m}$ $h^* = 0.75$ $f = 3.85\,\mathrm{Hz}$ $u = 0.00\,\mathrm{m\,s^{-1}}$	$T_w = 7.8\,°\mathrm{C}$ $\rho = 1000\,\mathrm{kg\,m^{-3}}$

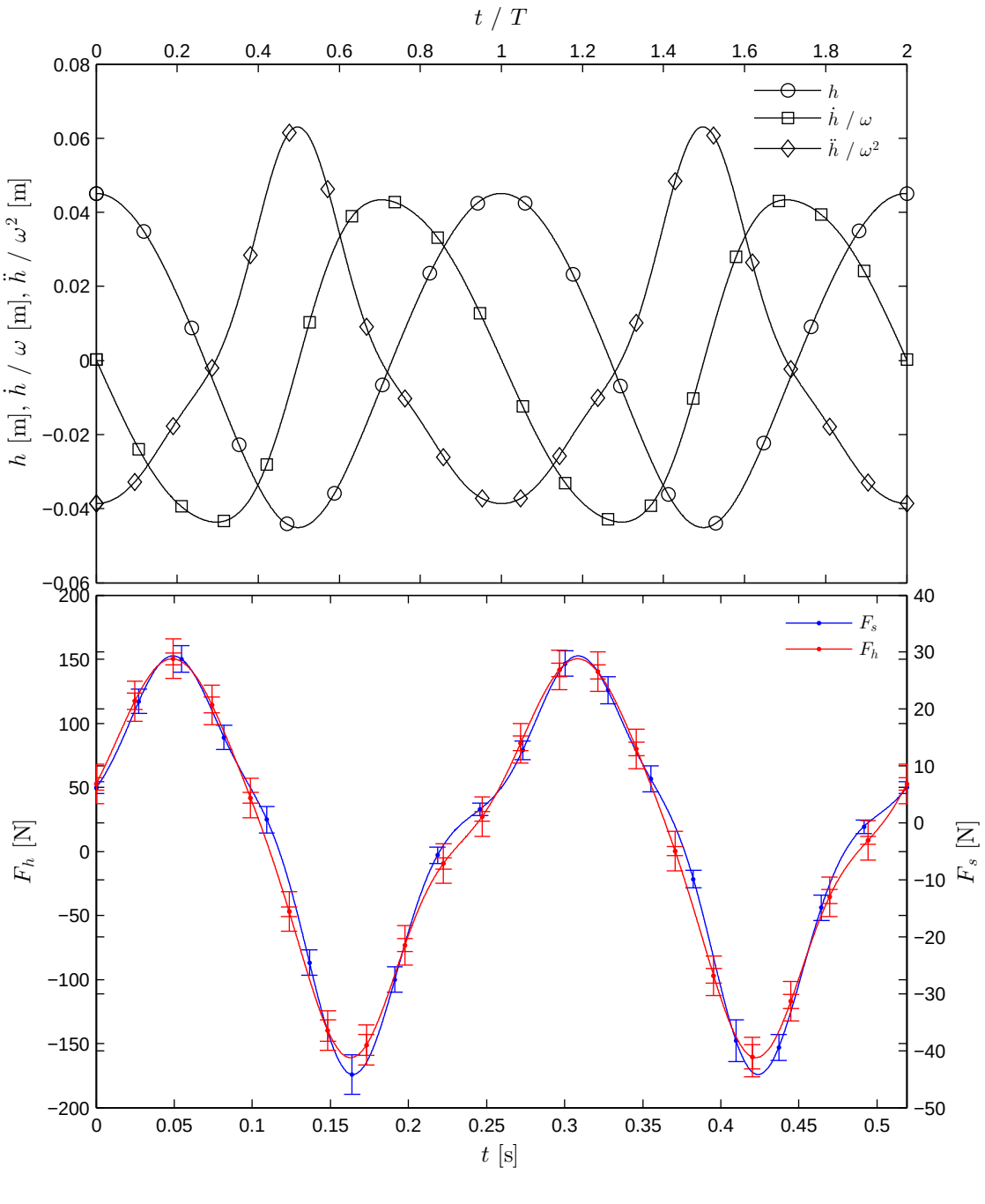

Object: NACA4415		Motion	Water
	$c = 0.060\,\mathrm{m}$ $L = 0.600\,\mathrm{m}$ $\theta = 40°$	$h_0 = 0.045\,\mathrm{m}$ $h^* = 0.75$ $f = 0.78\,\mathrm{Hz}$ $u = 0.00\,\mathrm{m\,s^{-1}}$	$T_w = 7.8\,°\mathrm{C}$ $\rho = 1000\,\mathrm{kg\,m^{-3}}$

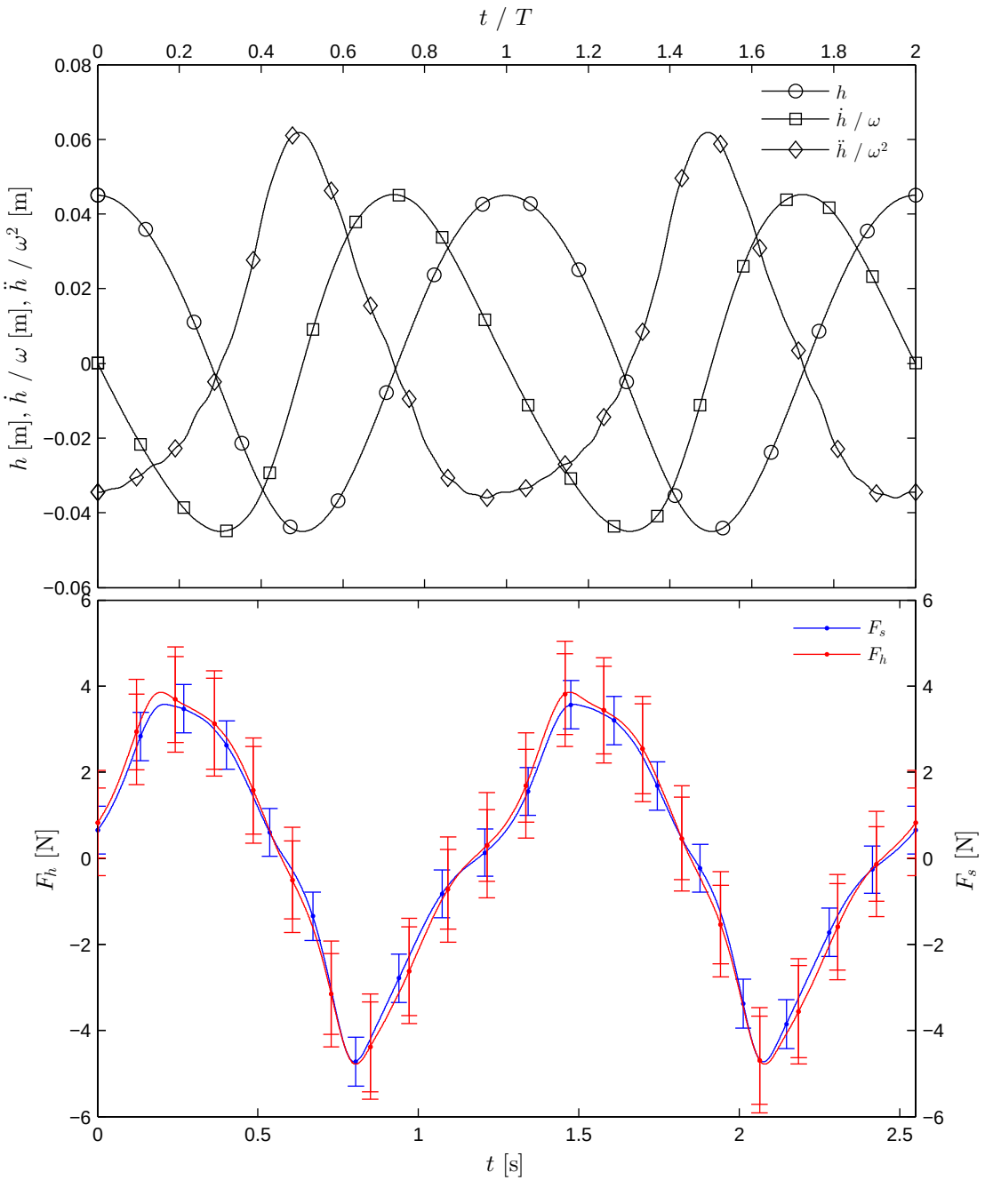

Object: NACA4415		Motion	Water
	$c = 0.060\,\mathrm{m}$ $L = 0.600\,\mathrm{m}$ $\theta = 40°$	$h_0 = 0.045\,\mathrm{m}$ $h^* = 0.75$ $f = 1.26\,\mathrm{Hz}$ $u = 0.00\,\mathrm{m\,s^{-1}}$	$T_w = 7.8\,°\mathrm{C}$ $\rho = 1000\,\mathrm{kg\,m^{-3}}$

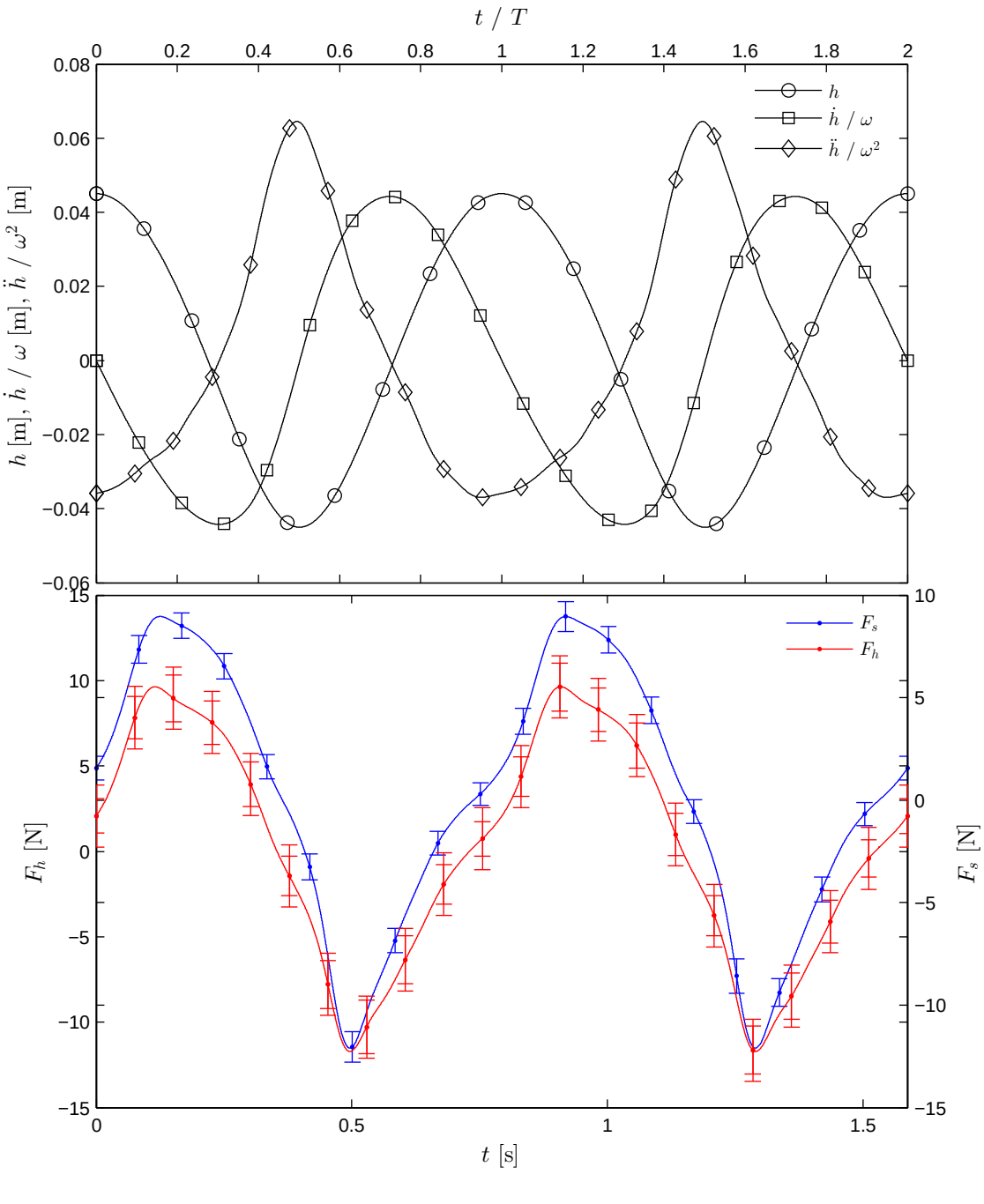

Object: NACA4415		Motion	Water
	$c = 0.060\,\mathrm{m}$ $L = 0.600\,\mathrm{m}$ $\theta = 40°$	$h_0 = 0.045\,\mathrm{m}$ $h^* = 0.75$ $f = 1.74\,\mathrm{Hz}$ $u = 0.00\,\mathrm{m\,s^{-1}}$	$T_w = 7.8\,°\mathrm{C}$ $\rho = 1000\,\mathrm{kg\,m^{-3}}$

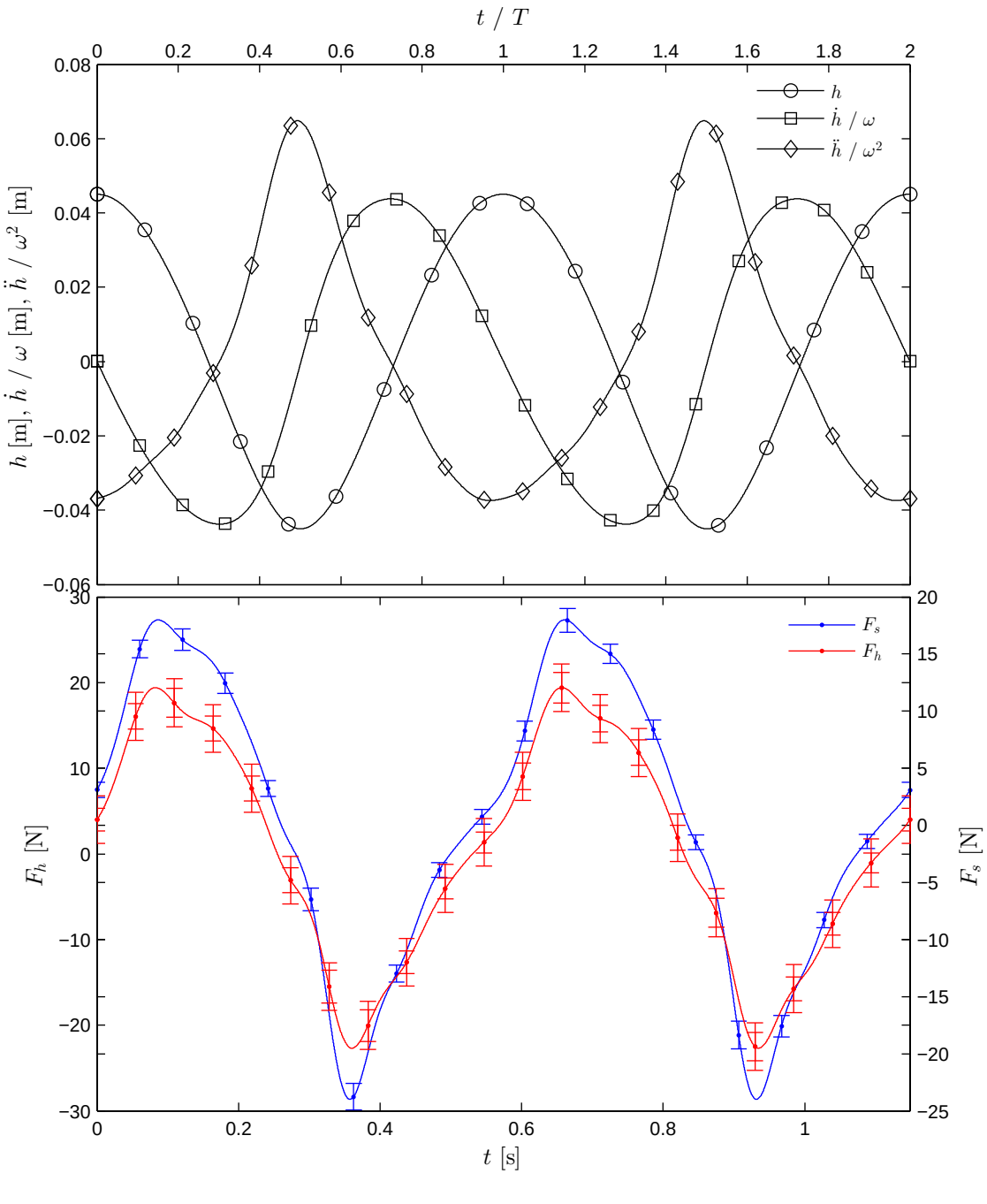

Object: NACA4415		Motion	Water
	$c = 0.060\,\mathrm{m}$ $L = 0.600\,\mathrm{m}$ $\theta = 40°$	$h_0 = 0.045\,\mathrm{m}$ $h^* = 0.75$ $f = 2.29\,\mathrm{Hz}$ $u = 0.00\,\mathrm{m\,s^{-1}}$	$T_w = 7.8\,°\mathrm{C}$ $\rho = 1000\,\mathrm{kg\,m^{-3}}$

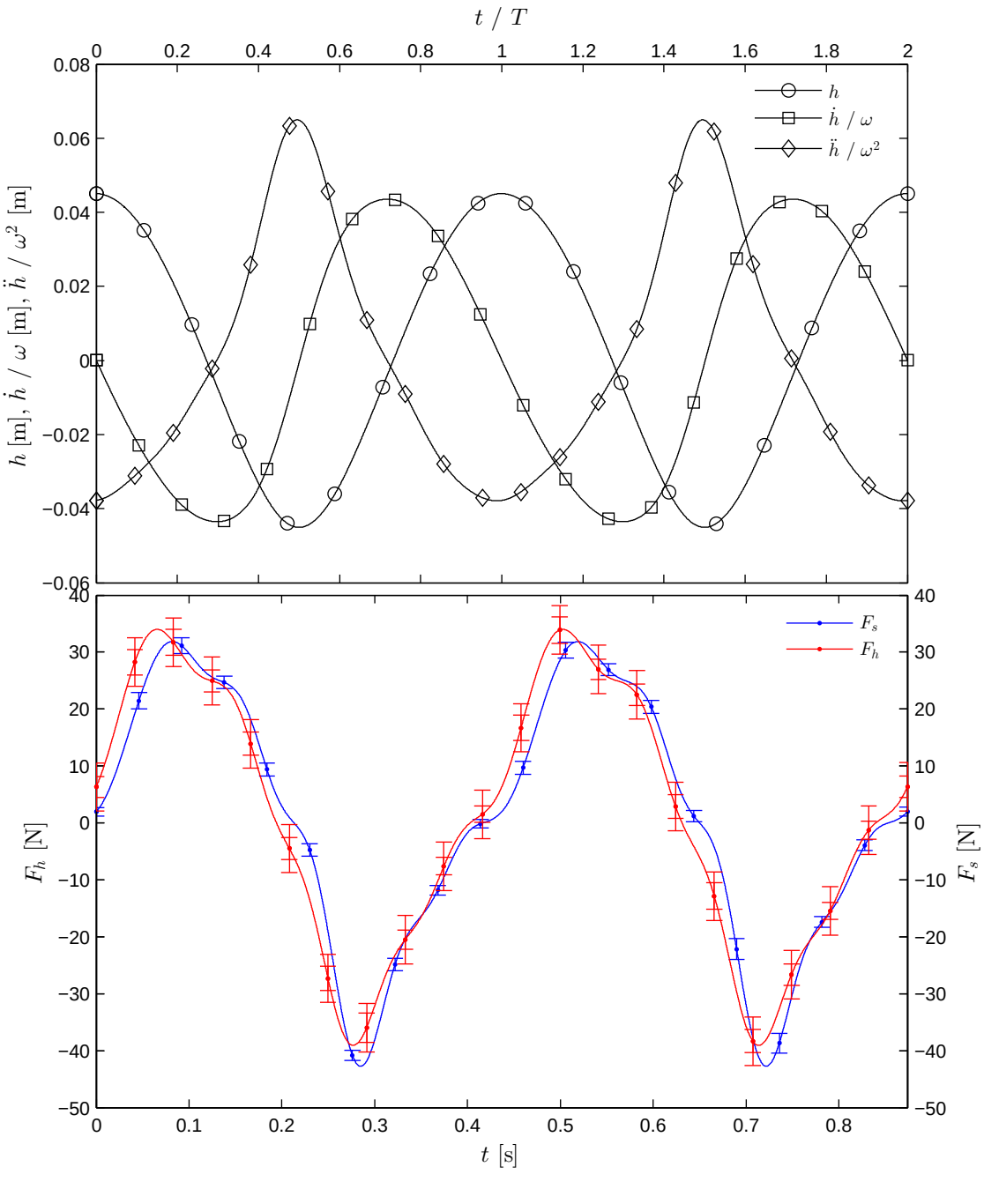

Object: NACA4415		Motion	Water
	$c = 0.060\,\mathrm{m}$ $L = 0.600\,\mathrm{m}$ $\theta = 40°$	$h_0 = 0.045\,\mathrm{m}$ $h^* = 0.75$ $f = 2.78\,\mathrm{Hz}$ $u = 0.00\,\mathrm{m\,s^{-1}}$	$T_w = 7.8\,°\mathrm{C}$ $\rho = 1000\,\mathrm{kg\,m^{-3}}$

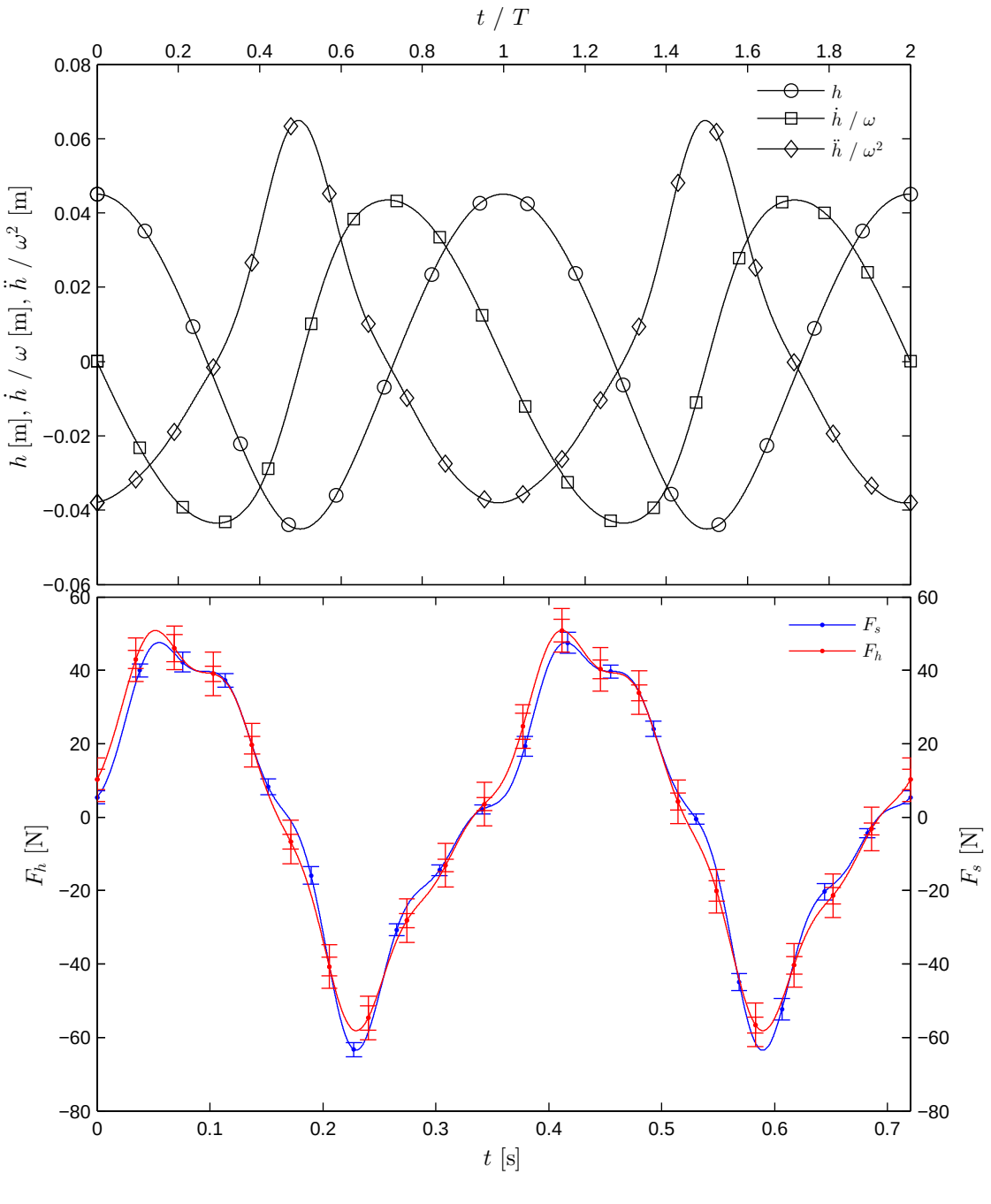

Object: NACA4415		Motion	Water
	$c = 0.060\,\mathrm{m}$ $L = 0.600\,\mathrm{m}$ $\theta = 40°$	$h_0 = 0.045\,\mathrm{m}$ $h^* = 0.75$ $f = 3.27\,\mathrm{Hz}$ $u = 0.00\,\mathrm{m\,s^{-1}}$	$T_w = 7.8\,°\mathrm{C}$ $\rho = 1000\,\mathrm{kg\,m^{-3}}$

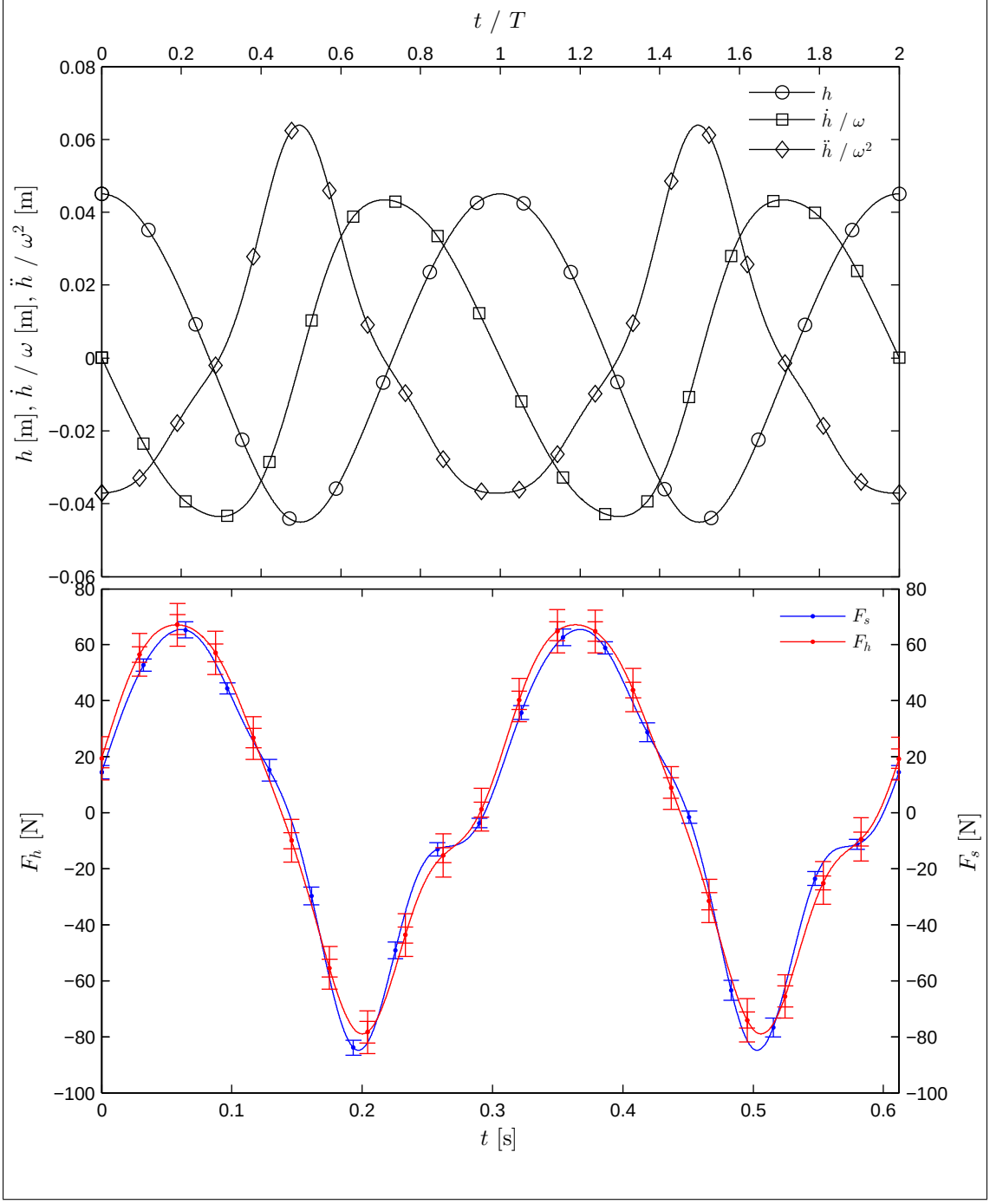

Object: NACA4415		Motion	Water
	$c = 0.060\,\mathrm{m}$ $L = 0.600\,\mathrm{m}$ $\theta = 40°$	$h_0 = 0.045\,\mathrm{m}$ $h^* = 0.75$ $f = 3.75\,\mathrm{Hz}$ $u = 0.00\,\mathrm{m\,s^{-1}}$	$T_w = 7.8\,°\mathrm{C}$ $\rho = 1000\,\mathrm{kg\,m^{-3}}$

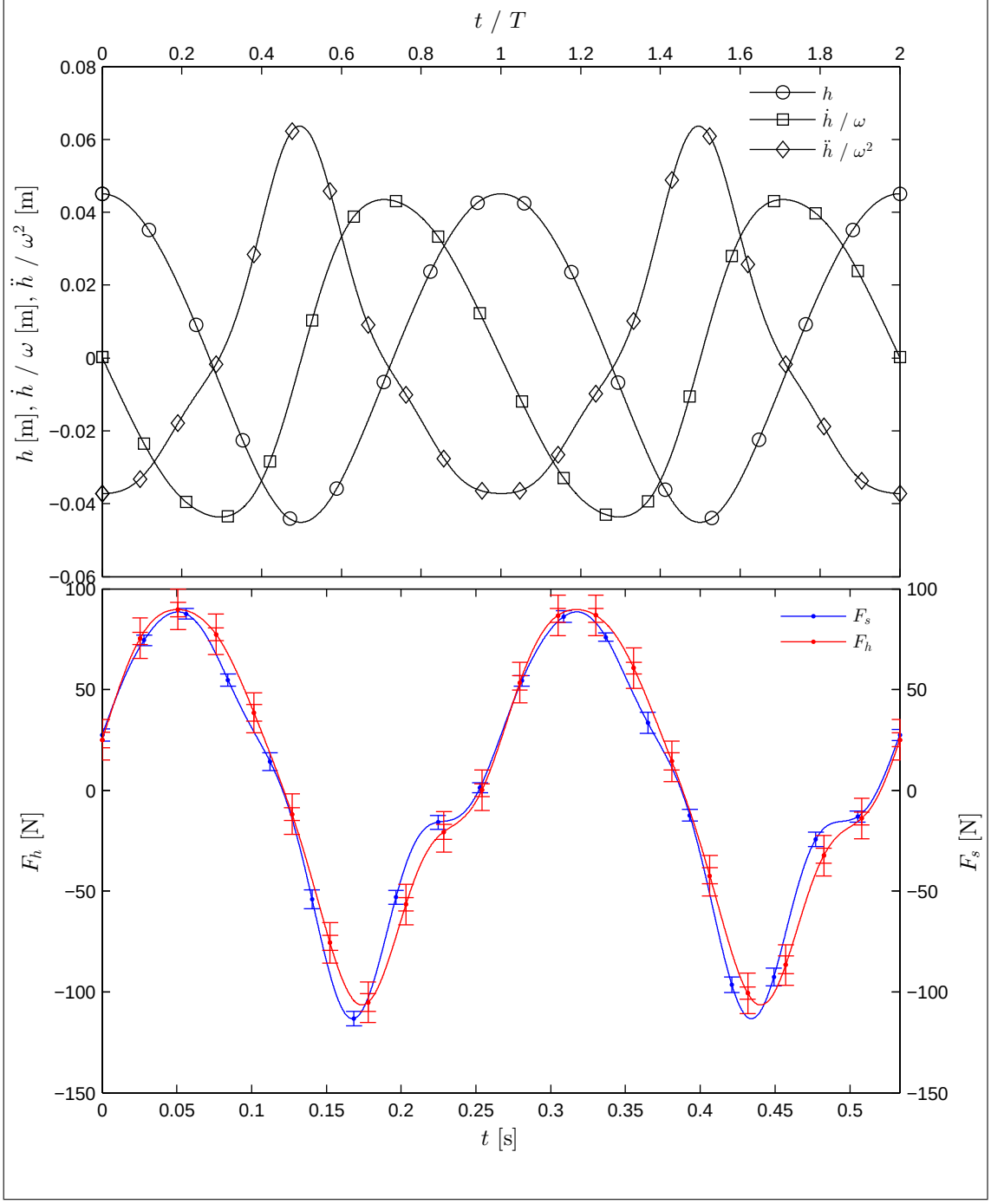

Object: NACA4415		Motion	Water
	$c = 0.060\,\mathrm{m}$ $L = 0.600\,\mathrm{m}$ $\theta = 0°$	$h_0 = 0.045\,\mathrm{m}$ $h^* = 0.75$ $f = 1.61\,\mathrm{Hz}$ $u = 0.52\,\mathrm{m\,s^{-1}}$	$T_w = 9.6\,°\mathrm{C}$ $\rho = 1000\,\mathrm{kg\,m^{-3}}$

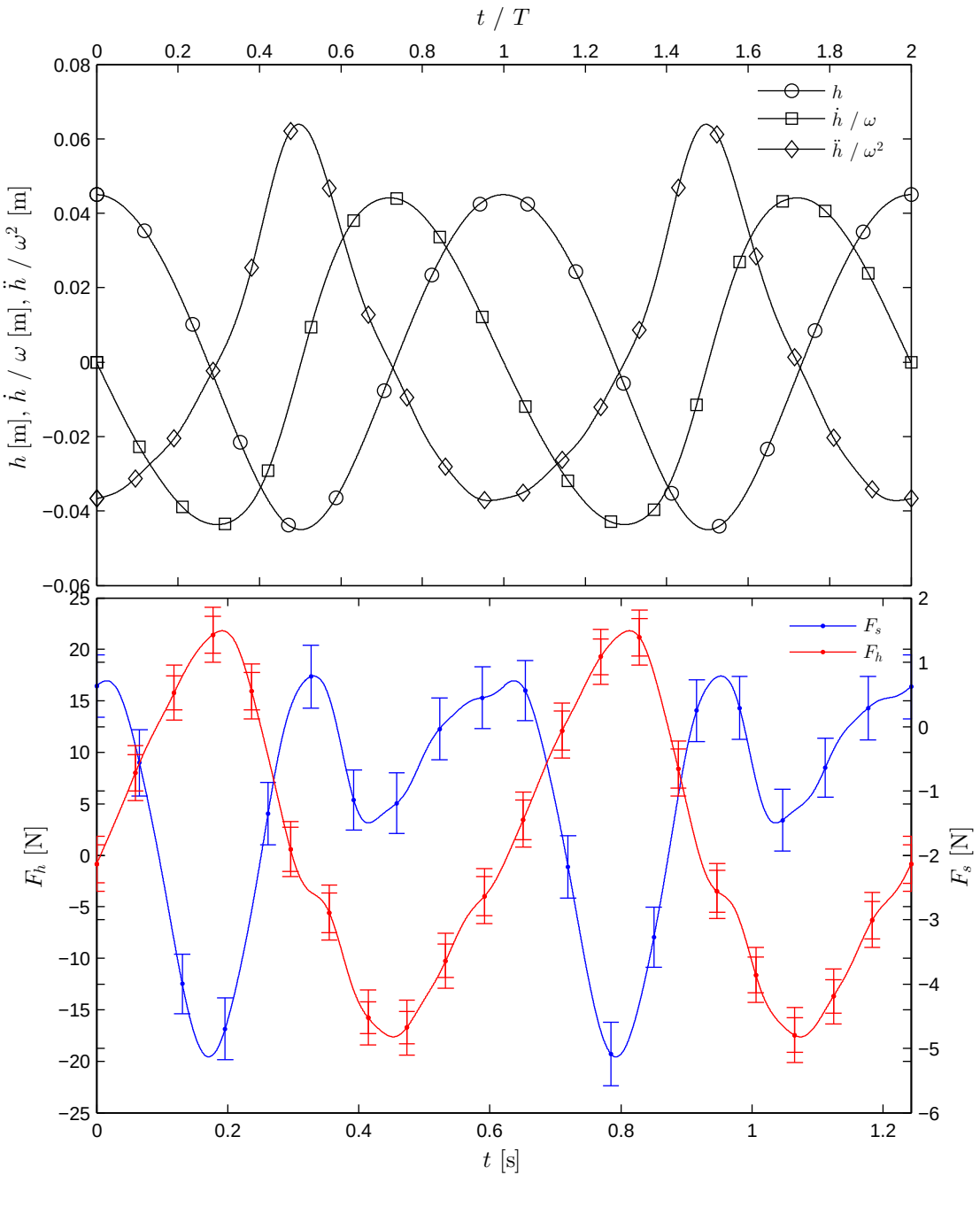

Object: NACA4415		Motion	Water
	$c = 0.060\,\mathrm{m}$ $L = 0.600\,\mathrm{m}$ $\theta = 0°$	$h_0 = 0.045\,\mathrm{m}$ $h^* = 0.75$ $f = 1.61\,\mathrm{Hz}$ $u = 0.99\,\mathrm{m\,s^{-1}}$	$T_w = 9.6\,°\mathrm{C}$ $\rho = 1000\,\mathrm{kg\,m^{-3}}$

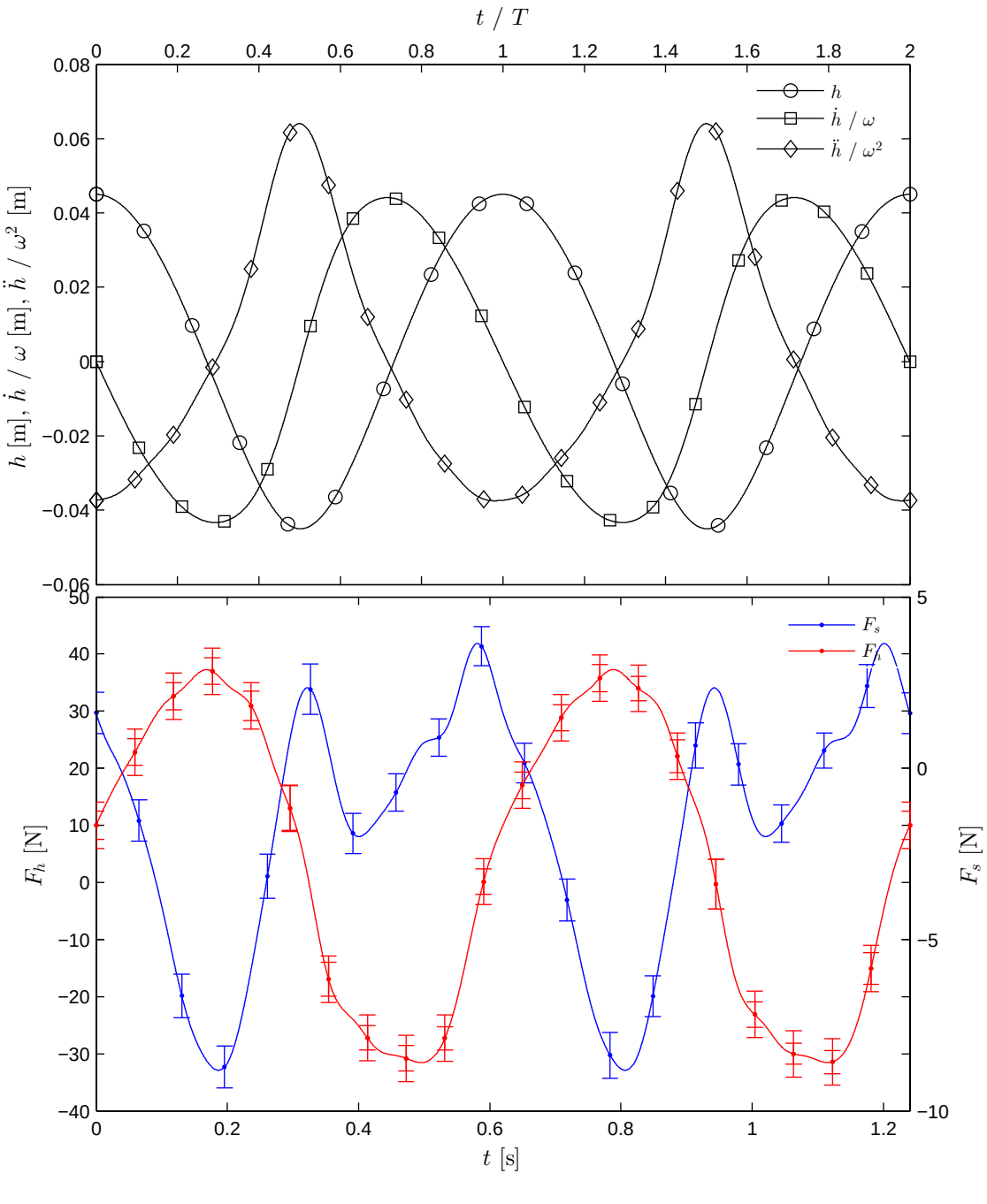

Object: NACA4415		Motion	Water
	$c = 0.060\,\mathrm{m}$ $L = 0.600\,\mathrm{m}$ $\theta = 0°$	$h_0 = 0.045\,\mathrm{m}$ $h^* = 0.75$ $f = 1.53\,\mathrm{Hz}$ $u = 1.49\,\mathrm{m\,s^{-1}}$	$T_w = 9.6\,°\mathrm{C}$ $\rho = 1000\,\mathrm{kg\,m^{-3}}$

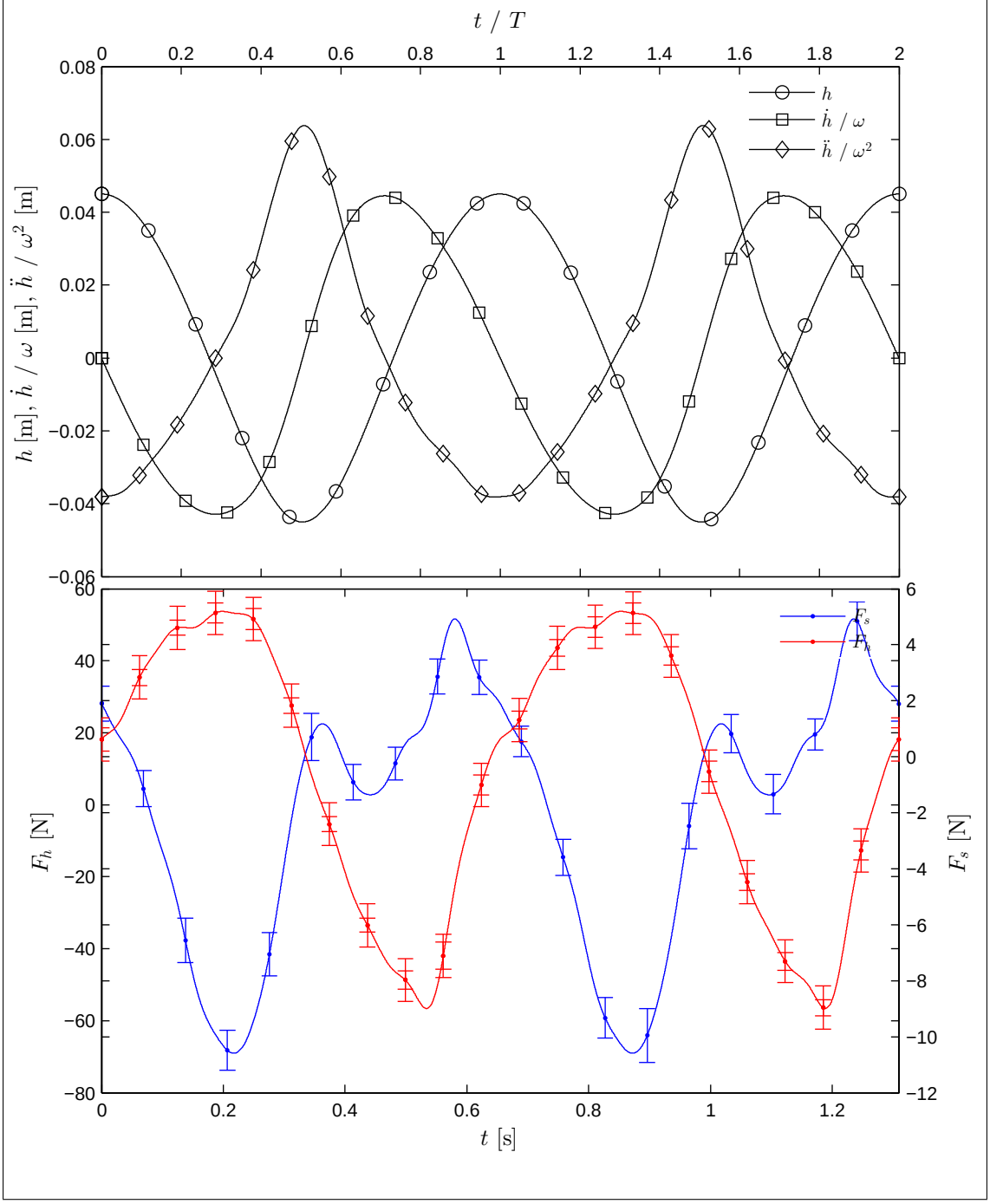

Object: NACA4415		Motion	Water
	$c = 0.060\,\mathrm{m}$ $L = 0.600\,\mathrm{m}$ $\theta = 0°$	$h_0 = 0.045\,\mathrm{m}$ $h^* = 0.75$ $f = 1.50\,\mathrm{Hz}$ $u = 1.97\,\mathrm{m\,s^{-1}}$	$T_w = 9.6\,°\mathrm{C}$ $\rho = 1000\,\mathrm{kg\,m^{-3}}$

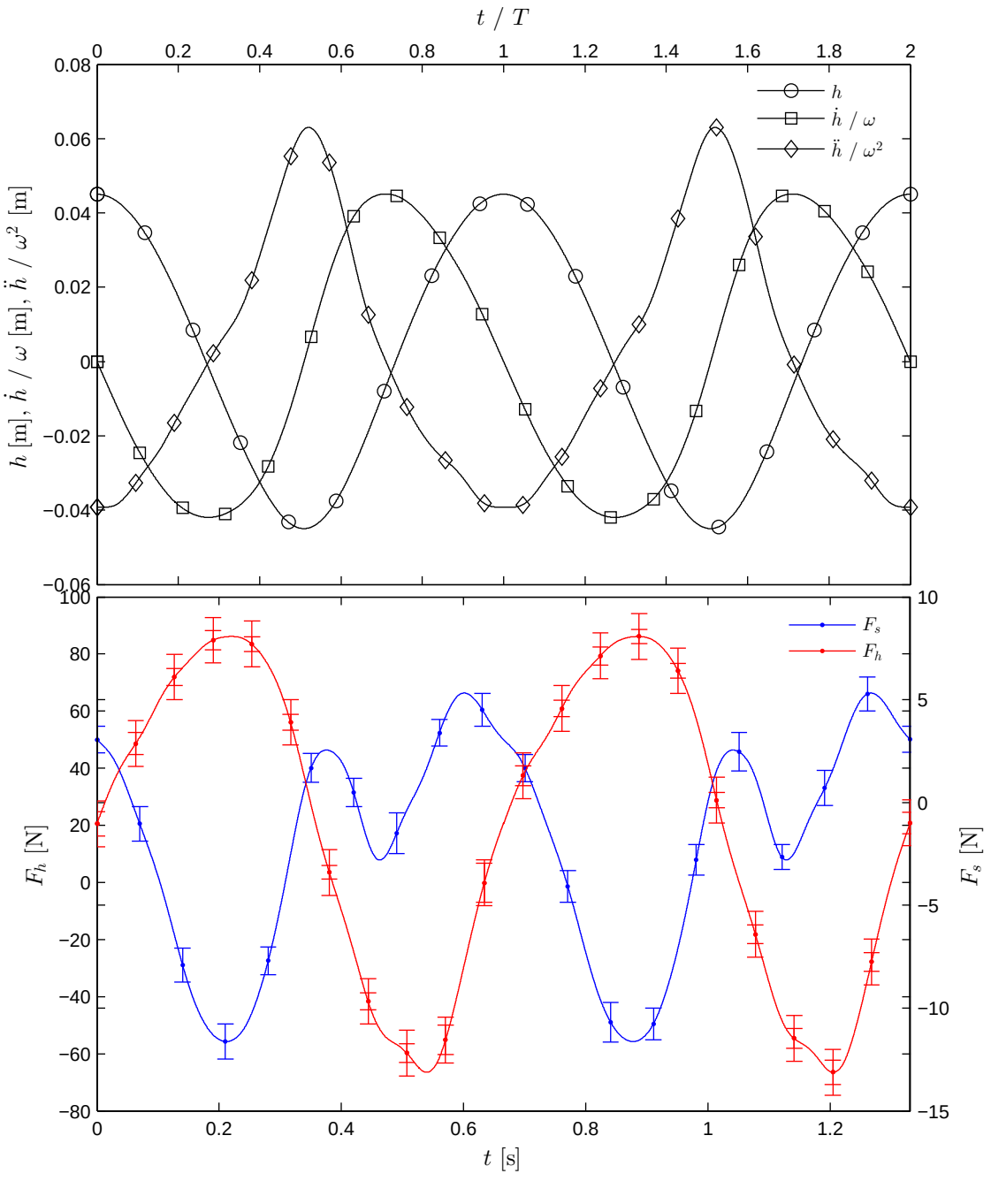

Object: NACA4415		Motion	Water
	$c = 0.060\,\mathrm{m}$ $L = 0.600\,\mathrm{m}$ $\theta = 0°$	$h_0 = 0.045\,\mathrm{m}$ $h^* = 0.75$ $f = 2.16\,\mathrm{Hz}$ $u = 0.52\,\mathrm{m\,s^{-1}}$	$T_w = 9.6\,°\mathrm{C}$ $\rho = 1000\,\mathrm{kg\,m^{-3}}$

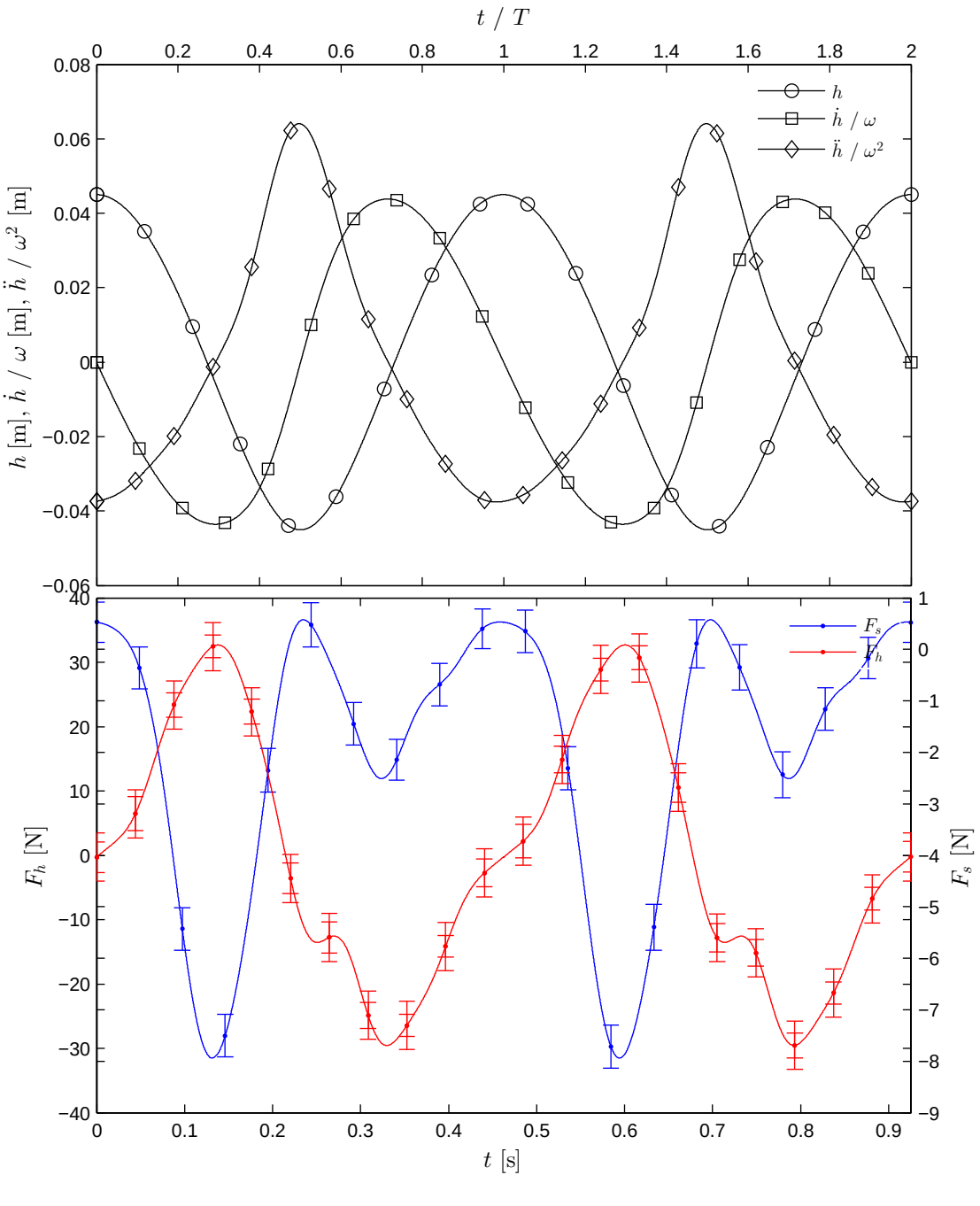

Object: NACA4415		Motion	Water
	$c = 0.060\,\mathrm{m}$ $L = 0.600\,\mathrm{m}$ $\theta = 0°$	$h_0 = 0.045\,\mathrm{m}$ $h^* = 0.75$ $f = 2.10\,\mathrm{Hz}$ $u = 0.99\,\mathrm{m\,s^{-1}}$	$T_w = 9.6\,°\mathrm{C}$ $\rho = 1000\,\mathrm{kg\,m^{-3}}$

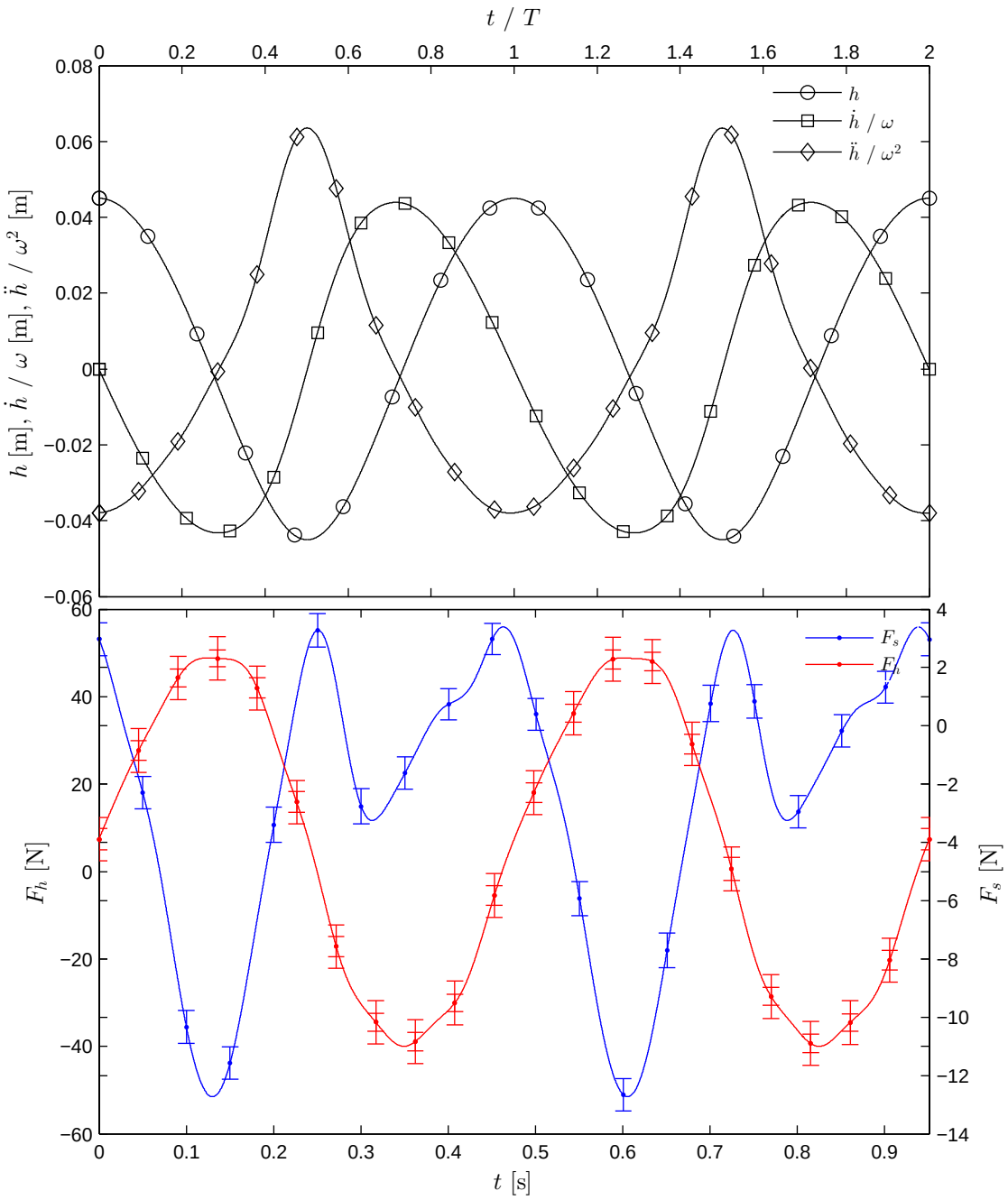

Object: NACA4415		Motion	Water
	$c = 0.060\,\mathrm{m}$ $L = 0.600\,\mathrm{m}$ $\theta = 0°$	$h_0 = 0.045\,\mathrm{m}$ $h^* = 0.75$ $f = 2.03\,\mathrm{Hz}$ $u = 1.49\,\mathrm{m\,s^{-1}}$	$T_w = 9.6\,°\mathrm{C}$ $\rho = 1000\,\mathrm{kg\,m^{-3}}$

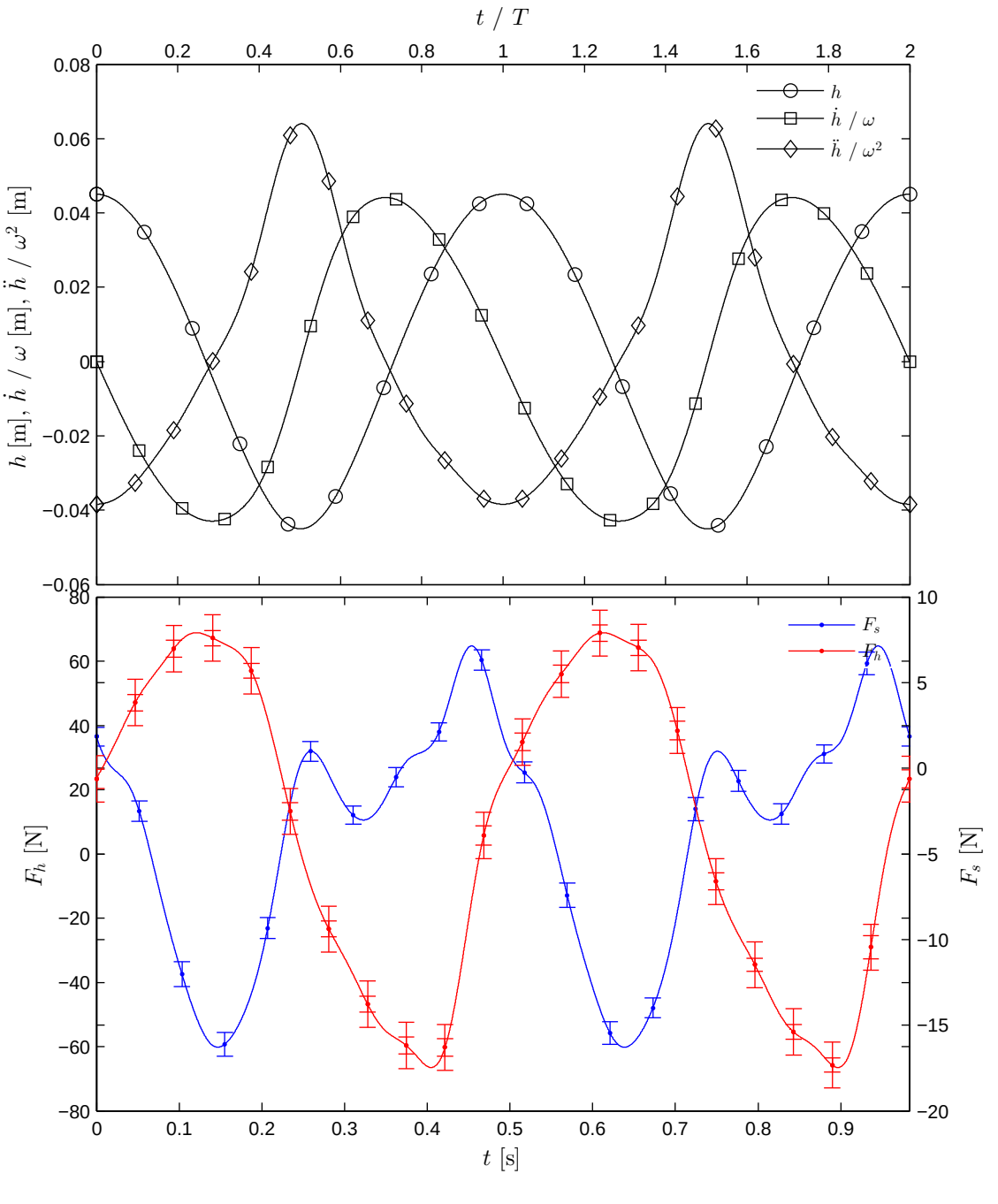

Object: NACA4415		Motion	Water
	$c = 0.060\,\mathrm{m}$ $L = 0.600\,\mathrm{m}$ $\theta = 0°$	$h_0 = 0.045\,\mathrm{m}$ $h^* = 0.75$ $f = 2.01\,\mathrm{Hz}$ $u = 1.97\,\mathrm{m\,s^{-1}}$	$T_w = 9.6\,°\mathrm{C}$ $\rho = 1000\,\mathrm{kg\,m^{-3}}$

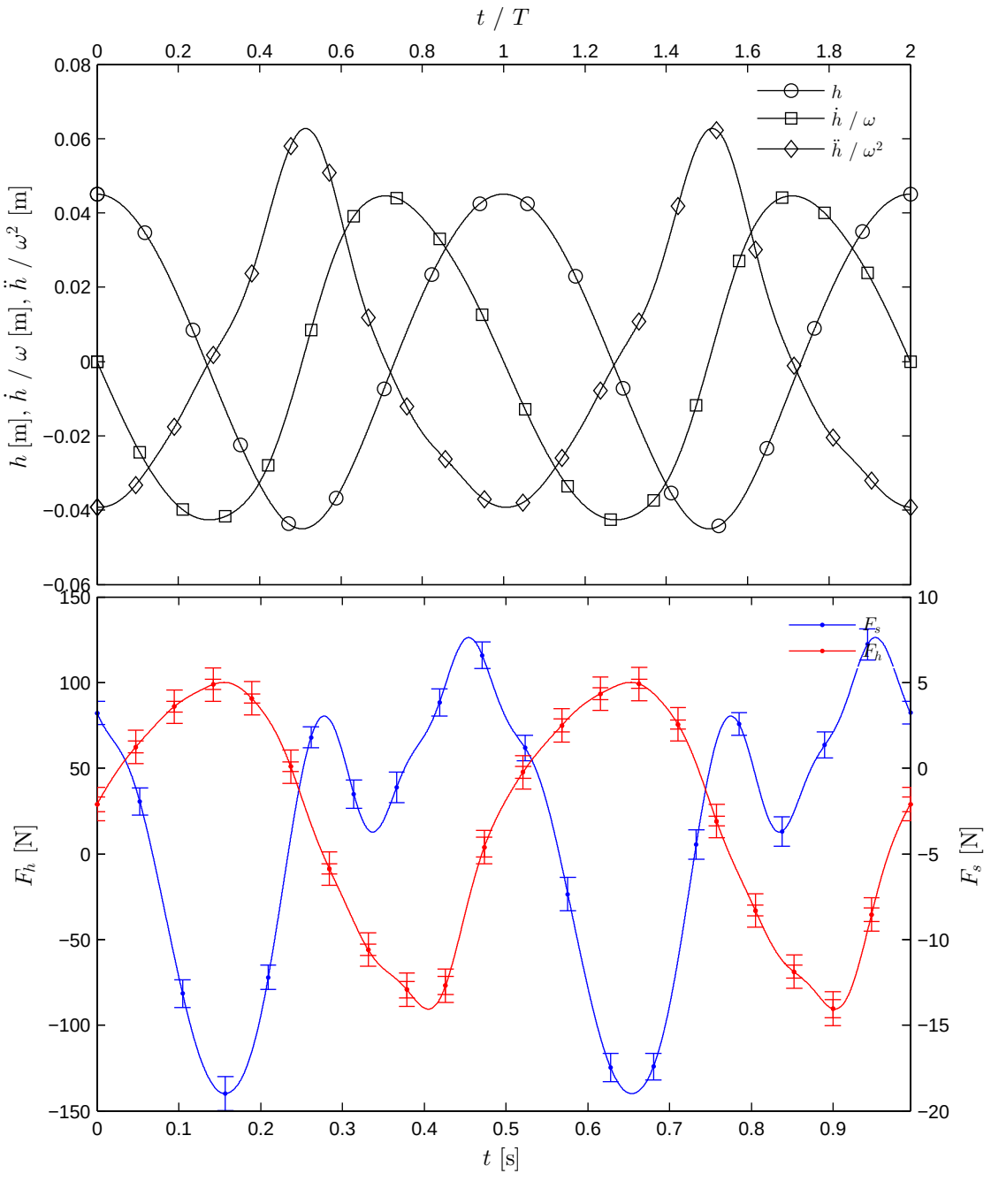

Object: NACA4415		Motion	Water
	$c = 0.060\,\mathrm{m}$ $L = 0.600\,\mathrm{m}$ $\theta = 0°$	$h_0 = 0.045\,\mathrm{m}$ $h^* = 0.75$ $f = 2.70\,\mathrm{Hz}$ $u = 0.52\,\mathrm{m\,s^{-1}}$	$T_w = 9.6\,°\mathrm{C}$ $\rho = 1000\,\mathrm{kg\,m^{-3}}$

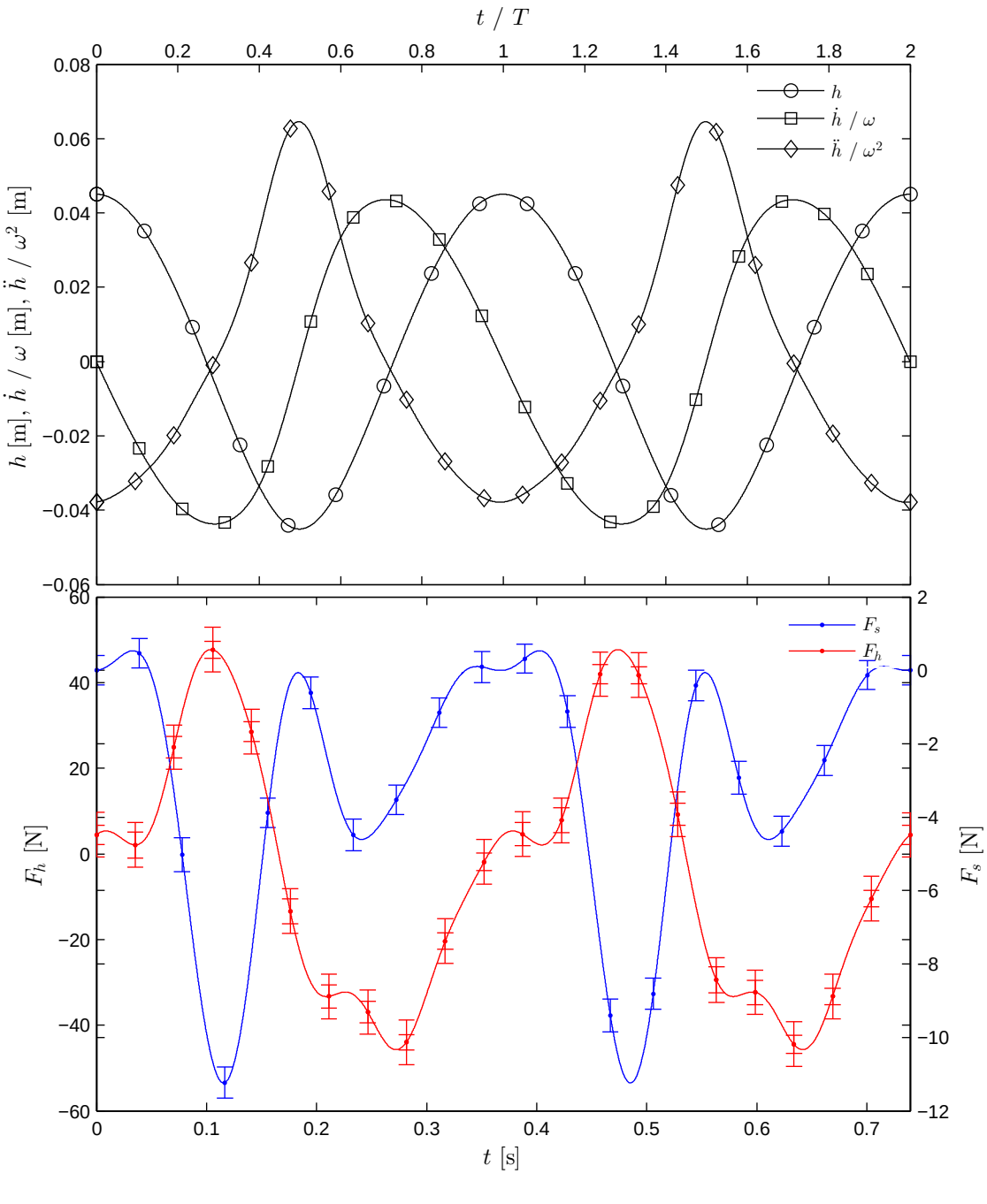

Object: NACA4415		Motion	Water
	$c = 0.060\,\mathrm{m}$ $L = 0.600\,\mathrm{m}$ $\theta = 0°$	$h_0 = 0.045\,\mathrm{m}$ $h^* = 0.75$ $f = 2.64\,\mathrm{Hz}$ $u = 0.99\,\mathrm{m\,s^{-1}}$	$T_w = 9.6\,°\mathrm{C}$ $\rho = 1000\,\mathrm{kg\,m^{-3}}$

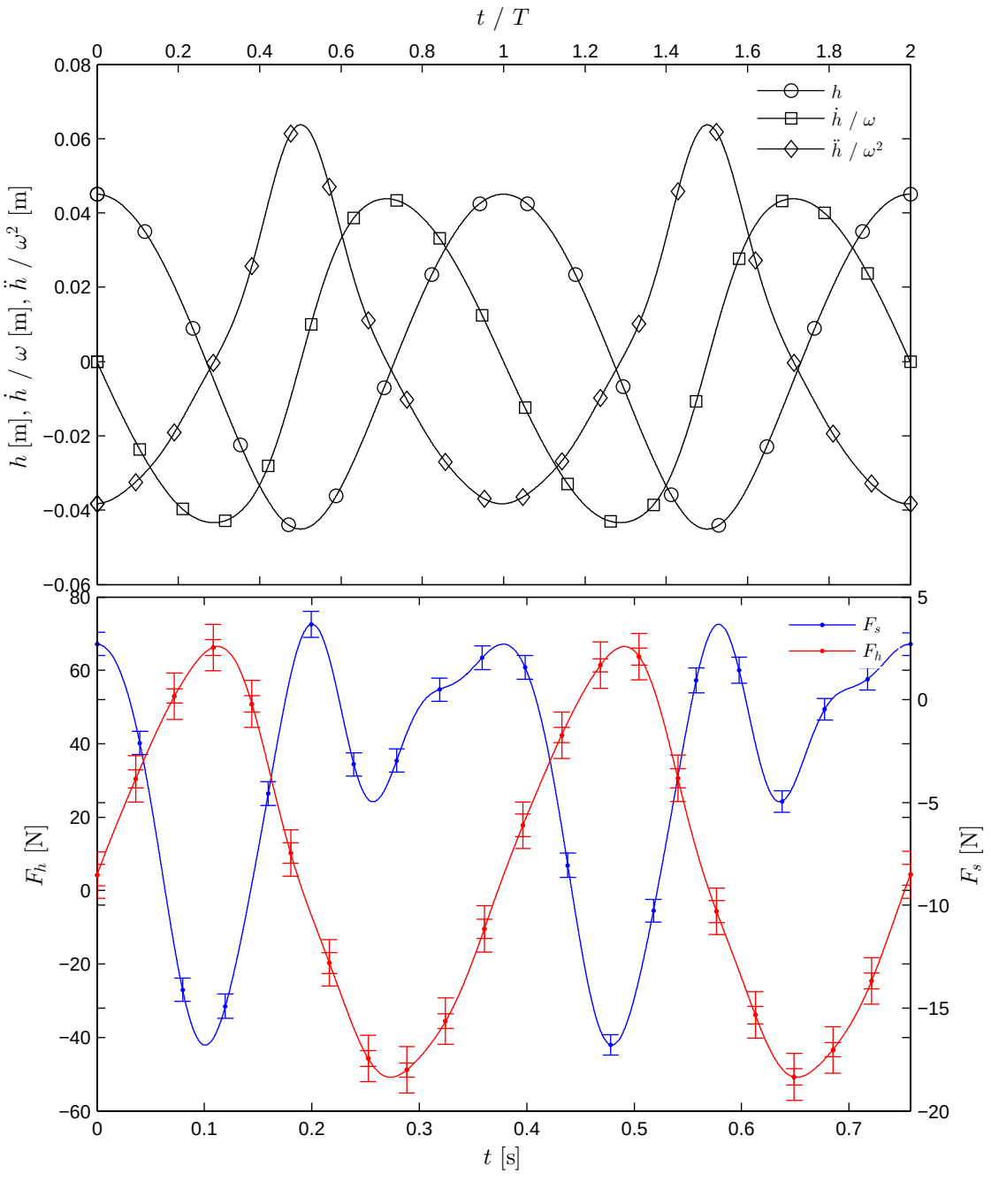

Object: NACA4415		Motion	Water
	$c = 0.060\,\mathrm{m}$ $L = 0.600\,\mathrm{m}$ $\theta = 0°$	$h_0 = 0.045\,\mathrm{m}$ $h^* = 0.75$ $f = 2.56\,\mathrm{Hz}$ $u = 1.49\,\mathrm{m\,s^{-1}}$	$T_w = 9.6\,°\mathrm{C}$ $\rho = 1000\,\mathrm{kg\,m^{-3}}$

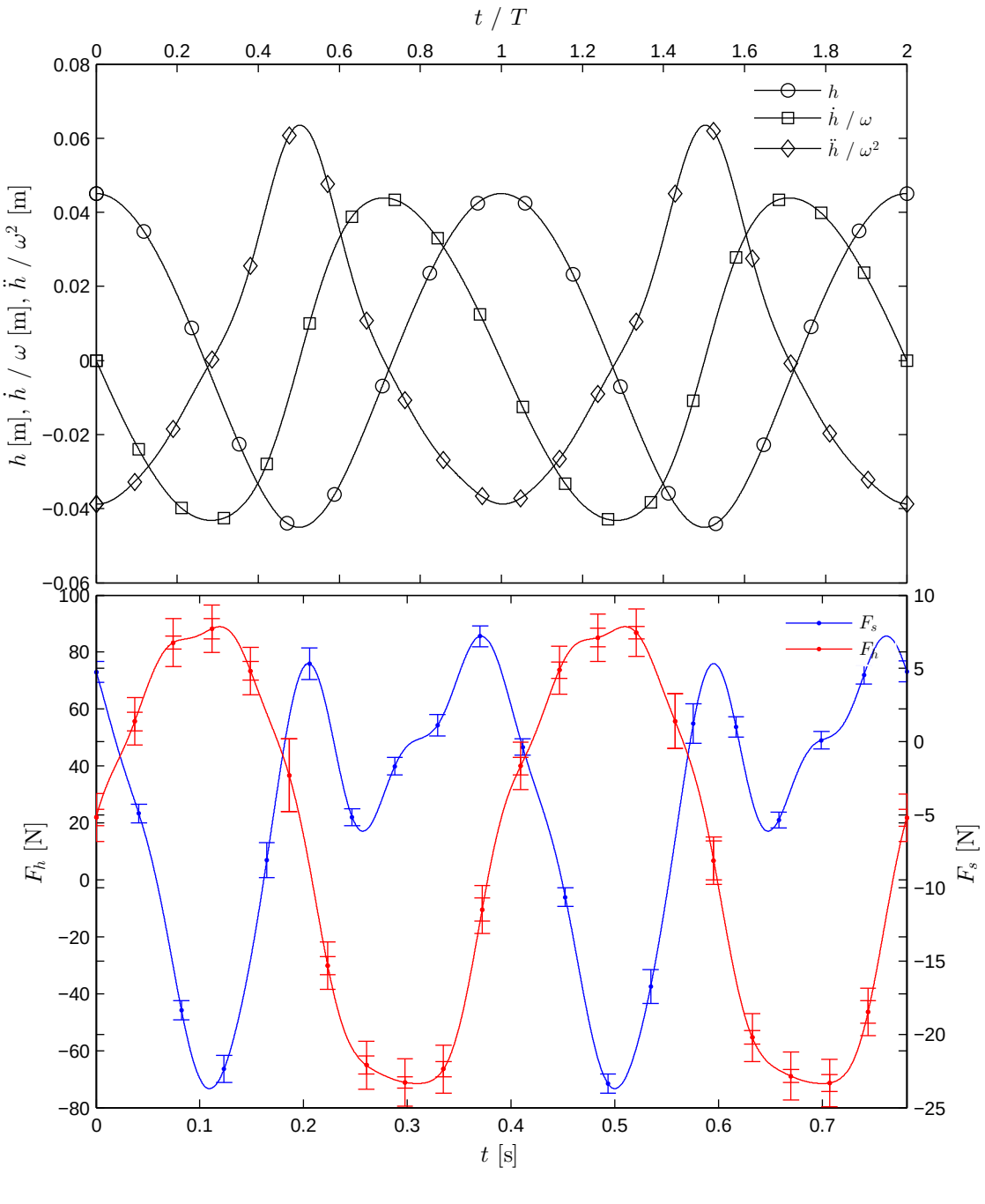

Object: NACA4415		Motion	Water
	$c = 0.060\,\mathrm{m}$ $L = 0.600\,\mathrm{m}$ $\theta = 0°$	$h_0 = 0.045\,\mathrm{m}$ $h^* = 0.75$ $f = 2.51\,\mathrm{Hz}$ $u = 1.97\,\mathrm{m\,s^{-1}}$	$T_w = 9.6\,°\mathrm{C}$ $\rho = 1000\,\mathrm{kg\,m^{-3}}$

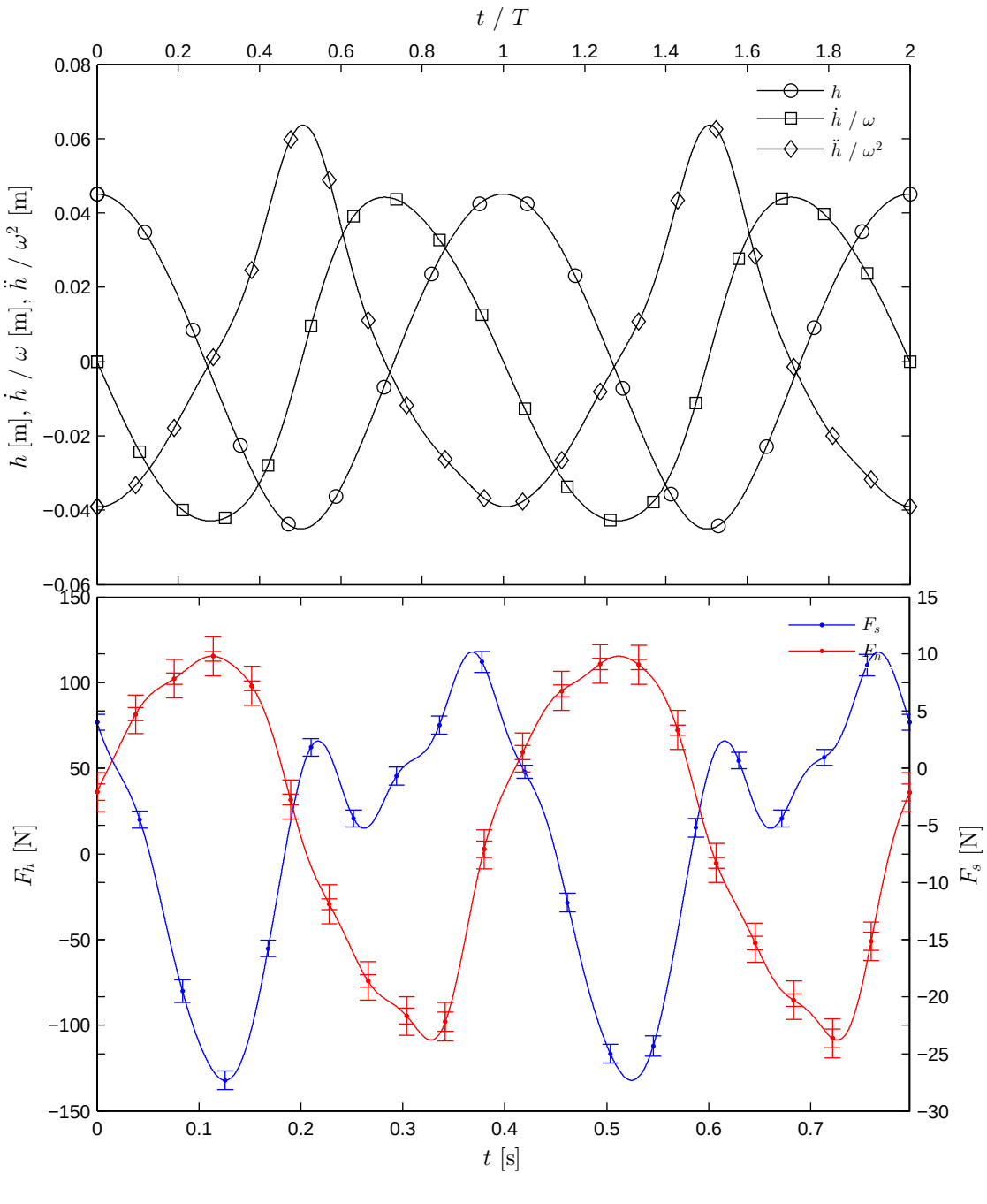

Object: NACA4415		Motion	Water
	$c = 0.060\,\mathrm{m}$ $L = 0.600\,\mathrm{m}$ $\theta = 0°$	$h_0 = 0.045\,\mathrm{m}$ $h^* = 0.75$ $f = 3.22\,\mathrm{Hz}$ $u = 0.52\,\mathrm{m\,s^{-1}}$	$T_w = 9.6\,°\mathrm{C}$ $\rho = 1000\,\mathrm{kg\,m^{-3}}$

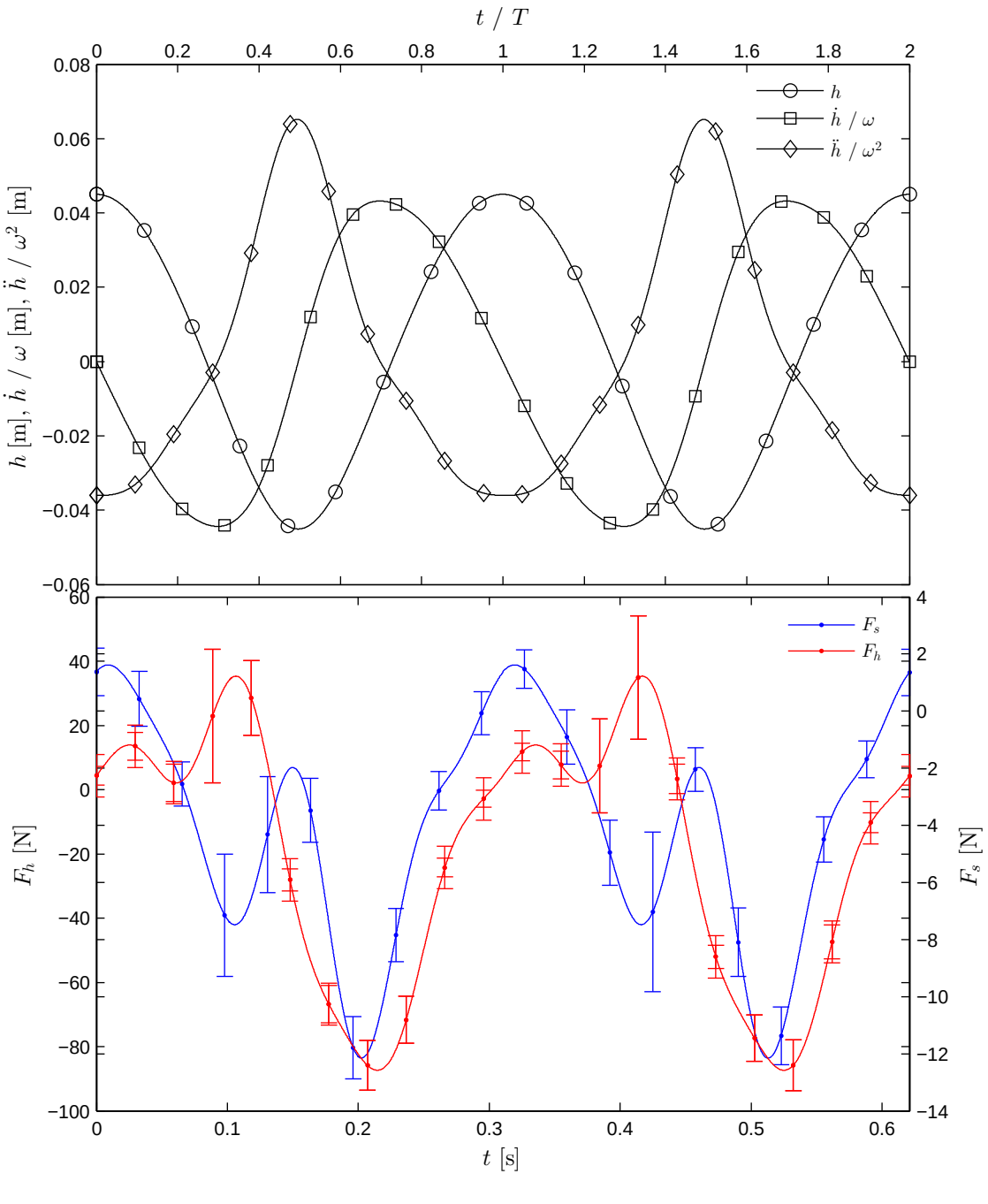

Object: NACA4415		Motion	Water
	$c = 0.060\,\mathrm{m}$ $L = 0.600\,\mathrm{m}$ $\theta = 0°$	$h_0 = 0.045\,\mathrm{m}$ $h^* = 0.75$ $f = 3.14\,\mathrm{Hz}$ $u = 0.99\,\mathrm{m\,s^{-1}}$	$T_w = 9.6\,°\mathrm{C}$ $\rho = 1000\,\mathrm{kg\,m^{-3}}$

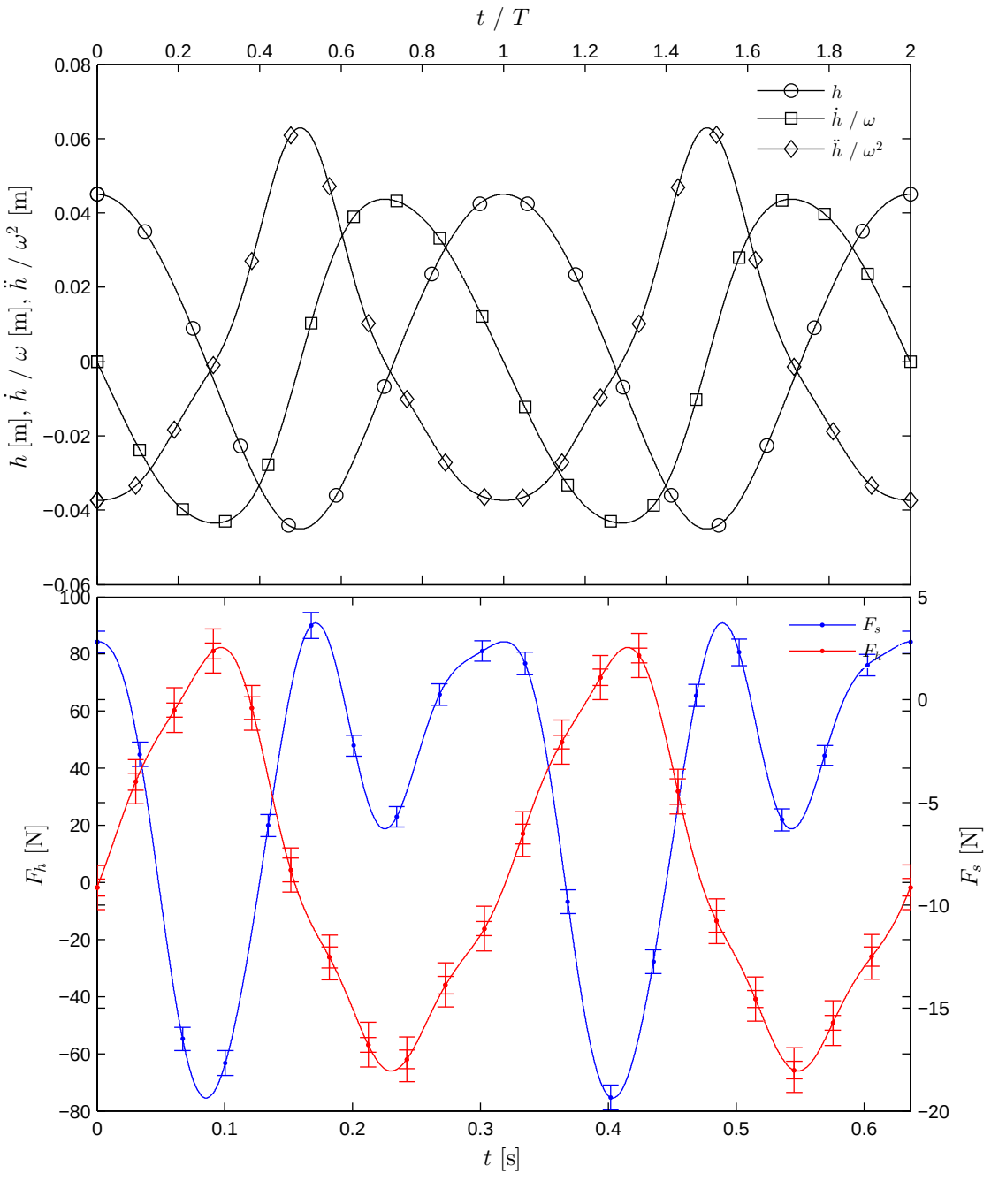

Object: NACA4415		Motion	Water
	$c = 0.060\,\mathrm{m}$ $L = 0.600\,\mathrm{m}$ $\theta = 0°$	$h_0 = 0.045\,\mathrm{m}$ $h^* = 0.75$ $f = 3.04\,\mathrm{Hz}$ $u = 1.49\,\mathrm{m\,s^{-1}}$	$T_w = 9.6\,°\mathrm{C}$ $\rho = 1000\,\mathrm{kg\,m^{-3}}$

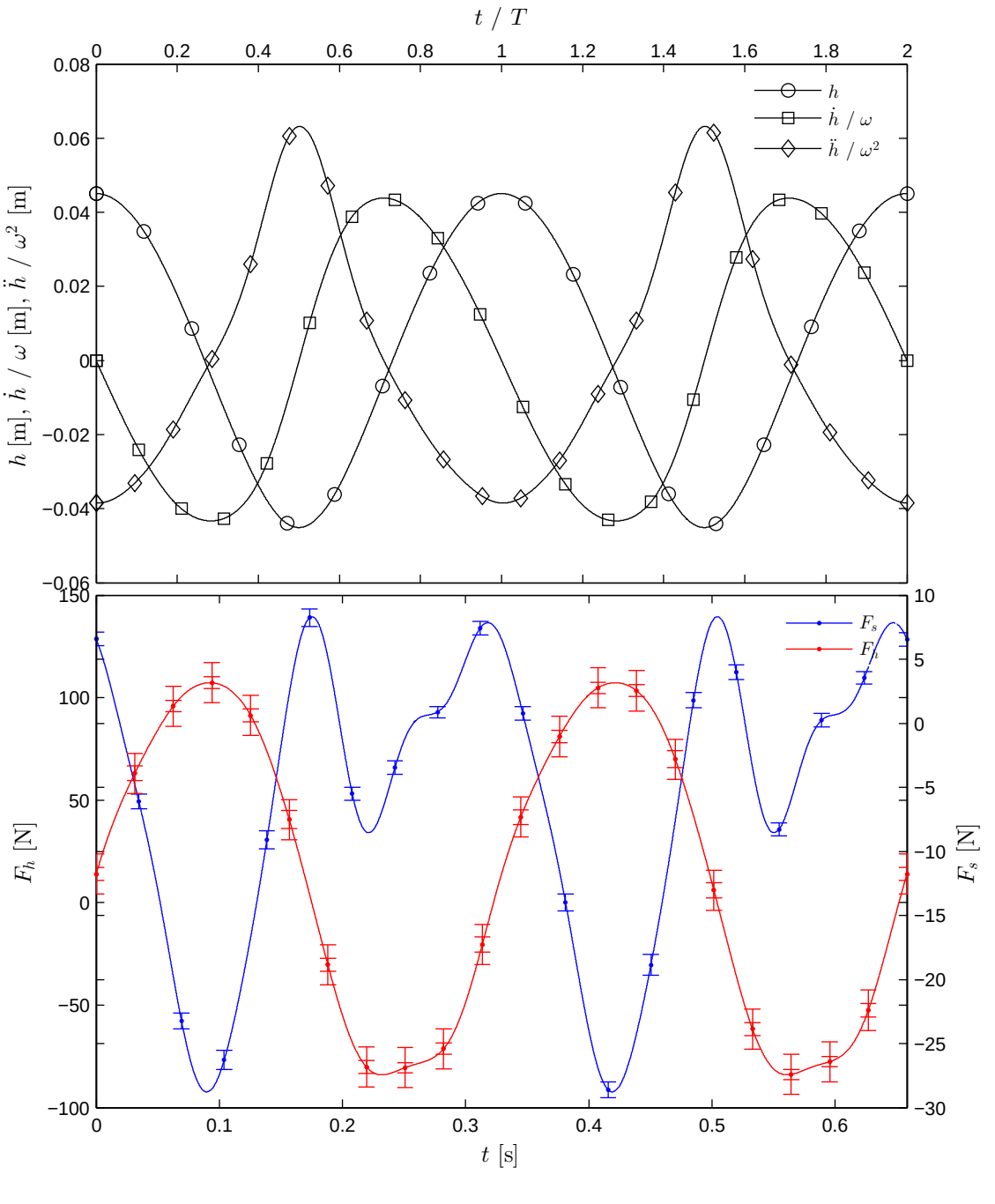

Object: NACA4415		Motion	Water
	$c = 0.060\,\mathrm{m}$ $L = 0.600\,\mathrm{m}$ $\theta = 0°$	$h_0 = 0.045\,\mathrm{m}$ $h^* = 0.75$ $f = 2.97\,\mathrm{Hz}$ $u = 1.97\,\mathrm{m\,s^{-1}}$	$T_w = 9.6\,°\mathrm{C}$ $\rho = 1000\,\mathrm{kg\,m^{-3}}$

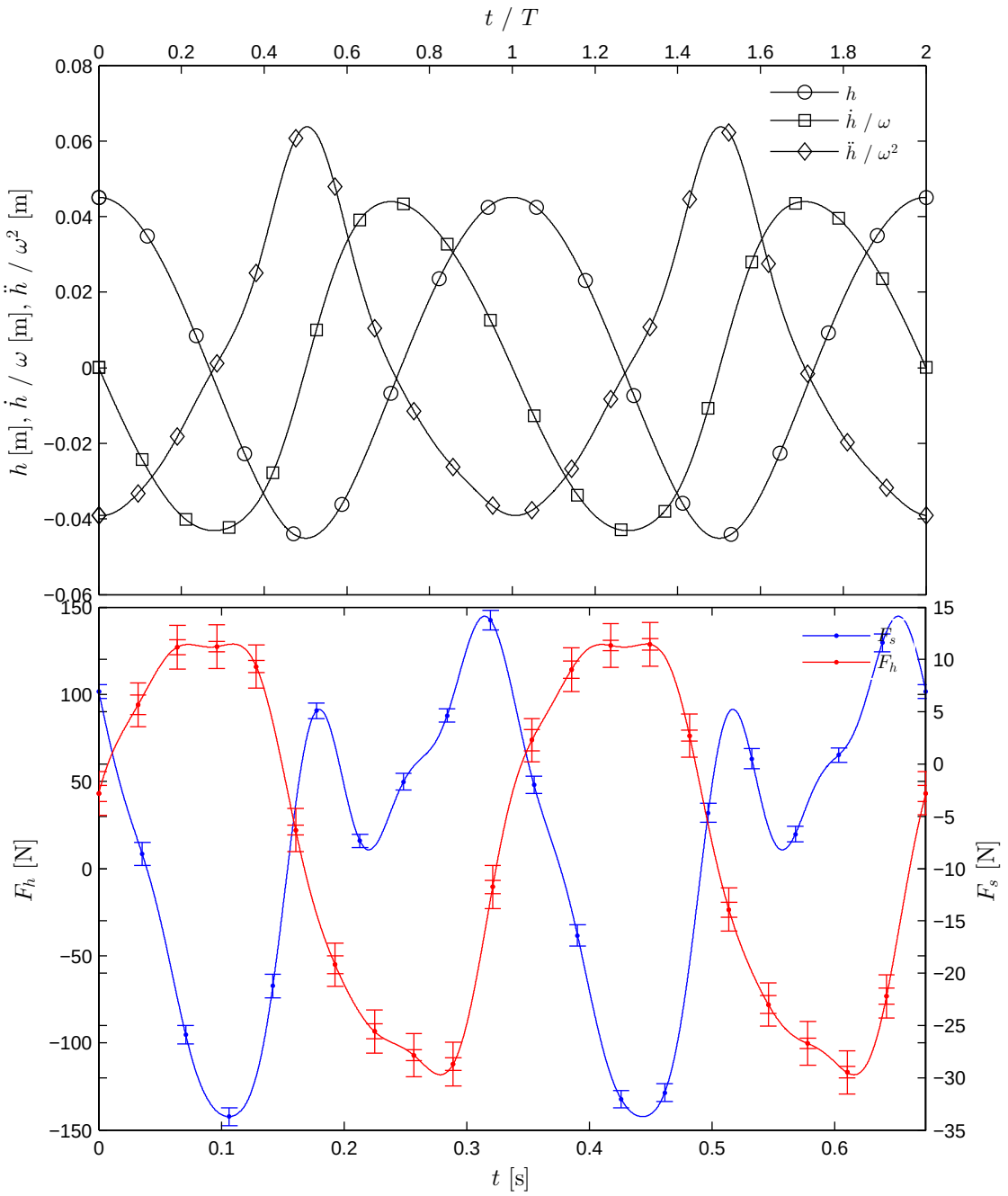

Object: NACA4415		Motion	Water
	$c = 0.060\,\mathrm{m}$ $L = 0.600\,\mathrm{m}$ $\theta = 0°$	$h_0 = 0.045\,\mathrm{m}$ $h^* = 0.75$ $f = 3.69\,\mathrm{Hz}$ $u = 0.52\,\mathrm{m\,s^{-1}}$	$T_w = 9.6\,°\mathrm{C}$ $\rho = 1000\,\mathrm{kg\,m^{-3}}$

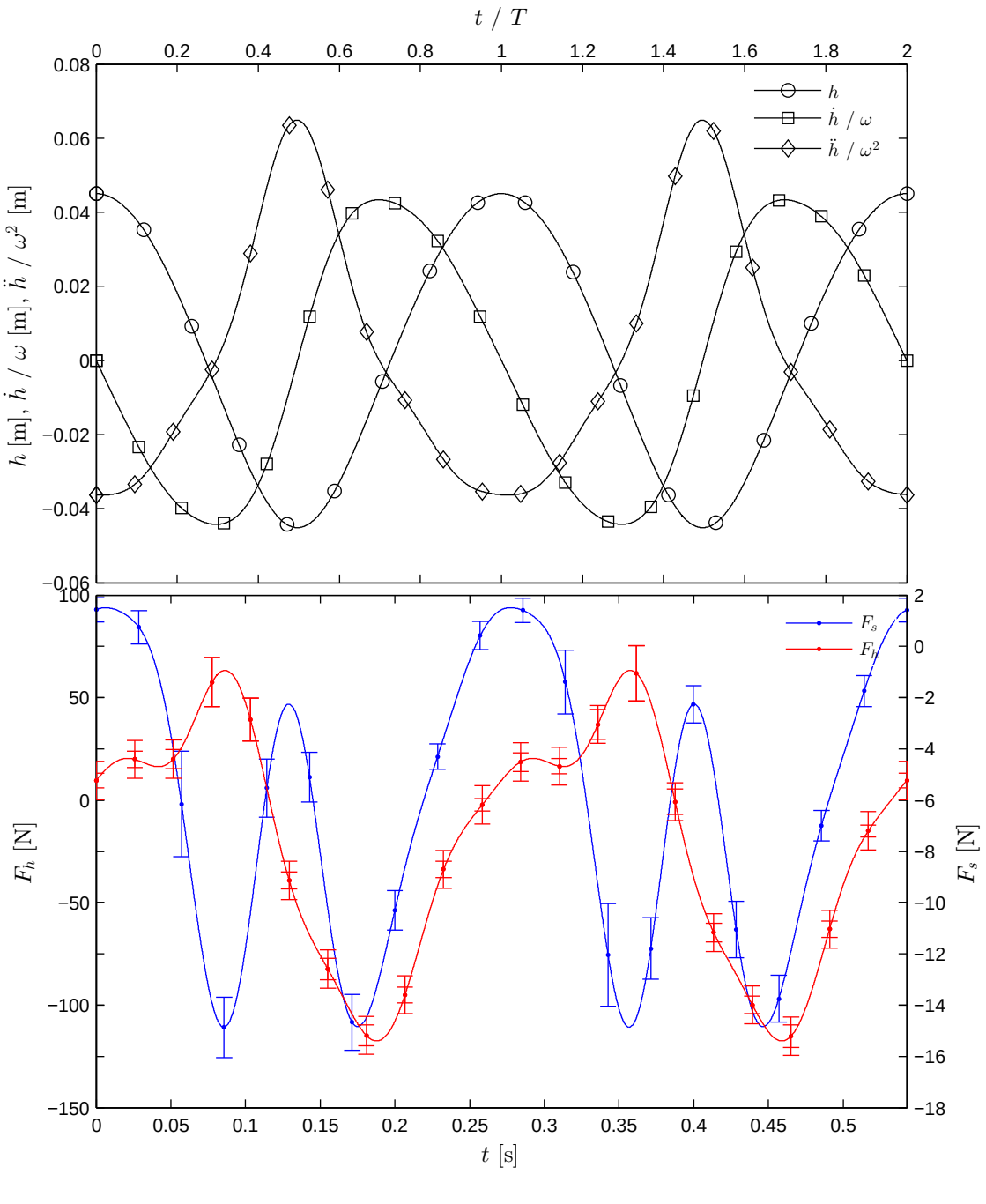

Object: NACA4415		Motion	Water
	$c = 0.060\,\mathrm{m}$ $L = 0.600\,\mathrm{m}$ $\theta = 0°$	$h_0 = 0.045\,\mathrm{m}$ $h^* = 0.75$ $f = 3.64\,\mathrm{Hz}$ $u = 0.99\,\mathrm{m\,s^{-1}}$	$T_w = 9.6\,°\mathrm{C}$ $\rho = 1000\,\mathrm{kg\,m^{-3}}$

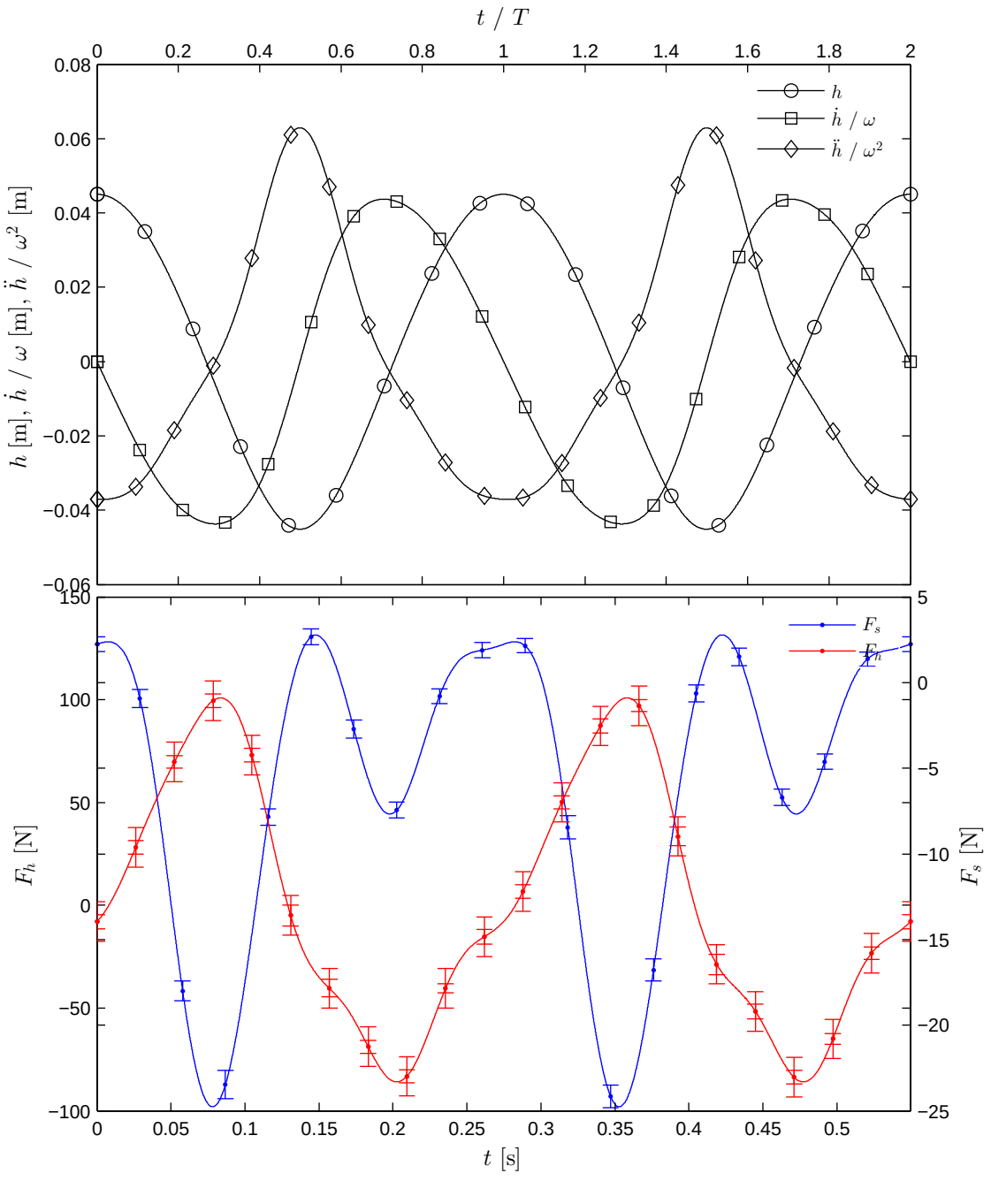

Object: NACA4415		Motion	Water
	$c = 0.060\,\mathrm{m}$ $L = 0.600\,\mathrm{m}$ $\theta = 0°$	$h_0 = 0.045\,\mathrm{m}$ $h^* = 0.75$ $f = 3.56\,\mathrm{Hz}$ $u = 1.49\,\mathrm{m\,s^{-1}}$	$T_w = 9.6\,°\mathrm{C}$ $\rho = 1000\,\mathrm{kg\,m^{-3}}$

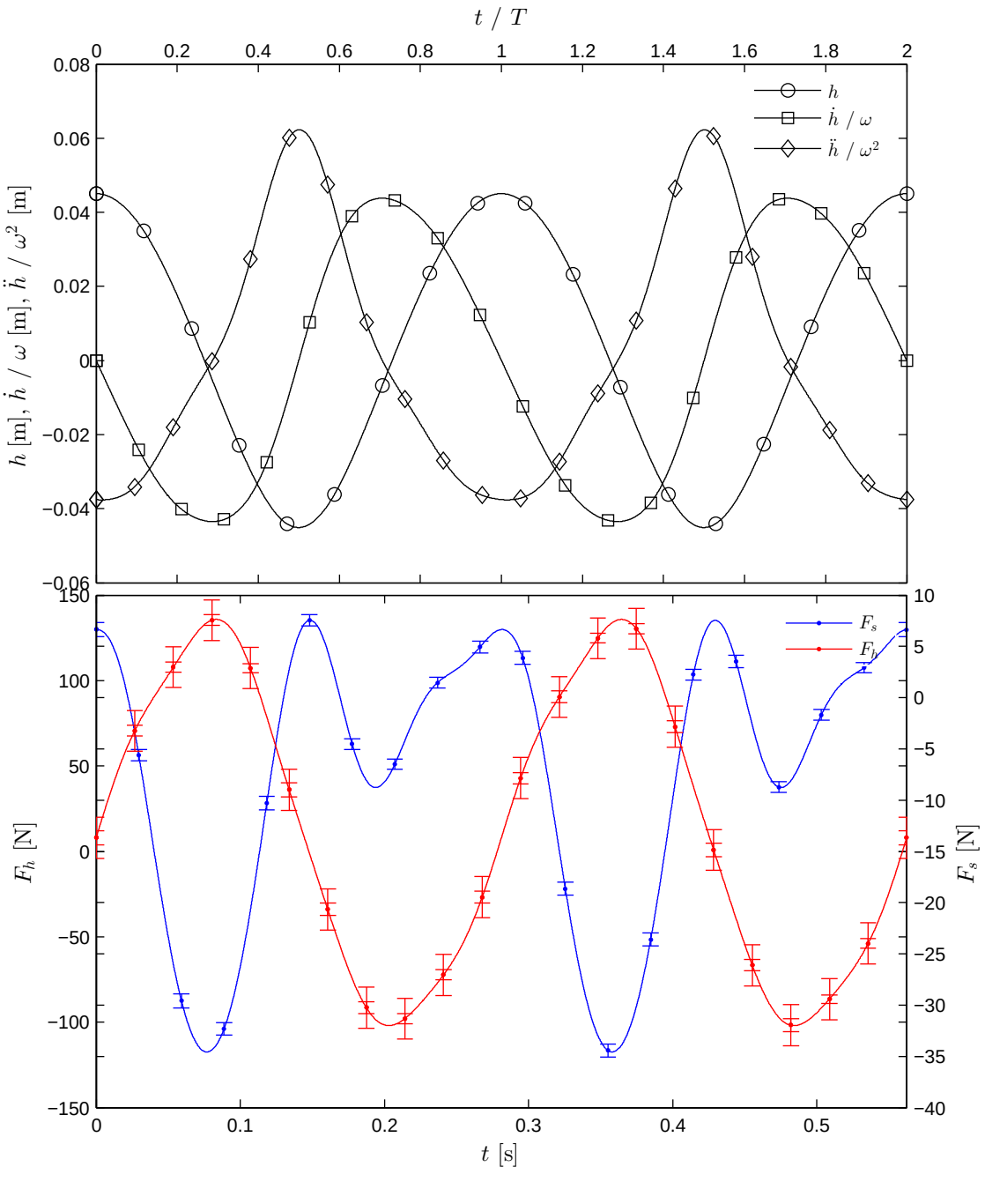

Object: NACA4415		Motion	Water
	$c = 0.060\,\mathrm{m}$ $L = 0.600\,\mathrm{m}$ $\theta = 0°$	$h_0 = 0.045\,\mathrm{m}$ $h^* = 0.75$ $f = 3.47\,\mathrm{Hz}$ $u = 1.97\,\mathrm{m\,s^{-1}}$	$T_w = 9.6\,°\mathrm{C}$ $\rho = 1000\,\mathrm{kg\,m^{-3}}$

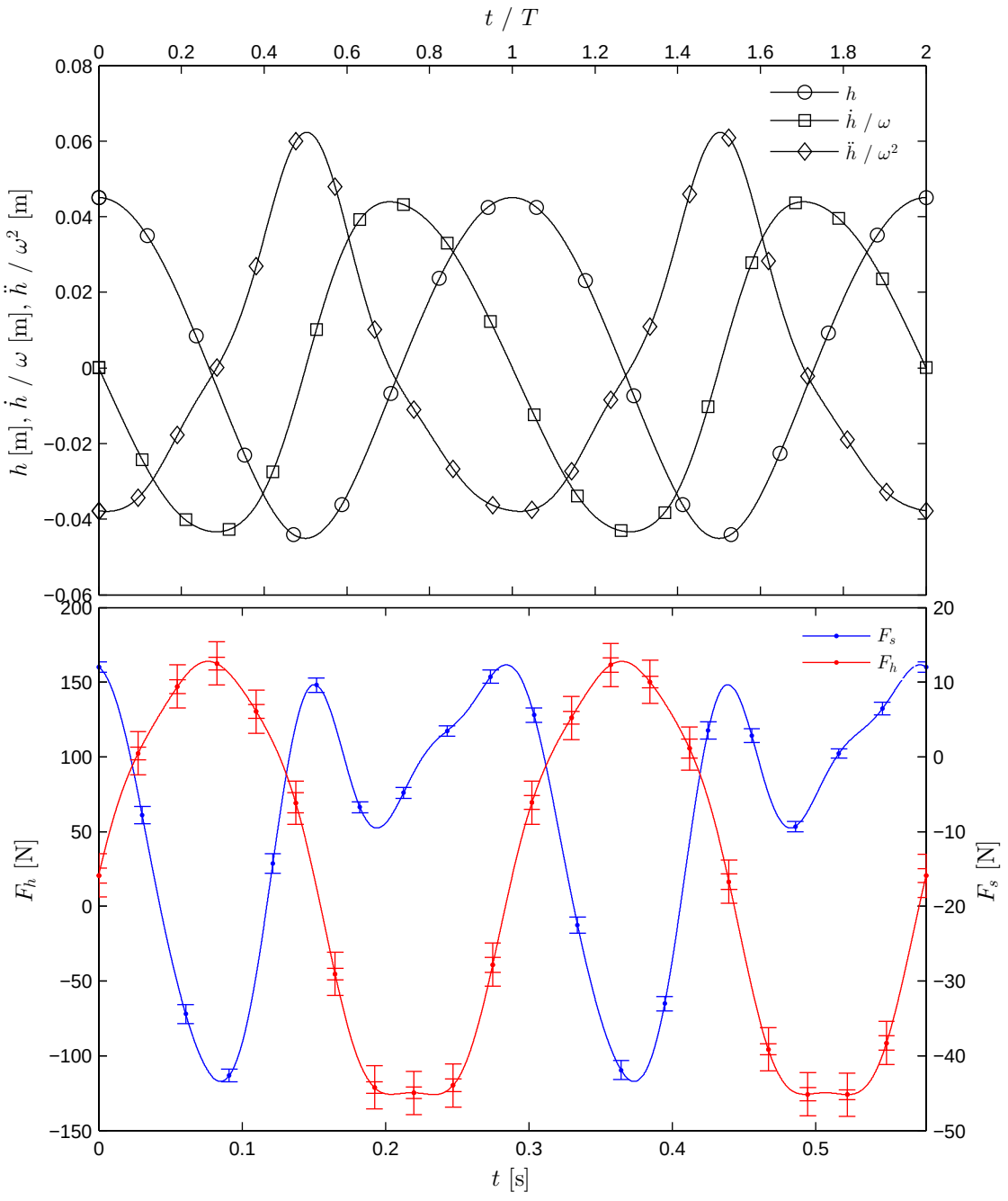

Glossary

Added mass describes an equivilant mass of fluid that is associated with providing a resisting inertial force against an object accelerating through that fluid.

Anguilliform is one of three major categories of swimming motions defined by Breder (1926). Anguilliform is described to be a serpentine motion like that of a flag waving in the wind. An eel is an anguilliform swimmer.

Aquaskipper a commercially available recreational watercraft that utilises a flapping wing propeller designed by Shane Chen for Inventist Inc. in 2003-2004.

Aqueon a flapping wing propeller for divers designed by Calvin Gongwer in the 1960's.

AUV stands for Autonomous Underwater Vehicle.

BBO Equation is an equation named after Alfred Barnard Basset, Joseph Valentin Boussinesq and Carl Wilhelm Oseen which is used to describe the forces on a particle in an unsteady flow at low Reynolds numbers.

BDC stands for Bottom Dead Centre, which refers to position of the experimental equipment where the oscillating object is furthest form the crank shaft, i.e. at the minimum heave position.

Carangiform is one of three major categories of swimming motions defined by Breder (1926). Carangiform swimming is the intermediate motion between the two extremes, Anguilliform and Ostraciiform. Carangiform swimming is displayed by most fish.

Cost of locomotion is a quantity which represents the energy used per unit distance travelled.

Cross-talk is an error included in force measurements due to a load cell having some sensitivity to forces or torques applied along axes other than the intend measurement axis.

Dorsoventral describes an anatomical axis that runs from the back to the belly.

Downforce describes a negative lift force.

Downstroke describes the portion of heaving motion while a negative heave velocity. i.e. as the object travels from the point of minimum heave position to the point of maximum heave position.

Drag is the component of a hydrodynamic force on a structure that is aligned with the flow. A drag force in the downstream direction is positive.

Dynamic error is error introduced into the force measurements due to the limited stiffness of the load cell assembly.

Dynamic uncertainty bounds describe an interval about a mean heave force measurement where the true (free from dynamic error), in-phase heave force is expected to lie. This interval is shown with heave force measurements to express uncertainty caused by compliance of the load cell assembly.

Effective velocity is the relative velocity of an object relative to a fluid. It equivilant to the vector sum of the fluid velocity and the negative object velocity.

Heave is a linear axis aligned with the vertical.

Heave-induced angle of attack is the angle of attack component due to a object having some velocity that is not parallel to the mainstream flow.

In-phase hydrodynamic forces are hydrodynamic forces that are in-phase with the acceleration of an object or a flow. They are proportional to the acceleration and are also referred to as inertial hydrodynamic forces.

Intermittent locomotion is a locomotion style that consists of an alternating series of thrusting and gliding periods.

Jet or jet wake describes an induced flow behind a structure that contains a net increase in streamwise momentum when compared to the mainstream flow. May also be referred to as a thrust wake.

Katzmayr Effect is when a steady foil in an oscillating flow generates thrust. This effect is named after Richard Katzmayr and is also referred to as the Knoller-Betz effect (after Richard Knoller and Albert Betz), or the Schmidt effect (after Wilhelm Schmidt).

Knoller-Betz Effect *see Katzmayr Effect.*

Lift is the component of a hydrodynamic force on a structure that is perpendicular to the flow. When lift a force is orientated parallel to the vertical, the upwards direction describes positive lift.

MAV stands for Micro Air Vehicle.

MOBL stand for Mutiny on the Boundary Layer. *see entry for Mutiny on the Boundary Layer*.

Mutiny on the Boundary Layer a pedal-powered watercraft with flapping wing propulsion designed and built by Parker MacCready during 1984 to 1986.

Neutral wake describes an induced flow behind a structure that has no net increase or decrease of streamwise momentum. This type of wake occurs when the vortices of a von Kármán street fall into a straight line..

Ostraciiform is one of three major categories of swimming motions defined by Breder (1926). Ostraciiform is described as a 'wig-wag motion', like a fan. An ostraciiform swimmer looks like it has a hinged tail that fans rapidly.

Out-of-phase hydrodynamic forces are hydrodynamic forces that are in-phase with velocity of an object or a flow. Drag forces are out-of-phase hydrodynamic forces.

Pitch describes rotation about the sway axis.

Pogo Foil a human-powered watercraft with flapping wing propulsion designed by Parker MacCready in 1989. Also known as the Preposterous Pogo Foil.

Pumpabike a commercially available recreational watercraft that utilises a flapping wing propeller designed by Michael Puzey.

Rajiform is a category of undulating swimming motion. Rajiform swimming is demonstrated well by most stingrays.

RMSE is the Root Mean Square Error.

Root-flapping is a type of flapping motion that comprises a combination of periodic rotary motion about an axis parallel to the surge axis and rotary motion about the pitching axis.

Schmidt effect *see Katzmayr Effect*.

SD is the Standard Deviation of a sample.

Stride length is the distance that a propeller travels forward per cycle. May also be referred to as the wave length of an oscillating propeller.

Surge is a linear axis aligned with the forward/backward directions of a vehicle, orthogonal to both the heave axis and the sway axis.

Sway is a linear axis aligned with the left/right directions of a vehicle, or port/starboard directions of a vessel, orthogonal to the heave and surge axis.

TDC stands for Top Dead Centre, which refers to position of the experimental equipment where the oscillating object is nearest to the crank shaft, i.e. at the maximum heave position.

Thrust Describes a negative drag force. A force that may propeller a vehicle forward.

Thunniform is a sub-group of carangiform swimming named after the tuna (Thunnus). Thunniform swimmers have a relatively stiff body, that only moves a small proportion of their body length. They also typically have a high-aspect ratio lunate tail.

Trampofoil a recreational watercraft that utilises a flapping wing propeller designed by Alexander Sahlin in 1998.

Upstroke describes the portion of heaving motion while a positive heave velocity. i.e. as the object travels from the point of maximum heave position to the point of minimum heave position.

Virtual mass describes an equivilant mass of fluid that is associated with providing a resisting inertial force against an object submerged in an acceleration flow.

VIV stands for Vortex-Induced Vibration, which describes motion induced by an external flow around a body.

von Kármán street is a wake pattern sometimes found behind a blunt body that comprises a series of vortices of alternating signs. This vortex pattern is named after Theodore von Kármán.

Wasserläufer a watercraft that utilises a flapping wing propulsion designed by Julius Schuck. Schuck demonstrated his invention on German television in 1953.

WDPS stands for Wave Devouring Propulsion System. This propulsion system was used to propel the Suntory Mermaid II.

Index